Xiao-Yu Yang *Editor*

Photo-Driven Seawater Splitting for Hydrogen Production

Springer

Photo-Driven Seawater Splitting for Hydrogen Production

Xiao-Yu Yang
Editor

Photo-Driven Seawater Splitting for Hydrogen Production

Springer

Editor
Xiao-Yu Yang
State Key Laboratory of Advanced
Technology for Materials Synthesis
and Processing
Wuhan University of Technology
Wuhan, China

Foshan Xianhu Laboratory of the Advanced
Energy Science and Technology
Guangdong Laboratory
Xianhu Hydrogen Valley
Foshan, China

Laoshan Laboratory
Qingdao, Shandong, China

ISBN 978-981-99-0509-6 ISBN 978-981-99-0510-2 (eBook)
https://doi.org/10.1007/978-981-99-0510-2

This Springer imprint is published by the registered company Springer Nature Singapore Pte Ltd.
The registered company address is: 152 Beach Road, #21-01/04 Gateway East, Singapore 189721, Singapore

Acknowledgement

This work was supported by the National Key Research and Development Program of China (2022YFB3805600, 2022YFB3805604),Program Fund of Non-Metallic Excellence and Innovation Center for Building Materials (2023TDA1-1),National Natural Science Foundation of China (22293020, 52201286, 52002414), Program for Changjiang Scholars and Innovative Research Team in University (IRT_15R52), PCSIRT, Guangdong Basic and Applied Basic Research Foundation (2022A1515011905, 2021A1515111131, 2019A1515110590), Jilin Province Science and Technology Development Plan (20220101248JC).

Contents

About the Editor

Prof. Dr. Xiao-Yu Yang received his Ph.D. from Jilin University (co-educated at FUNDP of Belgium). After Postdoctoral Fellowship at the FUNDP, he worked as "Chargé de Recherches" at the FNRS in Belgium. He is currently working as Full Professor at Wuhan University of Technology and Visiting Professor at Harvard University. His research is aimed at hierarchical assembly techniques, novel porous systems and hierarchical structured materials for the applications in energy, environment, catalysis and bioengineering.

Electrocatalytic Seawater Splitting

Jie Ying, Jiang-Bo Chen, Yuan Dong, and Xiao-Yu Yang

Abstract Seawater electrolysis opens a new opportunity to lower the cost of hydrogen production from current water electrolysis technologies. However, due to the different characters such as the existence of chloride ions and insoluble solids in seawater, the electrocatalysts are suffering from severely degraded activity and stability. This chapter focuses on recent developments made in the field of electrocatalytic seawater splitting. Firstly, the basic principles and features of electrocatalytic seawater splitting are discussed. Secondly, recently reported materials used for the both hydrogen evolution reaction (HER) and oxygen evolution reaction (OER) for electrocatalytic seawater splitting are described. Then, the current industrialization development of seawater electrolysis is introduced. Finally, several challenges and future perspectives in this field are summarized.

1 Preface

The energy crisis has become a critical issue worldwide. Fossil fuels, which comprise over 80% of the energy consumed by humans, are the cause of both the environmental crisis and climate alterations that significantly endanger the World. These problems in conjunction with non-renewability have urged mankind to seek alternative energy sources. One possible substitute for fossil materials is hydrogen (H_2), a clean and renewable energy source. This gas has a notably high energy density (for H_2 120 MJ kg^{-1} and for gasoline 44 MJ kg^{-1}) and when combusted it only produces water [1–8]. Thus, H_2 has been considered an excellent alternative energy

J. Ying (✉)
School of Chemical Engineering and Technology, Sun Yat-Sen University, Zhuhai 519082, China
e-mail: yingj5@mail.sysu.edu.cn

J.-B. Chen · Y. Dong · X.-Y. Yang
State Key Laboratory of Advanced Technology for Materials Synthesis and Processing (Wuhan), Foshan Xianhu Laboratory of the Advanced Energy Science and Technology Guangdong Laboratory (Xianhu Hydrogen Valley, Foshan), Laoshan Laboratory (168 Wenhai Middle Rd, Jimo District, Qingdao), Wuhan University of Technology, Wuhan 430070, China

X.-Y. Yang (ed.), *Photo-Driven Seawater Splitting for Hydrogen Production*,
https://doi.org/10.1007/978-981-99-0510-2_1

source to solve energy problems and mitigate the environmental crisis, which has aroused wide-spread attentions. Unfortunately, in the current industrial environment, H_2 is primarily generated from fossil fuels by reforming and cracking under critical conditions, but more advanced processes to produce this gas starting with nonhydrocarbon feedstocks are under current scrutiny. One approach, which has become "hot" research topic, is to produce H_2 through electrolytic water splitting [9–13].

A variety of technologies have been pursued to discover efficient large-scale and cost affective routes for electrolytic production of H_2, such as those employing mature liquid-electrolyte alkaline, high-temperature solid oxide, emerging proton exchange membrane (PEM), and anion exchange membrane (AEM) processes [14–16]. The two common components of all these electrolysis systems are a cathode where the H_2 evolution reaction (HER) occurs and an anode where the O_2 evolution reaction (OER) takes place [17].

Another much less-discussed requirement of water electrolysis is the availability of water sources. While readily used in laboratory studies, freshwater becomes a limiting issue when water splitting systems are deployed on a large scale in hot arid areas around the World. Because seawater (SW) in oceans represents 96.5% of the water reserves on the planet, it is an almost unlimited source [17, 18]. In addition to having direct access to SW, coastal arid zones of the Earth possess the prime ingredient needed for the electrolytic splitting process in the form of an ample supply of solar energy for photovoltaic electricity and the potential for generating electricity by using wind power. Therefore, the preferred locations for electrolytic production of H_2 are either those that receive high levels of solar irradiation like desert regions in the Middle East, South Africa, and the west coasts of the Americas, Australia, and China, or areas that have access to coastal wind power like the north coast of Europe, south coast of Alaska, southern tips of South America and Greenland, and small coastal areas of Australia and Asia. Deep-red areas in the World map shown in Fig. 1 are hyper-arid or arid coastal zones where direct SW electrolysis would be ideal for solar H_2 production [9].

While available in large quantities, SW is not suitable for use in current electrolysis systems because it contains electrochemically active anions that could interfere with the water splitting processes. Table 1 shows typical components of ocean SW, along with their redox reactions and corresponding electrochemical standard potentials (E_0) under alkaline and acidic conditions. Although the composition of SW throughout the world varies, the average concentrations of all ions present are ca. 3.5 wt% and SW has a pH in the 8.9–12 range. The dominant ions in SW are Na^+ and Cl^-, which is why an aqueous 0.5 M NaCl solution can be employed as a surrogate. In contrast to other ions, bromide and chloride are the most likely to undergo anodic oxidation that competes with the anodic oxidation of water. The presence of low concentrations of Br^- is the reason why its oxidation is typically neglected in SW electrolysis studies [19].

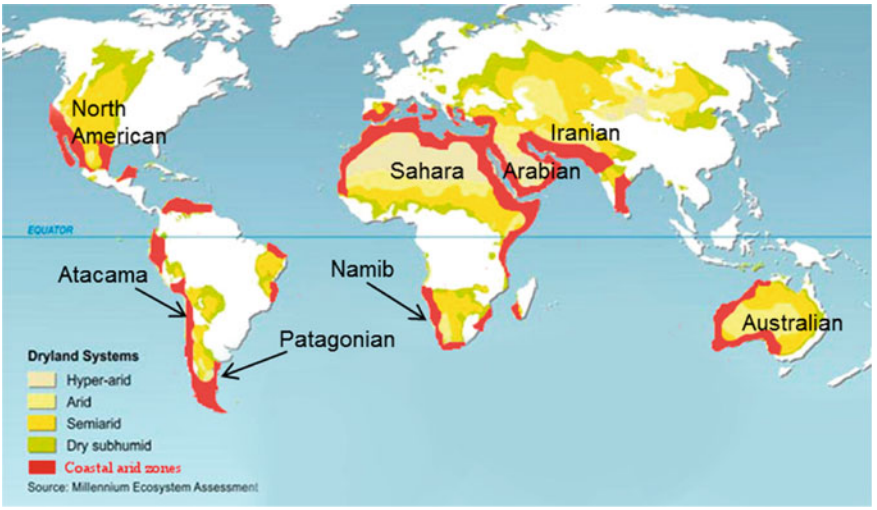

Fig. 1 Dry areas of the earth with coastal arid zones highlighted in red

2 Principles of Electrocatalytic SW Splitting

2.1 The Basic Principles for Electrocatalytic SW Splitting

Water splitting consists of two half-reactions, including HER, which occurs at the cathode, and OER, which occurs at the anode. Cathodic water splitting is a two-electron proton transfer process. In contrast, OER is a multi-electron transfer process, involving the loss of four protons per evolved oxygen molecule, which proceeds via several intermediates [17, 20, 21]. Depending on the nature of the electrolyte used, electrocatalytic water splitting follows different redox pathways that lead to O_2 evolution at the anode and H_2 evolution at the cathode [18]. In acidic electrolytes, the overall redox reactions taking place are those shown in Eqs. (1) and (2), while the redox reactions given in Eqs. (3) and (4) occur in alkaline electrolytes. In neutral electrolytes, the redox reactions involved are considered to be the same as those in basic electrolytes [22–24]. However, in SW the anodic process generating O_2 takes place in the competition with Cl^- oxidation (see below) [9].

$$\text{Cathode: } 2H^+(aq) + 2e^- \rightarrow H_2(g) \tag{1}$$

$$\text{Anode: } H_2O(l) \rightarrow 2H^+(aq) + O_2(g) \tag{2}$$

$$\text{Cathode: } 2H_2O(l) + 2e^- \rightarrow 2OH^-(aq) + H_2(g) \tag{3}$$

Table 1 Components of SW along with their concentrations and corresponding redox reactions and electrochemical standard potential E_0 at different pH values

	Conc	Conc		E^0		E^0
Species	[mol $kg_{H2O}{}^{-1}$]	[g $kg_{H2O}{}^{-1}$]	reaction Red. $\rightleftharpoons$ Ox at pH 0	[V_{SHE}]	Reaction Red. $\rightleftharpoons$ Ox at pH 14	[V_{SHE}]
H_2O			$2H_2O \rightleftharpoons O_2 + 4H^+ + 4e^-$	1.229	$H_2 + 2OH^- \rightleftharpoons 2H_2O + 2e^-$	−0.828
Cl^-	0.56576	20.0579	$2Cl^- \rightleftharpoons Cl_2(g) + 2e^-$ $Cl^- + 4H_2O \rightleftharpoons ClO_4{}^- + 8H^+ + 8e^-$ $Cl^- + 3H_2O \rightleftharpoons ClO_3{}^- + 6H^+ + 6e^-$ $Cl^- + H_2O \rightleftharpoons HClO + H^+ + 2e^-$ $Cl^- + 2H_2O \rightleftharpoons HClO_2 + 3H^+ + 4e^-$	1.358 1.389 1.451 1.482 1.570	$Cl^- + 4OH^- \rightleftharpoons ClO_2{}^- + 2H_2O + 4e^-$ $Cl^- + 2OH^- \rightleftharpoons ClO^- + H_2O + 2e^-$ $2Cl^- \rightleftharpoons Cl_2(g) + 2e^-$	0.76 0.89 1.358
$SO_4{}^{2-}$	0.02927	2.8117	$S_2O_6{}^{2-} + 2H_2O \rightleftharpoons 2SO_4{}^{2-} + 4H^+ + 2e^-$ $H_2SO3 + H_2O \rightleftharpoons SO_4{}^{2-} + 4H^+ + 2e^-$ $2SO_4{}^{2-} \rightleftharpoons S_2O_8{}^{2-} + 2e^-$	−0.22 0.172 2.010	$SO_3{}^{2-} + 2OH^- \rightleftharpoons SO_4{}^{2-} + H_2O + 2e^-$ $2SO_4{}^{2-} \rightleftharpoons S_2O_8{}^{2-} + 2e^-$	−0.93 2.010
Br^-	0.00087	0.0695	$2Br^- \rightleftharpoons Br_2(aq) + 2e^-$ $Br^- + H_2O \rightleftharpoons HBrO + H^+ + 2e^-$ $Br^- + 3H_2O \rightleftharpoons BrO_3{}^- + 6H^+ + 6e^-$	1.0873 1.331 1.423	$Br^- + 6OH^- \rightleftharpoons BrO_3{}^- + 3H_2O + 6e^-$ $Br^- + 2OH^- \rightleftharpoons BrO^- + H_2O + 2e^-$ $2Br^- \rightleftharpoons Br_2(aq) + 2e^-$	0.61 0.761 1.0873
F^-	0.00007	0.0013	$2F^- \rightleftharpoons F_2 + 2e^-$	2.866	$2F^- \rightleftharpoons F_2 + 2e^-$	2.866
Na^+	0.48616	11.1768	$Na \rightleftharpoons Na^+ + e^-$	−2.71	$Na \rightleftharpoons Na^+ + e^-$	−2.71
Mg^{2+}	0.05475	1.3307	$Mg \rightleftharpoons Mg^{2+} + 2e^-$	−2.372	$Mg \rightleftharpoons Mg^{2+} + 2e$	−2.372
Ca^{2+}	0.01065	0.4268	$Ca \rightleftharpoons Ca^{2+} + 2e^-$	−2.868	$Ca \rightleftharpoons Ca^{2+} + 2e^-$	−2.868
K^+	0.01058	0.4137	$K \rightleftharpoons K^+ + e^-$	−2.931	$K \rightleftharpoons K^+ + e^-$	−2.931
Sr^{2+}	0.00009	0.0079	$Sr \rightleftharpoons Sr^{2+} + 2e^-$	−2.899	$Sr \rightleftharpoons Sr^{2+} + 2e^-$	−2.899
$B(OH)_3$	0.00033	0.0204	$B(OH)_3 + 7H^+ + 8e^- \rightleftharpoons BH_4{}^- + 3H_2O$	−0.481		
$B(OH)_4{}^-$	0.00010	0.0079				
CO_2*	0.00001	0.0004				
HCO^{3-}	0.00183	0.1117				
$CO_3{}^{2-}$	0.00027	0.0162				
OH^-	0.00001	0.0002			$4OH^- \rightleftharpoons O_2 + 2H_2O + 4e^-$	0.401
H^+			$H_2 \rightleftharpoons 2H^+ + 2e^-$	0.0		

$$\text{Anode: } 2OH^{-}(aq) \rightarrow H_2O(1) + 2e^{-} + 1/2O_2(g) \quad (4)$$

Under standard conditions, the n Gibbs free energy value (ΔG) of water electrolysis is 237.2 kJ mol^{-1}, which corresponds to an equilibrium potential of 1.23 V. However, in practice, water electrolysis is carried out at voltages greater than 1.23 V due to kinetic barriers and poor energy utilization at both cathodes and anodes. Although water electrolysis occurs readily on catalytic electrode materials, it is hindered by several factors such as high activation energies, low ion and gas diffusion rates, and issues of particular relevance to electrolytic systems, including electrolyte concentrations, resistances of conducting wires and electrodes, and blockage of electrolyte diffusion. All of these problems lead to either large overpotentials or poor durability. Therefore, one of the main challenges facing the design of water electrolysis systems is the availability of scalable electrocatalysts that have excellent efficiencies and durability.

With respect to the HER, critical problems affecting the efficiency of direct SW splitting are the presence of various dissolved cations (Mg^{2+}, Na^{+}, $Ca^{2+,}$ etc.), bacteria/microbes, and small particles, all of which can poison or accelerate the degradation of the electrode/catalyst of the cathode. Specifically, as the current for electrolysis increases, the pH near the electrode surface dramatically increases, resulting in precipitation of $Mg(OH)_2$ and $Ca(OH)_2$ that obstruct the cathode active sites. Mayrhofer et al. demonstrated that even at medium current densities, the pH values near the electrode surface increased by 5–9 pH units compared to 4–10 pH values for lightly buffered media (Fig. 2). To overcome these dramatic pH fluctuations, buffers or additives are typically used to control pH. In addition, other strategies can be employed to overcome this problem like those that involve the use of suitable electrolysis cells and membranes that separate precipitated $Mg(OH)_2$ and $Ca(OH)_2$ [17].

Competing cathodic reactions of dissolved metal ions (such as Cu^{2+}, $Na^{+,}$ and Pb^{2+}) can also take place at characteristic electrolysis potentials (Fig. 3a). Therefore, to obtain long-time stability of HER electrocatalysts in SW, these undesired electrochemical processes need to be suppressed by using suitable membranes to separate

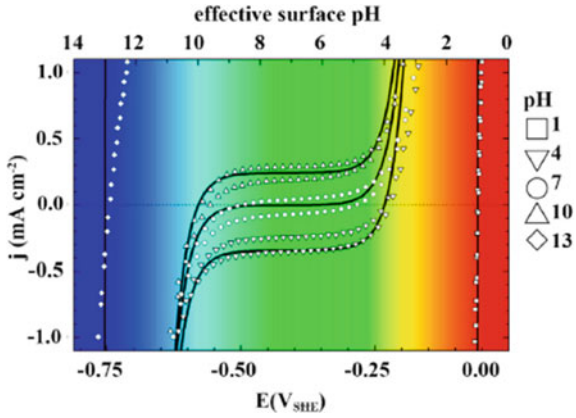

Fig. 2 The diagram of I-pH relationships

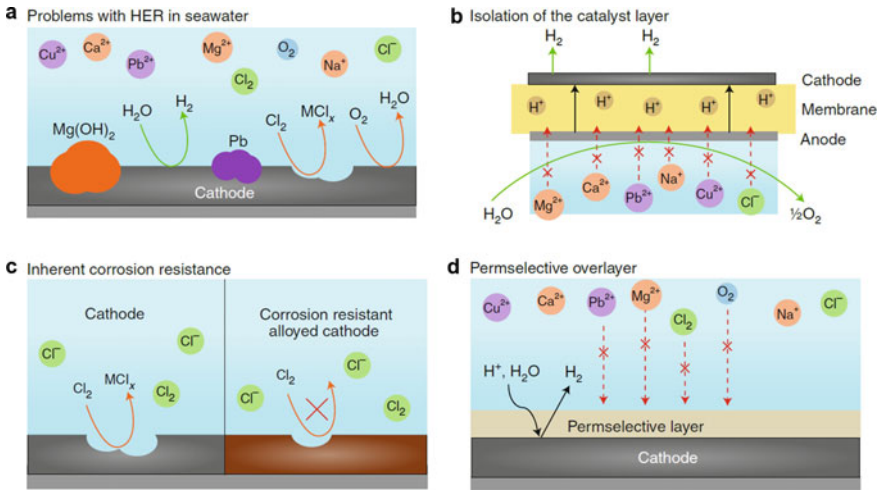

Fig. 3 Schematic diagram of electrocatalysts in SW

electrocatalysts from SW (Fig. 3b), catalysts with intrinsic corrosion resistance or selected surface chemistry (Fig. 3c), and perm-selective barrier layers to block access to the catalysts (Fig. 3d) [17].

SW contains a large amount of electrochemically active like Cl^- whose oxidation can be competitive with anodic OER. A consideration of standard redox potentials of possible anions in SW, chloride oxidation should be most competitive with the OER at the anode. This key issue was addressed in studies by Bennett in 1980, which showed that even though the electrolytic direct method of SW results in the evolution of hydrogen at the cathode with a high current efficiency, large amounts of hypochlorite are simultaneously generated at the anode. The chloride chemistry that occurs during electrolysis in aqueous solutions depends on the pH, applicable potential, and chloride ion concentration. Strasser et al. carried on a thorough analysis of the anodic OER in SW electrolysis, which resulted in the calculated Pourbaix diagram displayed in Fig. 4 that shows pH dependences of the OER and chloride oxidation [18, 25].

The main processes competing with OER formation are the chlorination reaction (ClER) at pH < 3 and hypochlorite formation at pH > 7.5. Hypochlorite formation is the main process that occurs at high anodic potentials of pH 3–7.5. Under acidic conditions, the ClER can occur by the process shown in Eq. (5), while under alkaline conditions hypochlorite is formed by the reaction given in Eq. (6).

$$2Cl^-(aq) \rightarrow Cl_2O(g) + 2e^-(E0 = 1.36\ V\ vs.\ SHE) \tag{5}$$

$$Cl^-(aq) + 2OH^-(aq) \rightarrow 2ClO^-(aq) + H_2O(l) + 2e^-(E_0 = 0.89\ V\ vs.\ SHE) \tag{6}$$

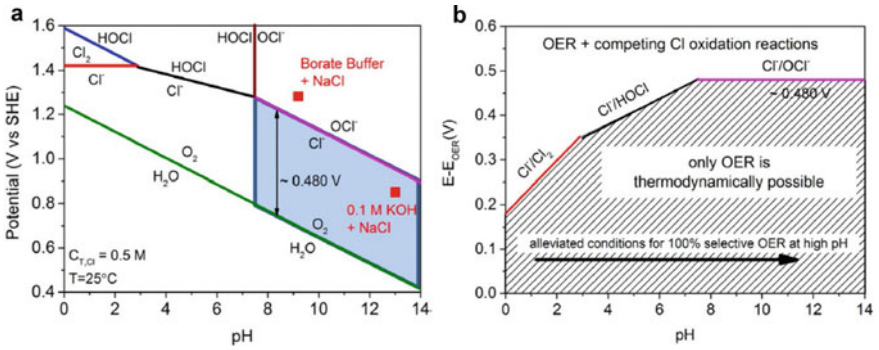

Fig. 4 **a** Pourbaix diagram for a simulated SW model. **b** Maximum permitted η for OER electrolyzer to ensure 100% selective OER

By observing Eqs. (5) and (6), it can be seen that the formation of ClER and hypochlorite is a two-electron process, which is kinetically more favorable than the four-electron OER. Therefore, ClER and hypochlorite formation occur more rapidly than the OER, whereas the OER is thermodynamically favored over hypochlorite formation. In contrast to the standard electrode potential of the ClER, that for hypochlorite formation is pH dependent as is shown in the Pourbaix diagram in Fig. 4a. Therefore, the OER occurs preferentially using an electrocatalyst operating at an η less than ca. 480 mV, whereas hypochlorite formation dominates when an electrocatalyst operating at an η greater than ca. 480 mV and an alkaline medium is used (Fig. 4b).

2.2 Features of Electrocatalytic SW Splitting

As mentioned above, 97% of water in the world is SW. However, the presence of up to 3.5% of various salts in SW (Fig. 5) and their propensity to undergo competitive electrochemical reactions limits the use of this abundant water source for hydrogen production by electrolytic water splitting. To overcome this limitation, an understanding of electrochemical reactions that can possibly take place in SW must first be gained. Needless to say, it is difficult and challenging to accomplish this task, as is reflected by the fact that very few studies addressing this issue have been conducted since the pioneering effort by Trasatti in 1984 [18, 26].

In an effort to understand the selectivity of electrocatalysts for OER and ClER, several key thermodynamic and kinetic parameters need to be evaluated. Using single-crystal RuO_2(110) and Pt(111) as model electrodes for the respective OER and HER, Over and his group determined the free energies, transition states (TS), and reaction intermediates (RI) in the OER or ClER and HER in both acidic and alkaline media. Single crystalline RuO_2(110) is composed of uncoordinated Ru sites (Ru_{cus}) containing an on-top (O_{ot}) and bridging oxygen O_{br}, which are saturated with

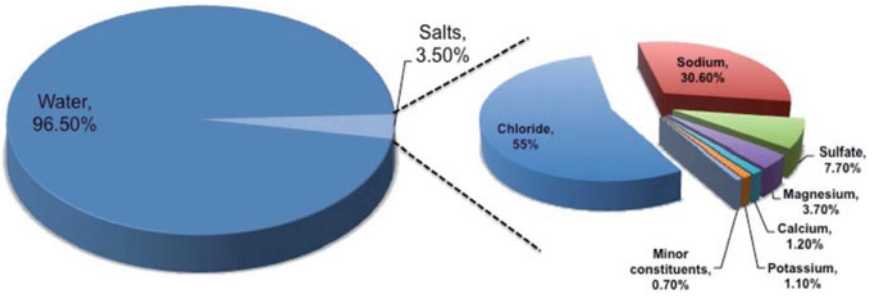

Fig. 5 Elementary distribution of SW

hydrogen in the form of OH_{br} depending on the overpotential utilized (see Fig. 6a). The Pourbaix diagram displayed in Fig. 6a, showing the OER and ClER over a pH range, shows that the O-caped RuO_2 surface is stable over pH values and a wide range of potential. Specifically, both the OER and ClER take place preferentially at potentials over 1.36 V, while at potentials above 1.49 V at pH values <4 where chlorine adsorption on O_{ot} dominates, the ClER process is more favored. The RuO_2 surface having the $1O_{br}1OH_{br} + 2O_{ot}$ composition is thermodynamically most favorable for the ClER reaction. The Volmer–Tafel, Volmer–Heyrovsky, or Krishtalik mechanisms are likely followed in the ClER. As depicted in Eqs. (7) and (8), this mechanism involves adsorption and discharge of the chloride ion in the Volmer step forming the intermediate Ru–O_{ot}Cl, then re-combination of adsorbed chlorine with free-chloride occurs in the Heyrovsky step, which is followed by release of Cl_2 [27].

$$Ru - O_{ot} + 2Cl^- \rightarrow \text{Ru-}O_{ot}Cl + e^- + Cl^- \text{(Volmer step)} \tag{7}$$

$$Ru - O_{ot}Cl + Cl^- \rightarrow Ru - O_{ot} + Cl_2 + e^- \text{(Heyrovsky step)} \tag{8}$$

Informed by the Tafel plot at acidic pHs shown in Fig. 6a, b more detailed understanding of the mechanism arises from studies in which varying overpotential values $\eta_{CER} > 0$ V are used. The free energy diagram indicates that Ru–O_{ot}Cl is the single intermediate, and the high TS free energy of the Heyrovsky step makes it rate determining. The energy of the TS for the Heyrovsky step (#2) is lowered by increasing the overpotential to a greater extent than is that of the Volmer step (#1) at $\eta_{CER} >$ 0.20 V.

The four-electron transfer OER takes place more slowly than the CER on the completely O-capped RuO_2(110) surface created by the coordination of uncoordinated Ru_{CUS} with O_{ot} at acidic pHs. The mechanism for this process is described by the four-step sequence shown in Eqs. (9)–(12).

$$2O_{ot} + H_2O \rightarrow 1O_{ot}1OOH_{ot} + H^+ + e^- \tag{9}$$

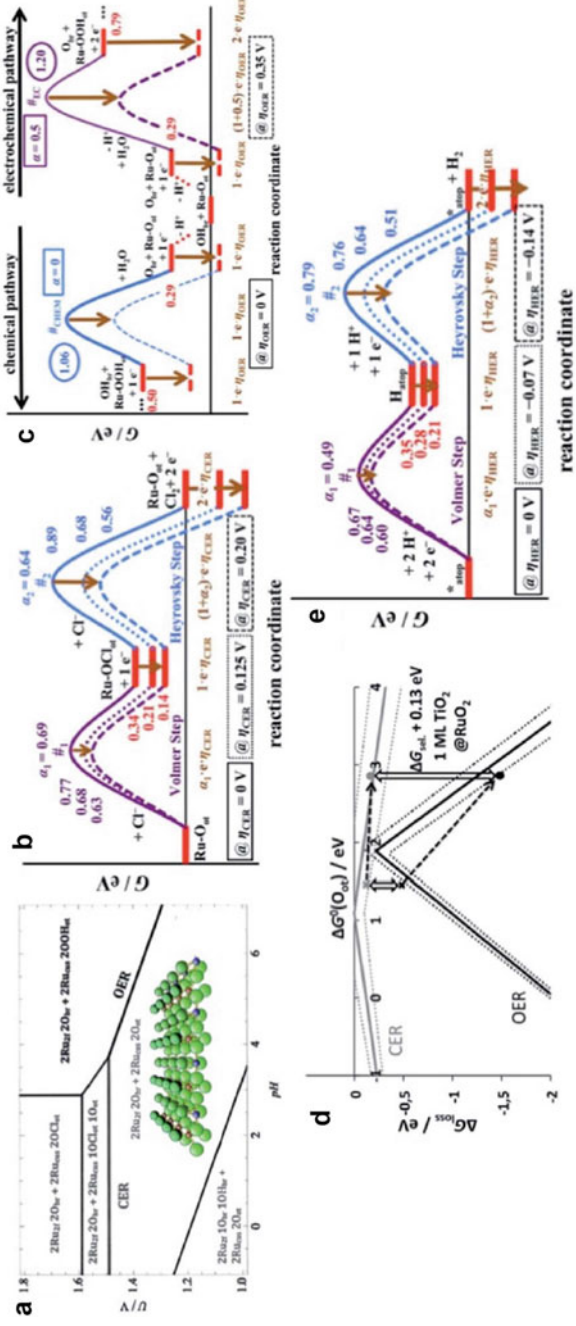

Fig. 6 **a** Pourbaix diagram of RuO_2(110). **b**, **c** Free energy diagram for the ClER (gray) and OER (black). **e** Free energy diagram for HER

$$1O_{ot}1OOH_{ot} \rightarrow 1O *_{ot} + O_2 + H^+ + e^- \quad (10)$$

$$1O *_{ot} + H_2O \rightarrow 1O_{ot}1OH_{ot} + H^+ + e^- \quad (11)$$

$$1O_{ot}1OH_{ot} \rightarrow 2O_{ot} + H^+ + e^- \quad (12)$$

As Over et al. suggested, water splitting leads to the adsorption of OH at the active O_{ot} site, H^+ on O_{br} to form OH_{br} or be released into the electrolyte. The diagram for the OER in Fig. 6c includes free energy changes for the competing chemical and electrochemical reactions leading to the formation of the corresponding intermediates. The diagram illustrates changes in the pathways occurring at different overpotentials and the reversible electrode potentials (i.e., hOER 1/4 0 V and at hOER > 0.3 V). Inspection of the diagram shows that at low overpotentials (ηOER < 0.3 V), the OER pathway is initiated combination of OH_{br} with Ru–O_{ot} at the surface, and proceeds through the pathway shown by the blue line (Fig. 6c). Yet, at hOER > 0.3 V, the initial active surface combination becomes O_{br} with Ru–O_{ot}), and the process proceeds through the electrochemical pathway represented by the violet line in Fig. 6c.

The results of the research show that thermodynamic barriers for the ClER and OER are not zero, suggesting that the O-capped RuO_2 surface might be manipulated to promote selective catalytic reactions. This hypothesis can be understood using the volcano diagram given in Fig. 6d. In this diagram, a larger $\Delta G_0(O_{ot})$ indicates limited Cl^- desorption, and a smaller value corresponds to limiting Cl^- adsorption. In contrast, for the OER, higher $\Delta G_0(O_{ot})$ values indicate OOH_{ot} decomposition, and smaller values lead to the restricted formation of OH_{ot}. It is important to note that both cases proceed with maximum activity at the middle of the higher and lower values. It is obvious to see that the volcano plot for CER is quite flat compared to OER, and the difference in the slopes reflects the different numbers of reaction intermediates. The difference in ΔG_{loss} values at a certain $\Delta G_0(O_{ot})$ defines the selectivity, and is quantified by ΔG_{sel}. The ΔG_{sel} value can be manipulated by weakening the Ru–O bond, i.e., which lowering the OER catalytic activity, and in another way, allowing for substantial selectivity, as exampled by the TiO_2(110) monolayer on RuO_2(110).

The cathodic reaction on the surface of the model single-crystal Pt(111) can be understood in terms of the Volmer–Tafel mechanism or the Volmer–Heyrovsky mechanism, the latter being preferred. The Volmer–Heyrovsky mechanism involves two steps, including proton adsorption on Pt surface (Volmer step) followed by a restructuring of adsorbed hydrogen with an H^+ ion (Heyrovsky step).

$$Pt - H\,Pt + 2H^+ + 2e^- \rightarrow \text{Pt-H Pt-H} + H + + e^- \text{(Volmer step)} \quad (13)$$

$$Pt - H\,Pt - H + H^+ + e^- \rightarrow Pt - H \cdot Pt + H_2 \text{(Heyrovsky step)} \quad (14)$$

As with RuO_2 in the OER or ClER, the fcc hollow sites on Pt(111) surface contain hydrogen atoms, while Pt atom sites remain unoccupied. As indicated by Eqs. (13) and (14), Pt atom sites are mainly involved in the reaction pathway. The free energy diagram for the HER (Fig. 6e) occurring via Volmer–Heyrovsky mechanism shows that the rate-limiting step of the two in the pathway depends on the applied overpotentials.

In SW electrolysis, the OER and HER vary with local pH changes at the electrodes with increases in pH occurring at the cathode and decreases in pH at the anode. The pH fluctuations are on the order of 5–9, which causes severe damage to the electrocatalysts even when a low current density of <10 mA cm^{-2} is utilized. Inspection of Pourbaix diagrams (Fig. 2b) shows that OER becomes less favorable and chlorate formation becomes more favorable as the pH at the anode decreases at a constant current density. However, hypochlorite formation is pH-independent in the 6.5–10.5 range, but it is dependent on the convective diffusion of ions. As shown in the Pourbaix diagram (blue dotted line in Fig. 2b), to carry out selective OER while avoiding CER at the anode, the pH of the medium should be >7.5. Control of pH at the electrode surface, required for carrying out a selective electrolytic process, can be achieved by using buffers to consume generated protons. While an electrolyte composed of 1 M KOH and 0.5 M NaCl is generally employed as a simulated SW (SSW) electrolyte in evaluations of electrocatalytic performances, borate (pH 9.2), carbonate (pH 8.6), or phosphate (pH 7) buffer have also been utilized. Notably, the amounts of borate and carbonate indigenously present in SW are too small to affect pH [18, 28, 29].

3 Materials Used for the HER in SW

3.1 Noble Metal-Based Materials

Catalysis of water splitting to form H_2 and O_2 is feasible only if hydrogen is absorbed in the form of metal(M)–H bonds. Thus, catalytic efficiency is optimal when the M-H adsorption energy is large, and the metal has a proper electronic configuration. Owing to these factors, noble metal-based nanomaterials like those containing Pt, Ru, Rh, and Ir are state-of-the-art catalysts for electrocatalytic water splitting. Guided by these considerations, studies aimed at designing ideal electrocatalysts for water splitting have focused mostly on noble metal-based nanomaterials [30].

3.1.1 Pt-Based Electrocatalysts

Pt-based alloys are benchmark electrocatalysts for the HER, owing to the fact that they exhibit the highest performances under acidic, alkaline, and neutral conditions [31–35]. However, the HER performance of these materials in SW is far less than

it is in freshwater-based electrolytic systems. With commercial Pt/C (20 wt%) in SSW, the overpotential of HER is in the range of 120–300 mV at a current density of 10 mA cm^{-2}, depending on the conditions employed. In addition to having large overpotentials, a current density loss of ca. 50% has been observed for Pt after 100 h continuous operation under alkaline conditions. Furthermore, investigations suggest that the reduction of current density is a result of the deterioration of the conductivity of the alkaline membrane rather than that of the Pt electrode. Scarcity and high costs greatly limit the use of Pt-based alloys in large-scale commercial applications [36]. To address these issues, strategies in which earth-abundant metals are incorporated into Pt are promising strategies.

Alloying with Mo, Ni, Co, Fe, or Cr modifies the electronic structure of Pt and enhances its charge transfer properties. Moreover, incorporating the alloy in a nanostructure form should lead to an expanded number of active sites that would enhance performance in the HER. Information about these issues was gained in a study by Zheng's group, which compared the HER performances in SW of Pt alloys including PtMo, PtNi, PtCo, PtFe, and PtCr that were fabricated on a Ti mesh using a cyclic voltammetric deposition. PtMo exists as nanoparticles (<10 nm) (Fig. 7a, b), in which Pt in a face-centered-cubic manner (Fig. 7c). Thus, incorporating alloying guest atoms into the host lattice alters the crystal size of Pt without changing its crystal structure and it introduces lattice distortions and defects. The Pt_{4f} band in the XPS spectrum of PtMo alloy is shifted downfield in comparison to that in pristine Pt. This change can be ascribed to the lowering of binding energies of Pt_{4f} core electrons by interactions of atomic orbitals of Pt and those of alloying guest atoms. The Mo 3d band in the XPS spectra of PtMo alloy also exhibits a downfield shift, showing that alloying causes induces a modification of the electronic structure of Mo. Charge transfer resistance measurements were carried out to explore if the interaction induces partial electron transfer from the Mo guest to Pt. The results show a clear order of charge transfer resistance. These effects are consistent with the observed HER activities of the Pt alloys (Fig. 7d). Notably, PtMo retains the high activity of the −800 mV overpotential during operation for 173 h, trends that are mimicked in the other Pt alloys (Fig. 7e, f). [37]

Jieshan Qiu et al. developed a template-engaged ultrafast aerosol drying strategy for generating multilevel hollow MXene that has a large surface area, high mass accessibility, excellent conductivity, and good aggregation resistance. Multilevel hollow MXene architectures are fabricated by using ultrafast drying of MXene aerosols on hard templates with desirable structures, dimensions, and chemical reactivities (Fig. 8a). Multilevel hollow MXene tailoring of ultra-fine Pt yields a multifunctional electrocatalytic interface that has high atomic utilization efficiency, good conductivity, efficient H^+/water adsorption, and large ionic/mass accessibility. Linear scan voltammetry (LSV) shows that 2.4% Pt@ mh-3D MXene with a mass loading of 0.2 mg cm^{-2} has a superior $\eta_j = 10$ of 280 mV compared to 20% Pt/C (308 mV) at a scan rate of 10 mV s^{-1}. After 50 sweeps, the 2.4% Pt@mh-3D MXene the $\eta_j = 10$ undergoes only a negligible increase indicating that it is highly stable during the HER in SW (Fig. 8b). In contrast, Pt/C is rapidly deactivated in SW where a 30% decrease of $\eta_j = 10$ occurs after 50 sweeps. The excellent durability of 2.4% Pt@mh-3D

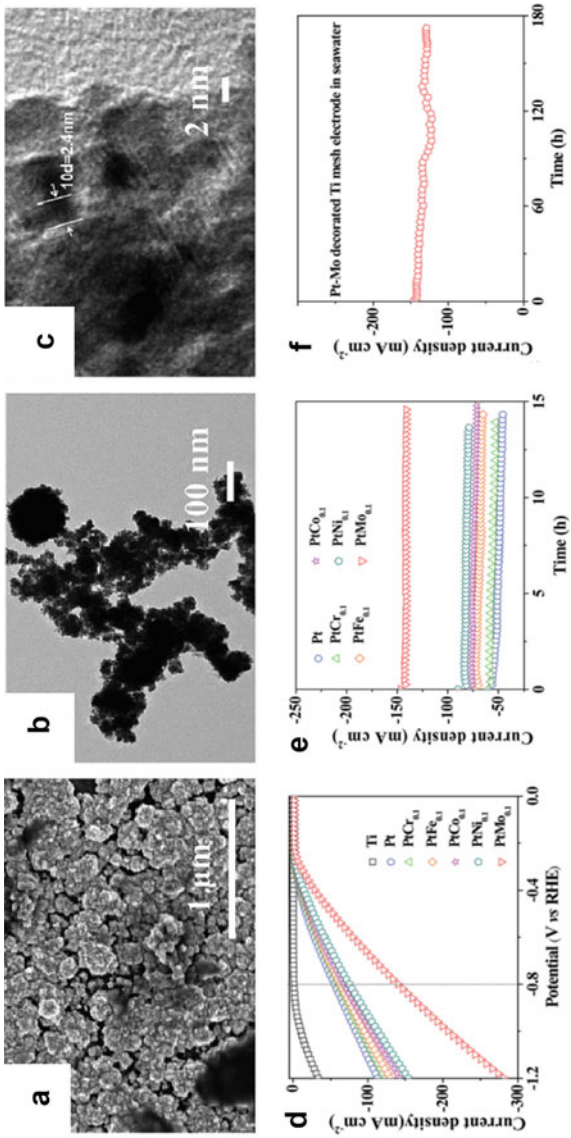

Fig. 7 **a** SEM image of a Ti mesh supported PtMo electrode. **b** TEM image and **c** HRTEM image of alloyed PtMo catalyst. **d** LSV of different electrodes in SW. Long-term stability of **e** Ti/Pt and Ti/PtM as well as **f** Ti/PtMo alloy in SW

MXene toward HER in SW was validated by using time-dependent current density measurements, which demonstrate that the potential of this catalyst remains stable for 250 h at a current density of 10 mA cm^{-2} (Fig. 8c). Figure 8d shows comparisons of the activity and durability for HER in SW of non-noble metal catalysts and 2.4% Pt@mh-3D MXene [38].

3.1.2 Ru-Based Materials

The use of Pt in large-scale applications is hindered by its high price and low availability. As a result, relatively inexpensive Ru has attracted increasing attention, especially because the Ru–H and Pt–H bond strengths are similar [39]. Pan's group devised the electrocatalyst Ru_{1+NPs}/N–C which is comprised of single-atom Ru sites and Ru nanoparticles deposited on mesoporous nitrogen-doped carbon (Fig. 9a, c) by using pyrolysis of $RuCl_3$-coordinated melamine formaldehyde resin (MF). The EDS-mapping image in Fig. 9b demonstrates that C, N, and Ru are evenly distributed on the surface of this material. The overpotential of Ru_{1+NPs}/N–C in SW is 375 mV when the current density is 10 mA cm^{-2}, and only 50 mV in SSW (Fig. 9d), which is comparable to that of the commercial Pt/C catalyst. Analysis of the i-t curve shows that Ru_{1+NPs}/N–C catalyst is stable for 24 h in both SSW and SW. The theoretical and experimental amounts of hydrogen generated in the HER promoted by Ru_{1+NPs}/N–C and Pt/C in SW and SSW were determined by using the drainage method. The faradic efficiency (FE) of the Ru_{1+NPs}/N–C catalyst for HER is 85.7% in SW and 98.2% in SSW, while the FE of the Pt/C catalyst is 76.3% in SW and 93.7% in SSW (Fig. 9e). The results indicate that Ru_{1+NPs}/N–C is highly selective for hydrogen production in SW electrolysis, but that the presence of higher levels of ionic impurities in SW compared to SSW causes lower faradic efficiency. Also, chronoamperometric curves show that the Ru-based catalyst has excellent stability under a variety of conditions (Fig. 9f).

Ru nanoparticles in Ru_{1+NPs}/N–C, which cause a decrease in an energy barrier, and the active site, where absorbed H^+ forms H_2, synergistically promote the production of H_2. This catalyst has a low overpotential over a wide pH range and a large rate. Due to the structural characteristics of both the single-atom Ru-N_4 site, Ru_{1+NPs}/N–C has high stability in alkaline/acidic SW [40].

Inspection of the top-view SEM images displayed in Fig. 10a, b shows that Ti mesh has a coarse surface comprised of bulky aggregates. After the deposition of Pt on the mesh, the surface is coated with a compact Pt film (Fig. 10c). High-resolution SEM (Fig. 10d) indicates that the Pt film consists of ~200 nm nanoparticles. When a mixture of Pt and Ru was used for electrodeposition, the Ti mesh becomes coated with a compact Pt–Ru alloy film containing cracks that includes homogenous nanoparticles with an approximate size of 100 nm (Fig. 10e, f). Interestingly, a ternary Pt–Ru–Mo alloy film on the Ti mesh created in the same manner has a porous topology with nanoparticles having an average diameter of around 30 nm (Fig. 10g, h). The increased in porosity and reduced nanoparticle size of the Pt–Ru–Mo alloy compared to that of Pt are beneficial for increasing the catalytically active area for hydrogen

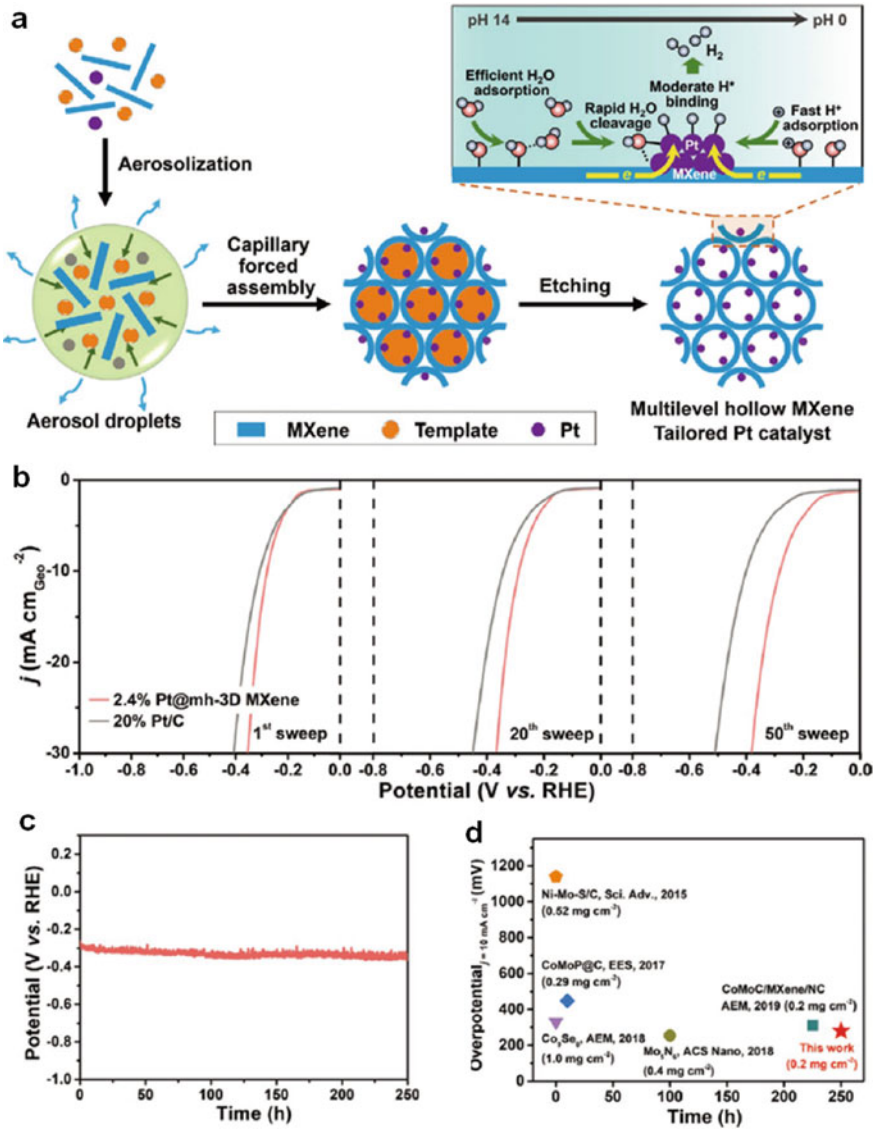

Fig. 8 **a** Schematic illustration of template-engaged ultrafast aerosol drying strategy. **b** LSV of samples and commercial Pt/C. **c** Long-time stability of samples. **d** Comparison of the activity and durability for HER in SW of samples and reported SW-workable electrocatalysts

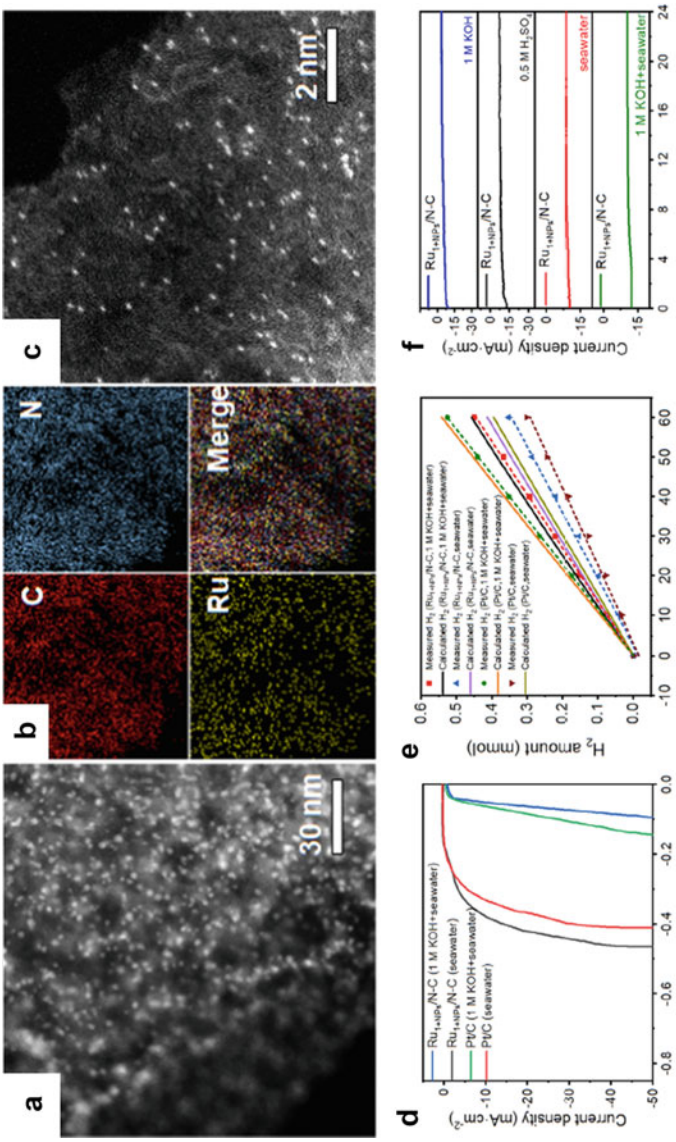

Fig. 9 **a** HRTEM, **b** EDS mapping and **c** HAADF-STEM image of the main sample. **d** LSV in SW. **e** FE of test samples. **f** I-t curves

adsorption. The respective current densities at −0.8 V of alloys including Pt–Ru, Pt–Ru–Fe, Pt–Ru–Co, Pt–Ru–Cr, Pt–Ru–Ni, and Pt–Ru–Mo are −45.04, −50.48, −55.02, −60.77, −65.00 and −69.54 mA cm^{-2} (Fig. 10i), which are markedly lower than that of for pure Pt (−39.61 mA cm^{-2}). The higher exchange current density and lower hydrogen evolution overpotential indicate that the alloys have increased catalytic activity.

Among those coated with the other alloys, the Pt–Ru–Mo-coated Ti mesh electrode has the highest SW splitting performance. The increase in electrocatalytic

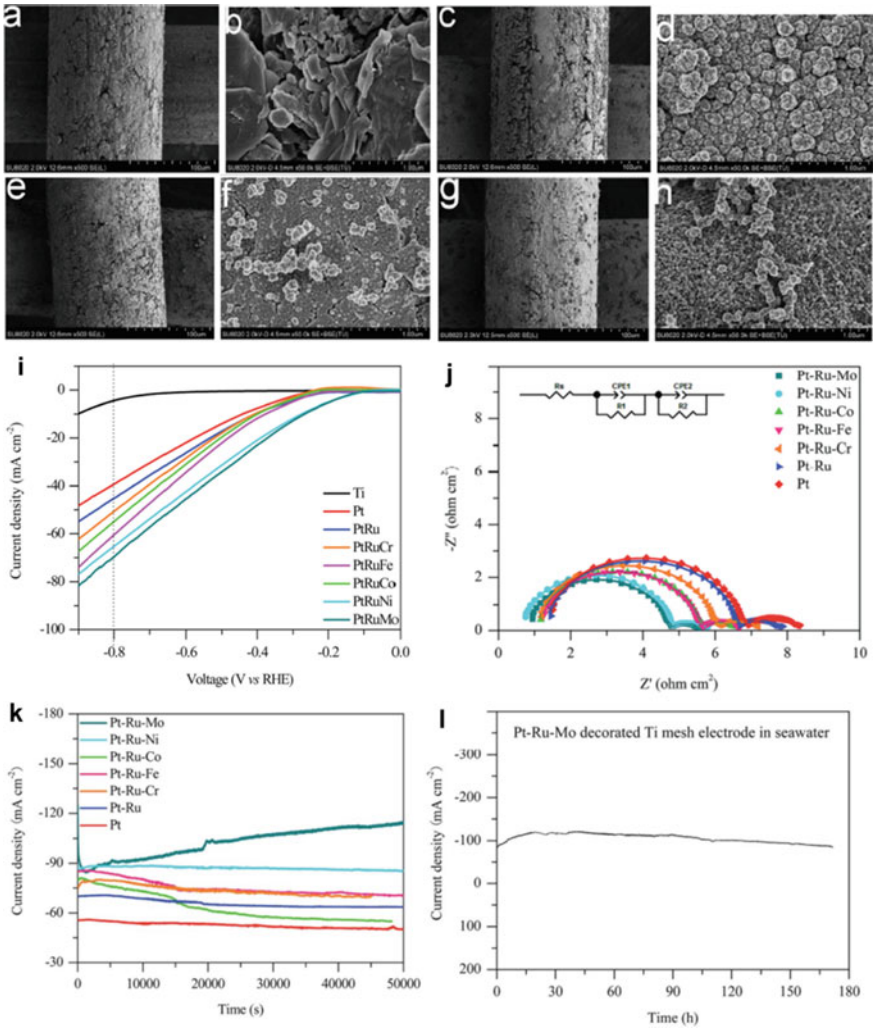

Fig. 10 SEM images of **a**, **b** Ti mesh, **c**, **d** pure Pt, **e**, **f** PtRu alloy, and **g**, **h** decorated Ti mesh. **i** Hydrogen evolution curves in SW. **j** EIS plots. **k** I-t curves. **l** U-t curves

activity is the result of synergistic alloying effects such as increased catalytically active area caused by increased nano-porosity, and the presence of electron-enriched Pt surface sites. Accordingly, the Brewer–Engel theory suggests that electrons are readily transferred to water molecules through Pt d orbitals, leading to O–H bond cleavage. The Pt–Ru–Mo-decorated Ti mesh electrode shows Rct value (Fig. 10j). The observation described above is which is consistent with the results of the Tafel analysis in showing that the Pt–Ru–Mo-coated electrode has superior catalytic activity for HER.

The stabilities of Pt–, Pt–Ru–, and decorated Ti mesh electrodes for HER in SW were researched by analyzing chronoamperometric curves recited at −0.8 V for 50,000 s (−13.9 h). The results show that only a 2.1% decrease for the Pt–Ru–Mo-decorated Ti mesh electrode occurs over 172 h (Fig. 10k and l), demonstrating its promise in systems that produce hydrogen from SW. The improved anticorrosion properties of the Pt–Ru–M alloys are a consequence of competitive dissolution reactions between the M species and Cl^- in SW. The metal species (Ru, Pt, Fe, Cr, Co, Mo, and Ni) in the catalysts react with dissolved Cl_2 to form corresponding metal chlorides. Along with its improved current density for HER, the long-term stability gives it a high potential for practical SW splitting application [41].

Tang et al. described the process for one-step electrode deposition of RuCo and RuCoMox alloys on Ti foil. The detailed observations summarized in Fig. 11a, b reveal that the $RuCoMo_7$ coated foil produced in this manner is composed of nanoparticles with a compact structure containing cracks. The loose structure for RuCo and the cracks for RuCoMo7 are expected to provide a large active surface for SW diffusion and adsorption. The onset potential of Ti foil supported RuCo electrode toward the HER is −0.25 V vs. RHE, and the Ti foil supported RuCoMox electrode exhibits a more negative onset potential for this process in the −0.35 to −0.37 V versus RHE range. At a potential of −1.4 V (vs. RHE), the current density of the Ti foil supported RuCo electrode is 210 mA cm^{-2}, which is larger than that of a Ti foil supported $RuCoMo_x$ electrode. Moreover, the current density is reduced from 130 mA cm^{-2} for Ti foil supported RuCoMo1 to 110 mA cm^{-2} for Ti foil supported $RuCoMo_7$ (Fig. 11c). The results suggest that the Ti foil supported RuCo electrode is more catalytically active for the HER than the Ti foil supported $RuCoMo_x$ electrode.

Operational stability of an electrode for HER is more important than catalytic efficiency in practical applications. Thus, the long-term stabilities of these electrodes in SW over 12 h at a constant potential of −1.2 V versus RHE were evaluated. As shown in Fig. 11d, the current density of the Ti foil supported RuCo electrode is reduced from 185 to 128 mA cm^{-2} over 12 h, reaching 70% of the original current density. Although the initial current density is only −85 mA cm^{-2} for the Ti foil supported $RuCoMo_x$ electrode, no obvious reduction occurs over 12 h, suggesting that it is relatively stable in SW. A possible reason for the excellent stability of the Ti foil supported RuCoMox electrode is that the Ru-3d core level peaks of RuO_2 do not change during HER and therefore protect against chemical dissolution or corrosion of Ru [42].

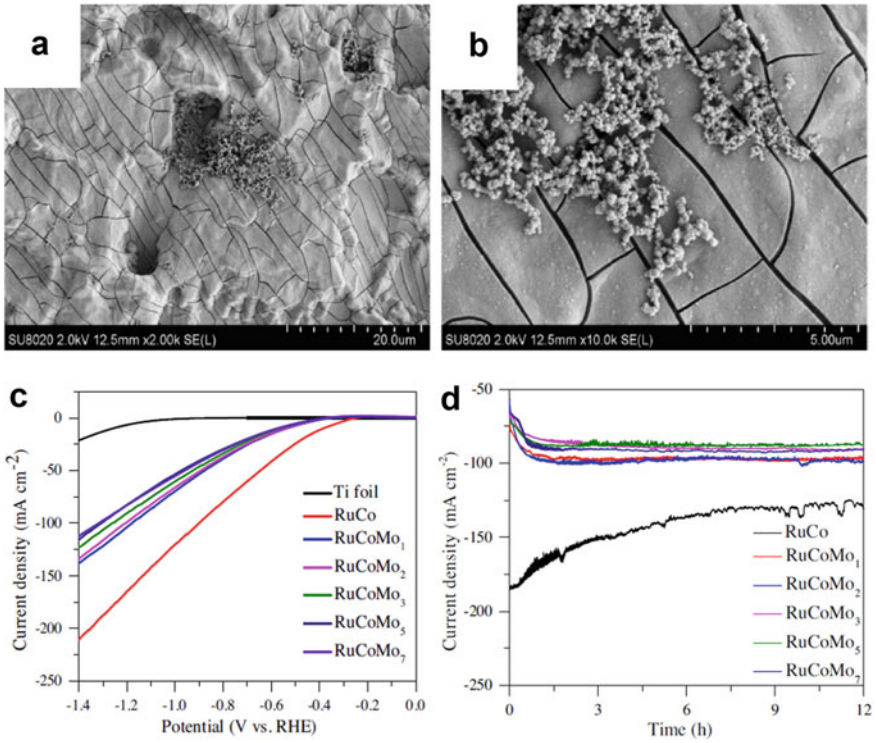

Fig. 11 **a**, **b** Ti foil supported $RuCoMo_7$ alloy electrode. **c** Polarization curves of all samples. **d** Chronoamperometric curves on Ti foil supported RuCo and $RuCoMo_x$ electrodes

3.2 Non-noble Metal-Based Materials

Despite the high activity of noble metal-based nanocatalysts for natural SW hydrogen production, their cost-effectiveness and absence of durability have largely hindered their use in industrial applications. As a result, exploration has been conducted to uncover non-noble-metal-based electrocatalysts that have high activities and stabilities. In the most recent years, transition metal-based electrocatalysts have been investigated because they possess different electronic configurations, high electrical conductivities, and optimized adsorption energies of intermediates [43–47].

3.2.1 Single-Atom Materials

Single-atom catalysts (SACs) containing uniformly distributed metal atoms (such as Co, Ni, Mo, and W) on a conductive substrate have been developed for the HER in alkaline freshwater. Differing from traditional nanoparticle/nanosheet catalysts, in which metal atoms are catalytically inactive owing to their inaccessibility to

substrates, SACs have higher atom utilization efficiencies and active site exposures that are desirable for efficient HER [40, 45, 48–50].

Wang's group described Ni single-atom electrocatalysts (Ni-SA/NC) containing $Ni–N_3–O_2$ and $Ni–N_4$ coordination, which they fabricated using a facile surfactant-assisted method (Fig. 12a). Also, these workers systematically investigated the catalytic performance of this material toward H_2 evolution in both alkaline freshwater and SW. Aberration-corrected high-angle annular dark-field scanning transmission electron microscope and annular bright-field images (Fig. 12b, c) show that Ni–SA/NC has a highly porous structure, consisting of twisted N-doped carbonaceous layers. Single Ni atoms are dispersed uniformly over the surfaces of the carbonaceous layers (Fig. 12d). The results of elemental concentration analysis (Fig. 12k) show that an increase of K and a decrease of Mg and Ca occur upon the addition of KOH to SW as a result of precipitation of $Mg(OH)_2$ and $Ca(OH)_2$. The LSV curve shows that Ni–SA/NC with a mass loading of 0.5 mg cm^{-2} (Fig. 12e) requires a very low overpotential of 139 mV to reach the current density of 10 mA cm^{-2}, a value that is much lower than those of Ni–NP/NC (151 mV) and NC (220 mV). The Tafel slope of the Ni–SA/NC was found to be 123 mV dec^{-1}, which differs only slightly from that in alkaline freshwater (Fig. 12f). Furthermore, Ni–SA/NC has high operational stability over 5000 operation cycles and it does not undergo activity decay during continuous electrolysis for 14 h (Fig. 12g). No changes in the distribution of Ni single atoms occur for Ni–SA/NC, indicating that it has high durability for the HER in SW (Fig. 12h, i). A chronoamperometry test for 14 h shows that the Na and K concentrations and the pH value of SW remain constant, and that concentration of dissolved Ni concentration is <0.1 ppm (Fig. 12k). A small reduction of the Ca concentration undergoes a small decrease during the electrolysis process, which is attributed to the formation of $Ca(OH)_2$ precipitates on the electrode surface.

DFT calculations were carried out using a computed hydrogen electrode model to gain insight into the reasons for the high HER performance of Ni–SA/NC (Fig. 12j). By viewing the diagram in Fig. 12j one can see $Ni–N_3$ stabilizes adsorbed hydrogen ($\Delta G = 0.69$ eV) whereas $Ni–N_4$ only weakly interacts with adsorbate ($\Delta G = 2.55$ eV). The finding that weak hydrogen adsorption occurs on $Ni–N_4$ (~2.43 eV) was described previously. In summary, a well-isolated dispersion of single Ni atoms anchored on porous N-doped carbon results in a large population of active sites with tunable coordination environments. The observations show that the development of low cost and highly efficient SACs for SW splitting is promising [45].

3.2.2 Metal Nitrides

Recently, transition metal nitrides (TMNs) have gained much attention as promising electrocatalyst materials for electrocatalytic processes (e.g., the HER and OER, and the oxygen reduction reaction). Because of their inherent electronic structure and good electrical conductivities, TMNs can potentially serve as replacements for noble metal catalysts for water splitting [51–53].

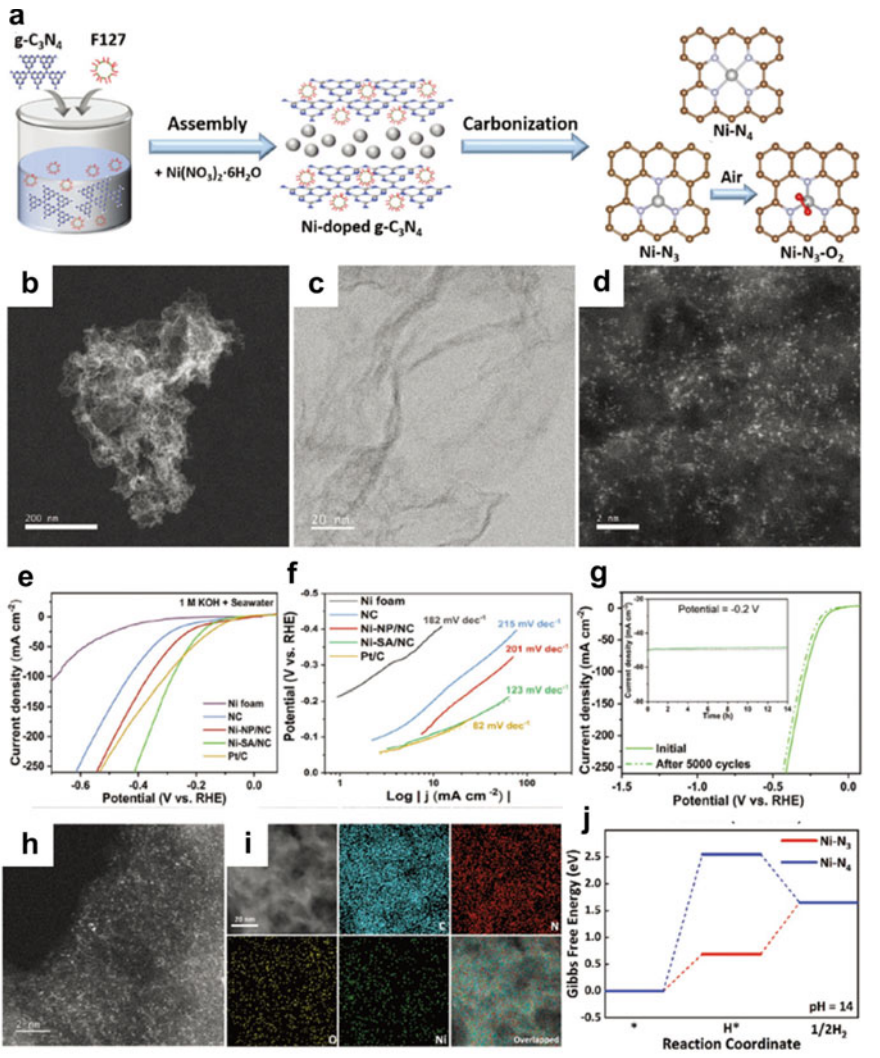

k

	Concentration of elements/ppm					pH
	Na	K	Mg	Ca	Ni	
Pure seawater	9694	342	1072	350	–	8.10
Alkaline seawater	9796	27 700	1042	337	–	13.80
Alkaline seawater after cycling for 14 h	9802	27 980	1023	262	<0.1	13.76

◀**Fig. 12** **a** Synthesis process and structural visualization. HAADF-STEM and ABF images of: **b** the 3D porous structure, **c** the plane structure, and **d** isolated Ni atoms. **e** LSV curves. **f** Tafel slopes. **g** LSV cures before and after 5000 CV cycles. **h** HAADF-STEM image and **i** STEM-EDS mappings of Ni–SA/NC after cycling. **j** Gibbs free energy diagram on the Ni–N_3 and Ni–N_4 structure at pH = 14, where H* denotes one hydrogen atom adsorbed on an adsorption site (*), and $1/2H_2$ refers to one gas-phase hydrogen molecule. **k** Concentration of elements after chronoamperometry test

Qiao's group described the metal-catalyzed phase transformation route (Fig. 13a). The formed 2D morphology of transparent and wrinkled Mo_5N_6 nanosheets can be observed using SEM and TEM imaging (Fig. 13b). The scanning TEM image in Fig. 13c shows that Mo_5N_6 has a hexagonal structure with an interplanar distance of 2.45 Å for MoN (110) facets, which is smaller than the 2.5 Å for the (200) facets. The presence of one set of diffraction spots in the SAED image reveals that Mo_5N_6 has single crystalline nature (Fig. 13d). Owing to rich metal-nitrogen bonding, the 2D Mo_5N_6 nanosheets have a higher HER activity in various electrolytes (pH 0–14) than those of conventional nitrogen-deficient TMNs. More significantly, Mo_5N_6 exhibits outstanding HER performance in SW and a catalytic current that remains stable over 100 h, both properties that are far superior to those of Pt/C benchmark and other TMNs (Fig. 13e–h). Specifically, Mo_5N_6 in the HER in SW requires an overpotential of 257 mV to produce 10 mA cm^{-2} of current density, a value that is lower than those of Pt/C and other nitrogen-deficient TMNs. Furthermore, the j_{10} overpotential (overpotential at a current density of 10 mA cm^{-2}) of MoN_6 is also lower than those of most non-noble metal catalysts reported thus far in the literature. More importantly, hydrogen production promoted by Mo_5N_6 in SW at an overpotential of 300 mV is extremely stable over a 100 h period. In comparison, the stability of Pt/C is much lower, retaining 5.5% of its catalytic current density after only 4 h of continuous operation. As has been documented in other studies, the poor stability of Pt/C is likely a result of poisoning by ions in SW which block active sites for hydrogen evolution. In addition, the 99.3% retention of catalytic current over 4 h of Mo_5N_6 is higher than those of MoN (55.0% for 4 h), $Ni_{0.2}Mo_{0.8}N$ (49.1% for 4 h), and Ni_3N (20.0% for 4 h) [54].

Because of their high corrosion resistance and electrical conductivity, and tunable electronic structure, two-dimensional (2D) TMNs such as W–N, Mo–N have shown promise as energy-related electrocatalysts. For example, a Ni_3N/W_5N_4 Janus nanostructure was prepared utilizing a three-step sequence involving a hydrothermal process, ion exchange, and nitridation (Fig. 14a). As shown in the image in Fig. 14b, Ni_3N/W_5N_4 is composed of intertwined nanoparticles and ultra-thin nanosheets. The high-resolution TEM (HRTEM) shows that this material has lattice spacings of 0.51 and 0.243 nm, which are ascribed to the (002) and (101) planes of hexagonal W_5N_4, and 0.218 nm and 0.188 nm interplanar spacings associated with the (002) and (102) planes of Ni_3N (Fig. 14c). A selected area electron diffraction (SAED) pattern of Ni_3N/W_5N_4 shows that the diffraction rings consist of discrete points assigned to (111) and (002) planes for Ni_3N, and (002) planes for W_5N_4 (Fig. 14d), indicating that this material has poly-crystalline character. As shown in Fig. 14e–i, the

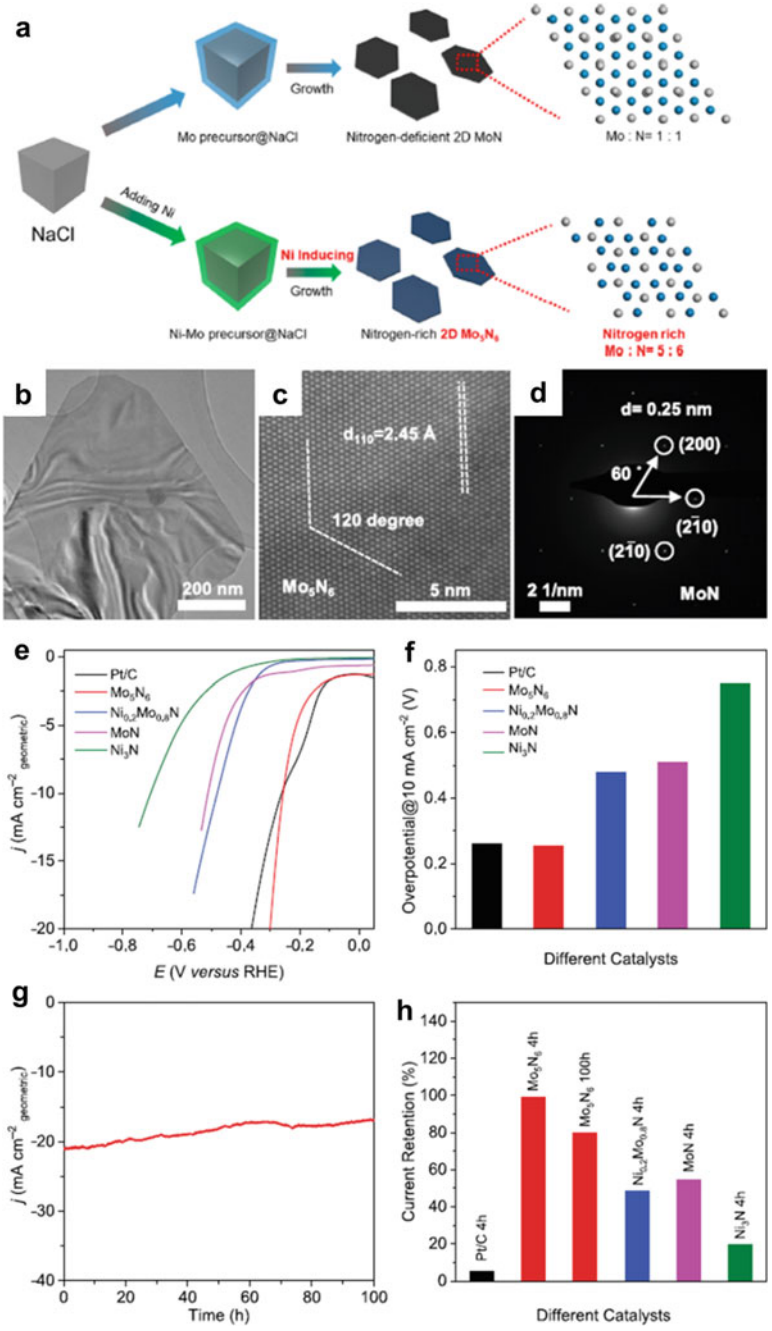

Fig. 13 **a** Synthesis diagram of MoN and Mo_5N_6 nanosheets. **b**, **c** TEM images of Mo_5N_6. **d** SAED pattern of MoN. **e** LSV curves of all samples. **f** Overpotentials of different samples. **g** I-t curve of Mo_5N_6. **h** Current retention of different samples

Ni_3N/ W_5N_4 electrode exhibits a lower overpotential and higher current density than those of pure Ni_3N and W_5N_4. The observation shows that the Janus interfaces are essential for the enhanced HER performance. Impressively, the Ni_3N/W_5N_4 Janus nanostructure has a Pt-like HER performance corresponding to an ultralow overpotential of 31 mV at 10 mA that is much lower than those of NiW–OH (289 mV), Ni_3N (166 mV), and W_5N_4 (80 mV). The Tafel slope for the Ni_3N/W_5N_4 hybrid electrode is ca. 34 mV dec^{-1}, suggesting that the mechanism for the process has the Heyrovsky step being rate determining. In contrast, the Ni_3N electrode has a Tafel slope of 143 mV dec^{-1}. Meanwhile, W_5N_4 with Tafel slope of 75 mV dec^{-1} has a higher water dissociation capability than Ni_3N, but the HER kinetics remain inferior to those of Ni_3N/W_5N_4. Together, the results demonstrate that the kinetics for the process promoted by Ni_3N/W_5N_4 are remarkably better than those of Ni_3N and W_5N_4 as a result of the synergetic effect of the Janus interface.

As can be seen by viewing the Nyquist plots in Fig. 14g, the Ni_3N/W_5N_4 heterostructure has a lower interface charge transfer resistance and superior electron transfer ability than those of Ni_3N and W_5N_4. This finding confirms the suggested more favorable kinetics for Ni_3N/W_5N_4. When tested in alkaline SW, Ni_3N/W_5N_4 has a catalytic activity that is similar to that of commercial Pt/C (Fig. 14k). As shown in Fig. 14l, Ni_3N/W_5N_4 also outperforms other TMNs catalysts. The structure and composition of the Ni_3N/W_5N_4 hybrid system have numerous advantageous features. Firstly, the multilevel nanostructures comprised of 2D W_5N_4 nanosheets and Ni_3N NPs expose more active sites and enhance mass transfer. Secondly, the barrier-free Janus interface has high electrical conductivity, and it also provides resistance to chloride ion-induced corrosion. Thirdly, confinement by the W_5N_4 nanosheets limits the growth and aggregation of Ni_3N nanoparticles. Finally, the W_5N_4 nanosheets exhibit super-hydrophilicity and a remarkable water dissociation capability, and the Ni_3N NPs have an appropriate H* adsorption free energy. These merits enable the Ni_3N/W_5N_4 Janus nanostructure to have Pt-like HER performance [52].

3.2.3 Metal Phosphides

In recent years, transition metal phosphides (TMPs) have received a lot of attention as HER electrocatalysts due to their high catalytic activity, and tunable structure and composition [55–58]. Cobalt molybdenum phosphide (CoMoP), which contains three HER-active elements, is a single crystalline bimetallic substance. Usually, the process for preparing stoichiometric CoMoP materials is complicated, and fabrication of CoMoP nanocrystals is even more difficult. However, recently CoMoP nanocrystals coated with few-layer N-doped carbon shells (CoMoP@C) were recently prepared on a large scale by using a simple one-step pyrolysis method starting with a mixture of $Co_{16}Mo_{16}P_{24}$ and dicyandiamide (DCA) (Fig. 15a). Figure 15b, c contains TEM images of CoMoP@C which show that it is comprised of an assembly of CoMoP@C nanoparticles of 5–20 nm in diameter. High-resolution TEM images (Fig. 15d) of a CoMoP@C indicate that the CoMoP core is wrapped by 3-layer graphitic carbon shells that effectively prevent CoMoP aggregation or

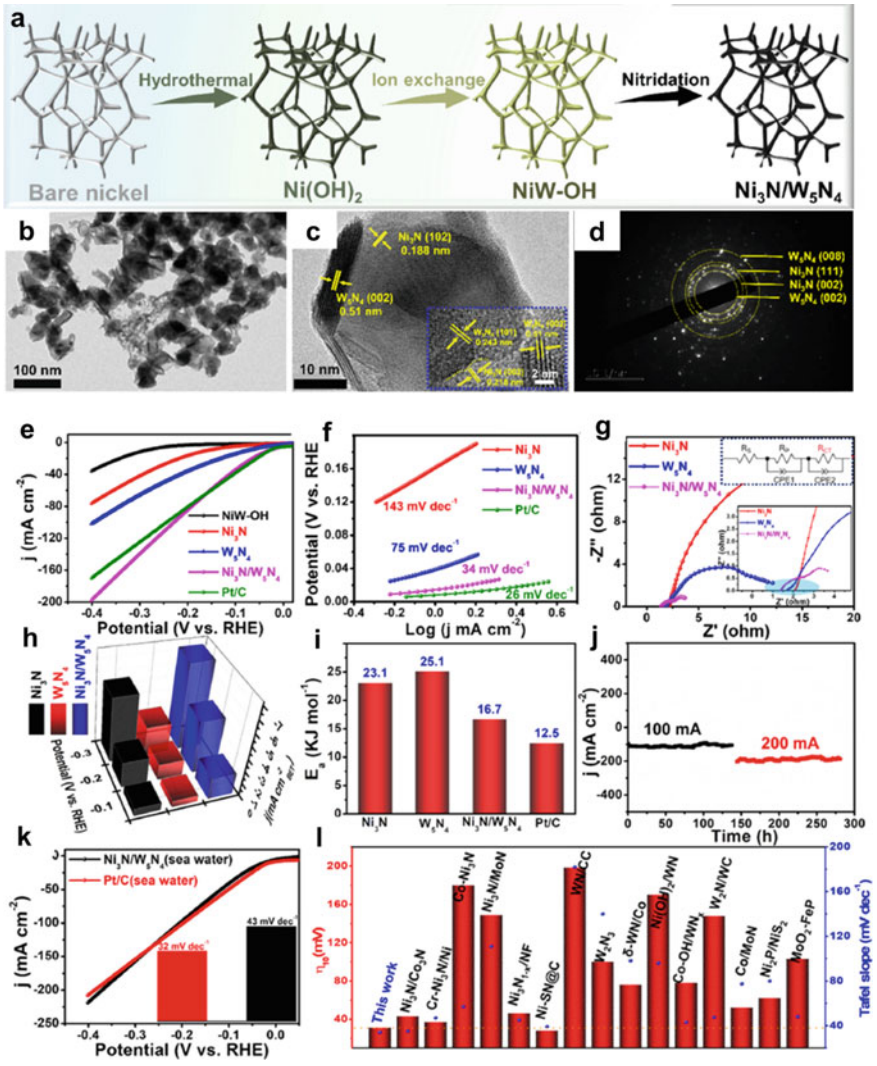

Fig. 14 **a** Schematic diagram of constructing the Ni_3N/W_5N_4 electrode with Janus nanostructures. **b** TEM image of catalysts. **c** HRTEM of Ni_3N/W_5N_4. **d** SAED pattern of this region. **e** LSV curves and **f** Tafel plots of Janus catalysts. **g** EIS of different catalysts. **h** Current density calculated. **i** Activation energies of samples. **j** I-t curves of the main sample. **k** LSV curves. **l** Comparison of overpotentials and Tafel slopes

oxidation of CoMoP nanocrystals. Also, images explore that the (112) crystal plane of orthorhombic CoMoP has a lattice stripe of 0.23 nm. Elemental mapping of CoMoP@C shows that the elements Mo,Co, P, C and N are uniformly distributed on the surface (Fig. 15e–j). In SSW, the activity of CoMoP@C does not decrease over 10 cycles, while the activities of 20% and 40% Pt/C dramatically decline during

this interval. The stability of the catalysts was evaluated by analyzing the curves of time-dependent current density, and 20% and 40% Pt/C were analyzed to evaluate the stability of the catalyst. The current density of CoMoP@C is stable for 20 h, while those of 20% and 40% Pt/C decrease. Furthermore, the HER activity of CoMoP@C is higher than that of 40% Pt/C in SSW after 12 h. However, the HER activity of the catalyst is influenced by complex components in SW (Yellow Sea, China). As illustrated in Fig. 15n, the activity of CoMoP@C distinctly decreases (<5%) during 20 cycles in SW, while those of 20% and 40% Pt/C decrease substantially. The Faradaic efficiency of CoMoP@C for the HER is 92.5% in SW (Fig. 15m). Time-dependent current density curves of CoMoP@C, and 20% and 40% Pt/C (Fig. 15o show that the current density of CoMoP@C remains stable for 10 h, while those of 20% and 40% Pt/C decrease. Also, the HER activity of CoMoP@C is higher than those of 20% and 40% Pt/C. Moreover, the current density of CoMoP NPs in SW was found to decrease by >75% after 3 h, likely a consequence of corrosion and poisoning by impurities in SW. In comparison, CoMoP@C has high stability as demonstrated by the observation that the current density remains stable for 10 h in SW as a result of poisoning protection by the N-doped carbon shell in CoMoP@C. Thus, CoMoP@C is an important model for designing promising HER electrocatalysts that can be used directly in SW splitting [59].

In a recent study, it was shown that heterostructured cobalt phosphides (CoP/Co_2P) have high water splitting activity because they contain highly active Co–P and Co–Co bonds. For example, Jiang's group demonstrated that porous CoP/Co_2P heterostructures can be fabricated by calcination at temperatures of 300, 400, and 500 °C, and direct phosphorization at 350 °C (Fig. 16a). The high-resolution TEM image in Fig. 16b shows that the interplanar spacings in C400P350 are 2.14 and 2.55 Å that correspond to the (220) plane of Co_2P and (200) plane of CoP. In addition, the selected area electron diffraction (SAED) patterns are indexed to the crystal planes of Co_2P (111), Co_2P (201), and CoP (200), which further demonstrate the co-existence of CoP and Co_2P phases in the CoP/Co_2P heterostructure (Fig. 16c). Figure 16 d–f displayed a plot of the HER current density versus the electrode potential. C400P350 exhibits low overpotentials of 87, 133, and 454 mV at the current density of 10 mA cm^{-2} in acidic, alkaline, and SW media, respectively. These values are lower than those of C300P350 and C500P350. It's worth mentioning that the HER performance for C400P350 in acid and alkaline media is superior to those of most reported co-based phosphide catalysts. The stability of C400P350 was examined by using chronopotentiometric analysis. Figure16g–i shows chronopotentiometric curves, recorded at a current density of 10 mA cm^{-2}, in alkaline, acidic, and SW media. The data demonstrate that only negligible degradation of C400P350 occurs during a 24 h electrocatalytic process, indicating the high stability of the porous CoP/Co_2P heterostructure over a wide pH range. The porous heterostructure endows CoP/Co_2P with a high specific surface area and abundant active interfaces, which when combined with enhanced active sites numbers and expedited charge transfer lead to the high HER activity in acidic, alkaline, and SW media [57].

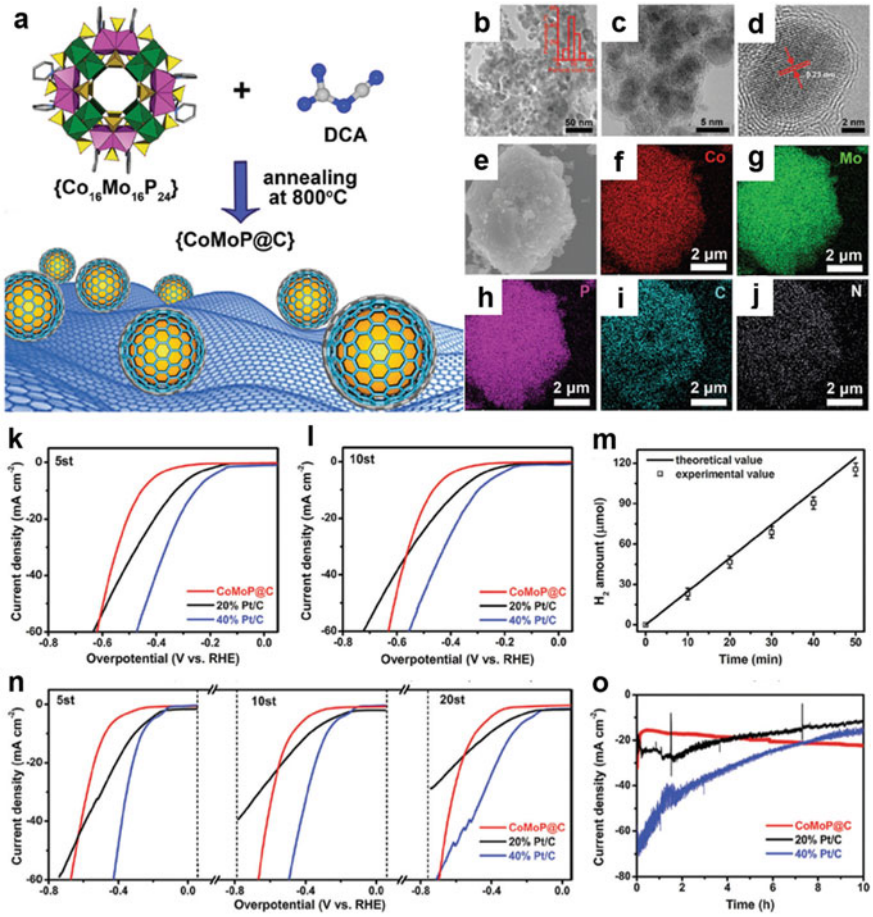

Fig. 15 **a** Diagram of the CoMoP@C catalyst. **b–d** TEM images of CoMoP@C. **e–j**HAADF-STEM and EDS mapping of CoMoP@C. **k**, **l** LSV curves of all samples. **m** FEs of CoMoP@C. **n** LSV curves of CoMoP@C. **o** I-t curve of all samples

3.2.4 Metal Chalcogenides

The use of metal chalcogenides as HER catalysts has attracted recent interest. Exploration of these materials began with theoretical and experimental studies by Nørskov et al. and Chorkendorff et al., which demonstrated that the widely used industrial catalyst for hydrodesulfurization of petroleum, is an efficient electrocatalyst for the HER in acidic media. The HER activity of MoS_2 is the result of an exposed edge surface that optimizes H* adsorption, whereas its (0001) basal planes are nearly inactive. This information motivated efforts to prepare MoS_2 nanostructures, including amorphous MoS_2, crystalline MoS_2, MoS_2-based hybrid materials, interlayer spacing expanded

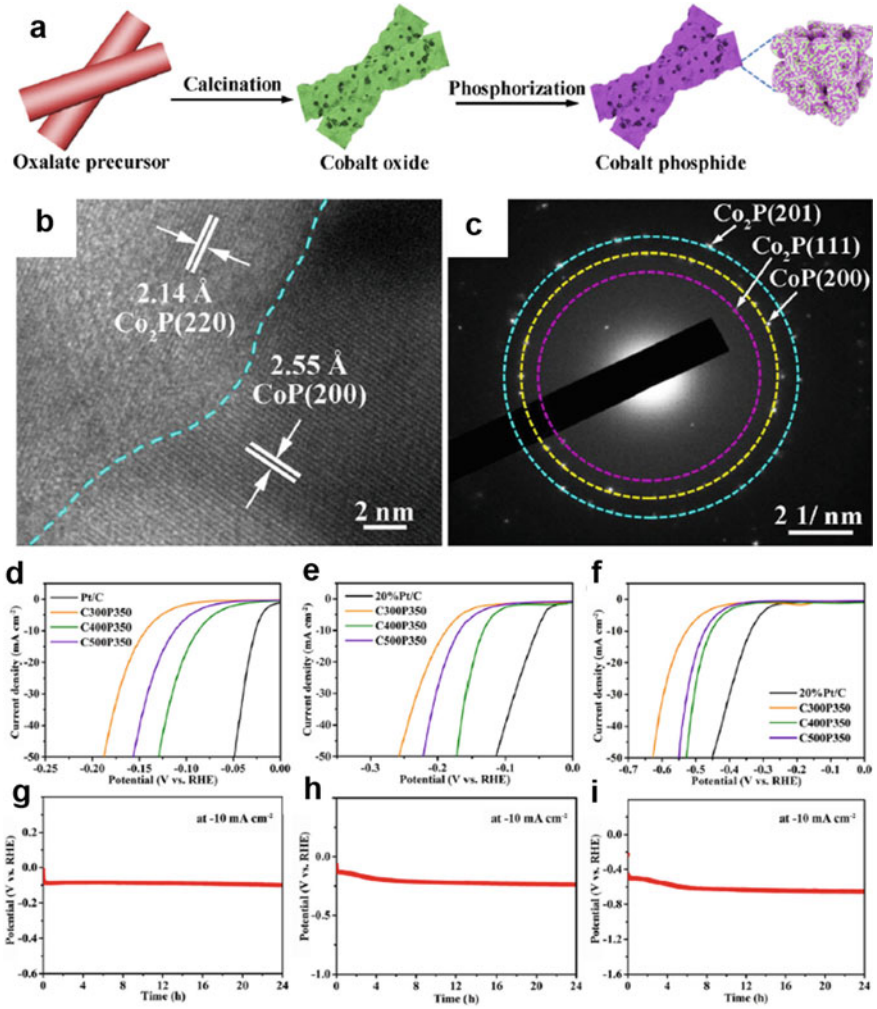

Fig. 16 **a** Diagram for CoP/Co_2P heterostructures. **b** High-magnification TEM images and **c** SAED pattern of C400P350. LSV curves in **d** 0.5 M H_2SO_4, **e** 1.0 M KOH, and **f** simulated SW. Chronopotentiometry curve with C400P350 as the HER catalyst in **g** 0.5 M H_2SO_4, **h** 1.0 M KOH and **i** simulated SW

MoS_2 structures, and structural mimics that have a large amount of maximally exposed edge sites [60].

In one investigation, Sun's group demonstrated that the core-shell rod-like material Cu_2S@Ni, having Cu_2S as the core and Ni as a shell on copper foam, promotes the HER in alkaline SW. The three-step synthesis of Cu_2S@Ni nanorod arrays begins with coating Cu foam with highly dense $Cu(OH)_2$ nanorods by using a simple strategy involving solution immersion ($Cu + S_2O_8^{2-} + 4OH^- + 2NH_4^+ \rightarrow Cu(OH)_2$

$+ 2SO_4^{2-} + 2NH_3 + 2H_2O$) (Fig. 17a). Next, the $Cu(OH)_2$ nanorod arrays are converted to Cu_2S by sulfurization using a Na_2S solution. Finally, the Ni layer, the active component in hydrogen evolution, is electrodeposited on the Cu_2S nanorod surface. The high-resolution TEM image shown in Fig. 17b, c shows the existence of a lattice fringe of 0.203 nm that is indexed to the (111) lattice plane of Ni. As shown in Fig. 17d, Cu and S atoms are concentrated in the middle of the nanorod, and those of Ni is located at the edge of the nanorod, which is consistent with the results of SEM and high-resolution TEM imaging. These features indicate that Cu_2S@Ni core-shell nanorods exist on the Cu foam surface. The nanorod array structure of Cu_2S@Ni not only modulates the reactivity of surface nickel through strong Ni–S interactions, but also creates active sites for catalytic HER. Density flooding theory (DFT) calculations show that the Ni–S interaction reduces the energy of hydrogen adsorbed on the nickel surface in Cu_2S@Ni, thereby increasing the HER activity. Due to their unique structure and interfacial modulation, Cu_2S@Ni nanorods have a high HER current density of ~500 $mAcm^{-2}$ [61].

Two-dimensional materials such as transition-metal dichalcogenides have drawn significant attention in various areas of materials science, such as energy generation and storage. Molybdenum disulfide (MoS_2) thin sheets have gained interest as a nonprecious HER electrocatalyst. However, the basal planes of MoS_2 are electrocatalytically inert. Therefore, MoS_2 thin sheets with reduced size and few layers should have better electrocatalytic performance because of the existence of abundant exposed sulfur edge sites. In this regard, Chen' group developed an environmentally sustainable method to fabricate a three-dimensional (3D) MoS_2 aerogel using a one-pot hydrothermal process. Figure18a shows a digital image of the lightweighted MoS_2 aerogel sample. Typical field emission scanning electron microscopy images of the MoS_2 aerogel show that it contains interconnected 3D porous networks with various uniform micropores of several micrometer diameters (Fig. 18b, c). The porous networks should enhance mass transfer and reduce the transportation of the electrolyte at the cathode. EDS-mapping analysis of the MoS_2 aerogel hybrid sample shows that it has a homogeneous distribution of C, Mo, and S (Fig. 18d–f), further confirming that agar is evenly anchored on the surface of MoS_2 thin sheets. As shown in Fig. 18g–n, the MoS_2 aerogel has an ultralow overpotential of 53 mV at a current density of 7 mA/g, a Tafel slope of 41 mV/dec, and stability for over 100 h in 0.5 M H_2SO_4. Moreover, the hydrothermal 3D MoS_2 aerogel has a HER performance that is superior to that of commercial Pt under neutral and alkaline conditions at a high overpotential. In SW, the hydrothermal 3D MoS_2 aerogel has an HER performance that is stable during 150 cycles, while the HER activity of commercial Pt dramatically decreases after 50 cycles. This effort has led to a significant breakthrough in developing nonprecious metal electrocatalyst systems for the HER [60].

3.2.5 Other Compounds

Over the past decade, various non-noble transition metal phosphides, nitrides, carbides, borides, and chalcogenides have been developed as electrocatalysts for the

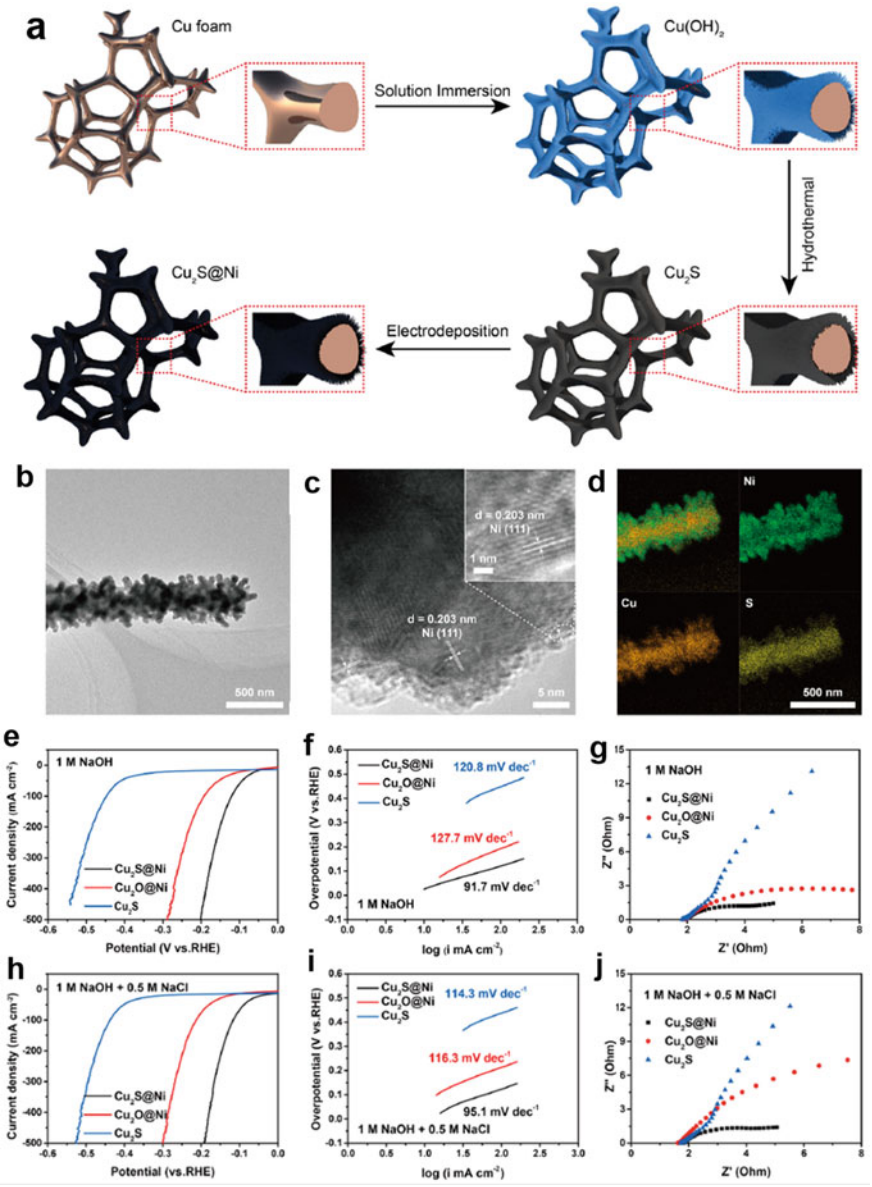

Fig. 17 **a** Synthetic illustration of Cu_2S@Ni nanorods. **b**, **c** TEM images of Cu_2S@Ni. **d** STEM-EDS of Cu_2S@Ni. **e**, **h** LSV curves of all samples. **f**, **i** Tafel plots of all samples. **g**, **j** EIS of all samples

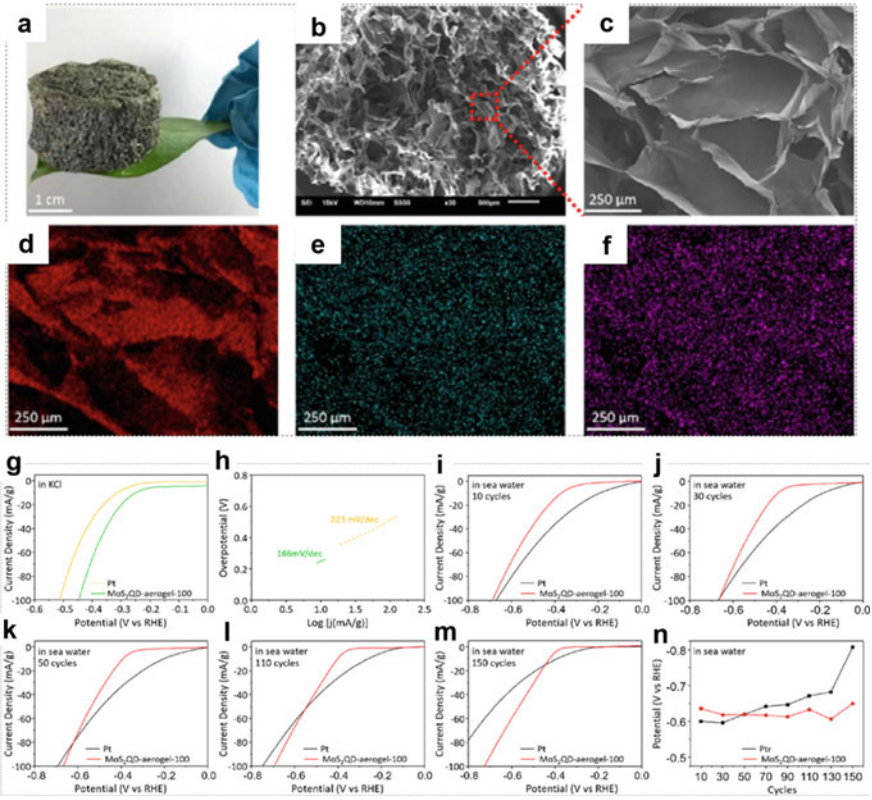

Fig. 18 **a** Photograph of the MoS_2 aerogel. **b**, **c** FESEM images of the MoS_2 aerogel. The elemental mapping images of **d** C, **e** Mo, and **f** S. **g** LSV curves and **h** Tafel slope of the MoS_2QD-aerogel-100 aerogel and Pt in neutral electrolyte. **i**–**m** LSV curves of the MoS_2QD-aerogel-100 aerogel and Pt in real SW. **n** Potential of the MoS_2QD-aerogel-100 aerogel and Pt in real SW at different cycles

HER. Several of these catalyst types have an activity close to or even exceeding that of the benchmark platinum. However, most newly developed catalysts only perform well in acidic or alkaline electrolytes and not in neutral media. Due to the environmental impact and expense of using acidic or alkaline electrolytes and the fact that most natural water sources (e.g., wastewater and SW) are neutral, uncovering electrocatalysts that generate H_2 under neutral conditions is an important goal. Thus, a large effort has been devoted to designing efficient catalysts for the HER in neutral media [48, 51, 62, 63].

Ren's group found that conductive nickel phosphide (Ni_xP) micro sheets coated on both sides with NiCoN nanoparticles in the form of sandwich-like nanostructures (NiCoN|Ni_xP|NiCoN) are electrically conductive and are good HER catalysts. Among the features causing enhanced activity is the high conductivity of both the NiCoN and Ni_xP. This allows for efficient charge transfer between the catalyst

surface and SW electrolyte, thereby enhancing HER kinetics. In addition, the three-dimensional (3D) hierarchical sandwich-like microsheet arrays have a high surface area and an abundance of active sites. Finally, the high corrosion-resistant arrays act as a stable backbone and the corrosion-resistant NiCoN nanoparticles act as strong protectors. The fabrication process of NiCoN|Ni_xP|NiCoN, shown in Fig. 19a, starts with the growth of Ni_xP microsheets by direct phosphorylation of commercial nickel foam. In this step, not only was a sandwich-like structure of the internal framework of the conductive Ni_xP produced, but also the corrosion resistance of the Ni foam was improved due to the metal phosphide being more stable in SW. The Ni_xP microsheet array covered Ni foam is then soaked in a solution of NiCo, dried under ambient conditions, and subjected to thermal nitridation to produce NiCoN nanoparticles. The three-dimensional porous skeleton of nickel foam maintains its integrity during high-temperature phosphorization, and the surface is evenly distributed and covered by perpendicularly aligned microsheet arrays (Fig. 19b, c). The transmission electron microscope (TEM) image in Fig. 19d shows that the Ni_xP microsheets have smooth surfaces, and the corresponding high-resolution TEM (HRTEM) image in Fig. 19e shows the existence of lattice fringes with an interplanar spacing of 0.29 nm, which are associated with the (200) plane of Ni_5P_4. The high magnification SEM image shown in Fig. 19g clearly demonstrates that the sides of the microflakes are homogeneously coated with a large number of nanoparticles, forming a three-dimensional layered sandwich-like nanostructure that exposes the active sites. In addition, the microflakes are interconnected to produce microvoids and highly porous structures with varying porosity. These properties facilitate SW electrolyte diffusion and bubble release. Figure 19h shows a TEM image of a single NiCoN|Ni_xP|NiCoN microsheet. This image shows that the material has a dense surface of attached nanoparticles. The HRTEM image in Fig. 19i shows the presence of lattice stripes with a planar spacing of 0.22 nm in the NiCoN|Ni_xP|NiCoN (002) plane. The scanning TEM (STEM) images of Ni, P, Co, and N and corresponding EDX elemental mapping images shown in Fig. 19j confirm that the material has a nanoparticle-modified microsheet structure and contains a homogeneous distribution of the four elements in sandwich-like microsheets.

Analysis of the polarization curve for the HER promoted by NiCoN|Ni_xP|NiCoN and those of Ni foam, Ni_xP, NiCoN, and Pt/C (Fig. 19k) shows that Ni_xP foam is more active than Ni foam, which has only an insignificant activity. NiCoN|Ni_xP|NiCoN catalyst has a much higher activity than those of Ni_xP and NiCoN. Pt/C exhibits the lowest overpotential of 90 mV (Fig. 19l). The NiCoN|Ni_xP|NiCoN also has the lowest Tafel slope of 139.2 mV dec^{-1} (Fig. 19m). As shown in Fig. 19n, NiCoN|Ni_xP|NiCoN also outperforms other TMs catalysts in the HER in natural SW and PBS electrolytes. The time-dependent overpotential curves (Fig. 19o) show that overpotentials at 10 mA cm^{-2} of all three Ni-based catalysts remain essentially stable with little increase occurring during long-term HER processes in SW. Compared with those of NixP and NiCoN, the stability curve of NiCoN|Ni_xP|NiCoN does not contain any fluctuations, which is a result of the 3D hierarchical sandwich-like nanostructure that enables the rapid release of gas bubbles. In summary, the large surface area and abundance of active sites in the 3D sandwich-like nanostructures, along with the improved

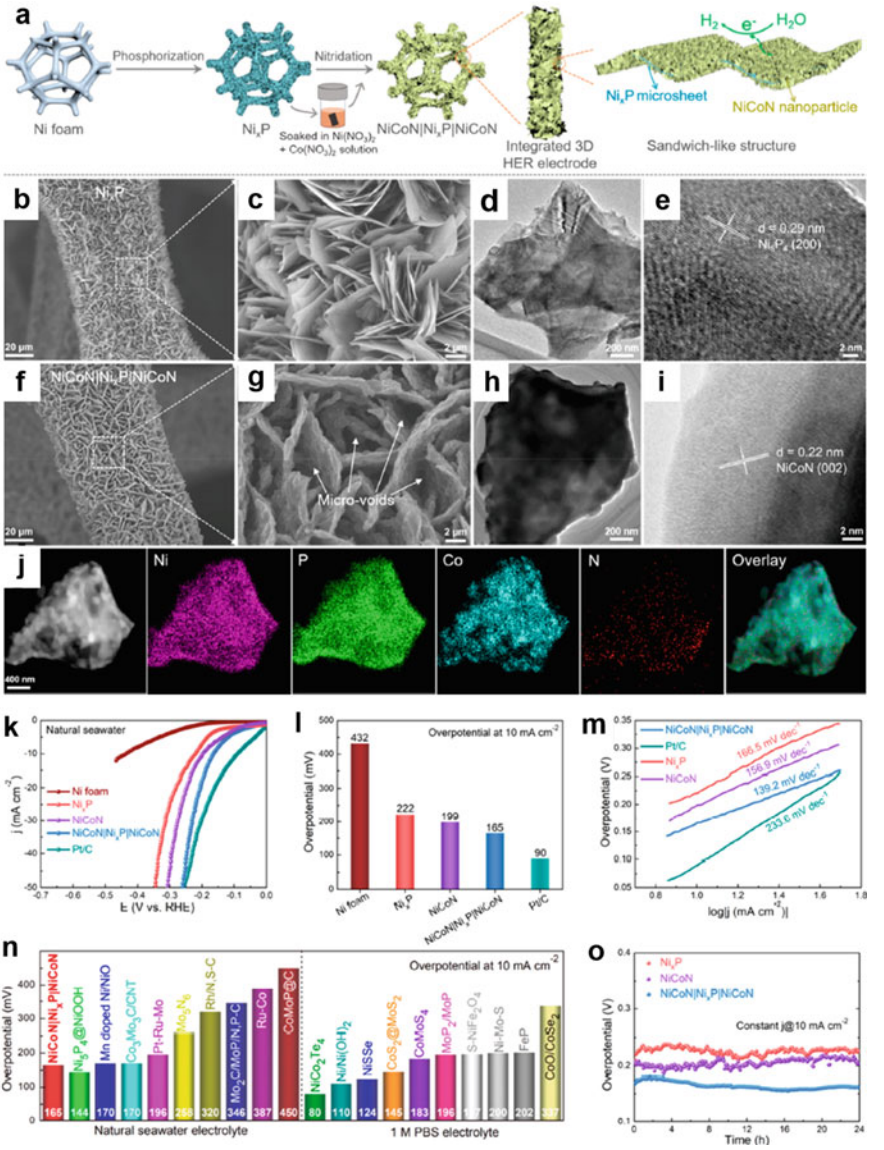

Fig. 19 **a** Diagram of the catalyst. **b**, **c** SEM, **d** TEM, and **e** HRTEM images of Ni_xP microsheet arrays. **f**, **g** SEM, **h** TEM, **i** HRTEM, and **j** STEM images and EDS of samples. **k** LSV curves, **l** overpotential, and **m** Tafel plots of all samples. **n** overpotential of the main sample and other reported HER catalysts. **o** I-t curves

intrinsic activity of active sites and efficient charge transfer ability arising from the high conductivities of Ni_xP and NiCoN, combine to give NiCoN|Ni_xP|NiCoN enhanced HER activity Also, the stability of this catalyst is a consequence of the corrosion resistance of the Ni_xP skeleton and the presence of anticorrosive NiCoN nanoparticles [64].

4 Materials Used for OER in SW

The anodic OER is a complex four-electron process that requires a significantly high η value of more than 300 mV in alkaline media even when the best electrocatalysts are utilized. To understand the nature of OER active sites and, thus, to design more active OER catalysts, an enormous effort has been made to correlate OER activity with parameters such as metal-OH (M–OH) bond energies, numbers of d-electrons, electron occupancies, and adsorption free energies ($\Delta G_O - \Delta G_{OH}$). These studies have resulted in the development of various types of catalysts that promote efficient OERs in alkaline electrolytes, including metal oxides/(oxy)hydroxides, metal nitrides, and metal chalcogenides.

4.1 Metal Oxides or (Oxy)hydroxides

The basic principle guiding the design of electrocatalysts that have enhanced efficiencies and selectivities for the OER is maximizing –OOH formation and minimizing formation of –OCl on the surface which diminishes the active chlorine species formation reaction (ACSFR). The generation of –OOH intermediates on surfaces of metal oxides can be enhanced by doping with metals having lower numbers of d-electrons than the host cation, while the formation of –OCl on the electrocatalyst can be minimized by performing the process in high pH media (pH > 6.0). Oxygen vacancies in the electrocatalyst lattice have also been shown to promote OER.

As early as 1955, Rüetschi and Delahay developed a correlation between the OER activity of electrocatalysts with M–OH bond energies. These workers found that η decreases in an approximately linear manner with increasing M–OH bond energies [65]. Later, Trasatti proposed that the enthalpy change associated with the transition of the metal from a lower to a higher oxidation state is a good parameter to judge OER efficiencies [66]. Specifically, it was demonstrated that RuO_2 and IrO_2, which have the lowest η values, are located at the top of a volcano-type curve. The experimentally derived relationship suggests that metal oxides that are difficult or readily oxidized are poor catalysts because their affinities for oxygen are either too weak or too strong, respectively.

In one investigation of metal oxide electrocatalysts, Ramani synthesized the oxygen vacancy-rich material $Pb_2Ru_2O_7$–x and compared its performance in the OER in neutral and alkaline SW with that of the benchmark catalyst RuO_2. The

study showed that $Pb_2Ru_2O_7$-x is more highly OER selective, active, and stable in alkaline SSW than in neutral SSW, and that RuO_2 has much lower OER selectivity, activity, and stability under both alkaline and neutral simulated SW conditions. The presence of the higher oxidation state Ru(V) at the surface and a large number of oxygen vacancies in $Pb_2Ru_2O_7$-x are responsible for the high OER selectivity and activity. Additionally, alkaline conditions suppress chlorine oxidation on the electrocatalyst surface especially when higher pH media (pH > 6.0) are used. No metal dissolution occurs with $Pb_2Ru_2O_7$-x under alkaline conditions (to the limit of ICP-OES) [67]. More importantly, –OOH intermediates on the surface metal oxides (e.g., RuO_2) are stabilized by doping with metals that have lower energy d-electrons than the host cation.

Sem images obtained in studies by Parrondo et al. show that pyrochlore structures of Pb and Ru can be generated using a modification of a wet chemical synthesis method under alkaline conditions. The particle sizes of spherically shaped pristine $Pb_2Ru_2O_{7-x}$ produced in this manner are in the range of 70–140 nm (Fig. 20a). The X-ray diffraction (XRD) spectrum (Fig. 20b) of synthesized $Pb_2Ru_2O_{7-x}$ contains peaks that match those of the pyrochlore phase (PDF, 00-002-1365; space group, Fd3m) of $Pb_2Ru_2O_7$ and no additional peaks corresponding to segregated Ru- and Pb-oxide or their mixed oxides are present. Because a large mismatch exists between the ionic sizes of Pb- and Ru-ions ($R_{Pb}/R_{Ru} > 1.5$), the probability that solid solutions or doped oxides are formed is low. Rietveld refinement of the XRD peaks of $Pb_2Ru_2O_{7-x}$ shows that the lattice constants are $a = b = c = 10.325$ Å, which is in good agreement with the reported values (Fig. 20c). $Pb_2Ru_2O_{7-x}$ has structural oxygen defects originating from a charge imbalance between Pb(II/IV) and Ru(IV/V). Because the standard potential difference between the OER and ACSFR increases with increasing pH, electrolysis promoted by $Pb_2Ru_2O_{7-x}$ was performed in alkaline SSW (0.6 M NaCl + 0.1 M NaOH). A 60-fold activity increase (1.57 V vs. RHE) and a reduction of 0.3 V for $\eta_j = 10$ were observed for the OER in alkaline simulated SW in comparison to neutral SSW (Fig. 20d). The current density using RuO_2 for alkaline SSW electrolysis is lower than it is in the process conducted in neutral media. A decrease in activity with an increase in pH on RuO_2 surface has been previously observed. At 10 mA/cm^2 for 2 h using a rotating disk electrode (RDE), $Pb_2Ru_2O_{7-x}$ does not undergo a potential drop at pH = 13 as compared to a 0.12 V change occurring at pH = 7 (Fig. 20e).

Wang devised a quenching method that induces Fe doping and vacancy generation on catalyst surfaces and found that doping effectively enhances the OER performance of $NiCo_2O_4$ nanowires. In the process used to prepare $NiCo_2O_4$@CC containing different metal ratios, hydrothermally synthesized NiCo–OH@CC is heated and then rapidly quenched by adding it to $FeSO_4$ solutions of different concentrations (Fig. 21a). The needle-like structures of the NiCo–OH@CC are assembled into nanoflower clusters that tightly and evenly cover the entire carbon cloth (Fig. 21b, c). A comparison of NiCo–OH@CC with 0.5Fe–$NiCo_2O_4$@CC formed by Fe doping shows that morphology is retained during the quenching process (Fig. 21d, e). Detailed structural information was obtained using TEM (Fig. 21f, g). The results of SEM imaging show that the surface of 0.5Fe–$NiCo_2O_4$@CC is no longer smooth

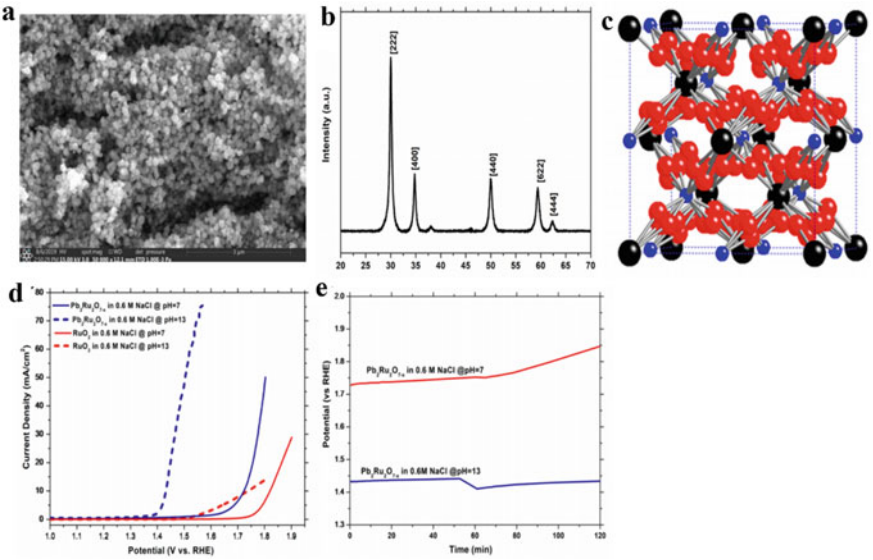

Fig. 20 **a** SEM images of $Pb_2Ru_2O_{7-x}$ samples. **b** XRD and **c** crystal structure of $Pb_2Ru_2O_7$-x. **d** LSV curves of $Pb_2Ru_2O_{7-x}$ and RuO_2. **e** U-t curves for $Pb_2Ru_2O_{7-x}$

and flat but rather it is porous and composed of numerous nanoparticles. The performance of 0.5Fe–$NiCo_2O_4$@CC in 1 M KOHis close to that in alkaline SSW, indicating that selective OER occurs in alkaline conditions (Fig. 21 h, i). In contrast, 0.5Fe–$NiCo_2O_4$@CC decays in neutral SW resulting in some active sites becoming buried. This observation matches one made in a previous investigation. The corresponding Tafel slope and charge transfer resistance of 0.5Fe–$NiCo_2O_4$@CC are both smaller than those of unquenched NiCo–OH@CC (Fig. 21k), suggesting that doping increases electron transport and conductivity (Fig. 21j). As expected, 0.5Fe–$NiCo_2O_4$@CC also exhibits a greatly enhanced ECSA (Fig. 21l) compared to that of NiCo–OH@CC. In addition, although has lower stability in SW than in alkaline freshwater, this catalyst retains a higher current density after long-term (20 h) operation than does that of the undoped catalyst (Fig. 21m). The combined results show that quenching brought about by rapid cooling from high temperature is a unique process for performing metal doping and surface vacancy generation. These alterations change the local electronic structure and coordination environment at or near the surface of $NiCo_2O_4$, which enables it to serve as an efficient OER electrocatalyst in both alkaline freshwater and SW [68].

Strasser et al. described the synthesis of NiFe LDH, which has a hexagonal nanoplate-like morphology that is typical of highly crystalline LDH materials (Fig. 22a, b). Reflections in the XRD spectrum of this material are assigned to a hydrotalcite structure (Fig. 22c), which is again typical of crystalline LDHs. The solvothermal synthesized NiFe LDH has high crystalline order, with narrow and well-defined reflections. The main peak in the spectrum at a 2q angle of 11.38,

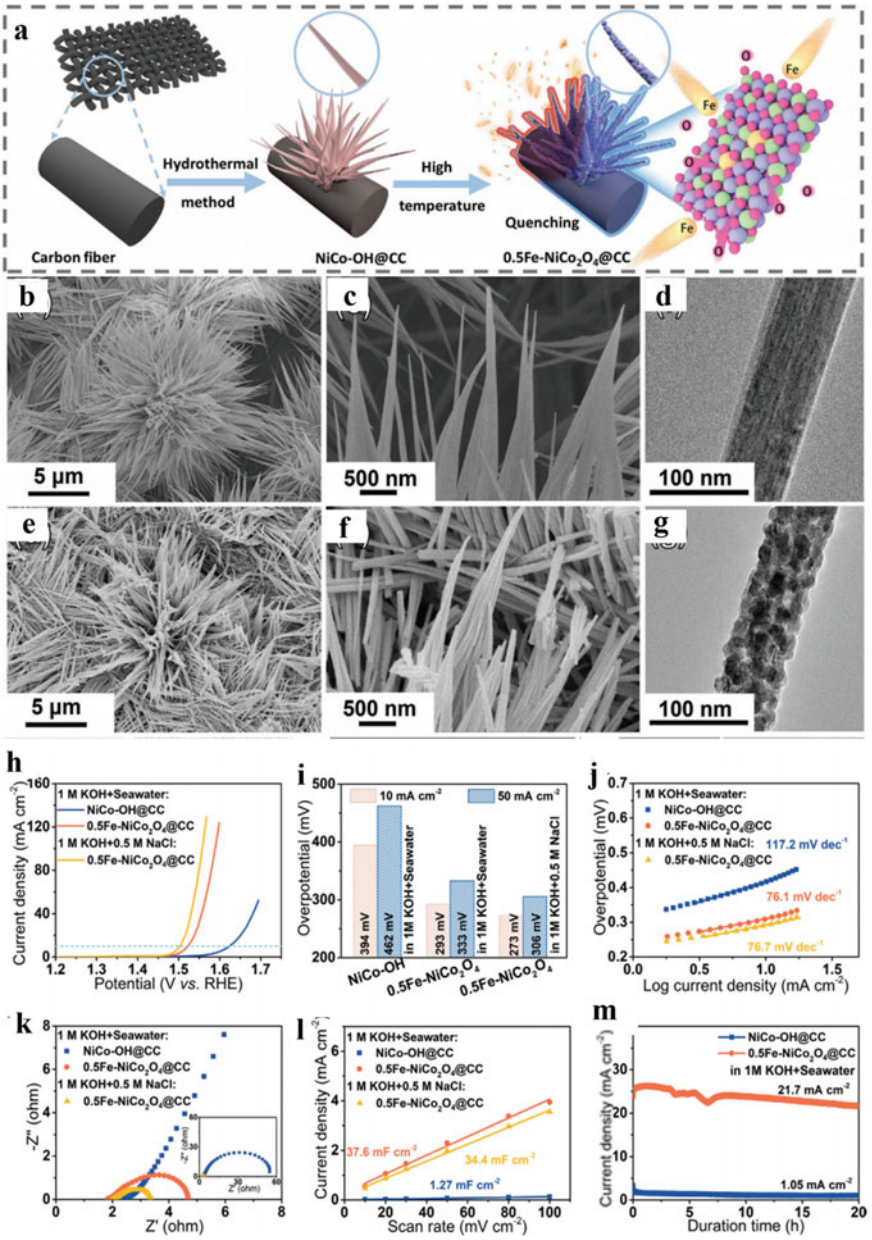

Fig. 21 **a** Schematic diagram of $NiCo_2O_4$@CC. SEM images of **b**, **c** NiCo–OH@CC and **d**, **e** 0.5Fe–$NiCo_2O_4$@CC. TEM images of **f** NiCo–OH (powder) and **g** 0.5Fe–$NiCo_2O_4$ (powder). **h** OER LSV curves of NiCo–OH@CC and 0.5Fe–$NiCo_2O_4$@CC catalyst. **i** Comparison of the overpotentials. **j** Tafel plots. **k** Nyquist plots, **l** double-layer capacitance (Cdl) plots, and **m** long-term stability evaluation of NiCo–OH@CC and 0.5Fe–$NiCo_2O_4$@CC over 20 h under a voltage of 1.55 V using the chronoamperometry method without iR corrections

labeled using Miller indexes (003), corresponds to diffraction from planes along the stacking direction. Therefore, the d-spacing of 7.8 nm, corresponding to the distance between the LDH layers, is comparable with that of NiFe LDH containing intercalated carbonate anions. The crystallite size obtained from the (003) peak width could be used to grossly estimate the nanoplate thickness, under the exclusion of vertically stacked multicrystalline domains. In this case, the Scherrer equation estimates a crystalline size of 15 ± 1 nm. Layers of edge sharing $[NiO_6]/[FeO_6]$ octahedra stacks exist along the c-axis in the crystal of NiFe LDH, along with OH groups on both sides, water and charge balancing anions (i.e., carbonate anions) intercalated between the layers. The pH of the medium has a pronounced effect on the electrochemical water splitting performance of these catalysts (Fig. 22d). Both the redox wave and OER occur at more positive potentials (vs. RHE) when the pH is lowered, and the OER overpotential increases ~110 mV (vs. RHE) at 1 mA cm^{-2}. Also, the difference between the potential between the redox peak maximum (for anodic) and minimum (for cathodic) increases as the pH is lowered. Specifically, the difference for the 50th cycle in the RHE scale is 119 ± 9 mV for pH 13 and 183 ± 10 mV for pH 9.2. These observations suggest that the reversibility of the nickel redox couple increases at lower pH. Finally, the data show that the area of the peak at pH 13 is larger than that at pH 9.2, which is consistent with greater accessibility to the reduced Ni. The overpotentials at 10 mA cm^{-2} and the Tafel slopes obtained from LSV experiments with chloride-free and chloride-containing electrolytes are given in Fig. 22e, f. The experimentally determined TOF in 0.1 M KOH an overpotential of 300 mV is ~0.03 s^{-1} [69].

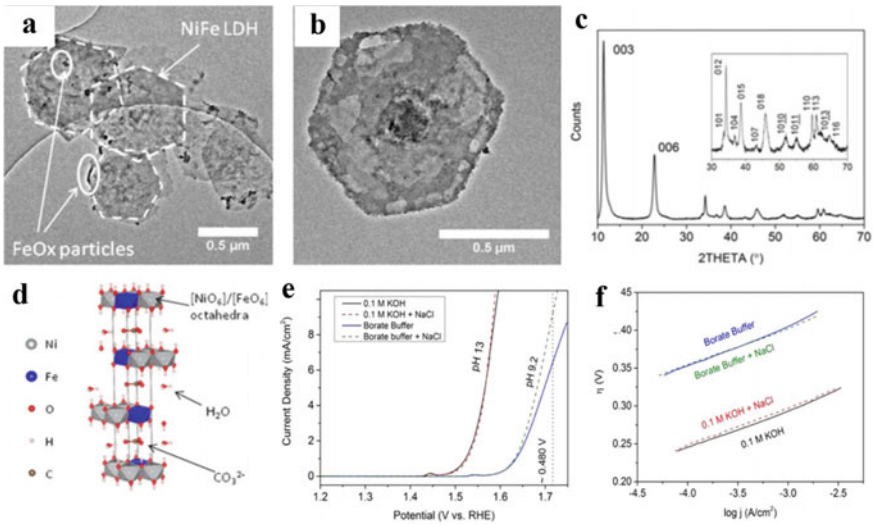

Fig. 22 **a**, **b** TEM images of sample. **c** XRD pattern and **d** Structure model of NiFe LDH. **e** LSV curves. **f** Corresponding Tafel plots

Choi et al. present the description of the development of a nickel-doped FeOOH as a highly efficient anion exchange membrane anode for alkaline SW electrolysis. (Fig. 23a). The Ni-doped FeOOH OER electrode was synthesized on Ni foam by soaking Ni foam in an aqueous $Fe(NO_3)_3$ solution. As shown in Fig. 23b**,** this process generates nanosheets that are uniformly distributed on the Ni foam surface which can be seen by using TEM (Fig. 23c). Selected area electron diffraction (SAED) patterns of the nanosheets contain diffraction bands indexed to the (021) and (002) planes (Fig. 23d). The X-ray diffraction (XRD) pattern of the electrode shows diffraction peaks (Fig. 23e), which are indexed to (110), (130), (021), (111), (121), and (140), respectively. The electrocatalytic OER activities of Ni-doped FeOOH in natural SW (Changwon, Republic of Korea) containing different electrolytes were determined. OER performances (Fig. 23f) in various media are in the following order: 1.0 M KOH > 1.0 M KOH + 0.5 M NaCl > 1.0 M KOH + SW. In contrast, the OER activities captured using iR uncorrected LSV follow a different tendency, with the highest performance being in 1.0 M KOH + 0.5 M NaCl (Fig. 23g). A comparison of catalytic activities at a current density of 100 mA cm^{-2} obtained from iR uncorrected/corrected LSV curves suggests that the difference may be related to the electrolyte conductivity (Fig. 23h). For example, compared to the 1.0 M KOH electrolyte, the one comprised of 1.0 M KOH + 0.5 M NaCl has a higher ionic conductivity. Thus, the OER performance of the uncorrected LSV curves is reversed in electrolytes containing 1.0 M KOH and 1.0 M KOH + 0.5 M NaCl. In addition, the pH of the 1.0 M KOH SW electrolyte was adjusted by the addition of 1.0 M KOH, resulting in the formation of precipitates such as Ca(OH)2 and Mg(OH)2 as by-products. Double layer capacitances (C_{dl}) in relation to the electrochemically active surface area were almost identical (9.4 mF), regardless of the electrolyte used (Fig. 23i). Thus, the observations suggest that the consumption of OH anions in 1.0 M KOH + SW leads to a decrease in OER performance. In addition, Ni-doped FeOOH is stable at 100 mA cm^{-2} for 80 h in all electrolytes (Fig. 23j), as reflected in the observation that 93% of the initial performance is maintained after the electrolytic process. Because the super-hydrophilicity of Ni-doped FeOOH leads to the efficient removal of generated oxygen, the cell voltage is retained due to the minimal mass transfer resistance in the AEM electrolyzer. AEM electrolyzers with nickel-doped FeOOH anodes in 1.0 M KOH + SW exhibit higher performance compared to reported AEM electrolyzers operating in 1.0 M KOH. [70]

4.2 Metal Nitrides

Practical electrolysis of SW requires the use of robust and efficient electrocatalysts that resist chloride corrosion, especially at the anode. The bottleneck that hinders the SW splitting process progress is the insoluble precipitate formation on the electrode surface, such as magnesium hydroxide, which is hazardous to the OER and

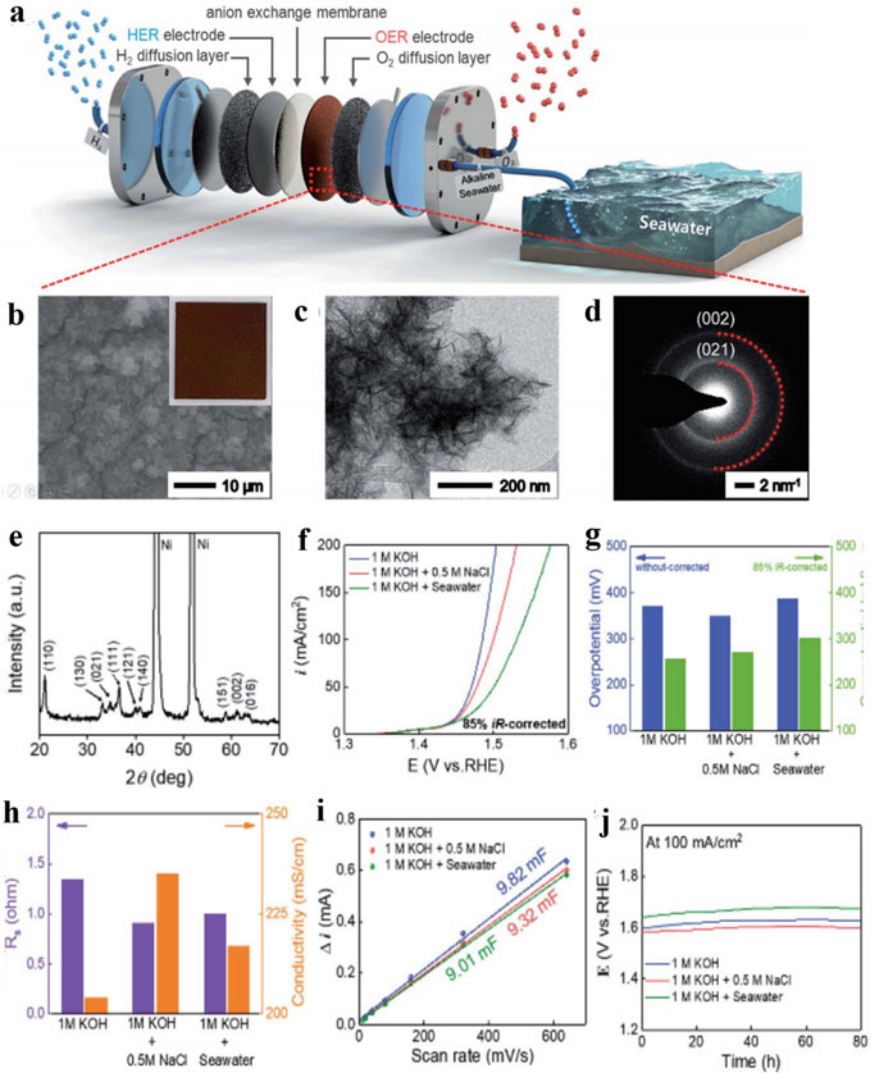

Fig. 23 **a** Diagram of hydrogen production. **b** SEM, **c** TEM, **d** SAED pattern, and **e** XRD patterns of Ni-doped FeOOH. **f** LSV curves of the samples. **g** Comparison of overpotential. **h** Comparison of Rs and electrolyte conductivity. **i** Double layer capacitance and **i** U-t curves of samples

HER catalysts. Transition metal nitrides (TMN) are highly corrosion-resistant, electrically conductive, and mechanically strong, making them interesting electrocatalysts for SW splitting. Recent studies have shown that the trimetallic nitride catalysts Ni_3N/Ni, NiMoN, and Ni–Fe–Mo are efficient non-noble metal electrocatalysts for splitting alkaline (1 M KOH) fresh water. For example, Ren's group developed

the heterostructured material NiMoN@NiFeN and employed it as an electrocatalyst for SW splitting. Interestingly, large surface area, high porosity, and strong synergistic effect between NiMoN and NiFeN greatly enhance the production and release of H_2 and O_2 in this system. The metal nitride NiMoN was synthesized by first generating $NiMoO_4$ nanorods on Ni foam in a tube furnace (Fig. 24a). SEM images reveal a large number of smooth surface nanorods uniformly distributed vertically on the surface of Ni foam (Fig. 24b). Soaking $NiMoO_4$ in the precursor ink containing $Fe(NO_3)_3$ and $Ni(NO_3)_2$ followed by thermal nitridation produces NiMoN@NiFeN nanorod morphology with rough and dense surfaces (Fig. 24c, d). The high-magnification SEM image clearly shows that the surfaces of the nanorods are uniformly coated with nanoparticles in the form of a unique 3D core-shell nanostructure that has an extremely large surface area and large numbers of active sites. The selected area electron diffraction (SAED) pattern of the NiMoN@NiFeN core-shell nanorods contains diffraction rings corresponding to NiMoN and NiFeN, confirming that a metal nitride phase has been produced (Fig. 24e). Also XRD patterns show that the material produced using thermal nitridation contains NiMoN and NiFeN (Fig. 24f). XPS survey spectra displayed in Fig. 24g demonstrate the presence of Ni, Mo, and N elements in NiMoN nanorods, Ni, Fe, and N in NiFeN nanoparticles, and Ni, Mo, Fe, and N in the core-shell NiMoN@NiFeN nanorods. These values are considerably smaller than those of NiFeN (348 and 417 mV), NiMoN (350 and 458 mV) and the benchmark IrO_2 electrode (430 and 542 mV) (Fig. 24h). Furthermore, NiMoN@NiFeN has a Tafel slope of 58.6 mV dec^{-1} that is lower than those of NiFeN (68.9 mV dec^{-1}), NiMoN (82.1 mV dec^{-1}), and IrO_2 electrodes (86.7 mV dec^{-1}), (Fig. 24i). The TOF value of 0.09 s^{-1} at an overpotential of 300 mV demonstrates the intrinsically high OER activity of the NiMoN@NiFeN catalyst. Impressively, 3D core-shell NiMoN@NiFeN has high durability during the OER in 1 M KOH. Specifically, the current densities of 100 and 500 mA cm^{-2} at constant overpotentials experience only slight decreases over 48 h OER, and the CV polarization curves remain unchanged (Fig. 24j). The interior NiMoN nanorods in this catalyst are highly conductive and have a large surface area, ensuring that efficient charge transfer occurs and the existence of numerous active sites. During the OER the outer NiFeN nanoparticles in the material form thin layers of amorphous NiFe oxide and NiFe oxy(hydroxide), which are not only responsible for the ORE selectivity of this catalyst but also for the corrosion resistance caused by chloride anions in SW. Moreover, the 3D core-shell nanostructures possessing multiple levels of porosity are favorable for SW diffusion and H_2/O_2 gas release [43].

Each exposed crystal facet has distinguishable adsorption energy for the OER intermediates and, thus, they have different catalytic activities. This is exemplified in a study in which Ho and co-workers synthesized α-Fe_2O_3 nanocrystals that have three facets including (012), (104), and (110). The Fe_2O_3 nanocrystals that contain a high indexed (012) facet only require a $\eta 10$ of 317 mV in 1 M NaOH (Fig. 25), a value that is superior to 388 mV and 422 mV needed for the respective Fe_2O_3 (104) and the (110) facets. This pattern of facet-dependent electrochemical activities is well correlated with the results of DFT theoretical calculations, which show that hematite nanocrystals that predominantly contain (110) facets interact strongly with

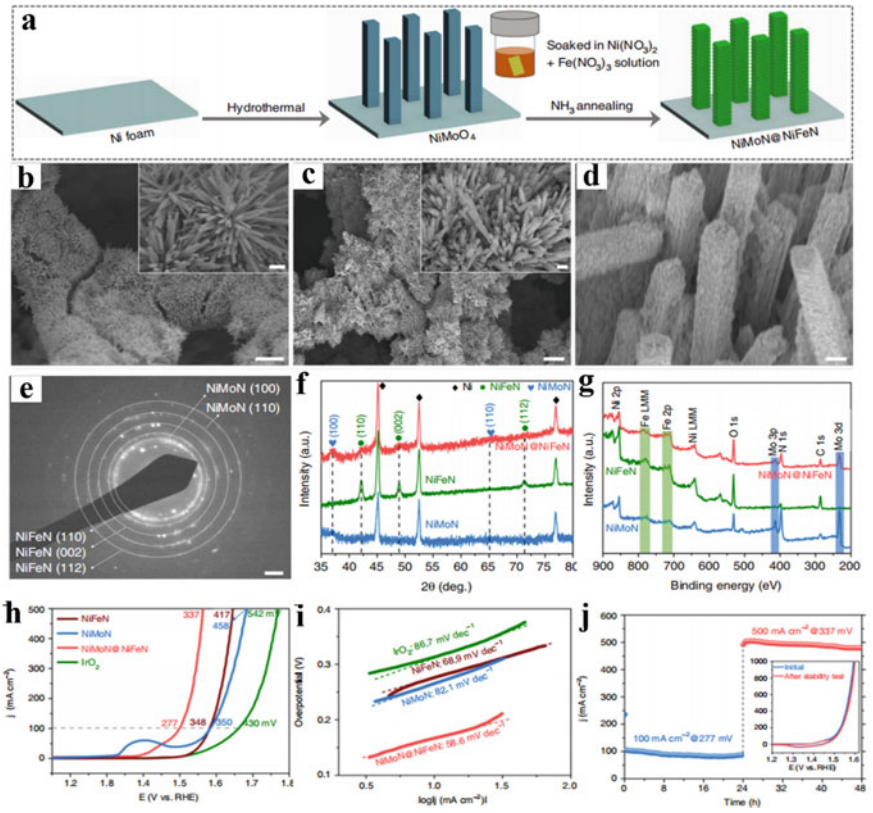

Fig. 24 **a** Synthesis diagram of samples. **b–d** SEM images. **e** SAED pattern. **f** XRD and **g** XPS survey. **h** LSV curves and **i** Tafel plots. **j** I-t curves

intermediates in the OER and the (104) facet interact only weakly with these species, which when combined result in unfavorable oxygen evolution. In contrast, Fe_2O nanocrystals having (012) facets have optimal adsorption/desorption values that lead to favorable OER catalysis. We note that, in spite of this finding, it is challenging to have precise control in generating nanocrystals with desired facets [71].

4.3 Metal Sulfides

Transition metal sulfides (TMSs) serve as versatile pre-catalysts on which surface reconstruction can be conducted to generate active TMOOH analogs that catalyze the OER in freshwater. Moreover, TMOOHs are typically self-doped by sulfur residues, which allows the multivalent coordination to sulfur to mediate the absorption of key OER intermediates and to increase electronic conductivity and chloride repulsion.

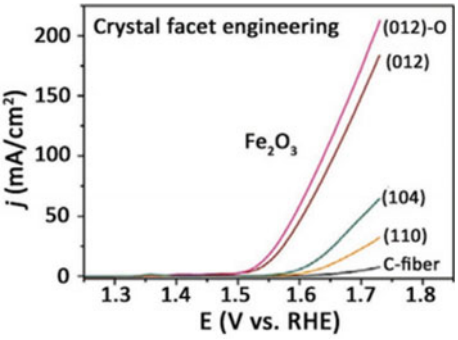

Fig. 25 Polarization curves of Fe_2O_3 with different crystal facets

Among non-PGM bifunctional catalysts, TMSs are prospective HER catalysts and pre-catalysts for the formation of oxidized surfaces to catalyze the post-hydrolysis dissociation of OER.

Yin's group described an outstanding anodic catalyst of this type for alkaline SW electrolysis. The catalyst comprises a three-dimensional standing array of heterolateral Ni_3S_2/Co_3S_4 (NiCoS) nanosheets grown homogeneously on Ni foam. The *in situ* fabricated Ni/Co (oxy) hydroxide surface layer contained a large number of active sites and excellent resistance to chloride corrosion. As illustrated in Fig. 26a–c, the commercial nickel foam (NF) has a three-dimensional (3D) macroporous structure with a smooth and clean surface. After the NiCoS nanosheets are grown, their surfaces are uniformly covered with vertically aligned nanosheet arrays forming interconnected nanowall structures with cavity sizes of 0.3–0.8 μm. The surface mesoporous layer is approximately 1.5 μm thick and is tightly rooted in the NF substrate. These vertical arrays of nanosheets expand the surface area for mass transfer and gas product release. As a result, the catalyst has a structure that favors high electrocatalytic performance. TEM images show that the surfaces of the synthesized NiCoS nanosheets have an ultra-thin texture due to their transparency to the electron beam (Fig. 26d). HRTEM images show the presence of two types of lattice stripes on the (110) face of Ni_3S_2 and the (311) face of Co3S4 with a planar spacing of 0.28 and 0.30 nm (Fig. 26e). The XRD pattern of the surface NiCoS nanosheets of this material contains diffraction peaks that are characteristic of those of Ni_3S_2 and Co_3S_4 along with signals for NF substrate (Fig. 26f). The NiCoS on Ni foam catalyst has overpotentials required to deliver current densities of 10 and 100 mA cm^{-2} of 220 and 270 mV, respectively, values that are much smaller than those of bare NF (430 and 520 mV), Ni_3S_2 (340 and 470 mV) and IrO_2 (313 and 430 mV) (Fig. 26g). Note that the anodic peak near 1.38 V in the CV forward scan of this catalyst is associated with the oxidative conversion of (NiCo)II to (NiCo)III/IV. The peak is more observable in the CV of the NiCoS catalyst than in CW of pure Ni_3S_2 or bare NF. This observation suggests that Ni–Co electronic interactions in NiCoS nanosheets lead to an increase in the number of high-valence metal active sites for the OER. NiCoS has a smaller Tafel slope of 42 mV dec^{-1} in contrast to those of bare NF

(88 mV dec^{-1}), Ni3S2 (116 mV dec^{-1}), and IrO_2 (66 mV dec^{-1}) (Fig. 26h), demonstrating again that it promotes rapid OERs. Also, Nyquist plots show that the NiCoS catalyst has much a smaller charge transfer resistance (R_{ct}) than those of bare NF and pure Ni_3S_2, which demonstrates that it has an excellent charge transfer capability for the OER (Fig. 26i). The calculated *C*dl values show that the NiCoS catalyst has a larger electrochemically active surface area (EASA) than do bare NF and pure Ni_3S_2 because of its 3D porous NSA structure containing an abundance of surface active sites (Fig. 26j).

The NiCoS catalyst has remarkable OER activity in SSW, as demonstrated by its requirement for overpotentials of 270, 360, and 430 mV to deliver respective current densities of 100, 500, and 1000 mA cm^{-2} (Fig. 26k). This OER performance is close to that in the 1 M aqueous KOH, suggesting that this catalyst requires an overpotential lower than 490 V to promote the CER in alkaline SSW. The NiCoS catalyst has lower OER activity in alkaline natural SW coming from the South China Sea, owing to the presence of small particulates, bacteria/microbes, and insoluble precipitates that block active sites on the electrode surface. This observation is consistent with the results of earlier studies of other electrodes in natural SW electrolysis.

Importantly, the NiCoS catalyst in the alkaline SW has respective current densities of 10, 100, and 500 mA cm^{-2} at overpotentials of 280, 360, and 440 mV (Fig. 26l). Furthermore, the current density of 100 mA cm^{-2} at an overpotential of 270 mV remains nearly constant over 100 h chronoamperometry in the alkaline SSW. Additionally, the overpotential of 360 mV needed to obtain a current density of 100 mA cm^{-2} is fairly constant during 100 h chronopotentiometry in SW (Fig. 26m).

The combined results show that the *in situ* generated amorphous S-doped NiCoOOH coating layer, generated on the surface of NiCoS during oxidative activation, is responsible for the highly selective OER activity of the electrocatalyst and its resistance to corrosion promoted by chloride ion in SW. Furthermore, the underlying NiCoS NSAs serve as a large area, conductive skeleton that is favorable for the formation and function of the active NiCoOOH species [72].

Iron and phosphorous dual-doped nickel selenide nanoporous films (Fe,P–$NiSe_2$ NFs Fig. 27a) were designed by Yang et al. for use as bifunctional catalysts for high efficiency SW electrolysis. Morphological analysis, performed using top-view and cross-sectional SEM, demonstrates that the film has a total thickness of 5 μm is entirely comprised of a nanoporous structure (Fig. 27b, c). A thin nanoporous layer (600 nm) of Fe, P–$NiSe_2$ present on the surface serves as the active site for catalytic reactions. An unreacted Fe–Ni alloy matrix remaining underneath the Fe, P–$NiSe_2$ layer functions as the conducting support to maintain structural integrity. The aberration-corrected annular bright-field scanning TEM image and selected area electron diffraction pattern show that this material has a well-defined lattice fingerprint and high crystallinity, with a slightly larger lattice spacing (0.32 nm) as compared to that of $NiSe_2$ (011) plane (0.31 nm). The enhancement is caused by doping (Fig. 27d). High-resolution high-angle annular dark-field (HAADF) STEM images of the region under the zone axis show the existence of lattice spacing of 0.296 nm corresponding to the $NiSe_2$ (101) plane (Fig. 27e). The enlarged HAADF-STEM image confirms the

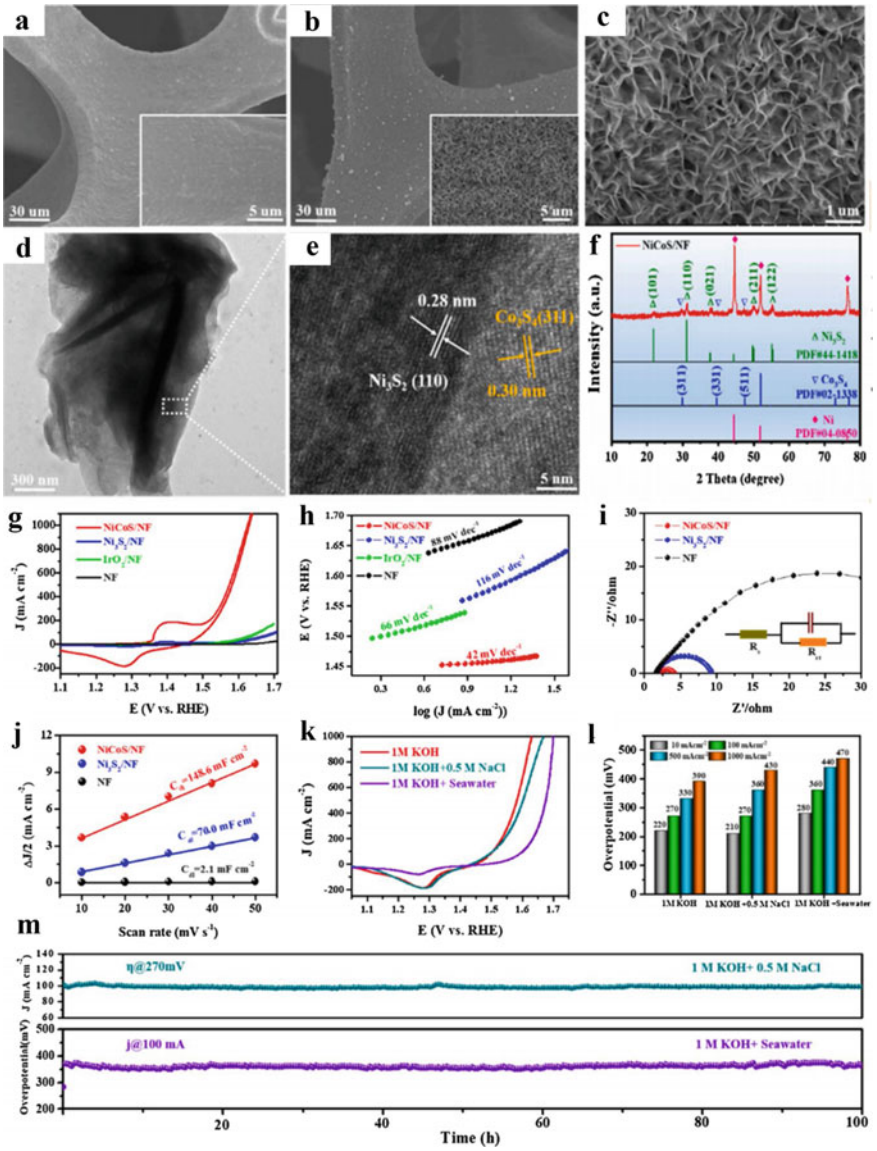

Fig. 26 **a–c** SEM images, **d**, **e** TEM images, **f** XRD pattern of samples. **g** CV curves, **h** Tafel plots, **i** EIS, and **j** Cdl for different catalysts. **k** CV curves and **l** comparison of overpotentials. **m** U-t curves

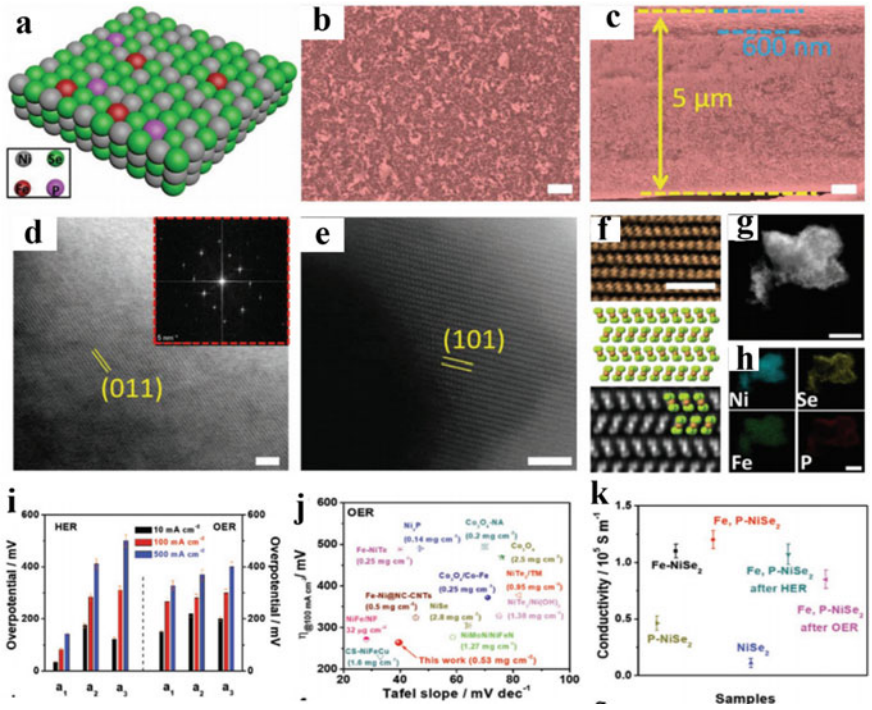

Fig. 27 **a** Structure model. **b** SEM image. **c** ABF-STEM image. **d**, **e** HAADF-STEM image. **f** Enlarged image from (**g**). **g** STEM image and **h** the corresponding EDS mapping. **i** Comparison of overpotentials. **j**, **k** Comparison of Tafel slopes and overpotentials

presence of the crystal structure of $NiSe_2$ (Fig. 27fh). The STEM image and corresponding energy-dispersive X-ray spectroscopy element mapping images prove that a homogeneous distribution of Ni, Se, Fe, and P is present throughout the nanoporous films.

Dual-doped Fe, P–$NiSe_2$ NFs have much lower OER overpotentials to reach current densities of 100 and 500 mA cm^{-2} (η of 266 and 317 mV, respectively) than do mono-doped Fe–NiSe2 NFs (η of 280 and 370 mV, respectively) and P–$NiSe_2$ NFs (η of 299 and 401 mV, respectively) (Fig. 27i). Importantly, all Ni-based catalysts have better OER performances than commercial IrO_2. Fe, P–$NiSe_2$ NFs is the best OER catalyst, demonstrated by it having the smallest η100 compared to those of previously reported catalysts (Fig. 27j, k) which need η values of 359 and 505 mV to reach current densities of 100 and 500 mA cm^{-2}, respectively. Doping by Fe increases the selectivity and Faraday efficiency (FE) of the dual-doped OER catalyst and doping with P improves electronic conductivity and prevents the dissolution of selenide by forming a passivation layer containing P–O species. The Fe-dopant is the primary active site for the HER, and it stimulates adjacent Ni atoms to function as active centers for the OER [73].

4.4 Compounds and Others

Owing to their low costs and high catalytic activities, transition metal-based materials are widely used as electrodes in alkaline water electrolysis systems. Besides introducing selectivity, Cl^- in SW causes corrosion of catalysts, especially when they are comprised of transition metal-based materials. Catalysts based on transition metal nitrides, phosphates and sulfides, and other substances, show good electrolytic performances and resist Cl^--induced corrosion in SW. Converting active metals to higher valence states is an effective strategy to inhibit Cl^- corrosion.

Ren et al. developed core-shell-structured material CoP_x@FeOOH and demonstrated that is an efficient OER catalyst in SW. In addition, its high chloride corrosion resistance and chemical stability enable CoP_x@FeOOH to perform well in alkaline SW. Owing to the presence of an HER-active CoP_x core, the CoP_x‖CoP_x @FeOOH electrode pair requires voltages of 1.710 and 1.867 V to attain respective current densities of 100 and 500 mA cm^{-2} in 1 M KOH SW. Moreover, the catalyst displays high Faradaic efficiency and long-term stability. This study led not only to the development of a new catalyst for selective SW electrolysis, but it also suggested new innovative approaches to design active and corrosion-resistant catalysts.

Kim and his colleagues observed that NCFPO/C NPs and NCFPO/C@CC are excellent electrocatalysts for alkaline SW splitting. The NCFPO/C NPs were prepared using a sol-gel method. X-ray diffraction (XRD) analysis was carried out on $Na_2Co_{1-x}FexP_2O_7$/C NPs (x = 0, 0.25, 0.5, 0.75, and 1). The diffraction peaks in the pattern of unsubstituted NCPO/C NPs (x = 0) are indexed to NCPO as a triclinic polymorph (Fig. 28a), which is isostructural to NFPO. Also, XRDs of NCFPO/C NPs (x = 0.25, 0.5, 0.75) contain the same patterns present in XRD of NCPO/C NPs, and no secondary peaks are observed. It is known that the difference in the cation sizes of Co^{2+} (0.89 Å) and Fe^{2+} (0.92 Å) is small. In addition, analysis of the FESEM image of NCFPO/C@ CC and its corresponding energy-dispersive X-ray spectroscopy (EDS) element map shows that the NCFPO/C NPs were uniformly coated in a thin layer on the CC surface (Fig. 28b–f). As can be observed, both NCPO/C and NCFPO/C have anodic peaks near 1.2–1.3 V (vs. RHE), corresponding to the $Co^{2+} \rightarrow Co^{3+}$ anodic reaction in the alkaline solution. Also, and the current density gradually increases over CV cycles, indicating that a surface change possibly occurs during the OER. The electrocatalytic OER performances of a freestanding NCFPO/C@CC (hereafter Co/Fe = 75:25 in NCFPO) electrode in both alkaline and alkaline saline solutions were determined. The information gained from polarization curves of NCFPO/C@CC in 0.1 M KOH and 0.5 M NaCl + 0.1 M KOH electrolytes and corresponding Tafel plots (Fig. 28 g, h) show that NCFPO/C@CC has a <480 mV overpotential at a current density of 100 mA cm^{-2} in an alkaline saline solution, in which only the OER is thermodynamically allowed (Fig. 28i, j). In addition, the high stability and durability of NCFPO/C@CC were demonstrated using CV and chronopotentiometry tests over a 100 h period (Fig. 28k). (Oxy)hydroxides generated at the surface of NCFPO/C NPs during the OER act as oxygen generation sites. No chlorine-derived species were detected in the alkaline saline solution after the

OER test, confirming the selectivity of this OER electrocatalyst in alkaline saline solution [74].

Mixed-phase metal hydroxide/oxide catalysts have been explored for use in SW splitting. Mixed Ni–Co hydroxides were synthetic by hydrothermal method using metal chelate complexes to control the growth of metal hydroxides. The SEM images of Ni–co hydroxides on nickel foam obtained by hydrothermal heating for 2, 4, 6, and 8 h are shown in Fig. 29a. After 2 h, an array of micro-rods formed on the surface of the Ni foam, and when the treatment time was increased to 4 h, petal-like Ni–Co hydroxides started to grow. The surface rod-like structure consisting of petals is the active catalytic region and is essential for generating high current densities for OER and HER. However, prolonged Ni–Co hydroxide precipitation hindered the three-dimensional network of nickel foam and thus the catalytic activity.

TEM and SEM images of the Ni–Co@NF, Fe@Ni–Co@NF, and GO@Fe@Ni–Co@NF catalysts, generated using 4 h hydrothermal treatment, are displayed in Fig. 29b, c. Inspection of the TEM image of Ni–Co@NF shows that ultra-thin sheets cover the micro-rods (Fig. 29d, e). A layer of Ni–Co hydroxide with an interlayer spacing of 0.474 nm can be seen on the surface in the HRTEM image of this catalyst. Furthermore, TEM-EDS elemental mapping shows that all elements are uniformly distributed. In the case of Fe@Ni–Co@NF, a homogeneous distribution of FeOOH nanoparticles with an average diameter of 7–9 nm covers the surfaces of the Ni–Co sheets (Fig. 29f–i). Interestingly, the size of the FeOOH nanoparticles on the Ni–Co sheets is much smaller (2–4 nm) in GO@Fe@Ni–Co@NF, possibly because the GO layer limits permeation of Fe ions into Ni–Co sheets during electrodeposition (Fig. 29j–m). Elemental mapping of the GO@Fe@Ni–Co@NF catalyst further confirms the existence of a uniform distribution of FeOOH nanoparticles on the Ni–Co sheets. SEM images show that in GO uniform coats Fe@Ni–Co@NF in GO@Fe@Ni–Co@NF.

A current density of 50 mA cm^2 was selected to compare the performances of these catalysts mainly because current densities associated with the metal redox peaks are much higher owing to the high specific capacitances of Ni–Co hydroxide-based materials. As shown in the LSV plot in Fig. 29n, Ni–Co@NF and Fe@Ni–Co@NF reach the 50 mA cm^{-2} current density at respective overpotentials of 313 and 246 m, and at 500 mA cm^{-2} they reach 401 and 312 mV. It should be noted that Fe@Ni–Co@NF catalyst requires an overpotential of 0.336 mV to reach the industrial-level 1000 mA cm^{-2} current density. Interestingly, graphene oxide overlayer containing GO@Ni–Co@NF and GO@Fe@Ni–Co@NF electrodes have slightly better performances than catalysts not possessing the GO overlayer. Specifically, GO@Ni–Co@NF reaches current densities of 50 and 500 mA cm^{-2} at respective overpotentials of 307 and 398 mV, and GO@Fe@Ni–Co@NF requires overpotentials of247 and 303 mV to reach these respective current densities. Both GO@Fe@Ni–Co@NF and Fe@Ni–Co@NF reach the industrial-level faradaic current density (1000 mA·cm^{-2}) at overpotentials that are lower than 480 mV. According to the Pourbaix diagram, oxidation of chloride is not thermodynamically feasible on either catalyst. It should be noted that the introduction of FeOOH into Ni–Co@NF leads to a significant enhancement of the OER activity.

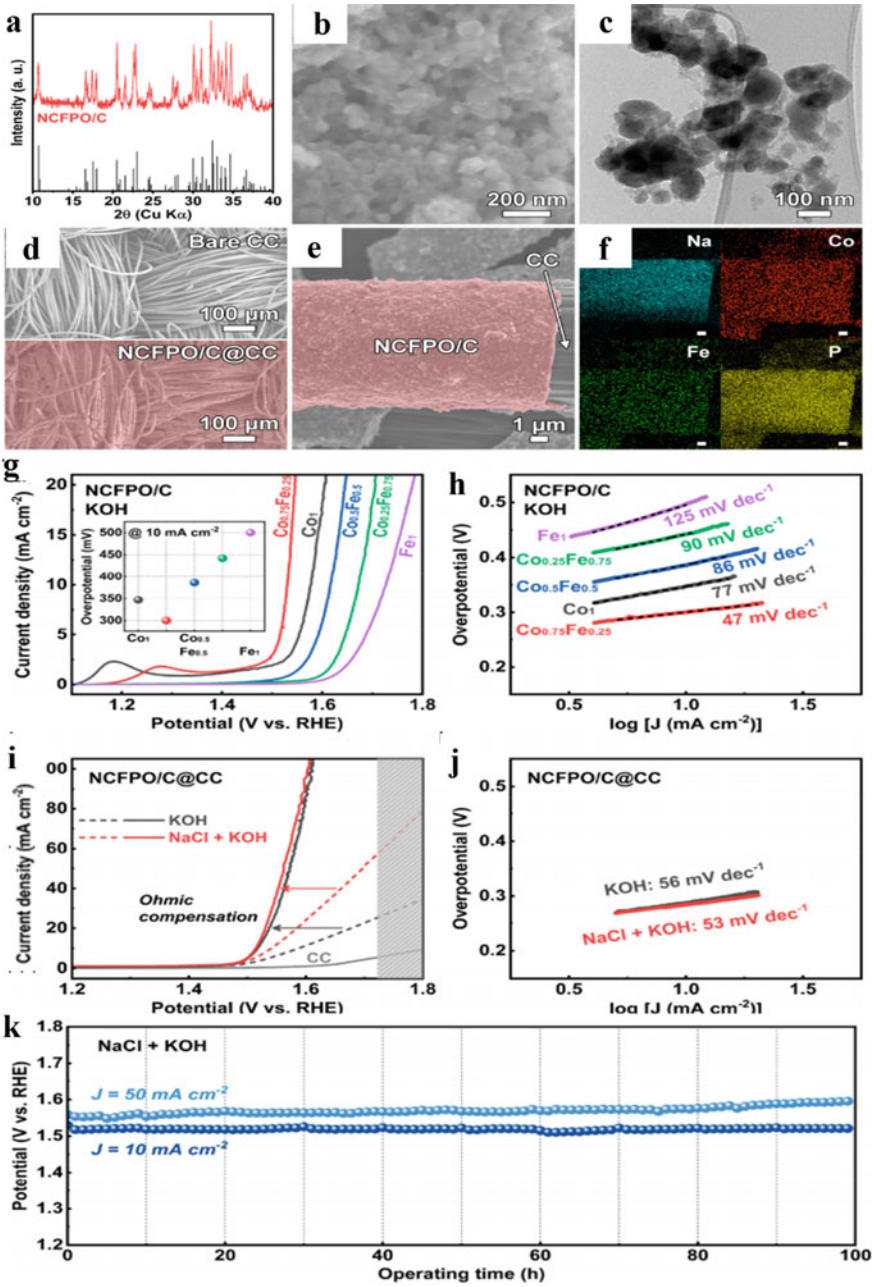

Fig. 28 **a** XRD pattern, **b** FESEM, and **c** TEM images of the samples. **d**, **e** FESEM images of samples and **f** the corresponding EDS mapping. **g** LSV curves and **h** Tafel plots of catalysts. **i** LSV curves and **j** Tafel plots of catalysts of NCFPO/C@CC. **k** U-t curves

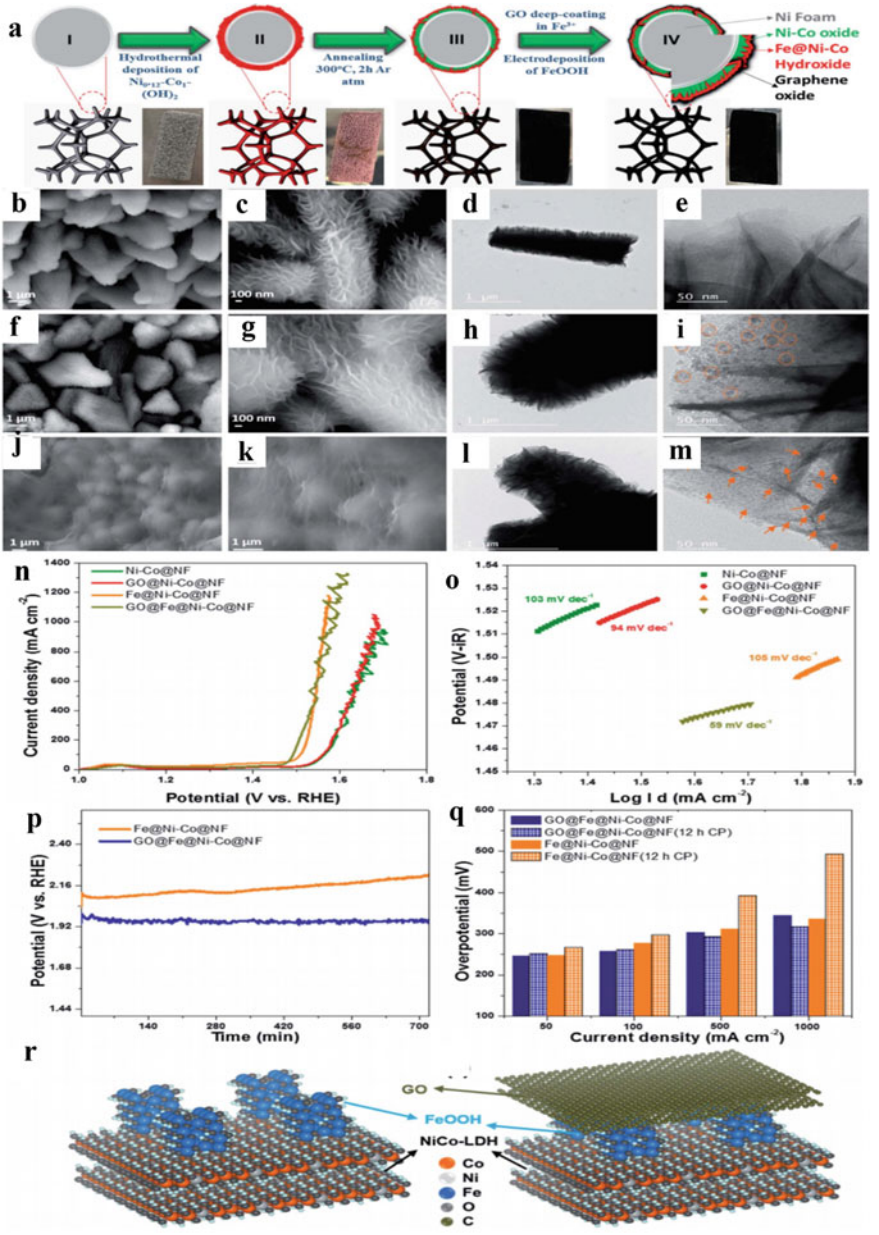

Fig. 29 **a** Schematic diagram of catalysts. **b–m** SEM images and TEM images of catalysts. **m** LSV curves. **o** The corresponding Tafel plots. **p** U-t curves. **q** OER overpotential comparisons. **r** Model of the outermost layer structure

Fe species, along with Ni and Co hydroxide needed to be present at the interface of Fe@Ni–Co@NF and GO@Fe@Ni–Co_2NF to achieve a high O_2 production. As seen in the Co 2p XPS spectra of the Fe@Ni–Co@NF and GO@Fe@Ni–Co_2NF, Co sites are electronically modified by Fe atoms to enhance OER activity relative to that of bare Ni–CO@NF. The respective RCTs of 2.74 and 2.01 for Go@Ni–Co@NF and GO@Fe@Ni–Co@NF show that the electrical conductivities of the catalysts are enhanced by introducing the GO layer. Furthermore, a comparison of the OER activities of catalysts with and without the GO layer at an overpotential of 260 mV shows that Ni–Co@NF, and Fe@Ni–Co@NF reach current densities of 17.16 and 59.57 $mA{\cdot}cm^{-2}$, respectively. In contrast, at a 260 mV overpotentials, the GO@Ni–Co@NF and GO@Fe@Ni–Co@NF catalysts have respective current densities of 19.26 and 90.65 $mA{\cdot}cm^{-2}$ (Fig. 29o–q).

The LSV curve of GO@Fe@Ni–Co@NF is non-smooth which is a result of oxygen bubble rupture at high current densities. In addition, the reduction of the graphene oxide layer on the catalyst occurred on the surface of GO@Fe@Ni–Co@NF (Fig. 29r). High-resolution EDS mapping of the affected area revealed that a carbon layer remained on the catalyst surface. The results show that the graphene oxide overlay on the surface of GO@Fe@Ni–Co@NF can be used as an efficient SW oxide electrocatalyst and can block chloride induced corrosion at high current densities. Also, the synergism between interfacial FeOOH NP and Ni–Co hydroxide 2D sheets lowers the OER overpotential and the metal oxide layer below the surface helps lower charge transfer resistance enabling generation [75].

Driven by the desire to discover materials to promote efficient electrolysis of SW, Gupta et al. prepared bimetallic oxy-boride (Co–Fe–O–B) nanostructures with varying Fe content using a hydrothermal method. The starting Co–O–B material is comprised of wire-like structures but mainly consists of nanoparticles (Fig. 30a). Interestingly, all Co–Fe–O–B structures have the same the morphology (Fig. 30b–e), consisting of cottonlike sheets covered by spherical particles. In the formation of Fe–O–B (Fig. 30f), the spherical morphology of the precursor is destroyed and small agglomerated clusters of sheets are formed. The boronation process was expected to disrupt the crystallinity of the surface of Co–O–B by diffusion of boron into peripheral areas while maintaining the core structure. This expectation is confirmed by the XRD spectra of the boronized materials, which have peaks for the component elements at the same positions as they are in Co–Fe–O (Fig. 30g) but with highly diminished intensities. In fact, most peaks in the spectra of Co–Fe–O–30 and Co–Fe–O–40 are suppressed by boronation and only those belonging to the pure Co_3O_4 phase are observable.

To establish the suitability of using this class of borides for the OER in SW, Co–Fe–O–B–10 was used as an anode in alkaline (0.5 M NaCl + 1 M KOH) and neutral (0.5 M NaCl) saline electrolytes containing Cl^- ions. The anodic polarization curves indicate that the most active Co–Fe–O–B–10 has comparable activities in both 1 M KOH and 1 M KOH + 0.5 M NaCl, and a low activity in 0.5 M NaCl. In the alkaline saline solutions, the electrocatalyst requires overpotentials of 294 and 434 mV to achieve 10 and 100 mA/cm^2, respectively (Fig. 30h). The long-term stability of Co–Fe–O–B–10 for OER in alkaline pure water and saline water was

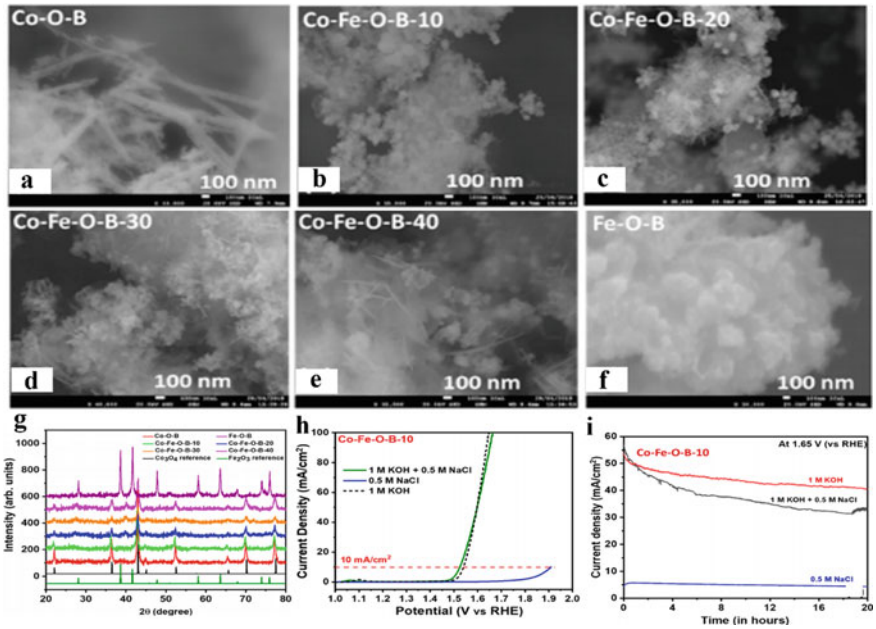

Fig. 30 **a–f** SEM images. **g** XRD patterns. **h** LSV curves. **i** I-t curves

assessed. Chronoamperometry tests on Co–Fe–O–B–10 in all three electrolytes at an applied potential of 1.65 V (vs. RHE) for 20 h (Fig. 30i) show that this electrode is highly stable in 1 M KOH (18% performance loss), and not in alkaline saline water where a current decrease of almost 35% takes place in 20 h.

The most active catalyst, Co–Fe–O–B–10, possesses a unique flower-like architecture comprised of small nanoparticles of Co_3O_4 encased in boron shells. Boron in cobalt boride prevents complete oxidation of Co sites and expedites the formation of active Co–OOH species. Reduction of Ni–Fe–based catalysts using $NaBH_4$ leads to the formation of oxygen vacancies and undercoordinated metal sites that improve conductivity and OER activity [76].

The electrocatalytic properties of highly porous N-doped carbons (PNCs), formed by thermolysis of nonporous Zn-based coordination polymers (CPs) containing nitrogen-containing ligands, have been described by Moon et al. 4-(Phenylazo)pyridine and Na_2FMA were employed as organic ligands in the nitrogen-containing CPs (Fig. 28a). Self-assembly of $Zn(NO_3)_2{\cdot}6H_2O$, Na_2FMA and 4-(phenylazo)pyridine yielded $[Zn(FMA)(4\text{-(phenylazo) pyridine})_2(H_2O)]{\cdot}(ZnCP_{azo}\text{-}1)$ as orange crystals (Fig. 31b, c), whose structure was determined using single crystal X-ray diffraction analysis. In the crystalline state, $ZnCP_{azo}$-1 possesses four crystallographically independent Zn atoms arranged in a distorted octahedral geometry. Zn^1 and Zn^4 are bonded to two carboxylate oxygens of two different FMA^{2-} moieties, two water molecules, and two pyridine nitrogens. Zn^2 and Zn^3 are coordinated to four carboxylate oxygens of three different FMA^{2-} ligands and two pyridine nitrogens.

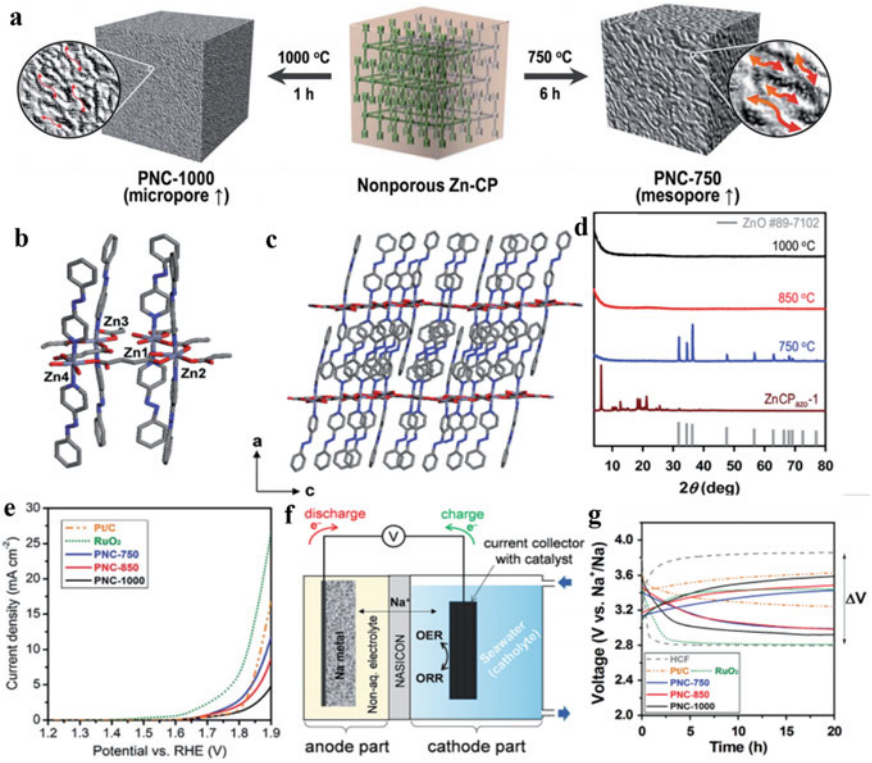

Fig. 31 **a** Schematic diagram of samples. **b**, **c** Structure model. **d** XRD patterns. **e** LSV curves. **f** Schematic drawing of the cell. **g** The initial charge–discharge voltage profiles of SW batteries

Fully coordinated Zn-FMA exists as 2D layers with 4-(phenylazo)pyridine groups in apical positions of each Zn^{2+} ion. The 2D layers are stacked in an interdigitated manner in which π-π interactions occurring between the pyridine rings.

The XRD pattern of the solid obtained by heating of $ZnCP_{azo}$-1 at 750 °C, referred to as PNC-700, corresponds to that of ZnO (Fig. 31d), formed by oxidation of Zn metal species during the cooling step. In contrast, the solids formed by heating $ZnCP_{azo}$-1 at 850 and 1000 °C (PNC850 and PNC-100, respectively) do not contain XRD peaks for ZnO, but instead very low intensity broad peaks exist at around 24 corresponding to carbon. OER activities were evaluated in N_2-saturated SW at 1600 rpm and 5 mV s^{-1}, and the resulting polarization graphs. The OERs (judged by E_{onset}, Fig. 31e) of PNC-750 and PNC-850 begin around 1.66 V, which is relatively high compared to that of the RuO_2 (E_{onset} 1.60 V), but slightly lower than that of the Pt/C. PNC-1000 has the lowest E_{onset} of substances in this series.

A schematic of a battery containing the PNCs is shown in (Fig. 31f). The cell comprises a sodium-metal anode (in an organic electrolyte) and a flowing opened cathode, which is separated by a NASICON ceramic electrolyte. During charging,

Na^+ ions diffused from the SW to the anode and were reduced by the NASICON separator to form Na metal, with OER at the cathode (air electrode.) Fig. 31g presents the initial charge and discharge curves of the cell at each step for 20 h with and without the addition of the PNC catalyst at 0.01 mA cm^{-2}. Cells with Pt/C or RuO_2 catalysts were also measured at the same conditions. Cells with only HCF air electrodes (no PNC) demonstrated charge and discharge voltages of 3.86 V and 2.80 V, respectively, as well as a large voltage gap of 1.06 V. The size of the gap is mainly due to the excessive overpotential resulting from the slower OER/ORR rate on the cathode during charging and discharging. In comparison, the PNC catalyst cells have relatively small voltage gaps, with the PNC-750, PNC-850, and PNC-1000 having voltage gaps of 0.44 V, 0.50 V, and 0.66 V, respectively. While the PNC samples have lower discharge voltages than the Pt/C samples, the charging voltages (which are OER dependent) are lower. Specifically, the PNC-750 has a smaller voltage gap than the Pt/C (0.39 V).

The above observations suggest that the structural properties of the parent CP are not conserved in the derived carbon material PNCs. On the contrary, the inherent physical and chemical properties that are introduced during the thermal conversion process are critical in determining the structural properties of the converted carbon material. By manipulating the transformation conditions, such as temperature, ramping rate, and retention time, the pore size of the PNCs can be regulated. Importantly, mesoporosity is a critical factor for control of the electrocatalytic activity and resultant performance of the PNCs in a SW battery [77].

A heterostructure of a Ni_3S_2 nanoarray with secondary Fe–$Ni(OH)_2$ lamellar edges that expose abundant active sites for SW oxidation has been developed by Hu et al. The lamellar-edged nanoarray initially grows perpendicular to the Ni foam surface and then becomes interlaced with the Ni foam skeleton (Fig. 32b–d). The ordered microstructure generated contains more open space for the permeation of the electrolyte and diffusion of the produced gas. Thin layers with clear interspaces in the form of a lamellar lace exist at the edges of the nanoplates.

Information about the structure of Fe–$Ni(OH)_2/Ni_3S_2$ was gained by using Raman spectroscopy (Fig. 32e). The Raman spectrum of this substance contains peaks for bond vibrations of Ni–S (from Ni_3S_2) at 188, 198, 221, 303, 322, and 349 cm^{-1}. The peak at ~450 cm^{-1} is assigned to a vibrational mode Ni–OH in Fe doped $Ni(OH)_2$ layer. The XPS survey spectrum revealed Ni, Fe, O, and S exist on the surface of Fe–$Ni(OH)_2/Ni_3S_2$. Synthesis of Fe–$Ni(OH)_2/Ni_3S_2$ nanoarray precursor on Ni foam (Fig. 32f).

Fe–$Ni(OH)_2/Ni_3S_2$ requires the low overpotential of 269 mV to reach a current density of 10 mA·cm^{-2}, while its precursors Ni_3S_2@NF and Ni foam require higher overpotentials (370 mV) to reach the same current density (Fig. 32g). Also, the Tafel slope of Fe–$Ni(OH)_2/Ni_3S_2$@NF is 46 mV·dec^{-1} (Fig. 32h). The small Tafel slope of that Fe–$Ni(OH)_2/Ni_3S_2$@NF, which indicates that it produces a large current density at a low overpotential, is driven by the high rate of the process, which could be linked to the structural merits of the presence of lamellar-edged nanoplates (see above). The results of EIS studies, conducted to assess charge transfer resistances (R_{ct}) (Fig. 32i), show that Fe–$Ni(OH)_2/Ni_3S_2$@NF has a smaller R_{ct} (~1.7 Ω) than bare Ni foam

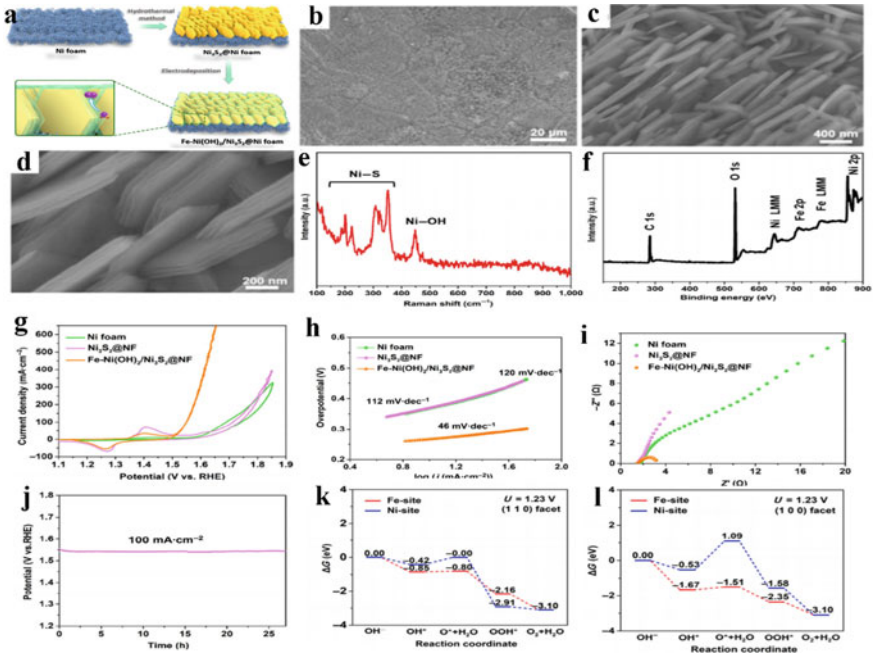

Fig. 32 **a** Schematic diagram for the synthesis. **b**–**d** SEM images. **d** TEM images. **e** Raman spectrum and **f** XPS survey spectra of the samples. **g** The CV curves and **h** Tafel plots. **i** EIS plots. **j** U-t curves. **k**, **l** DFT calculation of the Gibbs free energy changes

and Ni_3S_2@NF, suggesting that the OER promoted by this catalyst involves faster electron transfer steps. The micro-interface in the heterogeneous structure likely responsible for the favorability of charge transfer in the Faraday process.

Chronopotentiometry studies to evaluate durability show that Fe–$Ni(OH)_2/Ni_3S_2$@NF has reasonable stability in that negligible decay takes place over 27 h at a potential of 100 mA·cm^{-2} (Fig. 32j).

DFT calculations were performed using the well-accepted OER mechanism. Thermodynamic calculations suggest that the transformation of OH* to O* is endothermic and that it has the highest barrier in both (100) and (110) facets (Fig. 32k, l). This observation suggests that the rate determining step (RDS) for the OER promoted by $Ni(OH)_2/Ni_3S_2$@NF is *O formation. As expected, a lower thermodynamic barrier is confronted at the Fe-site (ΔG) than those at the two facets at the Ni-site, indicating that the Fe-site is more active for OER. In addition, DFT calculations demonstrate that the Fe rather than N species in lamellar edges are highly active and selective sites for the OER in SSW. Overall, these findings show that the superior electrocatalytic performance can be attained by designing hierarchical electrodes and introducing OER-preferred species that lead to large rates, long-term stability, and good selectivity in SW oxidation [78].

5 Bifunctional Materials Used for HER/OER in SW

As mentioned above, great efforts have been made to develop efficient OER and HER catalysts. However, various equipment and synthesis processes are required to produce catalysts that are selective for OER or HER. Therefore, the bifunctional catalysts with high catalytic activity for both OER and HER under alkaline conditions are very important. In 2014, the research report of Gr ä tzel group pointed out that NiFe LDH grown on NF can be used as a bifunctional electrocatalyst for water decomposition. In the three electrodes system, the OER of NiFe LDH electrode in 1 M KOH. The value is 240 mV and the HER is 210 mV. An electrolytic cell with this electrode requires a battery voltage of 1.7 V to achieve a current density of 10 $mA{\cdot}cm^{-2}$. Based on this groundbreaking research, many bifunctional electrocatalysts, including metals, metal oxides/(oxygen) hydroxides, nitrides, phosphides, and chalcogenides, have been gradually developed since then.

5.1 Metals

For efficient industrial-level water splitting, the sluggish kinetics of both the cathodic HER and anodic OER need to be overcome. Also, preparation of the two-electrode systems for water splitting remains challenging and most currently interesting electrocatalysts do not promote these processes simultaneously. For example, Pt-based catalysts have the highest HER activities but they only have moderate OER activities. Similarly, Ir and RuO_2 are state-of-the-art OER electrocatalysts but their performances in the HER are unsatisfactory. Thus, a large effort has been devoted to the development of efficient bifunctional HER and OER electrocatalysts.

Wang and colleagues synthesized functionalized Echinops-like Rh porous nanostructures (PNNS) by self-assembling ultra-fine subunit Rh nanosheets using a solvothermal method (Fig. 33a). The XRD pattern of the catalyst (Fig. 33b) contains four distinct broad peaks associated at 40.99°, 47.56°, 69.58°, and 84.10°. As shown in Fig. 33c–e, TEM and SEM images showed that the Rh nanostructures in the catalyst were evenly dispersed on the Rh-like porous nanostructures in acanthoderm. TEM examination of a single acanthoderm Rh porous nanostructure showed that the material was composed of secondary Rh nanosheets with porous structure, and the formation mechanism of acanthoderm rhPNNS involved self-assembly. High-resolution TEM images showed the presence of 0.220 nm lattice fringes (Fig. 33f), which was consistent with XRD analysis, which showed that the (111) lattice spacing of the face-centered cubic (fcc) Rh crystals was 0.220 nm. The corresponding selected electron diffraction (SAED) pattern contains bright discrete spots, confirming the high crystallinity of the material (Fig. 33g). The temporal evolution of Echinops-like Rh porous nanostructures was studied using TEM (Fig. 33h). In the initial stage of the process, ultra-fine and monodisperse Rh seed crystals of about 3 nm are generated,

suggesting that the formation of porous Rh nanostructures like Echinops is initiated by the generation and subsequent self-assembly of ultra-fine nanosheets.

LSV measurements show that the overpotential of Echinops-like Rh porous nanostructures in 1.0 M PBS at 10 mA cm^{-2} is 79.5 mV (Fig. 33i), a value that is much lower than that of commercial RuO_2 (139.4 mV). Additionally, Echinops-like Rh porous nanostructures have a Tafel slope of 88 mV dec^{-1} in 1.0 M PBS in contrast to the slope of 144 mV dec^{-1} for RuO_2 (Fig. 33j), suggesting that the OER promoted by Echinops-like Rh PNNSs takes place rapidly. The mass-specific activity of the PNNSs over repeated long-term operation remains constant, while that of the RuO_2 electrode decreases from 10.71 to 6.45 (Fig. 33k), indicating that Echinops-like Rh porous nanostructures have an excellent catalytic durability. In addition, LSV measurements show that the Echinops-like Rh PNNS has an excellent overall water splitting performance requiring a voltage of 1.61 V to achieve a current density of 10 mA cm^{-2} (Fig. 33l). This overpotential is much smaller than that of a Pt black‖RuO_2 based electrolyzer (1.89 V). Moreover, compared to a Pt black‖RuO_2 electrolyzer, one comprised of an Echinops-like Rh PNNS has outstanding catalytic durability during its use for electrolysis at 10 mA cm^{-2} over a 50 h period (Fig. 33m). A schematic illustration of the SW splitting cell is shown in Fig. 33n. Also, the Echinops-like Rh PNNS-based electrolyzer performs well in SW and exhibits outstanding durability (Fig. 33o). [79]

5.2 Metal Oxides or (Oxy)hydroxides

Transition metal oxides or (oxy)hydroxides have attracted much attention as electrocatalysts because of a balance between cost, performance, and robustness. In view of the fact that electrolytic hydrogen production from SW is a thermodynamically and kinetically unfavorable process, much thought has been given to the rational design of transition metal nano-composites that possess multi-functional active sites for simultaneous OER and HER. The material Ni–Co@NF has a dual function due to the synergy between the interface FeOOH NP and the Ni–Co hydroxide 2D sheet (Fig. 34a). This interaction effectively reduces OER overpotential so that higher current density can be achieved at low overpotential. At the same time, the lower metal oxide layer in the catalyst reduces the charge transfer resistance. TEM images showed an ultra-thin sheet covering Ni–Co@NF (Fig. 34b–e). The low distance between the b–Ni–Co LDH GO coating and the in situ carbon oxide layer effectively improves the working efficiency when Ni–Co@NF is used as the anode for SW oxidation. Lee constructed an alkaline SW cell, GO@Fe@Ni–Co@NF(+)//GO@Fe@Ni–Co@NF, which required very low cell voltages of 1.57 and 2.02 V to achieve current densities of 20 mA cm^{-2} and 1000 mA cm^{-2}, respectively, (Fig. 34f, g). Most importantly, this electrolyzer has excellent durability during alkaline SW splitting at an industrial-level current density. Specifically, no noticeable activity drop occurs during 378 h operation (Fig. 34h). If applicable to the design of other OER/HER electrocatalysts, observations made in this study would provide a groundwork for the development

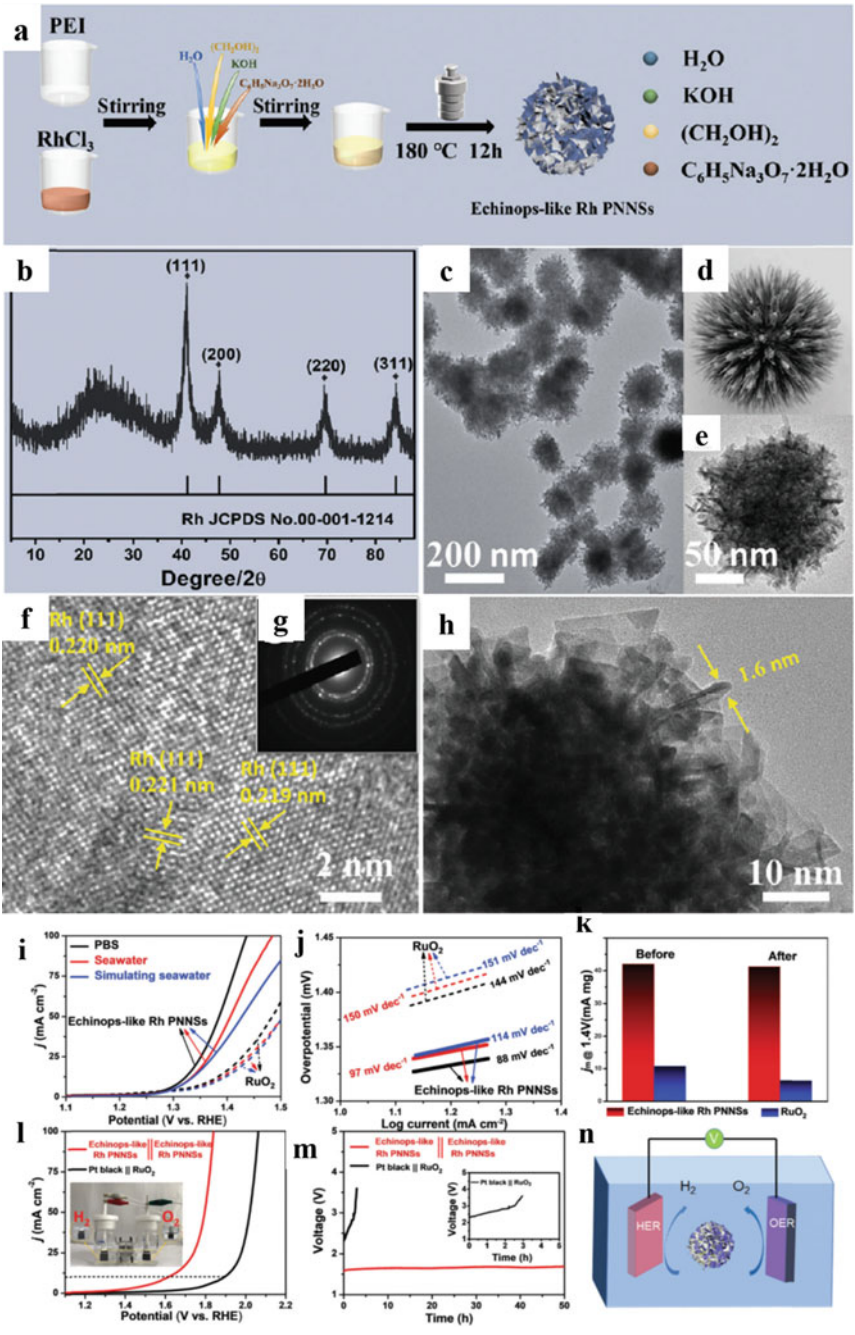
a
PEI
RhCl3
Stirring
Stirring
180 °C 12h
H2O
KOH
(CH2OH)2
C6H5Na3O7·2H2O
Echinops-like Rh PNNSs
b
(111)
(200)
(220)
(311)
Rh JCPDS No.00-001-1214
Degree/2θ
c
200 nm
d
e
50 nm
f
Rh (111) 0.220 nm
Rh (111) 0.231 nm
Rh (111) 0.219 nm
2 nm
g
h
1.6 nm
10 nm
i
PBS
Seawater
Simulating seawater
Echinops-like Rh PNNSs
RuO2
Potential (V vs. RHE)
j
RuO2
151 mV dec-1
144 mV dec-1
150 mV dec-1
114 mV dec-1
97 mV dec-1
88 mV dec-1
Echinops-like Rh PNNSs
Overpotential (mV)
Log current (mA cm-2)
k
Before
After
Echinops-like Rh PNNSs
RuO2
l
Pt black || RuO2
H2
O2
Potential (V vs. RHE)
m
Pt black || RuO2
Voltage (V)
Time (h)
n
H2
O2
HER
OER

◀**Fig. 33** **a** Synthesis process diagram of catalyst, **b** XRD pattern of catalyst, **c** TEM image of the morphological characteristics of catalyst, **d** the real Echinops in the ocean, **e** TEM image of a single Echinops-like catalyst, **f** HRTEM of catalyst to display lattice stripes, **g** Inset (**f**) is SAED image of catalyst, **h** TEM image of the catalyst with the details of nanoflakes, **i** comparison of oxygen evolution performance curves of different catalysts and **j** corresponding Tafel plots in (**i**), **k** histogram of catalyst performance change before and after stability test **l** the performance comparison of r water splitting electrolysis in seawater. **m** Chronopotentiometry curves reflect the stability of the catalyst in natural SW. **n** Schematic diagram of seawater splitting device. **o** E-t curve with periodic change

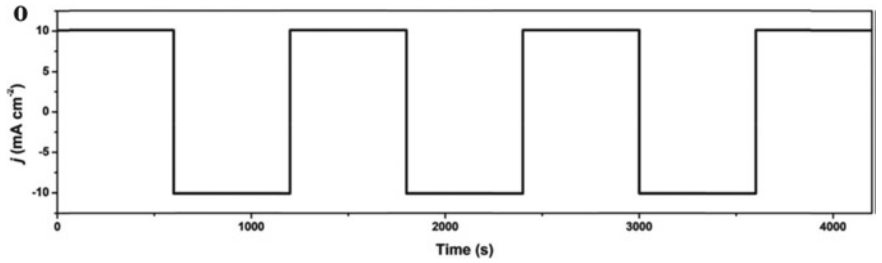

Fig. 33 (continued)

of economical and practical systems for hydrogen production through SW splitting [75].

Luo et al. developed a high-performance porous dendritic catalyst for alkaline SW splitting, whose design is based on a collaborative acceleration strategy (Fig. 35a). Typically, metal sulfate and metal hydrochloride with different ratios were dissolved in a multi-component plating buffer solution. Next, the pre-treatment Ni foam was immersed in the plating buffer solution. Temperature, current density, and time were adjusted during the electroplating to obtain an alloy layer with Cu, Ni, and Co adhered to the NF surface (CNC-A). The prepared CNC-A precursor was placed in the alkaline solution and then partially anodized. Then, the optimal Co/Ni-doped defect-rich Cu-based oxides (CNC-MO) with surface-vertical nanoneedle structure was formed. Finally, the Ni/Co-doped defect-rich Cu-based sulfides (CNC-MS) was further prepared by mixing sulfur source and CNC-MO through microwave treatment. The SEM in Fig. 35b refers to CNC-A, where the optimal texture of the alloy-coated surface is a mainly punctate protrusion texture. The main body is comprised of separated metal oxide nanostructure, and the outer layer is uniformly sulfurized (Fig. 35c). Comparing the overall polarization curves, it is found that the optimized non-noble-metal electrodes (non-noble-E; Overall-1) have a better performance than the noble-metal electrodes (noble-E; Overall-2) (Fig. 35d) and is also very competitive in low-grade water. A comparison of the overall performances of two electrolyzers created using noble-E and non-noble-E as electrodes showed that a voltage of 1.61 V drives non-noble-E to produce a current density of about 100 mA cm^{-2} (Fig. 35e), while noble-E produces only about 30 mA cm^{-2} (Fig. 35f) [80].

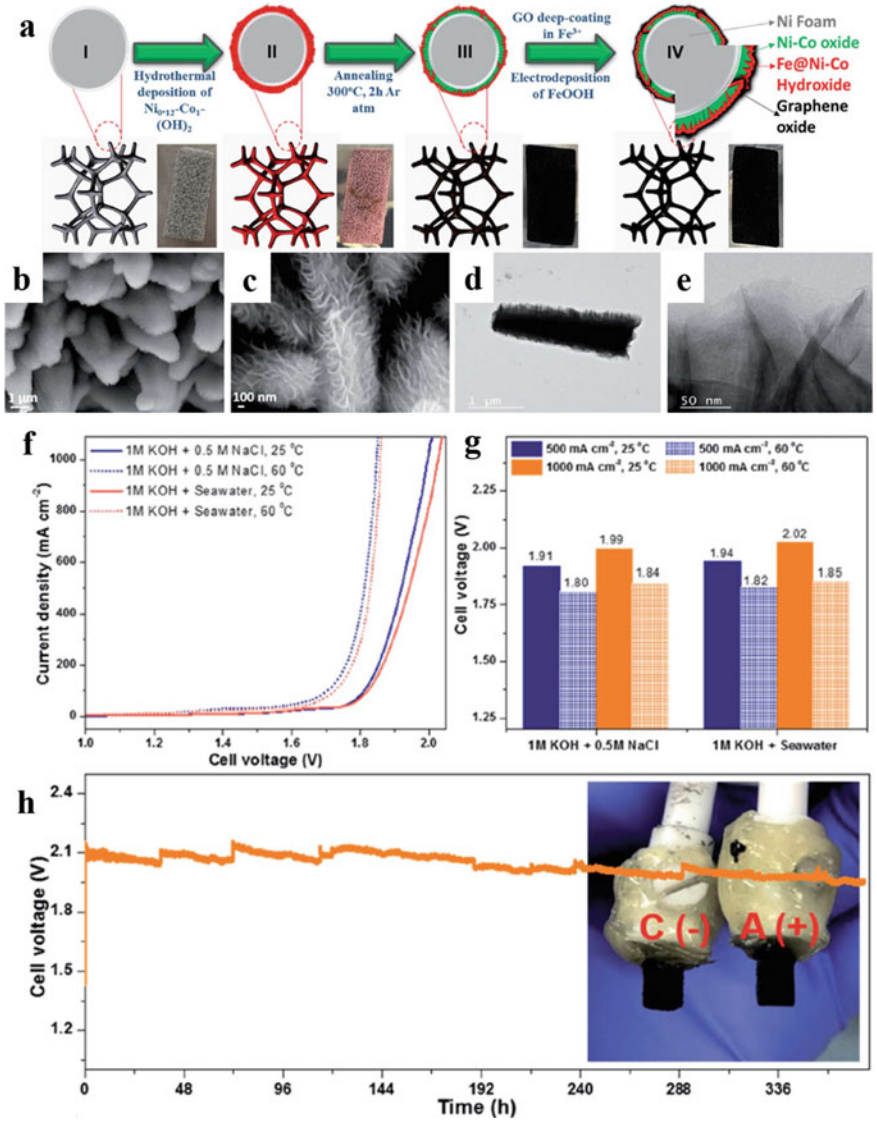

Fig. 34 **a** Schematic diagram of catalyst synthesis and structural changes at each stage of synthesis. **b**–**e** Morphological structure patterns of catalyst. **f** Polarization curves and **g** comparison of the required voltages of different catalysts. **h** Stability test in simulated seawater

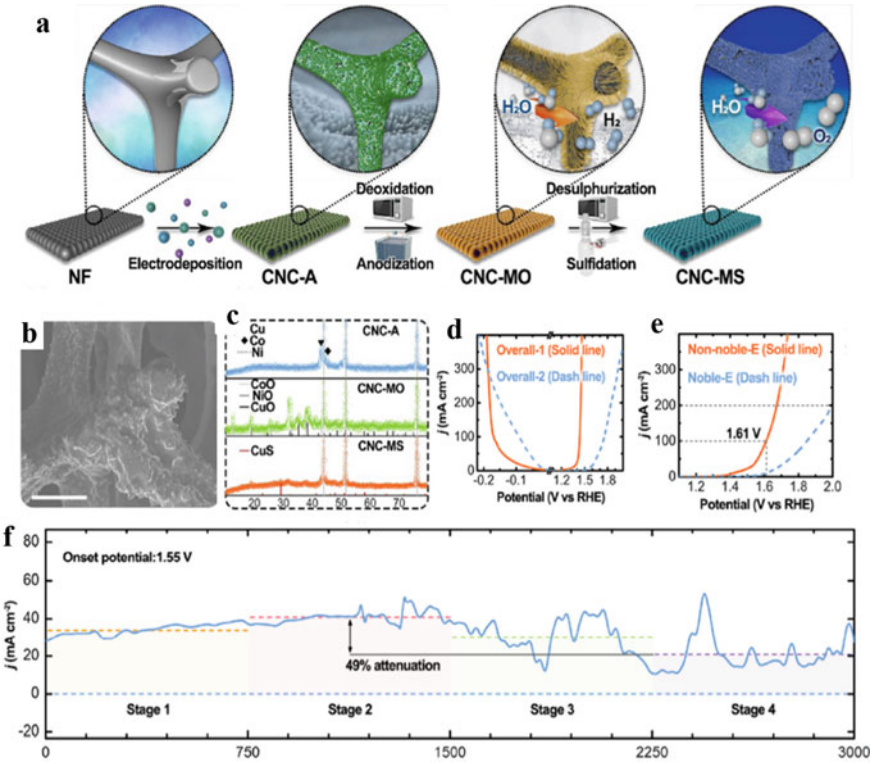

Fig. 35 **a** Diagram of the preparation pathway for the CNC-MO and CNC-MS catalysts. **b** SEM image of CNC-A. **c** XRD of CNC-A, CNC-MO, and CNC-MS. **d** Further comparison of HER and OER curves of noble-E and non-noble-E and their **e** cell voltage curves in overall water electrolysis. **f** Long-range chronoamperometric curves in 1 M KOH^+ World sea standard

To address the problem associated with competition between the OER and CER at the anode, an organic-oxidation assisted strategy was developed. In this approach, carbon paper supported Pt–Co_3O_4 electrocatalysts (denoted as Pt–Co_3O_4/CP) is used to promote a thermodynamically favorable methanol selective oxidation reaction (MSOR) and which takes place to the exclusion of the undesired OER and CER (Fig. 36a). Methanol oxidation leads to the simultaneous generation of hydrogen and valuable formate with significantly low energy consumption. Pt–Co_3O_4 has a nanosheet structure containing abundant nanopores, (Fig. 36b–e) which are beneficial electrolyte diffusion to active sites of the catalyst. An integrated two-electrode electrolyzer comprised of the bifunctional electrocatalysts Pt–Co_3O_4/CP and Pt–Co_3O_4 (Fig. 36f) has a required cell voltage of only 0.555 V in 2.0 M methanol to attain a current density of 10 mA cm^{-2}, which is 1022 mV lower than that in alkaline SSW (Fig. 36g). The integrated cell produces hydrogen and formate simultaneously with high faradaic efficiencies and it has long durability [30].

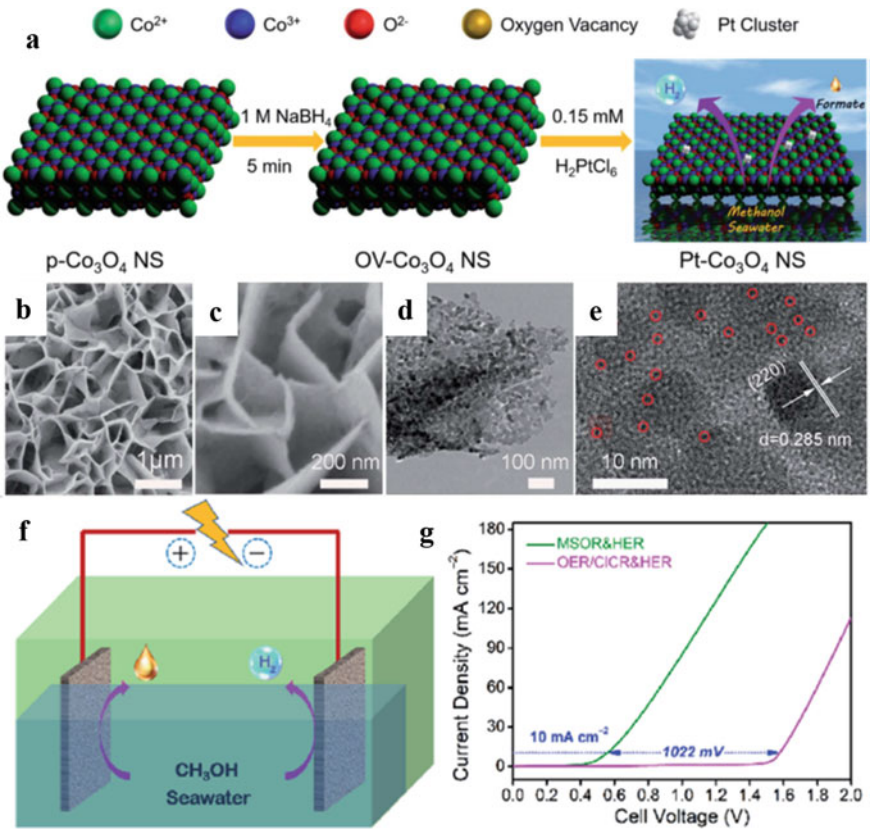

Fig. 36 **a** Diagram of the preparation of Pt–Co_3O_4/CP nanosheet electrocatalysts. **b**, **c** SEM images of Pt–Co_3O_4/CP. **d**, **e** TEM and HRTEM images of Pt–Co_3O_4 nanosheets. **f** Diagram of the Pt–Co_3O_4/CP as bifunctional electrocatalysts. **g** Comparison of sample performance with LSV curve (no iR compensation)

The interesting electrocatalyst Ru–CoO_x/NF was constructed through a series of steps initiated by uniformly distributing Co leaf-like zeolitic imidazolate framework (Co ZIF-L) arrays on NF using an in situ growth method to produce (Fig. 37a). Generated Co ZIF-L/NF is then annealed at 250 °C in air to generate CoO_x/NF, which is subsequently transformed to the target catalyst Ru–CoO_x/NF by incorporating Ru followed by calcination. The precursor Co ZIF-L/NF is comprised of vertical nanosheets with thicknesses of about 0.32 μm, evenly distributed on the foamed nickel substrate (Fig. 37b). Ru–CoO_x/NF also has a vertical nanosheet structure, indicating that no significant change in morphology takes place in the last two steps of the synthesis process (Fig. 37c). The ultralow Ru incorporated amorphous cobalt-based oxide, Ru–CoO_x/NF, serves as an effective catalyst for electrolysis in alkaline water and SW at high current densities. The overpotential of a Ru–CoO_x/NF||Ru–CoO_x/NF electrolyzer in SW is 630 mV (@100 mA cm^{-2}) and 1390 mV (@1000 mA cm^{-2}),

which are lower than those of the commercial electrocatalyst Pt/C/NF||RuO_2/NF (760 and 1530 mV corresponding to 100 and 1000 mA cm^{-2}) (Fig. 37d). The new electrocatalyst has high stability at a high current density (Fig. 37f). The electrolyzer containing Ru–CoO_x/NF requires ultralow respective voltages of 2.2 and 2.62 V to achieve a hydrogen production current density of 1000 mA cm^{-2} in alkaline water and SW. These values are better than those of commercial Pt/C and RuO_2 catalysts (Fig. 37e). The results of this study indicate that Ru–CoO_x/NF is a highly promising electrocatalysts for industrial applications and suggest that the current density in water electrocatalysis might be heightened by adjusting the crystallinity of the catalyst [81].

A group of Zr-doped LDH nanosheets that serve as electrocatalysts for water splitting was prepared by Lei et al. using electrodeposition on NF. XRD measurements (Fig. 38a) show that the materials generated after the introduction of Zr into CoFe-LDH have low degrees of crystallinity owing perhaps to the introduction of lattice distortion i when Zr^{4+} replaces Fe^{3+}. In contrast to the signal in the XRD pattern of CoFe/NF, the signal corresponding to Co 2p in CoFeZr/NF is shifted to a lower binding energy (Fig. 38b), which is likely caused by the introduction of Zr ions that enables charge transfer between Co and Zr to take place. The XRD patterns of CoFeZr/NF and CoFe/NF contain Fe^{3+} peaks at the same positions (Fig. 38c), along with peaks at 182.2 and 184.6 eV corresponding to Zr $3d_{5/2}$ and Zr $3d_{3/2}$ of Zr^{4+}, respectively (Fig. 38d). As TEM and SEM images displayed in Fig. 38e show, numerous nanosheet arrays exist on the NF surface in CoFeZr/NF. The TEM image in Fig. 38f demonstrates that this material has a nanosheet structure containing numerous exposed active sites that are responsible for the permeation of electrolytes. CoFeZr/NF and NiFeZr/NF catalysts are superior bifunctional OER and HER electrocatalysts in both alkaline SW and SSW. Notably, an electrolyzer comprised of this material has nearly the same overall water splitting activities in 1 M KOH and 1 M KOH + 0.5 M NaCl (Fig. 38g). Following 20 h of continuous electrolytic operation, CoFeZr/NF retains outstanding stability (Fig. 38h). That CoFeZr-LDH is a promising electrocatalyst is evidenced by the observation that its high OER and HER activity in alkaline SSW undergoes only a slight decay with time [82].

Electrolysis of SW can be utilized to both desalinate SW and produce high-purity hydrogen. Chloride ion in SW undergoes an oxidation reaction (ClOR) that competes with the OER and corrodes the electrodes. To avoid this process, an advanced bifunctional electrocatalyst based on NiFe layered double hydroxide (LDH)/FeOOH heterostructure nanosheets (NiFe LDH/FeOOH) on nickel-iron foam (INF) was prepared using a simple electrodeposition method. The material obtained when NaCl is not present in the electrodeposition process has XRD peaks at 11.3°, 22.7°, 33.5°, 34.4°, and 38.8° (Fig. 39a), which correspond to the respective (003), (006), (101), (01), and (015) planes of NiFe LDH. Electrodeposition in the presence of NaCl produces a material that contains these XRD peaks along with a new diffraction peak at 27.0°, corresponding to the (110) plane of FeOOH. This signal might arise because of loss of chloride ions might lead to an acceleration of oxygen corrosion that forms NiFe LDH/FeOOH. The Ni 2p XPS spectrum contains two major peaks at 855.6 and 873.5 eV, which correspond to Ni $2p_{3/2}$ and Ni $2p_{1/2}$, respectively (Fig. 39b).

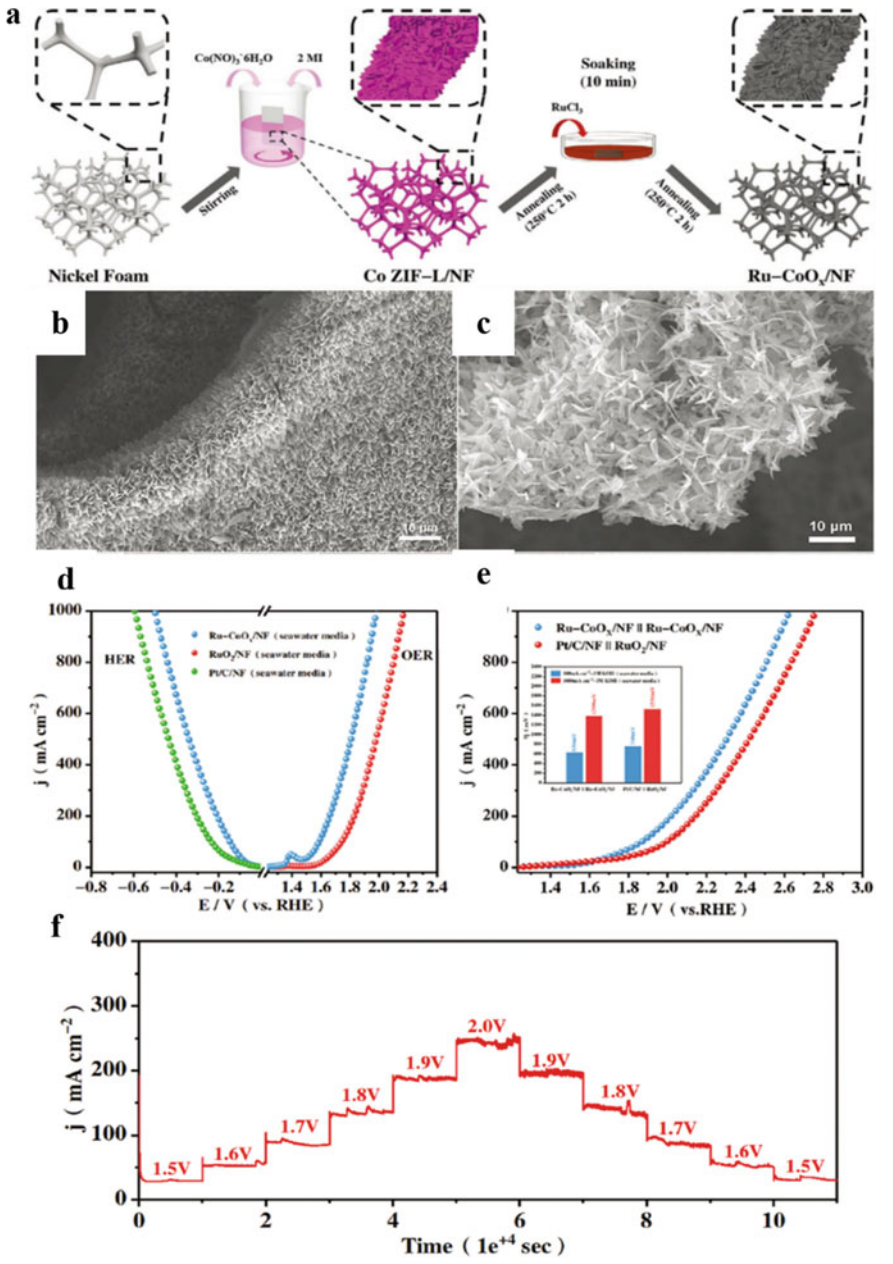

Fig. 37 **a** Diagram of the catalyst. Scanning electron microscope (SEM) images of **b** Co ZIF/L/NF and **c** Ru–CoO_x/NF. **d** Polarization curves of Ru–CoO_x/NF for HER and OER in SW media. **e** Polarization curves of Ru–CoO_x/NF||Ru–CoO_x/NF and Pt/C/NF||RuO_2/NF toward overall water splitting in SW media. Inset: the value of ΔE. **f** Ladder diagram of stability test under different voltages

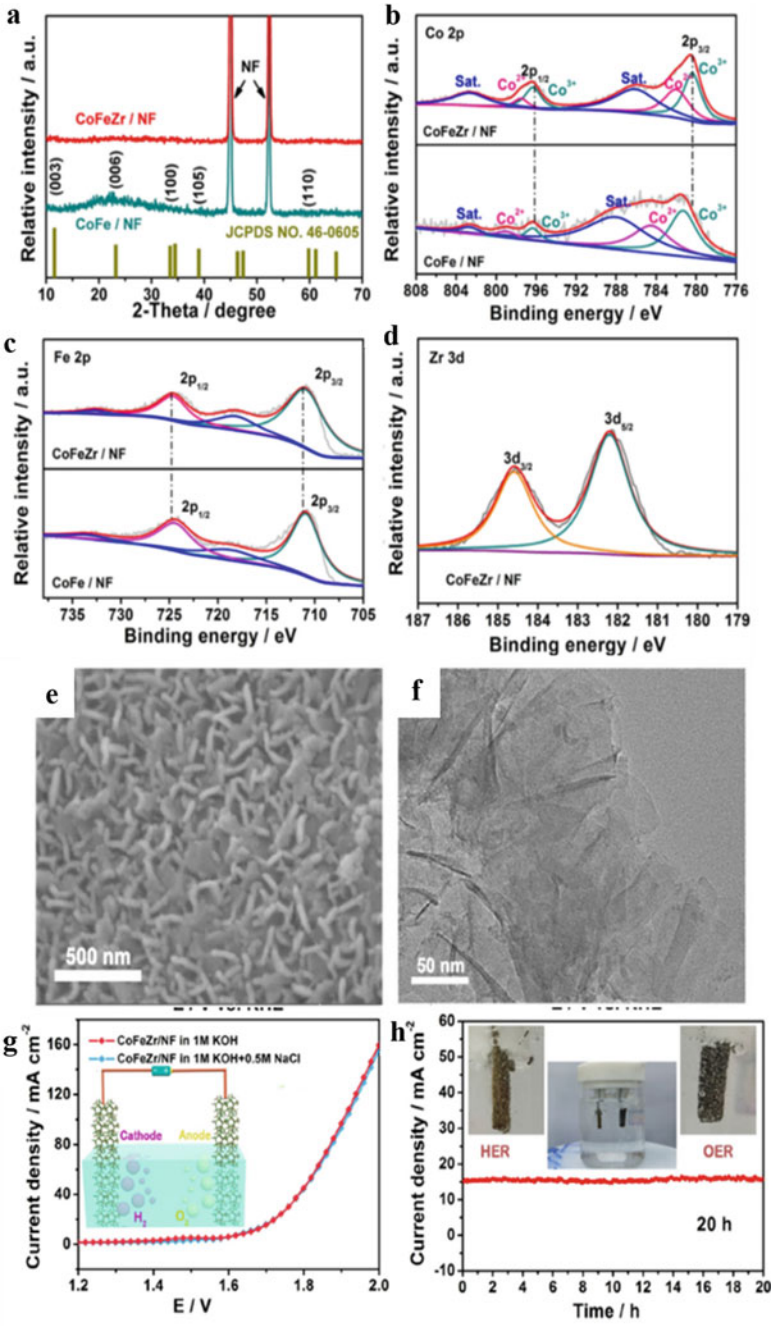
a
Relative intensity / a.u.
NF
CoFeZr / NF
(003)
(006)
(100)
(105)
(110)
CoFe / NF
JCPDS NO. 46-0605
10 20 30 40 50 60 70
2-Theta / degree
b
Co 2p
Sat.
Co2+
2p1/2
Co3+
Sat.
2p3/2
Co2+
Co3+
CoFeZr / NF
Sat.
Co2+
Co3+
Sat.
Co2+
Co3+
CoFe / NF
808 804 800 796 792 788 784 780 776
Binding energy / eV
c
Fe 2p
2p1/2
2p3/2
CoFeZr / NF
2p1/2
2p3/2
CoFe / NF
735 730 725 720 715 710 705
Binding energy / eV
d
Zr 3d
3d3/2
3d5/2
CoFeZr / NF
187 186 185 184 183 182 181 180 179
Binding energy / eV
e
500 nm
f
50 nm
g
Current density / mA cm-2
CoFeZr/NF in 1M KOH
CoFeZr/NF in 1M KOH+0.5M NaCl
Cathode
Anode
H2
O2
160
120
80
40
0
1.2 1.4 1.6 1.8 2.0
E / V
h
Current density / mA cm-2
HER
OER
20 h
60
50
40
30
20
10
0
-10
0 2 4 6 8 10 12 14 16 18 20
Time / h

◀**Fig. 38** **a** XRD patterns of as-synthesized samples. **b–d** High-resolution XPS spectra of different samples. **e** SEM and **f** TEM images for CoFeZr/NF catalyst. **g** LSV curves of catalyst in 1 M KOH and 1 M KOH + 0.5 M NaCl. **h** Durability test of the electrolyzer for 20 h in 1.0 M KOH + 0.5 M NaCl electrolyte

The Fe 2p XPS spectrum contains two major peaks at 711.9 and 725.3 eV associated with respective Fe $2p_{3/2}$ and Fe $2p_{1/2}$ (Fig. 39c). The presence of oxygen vacancies (O_v) in this material promotes its electroactivity for the OER by enhancing electrical conductivity (Fig. 39d), accelerating surface redox kinetics, and creating an abundance of active sites. The NiFe LDH/FeOOH electrode has excellent electrocatalytic activity and stability (Fig. 39g, h), which results from the strong interaction between FeOOH and NiFe LDH [44].

5.3 Metal Nitrides

Interest in metal nitrides as interstitial alloys in electrocatalysts is a consequence of their superior corrosion resistance, high conductivity and stability, and remarkable mechanical strength. The density of states in the d-band of the transition metal can be altered by the introduction of nitrogen dopants. Moreover, nitrogen doping reduces the d-band density, which leads to an enhancement of catalytic activity.

Yu et al. developed the three-dimensional core-shell metal nitride catalyst NiMoN@NiFeN, consisting of NiFeN nanoparticles uniformly distributed on NiMoN nanorods supported on Ni foam (Fig. 40a). In the first step of the preparative route, NiMoN was prepared by nitridation of $NiMoO_4$ without soaking in the precursor ink. Scanning electron microscope (SEM) images show that in this substance numerous nanorods with smooth surfaces are uniformly and vertically located on the surface of the Ni foam (Fig. 40b–d). The nanorods were soaked in the solution composed of $Fe(NO_3)_3$ and $Ni(NO_3)_2$, and then hot nitriding was performed to form NiMoN@NiFeN, which retained the good morphology of nanorods with the rough and dense surface. The surface of nanorods is uniformly and densely decorated with nanoparticles, forming a unique three-dimensional core-shell nanostructure with a large surface area and a large number of active sites (Fig. 40e). NiMoN@NiFeN is an active and durable catalyst for the OER of alkaline SW. When combined with a highly efficient HER catalyst consisting of NiMoN nanorods in a coupled electrode, the current densities reached industrial levels of 500 and 1000 mA cm^{-2}, and were performed at record low volt downs of 1.608 and 1.709 V, respectively, at alkaline SW integral splitting at 60 °C (Fig. 40f) [43].

Ni_xFe_yN@C/NF is composed of self-supported nickel-iron nitride microsheet arrays coated with carbon (Ni_3FeN@C) on commercial Ni foam. This material functions as an electrocatalyst for alkaline SW splitting (Fig. 41a). Ni_3FeN@C/NF, prepared by calcining glucose treated Ni_3Fe–OH/NF, retains the microsheet array structure of its precursor. The microsheets with microvoids in Ni_xFe_yN@C/NF not

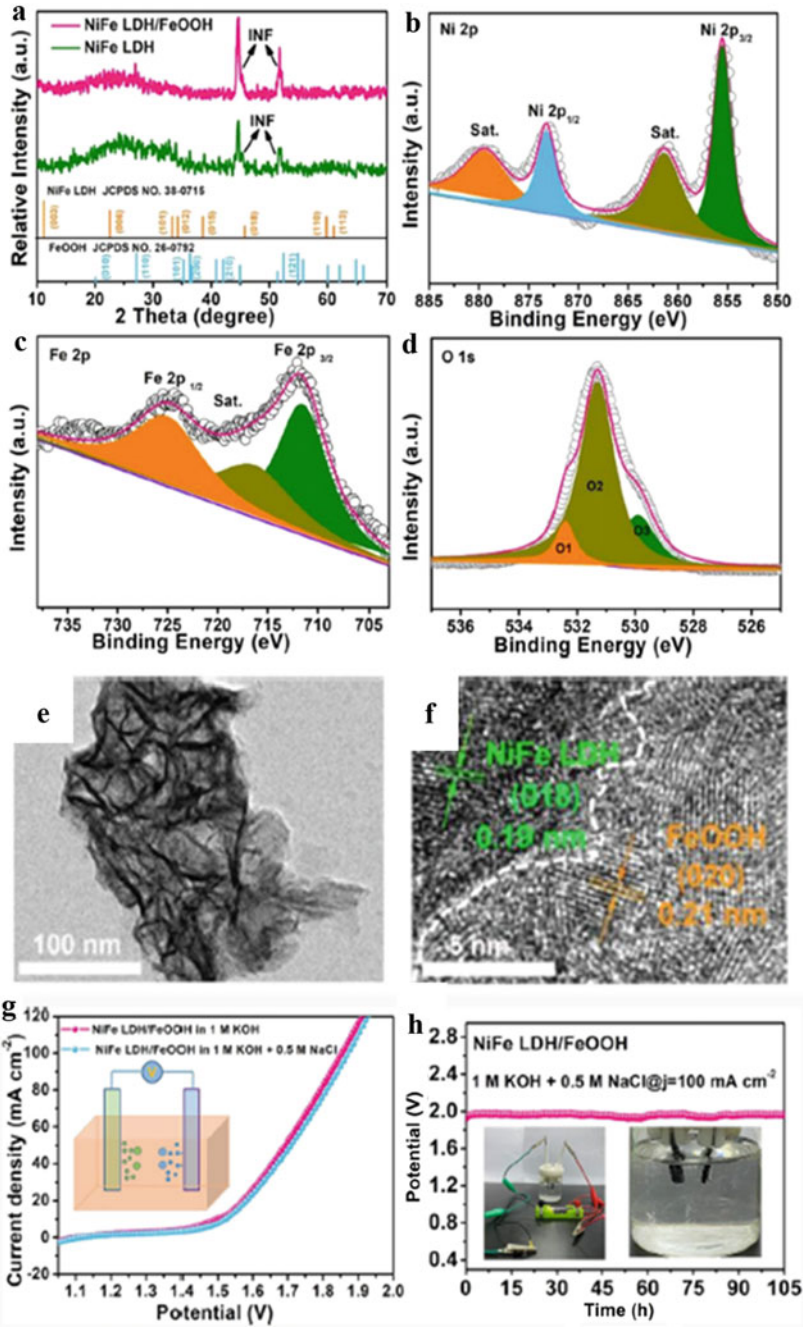
a
NiFe LDH/FeOOH
NiFe LDH
INF
INF
NiFe LDH JCPDS NO. 38-0715
FeOOH JCPDS NO. 26-0792
Relative Intensity (a.u.)
2 Theta (degree)
b
Ni 2p
Ni 2p3/2
Ni 2p1/2
Sat.
Sat.
Intensity (a.u.)
Binding Energy (eV)
c
Fe 2p
Fe 2p3/2
Fe 2p1/2
Sat.
Intensity (a.u.)
Binding Energy (eV)
d
O 1s
O2
O1
O3
Intensity (a.u.)
Binding Energy (eV)
e
100 nm
f
NiFe LDH
(018)
0.19 nm
FeOOH
(020)
0.21 nm
5 nm
g
NiFe LDH/FeOOH in 1 M KOH
NiFe LDH/FeOOH in 1 M KOH + 0.5 M NaCl
Current density (mA cm-2)
Potential (V)
h
NiFe LDH/FeOOH
1 M KOH + 0.5 M NaCl@j=100 mA cm-2
Potential (V)
Time (h)

◂**Fig. 39** **a** XRD patterns of different catalysts. **b–d** High-resolution XPS spectra of different samples. **e** TEM image and **f** HRTEM image of different catalysts. **g** LSV curves of catalyst in 1 M KOH and 1 M KOH + 0.5 M NaCl. **h** Durability test of the electrolyzer for 105 h in 1.0 M KOH + 0.5 M NaCl electrolyte

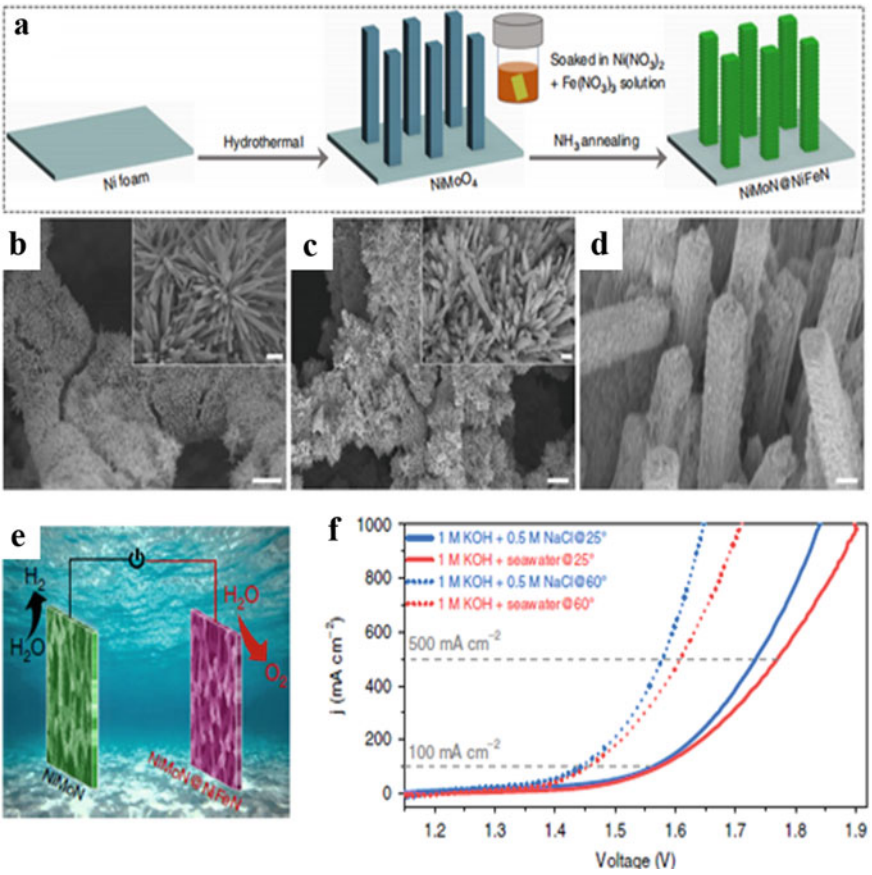

Fig. 40 **a** Diagram of the synthesis procedures for catalyst. SEM images of **b** NiMoN and **c**, **d** NiMoN@NiFeN. **e** Schematic diagram of catalyst electrolysis of seawater. **f** Comparison of polarization curves between alkaline simulated seawater and natural seawater

only provide a large surface area with abundant accessible active sites, but they also facilitate electrolyte diffusion and gas bubble release. The TEM image shows that the microsheets in Ni_3FeN@C are composed of interconnected nanoparticles (Fig. 41b–d). The carbon coating on the surface of Ni_3FeN microsheets not only inhibits the collapse of Ni_3FeN microsheets (Fig. 41e), but it also protects the interior Ni_3FeN from being poisoned and etched in SW. A device containing Ni_3FeN@C/NF as an anode and Ni_3N@C/NF as a cathode in a two-electrode alkaline SW electrolyzer

has a current density of 500 mA cm^{-2} at a low cell voltage of 1.91 V (Fig. 41f, g). The superior corrosion-resistance and electron conductivity are responsible for the 100 h durability of Ni_3FeN@C/NF (Fig. 41h). The findings suggest that transition metal nitrides coated with carbon are effective high-performance and durable hybrid electrocatalysts for hydrogen and oxygen production in SW [83].

5.4 Metal Phosphides

Metal phosphides have attracted much attention in recent years because of their high conductivity, stability, and metal-atom coordination properties. Metal phosphides have structures that are similar to those of metal-based hydrogenases. The metal and P sites in these materials serve as respective proton receptor and hydrogen receptor centers. Ma et al. described a new three-dimensional metal phosphide electrocatalyst that is created by depositing cobalt doped Fe_2P (Co–Fe_2P) on Ni foam (Fig. 42a). The Co–Fe_2P electrocatalyst is comprised of approximately 350 nm thick nanosheets emanating from the NF skeleton, which form a unique hyperbranched structure that has a large active area. The TEM image confirmed that the nanofibers in Co–Fe_2P are located at the edges of the nanosheets (Fig. 42b–d). The observed fringe spacings of 0.222 and 0.254 nm (Fig. 42e, f) correspond to the (111) and (200) planes of Fe_2P, respectively. The selected area electron diffraction (SAED) pattern of Co–Fe_2P contains rings corresponding to the (101), (200), (210), and (300) fringe planes of Fe_2P (Fig. 42g). The couple Co–Fe_2P//Co–Fe_2P is an efficient bifunctional electrocatalyst for the OER and HER in alkaline SSW (Fig. 42h), having a potential of 1.69 V to reach a current of 100 mA cm^{-2} (Fig. 42i) [84].

Indigenous scaling relationships between the adsorption energies of key intermediates in the OER cause large overpotential for SW splitting. By considering this relationship, Ren et al. developed the amorphous nickel-iron phosphide Ni_2P–Fe_2P that has a controllable morphology and high activity as an electrocatalyst for overall SW splitting. The heterogeneous Ni_2P–Fe_2P microsheet is synthesized by directly soaking Ni foam in a solution of hydrochloric acid and iron nitrate, followed by phosphidation (Fig. 43a). The TEM image of a slice of a Ni_2P–Fe_2P microsheet (Fig. 43b) shows that sheets have interplanar spacings of 0.221, 0.167, and 0.508 nm, corresponding to the (111) and (211) planes of Ni_2P and (100) plane of Fe_2P, respectively (Fig. 43c). A heterostructure, which induces an interfacial bonding effect that is beneficial for exposing more active sites, can be directly observed at the boundary between the Ni_2P and Fe_2P phases. Benefiting from a high intrinsic activity, an abundance of active sites, and a superior transfer coefficient, Ni_2P–Fe_2P has a high catalytic activity for overall water splitting (Fig. 43d), reflected in the fact that it achieves current densities of 100 and 500 mA cm^{-2} in 1 m KOH SW at voltages of 1.811 and 2.004 V, respectively. In addition, this electrocatalyst has robust durability in SW (Fig. 43e). This study shows that a general and economic approach exists for the fabrication of heterogeneous metallic phosphide catalysts for water/SW splitting [85].

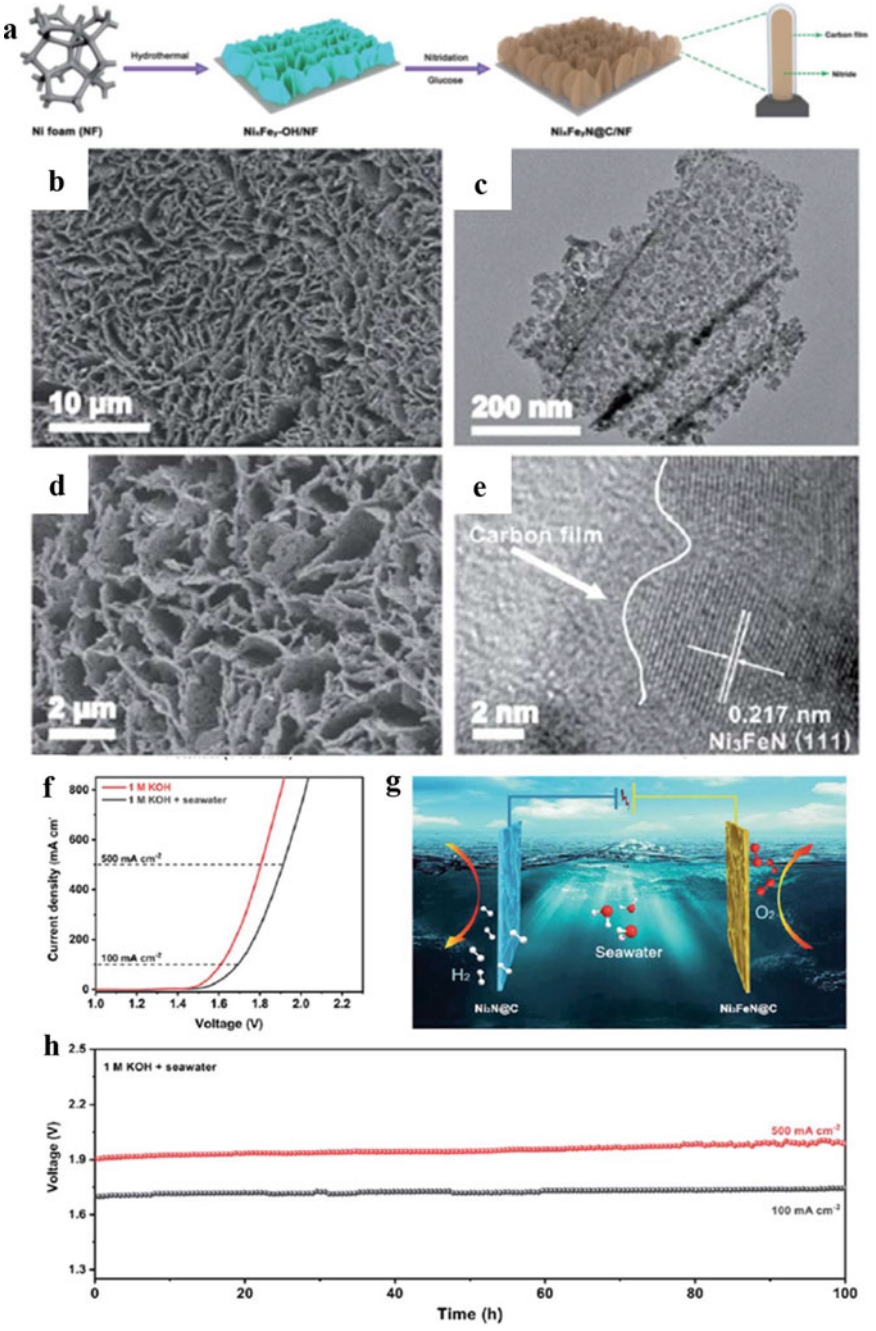
a
Hydrothermal
Nitridation
Glucose
Carbon film
Nitride
Ni foam (NF)
NixFey-OH/NF
NixFeyN@C/NF
b
10 μm
c
200 nm
d
2 μm
e
Carbon film
2 nm
0.217 nm
Ni3FeN (111)
f
1 M KOH
1 M KOH + seawater
500 mA cm-2
100 mA cm-2
Current density (mA cm-2)
Voltage (V)
g
H2
O2
Seawater
Ni3N@C
Ni3FeN@C
h
1 M KOH + seawater
500 mA cm-2
100 mA cm-2
Voltage (V)
Time (h)

◀**Fig. 41** **a** Diagram of the synthesis procedures of NixFeyN@C/NF. **b**, **d** SEM images of Ni_3FeN@C/NF; **c**, **e** TEM and HRTEM images of Ni_3FeN@C; **f** polarization curves of the electrolyzer tested in 1 M KOH and alkaline SW (1 M KOH + SW) electrolytes; **g** schematic illustration of the electrolyzer with Ni_3FeN@C/NF and Ni_3N@C/NF as the anode and cathode, respectively; **h** Stability test of 1 M KOH + seawater

5.5 Metal Chalcogenides

Transition metal dichalcogenides have recently attracted much attention owing to their excellent electrocatalytic activity, high chemical stability, and low cost. In one recent study in this area, Holade et al. devised a two-step method of production of heterogeneous materials involving combining oxidative aniline polymerization and calcination (Fig. 44a). The results of physical characterization show that this approach can be used to generate individual chalcogenides of nickel (NiS_x, x = 0, 2/3, 8/9, and 4/3) and cobalt (CoS_x, x = 0 and 8/9) on a carbon-nitrogen-sulfur nanostructure (Fig. 44b). Half-cell electrocatalytic measurements show that NaCl has no impact on the kinetics of the HER and OER occurring in dual electrode system comprised of PANI-Ni and PANI-Co. The high performances of these materials are maintained even when they are utilized in a single compartment electrolysis devise. The electrolytic process begins at a cell voltage of 1.6 V, which is close to the theoretical value of 1.45 V at 25 °C (Fig. 44c). Stability tests at 100 mA show that dual electrodes have substantiated stability with only 50 mV voltage change taking place after 17 h (Fig. 44d). The origin of the enhanced electrocatalytic performance and selectivity is the cooperative action of both the chalcogenides of nickel (NiS_x, x = 0, 2/3, 8/9, and 4/3) and cobalt (CoS_x, x = 0 and x = 8/9), the metal-support interaction and the open morphology of the bimetallic materials that expose more active sites. The results of this effort suggest new approaches on design novel, Pt-, Ru-, and Ir-free electrocatalysts for the SW electrolysis [86].

Three-dimensional cobalt selenide electrodes containing CoSe and Co_9Se_8 phases were synthesized by one-step calcination of Co foil with Se powder. Co–Se_1 and Co–Se_4 electrodes are composed of tens of nanometers of dense nanoparticles. The study of Co–Se_1 and Co–Se_4 fragments produced by electrode stripping (Fig. 45a–d) shows that the lattice stripes of Co–Se correspond to the CoSe (110) and Co_9Se_8 (440) planes, respectively, with a plane spacing of 0.181 and 0.185 nm, while the plane spacing of Co–Se_2 corresponds to the Co Se (102) and Co_9 Se_8 (44) planes respectively. This indicates that both Co–Se_1 and Co–Se_4 have CoSe and Co_9Se_8 phases. By controlling the mass ratio of added Se, the charge state of Co species can be controlled, and the performance of the prepared catalyst can be adjusted. In addition, when cobalt selenide is used as both anode and cathode, the entire SW electrolysis can be carried out at a current density of 10.3 mA cm^{-2} 1.8 V, which is three times that of the metal-based SW electrocatalyst Ir–C//Pt–C (2.9 mA cm^{-2}) at the same voltage (Fig. 45e). The electrocatalytic performance of the cobalt selenide electrode is significantly higher than that of integrated Ni/Ir–C and Ni/Pt–C electrodes (Fig. 45f).

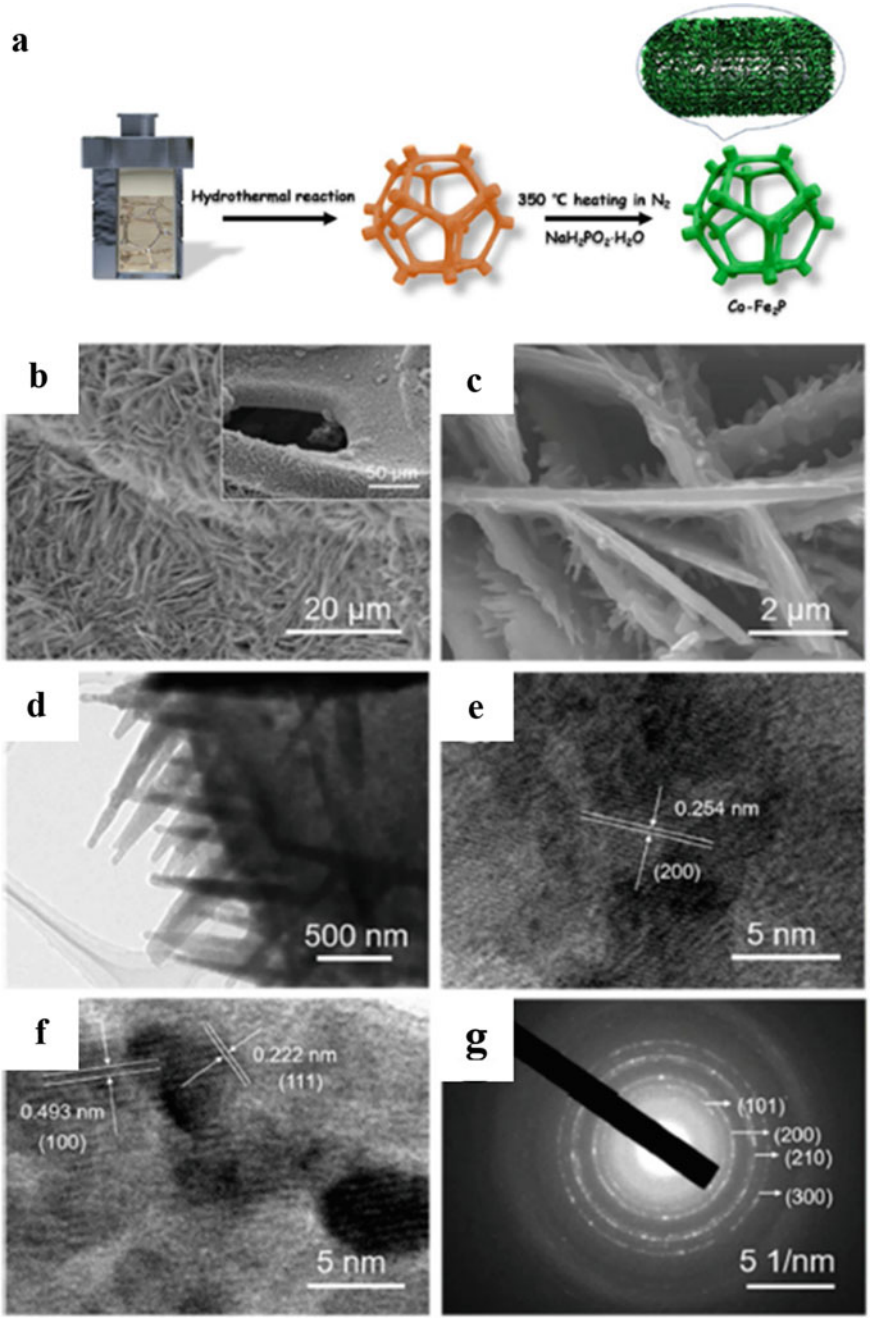
a
Hydrothermal reaction
350 °C heating in N2
NaH2PO2·H2O
Co-Fe2P
b
50 μm
20 μm
c
2 μm
d
500 nm
e
0.254 nm
(200)
5 nm
f
0.222 nm
(111)
0.493 nm
(100)
5 nm
g
(101)
(200)
(210)
(300)
5 1/nm

◀**Fig. 42** **a** Diagram of the synthesis procedures of the Co–Fe_2P. SEM (**b**, **c**), TEM (**d**–**f**), and SAED (**g**) images of the Co–Fe_2P electrocatalyst. **h** Polarization curves of Co–Fe_2P//Co–Fe_2P as electrocatalyst in simulated alkaline SW at 5 mV s^{-1}; **i** Durability test of the Co–Fe_2P electrolyzer in 1 M KOH electrolyte (a, 100 mA cm^{-2}), simulated alkaline SW (**b** 100 mA cm^{-2}) and simulated alkaline SW (**c** 250 mA cm^{-2}) at 25 °C

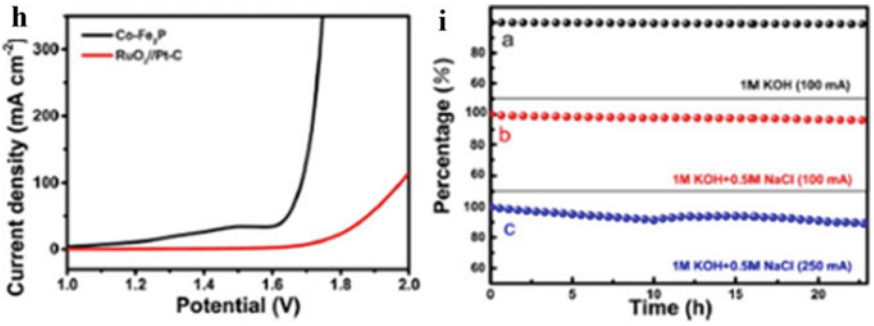

Fig. 42 (continued)

Therefore, these new bifunctional electrodes are ideal for practical large-scale water electrolysis [87].

Dai et al. designed the multilayer anode NiFe/NiS_x–Ni, consisting of a nickel–iron hydroxide (NiFe) layer uniformly coated on a nickel sulfide (NiS_x) layer located on porous Ni foam (Fig. 46a, b). With iR compensation, the overpotential applied to the NiFe/NiS_x–Ni anode to achieve an OER current density of 1500 mA/cm^2 in alkaline SSW is ~0.38 V, a value that is 110 mV lower than the 0.49 V threshold for chloride oxidation (Fig. 46c). The results of Faradaic efficiency tests conducted at 400, 800, and 1,000 mA/cm^2 all show the efficiency of the OER is nearly 100% (Fig. 46d). Two-electrode electrolysis using NiFe/NiS_x–Ni in 1 M KOH + 0.5 M NaCl occurs at cell voltages of 2.06 V, 2.27 V, and 2.44 V with respective current densities of 400, 800, and 1,000 mA/cm^2 (Fig. 46e). A continuous, highly OER active NiFe layer in this electrocatalyst along with in situ generated polyatomic sulfate and carbonate-rich passivating layers formed at the anode are responsible for chloride repulsion and the superior corrosion resistance during salt water splitting [88].

5.6 Compounds

In the past decade, various electrocatalysts-based non-noble transition metals, including those containing phosphides, nitrides, carbides, borides, and chalcogenides, have been developed as electrodes for both the HER and OER. Some of these demonstrate excellent activities that approach or even surpass those of benchmark Pt and RuO_2.

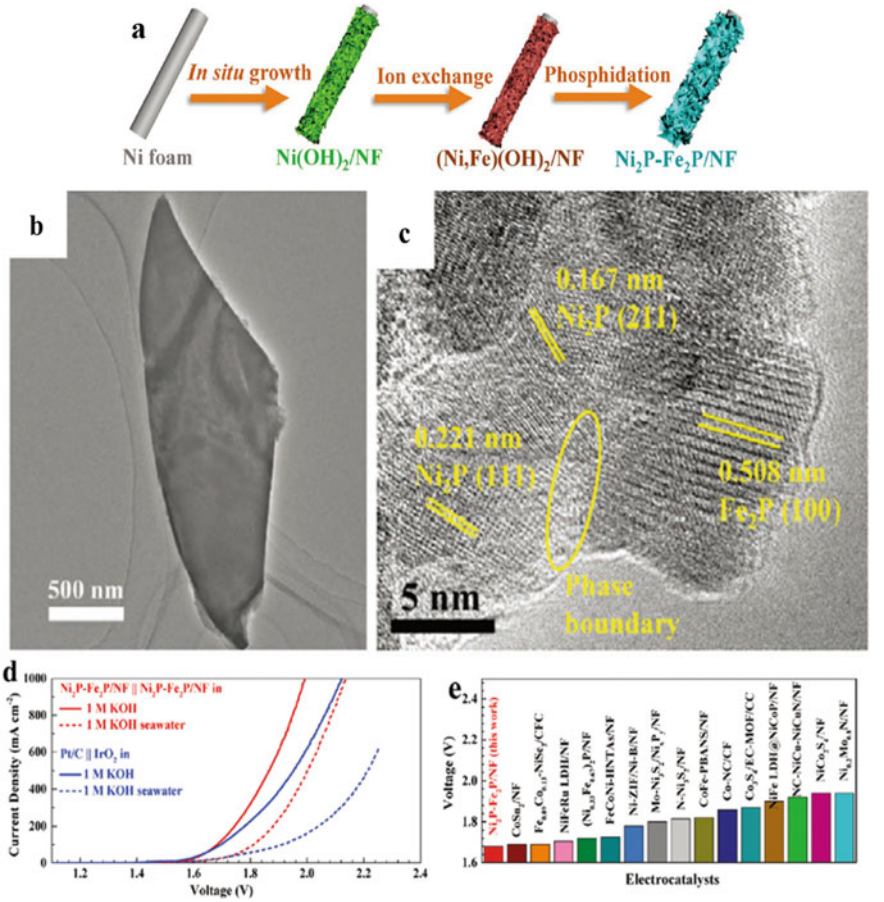

Fig. 43 **a** Diagram of the synthesis procedures of Ni_2P–Fe_2P/NF. **b** TEM and **c** HRTEM images of a slice of a Ni_2P–Fe_2P microsheet. **d** LSV performance of catalysts in 1 m KOH and 1 m KOH + SW. **e** Comparison of the voltages required to achieve a current density of 100 mA cm^{-2} for overall water splitting between Ni_2P–Fe_2P/NF and other self-supported bifunctional electrocatalysts

In recent studies, it has been reported that the catalyst composed of continuous cobalt cobalt oxide (Co–CoO) transverse heterostructure promotes the HER and OER in fresh water and SW under alkaline conditions (Fig. 47a–c). The synergistic effect produced by uniformly dispersed doped Rh and Co–CoO heterostructures produces rich active sites and excellent charge transfer capability, which together promote the HER and OER processes. Compared with the reference double electrode electrolytic cell composed of Pt/C/RuO2 1D–Cu@Co–CoO /In SSW (Fig. 47d) and SW (Fig. 47e), Rh on foam copper provides 1.60 and 1.70 V comparable battery voltage and long-term stability at 10 mA cm^{-2}, respectively. The results show that 1D Cu@Co–CoO /Rh is a promising catalyst for hydrogen production from fresh water and SW [89].

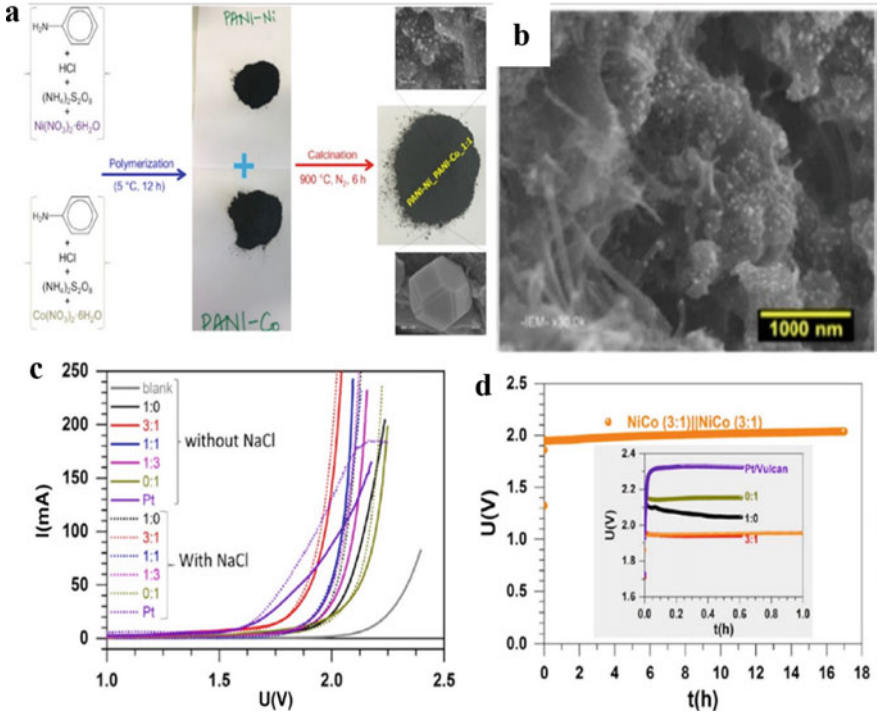

Fig. 44 **a** Schematic diagram of synthesis catalyst. **b** SEM images of the as-fabricated electrocatalysts. **c** LSV curves in 1 M NaOH in the absence (solid) and presence (dotted) of 1 M NaCl. **d** Chronopotentiometry curve recorded at 100 mA for different catalysts

Sun et al. made a nickel–cobalt phosphide/nickel–cobalt layered double hydroxide (NiCoP/NiCo–LDH) heterostructure supported on the nickel foam and showed that it plays a role as an electrocatalyst with high durability (Fig. 48a). TEM images show that NiCoP/Co LDH has a thin nanosheet structure (Fig. 48b–d). In the high-resolution TEM image, we can see the lattice stripes that match the (111) face of NiCoP and the (110) face of NiCo-LDH very well (Fig. 48e). NiCoP/NiCo LLDH heterostructure not only has excellent catalytic activity in alkaline medium, but also has excellent catalytic performance in SSW (1 M KOH + 0.5 M NaCl) (Fig. 48f, g). The current density of 50 mA cm^{-2} can be reached at a low overpotential of 1.66 V [90].

Raj et al. studied the double-layer anode, which contains dysprosium doped copper oxide (Cu0.98Dy0.02O) electrocatalyst layer, which is covered on copper sulfide (CuS) nano dendrites on stainless steel (SS) substrate (Fig. 49a, b). The double electrode electrolytic cell shows excellent performance, including the battery voltage of 1.95 V in 1 M KOH + 1.5 M NaCl, 1.70 V in 6 M KOH + 15 M NaCl, and the standard current density at 80 °C (Fig. 49c). Furthermore, an evaluation of long-term stability using chronopotentiometry analysis at a constant high current density of

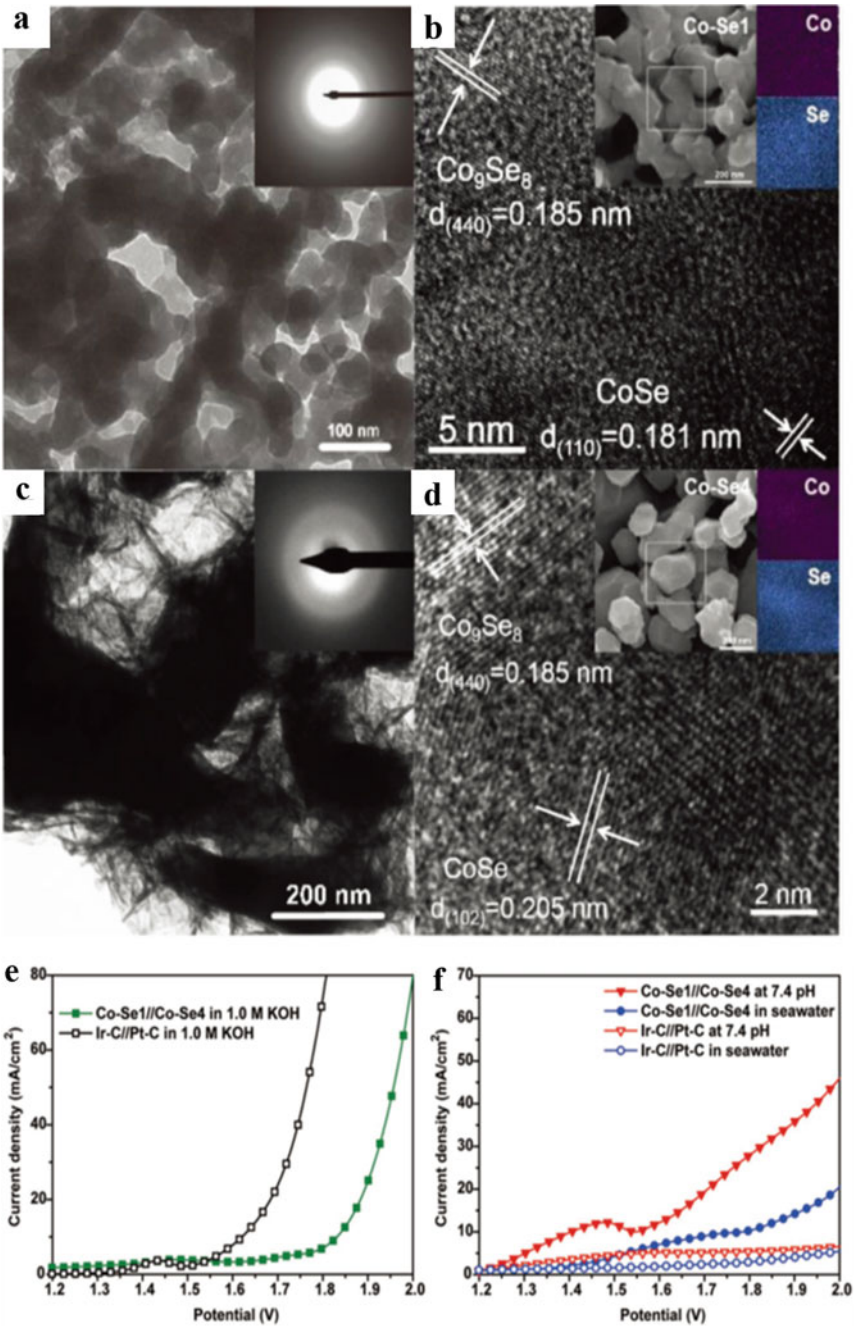

Fig. 45 TEM images and corresponding SAED pattern of **a** Co–Se1 and **c** Co–Se4; HRTEM images, (inset) SEM and elemental distribution mapping of **b** Co–Se1 and **d** Co–Se4. Polarization curves of different catalysts in **e** 1.0 m KOH and **f** buffer solution and SW

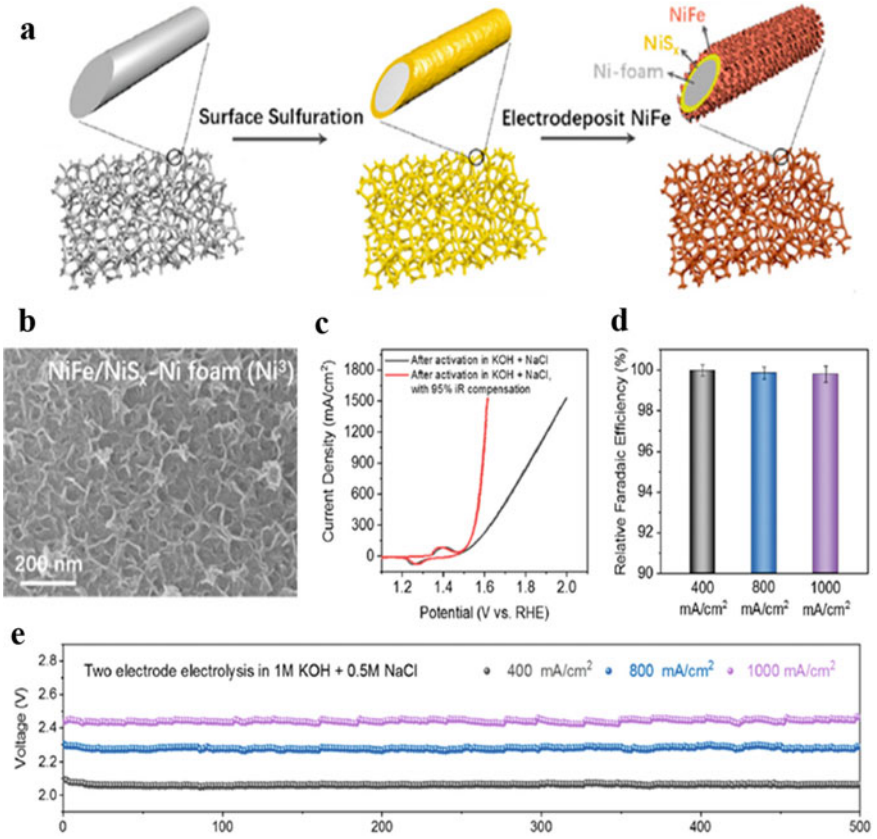

Fig. 46 **a** Schematic diagram of NiFe/NiSx–Ni foam (Ni_3) anode for SW splitting. **b** SEM images of electrodeposited NiFe on the NiSx surface. **c** CV scans with and without iR compensation of the 0.25 cm^2 Ni_3 anode shown in (**a**). **d** Comparison of oxygen production of electrolytic cells in seawater. **e** Comparison of stability tests of different catalysts under different current densities

50 mA cm^{-2} showed that this electrocatalyst is stable for a period of 12 h. A two-electrode electrolyzer comprised of this catalyst displays a constant cell voltage of 2.37 V in 1 M KOH + SW at 23 °C and 1.83 V in 6 M KOH + 1.5 M NaCl at 80 °C (Fig. 49d). The design of this material should advance the development of cheaper electrocatalysts for SW splitting for large-scale hydrogen production [91].

Highly stable 2D self-supporting catalytic electrode Ti@NiB has been developed for large-scale hydrogen production from alkaline SSW (1.0 M KOH + 0.5 M NaCl, pH = 14) (Fig. 50a). Ti@NiB is produced by electroless plating amorphous NiB on the surface of Ti plate at room temperature without the use of adhesives and other additives. When the reaction time to produce this material reaches 1 h, the size of 2–4 appears on the smooth titanium plate surface μ M honeycomb NiB particles (Fig. 50b–d). In addition, under low NiB load, there are several hole defects on the formed surface Ti@NiB. When the electroplating time reaches 1.5 h, the load of

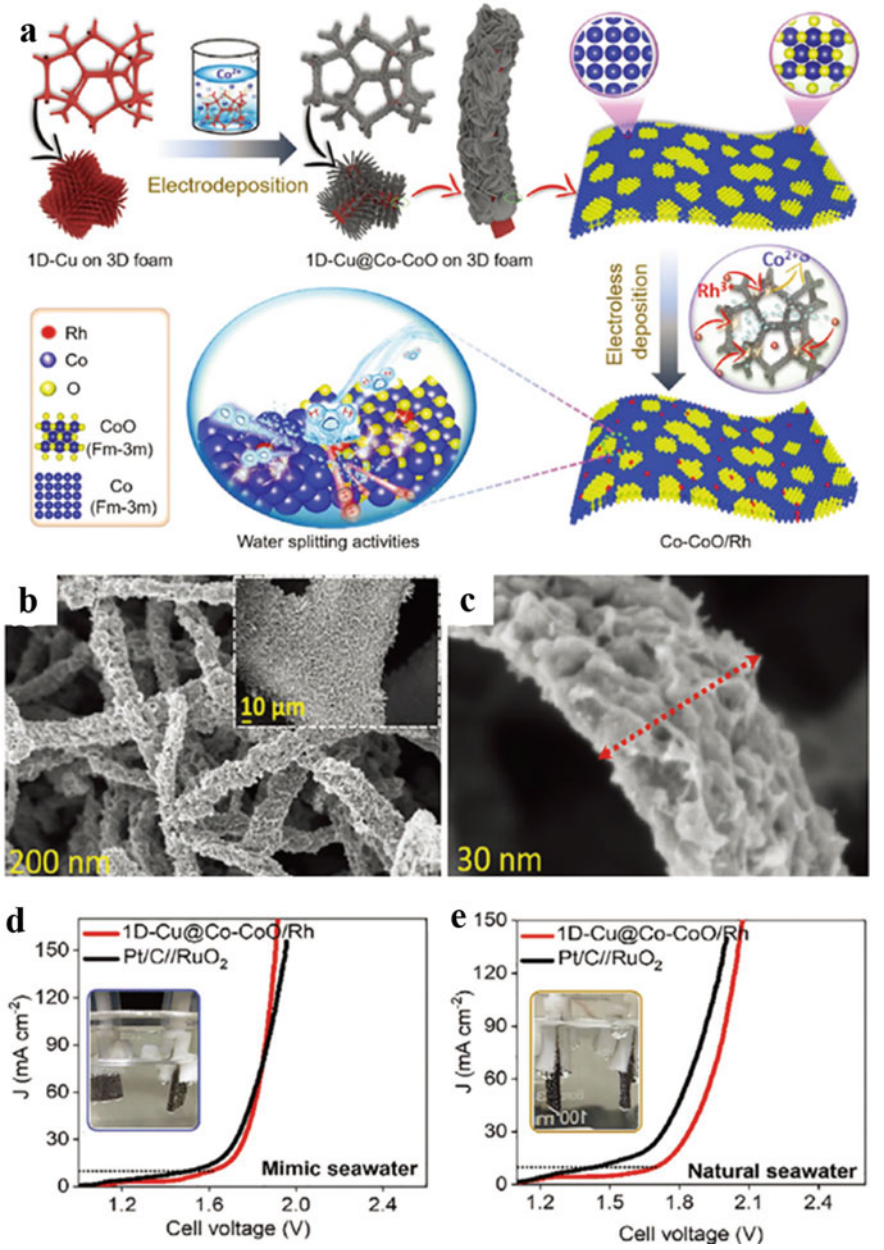

Fig. 47 **a** Schematic explanation for the preparation of core@shell 1D–Cu@Co–CoO/Rh material on a 3D foam. SEM images of **b**, **c** 1D–Cu@Co–CoO/Rh at different magnifications. V of electrolyzers coming from the 1D–Cu@Co–CoO/Rh catalyst and Pt/C//RuO_2 system in (**d**) mimic SW, and **e** natural SW under alkaline condition (inset: Optical images of the electrolyzers coming from 1D–Cu@Co–CoO/Rh catalyst working in different conditions)

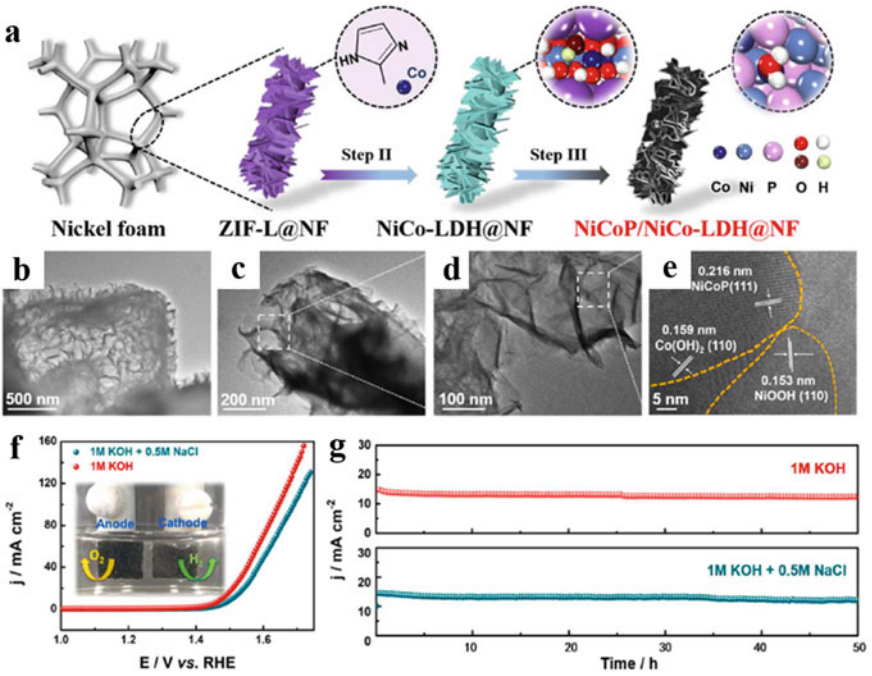

Fig. 48 **a** Diagram of the synthetic procedures for different electrocatalyst. **b–e** TEM images of NiCoP/NiCo-LDH at different magnifications. **f** Comparison of LSV performance curves of catalysts under different electrolyte conditions. **g** Chronoamperometric curves of the NiCoP/NiCo-LDH couple at an applied potential for 50 h

NiB becomes 3.2 mg·cm^{-2}, and the void defects disappear. Evenly distributed on the substrate with a diameter of 5 μ The NiB cell particles of m produced more active sites, thus improving the catalytic activity. Ti@NiB-1.5 Using 1.5 h of electroplating time, the current density of 20 mA·cm^{-2} can be reached at 1.75 V (Fig. 50e). At the same voltage, the bare titanium plate provides a current density of 5 mA·cm^{-2}, indicating that the NiB coating improves the electrocatalytic performance. After 40 h of continuous electrolysis at a constant voltage of 2.2 V, the current density has basically not changed, and the electrode surface has not changed significantly (Fig. 50f). This work provides a new strategy for designing electrodes with high activity and long-term durability [92].

6 Industrialization

In recent years, the great attention has been drawn to the use of hydrogen mainly as an automobile fuel. Imagine a vehicle that does not require gasoline but rather ages whose combustion generates water exclusively. At the present time, hydrogen

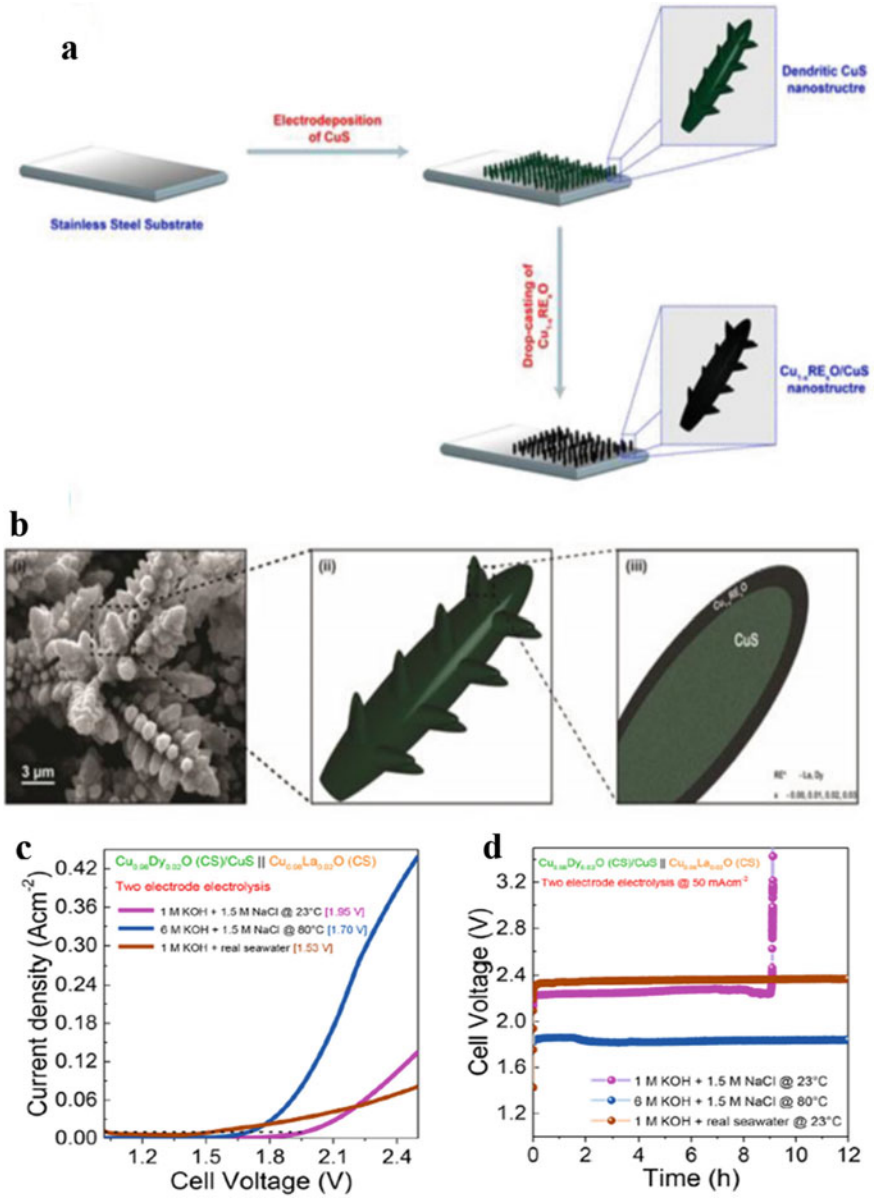

Fig. 49 **a** Diagram representation of anode fabrication and **b** SEM images and corresponding schematic diagram of nanostructures. **c** LSV for different catalysts in various electrolytes; (d) chronopotentiometric analysis for different catalysts in various electrolytes

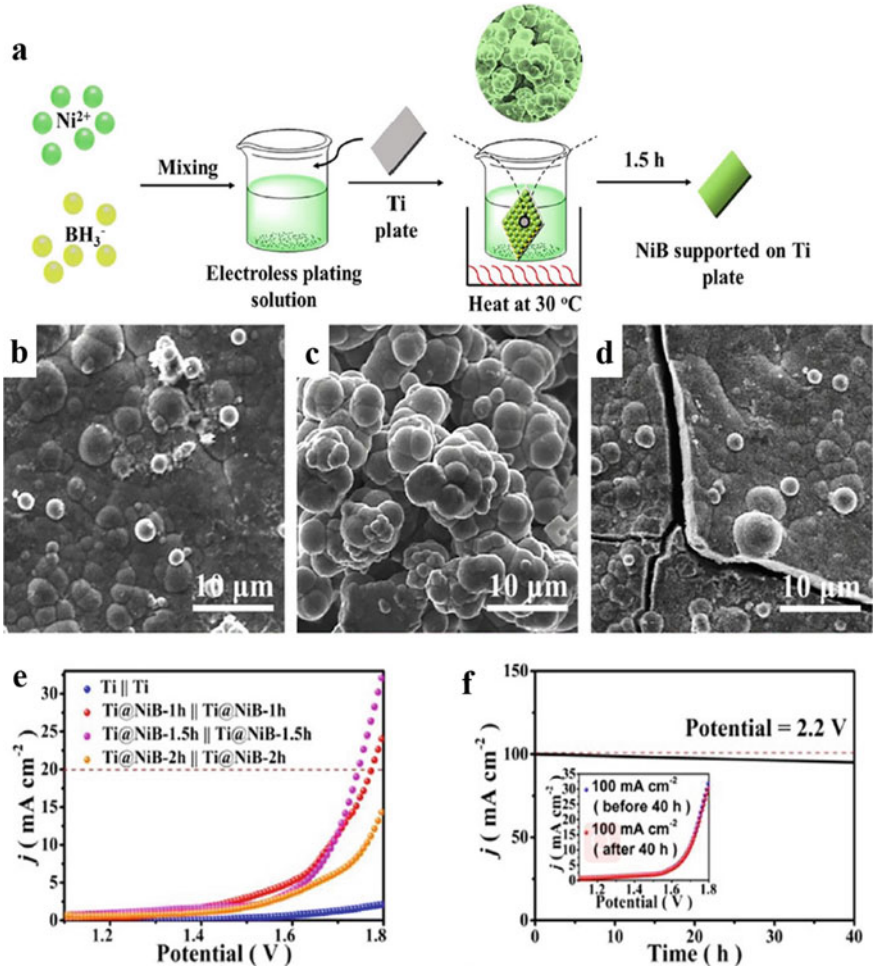

Fig. 50 **a** Illustration for preparing Ti@NiB bifunctional electrode. **b–d** SEM images for different catalysts. **e** LSV curves for different catalysts for overall water splitting; **f** chronopotentiometric measurement of overall water splitting. Inset is the LSV curves of Ti@NiB-1.5 h before and after overall water splitting

is expensive but scientists are searching for suitable methods to produce this gas at a low cost and on a large industrial scale. SW would almost be an endless source for hydrogen production using electrolytic water splitting. However, the traditional process for producing hydrogen from SW requires costly pre-purification steps to remove corrosive components or their precursors. Thus, a major goal of many current investigations is to develop systems that, along with low costs and large-scale operation capabilities, have long-term durability in electrolytic SW splitting. The aim of this chapter is to present a preliminary assessment of methods that have been developed for the direct generation of hydrogen from natural SW with a focus on the

progress that has been made, the knowledge gaps that remain, and future directions research in this area will take [28, 72].

Water electrolysis is perhaps the most promising future method for the efficient production of high-purity hydrogen (and oxygen), with inputs for this process coming from renewable solar or wind resources. In the 2007, the Bureau of Energy, Ministry of Economic Affairs of the Republic of China (Taiwan) listed the importance of hydrogen energy in a white paper on energy technology research and development. In this paper, a survey was made of various possible methods that can be employed to promote hydrogen production (Table 2) [93, 94]. This white paper also discussed the use of renewable energy for electrolysis of water and addressed the question of whether or not this method can incorporate the use of SW. Several possible approaches to produce hydrogen energy are shown in Fig. 51, with offshore wind power shown in Fig. 52 being one of the most promising [93, 95, 96].

The anode employed in hydrogen production in water electrolysis needs to be completely impervious to corrosive chlorine oxidation products that can be competitively generated by the oxidation of chloride. One approach is to use anodes that operate at potentials that do not promote chloride oxidant or that resist corrosion. In 2014, Xiamen University applied for a utility model patent of a device for hydrogen production in which electrolysis of SW is promoted using solar energy. The disclosure described a possible electrolytic cell, ion exchange membrane, cathode gas collection device, and inexpensive pole gas collection shop level device, along with a photoelectrocatalytic system that utilizes SW filtration and solar energy. Compared with traditional electricity powered systems, one that takes advantage of sunlight would have advantages in terms of cost and environmental compatibility.

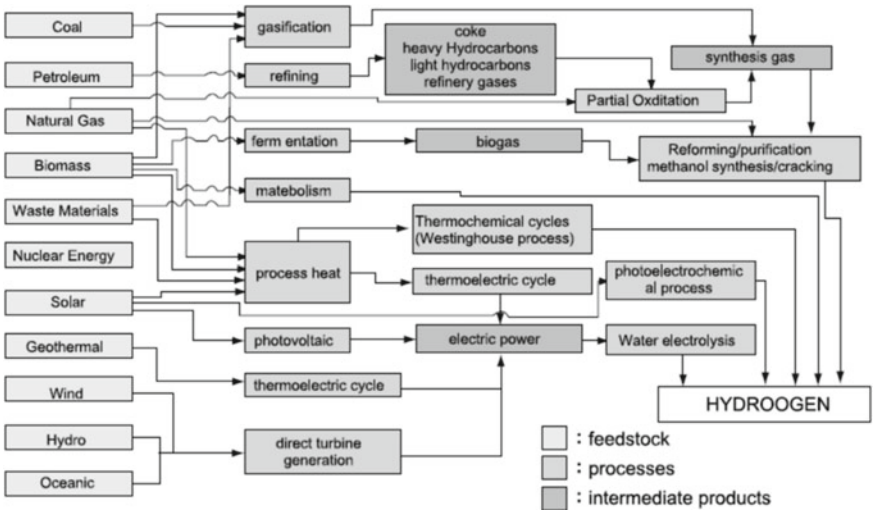

Fig. 51 Various approaches for hydrogen energy production

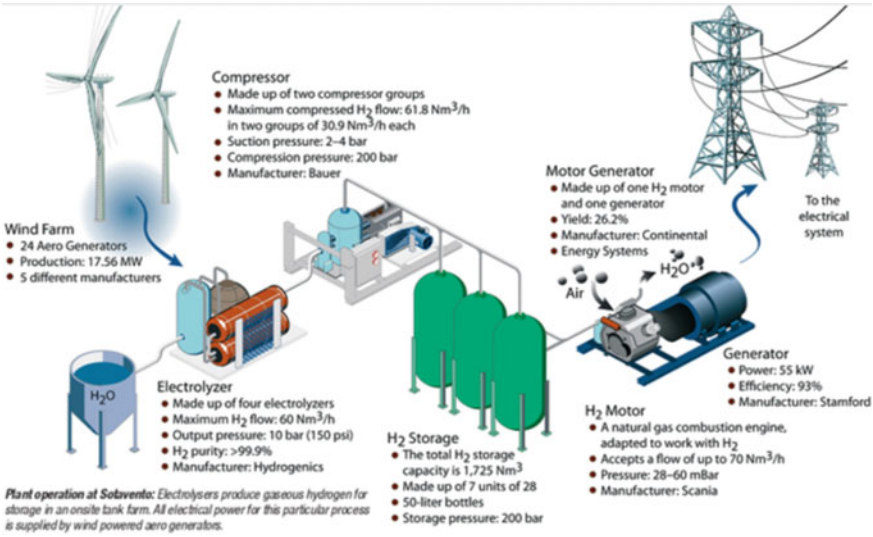

Fig. 52 Offshore wind power produces hydrogen exemplified by the Sotavento hydrogen-wind power plant

Table 2 The typical characteristics of the main electrolysis technologies [94]

	Low Temperature Electrolysis			High Temperature Electrolysis		
	Alkaline (OH^-) electrolysis		Proton Exchange (H^+) electrolysis	Oxygen ion(O^{2-}) electrolysis		
	Liquid	Polymer Electrolyte Membrane		Solid Oxide Electrolysis (SOE)		
	Conventional	Solid alkaline	H^+ - PEM	H^+ - SOE	O^{2-} - SOE	Co-electrolysis
Operation principles	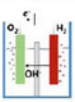	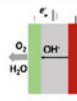	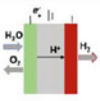	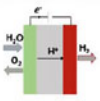	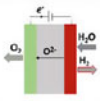	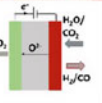
Charge carrier	OH^-	OH^-	H^+	H^+	O^{2-}	O^{2-}
Temperature	20-80°C	20-200°C	20-200°C	500-1000°C	500-1000°C	750-900°C
Electrolyte	liquid	solid (polymeric)	solid (polymeric)	solid (ceramic)	solid (ceramic)	solid (ceramic)
Anodic Reaction (OER)	$4OH^- \rightarrow 2H_2O + O_2 + 4e^-$	$4OH^- \rightarrow 2H_2O + O_2 + 4e^-$	$2H_2O \rightarrow 4H^+ + O_2 + 4e^-$	$2H_2O \rightarrow 4H^+ + 4e^- + O_2$	$O^{2-} \rightarrow {}^1/_2O_2 + 2e^-$	$O^{2-} \rightarrow {}^1/_2O_2 + 2e^-$
Anodes	Ni > Co > Fe (oxides) Perovskites: $Ba_{0.5}Sr_{0.5}Co_{0.8}Fe_{0.2}O_{3-\delta}$, $LaCoO_3$	Ni-based	IrO_2, RuO_2, $Ir_xRu_{1-x}O_2$ Supports: TiO_2, ITO, TiC	Perovskites with protonic-electronic conductivity	$La_xSr_{1-x}MnO_3$ + Y-Stabilized ZrO_2 (LSM-YSZ)	$La_xSr_{1-x}MnO_3$ + Y-Stabilized ZrO_2 (LSM-YSZ)
Cathodic Reaction (HER)	$2H_2O + 4e^- \rightarrow 4OH^- + 2H_2$	$2H_2O + 4e^- \rightarrow 4OH^- + 2H_2$	$4H^+ + 4e^- \rightarrow 2H_2$	$4H^+ + 4e^- \rightarrow 2H_2$	$H_2O + 2e^- \rightarrow H_2 + O^{2-}$	$H_2O + 2e^- \rightarrow H_2 + O^{2-}$ $CO_2 + 2e^- \rightarrow CO + O^{2-}$
Cathodes	Ni alloys	Ni, Ni-Fe, $NiFe_2O_4$	Pt/C MoS_2	Ni-cermets	Ni-YSZ Subst. $LaCrO_3$	Ni-YSZ perovskites
Efficiency	59-70%		65-82%	up to 100%	up to 100%	-
Applicability	commercial	laboratory scale	near-term commercialization	laboratory scale	demonstration	laboratory scale
Advantages	low capital cost, relatively stable, mature technology	combination of alkaline and H^+-PEM electrolysis	compact design, fast response/start-up, high-purity H_2	enhanced kinetics, thermodynamics: lower energy demands, low capital cost		+ direct production of syngas
Disadvantages	corrosive electrolyte, gas permeation, slow dynamics	low OH^- conductivity in polymeric membranes	high cost polymeric membranes; acidic: noble metals	mechanically unstable electrodes (cracking), safety issues: improper sealing		
Challenges	Improve durability/reliability; and Oxygen Evolution	Improve electrolyte	Reduce noble-metal utilization	microstructural changes in the electrodes: delamination, blocking of TPBs, passivation		C deposition, microstructural change electrodes

6.1 Electrolyzers

In addition to developing catalysts with durability and stability, it is also necessary to develop reasonable electrolytic cells to achieve high efficiency of water electrolysis. At present, the four main electrolytic cell configurations shown in Fig. 53 have been used for water separation.

Generally, PEMWE cathode and anode are separated by a solid acidic polymer electrolyte Nafion membrane (Fig. 53a), and water reacts with oxygen at the anode. The protons then reach the cathode through the proton exchange membrane. In this system, the use of SW will lead to the increase of local pH value of the cathode, which will affect the competitiveness of ClER. At the same time, the sodium ion membrane used as a proton transport agent will reduce the proton conductivity due to the influence of cationic impurities. In addition, although PEM isolates some impurities at the anode, cation substances such as $Mg^{2+}$and Ca^{2+}can still migrate from the anode to the cathode to produce metal salt deposits.

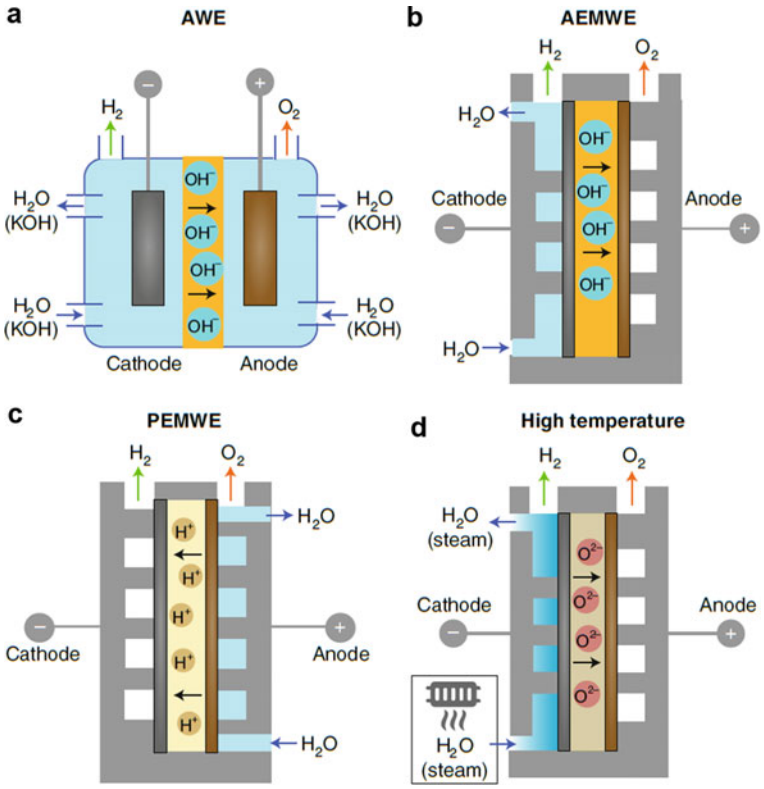

Fig. 53 Equipment for water electrolysis: **a** proton exchange membrane water electrolyzer (PEMWE), **b** anion exchange membrane water electrolyzer (AEMWE), **c** alkaline water electrolyzer (AWE), **d** high-temperature water electrolyzer

The AEMWE system consists of an anion exchange membrane (Fig. 53b). In this system, water is supplied to the cathode or/and anode. H_2 and OH^- are formed at the cathode, and OH^- migrates to the anode through the film. For SW electrolysis, due to the competitive reaction between OH^- and Cl^- oxidation, the anion exchange membrane must inhibit the migration rate of unnecessary anions. Based on the research, it is found that alkaline conditions seem more suitable for oxygen generation and reduction of Cl oxidation.

In the AWE device, the two compartments battery uses a porous membrane to conduct OH migration and prevent gas crossover (Fig. 53c). Alkaline electrolyte exists on both sides of the battery. Water is reduced at the cathode to produce H_2 and OH^-, which migrate to the anode through the diaphragm and then oxidize to form oxygen. The diaphragm used in AWE are materials like Zirfon that compared to membranes used in PEM/AEM are physically robust and unsusceptible to blockage. However, migration of anions and/or cations (like H^+, Na^+, OH^-, and Cl^-) across the diaphragm challenges this type of SW splitting systems.

The method of proton conduction ceramic membrane electrolysis (about 150–400 °C) or solid oxide electrolysis (about 800–1000 °C) using HTWE depends on the type of ions transmitted. For proton-conducting ceramic membrane electrolysis, water is only supplied to the anode, where it is oxidized to generate $H^-$and O_2. The protons then migrate to the cathode. In solid oxide electrolysis, water in the form of steam is sent to the cathode to generate hydrogen and hydroxide, which are sent to the anode to generate oxygen (Fig. 53d), which is more economical than electricity. In addition, high working temperature accelerates the reaction rate, which reduces the energy loss due to electrode polarization and improves the overall electrolysis efficiency. On the other hand, compared with the low-temperature electrolysis system, the high energy consumption and the limitation of preventing catalyst degradation are the disadvantages of HTWE system.

The configurations for electrolytic water splitting described above share common problems when they are applied to SW. Physical and chemical interference with ion exchange membranes and corrosion of metal components are the main concerns in designing systems for SW electrolysis. For example, contaminating cations such as Na^+, Mg^{2+}, and Ca^{2+} present in SW can degrade the performance of proton exchange membranes (PEMs) in PEMWE and HTWE. In addition, anions in SW such as Cl^-, Br^-, and SO^{4-} can have a negative effect on membrane performance in AEMWE, AWE, and HTWE. Moreover, bacteria/microbes and solid impurities/precipitates in SW could also lead to low efficiencies owing to physical/chemical interference. As a result, developing stabile membranes for use in SW is an important challenge that needs to be addressed. In this respect, pre-filtration of SW is one approach for extending the lifetimes of direct SW electrolyzers. To this end, simple filtration systems for natural SW that rely on membrane filtration techniques such as microfiltration and ultrafiltration are capable of solving problems associated with physical blockage by solid impurities, precipitates, and microbial contaminants. Also, to reduce metal component corrosion in electrolyzers, current collectors and separator plates that are made of titanium, graphite or stainless steel have been utilized [17, 97–99].

6.2 Purification Technique and Cost Analysis

As the price of renewable electricity continues to decrease, the development trend of hydrogen production through water electrolysis will increase globally. The limited source of high-purity water and the wide availability of SW together stimulate the research and development of direct SW electrolysis technology. Commercial water electrolysis requires more energy than reverse osmosis (SWRO) SW purification processes. Thus, the costs of SWRO can be considered and should not greatly contribute in determining the levelized cost for producing H_2 (<0.1 $ per kg H_2) from an SWRO-proton exchange membrane (SWRO-PEM) coupled process [100].

It is expected that the global market value of hydrogen energy will increase from US $142 billion in 2019 to US $209 billion in 2027. Although hydrogen is an energy carrier rather than an energy source, its production process needs to adapt to the environment and climate. Today, more than 95% of the 70 million tons of hydrogen produced annually is produced by SMR, which releases 830 million tons of carbon dioxide every year. Although the technical route of combining SMR with carbon capture and storage (CCS) technology is being tested, it is more worthwhile to use water electrolysis powered by low-carbon energy to produce sustainable hydrogen energy.

Currently, electrolytic cells based on alkaline electrolysis and proton exchange membrane (PEM) are two commercially available technologies. Alkaline electrolysis is an advanced commercial technology that has been in use since the 1920s. Several alkaline electrolytic cells with capacities of up to 165 MW were built in the last century, but almost all were decommissioned in the 1970s when SMR hydrogen production became popular. Alkaline cells have a lower capital cost than PEM systems because they do not require expensive catalysts. In addition, these systems have high system efficiency (approximately 55–70% low aggregation value), low current density (<0.45 cm^{-2}), and low operating pressure (<30 bar), and they do not have negative effects. In addition, the dynamic continuous operation of alkaline cells (unusual start-up and constant energy input) is limited (25–100% of rated load), which negatively affects efficiency and gas purity.

PEM water electrolysis was initiated by Grubb in the early 1950s and modified by General Electric Co. in the 1960s to overcome the shortcomings of alkaline electrolysis. The PEM system uses clean water, thus avoiding the need to recover and recycle corrosive potassium. Currently, the industry tends to use PEM systems due to their compact design, high efficiency (about 52–69% LHV) with high current density (<1–2 A^{-2}), fast response time, dynamic capability (0–160% nominal load), low temperature (20–80 °C), and the ability to produce ultra-pure hydrogen at high pressure (30–80 bar). Over the past few years, the cost of the PEM electrolytic cell group has been significantly reduced, so it is estimated that this technology will become the main way of sustainable hydrogen production up to 2030 [101–103].

6.2.1 Direct SW Electrolysis

One requirement of PEM water electrolysis is the need for high-purity water. The minimum requirement of the American Society for Testing and Materials (ASTM) is type II deionized (DI) water (resistivity > 1 M Ω cm^{-1}). ASTM defines Type II water as having resistivity >1 M Ω cm^{-1}, sodium, and chloride content <5 ug L^{-1}, and total organic carbon (TOC) <50 ppb. In contrast, the alkaline electrolyzer is less dependent on water, but if you want to maintain the long-term stability of its system, you still rely on high-purity water. The high-purity water required by the electrolysis system is produced by the combination of reverse osmosis (RO), multi-stage flash evaporation (MSF), electrodialysis (ED), and multiple effect distillation (MED), along with ensuing ion exchange or electrodeionization (EDI). In addition to the fact that SW is ~96.5% of earth's water resources, additional capital and operating costs associated with SW purification are a major factor that has spurred research into the development of systems for direct electrolysis of natural SW. In addition, this technology can be used in coastal arid areas lacking freshwater resources, where the amount of fresh water is small, but it is very easy to obtain opportunities for SW and renewable solar, wind, and geothermal power generation. Over the past decade, the investment in this field has generated more than 700 scientific publications and more than 340 patent applications, which has also been translated into a global allocation of millions of dollars (Fig. 54) [104, 105].

In addition to hydrogen production, SW electrolysis can be used to oxidize chlorides to produce chlorine or to produce oxygen through water oxidation process. Chlorine is a valuable industrial product, but the amount generated in the process of hydrogen formation will greatly exceed the global demand. Therefore, one major challenge in this area is the development of active and stable anode catalysts that are selective for the OER oxygen over the chlorine evolution reaction (ClER). The ClER is thermodynamically unfavorable compared to the OER (~480 mV higher in alkaline media), but it is a two-electron reaction in contrast to the OER which involves four electrons. This difference makes the OER more kinetically unfavorable. While some progress has been made in developing selective catalysts for the OER in alkaline SSW, reaching stable and industrially relevant current densities (>300 mA cm^{-2}) remains a major challenge when natural SW (pH ~ 8) is employed. It is worth noting that when the concentration of carbonate and borate ions in SW is very low, high current density cannot be maintained. Therefore, most systems that can achieve an industry related current density will add SW containing borate additives or other additives such as KOH. In addition, SW is essentially a non-buffer electrolyte. Therefore, during electrolysis, the pH value near the electrode surface will change adversely to the reaction (up to 5–9 pH units). In addition, the existence of other ions, bacteria, microorganisms, and small particles limits the stability and durability of catalysts and exchange membranes. Although a lot of resources and efforts have been invested in the development of this technology, it is still not commercialized [106].

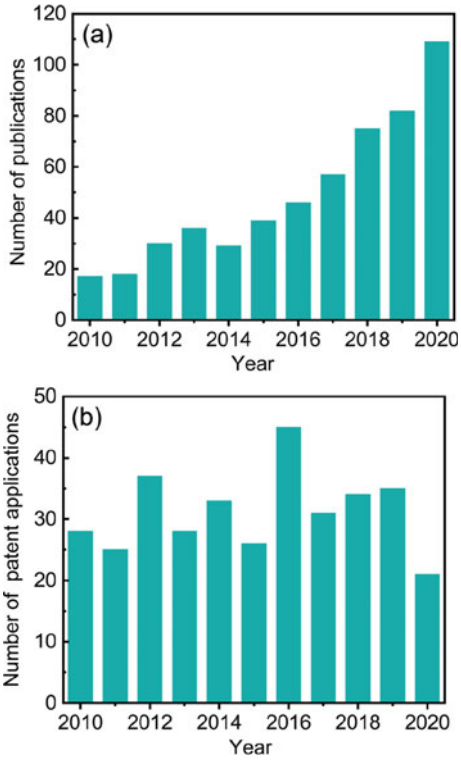

Fig. 54 **a** Annual number of publications extracted from https://www.dimensions.ai/, when a search for the topic "SW splitting" was performed. **b** Annual number of patent applications found in Patsnap database, when a search for the topic, i.e., "SW" and "electrolysis" was performed in the title, abstract, or claims

6.2.2 Desalination Technologies

In recent years, great progress has been made in seawater desalination technology through SWRO. The improvement of exchange membrane technology, high efficiency energy recovery technology, and reverse osmosis (RO) has fully reduced the corresponding energy demand, capital expenditure (CAPEX), and operating cost (OPEX). In the past decades, the energy demand of SWRO desalination plant has been reduced to less than 1/3 of the original. This resulted in the leveling cost of SWRO water being reduced to <0.6 USD/m^3, and the global desalination capacity increased 6.5 times (Fig. 55). By 2020, the total production capacity of fresh water has reached more than 100 million m^3/day. It is expected that this growth trend will be maintained in the future as the plants under construction are gradually put into use and the number of construction increases [104].

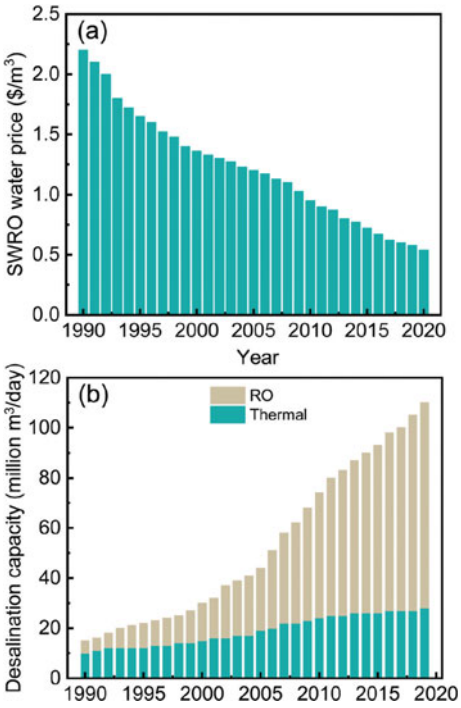

Fig. 55 **a** Histogram of the declining trend of SWRO desalinated water price and **b** Histogram of annual global installed capacity of reverse osmosis (RO) and thermal desalination process

6.3 SW Reverse Osmosis Coupled with Water Electrolysis

Figure 56 shows a PEM water electrolysis system that can produce 50 tons of hydrogen per day. It can be seen from the figure that this system is connected to SWRO plant to generate supply water. The system is powered by the existing fossil energy and renewable energy power generation grid. As shown in Fig. 57, the PEM Electrolysis Plant consists of an electrolytic cell bank and associated mechanical and electrical balance (BoP) components [14, 104, 107].

SWRO unit includes a reverse osmosis unit, which uses membrane and pump to separate salt from SW. With a high-pressure pump, water is forced to pass through a semi-permeable membrane with a dense separation layer (membrane composite membrane), allowing water to pass through, while removing dissolved salts and other impurities. In addition, in order to prevent reverse osmosis membrane (biological) scaling and scaling, SWRO system requires physical (such as dual media, sediment and carbon filter or low-pressure membrane such as ultrafiltration) and chemical (such as coagulant polymer, scale inhibitor, acid, chlorination/dechlorination) pretreatment steps, which vary with the complexity of feedwater. The carbon filter in the system can remove volatile organic compounds (VOCs), chlorine (intolerable to polyamide reverse osmosis membrane), and other pollutants, while the sediment filter

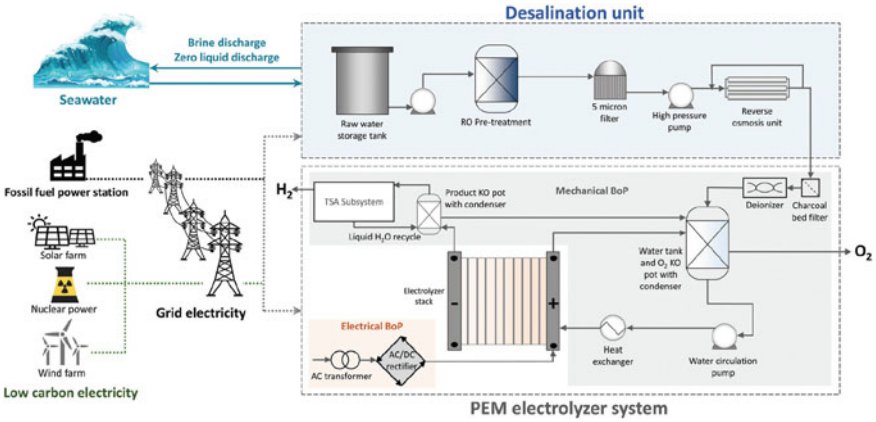

Fig. 56 Schematic diagram of grid power supply system

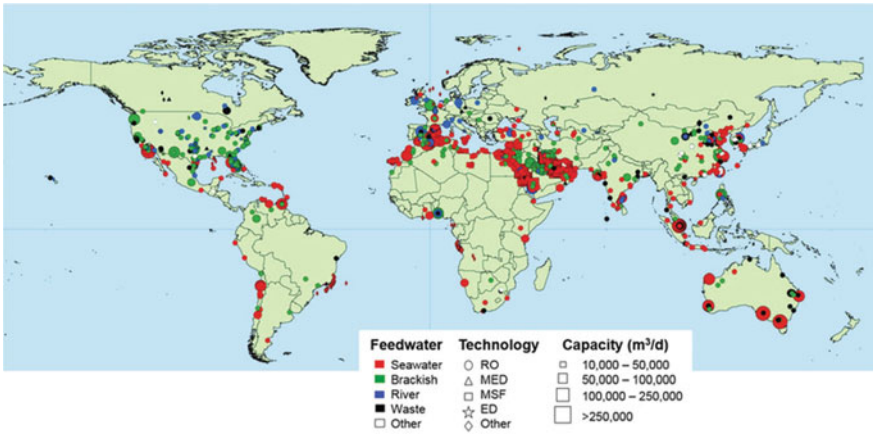

Fig. 57 Global distribution of large desalination units by capacity, water supply type, and desalination technology

can remove dirt, colloidal substances, and debris, and the reverse osmosis membrane can remove >99.8% of total dissolved solids (TDS).

As mentioned above, it is more reasonable for SWRO-PEM coupling system to be located in coastal areas receiving strong solar radiation and/or wind. Due to the sufficient seawater resources in these areas, most of them may have been equipped with relevant seawater desalination equipment (Fig. 57), so it is feasible to combine it with PEM water electrolyzer. If the technology is to be commercialized in the future, these areas are also identified for direct SW electrolysis [108].

The PEM electrolytic plant consumes 500 m^3 of SWRO water per day to produce 50 tons of hydrogen. Figure 58a shows the daily energy breakdown required to run the

coupled Swr-PEM process under industry standards, indicating that the actual energy consumption of such plants is lower (0.1% of total energy). Specifically, energy-intensive hydrolysis requires about 55.44 kWh (including BoP) to decompose 10 kg of water, while the same amount of water requires only 0.03 kWh after desalting. Figure 58b shows the capital expenditure details associated with the construction of the Wro-PEM plant. The capital cost of an SWRO plant also depends on the level of technology, the location of the plant, relevant environmental regulations, and the size of the plant. For example, a medium-sized reverse osmosis unit with a capacity of 10 million gallons per day (37,800 m^3 per day) would have a capital cost of about $80 million, while a smaller unit with a capacity of 500,000 gallons per day (1,890 m^3 per day) would cost less than a tenth of that. Unlike the previous broad approach, this analysis shows that the capex at the SWRO plant represents only about 3% of the total direct capex required for the coupling process (Fig. 58b). The detailed distribution of OPEX coupled with the SWRO-PEM process is shown in Fig. 58c. The OPEX of a PEM system depends primarily on the power consumption required to drive energy-intensive electrolysis, while other contributions come from operation and maintenance and battery pack replacement costs. On the other hand, typical OPEX for SWRO installations includes power consumption, membrane replacement, waste disposal, chemical consumption, labor, and operating maintenance costs. The OPEX of the SWRO unit represents only a small fraction (about 0.2%) of the total OPEX of the coupling process, with the power costs associated with the PEM cell (about 95%) accounting for the majority. We calculate that the average cost of hydrogen production is about $3.81 /kg without taking into account Swro-related factors. Otherwise, the cost will rise slightly to about $3.83/kg (Fig. 58d). This analysis shows that the use of SWRO water does not significantly increase H_2 production costs due to energy requirements and that capex and operating expenses for SWRO are higher than for PEM electrolysis [109].

7 Conclusion

The supply of SW in the sea is almost unlimited, and freshwater is a very precious commodity. In this case, SW electrolysis will also become an attractive electricity/hydrogen conversion and storage technology in the appropriate location and environment. This technology will be fully used and developed in areas where renewable energy supply is sufficient and seawater can be fully used. After reasonable design, the direct SW electrolyzer brings fewer engineering difficulties than the multi-step electrolyzer. The key electrochemical challenge facing these systems is to provide powerful and selective electrodes to suppress unexpected electrochemical processes related to pollutant and major chloride chemistry. As mentioned above, many highly active and selective electrocatalysts have been identified as electrode materials. However, new membrane and separation technologies need to be designed to improve the stability of direct SW electrolyzer. In addition, the additional multiple continuous purification steps may reduce the overall life of the SW electrolyzer,

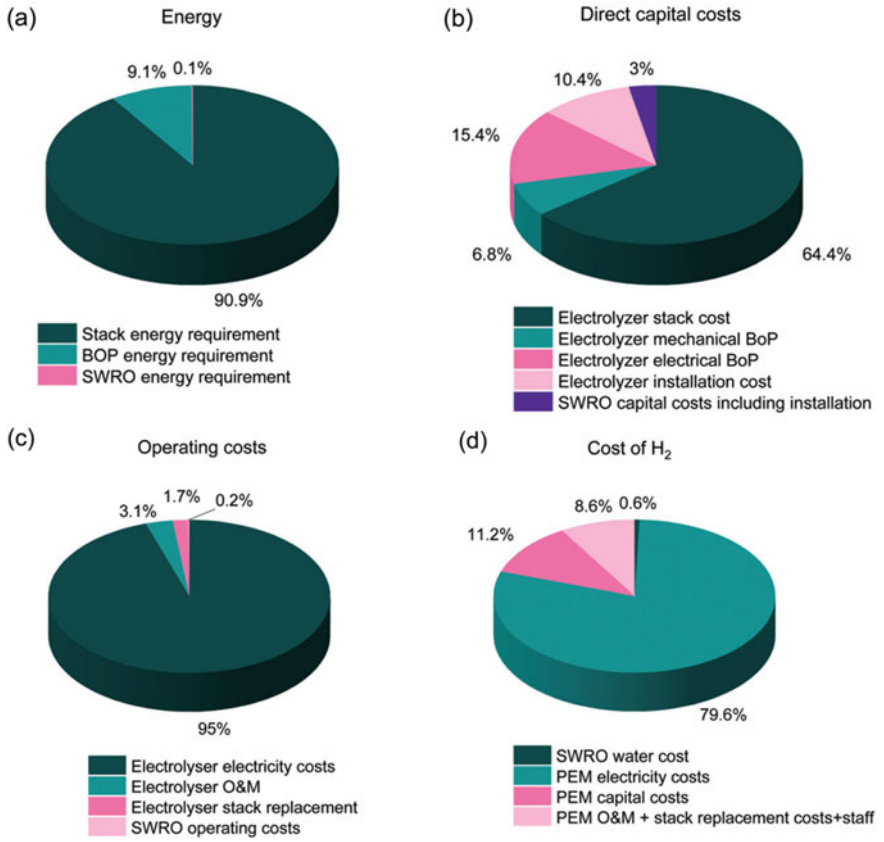

Fig. 58 Breakdown of the **a** daily energy requirement, **b** direct capital costs, **c** operating costs, and **d** levelized cost of hydrogen for an SWRO-PEM electrolysis plant operating at 50 tons H_2 per day capacity

because compared with a single direct SW separation unit, all existing methods (such as reverse osmosis system) require frequent maintenance.

In this chapter, we provided an overview of studies carried out to elucidate the basic principles and mechanistic features that are commonly used to evaluate catalysts for SW electrolysis. We surveyed almost all types of SW OER and HER electrocatalyst systems developed in past decades and discussed their synthetic strategies, reaction mechanisms, catalyst improvements, and relationships between structure and catalytic activity. We also highlighted several recent excursions into the industrialization of electrolyzers, along with purification techniques and cost analysis of SW reverse osmosis coupled with water electrolysis.

8 Outlook

Although the development of SW electrolysis has made great progress, there are still many challenges to achieve clean, economic, and sustainable large-scale hydrogen production.

The first key challenge is to design and develop highly reactive and selective electrocatalysts capable of inhibiting unnecessary electrochemical reaction processes associated with pollutants. That is, the selected catalyst needs to be stable against the oxidation of Cl_2, ClO^-, and other oxidants.

Secondly, how to use SW electrolysis to produce hydrogen and high-purity fresh water at the same time is another very important challenge. The use of advanced electrode materials and exchange membrane materials is one way to achieve this challenge.

Third, the abundance of ions in SW hinders electrocatalytic reactions in SW, which leads to undesired electrochemical reactions. Thus, removing ions from SW to improve the SW electrocatalytic efficiency is another major challenge. One way to solve this problem is to develop electrode materials that effectively use the ions in SW to produce high-value products and can simultaneously enhance SW splitting.

Fourthly, during the SW electrolysis process, the chemical state of the electrode material surface has changed greatly. Therefore, the actual reaction site of the catalyst may be very different from that of the original material. In order to better understand the electronic properties and catalytic mechanism of electrode materials, in situ test methods (synchrotron radiation and Operando) and catalytic mechanism studies are needed to determine the actual active sites. Research toward this goal will illuminate the clear structure-activity relationship required for the rational design of efficient SW electrocatalysts.

Finally, developing bifunctional electrocatalysts with high activity and durability for SW electrolysis is also a challenge, as many electrocatalysts developed to date are only highly active in semi-reactions of hydrolysis.

References

1. Sartbaeva A, Kuznetsov VL, Wells SA, Edwards PP (2008) Hydrogen nexus in a sustainable energy future. Energy Environ Sci 1(1):79
2. Ball M, Wietschel M (2009) The future of hydrogen—opportunities and challenges☆. Int J Hydrogen Energy 34(2):615–627
3. Brouwer J (2010) On the role of fuel cells and hydrogen in a more sustainable and renewable energy future. Curr Appl Phys 10(2):S9–S17
4. Marchenko OV, Solomin SV (2015) The future energy: Hydrogen versus electricity. Int J Hydrogen Energy 40(10):3801–3805
5. Singh AK, Singh S, Kumar A (2016) Hydrogen energy future with formic acid: a renewable chemical hydrogen storage system. Catal Sci Technol 6(1):12–40
6. Thomas JM, Edwards PP, Dobson PJ, Owen GP (2020) Decarbonising energy: the developing international activity in hydrogen technologies and fuel cells. J Energy Chem 51:405–415

7. Logan BE, Shi L, Rossi R (2021) Enabling the use of seawater for hydrogen gas production in water electrolyzers. Joule 5(4):760–762
8. Qazi UY (2022) Future of hydrogen as an alternative fuel for next-generation industrial applications; challenges and expected opportunities. Energies 15(13):4741
9. Wang C, Shang H, Jin L, Xu H, Du Y (2021) Advances in hydrogen production from electrocatalytic seawater splitting. Nanoscale 13(17):7897–7912
10. <science.285.5428.687.pdf>
11. Winebrake JJ, Creswick BP (2003) The future of hydrogen fueling systems for transportation. Technol Forecast Soc Chang 70(4):359–384
12. Feng W (2004) The future of hydrogen infrastructure for fuel cell vehicles in China and a case of application in Beijing. Int J Hydrogen Energy 29(4):355–367
13. Edwards PP, Kuznetsov VL, David WIF, Brandon NP (2008) Hydrogen and fuel cells: towards a sustainable energy future. Energy Policy 36(12):4356–4362
14. Barbir F (2005) PEM electrolysis for production of hydrogen from renewable energy sources. Sol Energy 78(5):661–669
15. Carmo M, Fritz DL, Mergel J, Stolten D (2013) A comprehensive review on PEM water electrolysis. Int J Hydrogen Energy 38(12):4901–4934
16. Litster S, McLean G (2004) PEM fuel cell electrodes. J Power Sources 130(1–2):61–76
17. Liu G, Xu Y, Yang T, Jiang L (2020) Recent advances in electrocatalysts for seawater splitting. Nano Mater Sci
18. Khatun S, Hirani H, Roy P (2021) Seawater electrocatalysis: activity and selectivity. J Mater Chem A 9(1):74–86
19. Dresp S, Dionigi F, Klingenhof M, Strasser P (2019) Direct electrolytic splitting of seawater: opportunities and challenges. ACS Energy Lett 4(4):933–942
20. Zhang J, Hu W, Cao S, Piao L (2020) Recent progress for hydrogen production by photocatalytic natural or simulated seawater splitting. Nano Res 13(9):2313–2322
21. Hausmann JN, Schlögl R, Menezes PW, Driess M (2021) Is direct seawater splitting economically meaningful? Energy Environ Sci 14(7):3679–3685
22. Zheng Y, Jiao Y, Vasileff A, Qiao SZ (2018) The hydrogen evolution reaction in alkaline solution: from theory, single crystal models, to practical electrocatalysts. Angew Chem 57(26):7568–7579
23. Chen Z, Duan X, Wei W, Wang S, Ni B-J (2019) Recent advances in transition metal-based electrocatalysts for alkaline hydrogen evolution. J Mater Chem A 7(25):14971–15005
24. Wang X, Zheng Y, Sheng W, Xu ZJ, Jaroniec M, Qiao S-Z (2020) Strategies for design of electrocatalysts for hydrogen evolution under alkaline conditions. Mater Today 36:125–138
25. Jiang S, Liu Y, Qiu H, Su C, Shao Z (2022) High selectivity electrocatalysts for oxygen evolution reaction and anti-chlorine corrosion strategies in seawater splitting. Catalysts 12(3):261
26. <ChemSusChem—2017—Fukuzumi—Fuel Production from Seawater and Fuel Cells Using Seawater.pdf>
27. Exner KS, Sohrabnejad-Eskan I, Over H (2018) A universal approach to determine the free energy diagram of an electrocatalytic reaction. ACS Catal 8(3):1864–1879
28. Wu D, Chen D, Zhu J, Mu S (2021) Ultralow Ru incorporated amorphous cobalt-based oxides for high-current-density overall water splitting in alkaline and seawater media. Small 17(39):e2102777
29. <A universal synthesis strategy for single atom dispersed cobalt_metal clusters heterostructure boosting hydrogen evolution catalysis at all pH values.pdf>
30. Xiang K, Song Z, Wu D, Deng X, Wang X, You W, Peng Z, Wang L, Luo J-L, Fu X-Z (2021) Bifunctional Pt–Co_3O_4 electrocatalysts for simultaneous generation of hydrogen and formate via energy-saving alkaline seawater/methanol co-electrolysis. J Mater Chem A 9(10):6316–6324
31. Xiao YX, Ying J, Tian G, Yang X, Zhang YX, Chen JB, Wang Y, Symes MD, Ozoemena KI, Wu J, Yang XY (2021) Hierarchically fractal PtPdCu sponges and their directed mass- and electron-transfer effects. Nano Lett 21(18):7870–7878

32. Xiao Y-X, Ying J, Chen J-B, Dong Y, Yang X, Tian G, Wu J, Janiak C, Ozoemena KI, Yang X-Y (2022) Confined ultrafine Pt in porous carbon fibers and their N-enhanced heavy d-π effect. Chem Mater 34(8):3705–3714
33. Xiao Y-X, Ying J, Tian G, Tao Y, Wei H, Fan S-Y, Sun Z-H, Zou W-J, Hu J, Chang G-G, Li W, Yang X-Y, Janiak C (2019) Highly dispersed PtPd on graphitic nanofibers and its heavy d-π effect. Appl Catal B 259:118080
34. Xiao YX, Ying J, Tian G, Zhang XQ, Janiak C, Ozoemena KI, Yang XY (2021) PtPd hollow nanocubes with enhanced alloy effect and active facets for efficient methanol oxidation reaction. Chem Commun 57(8):986–989
35. Dong Y, Ying J, Xiao YX, Chen JB, Yang XY (2021) Highly dispersed Pt nanoparticles embedded in N-doped porous carbon for efficient hydrogen evolution. Chem Asian J 16(14):1878–1881
36. Zheng W, Lee LYS, Wong KY (2021) Improving the performance stability of direct seawater electrolysis: from catalyst design to electrode engineering. Nanoscale 13(36):15177–15187
37. Zheng J, Zhao Y, Xi H, Li C (2018) Seawater splitting for hydrogen evolution by robust electrocatalysts from secondary M (M = Cr, Fe Co, Ni, Mo) incorporated Pt. RSC Adv 8(17):9423–9429
38. Xiu L, Pei W, Zhou S, Wang Z, Yang P, Zhao J, Qiu J (2020) Multilevel hollow MXene tailored low-Pt catalyst for efficient hydrogen evolution in full-pH range and seawater. Adv Funct Mater 30(47):1910028
39. Wang Y, Luo W, Li H, Cheng C (2021) Ultrafine Ru nanoclusters supported on N/S doped macroporous carbon spheres for efficient hydrogen evolution reaction. Nanoscale Adv 3(17):5068–5074
40. Wang S, Wang M, Liu Z, Liu S, Chen Y, Li M, Zhang H, Wu Q, Guo J, Feng X, Chen Z, Pan Y (2022) Synergetic function of the single-atom Ru-N_4 site and Ru nanoparticles for hydrogen production in a wide pH range and seawater electrolysis. ACS Appl Mater Interfaces 14(13):15250–15258
41. Li H, Tang Q, He B, Yang P (2016) Robust electrocatalysts from an alloyed Pt–Ru–M (M = Cr, Fe Co, Ni, Mo)-decorated Ti mesh for hydrogen evolution by seawater splitting. J Mater Chem A 4(17):6513–6520
42. Niu X, Tang Q, He B, Yang P (2016) Robust and stable ruthenium alloy electrocatalysts for hydrogen evolution by seawater splitting. Electrochim Acta 208:180–187
43. Yu L, Zhu Q, Song S, McElhenny B, Wang D, Wu C, Qin Z, Bao J, Yu Y, Chen S, Ren Z (2019) Non-noble metal-nitride based electrocatalysts for high-performance alkaline seawater electrolysis. Nat Commun 10(1):5106
44. Jiang K, Liu W, Lai W, Wang M, Li Q, Wang Z, Yuan J, Deng Y, Bao J, Ji H (2021) NiFe layered double hydroxide/FeOOH heterostructure nanosheets as an efficient and durable bifunctional electrocatalyst for overall seawater splitting. Inorg Chem 60(22):17371–17378
45. Zang W, Sun T, Yang T, Xi S, Waqar M, Kou Z, Lyu Z, Feng YP, Wang J, Pennycook SJ (2021) Efficient hydrogen evolution of oxidized Ni-N_3 defective sites for alkaline freshwater and seawater electrolysis. Adv Mater 33(8):e2003846
46. Zhang Y-C, Han C, Gao J, Pan L, Wu J, Zhu X-D, Zou J-J (2021) NiCo-based electrocatalysts for the alkaline oxygen evolution reaction: a review. ACS Catal 11(20):12485–12509
47. Su Y-Z, Xu Q-Z, Chen G-F, Cheng H, Li N, Liu Z-Q (2015) One dimensionally spinel $NiCo_2O_4$ nanowire arrays: facile synthesis, water oxidation, and magnetic properties. Electrochim Acta 174:1216–1224
48. Tran PKL, Tran DT, Malhotra D, Prabhakaran S, Kim DH, Kim NH, Lee JH (2021) Highly effective freshwater and seawater electrolysis enabled by atomic Rh-modulated Co-CoO lateral heterostructures. Small 17(50):e2103826
49. Lv XW, Liu XL, Suo YJ, Liu YP, Yuan ZY (2021) Identifying the dominant role of pyridinic-N-Mo bonding in synergistic electrocatalysis for ambient nitrogen reduction. ACS Nano
50. Wang XR, Liu JY, Liu ZW, Wang WC, Luo J, Han XP, Du XW, Qiao SZ, Yang J (208) Identifying the key role of pyridinic-N-Co bonding in synergistic electrocatalysis for reversible ORR/OER. Adv Mater 30(23):e1800005

51. <2019-pnas-NiFeNiSx-N-镍网载片状-全解水.pdf>
52. Ma F, Wang S, Gong X, Liu X, Wang Z, Wang P, Liu Y, Cheng H, Dai Y, Zheng Z, Huang B (2022) Highly efficient electrocatalytic hydrogen evolution coupled with upcycling of microplastics in seawater enabled via Ni3N/W5N4 janus nanostructures. Appl Catal B 307:121198
53. Jin H, Wang X, Tang C, Vasileff A, Li L, Slattery A, Qiao SZ (2021) Stable and highly efficient hydrogen evolution from seawater enabled by an unsaturated nickel surface nitride. Adv Mater 33(13):e2007508
54. Jin H, Liu X, Vasileff A, Jiao Y, Zhao Y, Zheng Y, Qiao SZ (2018) Single-crystal nitrogen-rich two-dimensional Mo_5N_6 nanosheets for efficient and stable seawater splitting. ACS Nano 12(12):12761–12769
55. Wu L, Yu L, Zhang F, McElhenny B, Luo D, Karim A, Chen S, Ren Z (2020) Heterogeneous bimetallic phosphide Ni_2P-Fe_2P as an efficient bifunctional catalyst for water/seawater splitting. Adv Funct Mater 31(1):2006484
56. Liu D, Ai H, Chen M, Zhou P, Li B, Liu D, Du X, Lo KH, Ng KW, Wang SP, Chen S, Xing G, Hu J, Pan H (2021) Multi-phase heterostructure of CoNiP/Cox P for enhanced hydrogen evolution under alkaline and seawater conditions by promoting H_2O dissociation. Small 17(17):e2007557
57. Liu G, Wang M, Xu Y, Wang X, Li X, Liu J, Cui X, Jiang L (2021) Porous CoP/Co_2P heterostructure for efficient hydrogen evolution and application in magnesium/seawater battery. J Power Sources 486:229351
58. Wu L, Yu L, McElhenny B, Xing X, Luo D, Zhang F, Bao J, Chen S, Ren Z (2021) Rational design of core-shell-structured CoP @FeOOH for efficient seawater electrolysis. Appl Catal B 294:120256
59. Ma Y-Y, Wu C-X, Feng X-J, Tan H-Q, Yan L-K, Liu Y, Kang Z-H, Wang E-B, Li Y-G (2017) Highly efficient hydrogen evolution from seawater by a low-cost and stable CoMoP@C electrocatalyst superior to Pt/C. Energy Environ Sci 10(3):788–798
60. Chen IP, Hsiao CH, Huang JY, Peng YH, Chang CY (2019) Highly efficient hydrogen evolution from seawater by biofunctionalized exfoliated MoS_2 quantum dot aerogel electrocatalysts that is superior to Pt. ACS Appl Mater Interfaces 11(15):14159–14165
61. Zhang B, Xu W, Liu S, Chen X, Ma T, Wang G, Lu Z, Sun J (2021) Enhanced interface interaction in Cu_2S@Ni core-shell nanorod arrays as hydrogen evolution reaction electrode for alkaline seawater electrolysis. J Power Sources 506:230235
62. Cui B, Hu Z, Liu C, Liu S, Chen F, Hu S, Zhang J, Zhou W, Deng Y, Qin Z, Wu Z, Chen Y, Cui L, Hu W (2020) Heterogeneous lamellar-edged Fe-Ni$(OH)_2$/Ni_3S_2 nanoarray for efficient and stable seawater oxidation. Nano Res 14(4):1149–1155
63. Liu W, Jiang K, Hu Y, Li Q, Deng Y, Bao J, Lei Y (2021) Zr-doped CoFe-layered double hydroxides for highly efficient seawater electrolysis. J Colloid Interface Sci 604:767–775
64. Yu L, Wu L, Song S, McElhenny B, Zhang F, Chen S, Ren Z (2020) Hydrogen generation from seawater electrolysis over a sandwich-like NiCoN|Ni_xP|NiCoN microsheet array catalyst. ACS Energy Lett 5(8):2681–2689
65. Rüetschi P, Delahay P (1955) Influence of electrode material on oxygen overvoltage: a theoretical analysis. J Chem Phys 23(3):556–560
66. Trasatti S (1984) Electrocatalysis in the anodic evolution of oxygen and chlorine. Electrochim Acta 29(11):1503–1512
67. Gayen P, Saha S, Ramani V (2020) Selective seawater splitting using pyrochlore electrocatalyst. Acs Appl Energ Mater 3(4):3978–3983
68. Yang J, Wang Y, Yang J, Pang Y, Zhu X, Lu Y, Wu Y, Wang J, Chen H, Kou Z, Shen Z, Pan Z, Wang J (2022) Quench-induced surface engineering boosts alkaline freshwater and seawater oxygen evolution reaction of porous $NiCo_2O_4$ nanowires. Small 18(3):2106187
69. Dionigi F, Reier T, Pawolek Z, Gliech M, Strasser P (2016) Design criteria, operating conditions, and nickel-iron hydroxide catalyst materials for selective seawater electrolysis. Chemsuschem 9(9):962–972

70. Park YS, Lee J, Jang MJ, Yang J, Jeong J, Park J, Kim Y, Seo MH, Chen Z, Choi SM (2021) High-performance anion exchange membrane alkaline seawater electrolysis. J Mater Chem A 9(15):9586–9592
71. Yu Z-Y, Duan Y, Feng X-Y, Yu X, Gao M-R, Yu S-H (2021) Clean and affordable hydrogen fuel from alkaline water splitting: past, recent progress, and future prospects. Adv Mater 33(31):2007100
72. Wang C, Zhu M, Cao Z, Zhu P, Cao Y, Xu X, Xu C, Yin Z (2021) Heterogeneous bimetallic sulfides based seawater electrolysis towards stable industrial-level large current density. Appl Catal B 291:120071
73. Chang J, Wang G, Yang Z, Li B, Wang Q, Kuliiev R, Orlovskaya N, Gu M, Du Y, Wang G, Yang Y (2021) Dual-doping and synergism toward high-performance seawater electrolysis. Adv Mater 33(33):2101425
74. Song HJ, Yoon H, Ju B, Lee D-Y, Kim D-W (2020) Electrocatalytic selective oxygen evolution of carbon-coated Na_2Co_1–$xFe_xP_2O_7$ nanoparticles for alkaline seawater electrolysis. ACS Catal 10(1):702–709
75. Jadhav AR, Kumar A, Lee J, Yang T, Na S, Lee J, Luo Y, Liu X, Hwang Y, Liu Y, Lee H (2020) Stable complete seawater electrolysis by using interfacial chloride ion blocking layer on catalyst surface. J Mater Chem A 8(46):24501–24514
76. Gupta S, Forster M, Yadav A, Cowan AJ, Patel N, Patel M (2020) Highly efficient and selective metal oxy-boride electrocatalysts for oxygen evolution from alkali and saline solutions. Acs Appl Energ Mater 3(8):7619–7628
77. Jeoung S, Sahgong SH, Kim JH, Hwang SM, Kim Y, Moon HR (2016) Upcycling of nonporous coordination polymers: controllable-conversion toward porosity-tuned N-doped carbons and their electrocatalytic activity in seawater batteries. J Mater Chem A 4(35):13468–13475
78. Cui B, Hu Z, Liu C, Liu S, Chen F, Hu S, Zhang J, Zhou W, Deng Y, Qin Z, Wu Z, Chen Y, Cui L, Hu W (2021) Heterogeneous lamellar-edged Fe-$Ni(OH)_2$/Ni_3S_2 nanoarray for efficient and stable seawater oxidation. Nano Res 14(4):1149–1155
79. Jiang X, Dong Z, Wang J, Zhang N, Xu G-R, Zhang W, Lai J, Li Z, Wang L (2021) Self-assembly of functionalized Echinops-like Rh porous nanostructure electrocatalysts for highly efficient seawater splitting. J Mater Chem C 9(26):8314–8322
80. Wang XH, Ling Y, Wu B, Li BL, Li XL, Lei JL, Li NB, Luo HQ (2021) Doping modification, defects construction, and surface engineering: design of cost-effective high-performance electrocatalysts and their application in alkaline seawater splitting. Nano Energy 87:106160
81. Wu D, Chen D, Zhu J, Mu S (2021) Ultralow Ru incorporated amorphous cobalt-based oxides for high-current-density overall water splitting in alkaline and seawater media. Small 17(39):2102777
82. Liu W, Jiang K, Hu Y, Li Q, Deng Y, Bao J, Lei Y (2021) Zr-doped CoFe-layered double hydroxides for highly efficient seawater electrolysis. J Colloid Interf Sci 604:767–775
83. Wang B, Lu M, Chen D, Zhang Q, Wang W, Kang Y, Fang Z, Pang G, Feng S (2021) NixFeyN@C microsheet arrays on Ni foam as an efficient and durable electrocatalyst for electrolytic splitting of alkaline seawater. J Mater Chem A 9(23):13562–13569
84. Wang S, Yang P, Sun X, Xing H, Hu J, Chen P, Cui Z, Zhu W, Ma Z (2021) Synthesis of 3D heterostructure Co-doped Fe2P electrocatalyst for overall seawater electrolysis. Appl Catal B 297:120386
85. Wu L, Yu L, Zhang F, McElhenny B, Luo D, Karim A, Chen S, Ren Z (2021) Heterogeneous bimetallic phosphide Ni_2P-Fe_2P as an efficient bifunctional catalyst for water/seawater splitting. Adv Funct Mater 31(1):2006484
86. Hajjar P, Lacour M-A, Masquelez N, Cambedouzou J, Tingry S, Cornu D, Holade Y (2021) Insights on the electrocatalytic seawater splitting at heterogeneous nickel-cobalt based electrocatalysts engineered from oxidative aniline polymerization and calcination. Molecules 26(19)
87. Zhao Y, Jin B, Zheng Y, Jin H, Jiao Y, Qiao S-Z (2018) Charge state manipulation of cobalt selenide catalyst for overall seawater electrolysis. Adv Energy Mater 8(29):1801926

88. Kuang Y, Kenney MJ, Meng Y, Hung W-H, Liu Y, Huang JE, Prasanna R, Li P, Li Y, Wang L, Lin M-C, McGehee MD, Sun X, Dai H (2019) Solar-driven, highly sustained splitting of seawater into hydrogen and oxygen fuels. Proc Natl Acad Sci 116(14):6624–6629
89. Tran PKL, Tran DT, Malhotra D, Prabhakaran S, Kim DH, Kim NH, Lee JH (2021) Highly effective freshwater and seawater electrolysis enabled by atomic Rh-modulated Co-CoO lateral heterostructures. Small 17(50):2103826
90. Wu Y, Tian Z, Yuan S, Qi Z, Feng Y, Wang Y, Huang R, Zhao Y, Sun J, Zhao W, Guo W, Feng J, Sun J (2021) Solar-driven self-powered alkaline seawater electrolysis via multifunctional earth-abundant heterostructures. Chem Eng J 411:128538
91. Rodney JD, Deepapriya S, Robinson MC, Das SJ, Perumal S, Sivakumar P, Jung H, Kim BC, Raj CJ (2021) Cu1-xRExO (RE = La, Dy) decorated dendritic CuS nanoarrays for highly efficient splitting of seawater into hydrogen and oxygen fuels. Appl Mater Today 24:101079
92. Zhang Y, Fu C, Fan J, Lv H, Hao W (2021) Preparation of Ti@NiB electrode via electroless plating toward high-efficient alkaline simulated seawater splitting. J Electroanal Chem 901:115761
93. Kingson A (2020) Opportunities and challenges of industrialization of hydrogen production from natural seawater 60–68
94. Sapountzi FM, Gracia JM, Weststrate CJ, Fredriksson HOA, Niemantsverdriet JW (2017) Electrocatalysts for the generation of hydrogen, oxygen and synthesis gas. Prog Energy Combust Sci 58:1–35
95. Calado G, Castro R (2021) Hydrogen production from offshore wind parks: current situation and future perspectives. Appl Sci 11(12):5561
96. Dinh VN, Leahy P, McKeogh E, Murphy J, Cummins V (2021) Development of a viability assessment model for hydrogen production from dedicated offshore wind farms. Int J Hydrogen Energy 46(48):24620–24631
97. Tong W, Forster M, Dionigi F, Dresp S, Sadeghi Erami R, Strasser P, Cowan AJ, Farràs P (2020) Electrolysis of low-grade and saline surface water. Nat Energy 5(5):367–377
98. Yu Z, Xu J, Meng L, Liu L (2021) Efficient hydrogen production by saline water electrolysis at high current densities without the interfering chlorine evolution. J Mater Chem A 9(39):22248–22253
99. Farràs P, Strasser P, Cowan AJ (2021) Water electrolysis: direct from the sea or not to be? Joule 5(8):1921–1923
100. Daiyan R, MacGill I, Amal R (2020) Opportunities and challenges for renewable power-to-X. ACS Energy Lett 5(12):3843–3847
101. van Renssen S (2020) The hydrogen solution? Nat Clim Chang 10(9):799–801
102. Tawiah P, Duer J, Bryant SL, Larter S, O'Brien S, Dong M (2020) CO2 injectivity behaviour under non-isothermal conditions—field observations and assessments from the Quest CCS operation. Int J Greenhouse Gas Control 92:102843
103. Idriss H (2021) Toward large-scale hydrogen production from water: what have we learned and what are the main research hurdles to cross for commercialization? Energy Technol 9(2):2000843
104. Khan MA, Al-Attas T, Roy S, Rahman MM, Ghaffour N, Thangadurai V, Larter S, Hu J, Ajayan PM, Kibria MG (2021) Seawater electrolysis for hydrogen production: a solution looking for a problem? Energy Environ Sci 14(9):4831–4839
105. <comparison_of_lifecycle.pdf>
106. Bayer P, Saner D, Bolay S, Rybach L, Blum P (2012) Greenhouse gas emission savings of ground source heat pump systems in Europe: a review. Renew Sustain Energy Rev 16(2):1256–1267
107. <Ayers_2010_ECS_Trans._33_3.pdf>
108. Jones E, Qadir M, van Vliet MTH, Smakhtin V, Kang SM (2019) The state of desalination and brine production: a global outlook. Sci Total Environ 657:1343–1356
109. Ghaffour N, Missimer TM, Amy GL (2013) Technical review and evaluation of the economics of water desalination: Current and future challenges for better water supply sustainability. Desalination 309:197–207

Photocatalytic Seawater Splitting

Yi Lu, Yi-Xuan Liu, Shang Cao, and Xiao-Yu Yang

Abstract Low-carbon technologies have attracted wide interest for researchers. Among them, H_2 production from seawater splitting via photocatalysis is the most promising approach due to its abundant resources, low cost, and ease of construction on the large scale. However, there are many differences between water and seawater splitting in photocatalytic reactions. The ionic components in seawater and precipitate generation during the photocatalytic reaction have great impacts on seawater splitting. In this chapter, we have thoroughly introduced the principle, performance evaluation parameter, and features of photocatalytic seawater splitting, and we also summarized the recent development of the most fabricated photocatalysts including their structure, defects, and performances. At last, we discussed the economic cost and practical value of photocatalytic hydrogen industrialization, briefly summarized the design of large-scale synthesis and catalytic systems for photocatalysts, and explored their cost competitiveness.

Keywords Photocatalytic seawater splitting · Hydrogen production · Large-scale synthesis · System design · Industrial application

Y. Lu (✉)
Institut Für Anorganische Chemie Und Strukturchemie, Heinrich-Heine-Universität Düsseldorf, Universitätsstraße 1, 40225 Düsseldorf, Germany
e-mail: yi.lu@uni-duesseldorf.de

Y.-X. Liu · S. Cao
State Key Laboratory of Advanced Technology for Materials Synthesis and Processing, Wuhan University of Technology, Wuhan 430070, China

X.-Y. Yang
State Key Laboratory of Advanced Technology for Materials Synthesis and Processing (Wuhan), Foshan Xianhu Laboratory of the Advanced Energy Science and Technology Guangdong Laboratory (Xianhu Hydrogen Valley, Foshan), Laoshan Laboratory (168 Wenhai Middle Rd, Jimo District, Qingdao), Wuhan University of Technology, Wuhan, Hubei, China

X.-Y. Yang (ed.), *Photo-Driven Seawater Splitting for Hydrogen Production*,
https://doi.org/10.1007/978-981-99-0510-2_2

1 Preface

Photocatalytic seawater splitting (PCSS) is an eco-friendly method to produce clean burning and storable H_2 from two renewable sources including solar irradiation and seawater. The simplicity and low operational costs give PCSS systems a high potential for producing this gas at industrial levels.

The PCSS reaction taking place in a reactor begins with light absorption by a photocatalyst (such as semiconductor materials), which causes a transition of an electron from the valence band to the conduction band while leaving a hole in the valence band. Semiconductors that have an energy difference between their valence and conduction bands (called the band gap) greater than 1.23 eV are capable of promoting the redox events that lead to water splitting H_2O. Many semiconductor materials developed thus far for photocatalytic water splitting (PCWS) such as TiO_2, g-C_3N_4, CdS, and WO_3 have remarkable performances.

Several options exist for using semiconductor technologies in devices that utilize sunlight for water splitting, including the photovoltaic (PV)-assisted electrochemical (PV-E), photoelectrochemical (PEC), and PCSS methods. Compared to the process in PCSS systems, in PV-E as well as PEC cells, hydrogen and oxygen are evolved at macroscopically distant locations. Therefore, the basic design of PCSS systems is not identical to those of the PEC and PV-E counterparts. While it is believed that PCSS systems are less expensive than others, to date, only laboratory-scale devices have been extensively explored. However, the approaches devised thus far are nor amenable to scale up to the kilogram level. Moreover, large numbers and types of dissolved salts are present in seawater, and these salts participate in a variety of photocatalyzed chemical reactions that result in the reduction of the activity and durability of the photocatalyst.

In this chapter, we discuss the basic operational principles of PCSS and review the state-of-the-art materials that have been developed as photocatalysts for these systems. We also analyze past studies that have revealed key principles for the design of photocatalysis and guidelines that can be used to fabricate more efficient materials. In the final section, we review the different types of devices that have been designed thus far for large-scale PCSS.

2 Principles

2.1 Mechanism for H_2 Production in PCSW Systems

The basic process involved in sunlight-promoted photocatalyzed water splitting to generate H_2 is depicted in Fig. 1. In the process, the energy of a photon is converted into chemical energy for water splitting that requires a large positive Gibbs free

energy change (Fig. 2). The overall process is similar to the one occurring in photosynthesis by green plants and, therefore, PCWS is regarded as artificial photosynthesis. From the viewpoint of the Gibbs free energy change, PCWS is distinguished from photocatalytic degradation reactions such as TiO_2 photocatalyzed oxidation of organic compounds using oxygen, which are generally thermodynamically downhill processes.

The stepwise sequence involved in the PCWS reaction begins with the absorption of a photon of light by the photocatalyst, which promotes the transition of an electron in the valence band to the higher energy conduction band. The light promoting this transition must have an energy equal to that of the band gap. This event forms an electron–hole pair in the form of a negative-electron (e^-) and positive-hole (h^+), which then migrate to the surface of the photocatalyst where they induce water splitting to produce H_2 and O_2 by serving as respective reducing and oxidizing agents. The mechanism followed in a PCWS reaction is depicted in Fig. 3.

Splitting water to form H_2 and O_2 (Eq. 1) is an energetically uphill process that has a standard Gibbs free energy change (ΔG_0) of 237 kJ/mol or 1.23 eV. To enable

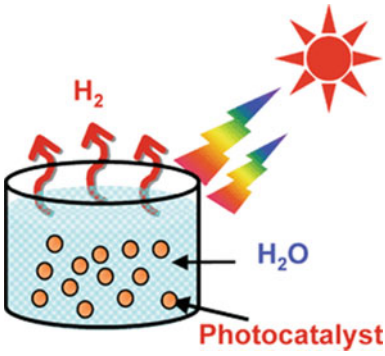

Fig. 1 Hydrogen production from water using photocatalyst under solar irradiation

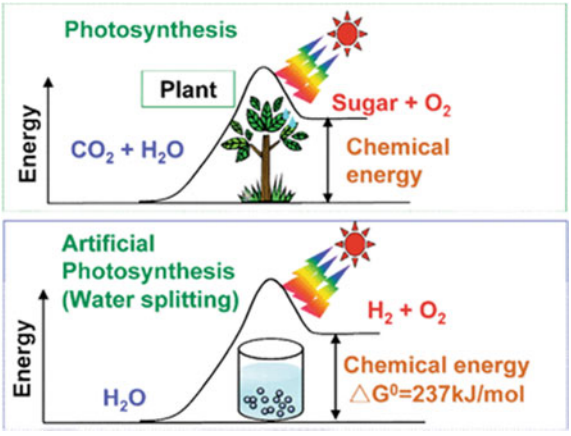

Fig. 2 Energetic changes in photosynthesis by green plants and PCWS

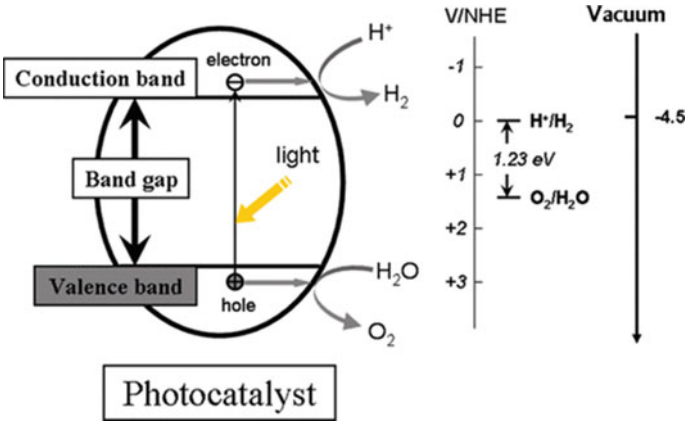

Fig. 3 Schematic diagram of the mechanism of PCWS for hydrogen and oxygen generation

both reduction and oxidation of H_2O by the photoexcited electron and hole (exciton), the reduction and oxidation potentials of water should lie within the band gap energy of the photocatalyst, with the energy of the conduction band being more negative than the reduction potential of H+/H_2 (0 V vs. normal hydrogen electrode (NHE)), and that of the valence band being more positive than the oxidation potential of O_2/H_2O (1.23 V). The electronic structures of semiconductor systems match well with the redox potential associated with transforming water into H_2 and O_2. Other factors, such as overpotentials, charge separation and mobility, and lifetime of the photogenerated electron and hole, affect the efficiency of photocatalytic generation of hydrogen from water splitting.

$$H_2O \rightarrow \frac{1}{2}O_2 + H_2;\ \Delta G = +237\,\mathrm{KJ/mol} \tag{1}$$

The second step in the mechanism for PCWS is charge separation and migration of the photogenerated electron and hole. Competing with these events is energy wasting charge recombination (both surface and bulk) that leads to deactivation by emitting light or generating phonons [1]. Moreover, the separation of an excited electron and hole sometimes has an energy barrier associated with the binding energies of these oppositely charged species. Efficient charge separation and transport is enhanced by avoiding bulk/surface charge recombination. Examples of the approaches that have been employed to facilitate charge separation and transport include incorporating an internal electric field and using high photoconductive semiconductor materials.

The final step in the PCWS process involves surface chemical reactions that lead to H_2 and O_2 formation. Importantly, for these reactions to take place efficiently it is necessary to have a large number of active sites on the semiconductor surface carrying the photoexcited electrons and holes. Cocatalysts such as Pt, NiO, and RuO_2 are typically utilized to introduce active sites for the reduction of water to evolve H_2. Active sites for holes are needed to promote 4-electron oxidation of water for O_2

evolution. It is necessary to use cocatalysts and photocatalysts that have unfavorable properties for this process.

2.2 *Measurement of the Performance of PCWS Systems*

Three metrics have been typically used to quantify the performance of PCWS systems including H_2 production rate, internal quantum yield (IQY) or apparent quantum yield (AQY), and solar-to-hydrogen (STH) conversion efficiency, which reflect three different aspects of the process (Scheme 1).

2.2.1 H_2 Production Rate

The activity of a PCWS system can be represented by the H_2 production rate (r, the amount of H_2 produced vs. reaction time and photocatalyst mass). The time and mass are the two factors determining the H_2 production rate, which is expressed by the amount of evolved H_2 or O_2 per unit irradiation time and the amount of photocatalysts ($\mu mol\ h^{-1}\ g^{-1}$ or $\mu mol\ h^{-1}\ mg^{-1}$) [2, 3]. However, many other factors influence the production rate including properties [4]. The use of different sets of parameters in studies in this area has led to confusion in comparing r directly, indicating that reporting protocols need to be standardized. Normalizing the r by using the mass of the photocatalyst is erroneous because r does not linearly increase with m owing to light-shielding effects (see Fig. 4) [5]. The light-shielding effects of photocatalysts occurring with increased photocatalyst mass is illustrated in Fig. 4. When the use of photocatalysts increases from m_1 in the graph, the shielding effect becomes more significant, and the gas evolution rate plateaus at high mass. Specifically, when a high mass of photocatalyst is present, numerous particles cannot participate in light absorption due to limited light penetration depth. Therefore, it is recommended that an r–m curve (Fig. 4) be provided when the efficiency of PCWS systems is given in terms of the H_2 evolution rate.

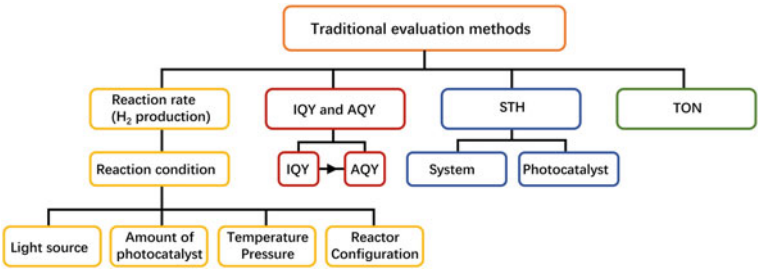

Scheme 1 Traditional methods to evaluate PCWS performance

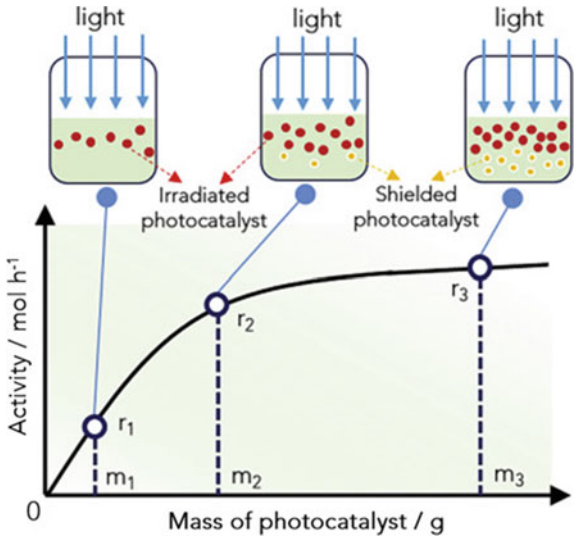

Fig. 4 The relationship between gas production rate and mass of photocatalyst

The H_2 production rate is governed by many factors, such as the temperature, pressure, and type of reaction system. To establish standard conditions for evaluating lab-based systems, we suggest using a temperature in the range of 10–25 °C that can be easily maintained through the use of a closed-water circulation system. An on-line gas chromatograph is normally used to measure gas evolution. However, the accumulation of H_2 and O_2 in the system will change the atmosphere and pressure, which leads to changes in gas evolution rates as the reaction progresses except when the rate is low. To minimize potential measurement errors, it is suggested that the system be calibrated under the same condition as those used in the overall water splitting reaction.

Under practical operating conditions, it is difficult to maintain a photocatalytic water splitting reactor at reduced pressures and temperatures. Therefore, determining the STH efficiency under ambient pressure and product gas analysis using a gas chromatograph are more acceptable. Also, it is best to utilize a flow reaction system that enables maintenance of the same atmosphere and pressure throughout the course of the process.

When photocatalysts have sufficiently high overall water splitting efficiencies, it is best to use the upward water displacement to quantify the amount of produced gas because this method does not rely on expensive equipment.

2.2.2 Internal Quantum Yield (IQY)

IQY has been defined by IUPAC as the number of electrons utilized for the reaction per number of absorbed photons in a given period time [6]. The electrons utilized for productive reactions are the number of molecules of reactant consumed or product

formed. Thus, IQY describes the efficiency of a photocatalyst that transforms light into active charges, which is independent of the photocatalyst's mass. At the early stage, the IQY was not widely used because of the great challenge associated with accurately measuring the absorption of photons [7, 8].

2.2.3 Apparent Quantum Yield (AQY)

Due to differences in conditions employed for photocatalytic reactions (especially irradiation conditions), direct comparisons of the activities of catalysts based on the amounts or rates of gases produced are not possible. Thus, at the current time, assessing the photocatalyst performance of PCWS systems requires the determination of both quantum yields and STH energy conversion efficiencies. Owing to light transmission and scattering, determining the actual number of photons absorbed by the photocatalyst is not possible. Hence, apparent quantum yield (AQY), or sometimes called the external quantum efficiency (EQE), calculated using Eq. (2), is used

$$\mathrm{AQY} = \frac{nR}{I} \tag{2}$$

in which n, R, and I represent the number of electrons or holes consumed, the quantity of gas molecules evolved in a specific time interval, and the number of incident photons reaching the photocatalytic system during the same time interval, respectively. It is important to determine the AQY as a function of irradiation wavelength.

The AQY provides insights into the intrinsic properties of a photocatalyst without knowing the mechanism of the overall water splitting or half-reaction. The AQY of a system can be diminished by energy wasting, such as charge recombination and back reactions, and is reflective of the quality of the semiconductor as well as those of the cocatalyst. Using the photocatalytic H_2 production reaction as an example, holes generated simultaneously with photoexcited electrons induce the formation of radicals, which can transfer electrons to the conduction band. In this case, one photon causes the production of two electrons for the HER, which can potentially lead to an AQY for HER over 100%. Therefore, it is important to understand the intrinsic nature of a photocatalyst in terms of light harvesting, separation efficiency, transfer kinetics, and utilization of carriers via surface catalytic reactions.

For the overall water splitting process, within experimental error the AQY calculated based on H_2 generation should be the same as that of O_2 generation. For photocatalytic half-reaction, AQY is the most significant parameter for evaluating the efficiency of a photocatalyst.

AQY is strongly dependent on the wavelengths of the incident photons due to varied absorption coefficients of a semiconductor at different irradiation wavelengths (λ) [9]. The setup for AQY measurements is similar to that used for a normal photocatalytic activity determination. Two critical criteria need to be met in making this

measurement. First, the AQY is normally evaluated at the maximum photocatalytic rate which is attained by using light corresponding to the absorption wavelength maximum of the photocatalyst. Second, monochromatic light should be employed by using combined band-pass and cut-off filters.

The standard actinometer method for the conversion of ferrioxalate ions into Fe^{2+} ions also provides an optional technology to determine the incident photon flux [10, 11]. Although the actinometer method also has some uncertainties, including the quantum yield of the reaction not actually being 100%, it can be used as a verification for the reliability measurements using photodetectors.

2.2.4 Solar-To-Hydrogen (STH) Efficiency

In 1985, Bolton et al. suggested that evaluations of PCWS systems should be based on the solar-to-hydrogen (STH) conversion efficiency. This is the most important parameter used to evaluate the water splitting device exposed to broadband solar Air Mass 1.5 Global (AM1.5 G) illumination under zero bias conditions [10]. During the past decades, this approach has gradually become accepted for evaluating the photocatalytic activity of PCWS [12, 13]. STH refers to the ratio of solar energy stored in formed H_2 to the incident solar energy as described in Eq. (3) [14].

$$\mathrm{STH} = \frac{\text{Output energy as } H_2}{\text{Energy of incident solar light}} = \frac{r_{H_2} \times \Delta G_r}{P_{\mathrm{sun}} \times S} \tag{3}$$

where P_{sun} is the energy flux of the sunlight, S is the irradiated area, r_{H_2} is the rate of H_2 production, and ΔG_r is the reaction Gibbs energy. Solar irradiation has an energy flux of 100 mW cm^{-2}. It should be noted that solar energy and H_2 are the only energy inputs and outputs, respectively, and that H_2 and O_2 evolved in a stoichiometric ratio [15]. Furthermore, it should be adjusted taking into account the experimental conditions when used in the calculation of STH efficiency, such as temperature and pressure.

The STH efficiency is considered to be the standard for the evaluation of photocatalyst performance. The intensity for STH measurement should be set as one sun, which is typically obtained via a solar simulator (AM 1.5G, 100 mW/cm^2). Calculating STH energy conversion efficiency using concentrated sunlight is not comparable arising by using a solar simulator because H_2 evolution rates on various photocatalysts are not proportional to the incident light intensity.

Due to the fluctuation of sunlight caused by weather and altitude, simulated light sources like a Xenon lamp, high-pressure mercury lamp, and solar simulators are used in laboratory research (Fig. 5A). The power spectra of Xenon and mercury lamps include a strong UV light region. However, mercury lamps emit this light as individual lines rather than a continuum, thus the spectral mismatch with sunlight is large. Therefore, solar simulators which simulate the standard sunlight (AM1.5G) with appropriate spectrum distribution and stable light intensity are highly recommended for the laboratory level comparisons.

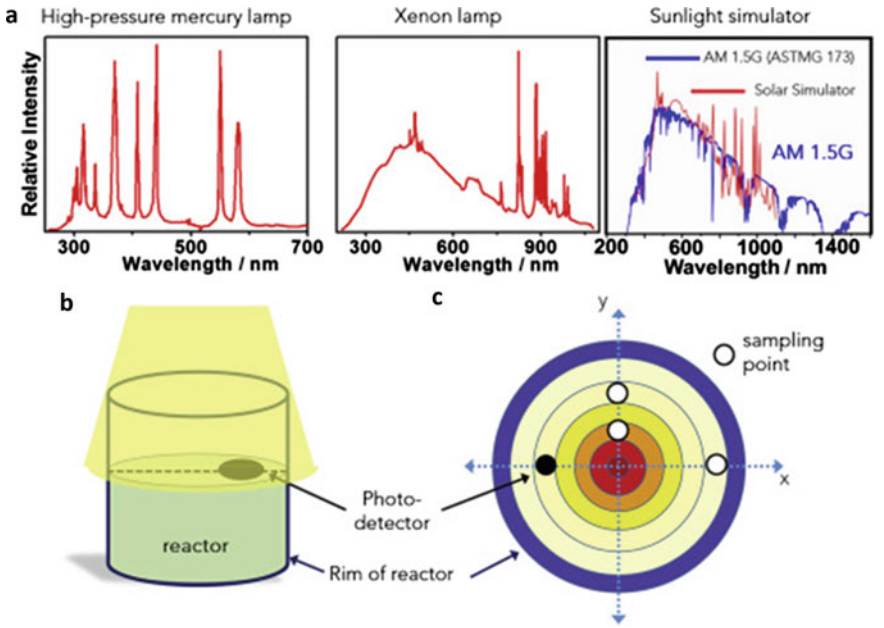

Fig. 5 **a** Typical power spectra of different light sources, **b** schematic diagram of light spot size and reactor, and **c** the Photon flux is calculated by measuring the light intensity in different areas via a light detector

In the case of uniformly distributed light intensity (Fig. 5B), the incident light intensity is relevant to the irradiation area and the distance of the reaction mixture from the light source. But the light intensity is distributed non-uniform within the irradiation area in practice (Fig. 5C), in which case a numerical integration needs to be performed to estimate the total intensity of input light. In this case, it is assumed that the light intensity is constant at the same distances from the center of the reactor (Fig. 5C) [9]. The first step in determining the STH energy conversion efficiency is the identification of the location of the highest light intensity region within the irradiation area. Starting at the maximum point, the intensity along the radial direction is then measured by changing the location of the photodetector along the *x*- and *y*-axis at the same intervals (Fig. 5C). After measuring the light intensity distribution within the irradiation area, the total incident photons can be measured with reasonable accuracy [4].

What is the difference between AQY and STH? Typically, AQY is measured at a specific wavelength or over a narrow range of wavelengths. Thus, there is no correlation between AQY and STH, because the effect of wavelength-dependent light absorption is fully considered in determining STH but not in AQY. Only in the case when STH is determined using a monochromatic light source can the two indicators be interconverted by using Eq. 4,

$$\mathrm{STH}_{\lambda} = \mathrm{AQE} \cdot \frac{\lambda \Delta G^{0}}{hcnN_{A}} \tag{4}$$

where STH_{λ} is the STH measured at wavelength λ, *h* is Planck's constant, c is the speed of light, and NA is Avogadro's number. Nevertheless, a high AQY at any wavelength is sufficient to indicate that efficient charge carrier separation, transport, and surface reactions have occurred which are also parameters for high STH over the entire solar spectrum. These physical processes are relatively independent of irradiation wavelength and can be described mathematically, which enables STH to be correlated to AQY to some extent. A detailed review on this aspect is found elsewhere [16, 17].

The theoretical limit for the STH efficiency is 31% in overall water splitting [18], which is the percentage of solar energy stored as chemical energy for hydrogen production. Considering inevitable losses, it has a practical limit of 11% [19]. But in practice, the STH efficiency of photocatalytic overall water splitting rarely exceeds 1%. One important reason for this is that only semiconductors that have E_g that is significantly larger than 1.23 eV have overall water splitting activity, such as some well-known examples like TiO_2, $SrTiO_3$, $NaTaO_3$, $Ga_{1-x}Zn_xN_{1-x}O_x$, and g-C_3N_4 [20–24]. The large E_g of these semiconductors prevents the utilization of most visible and infrared light, which accounts for over 95% of solar light received at sea level. Hence, enhancing the response of photocatalysts to visible light is an important goal for improving STH efficiency.

Another major factor leading to low STH efficiencies is energy (photon) wasting radiative or non-radiative recombination of photogenerated electrons and holes occurring in competition with promoting water splitting. Carrier diffusion length, which is the average distance a charge carrier travels in a semiconductor before recombination takes place, offers a way to intuitively compare the extent of recombination. This length typically ranges from over one millimeter for lightly doped silicon wafers to a few nanometers for the common photocatalyst TiO_2 [25, 26]. Short carrier diffusion lengths significantly impact photocatalytic efficiencies, which means that electrons/holes separation that happened deeper inside the bulk photocatalysts does not contribute to promoting surface redox reactions [16].

2.2.5 Ton

Turnover number (TON), defined as the number of reacted molecules to those of active sites (Eq. (5)), is usually used to assess the efficiencies of photocatalyst.

$$\mathrm{TON} = \frac{\text{Number of reacted molecules}}{\text{Number of active sites}} \tag{5}$$

In fact, the numbers of active sites present in photocatalysts is difficult to determine. Thus, Eq. (6)) or Eq. (7) is employed in determining TON.

$$\text{TON} = \frac{\text{Number of reacted electrons}}{\text{Number of atoms in a photocatalyst}} \tag{6}$$

$$\text{TON} = \frac{\text{Number of reacted electrons}}{\text{Number of atoms at the surface of a photocatalyst}} \tag{7}$$

However, these values cannot be applied to particulate photocatalysis systems due to the great challenge of identifying the number of active sites. However, most of the reported studies do not provide sufficient and exact experimental details, which leads to great difficulties in accurately evaluating and comparing photocatalytic performances. In addition, each of these evaluation parameters has its own insufficiencies or need for use of specific conditions. Only through a comprehensive and rational evaluation can the photocatalytic performance of a system be reasonably assessed and compared.

2.3 Features and Effects on the Performance

2.3.1 Salt Components

A large content of various salts is a characteristic feature of seawater. The main ionic components of >90% of these salts are Na^+, Mg^{2+}, Ca^{2+}, K^+, Cl^-, and $SO_4{}^{2-}$ [27]. Unfortunately, these salts have a great impact on PCSS, because the efficiencies of most photocatalysts are lower in natural or simulated seawater than in pure water [28–31], while only a few show the opposite behavior [32]. The mechanism by which ions in seawater control the water splitting process is still at an exploratory stage and, to date, no universal effects seem to apply to different systems. The main component of seawater is NaCl and most reports on splitting of seawater discuss the effects of Na^+ and Cl^- on the photocatalytic performance. For example, Li et al. found that Na^+ abundantly adsorbs on the surface of TiO_2 leading to enhance adsorption of sacrificial agents under alkaline or neutral conditions [28]. These agents readily combine with the photogenerated holes, facilitate charge separation, and reduce electron–hole recombination. It should be noted that at high NaCl concentrations (>1.0 mol L^{-1}), sacrificial agents undergo indirect Na^+-induced adsorption on the photocatalyst surface where they reduce the charge transfer efficiency of the photocatalyst [33].

Two different perspectives can be used to consider the effects of Cl^- on photocatalytic seawater splitting. Li et al. suggested earlier that although Cl^- reacts with holes, it also participates in reduction reaction with electrons in the conduction band (Eqs. (8) and (9)), thus decreasing the photocatalytic activity [28]. Ho et al. also speculated on the reason why the H_2 evolution rate was lower in seawater than in pure water [34]. The rate reduction can also be the reaction of the Cl^- in seawater with holes to generate Cl·, which competes with the H^+ reduction reaction (Eqs. (9) and (10)). No other chlorine-containing compounds are produced in the reaction, and

the Cl^- concentration remains unchanged, which is consistent with the speculation.

$$Cl^- + h^+ \rightarrow \cdot Cl \tag{8}$$

$$\cdot Cl + e^- \rightarrow Cl^- \tag{9}$$

$$Cl \cdot + Cl^- \rightarrow Cl \cdot_2^- \tag{10}$$

$$Cl \cdot_2^- + e^- \rightarrow 2Cl^- \tag{11}$$

Simamora et al. [35] suggested that many hydroxyl groups, such as in the form of $TiOH_2$ and Ti–OH, react with Cl^- on the surface of TiO_2 to form TiCl and reduce the photocatalytic activity. But in general, all the reasons presented above are speculative at this stage, and no additional experimental data has been provided to confirm the conclusion.

However, the results of some studies indicate that Cl^- has a positive effect on the efficiency of PCSS. For example, Ji et al. [36] proved that no decrease in Cl^- concentration occurs during a 6 h of photocatalytic reaction. Guan et al. found that although oxidation of Cl^- takes place to form Cl_2 (Cl_2/Cl^-, 1.36 V vs. NHE, pH = 0), the process is thermodynamically more difficult than oxidation of H_2O to form O_2 (O_2/H_2O, 1.23 V vs. NHE, pH = 0), since it is a two-electron redox process and kinetically more favorable [37]. Therefore, after the oxidation of Cl^- takes place, oxidation of water occurs (Eqs. (12) and (13)). Yang et al. postulated that holes are consumed by participation in the Cl^- oxidation reaction and, thereby, the rate of electron–hole recombination is lowered [38].

$$Cl_2 + H_2O \rightarrow H^+ + Cl^- + HClO \tag{12}$$

$$2HClO \rightarrow 2H^+ + 2Cl^- + O_2 \tag{13}$$

Lee et al. [36] tested the effects of NaCl, $MgCl_2$, $MgSO_4$, $CaSO_4$, K_2SO_4, K_2CO_3, and $MgBr_2$ on simulated seawater splitting. The results reveal that all these dissolved electrolytes except K_2SO_4 decrease the H_2 formation rate, and $MgCl_2$ is the most detrimental. A solution of natural seawater containing ca. 74% and 15% of Mg^{2+} and Cl^-, respectively, has the lowest activity with a twofold decreased hydrogen formation rate compared to that of pure water. Note that without $MgCl_2$, photocatalyst in simulated seawater has better performance than in seawater containing all seven salts, indicating that Mg^{2+} is the main deactivating species.

2.3.2 Sacrificial Agents

Sacrificial reagents are often introduced to enhance the separation of carriers in water splitting (Fig. 6). When the PCWS reaction is carried out in an aqueous solution containing a reducing reagent such as alcohols and sulfide ion, which serve as respective electron donors or hole scavengers, photogenerated holes are irreversibly reduced through oxidation of the reducing reagent instead of water. This process enriches the number of electrons in the photocatalyst which enhances the HER (Fig. 6a). When reducing reagents are present in biomass and compounds naturally occurring and industrial wastes, this reaction should be advantageous for hydrogen production [39]. On the other hand, photoexcited electrons are consumed by oxidizing agents (electron acceptors) such as Ag^+ and Fe^{3+} and thus resulted in an enhancement of the OER (Fig. 6b). Reactions using sacrificial reagents which affect the half-reactions involved in water splitting are often used to determine if a photocatalyst has the required thermodynamics and kinetics for H_2 and O_2 evolution. Even when a photocatalyst is capable of promoting these half-reactions, no guarantee exists that it will be able to induce the HER and OER in the absence of sacrificial reagents.

In spite of the fact that photocatalytic splitting using pure water can be achieved without employing sacrificial agents, most of those in which TiO_2 is the photocatalyst still utilize sacrificial agents. Notably, some work reported that inorganic and organic substances indigenously present in seawater can play roles of sacrificial agents to improve performance [40].

S^{2-}/SO_3^{2-} System

The S^{2-} and SO_3^{2-} ions can react with photogenerated holes to form S_n^{2-} and SO_4^{2-}, respectively; therefore, they could be used as sacrificial reagents in photocatalytic reactions [41–46]. However, oxidation of S^{2-} to form yellow polysulfides

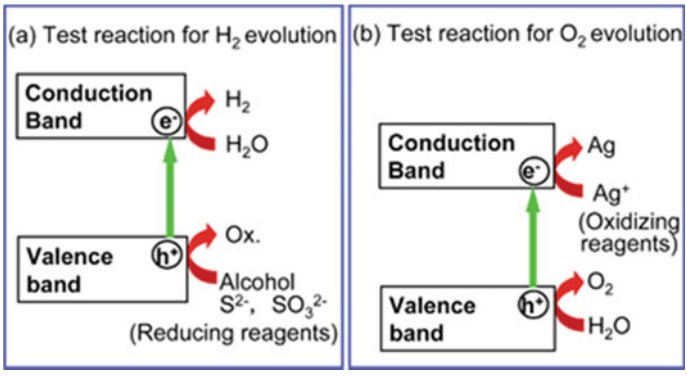

Fig. 6 Description of half-reactions of water splitting in the presence of sacrificial reagents

S_n^{2-} leads to a decrease in the rate of H_2 formation over time owing to competitive light absorption by S_n^{2-} in the visible region and reduction of S_n^{2-} is competitive with H_2O [43, 47]. Fortunately, SO_3^{2-} can act as an agent for regenerating S^{2-} from S_n^{2-} thus keeping the solution colorless [48]. Thus, the S^{2-}/SO_3^{2-} mixture has been widely used as an electron donor to improve photoactivity and photostability for H_2 production from water splitting [49–54]. The mechanism for the reaction occurring in the presence of S^{2-}/SO_3^{2-} as a sacrificial reagent is depicted in Eqs. (14)–(19).

$$\text{photocatalyst} + h\nu \rightarrow \text{h}^+ + \text{e}^- \tag{14}$$

$$2\text{e}^- + 2\text{H}_2\text{O} \rightarrow \text{H}_2 + 2\text{OH}^- \tag{15}$$

$$\text{SO}_3^{2-} + 2\text{OH}^- + 2\text{h}^+ \rightarrow \text{SO}_4^{2-} + 2\text{H}^+ \tag{16}$$

$$2\text{S}^{2-} + 2\text{h}^+ \rightarrow \text{S}_2^{2-} \tag{17}$$

$$\text{S}_2^{2-} + \text{SO}_3^{2-} \rightarrow \text{S}_2\text{O}_3^{2-} + \text{S}^{2-} \tag{18}$$

$$\text{SO}_3^{2-} + \text{S}^{2-} + 2\text{h}^+ \rightarrow \text{S}_2\text{O}_3^{2-} \tag{19}$$

Since $S_2O_3^{2-}$ can be oxidized by photogenerated holes to form SO_3^{2-} and subsequently to SO_4^{2-}, it also can be used as a sacrificial reagent during the photocatalytic reaction.

H_2S-Splitting System

Photocatalytic H_2 production from H_2S dissolved in water is particularly interesting [55–62]. This process, in which sulfide ions generated by the reaction of H_2S with hydroxide serve as sacrificial agents, could have practical applications to remove H_2S from natural gas and to desulfurize petrochemicals. As shown in (14) and (20)–(22), the overall process corresponds to H_2S splitting using two photons of visible light, which requires 39.3 kJ/mol.

$$\text{H}_2\text{S} + \text{OH}^- \rightarrow \text{HS}^- \tag{20}$$

$$2\text{HS}^- + 2\text{h}^+ \rightarrow \text{S}_2^{2-} + 2\text{H}^+ \tag{21}$$

$$2\text{H}^+ + 2\text{e}^- \rightarrow \text{H}_2 \tag{22}$$

Other Inorganic Sacrificial Reagents

Other inorganic compounds containing ions, such as Fe^{2+} [63], Ce^{3+}, [64] I^-, Br^-, and CN^-, [65] have been used as sacrificial reagents for hydrogen generation. These inorganic ions are easily oxidized by the photogenerated holes to form the corresponding Fe^{3+}, Ce^{4+}, I^{3-} (or IO^{3-}), Br_2, and OCN^- ions. Using I^- as an example, the mechanism for photocatalytic H_2 production is described in Eqs. (23)–(25).

$$2H^+ + 2e^- \rightarrow H_2 \tag{23}$$

$$3I^- + 2h^+ \rightarrow I_3^- \text{(in acidic solution)} \tag{24}$$

$$I^- + 6OH^- + 6h^+ \rightarrow IO_3^- + 3H_2O \text{(in basic solution)} \tag{25}$$

Some of the species, such as Fe^{3+}, Ce^{4+}, and IO^{3-}, can be easily reduced by photogenerated electrons and, thus, act as electron acceptors for photocatalytic O_2 production from aqueous solution [66, 67].

Organic Sacrificial Reagents

Organic compounds, for example, alcohols (methanol, ethanol, isopropanol, etc.) [68], carboxylic acids (formic acid, acetic acid, etc.), and aldehydes (formaldehyde, acetaldehyde, etc.) [69] could also be used as electron donors for photocatalysis. Among these, methanol has been most widely used, and the reaction is described in Eqs. (26)–(30) [70].

$$h^+ + H_2O \rightarrow \cdot OH + H^+ \tag{26}$$

$$CH_3OH + \cdot OH \rightarrow \cdot CH_2OH + H_2O \tag{27}$$

$$\cdot CH_2OH \rightarrow HCHO + H^+ + e^- \tag{28}$$

$$2H_2O + 2e^- \rightarrow H_2 + 2OH^- \tag{29}$$

$$\text{overall reaction} : CH_3OH \overset{h\nu,\text{catalyst}}{\rightarrow} HCHO + H_2 \tag{30}$$

Formaldehyde (HCHO) as the product can be further oxidized to form formic acid (HCOOH) and subsequently convert to CO_2 together with H_2 via Eqs. (31) and (32) [71]:

$$\mathrm{HCHO} + \mathrm{H_2O} \overset{h\nu,\text{catalyst}}{\rightarrow} \mathrm{HCOOH} + \mathrm{H_2} \tag{31}$$

$$\mathrm{HCOOH} \overset{h\nu,\text{catalyst}}{\rightarrow} \mathrm{CO_2} + \mathrm{H_2} \tag{32}$$

In these photocatalytic processes, organic compounds are oxidized by the photogenerated holes and the residual photogenerated electrons reduce water to form hydrogen. Thus, it is possible to design a bifunctional photocatalytic system in which organic pollutants in water act as electron donors to achieve photocatalytic production of hydrogen and simultaneous degradation of the pollutants [72]. Hashimoto et al. performed pioneering studies on photocatalytic H_2 production from fossil fuels and hydrocarbons in water where powdered Pt/TiO_2 is used as a suspended [73]. The mechanism in these reactions could be explained by Eqs. (14) and (33)–(39).

$$\mathrm{h^+} + \mathrm{H_2O} \rightarrow \cdot\mathrm{OH} + \mathrm{H^+} \tag{33}$$

$$\mathrm{H^+} + \mathrm{e^-} \rightarrow 1/2\mathrm{H_2} \tag{34}$$

$$\mathrm{RCH_2CH_3} + 2 \cdot \mathrm{OH} \rightarrow \mathrm{RCH_2CH_2OH} + \mathrm{H_2O} \tag{35}$$

$$\mathrm{RCH_2CH_2OH} \rightarrow \mathrm{RCH_2CHO} + \mathrm{H_2} \tag{36}$$

$$\mathrm{RCH_2CHO} + \mathrm{H_2O} \rightarrow \mathrm{RCH_2COOH} + \mathrm{H_2} \tag{37}$$

$$\text{Photo} - \text{Kolbe reaction} : \mathrm{RCH_2COOH} \rightarrow \mathrm{RCH_3} + \mathrm{CO_2} \tag{38}$$

$$\text{Overall reaction} : \mathrm{RCH_2CH_3} + 2\mathrm{H_2O} \overset{h\nu,\text{catalyst}}{\rightarrow} \mathrm{RCH_3} + 3\mathrm{H_2} + \mathrm{CO_2} \tag{39}$$

2.3.3 Cocatalysts

Electrocatalysts that specifically catalyze desired redox reactions when used in conjunction with a light-absorbing material are termed cocatalysts [4]. Cocatalysts continue to be materials of interest in the field of artificial photosynthesis. A cocatalyst can be vital for promoting the efficiency of charge separation and suppressing charge recombination of electrons and holes for photocatalytic water splitting. Specifically, the work functions or band levels of the cocatalysts need to be compatible with the Fermi-levels or electronic structures of the photocatalysts. When this occurs, desirable junctions (an Ohmic-type or Schottky-type contact) are generated that allow charges to flow in the correct direction at the interface.

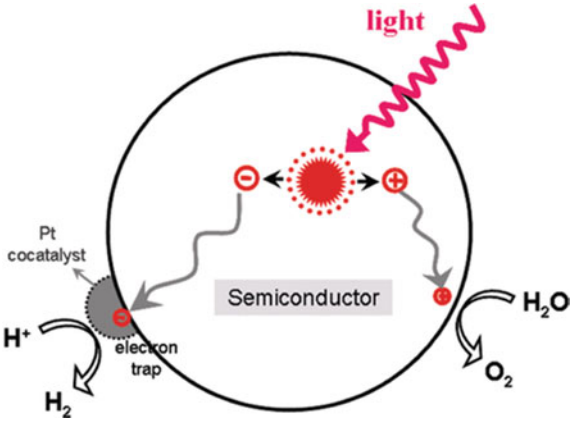

Fig. 7 Schematic diagram of charge transfer from inside to the surface

Generally speaking, cocatalysts are chosen from metals such as Pt, Rh, Ru, Ir, and Ni nanoparticles to accelerate H_2 evolution, and oxides of Co, Fe, Ni, Mn, Ru, and Ir function to accelerate O_2 evolution [74]. For a majority of the water splitting photocatalysts, a H_2 evolution cocatalyst is obligatory because of the existence of an insufficient overpotential for H^+ reduction compared to that for H_2O oxidation.

Transition metals, especially noble metals, are commonly used as cocatalysts in PCWS. For example, charge transfer between Pt and host photocatalyst is displayed in Fig. 7. In this system, photogenerated electrons transfer to the surface and are entrapped by the noble metal due to its lower Fermi energy level than the photocatalyst. Meanwhile, the photogenerated holes migrate to the surface of the host photocatalyst, resulting in the efficient separation of electrons and holes.

Noble Metal Cocatalysts

As a noble metal, Pt has been widely used as a cocatalyst in PCWS over many kinds of semiconductors including oxides [75–79], (oxy)sulfides [80–84], and (oxy)nitrides [85–88]. In all of these systems, the photocatalytic activity for hydrogen evolution is greatly enhanced. Until now, the highest photocatalytic activities for hydrogen production from water using visible light irradiation have been obtained using photocatalysts loaded with Pt as the cocatalyst [49, 50]. Other noble metals, for example, Au, [89–93] Ru, [94–96] Pd, [90, 97–99] Ag, [100–104], and Rh, [105–107] have also been employed as efficient cocatalysts. Iwase et al. [108] found that fine gold nanoparticles play an important role in creating active sites for H_2 evolution and enhancing charge separation. In addition, as compared to that on a Pt cocatalyst, the back-reaction between H_2 and O_2 to produce water is negligible on the Au. This phenomenon leads to improved overall water splitting photocatalytic activities of some titanate, niobate, and tantalate photocatalysts. Hara et al. [95] reported that H_2 evolution was unusually enhanced by Ru on a TaON photocatalyst under visible light irradiation. Note that other noble metals such as Pt, Ir, and Rh are ineffective in

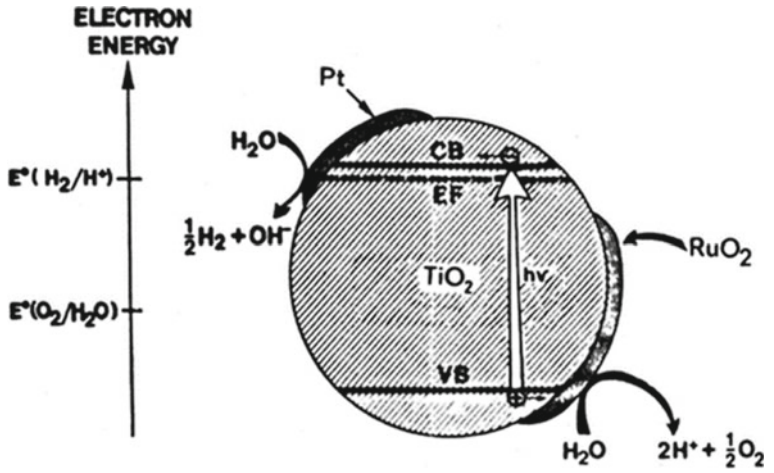

Fig. 8 Electron and hole transfer and chemical reactions on Pt/RuO_2-TiO_2 composite catalyst

promoting H_2 evolution under these conditions. The authors deduced that the electronic structure of the interface facilitates electron transfer from TaON to Ru that results in charge separation.

Transition Metal Oxide Cocatalysts

Some transition metal oxides such as RuO_2 [109–114] and NiO [115–118] act as efficient cocatalysts in photocatalytic reactions. Domen et al. found that β-Ge_3N_4 alone exhibits low photocatalytic activity [112, 119]. However, when loaded with RuO_2, β-Ge_3N_4 becomes photocatalytically active under UV irradiation ($\lambda > 200$ nm).

Borgarello et al. observed a pronounced synergistic effect on catalytic activity when both RuO_2 and Pt are co-deposited on TiO_2 particles [120]. As shown in Fig. 8, during the Pt/RuO_2-TiO_2 promoted water photosplitting reaction, Pt likely creates an ohmic contact whereas a Schottky barrier is formed by RuO_2. These effects direct electron flow to Pt sites and holes are trapped by RuO_2, resulting in enhanced charge separation.

In a series of studies, Maeda and co-workers explored the effect of loading Cr–M (M being one of the transition metals, Fe, Co, Ni, Cu, Ru, Rh, Pd, Ag, Ir, or Pt) using a co-impregnation method to form mixed oxide cocatalyst onto $(Ga_{1-x}Zn_x)(N_{1-x}O_x)$ [121–124]. The largest improvement in activity occurs by loading with the Rh–Cr mixed oxide (1 wt% Rh and 1.5 wt% Cr) followed by calcination at 623 K. It was proposed that the presence of Cr–Rh mixed oxide facilitates charge transfer from the photocatalyst to the cocatalyst. It is also possible that loading the mixed oxide also promotes the creation of active sites for hydrogen evolution, which results in the inhibition of charge recombination and enhanced photocatalytic activity [125].

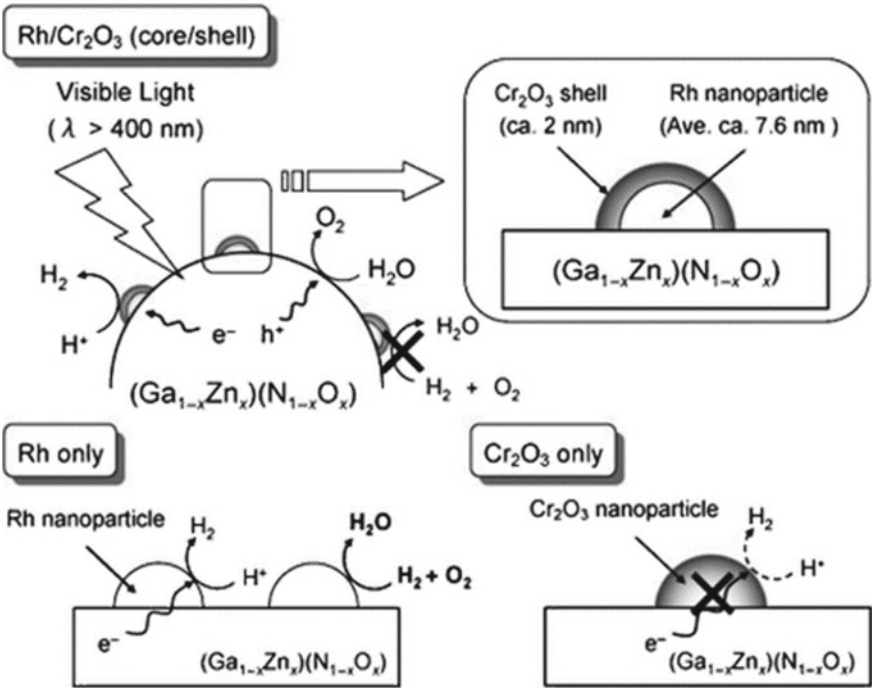

Fig. 9 Schematic diagram of PCWS and the corresponding reactions on supported Rh and Cr_2O_3 nanoparticles

Maeda et al. have synthesized noble metal/Cr_2O_3 core/shell nanoparticles as a cocatalyst for PCWS [126–128]. Fig. 9 shows a schematic of the mechanism for overall water splitting on Rh/Cr_2O_3 core/shell-loaded $(Ga_{1-x}Zn_x)(N_{1-x}O_x)$. The mode of operation in this system is quite different from those containing other cocatalysts such as the Rh–Cr mixed oxide [129]. The activity enhancement is primarily due to the suppression of undesired H_2–O_2 recombination and/or O_2 photoreduction, and possibly protection of the core from corrosion. Among the core materials examined, Rh species exhibit relatively high performances. Interestingly, with the assistance of Mn_3O_4 nanoparticle co-loading, the photocatalytic activity for overall water splitting of $(Ga_{1-x}Zn_x)(N_{1-x}O_x)$, containing core/shell-structured Rh/Cr_2O_3 nanoparticles, is improved. In this system, Mn_3O_4 nanoparticles function as O_2 evolution sites, and Rh/Cr_2O_3 nanoparticles serve as H_2 evolution sites [130].

Tian et al. [131] investigated Pt, RuO_2, and NiO_x nanoparticles loading on the narrow band gap photocatalysts $K_4Ce_2M_{10}O_{30}$ (M = Ta, Nb). The photocatalytic activity was markedly elevated by loading with cocatalysts, especially NiO_x which creates a NiO/Ni double-layered structure. This observation resulted in enhanced electron migration from the conduction band of $K_4Ce_2M_{10}O_{30}$ to the NiO/Ni. Hwang et al. synthesized a series of metal oxide-loaded $Sr_2Nb_2O_7$ photocatalysts using the impregnation method followed by redox treatment [11]. The system that uses

NiO_x as a cocatalyst was found to have the highest water splitting activity. Redox pretreatment to produce a double-layered structure is proven to be important to achieve high activity of the NiO_x-loaded catalysts. This phenomenon is ascribed to improved electron–hole separation by nickel in the p-type/n-type junction between NiO_x and $Sr_2Nb_2O_7$ that is created by redox pretreatment. However, this marked dependence on pretreatment does not exist for other metal oxides explored in this study. Also, various metal oxides (MO_x: M = Cr, Mn, Fe, Co, Cu, Ru, Ag, Ce, Sm, and Pb) were included as a second component of NiO_y cocatalyst to improve the activity of the photocatalyst NiO_y–$K_2La_2Ti_3O_{10}$. Among those fabricated, only CrO_x-NiO_y–$K_2La_2Ti_3O_{10}$ displays higher photocatalytic activity and durability over longer periods of irradiation as compared to those of the parent NiO_y–$K_2La_2Ti_3O_{10}$ [132].

Nonmetal-Oxide Cocatalysts

Transition metal sulfides have been explored as cocatalysts for PCWS. Zong and co-workers showed that MoS_2 is a novel cocatalyst for PCWS. They found that the activity of CdS is more greatly increased by loading with MoS_2 than that by loading with Pt [133, 134]. In this system, coupling and formation of junctions between MoS_2 and CdS improves charge separation that leads to higher activity. MoS_2 nanoparticle cocatalysts were also found to be effective in enhancing H_2 evolution over CdSe nanoribbons [135].

Tabata et al. [136] found that dispersing transition metal sulfides such as NiS, FeS, Ru_2S_3, Ag_2S, CoS, and PdS increases the photocatalytic activity of $CuGa_3S_5$. It is postulated that transition metal sulfides in this system accept photogenerated electrons from $CuGa_3S_5$ for reductive conversion of H^+ to H_2.

Note that the stability of GaN:ZnO during the prolonged photocatalytic reaction (>6 months) is retained to a certain extent when an O_2 evolution cocatalyst is deposited on a H_2 evolution catalyst. For example, co-deposition suppresses oxidative deactivation of GaN:ZnO thereby prolonging its lifetime. Also, Al-doped $SrTiO_3$ with $RhCrO_x$ and CoO_y cocatalysts has constant gas evolution activity during a 6 h water splitting, whereas the activity of $RhCrO_x$-loaded Al-doped $SrTiO_3$ decreases to 60% under the same conditions (Fig. 10a) [137]. The gas evolution rate of this photocatalyst coloaded with $RhCrO_x$ and CoO_y using simulated sunlight remains almost unchanged over 150 h and then gradually decreases to 64% after 1000 h (Fig. 10b).

Although the dual cocatalyst tactic can be used to enhance the performance and durability of particulate photocatalysts, it must be thoughtfully applied to obtain a synergistic effect of double cocatalysts. Factors that need to be considered include careful control of the locations of the H_2 and O_2 evolution cocatalysts and meticulous optimization of the loading amount of each cocatalyst. The results of one study showed that randomly dispersed NiO on $NaTaO_3$ cubes with exposed isotropic facets is reduced in situ to form metallic Ni at reduction sites while being retained as NiO at oxidation sites. Thus, this material functions as a dual cocatalyst with a photocatalytic

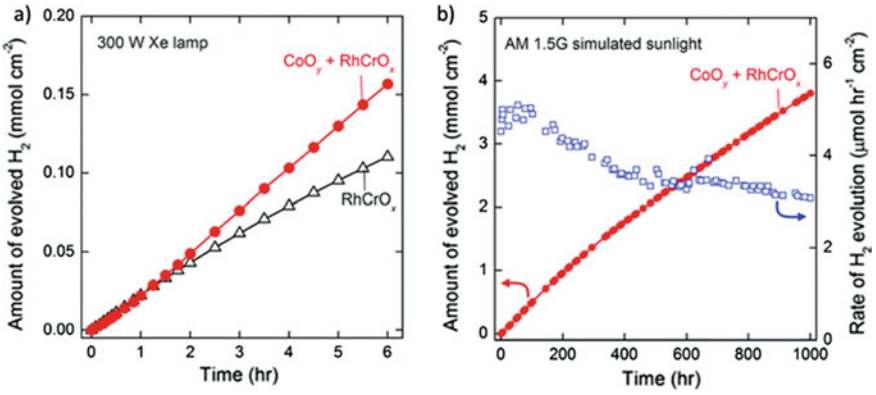

Fig. 10 Time courses of H_2 production under different light irradiations. **a** 300 W Xe lamp and **b** simulated sunlight

performance that is improved over that of NiO selectively deposited only at the reduction sites of $NaTaO_3$ [138]. The balance between in situ formed Ni and NiO, as well as their locations, are important factors governing the promotion of the overall water splitting activity of $NaTaO_3$.

2.3.4 Light Source

Typical photocatalytic systems in laboratory studies include either internal or external irradiation-type reactors, depending on the light source used [13, 139]. Internal irradiation reactors with the longest cut-off wavelengths higher than 400 nm usually have high gas evolution rates because the particle suspensions are close to the light source. Because of irregular light intensity distribution and irradiation areas, apparent quantum yields of photocatalysts cannot be precisely measured using this reactor.

Thus, analysis of wavelength-dependent gas evolution and quantum yields requires the use of an external irradiation-type reactor [9]. The light sources used in these reactors determine the performance of the photocatalyst. Xenon (Xe) and mercury (Hg) lamps, AM1.5 G, and light-emitting diodes (LED) are the most widely used light sources in laboratory studies [3, 140–142]. However, big differences exist between these sources and, thus, developing a uniform standard is not possible. Both spectral ranges and light intensities vary greatly for different sources. Moreover, different incident photon fluxes can lead to different photocatalytic performances. As a result of these factors, most reports do not contain sufficient information to compare and evaluate the efficiencies of photocatalysts and other reactor components.

The three main deficiencies that can be identified are listed below.

(1) Ambiguous or incomplete information regarding light sources. The actual light intensity used in the experiment is as important as the light brand, type, and power.

(2) Absence of data about attenuation of incident photon flux during operation. Each light source has a specific life span. Changes in radiation output occur, thus, it is best to measure light intensity at both the start and end of the test period. If the light source is decaying, photon flux may decrease significantly over the operation time.
(3) Incomplete description of the configuration of the light source and reactor. The actual light intensity reaching the reaction surface greatly depends on the material the reactor is composed of, the distance between the light source and the reactor, and the irradiated area of the reactor. Even using the same weight of photocatalyst, different irradiation areas with different suspension conditions can lead to diverse photocatalytic performances.

The lack and inconsistency of accurate information regarding the light source prevent comparisons of experimental results. It has been shown that irradiation at different wavelengths, even within the same visible wavelength range, can lead to different photocatalytic performances (Fig. 11 a) [143]. Also, when the light intensities are different, the rate of H_2 production varies significantly even for the same photocatalyst (Fig. 11 b). Moreover, different light sources may promote different reaction mechanisms [144, 145]. Therefore, details on the wavelength of the light source, light intensity or density, and irradiation area on the surface of the photocatalytic system need to be specified.

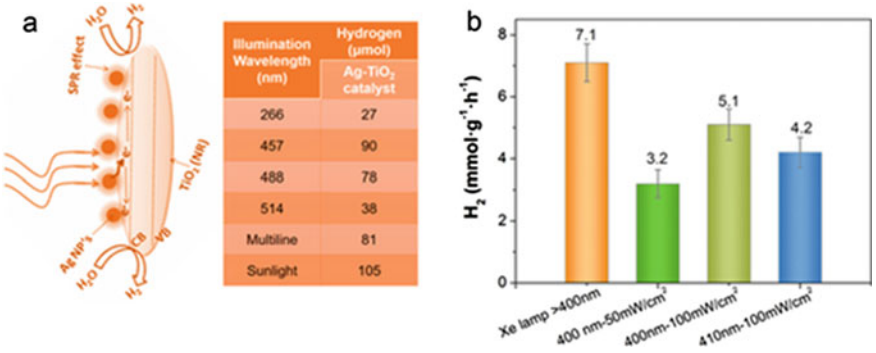

Illumination Wavelength (nm)	Hydrogen (μmol) Ag-TiO_2 catalyst
266	27
457	90
488	78
514	38
Multiline	81
Sunlight	105

Fig. 11 **a** H_2 production under different lighting conditions. **b** The efficiency of the photocatalytic dehydrogenation of formic acid (H_2 production) at different wavelengths or intensities for Pt/C_3N_4 photocatalyst after 5 h of irradiation

3 Materials Used for PCSS

3.1 Introduction (Material Type, Synthesis, Structure, Characteristic Properties, and Performance in Seawater Splitting)

Hydrogen, a clean and storable energy source with a high energy density of 142 MJ kg^{-1}, through photochemical water splitting with abundant seawater would address challenging issues such as the increasing energy demand and depletion of fossil fuels. In addition, it could also alleviate the consumption of scarce fresh water and have use in arid coastal areas. In this chapter, the earth-abundant photocatalysts including TiO_2, conjugated polymers, solid solution materials, and other semiconductor nanomaterials that have been developed for seawater splitting are discussed.

3.2 TiO_2-based Materials

Due to merits associated with high stability, low cost, and low toxicity, TiO_2-based photocatalysts have attracted extensive attention and have become the most widely used for PCSS. All reported TiO_2 photocatalysts are based on structure design, modification by other semiconductors, defect engineering, and so on.

In a series of studies on PCSS using TiO_2 materials, Yang et al. [146] using calcination at high temperatures prepared nano-TiO_2, referred to as TiO_2-OH, a material that has surface hydroxyl groups and high crystallinity. The morphology and structure of TiO_2-OH revealed by TEM images consist of aggregates of uniform TiO_2 nanocrystals with uniform sizes ranging from 30 to 40 nm. As can be seen in the magnified TEM images (Fig. 12a, b), single TiO_2 nanocrystals contain inner defect-like pores with a size of about 4 nm. Experimental measurements show the TiO_2-OH has defects (Fig. 12c). The rich array of surface hydroxyl groups and Ti-vacancies in TiO_2 significantly enhance its activity in photocatalytic H_2 production from (sea)water (Fig. 12d). [146, 147] Their group also developed a low-temperature method to introduce oxygen/metal vacancies in TiO_2 that increase the interfacial n-p effect. Interfacial n-p homojunctions of TiO_2 are fabricated by directly decorating interfacial p-type TiO_2 with Ti-vacancy around n-type TiO_2 nanocrystals.

Beads of TiO_2 that are calcined at 350 °C show a uniform diameter of about 500–600 nm (Fig. 13a) and consist of uniform nanoparticles with a diameter of about 15 nm (Fig. 13b). The nanocrystals with a size of around 8–10 nm (Fig. 13c, blue areas) are bonded together through an interconnecting amorphous/semi-crystalline interface of around 1–4 nm (Fig. 13c, yellow areas). The amorphous/semi-crystalline/highly crystalline phase can be well visualized by viewing the HRTEM image and inverse FFT in Fig. 13d, e. This highly crystalline/semi-crystalline/amorphous phase is coherent

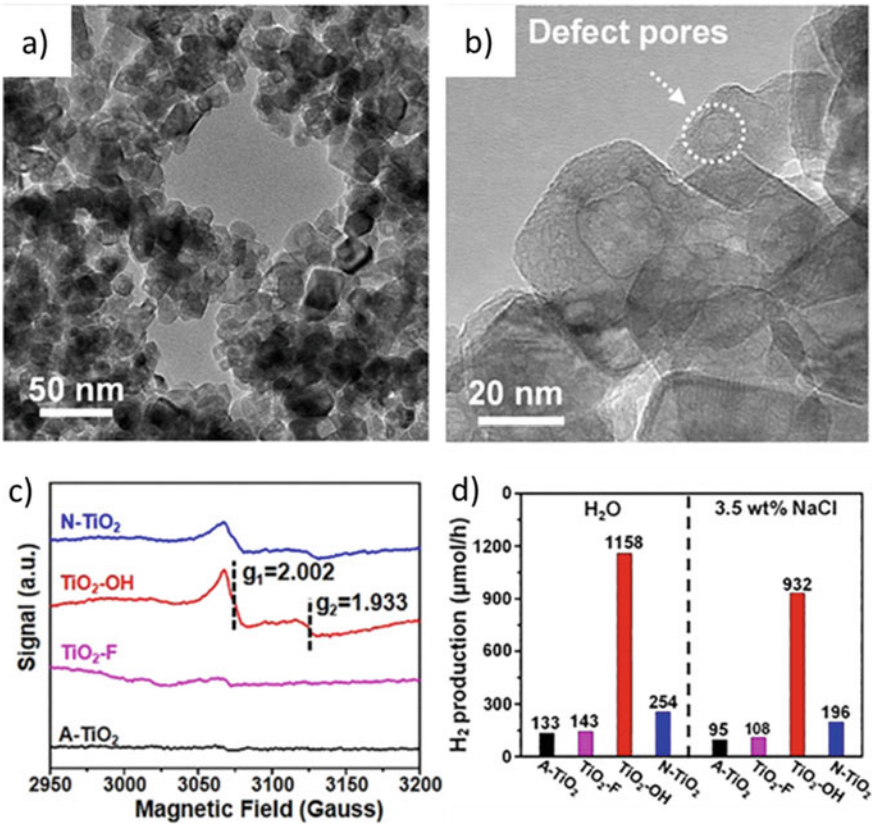

Fig. 12 **a**, **b** TEM images of TiO_2-OH, **c** EPR spectra, and **d** photocatalytic H_2 production rates from (sea)water of different samples

at the atomic scale, and defect generation mainly occurs at the interface region. In the EPR spectrum of TiO_2-350, the sharp peak corresponding to $g_{yy} = 2.001$ is assigned to oxygen vacancies and the high intensity of this peak means that TiO_2-350 has the highest level of oxygen vacancies of all the samples treated at different temperatures. The EPR signals at $g_{zz} = 2.020$ and $g_{xx} = 1.98$ are attributed to O^{2-} and Ti^{3+}.

To determine the Ti-vacancies in TiO_2, Yang et al. performed a 2D1H TQ-SQ magic-angle spinning (MAS) NMR experiment. Signals in the spectrum at (7.10, 7.10 + 7.10 + 1.84) (Fig. 14a) demonstrate the presence of Ti–OH species near the solid surface ($\delta_H = 1.84$ ppm) exist in TiO_2-A, and Ti–OH species from broken Ti–O–Ti bonds ($\delta_H = 7.10$ ppm) which were forming hydrogen bonds. At 250 °C, the signals at (6.00, 6.00 + 6.00 + 6.00) (Fig. 14b) show that Ti-vacancies start to form, and Ti–OH species from broken Ti–O–Ti bonds and surface Ti–OH groups are in the phases. When the temperature reaches 350 °C, Ti–OH nests remain and almost no other Ti–OH species are present in the bulk (Fig. 14c). Further increasing

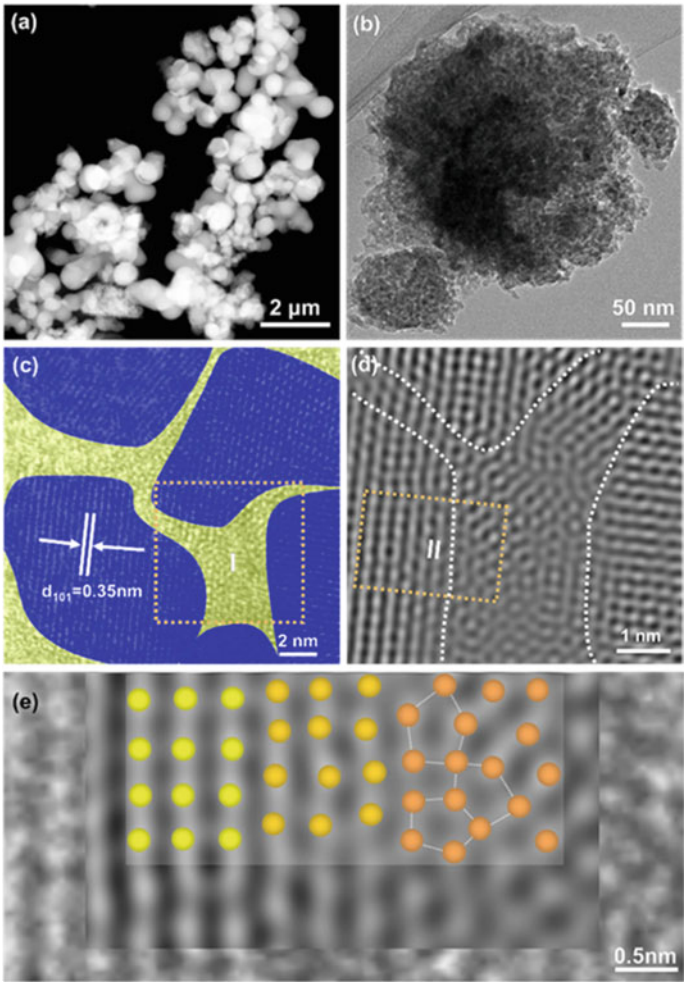

Fig. 13 The morphology of TiO_2 via TEM and corresponding Inverse FFT

the temperature only causes the loss of Ti–OH nests, and only Ti–OH species from broken Ti–O–Ti bonds and surface Ti–OH species remain (Fig. 14d–h).

As foreign phase-junctions, nanocarbons are very efficient dopants for semiconductor fabrication [148, 149]. Yang et al. found that graphene nanosheets or nanodots can capture oxygen atoms of TiO_2 thereby creating O- and Ti-vacancies. This group developed a two-step calcination treatment, involving starting at 500 °C calcination in an Ar flow and followed by 350 °C calcination in air. Application of this procedure enabled the formation of a junction of O-vacancies and Ti-vacancies in TiO_2 with the assistance of reduced graphene oxide (rGO) sheets [150]. As shown in Fig. 15a, rGO sheets have a thickness of about 3–5 nm that is intimately coated on the external

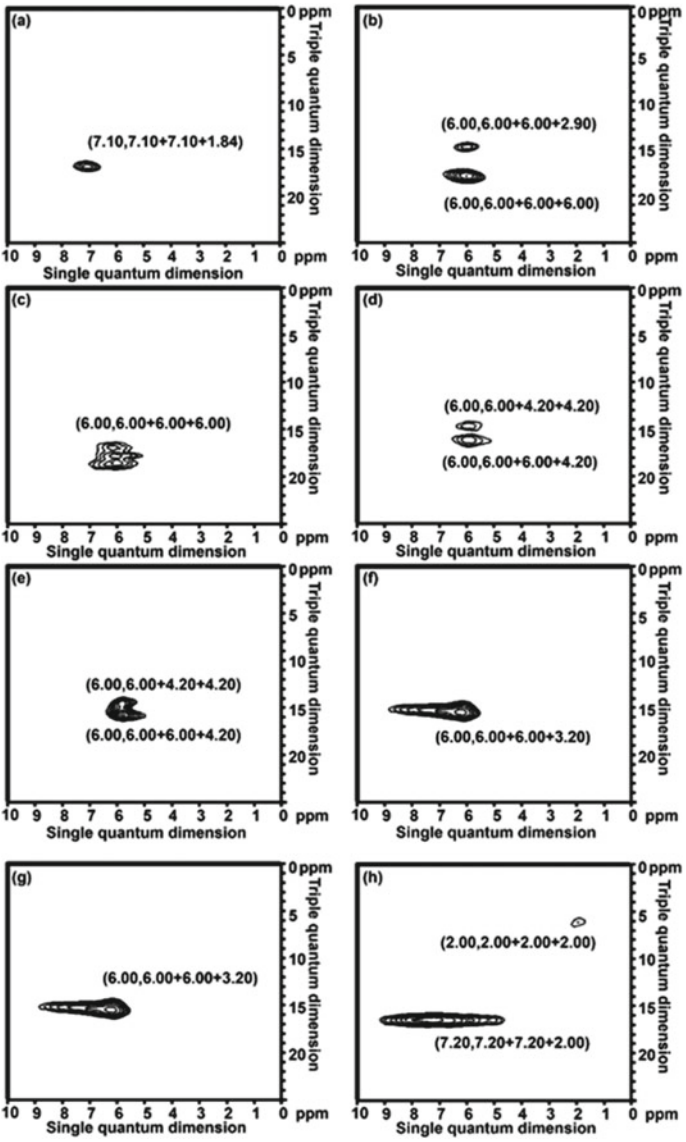

Fig. 14 1H TQ-SQ MAS NMR spectra of **a** TiO_2-A, **b** TiO_2-250, **c** TiO_2-350, **d** TiO_2-450, **e** TiO_2-550, **f** TiO_2-650, **g** TiO_2-750, and **h** TiO_2-850

surface of TiO_2 beads (Fig. 15a). It also shows a strong electron paramagnetic resonance (EPR) signal at $g = 2.002$ in the spectrum of TiO_2@rGO, which is attributed to O-vacancies in TiO_2 lattices, while the weak signal at $g = 1.965$ in that of TiO_2@rGO is related to the Ti^{3+} defects associated with O-vacancies (Fig. 15b) [151]. Interfacial junction of O-vacancies and Ti-vacancies significantly enhances t transport of

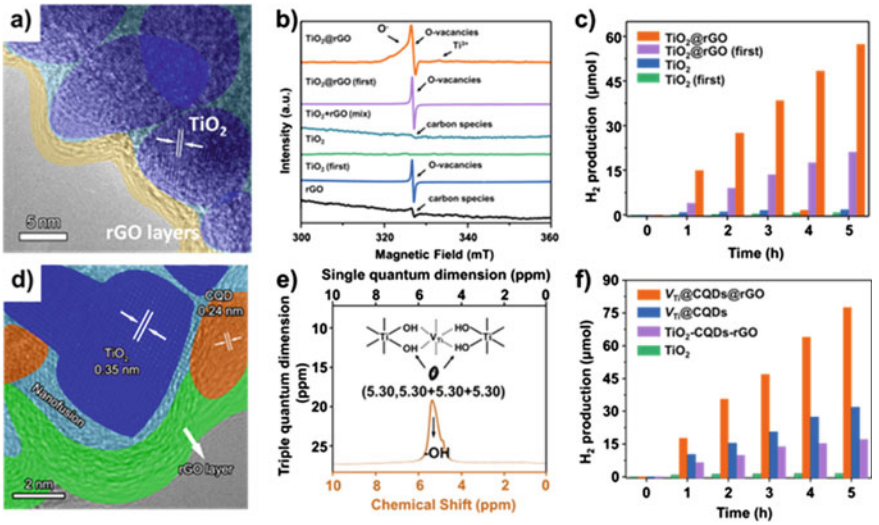

Fig. 15 **a**, **d** Structure, **b**, **e** defects, and **c**, **f** photocatalytic H_2 production from PCSS

interfacial carrier. The final sample exhibits a H_2 production rate of 570 μmol/h g^{-1} from seawater splitting (Fig. 15c).

Next, Yang and co-workers constructed a spatially ternary titanium-defected TiO_2@carbon quantum dots@reduced graphene oxide (denoted as V_{Ti}@CQDs@rGO) to demonstrate the cascade effect of charges [152]. The clear lattice fringes of TiO_2 and CQDs in the HRTEK image are in agreement with the anatase TiO_2 (101) planes and (110) lattice fringes of graphite, respectively (Fig. 17d). The uniform distribution of CQDs in overall mesostructured TiO_2 nanocrystals and outer coating of rGO can be clearly observed in this image. The Ti–OH nests with pairs of off-diagonal peaks at (5.3, 5.3 + 5.3 + 5.3) and (5.5, 5.5 + 5.5 + 5.5) appear in V_{Ti}@CQDs@rGO (Fig. 17e), which are attributed to Ti–OH nests referring to the Ti-vacancies, and almost no other Ti–OH species are present [153]. As components of the photo-energy conversion efficiency (η_c) of the cascade photo-conversion system, charge separation efficiency (η_{cs}) depends on the charge separation from the inner lattice to the Ti-vacancies, charge separation efficiency (η_{ct}) depends on the charge transport from the Ti-vacancies to the CQDs, and charge utilization efficiency (η_{cu}) depends on the charge collection and utilization from the CQDs and TiO_2 nanocrystals to the rGO sheets. This spatial heterojunction exhibits a H_2 production rate of 750 μmol/h g^{-1} from seawater splitting, which is 4.4-fold higher than that arising from a random surface heterojunction (Fig. 17f).

Zeng et al. [30] display an uncomplicated post-processing method to synthesize a Ti^{3+} self-doped titanium-silicon material with corrosion resistance. These workers demonstrated that Ti–O–Si materials created using different calcination temperatures serve as a highly efficient and convenient catalyst for the photogeneration of hydrogen from water and simulated seawater. The optimized Ti–O–Si (400) material has an

impressive 10-times enhanced photocatalytic H_2 production performance that is 43.1 times that of TiO_2 nanoparticles in water and simulated seawater.

Yang et al. [154] developed nonmetal plasmonic MoS_2@TiO_2 heterostructures for highly efficient photocatalytic H_2 generation. A combination of physical vapor deposition (PVD) and chemical vapor deposition (CVD) strategies was used to create few-layered MoS_2 nanoflake uniform coatings of different thicknesses on the inner surface of anodized TiO_2 nanocavities (referred to as MoS_2@TiO_2) to produce a highly ordered 3D hierarchical configuration (Fig. 16a). CVD sulfurization was carried out at 400 °C for 10 min on these coated TiO_2 arrays (abbreviated as MoS_2(10)@TiO_2, $MoS_2$20)@TiO_2, MoS_2(30)@TiO_2, respectively). In the bright-field (BF) STEM image of MoS_2 nanoflakes shown in Fig. 16b, a relationship with respect to the atomic number (Z) reveals the presence of sandwich structured MoS_2 and S-vacancies identified by blue dashed circles and blue arrows in Fig. 16c. These structures display intense LSPR throughout regulating the S stoichiometry of MoS_2 surfaces. The photocatalytic activities of members of the series of MoS_2@TiO_2 cocatalysts for H_2 under simulated solar light illumination (Fig. 16d, e). Pure TiO_2, sulfurized TiO_2, and MoO_3@TiO_2 hybrid are nearly photocatalytically inert toward H_2 production, associated with a reaction rate lower than 10 μmol h^{-1}. Notably, photocatalytic activity is greatly enhanced by the presence of the MoS_2 loading, reaching a maximum value of 84 μmol h^{-1} for MoS_2(30)@TiO_2 which is 8 times larger than that of pure TiO_2.

Ho et al. designed the SiO_2/Ag@TiO_2 core–shell solar thermal collector that possesses photothermic properties needed for highly targeted interfacial phase transition reactions that are synergistically favorable for both seawater splitting and desalination reactions [34]. In Fig. 17a is shown the photocatalytic performance trend in simulated seawater under full spectrum irradiation. Both SiO_2@TiO_2 and TiO_2 spheres undergo increases from 156 μmol g^{-1} h^{-1} to 192 μmol g^{-1} h^{-1} and from 138 μmol g^{-1} h^{-1} to 156 μmol g^{-1} h^{-1}, respectively. H_2 generation rates for the splitting of simulated seawater catalyzed by all three materials are lower than those for the splitting of pure water.

In this effort, chloride concentration as a function of time was measured during photocatalytic hydrogen generation reaction of the SiO during the photocatalytic hydrogen generation reaction during the photocatalytic hydrogen generation reaction catalyzed by the SiO_2/Ag@TiO_2 core–shell nanocomposite during the photocatalytic hydrogen generation reaction using a chloride ion selective electrode. Hydrogen is produced at a steady rate of 370 μmol g^{-1} h^{-1} under UV light irradiation and 857 μmol g^{-1} h^{-1} under full solar spectrum irradiation (Fig. 17). Concomitantly, the chloride concentration remains unchanged throughout the process (Fig. 17b) and, hence, no chloride derived compounds are produced. Based on these findings, seawater collected from the Strait of Singapore, combined with glycerol in a 20% v/v ratio, was subjected to photocatalytic hydrogen production. The results show that the photocatalytic performance using actual seawater was better than that utilizing simulated seawater. The second issue assessed is the stability of the photocatalyst. These workers found that the hydrogen generation rate remains relatively constant

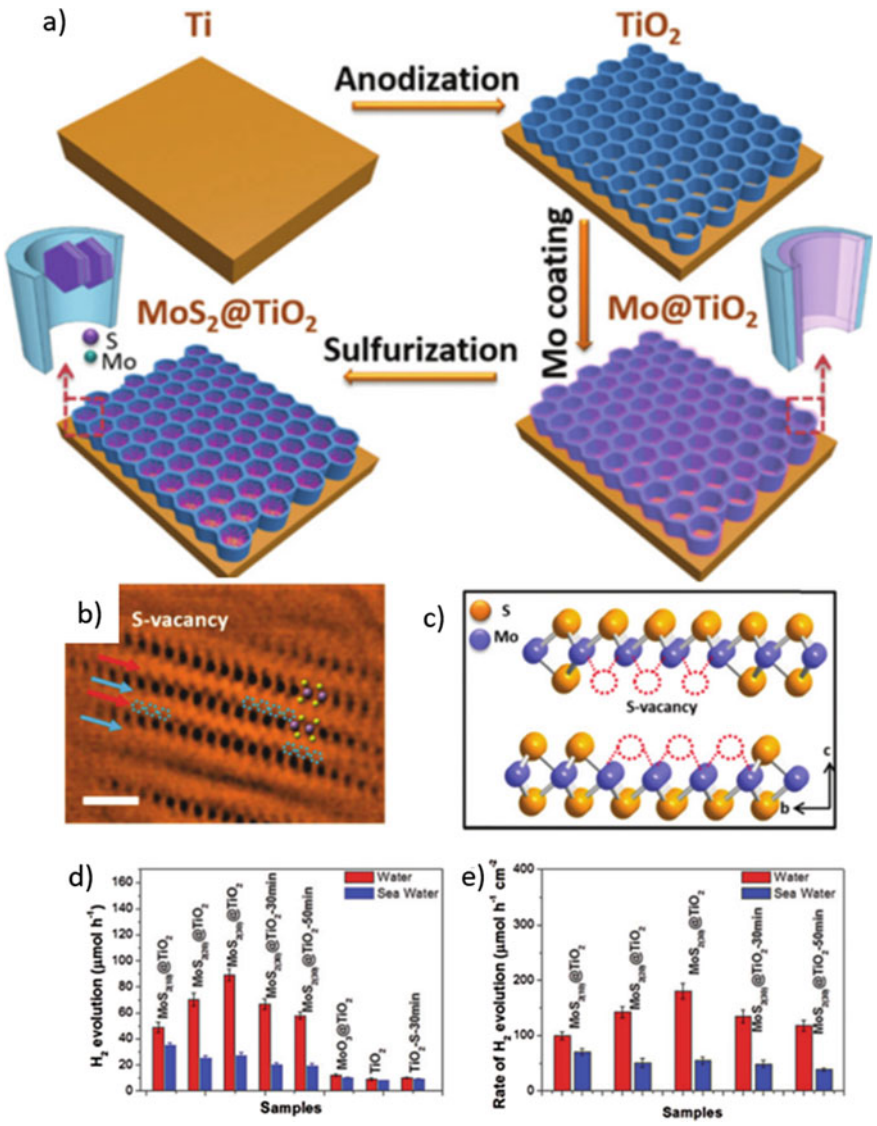

Fig. 16 **a** Synthesis process of the MoS_2@TiO_2 heterostructure. **b**, **c** BF-STEM image, and **d**, **e** H_2 production rate over different samples in water and seawater condition

at about 7% during the process (Fig. 17c) which suggests that the SiO_2/Ag@TiO_2 core–shell nanocomposite is chemically stable during seawater splitting.

Wu et al. [155] investigated the Pt/GaP-TiO_2-SiO_2:Rh (PGTSR) composite composed of the d^0 metal oxide photocatalyst TiO_2 and d^{10} photocatalyst (GaP). The noble metal Pt and supporter SiO_2 are employed to enhance the transfer of the

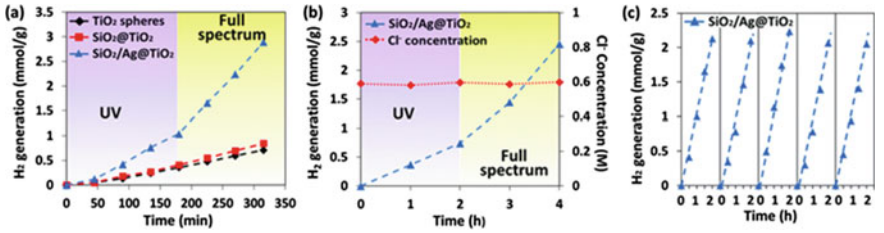

Fig. 17 **a** H_2 production of different samples in simulated seawater. **b** H_2 production and chlorine concentration of $SiO_2/Ag@TiO_2$. **c** Cycling test for H_2 production

photogenerated electrons and the adsorption capacity of the composite. The photocatalytic performance and stability of the prepared photocatalyst were evaluated by measuring the hydrogen and oxygen generation from pure water or seawater in a single photoreactor without using sacrificial agents. This PCSS system achieved a HER/OER ratio of 41.5/26.1 μmol g^{-1}.

3.3 Polymer-Based Materials

A series of water splitting systems that utilize UV light have been developed since 1980. However, it is unlikely that STH efficiencies of these systems will reach the threshold value required to make the cost of hydrogen production by this process competitive with those of fossil fuels [156]. UV light (i.e., $\lambda < 400$ nm) only accounts for approximately 5% of the solar spectrum. In contrast, visible light (400 nm $< \lambda <$ 800 nm) represents more than 50% of the solar spectrum, and close to a 16% STH efficiency is possible by using visible light-absorbing photocatalysts that utilize >600 nm sunlight with 100% efficiency [157]. Therefore, developing long-wavelength-responsive photocatalysts is a critical aspect of truly efficient renewable hydrogen production.

Conjugated polymers are new types of photocatalysts that have been developed for water splitting since they have similar band structures with semiconductors. Early studies primarily of these materials focused on the photocatalytic half-reactions promoted by polymeric carbon nitride (PCN) [158, 159]. After persistent efforts, by loading suitable cocatalysts on PCN loaded with suitable cocatalysts were identified that promote water splitting using both UV and visible light [160]. In addition, single-site cocatalysts have been found to significantly improve catalytic performance. A conjugated polymer, comprised of 1,3-diyne-linked conjugated microporous polymer nanosheets (CMPNs) and synthesized via the oxidative coupling of terminal alkynes, was found to function as a visible light-responsive photocatalyst for overall water splitting [161]. Although the efficiencies of processes promoted by conjugated polymers are relatively low, their performances can be improved by

using the crystallinities of the polymers [162]. In addition, the incorporation of functional groups can be used to tune band gaps and enhance charge separation, and high-efficiency cocatalysts, doping, and morphologic control can be employed to enhance activities.

In 2015, Kang et al. [163] described the design and fabrication of a metal-free carbon nanodot-carbon nitride (C_3N_4) nanocomposite and demonstrated its impressive performance for photocatalytic-solar water splitting. The measured wavelength-dependent quantum efficiencies of the system are 16% for $\lambda = 420 \pm 20$ nm, 6.29% for $\lambda = 580 \pm 15$ nm, and 4.42% for $\lambda = 600 \pm 10$ nm, and the overall solar energy conversion efficiency is 2.0%. Even though seawater was not used for these measurements, they highlight the bright future that this low-cost, Earth-abundant, environmentally friendly, and stable material has in H_2 production.

Xiang et al. [164] developed the organic hybridized photocatalyst, COP-TF@CNi_2P), comprised of a carbon-encapsulated nickel phosphide, as a cocatalyst loaded on a fully conjugated organic polymer (Fig. 18a). COP-TF@CNi_2P exhibits has a photocatalytic H_2 evolution rate up to 2500 μ mol g^{-1} h^{-1} ($\lambda \geq 400$ nm) using seawater and it maintains 92% of its initial efficiency after 16 intermittent cycles occurring over a half month (Fig. 18b, c). The excellent activity and long-term stability of this material are ascribed to the presence of a tight combination between CNi2P and pristine COP-TF, which is conducive to the transfer of photoexcited electrons to the surface of CNi_2P and its resistance to shedding during photocatalytic hydrogen evolution.

Huang et al. [165] reported the results of a study of an electrostatically induced supramolecular approach in which small molecules form self-assembled superstructures as they provide a platform for loading Pt nanoparticle catalyst and facilitate charge transfer. This group took unprecedented advantage of chloride ions in seawater to promote superstructure formation by their electrostatic interactions with the fine-designed conjugated small-molecule PorFN. The observations show that the photocatalytic activity of the system in simulated seawater reached 10.8 mmol h^{-1} g^{-1}.

Yu et al. [166] described the thioether-functionalized covalent organic framework, TTR-COF, and its use in visible light-driven photocatalytic H_2 production from seawater (Fig. 19a). Owing to the specific affinity of thioether groups for Au ions, TTR-COF selectively adsorbs Au over other alkaline and alkaline-earth metal cations in seawater, to produce a uniform loading of Au as a cocatalyst. This loading along with the highly conjugated structure containing triazine units in TTR-COF contributes to enhancing the visible light harvesting and photoinduced charge generation and separation ability, as well as the stability of the system. The results suggest that COFs have great potential for photocatalytic H_2 production from seawater. TTR-COF also has an ability to selectively capture Au ions over other common transition and basic metal ions (Fig. 19b). The H_2 evolution capacity of TTR-COF is up to 1720 μ mol g^{-1} in a 4 h reaction and is stable at that level for at least 20 h (Fig. 19c). Moreover, TTR-COF displays continuous and stable H_2 production of 501 μmol g^{-1} and an H_2 evolution rate of 141 μmol h^{-1} g^{-1} over a 20 h irradiation

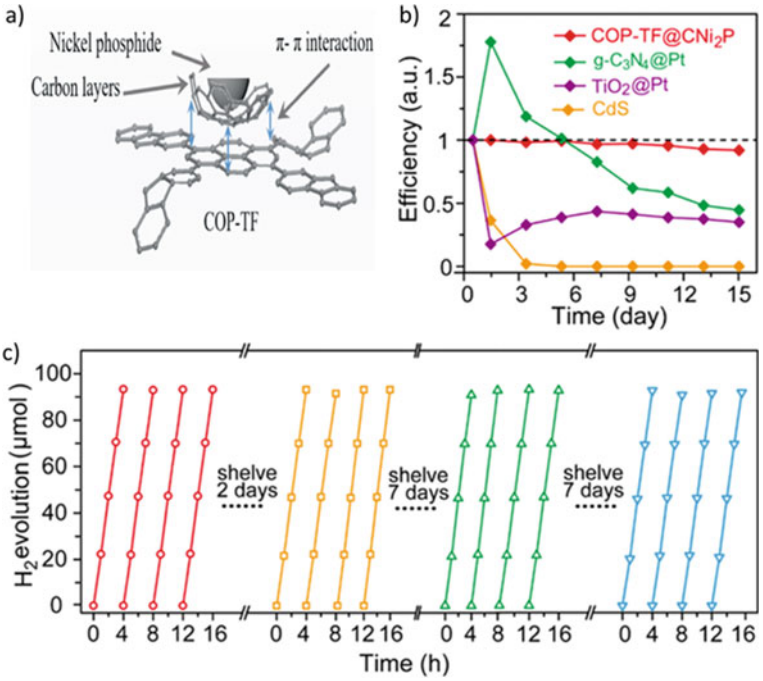

Fig. 18 **a** Structure diagram of CNi_2P and COP-TF. **b** Photocatalytic stabilities of different samples in seawater. **c** Cycling test of H_2 production from seawater

time (Fig. 19d), although a relatively higher H_2 evolution rate was obtained using TFPT-COF (Fig. 19e).

Babu et al. [167] demonstrated the success of solar seawater splitting by using a two-dimensional polymer catalyst derived from metalloporphyrin-bearing multi-hydroxyl groups. A bimetallic (Co and Ni) derivative of the porphyrin 2D-polymer exhibits excellent long-term durability over 15 cycles of H_2 and O_2 generation in 200 d from pure water. Detailed studies using rivers and seawaters also show that the catalyst has reliable performance over repeated cycles.

Studies by Lyutakov et al. [168] resulted in the formation of rationally designed two-dimensional (2D) flexible heterostructures with photocatalytic activity for the production of "clean" hydrogen under NIR illumination. The system displays a hydrogen production rate exceeding that of most other 2D materials and it has the ability to use the seawater. The material has a hybrid bimetallic (Au/Pt) periodic structure, which is covalently grafted with a metal–organic framework MIL-101(Cr). The periodic gold structure effectively supports a plasmon-polariton wave to excite the hot electrons, which are injected into the Pt and MIL-101(Cr) layers. The Pt and MIL-101(Cr) structures contain catalytic sites, which are saturated with hot electrons that efficiently initiate water splitting and hydrogen production. The MIL-101(Cr) layer also serves to repel generated hydrogen bubbles. The results of mechanistic studies

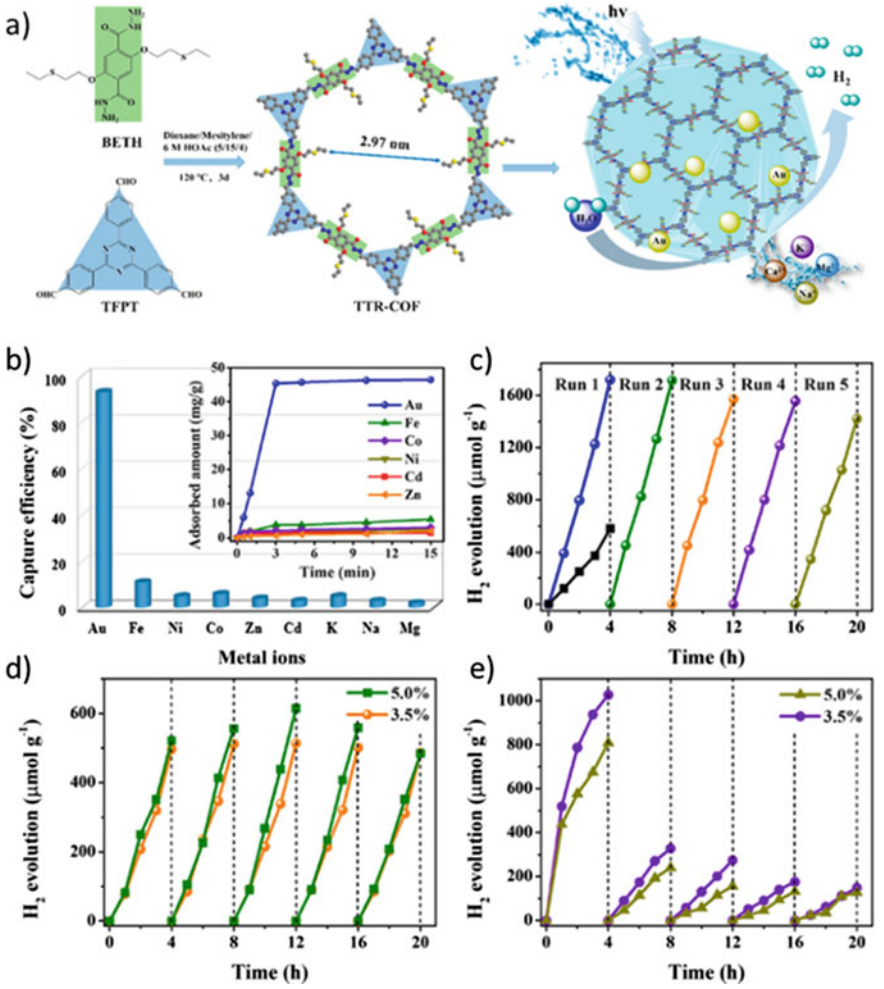

Fig. 19 **a** Synthesis and application of TTR-COF in PCSS. **b** Capture efficiency for various metal ions of TTP-COF from H_2O. Inset: adsorption curve of various metal ions, **c** Photocatalytic performances of TTR-COF and TTB-COF (black) in water, Photocatalytic performances of **d** TTR-COF and e) TTB-COF (black) in seawater conditions

reveal the catalytic role played by every element in the 2D flexible heterostructures. A maximum hydrogen output was achieved under plasmon resonance excitation in the NIR range, and it could be controlled by varying the applied LED wavelength. Moreover, water or seawater is converted into H_2 at 193.5 μmol h^{-1} cm^{-2} rate under irradiation with the NIR part of the solar spectrum.

3.4 Solid Solution-Based Materials

Solid solution photocatalysts can optimize the band structures of materials, leading to a reduction of the band gap of photocatalysts, broadening the light absorption range, and improving the sunlight utilization rate. Thus, these photocatalysts provide a more controllable way to realize continuous regulation of the physicochemical properties of materials [169, 170]. Furthermore, their optimized band structures may promote the delocalization of photogenerated electrons, which boosts diffusion and disconnection of photogenerated carriers and improvement of photocatalytic performances [171]. Finally, solid solution materials enable better adjustability in compositions and structures than single component materials which considerably affect photocatalytic performance [172].

K. Domen was the first to use a solid solution as a photocatalyst for overall water splitting under visible light irradiation ($\lambda > 400$ nm). [173] To devise a new d_{10}-(oxy)nitride having a visible light response, the attention of this group initially focused on gallium nitride (GaN). Since both GaN and ZnO have wurtzite structures with similar lattice parameters [174, 175]. They participate in forming a solid solution (Fig. 20a). The expected band structure of the GaN–ZnO solid solution $(Ga_{1-x}Zn_x)(N_{1-x}O_x)$) is illustrated in Fig. 20b [23]. Experiments confirmed that by using Xe (300 W) irradiation, the GaN:ZnO photocatalyst system functions at wavelengths as long as 460 nm and has an average apparent quantum efficiency in the range of 300–480 nm of 0.14% [173]. Upon modification by using suitable cocatalysts (such as $RH_{2-y}Cr_yO_3$), GaN:ZnO becomes active for the H_2 evolution under visible light ($400 < \lambda < 500$ nm). The rate of visible light water splitting producing H_2 and O_2 continuously in stoichiometric amounts remains unchanged for 3 months (2160 h). After 6 months of operation, a 50% loss of initial activity occurs. Regeneration of deactivated catalysts was attempted by the reloading of the $RH_{2-y}Cr_yO_3$ cocatalyst. The degree of activity regeneration was found to depend on the reloading amount, with up to 80% of the initial activity for H_2 evolution being recovered optimally. It was also found that the deactivation of GaN:ZnO is suppressed to some extent by prior co-loading of an O_2 evolution cocatalyst, which helps to suppress oxidative decomposition of GaN:ZnO by valence band holes, thereby improving durability [176]. Furthermore, these workers investigated the effects of electrolytes on photocatalytic activity in seawater [177]. The cocatalyst $RH_{2-y}CryO_2$ was found to selectively promote photoreduction of H^+, while RuO_2 functions as both H_2 evolution and efficient O_2 evolution sites.

Zhang et al. [178] employed a simple mechanical mixing method to combine $Cd_xZn_{1-x}Se$ and CoP. They found that the $Cd_xZn_{1-x}Se$ energy band could be tuned by changing Cd concentrations due to the acceptance of photoelectrons on CoP nanoparticles. The higher CB generates electrons with stronger reduction capacity for H_2 evolution. Considering various electrolytes exist in natural seawater besides NaCl, Li et al. studied possible reactions of ions during the photocatalytic process. These workers synthesized $ZnS_{1-x-0.5y}O_x(OH)_y$–ZnO photocatalyst with NiS loading by using two methods [179]. When $Na_2S{\cdot}9H_2O$ and Na_2SO_3 are added as sacrificial

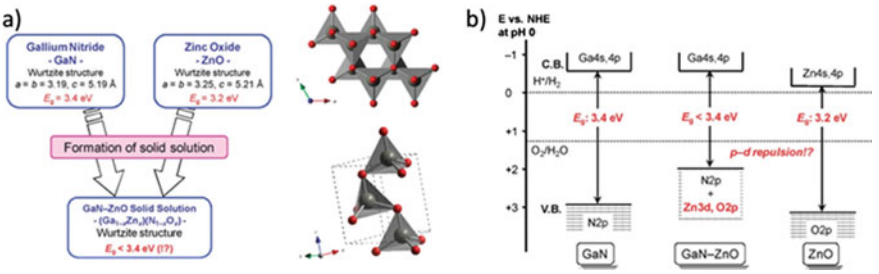

Fig. 20 **a** Crystal data and structure of GaN and ZnO and **b** band structures of different samples

agents to seawater, a precipitate of a mixture of $Mg(OH)_2$ and $CaSO_3$ is produced. Although the surfaces of both the precipitate and photocatalyst are negatively charged in the seawater-electron donor reaction system, part of the precipitate particles cover the active sites of the photocatalyst. The precipitate can also screen light absorbed by the photocatalyst. The surface charge of the modified photocatalyst changes to more negative when NiS loaded, which leads to decreasing coverage of the photocatalyst surface with the precipitate particles due to increased electrostatic repulsion. Thus, the detrimental effect of precipitation decreases, and the photoactivity of the modified photocatalyst in seawater-electron donors with the precipitate is higher than that in pure water-electron donors without the precipitate.

Chai et al. [180] prepared a photocatalytic system comprised of p-doped $Zn_{0.5}Cd_{0.5}S$ (pZCS) and CoP as a noble-metal-free cocatalyst for photocatalytic HER in both pure water and seawater. Through a series of detailed characterization experiments, they deduced that the P atoms interstitially doped into the lattice framework amplify the S-vacancies present in ZCS. The electron trapping effect becomes even more pronounced because the P dopant shifts the Fermi level to a location that is in closer proximity to the midgap state. The multiple extents of electron entrapment within the composite result in highly efficient HEP in pure water and 3864.1 $\mu mol\ g^{-1}\ h^{-1}$ in seawater. Overall, this study offers new insight into photocatalytic seawater splitting by highlighting a new approach to produce a composite that functions as an innate dual-stage electron trapping system for hindering charge carrier recombination.

Huang et al. [181] prepared $Cd_{0.5}Zn_{0.5}S/Ti_3C_2$ composites containing Ti_3C_2 nanosheets that have excellent metal conductivity with $Cd_{0.5}Zn_{0.5}S$ to form a non-precious Schottky photocatalyst. The rate of hydrogen production promoted by this composite in seawater is 9.071 $mmol\ g^{-1}\ h^{-1}$, which is 33 times higher than that of Pt-loaded photocatalysts in seawater. In addition, Silva [182] prepared selenium/selenide containing Cd and Zn in aqueous solution at room temperature by using co-precipitation. The cubic structure formed has a wide size distribution of CdSe and ZnSe solids and produces 16% more hydrogen in natural seawater with added lactic acid as a sacrificial agent than in deionized water. The hydrogen production rate of $Cd_{0.5}Zn_{0.5}S_{0.1}Se_{0.9}$ is 350 $umol\ g^{-1}\ h^{-1}$, and the CdSe composite $Zn_5(OH)_8Cl_2{\cdot}H_2O$ produces hydrogen at a rate of 395 $umol\ g^{-1}\ h^{-1}$. Based on considerations of a

computational phase diagram, band gap, and band edge position, Gerbrand Ceder et al. [183] devised the solid solution $Ta_{3x}Ti_{3-3x}O_{3-3x}N_{2+3x}$ as a promising water splitting photocatalyst. The minimal band gap is around 2.0 eV, indicating that high efficiency under solar illumination may be achieved.

3.5 Other Types of Materials

Wu et al. [184] designed and synthesized few-layer heterostructure ReS_2 nanosheets with a lateral metallic T and semiconducting Td phase interface, in which cationic vacancies are intentionally introduced as active sites. Six representative samples of seawater of different salinities including 0.8 (Baltic Sea), 2.8 (Yellow Sea), 3.6 (Caribbean Sea), 3.9 (Arabian Sea), 10 (Dead Sea), and 36wt% (saturated salt solution) were analyzed. The plot in Fig. 21a shows that the H_2 production rate increases with increasing salinity. The process promoted by T3 in saturated salt solution exhibits the highest hydrogen evolution activity with a hydrogen production rate of 216 μmol cm^{-2} h^{-1}, and the hydrogen production efficiency in Arabian seawater is slightly larger than that in freshwater (0.5 M sodium sulfate solution). The sample from the East Sea, China, was further tested to evaluate the EC performance of T3 in the presence of light. The hydrogen production rate is higher in real seawater than in simulated seawater (Fig. 21b) because cations such as Na^+, Mg^{2+}, Ca^{2+}, K^+, and B^{3+} present in the former improve conductivity. The performance lasts over a long period without obvious decay compared to that promoted by nanosheets with S-vacancies (Fig. 21c). Compared to S-vacancies, the Re vacancies in the ReS_2 nanosheets adsorb H^+ ions more easily than they do the other five cationic ions. Hence, degeneration of active sites is avoided as manifested in the durability of the system (Fig. 21c, d). The study demonstrates that T@Td-ReS_2 nanosheets are practical and versatile photocatalysts in different environments.

Tang et al. [185] constructed an IR-driven PCSS system based on WO_2-Na_xWO_3 ($x > 0.25$) by reduction of semiconductor Na_xWO_3 ($x < 0.25$) nanowire bundles at high temperatures. During the calcination process, the nanowire bundles are reconstructed into micron-sized crystals. The residual reducing agents and carbon particles mostly exist either independently or on the surface of the micron-sized crystals. The seawater splitting activity of this system was demonstrated. In addition to the tungsten conductive oxides, other hybrid conductive oxides with the general formula of MO_2-A_xMO_3 (M = V, Mo, Ta, Re, Nb, Tc, Ru; A = Na, K, Sr) in the material have potentially similar photocatalytic properties.

Wang et al. [186] prepared (Ni-ZnO)@C core–shell and yolk-shell nanoparticles for photocatalytic H_2 production from seawater. The average particle diameters of the embedded photoactive species (Ni and ZnO) in the carbon-shell are in the range of 7–23 nm. The collision frequency between water and photoactive sites is also highly increased within the confined space in the nanoreactors. The photocatalytic splitting of seawater promoted by the nanoreactors has a 5.01 mmol/h gcat yield of H_2.

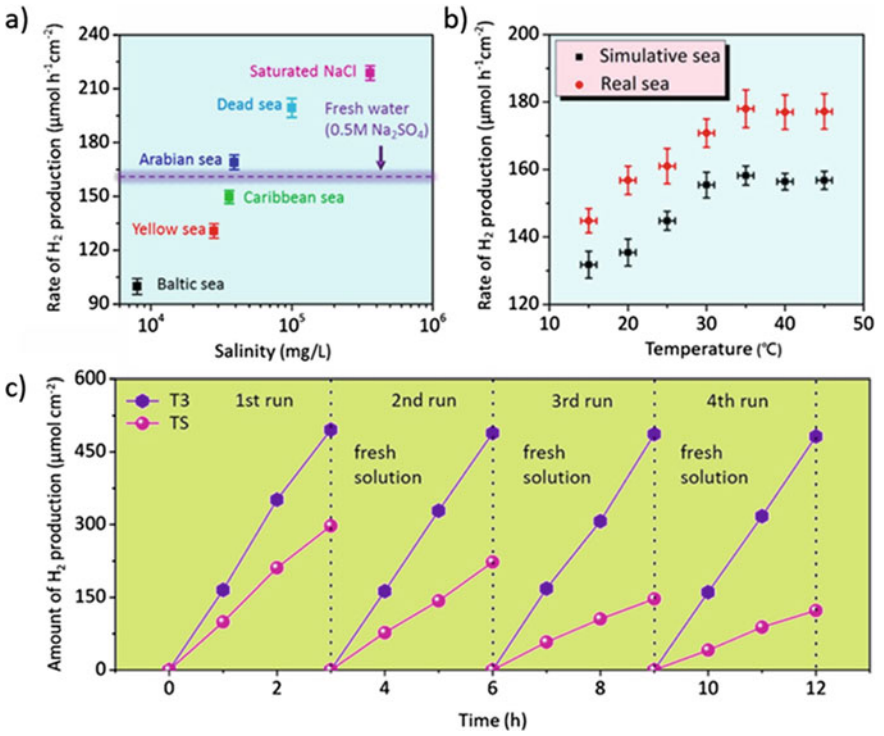

Fig. 21 H_2 production rate in **a** different concentrations of seawater and **b** simulated and natural seawater at different temperatures. **c** Cycling test of H_2 production of T3 and TS in natural seawater

Mu-Hsiang Hsu et al. [187] have developed the Ce-doped ZnO/ZnS photocatalyst. The results of XPS Ce 3d spectra indicate that a mixed valence state (Ce^{3+} and Ce^{4+}) is present in the photocatalysts. The activity for optimized Ce-doped ZnO/ZnS photocatalyst in an aqueous NaCl solution containing electron donors (Na_2S and Na_2SO_3) (1200 μmol/g/h) is 5.2 times as high as that of undoped ZnO/ZnS photocatalyst. The improved activity using Ce doping originates from empty or half-filled Ce4f electron configurations which make the redox cycle between Ce^{3+} and Ce^{4+} rapid and repeatable. The recycled photocatalyst has only a limited activity loss, with the H_2 production rate for the fourth cycle being 85% of the first.

Kang et al. [31] report the results of studies of a CDs-CdS photocatalyst, comprised of cadmium sulfide (CdS) cocatalyst and carbon dots (CDs) as cocatalyst. A series of CDs/CdS composites were observed to be efficient hydrogen production photocatalysts in both water and seawater. Four typical morphologies of CDs/CdS composites have been successfully synthesized with different sulfur sources and solvents. As shown in Fig. 22a, CDs/CdS composites were rod-like CDs/CdS-R with a diameter from 50 to 60 nm, CDs/CdS-S nanosheets with thin layers (Fig. 22b), CDs/CdS nanospheres with uniform size (diameter around 60 nm) and distribution with vesicle-like structure (Fig. 22c), and irregular large bulk CDs/CdS-I composites not having a

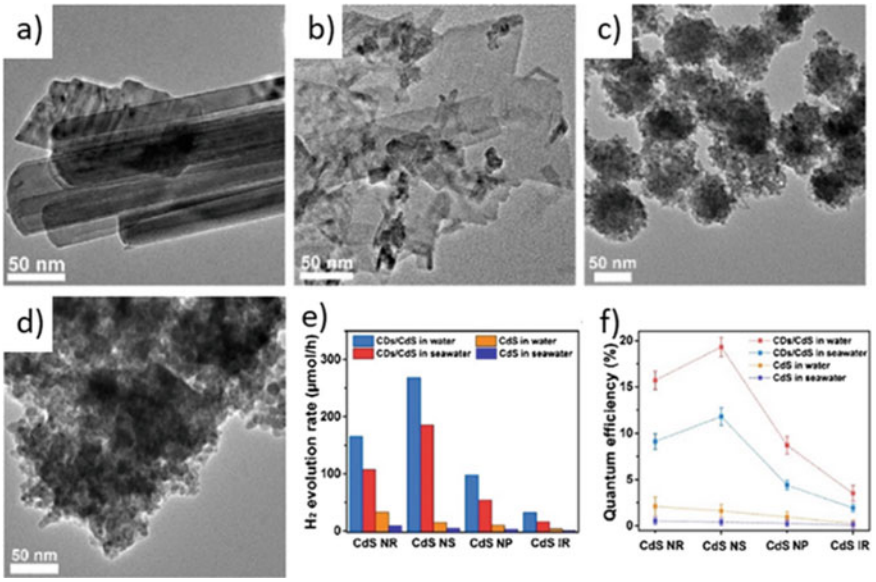

Fig. 22 **a**–**d** TEM images of different samples. **e** Photocatalytic performance of different samples in water and seawater. **f** AQE tests for different samples

characteristic morphological structure (Fig. 22d). The introduction of CDs into CdS nanocrystals remarkably enhances photocatalytic activity. Figure 25e shows that the composite photocatalysts have photocatalytic activity in seawater, corresponding to 65%, 70%, 55%, and 50% of those in water, respectively. On the contrary, CdS not loaded with CDs exhibits low activity, which is even lower in seawater (30% of that in water). The AQY values under optimal conditions with irradiation at 420 nm are 15.7%, 19.3%, 8.7%, and 3.5% for CDs/CdS-R, CDs/CdS-S, CDs/CdS-N, and CDs/CdS-I, respectively. In contrast, a AQY value of 2.1% is obtained using CdS-R, which is lower that the lowest value for CDs/CdS-I. In seawater, CDs/CdS composites maintain about 50–60% of their AQYs in water with the highest value being 11.8% for CDs/CdS-S. Additionally, the highest AQY value in seawater for CdS is only 0.53% while the lowest is 0.07%.

4 Industrialization

4.1 Introduction

Global energy consumption has increased by about 1.7% annually over the past 10 years and reached 17.9 TW (terawatts) in 2017, a value that is estimated to increase to 22 TW by 2030. About 80% of the energy consumption relies on fossil fuels during

the period of transition, and carbon dioxide emissions should also increase over the next several decades. In the early 1970s, Fujishima and Honda reported the results of a study of photochemical water oxidation on a TiO_2 photoanode. Although an electrical or chemical bias was necessary to drive the process, this phenomenon now known as the Honda-Fujishima effect laid the foundation for using semiconducting materials in the thermodynamically uphill water splitting reaction to convert light into chemical and storable energy. Photocatalytic hydrogen production is among a group of catalytic processes that could potentially address the above challenges, and it can contribute to the realization of sustainable societies. However, many obstacles exist in developing a practical and renewable solar-driven H_2 production technology. An economic analysis of solar H_2 production by the U.S. Department of Energy estimated that a photocatalytic system with an STH efficiency of 5% would produce H_2 at a cost of \$2.30 kg^{-1}. Recent progress shows that achieving the goal of attaining a 5% STH efficiency for photocatalytic H_2 production is not far off. The results obtained thus far suggest that the photocatalysis approach is a promising strategy for large-scale solar H_2 production because the reactor designed for this purpose is easily scaled up. However, a major issue still to be considered is the need to separate H_2 and O_2 from the explosive product gas mixture [188].

In this chapter, we introduce the economic cost and practical value of photocatalytic hydrogen industrialization and briefly summarize the design of large-scale synthesis and catalytic systems for photocatalysts and explore their cost competitiveness.

4.2 Economical Costs versus Practical Value

The United States Department of Energy (US DOE) had estimated that the maximum cost of hydrogen in 2020 of US\$ 2–4 kg^{-1} would make this gas an economically viable fuel [189]. The cost of photoelectrochemical hydrogen production was predicted to be US\$ 5.7 kg^{-1} in 2020 and to decrease to US\$2.1 kg^{-1} in the more distant future based on market competition. In 2013, Pinaud et al. conducted a techno-economic analysis of the cost of producing hydrogen using various photocatalytic and photoelectrochemical systems (Fig. 23) [190]. Based on assumptions of the STH values of 10% and 5% and a common lifetime of five years, the analysis estimated that the cost would be US\$1.6 and US\$3.2 kg^{-1} for respective single and dual bed particle suspension systems. Using assumed STH values of 10% and 15% and a lifetime of 10 years, hydrogen generated using photoelectrochemical systems with fixed planar and tracking concentrator arrays was predicted to cost US\$10.4 and US\$4.0 kg^{-1}, respectively. Because suspended photocatalyst systems containing simple plastic bag reactors are expected to have lower capital costs than photoelectrochemical systems, the cost of their implementation could meet the target hydrogen price of US\$2–4 kg^{-1} suggested by the US DOE. If significant improvements are made in STH efficiencies and cell lifetimes, it might be possible to utilize additional energy and material inputs and still maintain costs in the target region.

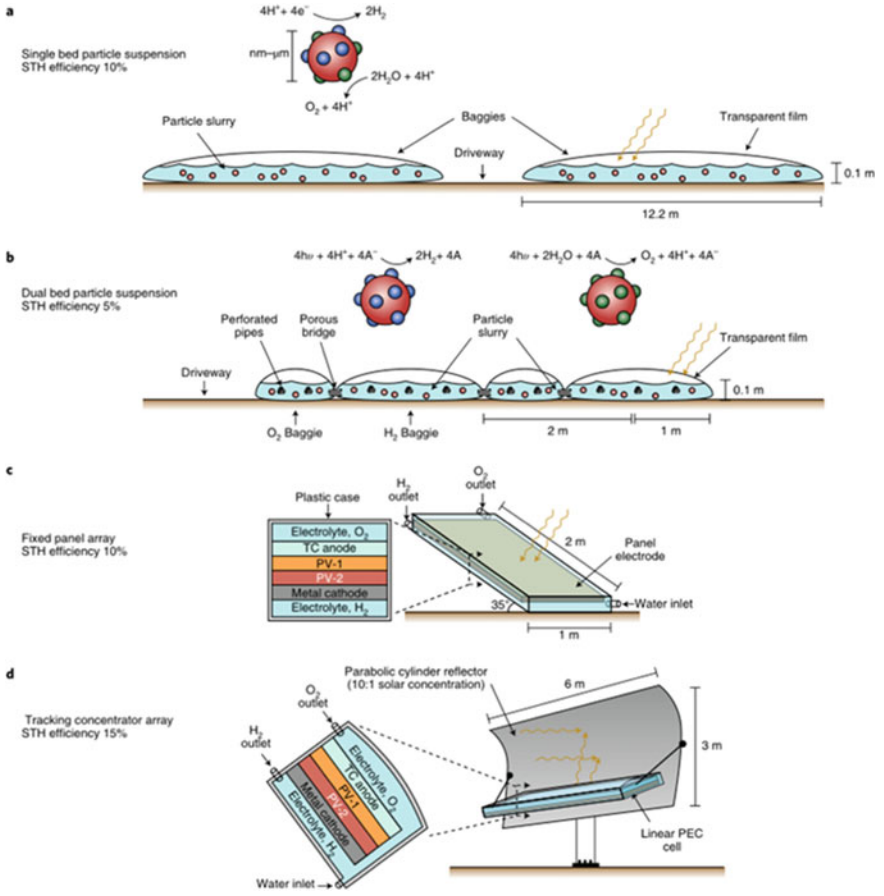

Fig. 23 Four different types of reactors. **a** Single bed type, **b** dual bed type, **c** fixed panel array type, and **d** tracking concentrator array type

In earlier evaluations, the cost of solar hydrogen production was estimated by assessing the capital and operating costs of the systems [190]. However, the allowable cost can also be estimated using the resulting hydrogen and oxygen products as metrics [191]. Fig. 24 gives an overview of a blueprint of photocatalytic H_2 production plant with an area of 100 m * 100 m. In this setup, 228 kg of hydrogen is produced and 2 tons of water is consumed daily. Assuming an STH efficiency of 10%, daily AM1.5 G irradiation for 7.6 h (corresponding to 317 W m^{-2}), a lifetime of 10 years, and an annual depreciation rate of 4%. Using this approach, the cost of the system was calculated to be US$136 m^{-2}, and the respective prices of H_2 and O_2 would be US$3.5 kg^{-1} and US$0.1 kg^{-1}. However, solar irradiance is typically 240 W m^{-2} at most, [190]. So the accurate cost would be US$102 m^{-2}. It is estimated that the balance of system expenses alone will exceed the target [192]. Thus, a significant

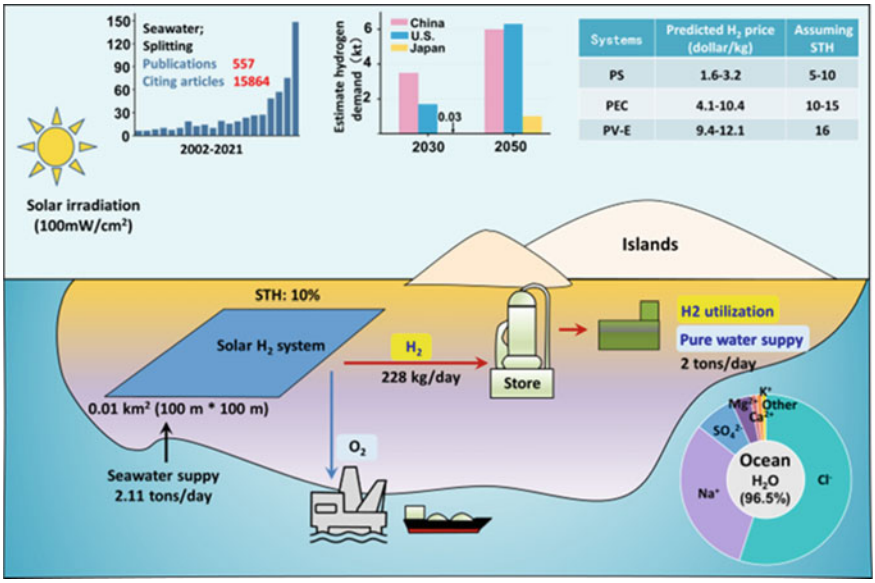

Fig. 24 A proposed scheme for large-scale H_2 production via solar seawater splitting

need exists for developing new materials and techniques for photocatalytic systems for hydrogen generation.

Before solar hydrogen take the place of fossil fuels, many hurdles facing solar photochemical water splitting must be overcome. To make solar hydrogen a feasible fuel, the design principle of photocatalytic systems must be coupled with uncovering low-cost, stable, and efficient materials. Specifically, the ultimate goal is to reach >10% efficiency, >10 years of stability, and a hydrogen cost that is competitive on an energy equivalent basis with those of fossil fuels.

In 2020, Domen et al. [193] reported the development of a 100-m^2 scale prototype solar hydrogen production system consisting of an array of 1,600 reactor units composed of mass-produced $SrTiO_3$:Al as the photocatalyst and loaded with Rh, Cr, and Co as cocatalysts. The photocatalyst was fabricated as individual units with the light receiving areas of 625 cm^2, and gaps between the ultraviolet-transparent glass windows and photocatalyst sheets adjusted to 0.1 mm (Fig. 25a, b) to minimize the water load and prevent accumulation and ignition of the product gases. A 100-m^2 water splitting photocatalyst panel array, consisting of $33\frac{1}{3}$ modules of 3 m^2 each, is shown in Fig. 28c. The entire hydrogen production system operated under field conditions for more than a year reached a maximum STH of 0.76% under natural sunlight.

It should be noted that economically large-scale H_2 production by water splitting, let alone seawater splitting, using photocatalysis is still a challenge. Observations made by Domen and colleagues should inspire and encourage other researchers.

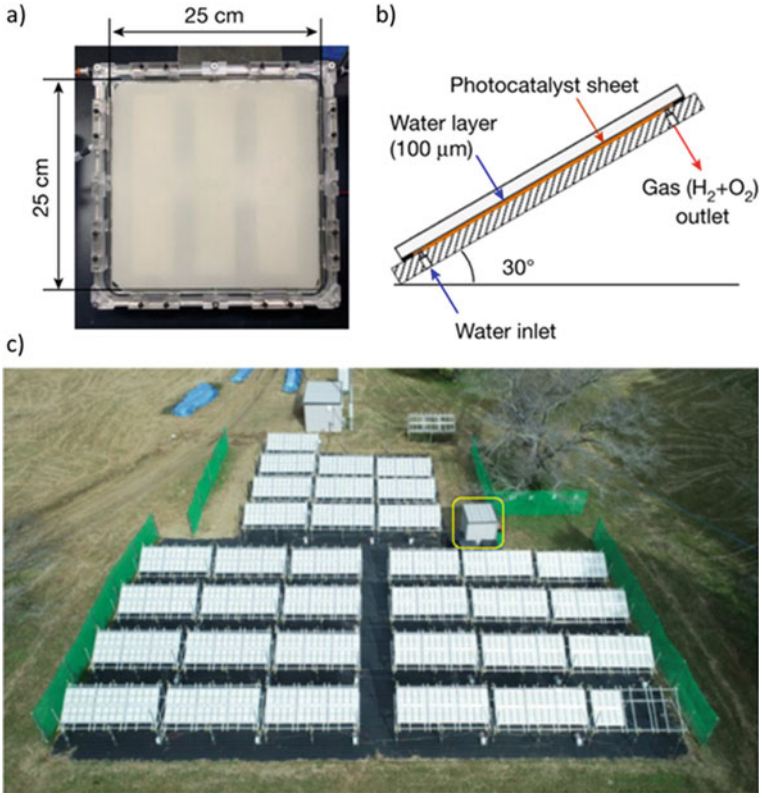

Fig. 25 A 100-m^2 solar panel reactor for H_2 production. **a** A picture of a panel photoreactor unit. **b** Side view of the panel reactor unit. **c** An 100-m^2 solar hydrogen production system

Their results indicate the timescale needed for developing a successful system for the production of hydrogen.

4.3 Large-Scale Synthesis of Photocatalysts

4.3.1 Large-Scale Batch Synthesis

To date, batch-wise wet chemical processing has remained the dominant method for laboratory synthesis of photocatalysts. This approach requires minimal investment in equipment and is supported by extensive knowledge available in the literature. The self-contained apparatus also contained components for reagent storage, product separation, and waste gas treatment (Fig. 26). Importantly, the produced nanocrystals are separated using ultrafiltration, which requires a lower energy input

than centrifugation. The catalyst generated in this manner has an energy conversion efficiency of up to 4.3% and an AQY of 40.5% at 425 nm, which is nearly equal to the activity of a similar catalyst synthesized in a 130-fold smaller batch. However, the particle size distribution and catalytic activity are noticeably worse than those obtained using a twofold diluted, laboratory-scale synthesis system that does not require stirring [194]. This observation highlights the difficulty associated with the scale-up of process employed for nanomaterials synthesis using batch-wise wet chemical systems.

Besides increasing the batch size, improving the throughput of batch-wise synthesis is an alternative route, for example, shortening the processing time or increasing the reaction temperature. Completion of reactions, required to obtain reasonable yields, can be achieved by using more efficient heating methods such as microwave heating. For example, α-Fe_2O_3 particles with an average size of 200 nm have been fabricated in a 5 L microwave-heated hydrothermal reactor, and the production rate is claimed to be comparable to 2.1 m^3 conventional reactors [195]. Many photocatalysts have been prepared by using similar methods where the required reaction time, typically a few minutes to hours, is an order of magnitude lower than those utilizing conventional hydrothermal methods [196]. However, the photocatalysts that are synthesized using microwave-assisted methods have not yet exceeded the gram scale in laboratory research, mainly because of the limited penetration of 2.45 GHz microwaves [197].

Lasers and direct currents have also been used for efficient heat delivery. In the former method, optical energy is converted to heat that melts/vaporizes a starting

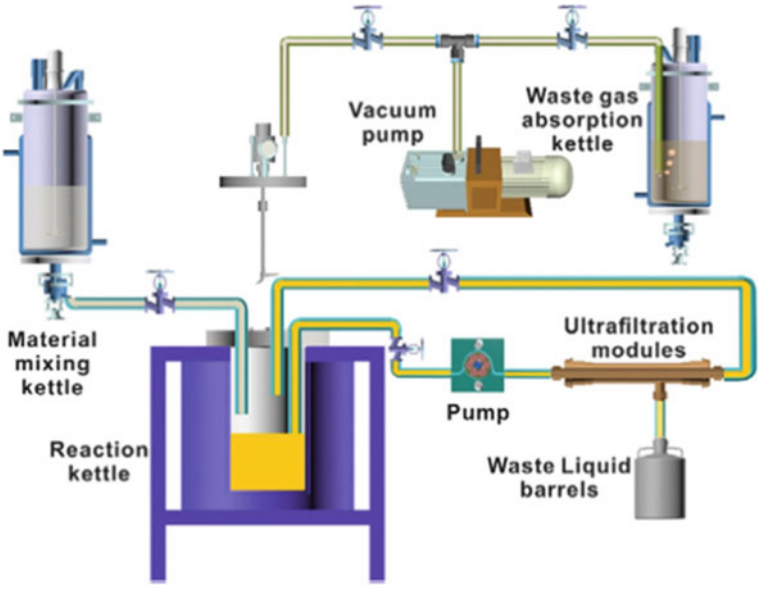

Fig. 26 Schematic diagram of a pilot plant in large-scale batch hydrothermal synthesis mode

material, which is then transferred to the reaction medium [198]. Similar to lasers, high voltages applied to solid–liquid interfaces generate localized heating through plasma discharge. This method has been employed in the one-step synthesis of TiO_2-x [199, 200], which is promoted by applying high voltage pulses to Ti electrodes immersed in NH_4NO_3 or HNO_3 electrolyte. It was suggested that metallic Ti melted/vaporized by the plasma at the cathode transfers heat to the electrolyte while being partially oxidized. In both of these heating methods, the amount of materials converted to heat by each laser/electrical pulse is microscopic, but production of the extreme temperatures occurs within 1 ms. As most of the input energy is delivered to the solid–liquid interface instead of the bulk mixture, these methods are energy-efficient and, hence, they have the potential for scale-up provided that low-cost processes exist for economic processes for product recovery.

Solid-state synthesis uses much higher precursor concentrations and hence it makes more efficient use of reactor volumes than wet chemistry. Due to sluggish diffusion and interaction between solid precursors, which necessitates the use of high temperatures for acceptable reaction rates, these processes are slow, energy-intensive, and accompanied by severe sintering. The high temperatures facilitate the removal of structural defects from the semiconductor crystals and improve carrier diffusion lengths. The negative effects of small surface areas can be compensated for by an increase in the number of charge carriers reaching catalytic sites. Furthermore, this method, which is applicable for industrial-level production, has a close to 100% yield based on the metal. Despite the fact that throughputs employed in research laboratories are limited to several grams, solid-state synthesis has great potential for use in the production of photocatalysts on large scales.

Similar to using wet chemical methods, solid-state synthesis of photocatalysts has also taken advantage of microwave heating. However, heating efficiency depends on the properties of the materials being processed, and it is modulated by the copious amount of solvent present in wet chemical but not solid-state synthesis systems. Microwave heating in solid-state mixtures is therefore non-uniform due to inhomogeneity. The strong microwave absorber CuO has been used as a medium to deliver heat to a reaction mixture. Although the uniformity of heating is affected, the reaction time is reduced to 18 min from the 3–4 h required using conventional heating. The product generated in this manner has a 50% improved PCWS activity compared with that using g-C_3N_4 synthesized in a furnace, because it has higher crystallinity.

A solid phase reaction can not only be accelerated using efficient heating but also by a flux which forms a melt that acts like a solvent to promote local diffusion of reactants. Recently, this method has been improved by increasing the amount of flux so that a significant fraction if not all of the precursors are in the solution phase during the reaction [201]. The resulting molten salt process enables the controllable formation of nanocrystals because crystal nucleation and growth occur more uniformly than in conventional solid-state synthesis systems. In this sense, this process parallels wet chemical synthesis with the exception of having significantly higher reactant concentrations. For example, Sr-doped $NaTaO_3$ nanocubes with sizes of 20–60 nm have been synthesized in molten NaCl–KCl and the material generated has remarkable overall water splitting activity under UV radiation [202].

4.3.2 Large-Scale Continuous Synthesis

Batch-wise synthesis requires that reactors be evacuated and recharged which leads to long down-times and batch-to-batch variations caused by non-linear heat/mass transport, particularly when using wet chemical processes. As a result, the use of continuous processes is preferred for industrial-level production. Considerable studies have been conducted since the 1990s on continuous hydrothermal flow synthesis (CHFS) of inorganic nanomaterials [203]. In contrast to laboratory-scale batch synthesis where the reaction mixture is usually heated for several hours at temperatures up to 200 °C, industrial-level production usually utilizes temperatures of 200–400 °C, thus, reducing the required residence time to a few seconds or minutes. In order to achieve these high temperatures in an even smaller timescale before the product formation starts, precursor solutions are often heated by direct mixing with supercritical water. Using this approach, small sizes of metal oxide, hydroxide, sulfide, and phosphate nanoparticles (less than 100 nm) have achieved a kg h^{-1} scale. Figure 27 contains a schematic diagram of a representative CHFS system.

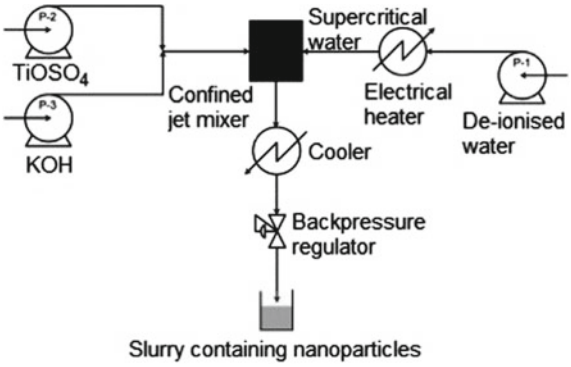

Fig. 27 Schematic diagram of a CHFS system

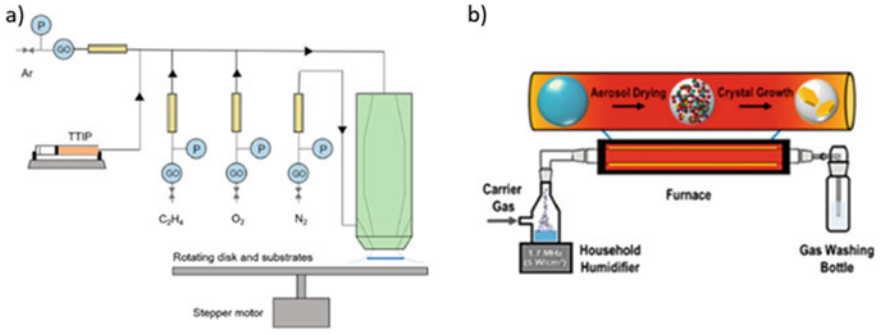

Fig. 28 **a** Schematic diagram of vapor-fed flat flame aerosol synthesis. **b** Schematic diagram of a ultrasonic spray pyrolysis process

While many photocatalytically active materials including TiO_2, α-Fe_2O_3, CdS, ZnO, and WO_3 have been prepared by this method, [204] research works on their PCWS activity have been extensively reported. Makwana et al. synthesized anatase TiO_2 with $TiOSO_4$ and KOH, and the fabricated sample has tunable sizes of 5–18 nm and displayed high PCWS activity. More recently, a 5 nm Ti^{3+}-doped TiO_2/C composite was synthesized on a small scale using 45 mmol h^{-1} throughput of the Ti precursor [205]. The composite has a higher hydrogen evolution activity than that of commercial TiO_2. In an earlier study, a similar activity was achieved by employing $K_2Ti_6O_{13}$ nanofibers. This material was synthesized using a residence time of ~2 s and a production rate of 0.3 g h^{-1}. Notably, the throughput of CHFS still has a bottleneck associated with time-consuming product separation.

Although not used often in chemistry, gas-phase synthesis is by far the most useful method for industrial production. For example, carbon black, fumed silica, and the commercial P25 et al. are fabricated using a type of gas-phase process called flame aerosol synthesis (FAS), which was first commercialized in the 1940s. In FAS, precursors and supporting fuels in the forms of either vapors or atomized liquids are introduced continuously into a flame, where they undergo pyrolysis to form nanoparticles along with exhaust gases which can be recovered by using cyclone separators or filters.

Wu et al. [206] reported that a methanol solution of a FAS-derived 10–20 nm TiO_2 photocatalyst promotes photocatalytic H_2 evolution with a AQY of 39.4% at 360 nm. TiO_2 was synthesized by feeding vaporized titanium(IV) tetraisopropoxide along with ethylene, oxygen, and argon into a flat flame on the surface of a rotating collection disk (Fig. 28a). Fast quenching of metastable intermediates before rutile crystallization leads a TiO_2 II phase during this process [207]. A flame is not the only heat source that can be used for the gas-phase synthesis of nanomaterials. As depicted in Fig. 28b, the so-called ultrasonic spray pyrolysis process, in which a conventional tube furnace is used to continuously dry and pyrolyze fine droplets of precursor solution without combustion, can also be employed for this purpose. Compared with FAS, ultrasonic spray pyrolysis does not involve rapid heating of precursors, which causes incomplete vaporization of droplets before a significant amount of product forms. The resulting particles in the form of polycrystalline aggregates retain the shape of the precursor droplets. It has been noted that despite the large potential of using gas-phase nanomaterial synthesis at commercial levels, short residence times of particles prevent the healing of structural defects which compromises photocatalytic activity [208]. Thus, to achieve desirable results, this approach could be used in combination with an annealing or wet chemical step. In addition, how species adsorbed on nanoparticles affect morphological control during FAS is poorly understood.

4.4 System Design

4.4.1 Reactors Design

Conventionally, laboratory-scale PCWS use suspensions of particulate photocatalysts in flask-type reactors. However, the difficulty in the scale-up of suspension systems might be reflected in the absence of large-scale demonstrations with appreciable STH values. This approach has difficulties on large scales for several reasons. Firstly, considering the larger volumes of water required, minimizing of reactor costs is still challenging. For example, a 1 cm depth of water in a reactor has a mass that reaches 10 kg m^{-2}. Thus, large-scale use of these types of reactors is not feasible considering that the target cost for the entire system needs to be US$102 m^{-2} [209]. Secondly, sedimentation of particulate photocatalysts in the reactor leads to an insufficient irradiation unless stirring is used. Tubular reactors coupled with compound parabolic concentrators (CPC) have been examined for large-scale outdoor operation of PCWS reactions using sacrificial reagents. [210] No daily light tracking is required when CPCs are utilized. In a system developed by Jing et al., the CPC has a maximum half incident angle of 14°, aperture length of 0.4 m, and total length of 1.5 m, along with 1.6 m long Pyrex glass reactor tubes. This configuration has a concentration factor of four. Thirdly, recovering suspended catalytic powder using filtration or centrifugation is energy- and time-consuming. Processes associated with spent photocatalyst replacement would be simpler considering the large footprints of PCWS systems. Because fixed particulate photocatalysts address these problems, it has been suggested that photocatalysts should be generated as planar panel modules such as those used in photovoltaic systems.

Water splitting systems using photocatalyst powders thinly fixed on substrates have been described in several recent publications [211, 212]. It is possible to fix particulate photocatalysts onto substrates by using drop-cast methods along with silica binders. Controlling the hydrophilicity and porosity of these layers is important to preserve the intrinsic activities of particulate photocatalysts fixed to substrates. For example, photocatalyst particles fixed on glass substrates exhibit lower activities than suspensions of the same materials [137, 211]. This activity retardation is caused by the inefficiency of penetration of water and desorption of gaseous products from the dense particulate photocatalyst layer. Hydrophilic silica particles accelerate water splitting promoted by photocatalyst panels because they create voids in the particles and, thus, promote the diffusion of substances in solutions and product gas bubbles. The properties of Z-scheme-type sheets of OER and HER photocatalysts fixed on conductive materials have been reviewed recently [213–215]. The size of the photocatalyst sheet can be scaled up without special consideration being given to electron and mass transfer between the OER and HER photocatalysts.

In 2015, Schröder et al. [212] described a 0.76 m^2 flat panel-type reactor employing a C_3N_4 photocatalyst and triethanolamine as a sacrificial electron donor. The reactor contained a reactor body composed of an etched Teflon plate (6 mm in depth), exchangeable stainless-steel plates coated with the photocatalyst using a

Nafion binder, a plexiglass window (8 mm in thickness), a reaction solution reservoir (10 vol% aqueous triethanolamine), and a pump for circulation (Fig. 29). The photocatalytic H_2 production rate has decreased by 40% after continuous operation over 30 d. Unfortunately, the STH efficiency of this device was not correctly calculated due to the participation of the sacrificial reagent. In fact, a majority of the energy stored as hydrogen in this system originates from the chemical energy of the sacrificial reagent and not from the solar energy harvested by photocatalysis.

K. Domen et al. [137] has reported panel-type reactors intended for large-scale via highly active $SrTiO_3$:Al photocatalyst sheets. $SrTiO_3$:Al has an absorption edge of 390 nm and a wide band gap of 3.2 eV. In a scaled-up system, $SrTiO_3$:Al materials were fabricated by depositing the $SrTiO_3$:Al photocatalyst on frosted glass plates. The plates were immersed in a laboratory-scale panel-type reactor filled with water. Under UV light illumination over the entire plate, the rate of hydrogen and oxygen evolution was tested to reach 5.6 mL cm^{-2} h^{-1}. During the process, small bubbles of hydrogen and oxygen migrate upward due to the buoyant force without forced convection. The STH of the water splitting reaction reaches 10%, while producing a mixture of hydrogen and oxygen at a rate of 5.6 mL cm^{-2} h^{-1}. In addition, they constructed 1 m^2 panel reactors by using plexiglass plates for the body and window, and 8 g m^{-2} $SrTiO_3$:Al sheets and distilled water were loaded into the device (Fig. 30). The STH efficiency of this reactor for non-sacrificial solar-driven water splitting under natural

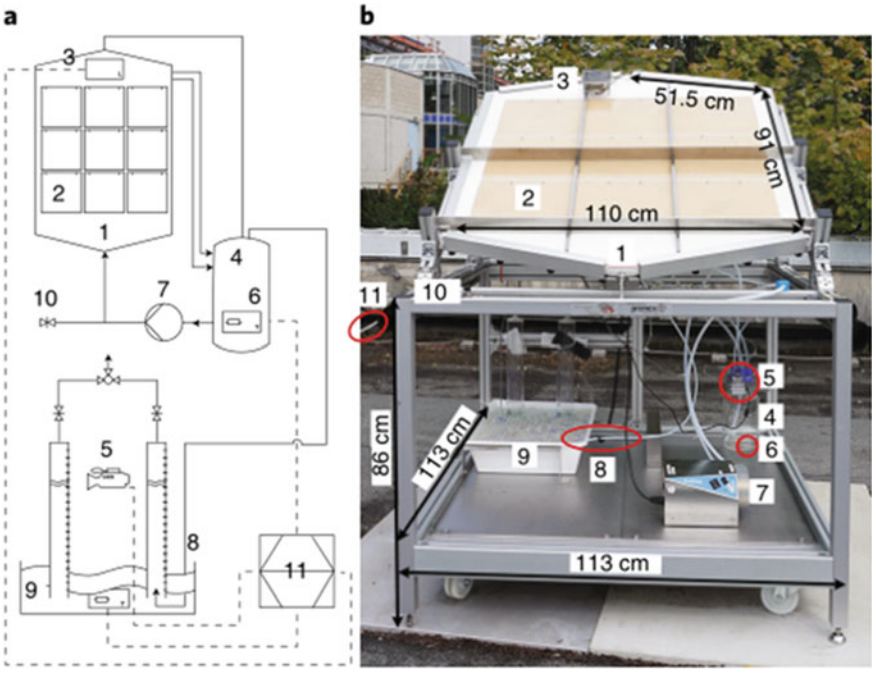

Fig. 29 **a** Schematic diagram and **b** photograph of large-scale photoreactor

sunlight was estimated to be 0.4%. This value is very close to that obtained during laboratory-scale experiments. The results suggest that a panel-type reactor with an area greater than 1 m^2 could obtain STH of 10% under AM1.5 G irradiation without using forced convection.

One of the critical issues that needs to be considered in creating scaled-up or overall water splitting reactors is the fire/explosion hazard arising from the fact that H_2 and O_2 are generated simultaneously. The produced H_2 could be diluted with an inert gas, for example, N_2 or CO_2, so that its concentration is below the lower flammability limit before being separated by selective permeable membranes [216, 217]. However, considering that hydrogen's lower flammability limit is only 4% (in air/oxygen, at normal temperatures and pressures). However, the large amount of diluent required limits the process.

A shallow funnel-shaped photoreactor without active stirring has a similar STH as that of an ordinary stirred tank photoreactor [218]. In Fig. 31 a, b is shown the reactor in which a slurry is introduced tangentially to induce mixing. Notably, a 44% improvement in AQY was obtained in a more recent study using Pt/TiO_2 catalyst beads in a fluidized bed reactor rather than a recirculating suspension of Pt/TiO_2 nanoparticles [219]. The system also included a sparger downstream of the reactor to extract H_2 and O_2 with an inert gas (Fig. 31c). Efficient mass transfer and fast removal of product gasses are proven to be key factors leading to high AQY because they suppress reverse reactions via a computational modeling [220].

Low-pressure operation on large scales is a burden unless the sacrificial reagent is waste or can be simply regenerated. Specifically, the production of hydrogen as a

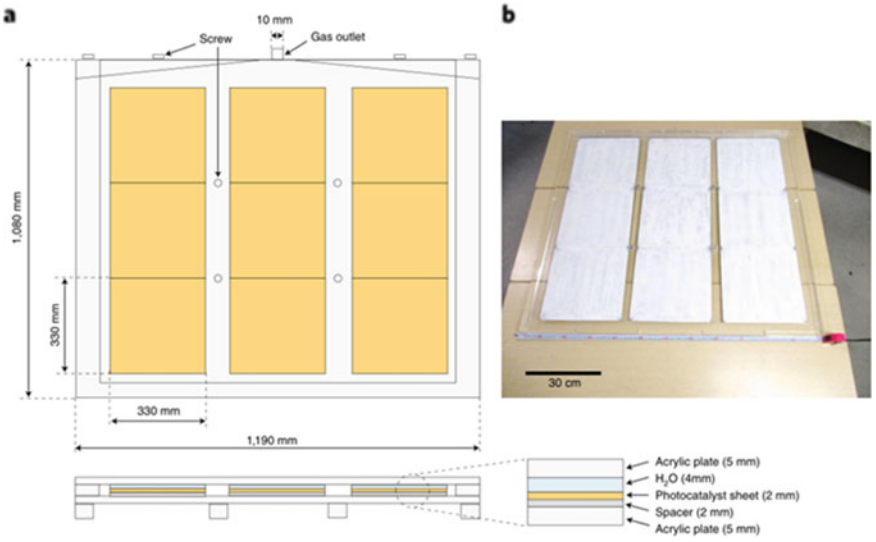

Fig. 30 **a** Schematis of a 1 × 1 m panel-type reactor containing photocatalyst coating sheets and **b** a photograph of a 1 × 1 m panel containing $SrTiO_3$:Al photocatalyst

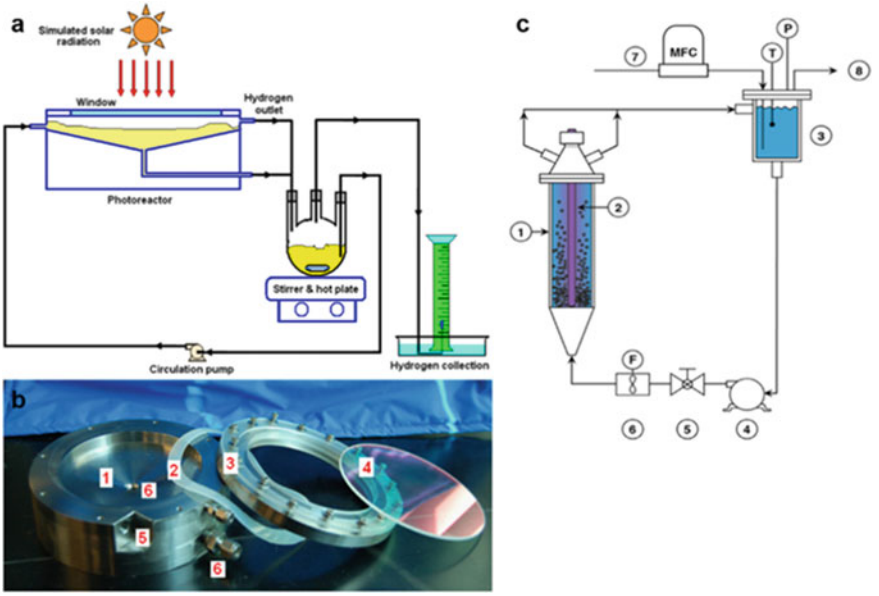

Fig. 31 **a** Schematic diagram of flow photoreactor and **b** a photograph of laboratory-scale flow photoreactor. **c** Schematic diagram of a fluidized bed photoreactor system

basic feedstock at the expense of using downstream chemicals cannot be justified. With this in mind, a hybrid photocatalytic-solar thermal cycle has been devised [221] in which photocatalytic hydrogen production occurs together with the oxidation of aqueous $(NH_4)_2SO_3$ to form $(NH_4)_2SO_4$ by photogenerated holes, which then passes through a metal oxide-assisted multistep solar thermal process to regenerate a more recent study and produce oxygen.

4.4.2 Optical Design

The design of a photoreactor needs to consider the maximum exposure of catalyst particles to solar radiation. The simplest way is comprised of a flat panel-type container (Fig. 32a), which has been proven to be a cost-effective approach to water treatment [222]. However, for water splitting the reactor needs to be sealed with a highly UV transparent cover, which leads to capital cost increases. In typical laboratory studies, quartz glass is employed as the cover. However, the use of this type of glass in large reactors is too costly. While thin borosilicate and soda lime glass have satisfactory transparencies in the UV region, when they are utilized to cover large areas, their thicknesses need to be large to support their weights, which leads to UV transmission decreases. Polymethyl acrylate is commended for use as alternative [218], but its reliability under constant exposure to direct sunlight is questionable.

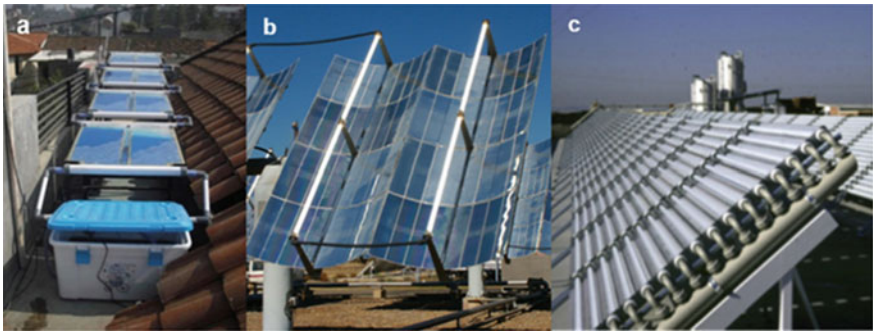

Fig. 32 **a** Flat panel-type photoreactors. **b** Tubular photoreactors with parabolic trough collectors and **c** tubular photoreactors with compound parabolic collectors

Based on the above reasons, tubular glass reactors have become the compromise between transparency and mechanical strength. Moreover, flat panel reactors were employed in recent pilot-scale trials of PCWS as elaborated further in Progress in pilot tests due to its low cost and ease of reactor construction on such scales [211].

To fully utilize the surface area of a tubular reactor, light reflectors have been employed to enable illumination of the underside of the reactor. Originating from solar thermal engineering studies, the old-type reflectors have single parabolic profiles. This configuration, known as a parabolic trough (Fig. 32b), only reflects incident light that is perpendicular to the aperture of the reactor tube at the focal point. Thus, all the diffuse light is not utilized [223]. Compound parabolic collectors (CPCs, Fig. 33a) are now the most of the reflectors used for water splitting devices, which allow some diffuse light to reach the reactor tube (Fig. 32c). Furthermore, a new type of reflector geometry has been developed recently for the improvement of the uniformity of illumination on the tube surface (Fig. 33b) [224].

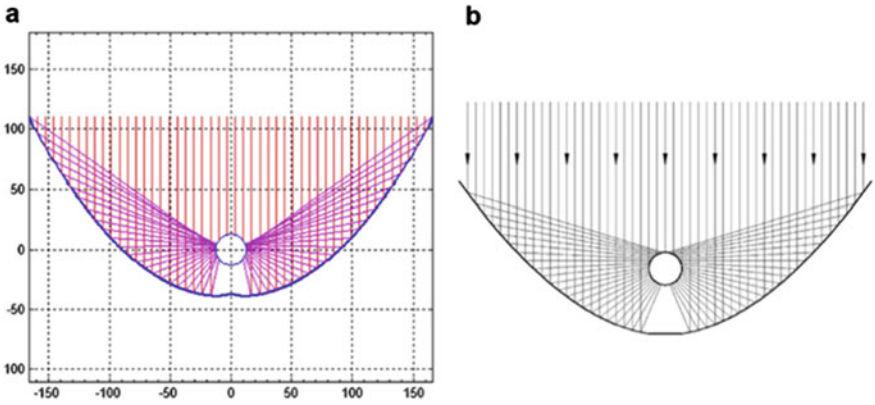

Fig. 33 Schematic diagram of **a** typical parabolic collector and **b** surface illumination uniform collector

4.5 Technology Cost Competitiveness

Unlike in fundamental research where gaining insight into processes that occur is the most important goal, applied technologies depend on profitability. Most of the solar H_2 production technologies discussed in this chapter are at the research stage only. Economic assessments of these approaches are made difficult by the unavailability of key data, which necessitates that coarse assumptions be made. As a consequence, direct comparison between different systems provides little insight into the relative viabilities of hydrogen-generating devices. Nevertheless, rough comparisons can provide perspectives for designing future investigations.

Considering that photovoltaics and water electrolysis are well-established industrial processes, modular PEC water splitting has received the greatest techno-economic study thus far. As shown in Table 1, the levelized cost of hydrogen (LCH), estimated by different authors, varies from 4.7 to over 13 USD kg^{-1}. An important assumption that leads to differences in the estimates is the capacity factor of the electrolyzer unit, i.e., the ratio of the average actual production rate to the design capacity. This factor directly influences the size and hence capital cost of the electrolyzer. To obtain the lowest LCH, an assumption is made that the electrolyzer operates at constant full capacity, which is equal to that designed for hydrogen production [225]. For a model that includes a minimal size electrolysis plant, the capital cost would be less than 15% of the LCH in the case of a PEM electrolyzer, a value similar to that for a grid-powered electrolyzer [226]. One way of estimating the size of an electrolyzer at the upper end of LCHs is to make its capacity equal to the peak power of the photovoltaic plant, in other words to assume that all photovoltaic power is utilized by the electrolyzer [192, 227]. This consideration significantly increases the contribution of the electrolyzer cost to LCH which can be up to 40%. In this design, the electrolyzer capacity is severely underused.

It has been proposed that grid electricity be used as supplemental to photovoltaic power to keep the electrolyzer operating at full capacity [192]. Because at the current time contributions to the grid are dominated by nonrenewable energy sources, a design of this type would have a high carbon footprint, along with estimated LCHs being higher than that of grid-powered electrolysis (6.6 versus 5.9 USD kg^{-1}).

Remarkably low LCHs of 2.1 and 4.2 USD kg^{-1} have been estimated for single semiconductor and Z-scheme PCWS systems, respectively. Both values are within the U. S. Department of Energy target and, thus, they are potentially competitive with hydrogen generation by methane steam reforming having an estimated cost of approximately 1.4 USD kg^{-1} [156, 192]. However, this is an optimistic outlook rather than an estimation based on the current state-of-the-art technologies.

Table 1 Various solar hydrogen production technologies and their economic assessment

Type	Scale	STH or H_2 productivity	LCH(USD kg^{-1})
Reforming	–	–	1.4
Photocatalytic, single semiconductor	$10td^{-1}$	10%	2.1
Oxygenic biophotolysis	$10td^{-1}$	9.2%	3.9
Photocatalytic, Z-scheme	$10td^{-1}$	5%	4.2
Photovoltaic PEM electrolysis	$1td^{-1}$	10.8%	4.7
Integrated PEC, 10× solar concentration, and tracking	$10td^{-1}$	15%	5.3
Anoxic biophotolysis	$10td^{-1}$	5.2%	5.5
Integrated photovoltaic-concentrated solar thermal SOSE	$8MW_{PV}$	–	5.7
Grid-assisted photovoltaic PEM electrolysis	$10td^{-1}$	9.8%	6.6
Integrated photovoltaic-concentrated solar thermal SOSE	$0.4td^{-1}$	9.9%	6.6
Solar thermal hybrid H_2SO_4	$50MW_{th}$ $10.2td^{-1}$	–	6.9
Anoxic biophotolysis by immobilized green algae	$10td^{-1}$	2.25%	7.9
Photovoltaic SOSE	$0.4td^{-1}$	6.3%	8.4
Solar thermal $NiFe_2O_4$	$50MW_{th}$ $11.4td^{-1}$	–	8.6
Integrated PEC, 10× solar concentration, and tracking	$10td^{-1}$	20%	10.0
Photovoltaic electrolysis	–	11.5%	10.0
Photovoltaic electrolysis, 10× solar concentration	–	–	10.1
Integrated PEC, fixed panel	$10td^{-1}$	9.8%	12.3
Photovoltaic SOSE	–	–	12.8
Photovoltaic PEM electrolysis	$10td^{-1}$	9.8%	13.1
Integrated PEC, fixed panel	$10td^{-1}$	10%	13.6
Photo-fermentation	$10td^{-1}$	3.5% (1.5%)	13.6 (18.3)
Solar thermal CeO_2	$90MW_{th}$	13.4%	14.7
Integrated dark/photo-fermentation	$1.3td^{-1}$	0.33 $mmolL^{-1}$ h^{-1}	25.1
Integrated dark/photo-fermentation	$1.4td^{-1}$	0.5 $mmolL^{-1}$ h^{-1}	37.5
Solar thermal $NiFe_2O_4$	$90MW_{th}$	6.4%	43.8

(continued)

Table 1 (continued)

Type	Scale	STH or H_2 productivity	LCH(USD kg^{-1})
Integrated dark/photo-fermentation	$27.1td^{-1}$	$0.21mmolL^{-1}\ h^{-1}$	62.6

5 Perspectives

PCWS has attracted wide interest for the past 50 years and achieved significant improvements reaching solar-to-hydrogen conversion efficiencies η_{STH} of nearly 2% during the last 10 years. Thus, efficiency is one of the many considerations guiding the selection of a solar hydrogen production technology. This technology used in seawater splitting has attracted attention in only the recent 5 years. Among the recent studies on PCSS, TiO_2 is the most widely used semiconductor material, and the stability of the photocatalyst plays a significant role. However, only part of the reported efforts give an evaluation of the stability of the photocatalyst. Different kinds of inorganic salts (NaCl, $MgCl_2$, etc.), organic matter, and microorganisms exist in seawater. As a result, the activities and durabilities of photocatalysts can be lower when used in seawater rather than pure water. For estimating the effects of ions, it is generally believed that Na^+ has a positive effect on photocatalytic water splitting, but the influence of Cl^- remains controversial. Nevertheless, it should be noted that the effects strongly depend on the photocatalysts used.

Although there have been a few reports on the use of electrocatalysis and photoelectrocatalysis for water splitting, photocatalysis has advantages over these approaches that include (1) the design of the photocatalytic device is cheap and easy maintenance, and (2) the reaction does not require additional electrolytes, reducing costs of product separation. Thus, the development of highly efficient PCSS systems for H_2 production is highly desirable.

Compared with PCWS, the development of the PCSS has three significant advantages. Firstly, it not only makes full use of abundant seawater resources, opening up scenes and solving the problem of lack of freshwater, but it also greatly reduces the cost and avoids the desalination process, which is more in line with actual application requirements. Secondly, the inorganic salts and other impurities may improve the efficiency of PCWS in some systems. Finally, other high-value-added by-products such as ClO^- can be produced.

Several questions should be posed at the outset of studies of photocatalytic seawater splitting. One concerns possible approaches that can be taken to decrease structural defects, lower surface reaction barriers, and control particle morphology in order to utilize as many photoexcited carriers as possible in narrow band gap photocatalysts. Next, how can backward reactions be suppressed while separating the H_2 and O_2 products in overall water splitting systems? Also, how can water splitting devices be scaled up for practical applications without significant decreases in performance? Minimization of the negative effects of electron mediators used in PCSS needs to be considered. Finally, the question of how visible light-responses

photocatalysts can be stabilized and verified during the water splitting process needs to be addressed.

6 Conclusion

In this chapter, we highlighted recent progress made in studies of PCWS, with the goal of inspiring future efforts in this important field. The development and utilization of sustainable and clean solar energy is the goal of investigations aimed at solving the intertwined energy and environmental dilemma.

Firstly, a brief introduction was given to describe the conceptual basis of PCSS and PCWS, including evaluation parameters such as IQY, AQY, STH, and TON, and the effects of salt, sacrificial agents, cocatalysts, and light sources.

Secondly, we provided a brief introduction to the extensively studied materials for PCSS, ranging from their structures, defects, and optical and electronic properties. Major challenges still exist in many areas, including optimization of the photocatalytic materials and the overall systems. Developing long-wavelength-responsive photocatalysts are beneficial to achieve high STH efficiencies. Inhibiting back reactions of hydrogen and oxygen by applying coating layers to cocatalysts and photocatalysts can further improve efficiencies. Developing more visible light-responsive photocatalysts for use in seawater splitting is the most important task for enabling large-scale H_2 production by using photocatalysis technology.

Finally, it is important to design new water splitting devices for the development of practical systems. Particulate Photocatalysts are proven to be easily scaled up at low cost, but they have critical disadvantages. These include challenges associated with constructing inexpensive large-size reactors, maintaining suspensions over large areas using pumping and stirring, and reclaiming used photocatalysts from the system. Essentially, a combination of highly efficient photocatalysts, inexpensive scalable devices, and innovative technologies for the construction and operation of large-scale photocatalytic plants is required to realize a future sustainable energy source based on hydrogen.

References

1. Linsebigler AL, Lu G, Yates JT (1995) Photocatalysis on TiO_2 surfaces: principles, mechanisms, and selected results. Chem Rev 95:735–758
2. Cao S, Wang CJ, Fu WF, Chen Y (2017) Metal phosphides as co-catalysts for photocatalytic and photoelectrocatalytic water splitting. Chemsuschem 10:4306–4323
3. Cao S, Chen Y, Wang CJ, Lv XJ, Fu WF (2015) Spectacular photocatalytic hydrogen evolution using metal-phosphide/CdS hybrid catalysts under sunlight irradiation. Chem Commun (Camb) 51:8708–8711

4. Fabian DM, Hu S, Singh N, Houle FA, Hisatomi T, Domen K, Osterloh FE, Ardo S (2015) Particle suspension reactors and materials for solar-driven water splitting. Energy Environ Sci 8:2825–2850
5. Serpone N (1997) Relative photonic efficiencies and quantum yields in heterogeneous photocatalysis. J. Photochem Photobiol A 104:1–12
6. Kuhn HJ, Braslavsky SE, Schmidt R (2004) Chemical actinometry (IUPAC Technical Report). Pure Appl Chem 76:2105–2146
7. Buriak JM, Jones CW, Kamat PV, Schanze KS, Schatz GC, Scholes GD, Weiss PS (2016) Virtual issue on best practices for reporting the properties of materials and devices. Chem Mater 28:3525–3526
8. Kisch H (2010) On the problem of comparing rates or apparent quantum yields in heterogeneous photocatalysis. Angew Chem 122:9782–9783
9. Wang Z, Li C, Domen K (2019) Recent developments in heterogeneous photocatalysts for solar-driven overall water splitting. Chem Soc Rev 48:2109–2125
10. Bolton JR (1996) Solar photoproduction of hydrogen: a review. Sol Energy 57:37–50
11. Hwang DW, Kim HG, Kim J, Cha KY, Kim YG, Lee JS (2000) Photocatalytic water splitting over highly donor-doped (110) layered perovskites. J Catal 193:40–48
12. Cao S, Piao L (2020) Considerations for a more accurate evaluation method for photocatalytic water splitting. Angew Chem Int Ed Engl 59:18312–18320
13. Qureshi M, Takanabe K (2017) Insights on measuring and reporting heterogeneous photocatalysis: efficiency definitions and setup examples. Chem Mater 29:158–167
14. Chen S, Takata T, Domen K (2017) Particulate photocatalysts for overall water splitting. Nat Rev Mater 2:1–17
15. Wang Z, Hisatomi T, Li R, Sayama K, Liu G, Domen K, Li C, Wang L (2021) Efficiency accreditation and testing protocols for particulate photocatalysts toward solar fuel production. Joule 5:344–359
16. Liu G, Sheng Y, Ager JW, Kraft M, Xu R (2019) Research advances towards large-scale solar hydrogen production from water. EnergyChem 1
17. Takanabe K (2017) Photocatalytic water splitting: quantitative approaches toward photocatalyst by design. ACS Catal 7:8006–8022
18. Bolton JR, Strickler SJ, Connolly JS (1985) Limiting and realizable efficiencies of solar photolysis of water. Nature 316:495–500
19. Seitz LC, Chen Z, Forman AJ, Pinaud BA, Benck JD, Jaramillo TF (2014) Modeling practical performance limits of photoelectrochemical water splitting based on the current state of materials research. Chemsuschem 7:1372–1385
20. Ma Y, Wang X, Jia Y, Chen X, Han H, Li C (2014) Titanium dioxide-based nanomaterials for photocatalytic fuel generations. Chem Rev 114:9987–10043
21. Ham Y, Hisatomi T, Goto Y, Moriya Y, Sakata Y, Yamakata A, Kubota J, Domen K (2016) Flux-mediated doping of $SrTiO_3$ photocatalysts for efficient overall water splitting. J Mater Chem A 4:3027–3033
22. Kato H, Asakura K, Kudo A (2003) Highly efficient water splitting into H_2 and O_2 over lanthanum-doped $NaTaO_3$ photocatalysts with high crystallinity and surface nanostructure. J Am Chem Soc 125:3082–3089
23. Maeda K, Domen K (2010) Solid solution of GaN and ZnO as a stable photocatalyst for overall water splitting under visible light. Chem Mater 22:612–623
24. Ong W-J, Tan L-L, Ng YH, Yong S-T, Chai S-P (2016) Graphitic carbon nitride (g-C_3N_4)-based photocatalysts for artificial photosynthesis and environmental remediation: are we a step closer to achieving sustainability? Chem Rev 116:7159–7329
25. Sayad Y, Kaminski A, Blanc D, Nouiri A, Lemiti M (2009) Determination of diffusion length in photovoltaic crystalline silicon by modelisation of light beam induced current. Superlattices Microstruct 45:393–401
26. Salvador P (1984) Hole diffusion length in n-TiO_2 single crystals and sintered electrodes: photoelectrochemical determination and comparative analysis. J Appl Phys 55:2977–2985

27. Millero FJ, Feistel R, Wright DG, McDougall TJ (2008) The composition of standard seawater and the definition of the reference-composition salinity scale. Deep Sea Res Part I: Ocean Res Pap 55:50–72
28. Li Y, He F, Peng S, Gao D, Lu G, Li S (2011) Effects of electrolyte NaCl on photocatalytic hydrogen evolution in the presence of electron donors over Pt/TiO2. J Mol Catal A: Chem 341:71–76
29. Li Y, He F, Peng S, Lu G, Li S (2011) Photocatalytic H_2 evolution from NaCl saltwater over $ZnS_{1-x-0.5y}O_x(OH)_y$–ZnO under visible light irradiation. Int J Hydrogen Energy 36:10565–10573
30. Song T, Zhang P, Wang T, Ali A, Zeng H (2018) Constructing a novel strategy for controllable synthesis of corrosion resistant Ti^{3+} self-doped titanium–silicon materials with efficient hydrogen evolution activity from simulated seawater. Nanoscale 10:2275–2284
31. Zhu C, Liu Ca, Fu Y, Gao J, Huang H, Liu Y, Kang Z (2019) Construction of CDs/CdS photocatalysts for stable and efficient hydrogen production in water and seawater. Appl Catal B: Environ 242:178–185
32. Gao H, Yan S, Wang J, Zou Z (2014) Ion coordination significantly enhances the photocatalytic activity of graphitic-phase carbon nitride. Dalton Trans 43:8178–8183
33. Li Y, Lu G, Li S (2001) Photocatalytic hydrogen generation and decomposition of oxalic acid over platinized TiO_2. Appl Catal A Gen 214:179–185
34. Gao M, Connor PKN, Ho GW (2016) Plasmonic photothermic directed broadband sunlight harnessing for seawater catalysis and desalination. Energy Environ Sci 9:3151–3160
35. Simamora AJ, Chang F-C, Wang HP, Yang TC, Wei YL, Lin WK (2013) H_2 Fuels from photocatalytic splitting of seawater affected by nano-TiO_2 promoted with CuO and NiO. Int J Photoenergy 2013:419182
36. Ji SM, Jun H, Jang JS, Son HC, Borse PH, Lee JS (2007) Photocatalytic hydrogen production from natural seawater. J Photochem Photobiol A 189:141–144
37. Guan X, Chowdhury FA, Pant N, Guo L, Vayssieres L, Mi Z (2018) Efficient unassisted overall photocatalytic seawater splitting on GaN-based nanowire arrays. J Phys Chem C 122:13797–13802
38. Yang C, Qin J, Rajendran S, Zhang X, Liu R (2018) WS_2 and C-TiO_2 nanorods acting as effective charge separators on g-C_3N_4 to boost visible-light activated hydrogen production from seawater. Chemsuschem 11:4077–4085
39. Kawai T, Sakata T (1979) Hydrogen evolution from water using solid carbon and light energy. Nature 282:283–284
40. Zhang J, Hu W, Cao S, Piao L (2020) Recent progress for hydrogen production by photocatalytic natural or simulated seawater splitting. Nano Res 13:2313–2322
41. Shen S, Guo L (2006) Structural, textural and photocatalytic properties of quantum-sized In_2S_3-sensitized Ti-MCM-41 prepared by ion-exchange and sulfidation methods. J Solid State Chem 179:2629–2635
42. Shen S, Guo L (2008) Growth of quantum-confined CdS nanoparticles inside Ti-MCM-41 as a visible light photocatalyst. Mater Res Bull 43:437–446
43. Koriche N, Bouguelia A, Aider A, Trari M (2005) Photocatalytic hydrogen evolution over delafossite. Int J Hydrogen Energy 30:693–699
44. Saadi S, Bouguelia A, Derbal A, Trari M (2007) Hydrogen photoproduction over new catalyst $CuLaO_2$. J Photochem Photobiol A 187:97–104
45. Boudjemaa A, Bouarab R, Saadi S, Bouguelia A, Trari M (2009) Photoelectrochemical H_2-generation over spinel $FeCr_2O_4$ in X_2-solutions (X_{2-}=S_{2-} and SO_{32-}). Appl Energy 86:1080–1086
46. Hirai T, Nomura Y, Komasawa I (2003) Immobilization of RuS_2 nanoparticles prepared in reverse micellar system onto thiol-modified polystyrene particles and their photocatalytic properties. J Nanopart Res 5:61–67
47. Younsi M, Saadi S, Bouguelia A, Aider A, Trari M (2007) Synthesis and characterization of oxygen-rich delafossite $CuYO_{2+x}$-Application to H_2-photo production. Sol Energy Mater Sol Cells 91:1102–1109

48. Bessekhouad Y, Trari M (2002) Photocatalytic hydrogen production from suspension of spinel powders AMn_2O_4(A=Cu and Zn). Int J Hydrogen Energy 27:357–362
49. Bao N, Shen L, Takata T, Domen K (2008) Self-Templated synthesis of nanoporous CdS nanostructures for highly efficient photocatalytic hydrogen production under visible light. Chem Mater 20:110–117
50. Yan H, Yang J, Ma G, Wu G, Zong X, Lei Z, Shi J, Li C (2009) Visible-light-driven hydrogen production with extremely high quantum efficiency on Pt–PdS/CdS photocatalyst. J Catal 266:165–168
51. Shen S, Guo L, Chen X, Ren F, Mao SS (2010) Effect of Ag_2S on solar-driven photocatalytic hydrogen evolution of nanostructured CdS. Int J Hydrogen Energy 35:7110–7115
52. Koriche N, Bouguelia A, Trari M, Photocatalytic hydrogen production over new oxide $CuLaO_{2.62}$. Int. J. Hydrogen Energy 31:1196–1203
53. Zhang X, Jing D, Guo L (2010) Effects of anions on the photocatalytic H_2 production performance of hydrothermally synthesized Ni-doped $Cd_{0.1}Zn_{0.9}S$ photocatalysts. Int. J. Hydrogen Energy 35:7051–7057
54. Zhang K, Jing D, Chen Q, Guo L (2010) Influence of Sr-doping on the photocatalytic activities of CdS–ZnS solid solution photocatalysts. Int J Hydrogen Energy 35:2048–2057
55. Lu G, Li S (1992) Hydrogen production by H2S photodecomposition on $ZnFe_2O_4$ catalyst. Int J Hydrogen Energy 17:767–770
56. Gurunathan K, Baeg J-O, Lee SM, Subramanian E, Moon S-J, Kong K-J (2008) Visible light active pristine and Fe^{3+} doped $CuGa_2O_4$ spinel photocatalysts for solar hydrogen production. Int J Hydrogen Energy 33:2646–2652
57. Gurunathan K, Baeg J-O, Lee SM, Subramanian E, Moon S-J, Kong K-J (2008) Visible light assisted highly efficient hydrogen production from H_2S decomposition by $CuGaO_2$ and $CuGa_{1-x}In_xO_2$ delafossite oxides bearing nanostructured co-catalysts. Catal Commun 9:395–402
58. Subramanian E, Baeg J-O, Lee SM, Moon S-J, Kong K-J (2008) Dissociation of H_2S under visible light irradiation ($\lambda \geq 420$nm) with $FeGaO_3$ photocatalysts for the production of hydrogen. Int J Hydrogen Energy 33:6586–6594
59. Barbeni M, Pelizzetti E, Borgarello E, Serpone N, Grätzel M, Balducci L, Visca M (1985) Hydrogen from hydrogen sulfide cleavage. Improved efficiencies via modification of semiconductor particulates. Int. J. Hydrogen Energy 10:249–253
60. De GC, Roy AM, Bhattacharya SS (1995) Photocatalytic production of hydrogen and concomitant cleavage of industrial waste hydrogen sulphide. Int J Hydrogen Energy 20:127–131
61. Naman SA, Aliwi SM, Al-Emara K (1986) Hydrogen production from the splitting of H_2S by visible light irradiation of vanadium sulfides dispersion loaded with RuO_2. Int J Hydrogen Energy 11:33–38
62. Linkous CA, Muradov NZ, Ramser SN (1995) Consideration of reactor design for solar hydrogen production from hydrogen sulfide using semiconductor particulates. Int J Hydrogen Energy 20:701–709
63. Ohmori T, Mametsuka H, Suzuki E (2000) Photocatalytic hydrogen evolution on InP suspension with inorganic sacrificial reducing agent. Int J Hydrogen Energy 25:953–955
64. He C-H, Yang OB (2003) Hydrogen Evolution by Photocatalytic Decomposition of Water under UV Irradiation over $K[Bi_3PbTi_5O_{16}]$ Perovskite: Effect of Cerium Species. Ind Eng Chem Res 42:419–425
65. Lee SG, Lee S, Lee H-I (2001) Photocatalytic production of hydrogen from aqueous solution containing CN− as a hole scavenger. Appl Catal A-Gen 207:173–181
66. Bamwenda GR, Uesigi T, Abe Y, Sayama K, Arakawa H (2001) The photocatalytic oxidation of water to O_2 over pure CeO_2, WO_3, and TiO_2 using Fe^{3+} and Ce^{4+} as electron acceptors. Appl Catal A Gen 205:117–128
67. Ohno T, Tanigawa F, Fujihara K, Izumi S, Matsumura M (1999) Photocatalytic oxidation of water by visible light using ruthenium-doped titanium dioxide powder. J Photochem Photobiol A 127:107–110

68. Galińska A, Walendziewski J (2005) Photocatalytic water splitting over Pt−TiO_2 in the presence of sacrificial reagents. Energy Fuels 19:1143–1147
69. Zieliñska B, Borowiak-Palen E, Kalenczuk RJ (2008) Photocatalytic hydrogen generation over alkaline-earth titanates in the presence of electron donors. Int J Hydrogen Energy 33:1797–1802
70. Chiarello GL, Forni L, Selli E (2009) Photocatalytic hydrogen production by liquid- and gas-phase reforming of CH3OH over flame-made TiO_2 and Au/TiO_2. Catal Today 144:69–74
71. Chen T, Wu G, Feng Z, Hu G, Su W, Ying P, Li C (2008) In situ FT-IR study of photocatalytic decomposition of formic acid to hydrogen on Pt/TiO_2 catalyst. Chin J Catal 29:105–107
72. Patsoura A, Kondarides DI, Verykios XE (2007) Photocatalytic degradation of organic pollutants with simultaneous production of hydrogen. Catal Today 124:94–102
73. Hashimoto K, Kawai T, Sakata T (1984) Photocatalytic reactions of hydrocarbons and fossil fuels with water. Hydrogen production and oxidation. The Journal of Physical Chemistry 88:4083–4088
74. Chen S, Takata T, Domen K (2017) Particulate photocatalysts for overall water splitting. Nat Rev Mater 2:17050
75. Sayama K, Arakawa H (1996) Effect of carbonate addition on the photocatalytic decomposition of liquid water over a ZrO_2 catalyst. J Photochem Photobiol A 94:67–76
76. Jing DW, Zhang YJ, Guo LJ (2005) Study on the synthesis of Ni doped mesoporous TiO_2 and its photocatalytic activity for hydrogen evolution in aqueous methanol solution. Chem Phys Lett 415:74–78
77. Ebina Y, Sasaki T, Harada M, Watanabe M (2002) Restacked perovskite nanosheets and their Pt-loaded materials as photocatalysts. Chem Mater 14:4390–4395
78. Kudo A, Mikami I (1998) New In_2O_3(ZnO)(m) photocatalysts with laminal structure for visible light-induced H_2 or O_2 evolution from aqueous solutions containing sacrificial reagents. Chem. Lett. 1027–1028
79. Ikuma Y, Bessho H (2007) Effect of Pt concentration on the production of hydrogen by a TiO_2 photocatalyst. Int J Hydrogen Energy 32:2689–2692
80. Ogisu K, Ishikawa A, Teramura K, Toda K, Hara M, Domen K (2007) Lanthanum-indium oxysulfide as a visible light driven photocatalyst for water splitting. Chem Lett 36:854–855
81. Ogisu K, Ishikawa A, Shimodaira Y, Takata T, Kobayashi H, Domen K (2008) Electronic band structures and photochemical properties of La-Ga-based oxysulfides. J Phys Chem C 112:11978–11984
82. Jang JS, Joshi UA, Lee JS (2007) Solvothermal synthesis of CdS nanowires for photocatalytic hydrogen and electricity production. J Phys Chem C 111:13280–13287
83. Bessekhouad Y, Mohammedi M, Trari M (2002) Hydrogen photoproduction from hydrogen sulfide on Bi2S3 catalyst. Sol Energy Mater Sol Cells 73:339–350
84. Bao NZ, Shen LM, Takata T, Lu DL, Domen K (2006) Highly ordered Pt-loaded CdS nanowire arrays for photocatalytic hydrogen production under visible light. Chem Lett 35:318–319
85. Hara M, Hitoki G, Takata T, Kondo JN, Kobayashi H, Domen K (2003) TaON and Ta_3N_5 as new visible light driven photocatalysts. Catal Today 78:555–560
86. Hitoki G, Takata T, Kondo JN, Hara M, Kobayashi H, Domen K (2002) An oxynitride, TaON, as an efficient water oxidation photocatalyst under visible light irradiation (lambda <= 500 nm). Chem. Commun. 1698–1699
87. Kasahara A, Nukumizu K, Takata T, Kondo JN, Hara M, Kobayashi H, Domen K (2003) $LaTiO_2N$ as a visible-light (<= 600 nm)-driven photocatalyst (2). J Phys Chem B 107:791–797
88. Xiao W, Yuan H, Zhang W, Shangguan W (2007) TiN film with (111) preferred orientation as a visible-light-driven photocatalyst for hydrogen evolution from water decomposition. Mater Chem Phys 105:6–9
89. Chiarello GL, Selli E, Forni L (2008) Photocatalytic hydrogen production over flame spray pyrolysis-synthesised TiO_2 and Au/TiO_2. Appl Catal B-Environ 84:332–339
90. Sreethawong T, Yoshikawa S (2005) Comparative investigation on photocatalytic hydrogen evolution over Cu-, Pd-, and Au-loaded mesoporous TiO_2 photocatalysts. Catal Commun 6:661–668

91. Bae E, Choi W (2003) Highly enhanced photoreductive degradation of perchlorinated compounds on dye-sensitized metal/TiO_2 under visible light. Environ Sci Technol 37:147–152
92. Arabatzis IM, Stergiopoulos T, Andreeva D, Kitova S, Neophytides SG, Falaras P (2003) Characterization and photocatalytic activity of Au/TiO_2 thin films for azo-dye degradation. J Catal 220:127–135
93. Tai YW, Chen JS, Yang CC, Wan BZ (2004) Preparation of nano-gold on $K_2La_2Ti_3O_{10}$ for producing hydrogen from photo-catalytic water splitting. Catal Today 97:95–101
94. Tsuji I, Kato H, Kudo A (2005) Visible-light-induced H_2 evolution from an aqueous solution containing sulfide and sulfite over a ZnS-$CuInS_2$-$AgInS_2$ solid-solution photocatalyst. Angew Chem Int Ed 44:3565–3568
95. Hara M, Nunoshige J, Takata T, Kondo JN, Domen K (2003) Unusual enhancement of H-2 evolution by Ru on TaON photocatalyst under visible light irradiation. Chem. Commun. 3000–3001
96. Navarro RM, del Valle F, Fierro JLG (2008) Photocatalytic hydrogen evolution from CdS-ZnO-CdO systems under visible light irradiation: effect of thermal treatment and presence of Pt and Ru cocatalysts. Int J Hydrogen Energy 33:4265–4273
97. Sano T, Kutsuna S, Negishi N, Takeuchi K (2002) Effect of Pd-photodeposition over TiO_2 on product selectivity in photocatalytic degradation of vinyl chloride monomer. J Mol Catal A-Chem 189:263–270
98. Wang X, He Z, Zhong S, Xiao X (2007) Photocatalytic synthesis of hydrocarbon oxygenates from C_2H_6 and CO_2 over Pd-MoO_3/SiO_2 catalyst. J Nat Gas Chem 16:173–178
99. Jin S, Shiraishi F (2004) Photocatalytic activities enhanced for decompositions of organic compounds over metal-photodepositing titanium dioxide. Chem Eng J 97:203–211
100. Ke D, Peng T, Ma L, Cai P, Jiang P (2008) Photocatalytic water splitting for O_2 production under visible-light irradiation on BiVO4 nanoparticles in different sacrificial reagent solutions. Appl Catal A-Gen 350:111–117
101. Georgekutty R, Seery MK, Pillai SC (2008) A highly efficient Ag-ZnO photocatalyst: synthesis, properties, and mechanism. J Phys Chem C 112:13563–13570
102. Lu W, Gao S, Wang J (2008) One-pot synthesis of Ag/ZnO self-assembled 3D hollow microspheres with enhanced photocatalytic performance. J Phys Chem C 112:16792–16800
103. Anandan S, Sathishkumar P, Pugazhenthiran N, Madhavan J, Maruthamuthu P (2008) Effect of loaded silver nanoparticles on TiO_2 for photocatalytic degradation of Acid Red 88. Sol Energy Mater Sol Cells 92:929–937
104. Hou X-G, Huang M-D, Wu X-L, Liu A-D (2009) Preparation and studies of photocatalytic silver-loaded TiO_2 films by hybrid sol-gel method. Chem Eng J 146:42–48
105. Pal B, Ikeda S, Kominami H, Kera Y, Ohtani B (2003) Photocatalytic redox-combined synthesis of L-pipecolinic acid from L-lysine by suspended titania particles: effect of noble metal loading on the selectivity and optical purity of the product. J Catal 217:152–159
106. Sasaki Y, Iwase A, Kato H, Kudo A (2008) The effect of co-catalyst for Z-scheme photocatalysis systems with an Fe^{3+}/Fe^{2+} electron mediator on overall water splitting under visible light irradiation. J Catal 259:133–137
107. Pal B, Torimoto T, Okazaki K-I, Ohtani B (2007) Photocatalytic syntheses of azoxybenzene by visible light irradiation of silica-coated cadmium sulfide nanocomposites. Chem Commun 483–485
108. Iwase A, Kato H, Kudo A (2006) Nanosized Au particles as an efficient cocatalyst for photocatalytic overall water splitting. Catal Lett 108:7–10
109. Ebina Y, Sakai N, Sasaki T (2005) Photocatalyst of lamellar aggregates of RuOx-loaded perovskite nanosheets for overall water splitting. J Phys Chem B 109:17212–17216
110. Kadowaki H, Saito N, Nishiyama H, Kobayashi H, Shimodaira Y, Inoue Y (2007) Overall splitting of water by RuO_2-loaded $PbWO_4$ photocatalyst with d(10)s(2)-d(0) configuration. J Phys Chem C 111:439–444
111. Arai N, Saito N, Nishiyama H, Shimodaira Y, Kohayashi H, Inoue Y, Sato K (2008) Photocatalytic activity for overall water splitting of RuO_2-loaded $Y_xIn_{2-x}O_3$ (x=0.9–1.5). J. Phys. Chem. C 112:5000–5005

112. Sato J, Saito N, Yamada Y, Maeda K, Takata T, Kondo JN, Hara M, Kobayashi H, Domen K, Inoue Y (2005) RuO_2-loaded beta-Ge3N4 as a non-oxide photocatalyst for overall water splitting. J Am Chem Soc 127:4150–4151
113. Lee Y, Terashima H, Shimodaira Y, Teramura K, Hara M, Kobayashi H, Domen K, Yashima M (2007) Zinc germanium oxynitride as a photocatalyst for overall water splitting under visible light. J Phys Chem C 111:1042–1048
114. Arai N, Saito N, Nishiyama H, Domen K, Kobayashi H, Sato K, Inoue Y (2007) Effects of divalent metal ion (Mg^{2+}, Zn^{2+} and Be^{2+}) doping on photocatalytic activity of ruthenium oxide-loaded gallium nitride for water splitting. Catal Today 129:407–413
115. Miseki Y, Kato H, Kudo A (2005) Water splitting into H_2 and O_2 over Cs2Nb4O11 photocatalyst. Chem Lett 34:54–55
116. Kato H, Kudo A (2001) Water splitting into H2 and O-2 on alkali tantalate photocatalysts ATaO(3) (A = Li, Na, and K). J Phys Chem B 105:4285–4292
117. Sreethawong T, Suzuki Y, Yoshikawa S (2005) Photocatalytic evolution of hydrogen over mesoporous TiO_2 supported NiO photocatalyst prepared by single-step sol-gel process with surfactant template. Int J Hydrogen Energy 30:1053–1062
118. Lin H-Y, Chen Y-F, Chen Y-W (2007) Water splitting reaction on NiO/$InVO_4$ under visible light irradiation. Int J Hydrogen Energy 32:86–92
119. Maeda K, Domen K (2007) New non-oxide photocatalysts designed for overall water splitting under visible light. J Phys Chem C 111:7851–7861
120. Kawai T, Sakata T (1980) Conversion of carbohydrate into hydrogen fuel by a photocatalytic process. Nature 286:474–476
121. Maeda K, Teramura K, Lu D, Takata T, Saito N, Inoue Y, Domen K (2006) Characterization of Rh-Cr mixed-oxide nanoparticles dispersed on $(Ga_{1-x}Zn_x)(N_{1-x}O_x)$ as a cocatalyst for visible-light-driven overall water splitting. J Phys Chem B 110:13753–13758
122. Maeda K, Teramura K, Saito N, Inoue Y, Domen K (2006) Improvement of photocatalytic activity of $(Ga_{1-x}Zn_x)(N_{1-x}O_x)$ solid solution for overall water splitting by co-loading Cr and another transition metal. J Catal 243:303–308
123. Maeda K, Teramura K, Domen K (2007) Development of cocatalysts for photocatalytic overall water splitting on $(Ga_{1-x}Zn_x)(N_{1-x}O_x)$ solid solution. Catal Surv Asia 11:145–157
124. Maeda K, Lu D, Teramura K, Domen K (2008) Direct deposition of nanoparticulate rhodium-chromium mixed-oxides on a semiconductor powder by band-gap irradiation. J Mater Chem 18:3539–3542
125. Hisatomi T, Miyazaki K, Takanabe K, Maeda K, Kubota J, Sakata Y, Domen K (2010) Isotopic and kinetic assessment of photocatalytic water splitting on Zn-added Ga_2O_3 photocatalyst loaded with $Rh_{2-y}CryO_3$ cocatalyst. Chem Phys Lett 486:144–146
126. Maeda K, Teramura K, Lu D, Saito N, Inoue Y, Domen K (2006) Noble-metal/Cr_2O_3 core/shell nanoparticles as a cocatalyst for photocatalytic overall water splitting. Angew Chem Int Ed 45:7806–7809
127. Maeda K, Teramura K, Lu D, Saito N, Inoue Y, Domen K (2007) Roles of Rh/Cr_2O_3 (core/shell) nanoparticles photodeposited on visible-light-responsive $(Ga_{1-x}Zn_x)(N_{1-x}O_x)$ solid solutions in photocatalytic overall water splitting. J Phys Chem C 111:7554–7560
128. Maeda K, Lu D, Teramura K, Domen K (2010) Simultaneous photodeposition of rhodium-chromium nanoparticles on a semiconductor powder: structural characterization and application to photocatalytic overall water splitting. Energy Environ Sci 3:471–478
129. Maeda K, Sakamoto N, Ikeda T, Ohtsuka H, Xiong A, Lu D, Kanehara M, Teranishi T, Domen K (2010) Preparation of core-shell-structured nanoparticles (with a noble-metal or metal oxide core and a chromia shell) and their application in water splitting by means of visible light. Chem Eur J 16:7750–7759
130. Maeda K, Xiong A, Yoshinaga T, Ikeda T, Sakamoto N, Hisatomi T, Takashima M, Lu D, Kanehara M, Setoyama T, Teranishi T, Domen K (2010) Photocatalytic overall water splitting promoted by two different cocatalysts for hydrogen and oxygen evolution under visible light. Angew Chem Int Ed 49:4096–4099

131. Tian M, Shangguan W, Yuan J, Wang S, Ouyang Z (2007) Promotion effect of nanosized Pt, RuO_2 and NiOx loading on visible light-driven photocatalysts K4Ce2M10O30 (M = Ta, Nb) for hydrogen evolution from water decomposition. Sci Technol Adv Mater 8:82–88
132. Thaminimulla CTK, Takata T, Hara M, Kondo JN, Domen K (2000) Effect of chromium addition for photocatalytic overall water splitting on Ni-$K_2La_2Ti_3O_{10}$. J Catal 196:362–365
133. Zong X, Wu G, Yan H, Ma G, Shi J, Wen F, Wang L, Li C (2010) Photocatalytic H_2 evolution on MoS_2/CdS catalysts under visible light irradiation. J Phys Chem C 114:1963–1968
134. Zong X, Yan H, Wu G, Ma G, Wen F, Wang L, Li C (2008) Enhancement of photocatalytic H_2 evolution on CdS by loading MoS_2 as cocatalyst under visible light irradiation. J Am Chem Soc 130:7176–7177
135. Frame FA, Osterloh FE (2010) CdSe-MoS_2: a quantum size-confined photocatalyst for hydrogen evolution from water under visible light. J Phys Chem C 114:10628–10633
136. Tabata M, Maeda K, Ishihara T, Minegishi T, Takata T, Domen K (2010) Photocatalytic hydrogen evolution from water using copper gallium sulfide under visible-light irradiation. J Phys Chem C 114:11215–11220
137. Goto Y, Hisatomi T, Wang Q, Higashi T, Ishikiriyama K, Maeda T, Sakata Y, Okunaka S, Tokudome H, Katayama M, Akiyama S, Nishiyama H, Inoue Y, Takewaki T, Setoyama T, Minegishi T, Takata T, Yamada T, Domen K (2018) A particulate photocatalyst water-splitting panel for large-scale solar hydrogen generation. Joule 2:509–520
138. Zhang Q, Li Z, Wang S, Li R, Zhang X, Liang Z, Han H, Liao S, Li C (2016) Effect of redox cocatalysts location on photocatalytic overall water splitting over cubic $NaTaO_3$ semiconductor crystals exposed with equivalent facets. ACS Catal 6:2182–2191
139. Kudo A, Miseki Y (2009) Heterogeneous photocatalyst materials for water splitting. Chem Soc Rev 38:253–278
140. Chen X, Liu L, Yu Peter Y, Mao Samuel S (2011) Increasing solar absorption for photocatalysis with black hydrogenated titanium dioxide nanocrystals. Science 331:746–750
141. Tao X, Zhao Y, Mu L, Wang S, Li R, Li C (2018) Bismuth tantalum oxyhalogen: a promising candidate photocatalyst for solar water splitting. Adv Energy Mater 8:1701392
142. Cai J, Wu M, Wang Y, Zhang H, Meng M, Tian Y, Li X, Zhang J, Zheng L, Gong J (2017) Synergetic enhancement of light harvesting and charge separation over surface-disorder-engineered TiO_2 photonic crystals. Chem 2:877–892
143. Rather RA, Singh S, Pal B (2017) Visible and direct sunlight induced H_2 production from water by plasmonic Ag-TiO_2 nanorods hybrid interface. Sol Energy Mater Sol Cells 160:463–469
144. Si Y, Cao S, Wu Z, Ji Y, Mi Y, Wu X, Liu X, Piao L (2018) What is the predominant electron transfer process for Au NRs/TiO_2 nanodumbbell heterostructure under sunlight irradiation? Appl Catal B Environ 220:471–476
145. Si Y, Cao S, Wu Z, Ji Y, Mi Y, Wu X, Liu X, Piao L (2017) The effect of directed photogenerated carrier separation on photocatalytic hydrogen production. Nano Energy 41:488–493
146. Xiao S-T, Wu S-M, Dong Y, Liu J-W, Wang L-Y, Wu L, Zhang Y-X, Tian G, Janiak C, Shalom M, Wang Y-T, Li Y-Z, Jia R-K, Bahnemann DW, Yang X-Y (2020) Rich surface hydroxyl design for nanostructured TiO_2 and its hole-trapping effect. Chem Eng J 400:125909
147. Zhang YX, Wu SM, Tian G, Zhao XF, Wang LY, Yin YX, Wu L, Li QN, Zhang YX, Wu JS (2021) Titanium vacancies in TiO_2 nanofibers enable highly efficient photodriven seawater splitting. Chem–A Eur J 27:14202–14208
148. Vilatela JJ, Eder D (2012) Nanocarbon composites and hybrids in sustainability: a review. Chemsuschem 5:456–478
149. Christoforidis KC, Fornasiero P (2017) Photocatalytic hydrogen production: a rift into the future energy supply. ChemCatChem 9:1523–1544
150. Lu Y, Liu Y-X, He L, Wang L-Y, Liu X-L, Liu J-W, Li Y-Z, Tian G, Zhao H, Yang X-H, Liu J, Janiak C, Lenaerts S, Yang X-Y, Su B-L (2020) Interfacial co-existence of oxygen and titanium vacancies in nanostructured TiO2 for enhancement of carrier transport. Nanoscale 12:8364–8370
151. Wang S, Pan L, Song J-J, Mi W, Zou J-J, Wang L, Zhang X (2015) Titanium-defected undoped anatase TiO_2 with p-type conductivity, room-temperature ferromagnetism, and remarkable photocatalytic performance. J Am Chem Soc 137:2975–2983

152. Lu Y, Liu X-L, He L, Zhang Y-X, Hu Z-Y, Tian G, Cheng X, Wu S-M, Li Y-Z, Yang X-H, Wang L-Y, Liu J-W, Janiak C, Chang G-G, Li W-H, Van Tendeloo G, Yang X-Y, Su B-L (2020) Spatial heterojunction in nanostructured TiO_2 and its cascade effect for efficient photocatalysis. Nano Lett 20:3122–3129
153. Wu S-M, Liu X-L, Lian X-L, Tian G, Janiak C, Zhang Y-X, Lu Y, Yu H-Z, Hu J, Wei H, Zhao H, Chang G-G, Tendeloo G, Wang L-Y, Yang X-Y, Su B-L (2018) Homojunction of oxygen and titanium vacancies and its interfacial *n–p* effect. Adv Mater 30:1802173
154. Guo L, Yang Z, Marcus K, Li Z, Luo B, Zhou L, Wang X, Du Y, Yang Y (2018) MoS_2/TiO_2 heterostructures as nonmetal plasmonic photocatalysts for highly efficient hydrogen evolution. Energy Environ Sci 11:106–114
155. Dang HV, Wang YH, Wu JCS (2021) Z-scheme photocatalyst Pt/GaP-TiO2-SiO2:Rh for the separated H_2 evolution from photocatalytic seawater splitting. Appl Catal B: Environ 296:120339
156. Pinaud BA, Benck JD, Seitz LC, Forman AJ, Chen Z, Deutsch TG, James BD, Baum KN, Baum GN, Ardo S, Wang H, Miller E, Jaramillo TF (2013) Technical and economic feasibility of centralized facilities for solar hydrogen production via photocatalysis and photoelectrochemistry. Energy Environ Sci 6:1983–2002
157. Hisatomi T, Kubota J, Domen K (2014) Recent advances in semiconductors for photocatalytic and photoelectrochemical water splitting. Chem Soc Rev 43:7520–7535
158. Wang X, Maeda K, Thomas A, Takanabe K, Xin G, Carlsson JM, Domen K, Antonietti M (2009) A metal-free polymeric photocatalyst for hydrogen production from water under visible light. Nat Mater 8:76–80
159. Zheng Y, Lin L, Wang B, Wang X (2015) Graphitic carbon nitride polymers toward sustainable photoredox catalysis. Angew Chem Int Ed 54:12868–12884
160. Lin L, Wang C, Ren W, Ou H, Zhang Y, Wang X (2017) Photocatalytic overall water splitting by conjugated semiconductors with crystalline poly(triazine imide) frameworks. Chem Sci 8:5506–5511
161. Wang L, Wan Y, Ding Y, Wu S, Zhang Y, Zhang X, Zhang G, Xiong Y, Wu X, Yang J, Xu H (2017) Conjugated microporous polymer nanosheets for overall water splitting using visible light. Adv Mater 29:1702428
162. Lin L, Yu Z, Wang X (2019) Crystalline carbon nitride semiconductors for photocatalytic water splitting. Angew Chem Int Ed 58:6164–6175
163. Liu J, Liu Y, Liu N, Han Y, Zhang X, Huang H, Lifshitz Y, Lee S-T, Zhong J, Kang Z (2015) Metal-free efficient photocatalyst for stable visible water splitting via a two-electron pathway. Science 347:970–974
164. Liu Y, Xiang Z (2019) Fully conjugated covalent organic polymer with carbon-encapsulated Ni_2P for highly sustained photocatalytic H_2 production from seawater. ACS Appl Mater Inter 11:41313–41320
165. Yang X, Hu Z, Yin Q, Shu C, Jiang XF, Zhang J, Wang X, Jiang JX, Huang F, Cao Y (2019) Water-soluble conjugated molecule for solar-driven hydrogen evolution from salt water. Adv Funct Mater 29:1808156
166. Li L, Zhou Z, Li L, Zhuang Z, Bi J, Chen J, Yu Y, Yu J (2019) Thioether-functionalized 2D covalent organic framework featuring specific affinity to Au for photocatalytic hydrogen production from seawater. ACS Sustain Chem Eng 7:18574–18581
167. Ranjeesh KC, George L, Maibam A, Krishnamurty S, Babu SS (2021) A durable Metallo-porphyrin 2D-polymer for photocatalytic hydrogen and oxygen evolution from river and sea waters. ChemCatChem 13:1717–1721
168. Guselnikova O, Trelin A, Miliutina E, Elashnikov R, Sajdl P, Postnikov P, Kolska Z, Svorcik V, Lyutakov O (2020) Plasmon-induced water splitting—through flexible hybrid 2D architecture up to hydrogen from seawater under NIR light. ACS Appl Mater Inter 12:28110–28119
169. Tao Jing YD (2017) Development of solid solution photocatalytic materials. Acta Phys Chim Sin 33:295–304
170. Hart JN, Allan NL, Claeyssens F (2011) Ternary silicon germanium nitrides: a class of tunable band gap materials. Phys Rev B 84:245209

171. Ouyang S, Ye J (2011) β-AgAl1-xGaxO$_2$ solid-solution photocatalysts: continuous modulation of electronic structure toward high-performance visible-light photoactivity. J Am Chem Soc 133:7757–7763
172. Tsuji I, Kato H, Kudo A (2006) Photocatalytic hydrogen evolution on ZnS−CuInS$_2$−AgInS$_2$ solid solution photocatalysts with wide visible light absorption bands. Chem Mater 18:1969–1975
173. Maeda K, Takata T, Hara M, Saito N, Inoue Y, Kobayashi H, Domen K (2005) GaN:ZnO solid solution as a photocatalyst for visible-light-driven overall water splitting. J Am Chem Soc 127:8286–8287
174. Schulz H, Thiemann KH (1977) Crystal structure refinement of AlN and GaN. Solid State Commun 23:815–819
175. García-Martínez O, Rojas RM, Vila E, de Vidales JLM (1993) Microstructural characterization of nanocrystals of ZnO and CuO obtained from basic salts. Solid State Ionics 63–65:442–449
176. Ohno T, Bai L, Hisatomi T, Maeda K, Domen K (2012) Photocatalytic water splitting using modified GaN:ZnO solid solution under visible light: long-time operation and regeneration of activity. J Am Chem Soc 134:8254–8259
177. Maeda K, Masuda H, Domen K (2009) Effect of electrolyte addition on activity of ($Ga_{1-x}Zn_x$)($N_{1-x}O_x$) photocatalyst for overall water splitting under visible light. Catal Today 147:173–178
178. Qiu B, Zhu Q, Xing M, Zhang J (2017) A robust and efficient catalyst of CdxZn1−xSe motivated by CoP for photocatalytic hydrogen evolution under sunlight irradiation. Chem Commun 53:897–900
179. Li Y, Lin S, Peng S, Lu G, Li S (2013) Modification of $ZnS_{1-x-0.5y}O_x(OH)_y$–ZnO photocatalyst with NiS for enhanced visible-light-driven hydrogen generation from seawater. Int J Hydrogen Energy 38:15976–15984
180. Chew Y-H, Ng B-J, Tang J-Y, Tan L-L, Chai, SP (2021) A synergistic combination of P-doped $Zn_{0.5}Cd_{0.5}S$ and CoP for dual-stage electron trapping and its application in seawater splitting. Solar RRL 5:2100016
181. Zeng G, Cao Y, Wu Y, Yuan H, Zhang B, Wang Y, Zeng H, Huang S (2021) $Cd_{0.5}Zn_{0.5}S/Ti_3C_2$ MXene as a Schottky catalyst for highly efficient photocatalytic hydrogen evolution in seawater. Appl Mater Today 22:100926
182. Lopes PAL, Maia DLdS, Silva LA (2020) Chalcogenide nanoparticles like $Cd_xZn_{(1-x)}SySe_{(1-y)}$ applied to photocatalytic hydrogen production from natural seawater under visible light irradiation. Mater Today Commun 25:101503
183. Wu Y, Ceder G (2013) First principles study on Ta_3N_5:$Ti_3O_3N_2$ solid solution as a water-splitting photocatalyst. J Phys Chem C 117:24710–24715
184. Zhou G, Guo Z, Shan Y, Wu S, Zhang J, Yan K, Liu L, Chu PK, Wu X (2019) High-efficiency hydrogen evolution from seawater using hetero-structured T/Td phase ReS_2 nanosheets with cationic vacancies. Nano Energy 55:42–48
185. Cui G, Wang W, Ma M, Xie J, Shi X, Deng N, Xin J, Tang B (2015) IR-driven photocatalytic water splitting with WO_2–Na_xWO_3 hybrid conductor material. Nano Lett 15:7199–7203
186. Yang TC, Chang FC, Wang HP, Wei YL, Jou CJ (2014) Photocatalytic splitting of seawater effected by (Ni–ZnO)@C nanoreactors. Mar Pollut Bull 85:696–699
187. Chang C-J, Huang K-L, Chen J-K, Chu K-W, Hsu M-H (2015) Improved photocatalytic hydrogen production of ZnO/ZnS based photocatalysts by Ce doping. J Taiwan Inst Chem Eng 55:82–89
188. Kim JH, Hansora D, Sharma P, Jang J-W, Lee JS (2019) Toward practical solar hydrogen production - an artificial photosynthetic leaf-to-farm challenge. Chem Soc Rev 48:1908–1971
189. https://www.energy.gov/eere/fuelcells/doe-technical-targets-hydrogen-production-photoelectrochemical-water-splitting.
190. Pinaud BA, Benck JD, Seitz LC, Forman AJ, Chen Z, Deutsch TG, James BD, Baum KN, Baum GN, Ardo S (2013) Technical and economic feasibility of centralized facilities for solar hydrogen production via photocatalysis and photoelectrochemistry. Energy Environ Sci 6:1983–2002

191. Setoyama T, Takewaki T, Domen K, Tatsumi T (2017) The challenges of solar hydrogen in chemical industry: how to provide, and how to apply? Faraday Discuss 198:509–527
192. Shaner MR, Atwater HA, Lewis NS, McFarland EW (2016) A comparative technoeconomic analysis of renewable hydrogen production using solar energy. Energy Environ Sci 9:2354–2371
193. Nishiyama H, Yamada T, Nakabayashi M, Maehara Y, Yamaguchi M, Kuromiya Y, Nagatsuma Y, Tokudome H, Akiyama S, Watanabe T, Narushima R, Okunaka S, Shibata N, Takata T, Hisatomi T, Domen K (2021) Photocatalytic solar hydrogen production from water on a 100–m^2 scale. Nature 598:304–307
194. Liu M, Wang L, Lu G, Yao X, Guo L (2011) Twins in Cd1−xZnxS solid solution: Highly efficient photocatalyst for hydrogen generation from water. Energy Environ Sci 4:1372–1378
195. Hwang J-Y, Shi S, Xu Z, Peterson KW (2006) synthesis of monodispersed iron oxide particles by a large-scale microwave reactor. Chem Eng Commun 193:1586–1591
196. Pan L, Liu X, Sun Z, Sun CQ (2013) Nanophotocatalysts via microwave-assisted solution-phase synthesis for efficient photocatalysis. J. Mater. Chem. A 1:8299–8326
197. Thostenson ET, Chou TW (1999) Microwave processing: fundamentals and applications. Compos A Appl Sci Manuf 30:1055–1071
198. Xiao J, Liu P, Wang CX, Yang GW (2017) External field-assisted laser ablation in liquid: An efficient strategy for nanocrystal synthesis and nanostructure assembly. Prog Mater Sci 87:140–220
199. Jedsukontorn T, Ueno T, Saito N, Hunsom M (2017) Facile preparation of defective black TiO_2 through the solution plasma process: Effect of parametric changes for plasma discharge on its structural and optical properties. J Alloys Compd 726:567–577
200. Zhang Z-K, Bai M-L, Guo D-Z, Hou S-M, Zhang G-M (2011) Plasma-electrolysis synthesis of TiO2 nano/microspheres with optical absorption extended into the infra-red region. Chem Commun 47:8439–8441
201. Kimura T (2011) In: Advances in ceramics-synthesis and characterization, processing and specific applications, pp. 75–100
202. Sun J, Chen G, Pei J, Jin R, Wang Q, Guang X (2012) A simple approach to strontium sodium tantalite mesocrystals with ultra-high photocatalytic properties for water splitting. J Mater Chem 22:5609–5614
203. Darr JA, Zhang J, Makwana NM, Weng X (2017) Continuous hydrothermal synthesis of inorganic nanoparticles: applications and future directions. Chem Rev 117:11125–11238
204. Makwana NM, Tighe CJ, Gruar RI, McMillan PF, Darr JA (2016) Pilot plant scale continuous hydrothermal synthesis of nano-titania; effect of size on photocatalytic activity. Mater Sci Semicond Process 42:131–137
205. Weng X, Zeng Q, Zhang Y, Dong F, Wu Z (2016) Facile approach for the syntheses of ultrafine TiO_2 nanocrystallites with defects and C heterojunction for photocatalytic water splitting. ACS Sustain Chem Eng 4:4314–4320
206. Wu S, Wang W, Tu W, Yin S, Sheng Y, Manuputty MY, Kraft M, Xu R (2018) Premixed stagnation flame synthesized TiO_2 nanoparticles with mixed phases for efficient photocatalytic hydrogen generation. ACS Sustain Chem Eng 6:14470–14479
207. Manuputty MY, Dreyer JAH, Sheng Y, Bringley EJ, Botero MariaL, Akroyd J, Kraft M (2019) Polymorphism of nanocrystalline TiO_2 prepared in a stagnation flame: formation of the TiO_2-II phase. Chem Sci 10:1342–1350
208. Teoh WY (2013) A perspective on the flame spray synthesis of photocatalyst nanoparticles. Materials 6
209. Xing Z, Zong X, Pan J, Wang L (2013) On the engineering part of solar hydrogen production from water splitting: photoreactor design. Chem Eng Sci 104:125–146
210. Jing D, Liu H, Zhang X, Zhao L, Guo L (2009) Photocatalytic hydrogen production under direct solar light in a CPC based solar reactor: reactor design and preliminary results. Energy Convers Manage 50:2919–2926
211. Xiong A, Ma G, Maeda K, Takata T, Hisatomi T, Setoyama T, Kubota J, Domen K (2014) Fabrication of photocatalyst panels and the factors determining their activity for water splitting. Catal Sci Technol 4:325–328

212. Schröder M, Kailasam K, Borgmeyer J, Neumann M, Thomas A, Schomäcker R, Schwarze M (2015) Hydrogen evolution reaction in a large-scale reactor using a carbon nitride photocatalyst under natural sunlight irradiation. Energy Technol 3:1014–1017
213. Wang Q, Hisatomi T, Suzuki Y, Pan Z, Seo J, Katayama M, Minegishi T, Nishiyama H, Takata T, Seki K (2017) Particulate photocatalyst sheets based on carbon conductor layer for efficient Z-scheme pure-water splitting at ambient pressure. J Am Chem Soc 139:1675–1683
214. Tilley SD, Lany S, Van de Krol R (2018) Advances in photoelectrochemical water splitting: theory. Royal Society of Chemistry, Experiment and Systems Analysis
215. Sun S, Hisatomi T, Wang Q, Chen S, Ma G, Liu J, Nandy S, Minegishi T, Katayama M, Domen K (2018) Efficient redox-mediator-free Z-scheme water splitting employing oxysulfide photocatalysts under visible light. ACS Catal 8:1690–1696
216. Alsayegh S, Johnson JR, Ohs B, Lohaus J, Wessling M (2017) Systematic optimization of H2 recovery from water splitting process using membranes and N_2 diluent. Int J Hydrogen Energy 42:6000–6011
217. Alsayegh S, Johnson JR, Wei X, Ohs B, Lohaus J, Wessling M (2017) CO2 aided H2 recovery from water splitting processes. Int J Hydrogen Energy 42:21793–21805
218. Huang C, Yao W, T-Raissi A, Muradov N (2011) Development of efficient photoreactors for solar hydrogen production. Solar Energy 85:19–27
219. Reilly K, Fang B, Taghipour F, Wilkinson DP (2017) Enhanced photocatalytic hydrogen production in a UV-irradiated fluidized bed reactor. J Catal 353:63–73
220. Reilly K, Wilkinson DP, Taghipour F (2018) Photocatalytic water splitting in a fluidized bed system: Computational modeling and experimental studies. Appl Energy 222:423–436
221. Vagia EC, Muradov N, Kalyva A, T-Raissi A, Qin N, Srinivasa AR, Kakosimos KE (2017) Solar hybrid photo-thermochemical sulfur-ammonia water-splitting cycle: Photocatalytic hydrogen production stage. Int J Hydrogen Energy 42:20608–20624
222. Braham RJ, Harris AT (2009) Review of major design and scale-up considerations for solar photocatalytic reactors. Ind Eng Chem Res 48:8890–8905
223. Fuqiang W, Ziming C, Jianyu T, Yuan Y, Yong S, Linhua L (2017) Progress in concentrated solar power technology with parabolic trough collector system: A comprehensive review. Renew Sustain Energy Rev 79:1314–1328
224. Yang Y, Wei Q, Hou J, Liu H, Zhao L (2016) Solar concentrator with uniform irradiance for particulate photocatalytic hydrogen production system. Int J Hydrogen Energy 41:16040–16047
225. Touili S, Alami Merrouni A, Azouzoute A, El Hassouani Y, Amrani A-I (2018) A technical and economical assessment of hydrogen production potential from solar energy in Morocco. Int J Hydrogen Energy 43:22777–22796
226. Chen H, Bo R, Tran-Phu T, Liu G, Tricoli A (2018) One-step rapid and scalable flame synthesis of efficient WO_3 photoanodes for water splitting. ChemPlusChem 83:569–576
227. Yadav D, Banerjee R (2018) Economic assessment of hydrogen production from solar driven high-temperature steam electrolysis process. J Clean Prod 183:1131–1155

Photoelectrocatalytic Seawater Splitting

Si-Ming Wu, Shi-Tian Xiao, Yi-Tian Wang, and Xiao-Yu Yang

Abstract Hydrogen is a renewable and eco-friendly energy source which has become the focus of attention. Solar energy is the most abundant renewable energy, and seawater is the most abundant natural resource on the earth. Using photoelectrocatalytic seawater splitting to produce hydrogen has become one of the ideal ways to solve the practical energy problem and alleviate the shortage of freshwater resources. This part summarizes the recent research work on the photoelectrocatalytic for seawater splitting, clarifies the research content and mechanisms, and discusses the implementation and challenges of photoelectrocatalytic seawater splitting.

Keywords Photoelectrocatalytic · Seawater splitting · Hydrogen · Photocatalysis · Photoelectrode

1 Preface

In this chapter, we discuss the basic principles that serve as the foundation of photoelectrocatalytic (PEC) water-splitting technologies, along with recent advances that have been made in developing eco-friendly and efficient systems for the production of clean H_2 using solar power and abundant seawater. In a PEC device, a photoactive electrode (photoelectrode) is typically a semiconductor (SC) that absorbs light having an energy that is larger than the bandgap of SC. Light absorption promotes an electron to move from the valence band (VB) to the conduction band (CB) in the photoelectrode, leaving a corresponding hole (h^+) in the VB. A hole–pair electron then moves from the surface of the excited photoelectrode to the electrolyte to promote the water splitting [1, 2].

Recently, a host of novel nanomaterials have been developed that have applications in PEC seawater splitting systems. Specifically, photoactive semiconductor (SC)

S.-M. Wu (✉) · S.-T. Xiao · Y.-T. Wang · X.-Y. Yang
State Key Laboratory of Advanced Technology for Materials Synthesis and Processing (Wuhan), Foshan Xianhu Laboratory of the Advanced Energy Science and Technology Guangdong Laboratory (Xianhu Hydrogen Valley, Foshan), Laoshan Laboratory (168 Wenhai Middle Rd, Jimo District, Qingdao), Wuhan University of Technology, Wuhan 430070, China
e-mail: wusiming@whut.edu.cn

X.-Y. Yang (ed.), *Photo-Driven Seawater Splitting for Hydrogen Production*,
https://doi.org/10.1007/978-981-99-0510-2_3

materials, such as TiO_2, ZnO, Fe_2O_3, and WO_3, which have various nanostructures including 0D nanoparticles, 1D nanorods/nanowires/nanotubes, 2D nanosheets, and 3D complex structures have been shown to display impressive PEC performances [3]. The wide range of chemical compositions and different structural dimensions [4] of these materials makes it possible to tune their physical properties. Advances made in both photocatalysis and electrocatalysis have guided the design of PEC seawater splitting systems that display highly advantageous features of selectivity and long-term stability [5].

Highly stable low-cost seawater splitting PEC systems required for industrial-level applications need to have properties that match specific criteria. For example, driving the PEC water-splitting process requires a low overpotential to have a high solar-to-hydrogen (STH) conversion efficiency. Secondly, PEC water-splitting systems need to be simple and space-saving, which means they must be comprised of a minimal number of components (wires, electrodes, reactor, etc.). Thirdly, costs for fabricating PEC systems must be low, a goal that can be realized by making a PEC system by combining light absorption and water-splitting catalysts. Finally, to be applicable, PEC cells must have long-term stabilities in seawater [6, 7].

2 Principles Serving as the Foundation of Photoelectrocatalytic Water Splitting

2.1 Introduction

Since the time Fujishima and Honda discovered that rutile TiO_2/Pt serves as a photocathode for PEC hydrogen production, [1] many research efforts have been carried out on PEC water splitting. Because climate changes have become more intense in recent years, developing systems that convert recyclable energy sources into clean energy have become an obvious goal of many investigations. The ocean has 97% of the world's water resources which cannot be desalinated in an economical manner. A highly promising general strategy to accomplish this objective is based on the PEC water-splitting process which converts sustainable solar energy into the clean energy generator H_2 and utilizes abundant seawater (SW). In this chapter, this strategy is described by first discussing the basic principles that serve as the foundation of photoelectrocatalytic (PEC) water splitting. Next, a summary is given on recent advances that have been made in developing eco-friendly and efficient PEC systems for clean H_2 production using solar power and abundant seawater. The chapter concludes by discussing hurdles that still need to be overcome to fabricate industrial-scale PEC systems for SW splitting [8, 9].

2.2 Mechanism of PEC Water Splitting

PEC combines features of electrocatalysis (EC) and photocatalysis. Like in EC systems, an external electronic circuit connecting the electrodes in PEC cells, with the difference being that in PEC cells one or both electrodes contain photoactive materials (photocatalysts) as thin film distributed on the substrates. Materials that commonly serve as photoanodes and photocathodes are n-type (e.g., TiO_2) and p-type SCs (e.g., Cu_2O), respectively. In a PEC cell, what electrolyte is used depends on the nature of the electrode. For example, when TiO_2 anodes are utilized, the electrolyte is preferably alkaline. The counter electrodes are typically comprised of Pt [9–11].

The mechanistic pathway followed in PEC is a combination of those operating in photocatalysis and electrocatalysis. As shown in Fig. 1, in a PEC cell containing water, illumination of a SC containing photoanode that is separated from the cathode promotes photocatalysis of the hydrogen evolution reaction (HER) and oxygen evolution reaction (OER) simultaneously. The specific electronic band structure of the SC, which consists of a full valence band (VB) and an empty conduction band (CB) and a small bandgap energy (E_g), is responsible for the chain of events that occur after illumination of the cell. Specifically, irradiation of the SC using light that has an energy greater than E_g promotes a VB-to-CB (e^-_{CB}) transition of an electron forming a hole which has a positive charge in the VB (h^+_{VB}) (Eq. 1). The photogenerated charge carriers h^+_{VB} and e^-_{CB} on the photoanode can be efficiently separated by applying a bias voltage. The hole created in this manner migrates to the photocatalyst surface, and then it is transferred to aqueous electrolyte solution where it initiates water oxidation to produce O_2 (Eq. (2)). The remaining electron in the CB is also transferred to the electrolyte solution where it promotes reduction of protons to form H_2 (Eq. (3)) [12, 13]:

$$SC + h\nu \rightarrow h^+_{VB} + e^-_{CB} \tag{1}$$

$$OER: 2H_2O\,(l) + 4h^+_{VB} \rightarrow O_2(g) + 4H^+ \tag{2}$$

$$HER: 4H^+ + 4\,e^-_{CB} \rightarrow 2\,H_2(g) \tag{3}$$

2.3 Features of PEC Water Splitting and Effects on the Performance

PEC methods are highly promising. The PEC performance of a system is often evaluated through the rate of hydrogen production and current density that can be determined by employing linear sweep voltammetry (LSV). Photogenerated current density is a common parameter used to evaluate the PEC performance. Several factors

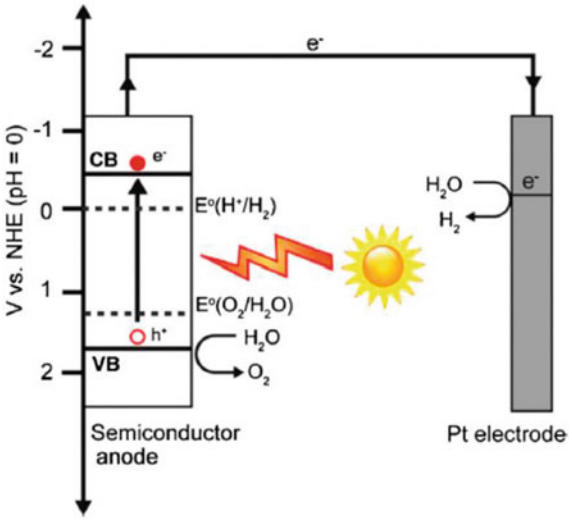

Fig. 1 PEC water splitting cell based on n-type SC as photoanode

govern performances of PEC systems including the SCs used as photoelectrodes, properties of electrolytes, bias utilized, and light source. In this regard, a systematic understanding of the PEC system and process is needed to develop new approaches to promote PEC cells with high performance [14, 15].

2.3.1 Photoelectrodes

In a water-splitting system based on PEC, n-type SCs are often used as photoanodes to promote HER and p-type SCs are used as photocathodes to drive OER. Several different configurations (presented schematically in Fig. 2), differing in the photoelectrode(s) being illuminated, have been employed in the design of PEC cells. Another system, using both HEC and OEC, contains two light-absorbing electrodes in a tandem, such as photoanode–photocathode cell or a tandem photoanode–photovoltaic (PEC-PV) cell to realize unbiased operation. Details about these different PEC systems will be given in Part 4.3 [16–18].

2.3.2 Electrolyte

The composition and pH of an electrolyte influence the performance of a PEC cell. When used for SW splitting, a neutral electrolyte comprised of seawater is utilized. Studies of the effect of the concentration of NaCl, the main component in natural SW, show that a certain range of higher concentrations lead to increase in electrolyte

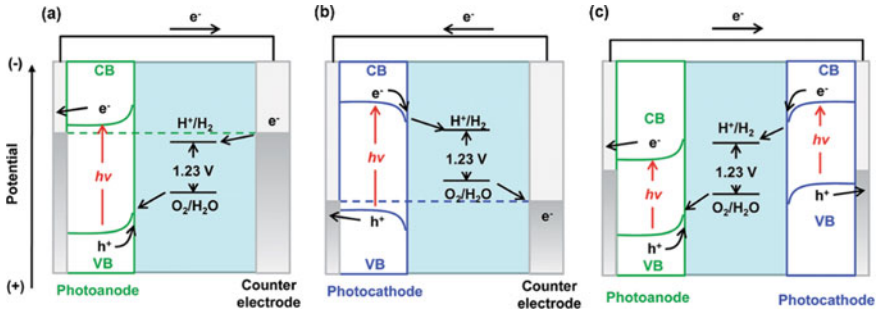

Fig. 2 Schematics of various PEC water-splitting systems using, **a** a photoanode and a counter cathode, **b** a photocathode and a counter anode, and **c** series-connected photoanode and photocathode

conductivity, the charge transfer rate, and the corresponding photocatalytic performance. However, compared with natural SW, NaCl solutions lack other salt components, such as $MgCl_2$ and Na_2SO_4. As a result, the performance of a PEC system is always better when it used for natural SW splitting. However, if the concentration of electrolyte is too high, the efficiency of hydrogen production will decrease. Finally, the temperature of the electrolyte also affects the efficiency of hydrogen production, where increases lead to improvement of the efficiency [10, 19].

2.3.3 Bias

When a wide energy bandgap SC (e.g., TiO_2) is used, the band edges are not suitable for water splitting. In these cases, an additional voltage or bias is often applied to simulate the decomposition potential of water under ideal conditions (1.23 V vs SHE). In this situation, also the photoelectrode typically contains an electrocatalyst with minimal overpotential. Bias potentials, typically in the 0.5–3 V range, promote the separation of electron and hole, reduce the recombination rate, and increase the photogenerated current density. However, a bias voltage should be sufficiently high to bring about optimization of the hydrogen production rate while minimizing energy waste [20].

2.3.4 Light Source

While UV–visible light sources have been used in experimental studies, most researchers utilize the AM 1.5G system to simulate a solar light source. PEC performance is typically higher under UV–visible light rather than sunlight or visible illumination because of typical differences in light intensities of the two types of sources. The intensity of the light source affects the performance of photoelectrochemical catalysts. In an appropriate range of intensities, the hydrogen evolution

performance increases with increasing light intensity, but this trend does not continue when the intensity is too high. Also, not all photocatalytic materials have visible light responses, hence they have a higher performance under illumination from a UV–visible light source. Hence, the light source and intensity in experimental PEC studies are usually selected to be in an economical range.

3 Materials Used in PEC Seawater Splitting Systems

3.1 Introduction

As discussed above, in PEC cells, photogenerated charge carriers on the photoelectrodes efficiently separate when a bias voltage is applied, and this leads to increase in photocatalytic activity. Also, ideal materials for photoanodes are n-type and p-type SCs and they are typically paired with appropriate electrolytes. Light absorption ranges of the photoelectrodes are related to bandgap energies of the SCs. Thus, a larger photocurrent density occurs when an SC with a narrow bandgap is employed, but this is accompanied by a lower photovoltage which needs to be high enough to promote water splitting. Thus, the compromise between photocurrent density and photovoltage determines the optimum SC bandgap energy for achieving a high STH efficiency. The properties of SCs such as TiO_2, WO_3, $BiVO_4$, Si, and CdS adhere to this criterion [21–23].

3.2 Understanding the PEC SW Splitting Mechanisms

3.2.1 Effect of Ions on Activity

Key technological challenges confront the use of SW as a source of hydrogen in PEC systems because of the presence of a wide variety of ions which can affect performance (Table 1). The results of studies by Ji et al., testing the effects of NaCl, $MgCl_2$, $MgSO_4$, $CaSO_4$, K_2SO_4, K_2CO_3, and $MgBr_2$ on a PEC system using simulated sea water (SSW), show that, in comparison to pure water, these ions decrease the rates of H_2 formation, and that K_2SO_4 and $MgCl_2$ are the most detrimental. A PEC cell has lowest activities when ca. 74% and 15% of the respective Mg^{2+} and Cl^- are in SW as is reflected in ca.2-fold decreased rate of H_2 production by compared to that in pure water. This group also found that PEC system in SSW without $MgCl_2$ displays a higher performance compared to its use in SW containing all seven salts. Hence, it should be beneficial if Mg^{2+} were absent which despite having membrane-related issues can be accomplished using a multilayer membrane that is known to reject 98% of this ion from seawater [24, 25].

Table 1 Ion concentrations © in natural SW. Based on values from Refs. [7, 24–28]

Solute (ion)	C (g kg^{-1} seawater)
Cl^-	20.058
Na^+	11.177
SO_4^{2-}	2.812
Mg^{2+}	1.331
Ca^{2+}	0.427
K^+	0.414
HCO_3^-	0.112
Br^-	0.070
$B(OH)_3$	0.020
CO_3^{2-}	0.016
Sr^{2+}	0.008
$B(OH)_4^-$	0.008
F^-	0.001

The effects of anions on PEC-promoted H_2 production have been investigated. Although Krivec et al. demonstrated that chloride ion has a detrimental effect by blocking active sites on TiO_2, the presence of other anions can be beneficial. In addition, Cl^- inhibits side reactions forming peroxo species which cause significant activity decrease. Also, stabilizing co-catalysts such as Co oxides is effective against peroxo formation on WO_3. As well, peroxide compounds are poisons for C_3N_4 photocatalysts. Therefore, Liu et al. developed an extra stabilizing carbon dot (CD) co-catalyst, which degrades peroxide species leading to stability for at least 200 d. Zhu et al. showed that these CDs block the negative effects of various ionic species in SW [26]. In addition, they promote efficient charge separation in CDs/CdS composites which leads to a H_2 evolution rate that is 265 times higher than that using unmodified CdS. The large abundance of various ions in SW (Table 1) represents a technological challenge to developing efficient PEC water-splitting systems that utilize SW [7, 26–28].

3.2.2 Effects on Stability

Detrimental effects of inorganic ions on PEC systems can arise from scaling and corrosion which have major impacts on long-term stability. However, Ichikawa observed that the surface of a thin anatase TiO_2 film remains clean and deposit free in SW.

The effects of photoelectrode materials on PEC activities are highly dependent on the nature of the SC used. For both the HER and OER, often chemically stable photocatalysts are used in conjunction with co-catalysts. Similar problems exist with photocathodes employed for PECs. To stabilize the cathodes, chemically stable oxides have been employed as protecting layers. Kawde et al. [29] showed that TiO_2

serves an effective protection layer for p-Si photocathode with NiO_x. In the absence of the extra layer, silicon oxidizes rapidly, but no decline in activity occurs during a 5 h illumination period when the photocathode is protected. As a final remark, in several studies, it was shown that salts in seawater can serve as protectants when corrosion and scaling issues are resolved [30, 31].

3.3 Metal Oxides Materials for Seawater Splitting

3.3.1 TiO_2-based Photoelectrodes

Titanium dioxide (TiO_2) is widely used as an SC for photoelectrodes due to its high photostability, low production cost, and eco-friendliness. The protective action of TiO_2 against corrosion has made its use attractive for PEC systems in seawater. As a photoelectrode, titanium dioxide is usually used in the form of anodized titanium dioxide nanotubes or nanorods, which have enhanced light absorption and the ability to achieve high STH efficiencies. The main strategies employed so far to enhance output include element doping, nanostructure control, and using nanocomposites. The nanocomposites most wildly used include TiO_2 composited with 0D (1D, 2D, and 3D) photoactive materials [32–37].

Misra et al. used anodized and annealed titanium oxide nanotubes as photoanodes for PEC water splitting for hydrogen generation. The photoconversion efficiencies of an array of TiO_2 tubes (Fig. 3a, b) annealed at 350 °C for 6 h in nitrogen under external applied potentials and visible light illumination are about 4% in 1 M KOH and 2.5% in NaCl solutions (Fig. 3c). The authors proposed models to describe this system and understand its mechanism in terms of VB and CB energy levels at the SC–electrolyte interface (Fig. 3d). In the TiO_2/KOH system, a maximum band bending occurs when the electrolyte's Fermi level is close to that of the valence band of the material in an n-type SC. Thus, maximum band bending will occur in KOH solution because its Fermi level is close to that of O_2/H_2O and the valence band. The degree of band bending determines the magnitude of the developed photopotential [27, 38].

Yoon et al. investigated a PEC hydrogen evolution system that contains tubular anodized TiO_2 electrodes (ATTE) as the photoanode and the cathode (Fig. 4b). An immobilized hydrogenase enzyme and external bias are included in this system, which functions utilizing various electrolytes composed of SW samples produced by membrane desalination (Fig. 4a). The rate of hydrogen evolution of the PEC system using nanofiltration (NF) retentate I was ca. 105 $\mu mol\ cm^{-2}\ h^{-1}$ (Fig. 4c), when enzyme is immobilized on the cathode (ca. 3.66 units per 1 cm^2 area) and a solar cell derived external bias of 2.0 V (Fig. 4d) [39].

Barreca et al. developed a Fe_2O_3–TiO_2-based PEC system that utilizes SW. Fe_2O_3–TiO_2 gas has a nanoscale structure (Fig. 5a), and that of well-developed upward growing hematite needles comprise the Fe_2O_3 nanodeposit whose assembly creates an open, porous structure. This unusual texture enabled deposition of an ALD TiO_2 coating even in inner regions of the nano-heterostructure. J–E curves

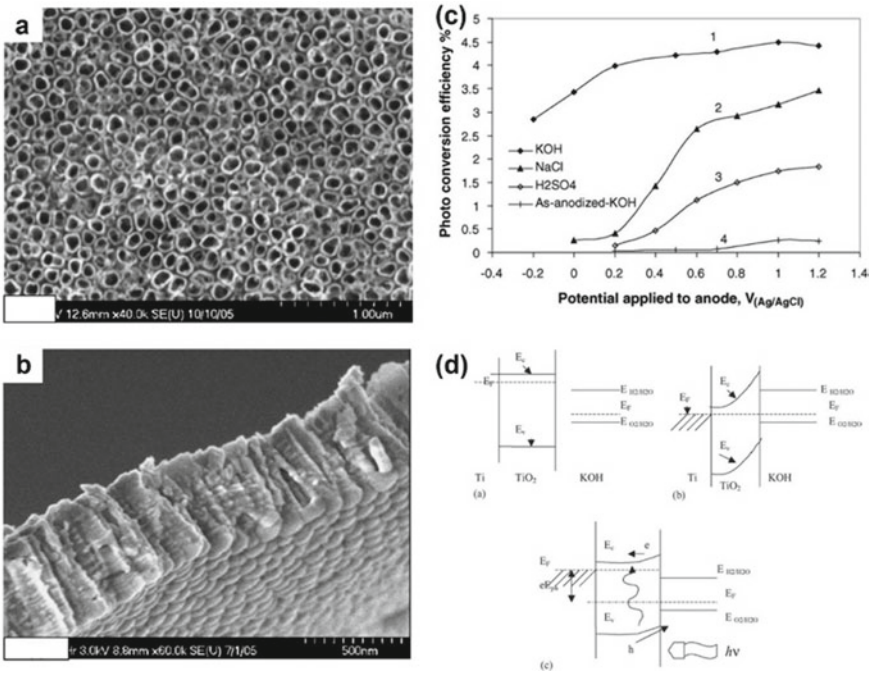

Fig. 3 Morphology of vertically oriented arrays of anodized titanium oxide nanotubes: **a** top and **b** side views of the surface. **c** Photoconversion efficiency of annealed (350 °C for 6 h in N_2) TiO_2 nanotubular arrays in different electrolytes as a function of anode potential. **d** Schematic of energy levels in SC and electrolyte interfaces

were obtained for specimen 400_H and for bare Fe_2O_3 using simulated seawater and solar illumination. In the latter case, an increase in photocurrent density of ca.0.2 mA cm^{-2} (at 1.23 V_{RHE}) occurs when a potential is applied. Interestingly, sample 400_H reached j values of ca. 0.4 mA cm^{-2} (at 1.23 V_{RHE}) under these conditions (Fig. 5b). These result data show that the implementation of the Fe_2O_3–TiO_2 materials is a key step in future designs of photoanodes for real-world devices. Another interesting observation is that the system's Fermi level energy is lowered with an increase in the positive bias, a change that also enhances band bending at the interfaces, which becomes more pronounced when the applied potential is raised. We believe that high photocurrents of the cell take place only after the valence band energy of Fe_2O_3 shifts to lower values with respect to the TiO_2 valence band edge at the electrolyte interface. This change promotes hole transfer from Fe_2O_3 to TiO_2. This suggestion gains support from the observation that no photocurrent plateau is reached for the TiO_2-functionalized specimens (Fig. 5c), which is attributed to an enhancement in the driving force for hole transfer through TiO_2 upon increasing anodic potential [40].

In a recent effort, Li et al. prepare TiO_2@g-C_3N_4 nanorod arrays containing different mass ratios of g-C_3N_4 [7]. The arrays were then decorated with Co-Pi

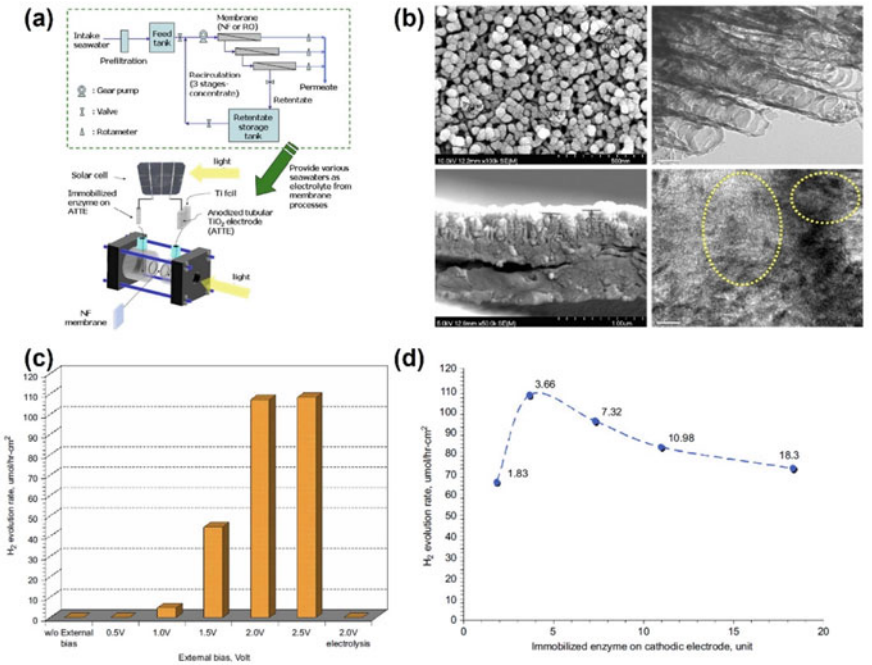

Fig. 4 **a** Schematic representation of the membrane desalination process and the system used for the light-sensitized enzymatic production of hydrogen using an anodized tubular TiO_2 photoanode, solar cell, and enzyme-immobilized cathode. **b** Characterization of the surface of a tubular TiO_2 electrode anodized at 20 V for 45 min in 0.5% HF at 5 °C and annealed at 650 °C for 5 h. **c** Effect on hydrogen evolution rate of external bias with the different solar cells with the NF retentate as electrolyte. **d** Effect of the amount of Pfu enzyme on hydrogen evolution rate

particles to offset the inadequacy of g-C_3N_4 (Fig. 6a). The TiO_2 nanorods can also be grown on the surface of an FTO. As can be seen by viewing Fig. 6b, the pristine TiO_2 nanorods have a tetragonal shape with an average diameter of about 200 nm, and the entire TiO_2 surface is evenly covered and forms good interfacial contact with g-C_3N_4. The transient photocurrent response of pristine TiO_2 is 0.42 mA cm^{-2} in aqueous 0.1 M Na_2SO_4 under 100 mW cm^{-2} (AM 1.5G) intermittent illumination at 1.23 V (vs. RHE) (Fig. 6c). The photocurrent density of TiO_2@g-C_3N_4 arrays increase during several on–off cycles. The photoresponse of CCNRs in seawater at 0.63 V (V_{RHE} = 1.23 V) under continuous 10 h illumination (100 mW cm^{-2}, AM 1.5G) was obtained using photocurrent—time (I–t) measurements (Fig. 6d). Before initiation of light irradiation, the photocurrent is almost zero. After illumination begins, the photocurrents sharply increase to a maximum of 1.82 mA cm^{-2}, and then decease slightly to ca. 1.64 mA cm^{-2} in a short time. The authors also proposed a mechanism for operation of this PEC cell (Fig. 6e) in which the CCNRs composite structure functions effectively to suppress charge recombination [7, 41, 42].

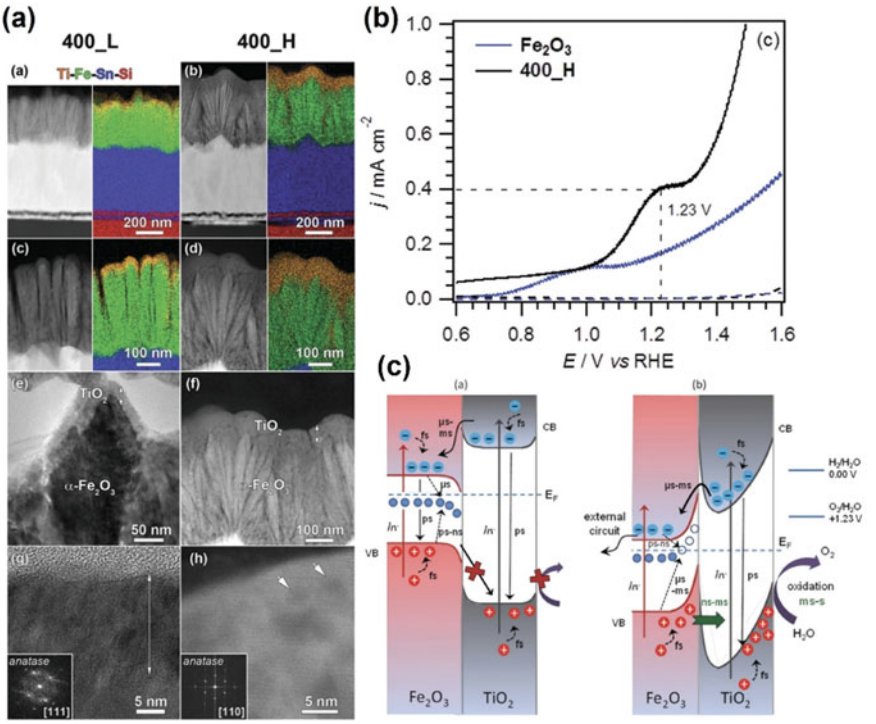

Fig. 5 **a** TEM of Fe_2O_3–TiO_2 photoanodes. **b** J–E curves for bare Fe_2O_3 and 400_H in a simulated seawater solution under solar illumination. **c** Energy level diagrams showing photoactivated charge transfer processes and related timescales: **a** without and **b** with the application of a positive external bias to Fe_2O_3–TiO_2 photoanodes

Using electrochemical methods, Boonserm et al. investigated the PEC response and corrosion behavior of CdS/TiO_2 nanocomposite films in aerated 0.5 M NaCl under white light illumination. The nanoporous TiO_2 film has a honeycomb structure containing 50–100 nm diameter pores (Fig. 7a). CdS/TiO_2 nanocomposite films created using 10 chemical deposition dipping cycles showed that the CdS nanoparticles are distributed uniformly over the film's inner and outer surfaces (Fig. 7b). The response rank was CdS(10)/TiO_2 (494.2 μA cm^{-2}), followed sequentially by CdS(15)/TiO_2 (117.1 μA cm^{-2}) and CdS(5)/TiO_2 (83.8 μA cm^{-2}), and non-sensitized TiO_2 is lowest. The results indicate that the CdS(10)/TiO_2 film has an optimal amount of CdS on the nanoporous TiO_2 surface to effectively enhance efficiency of electron–hole pair separation. The photocoupling current density of the CdS(10)/TiO_2 film has a maximum at 388 μA cm^{-2}, after which it continuously decreases (Fig. 7c) and at 4 h a quasi-steady state between potential and current density is attained (Fig. 7d). The diagram in Fig. 7e describes precipitation of the corrosion products, during which CdO formed by reaction of cadmium ions with superoxide radicals is released from photocorrosion in an aerated environment. In

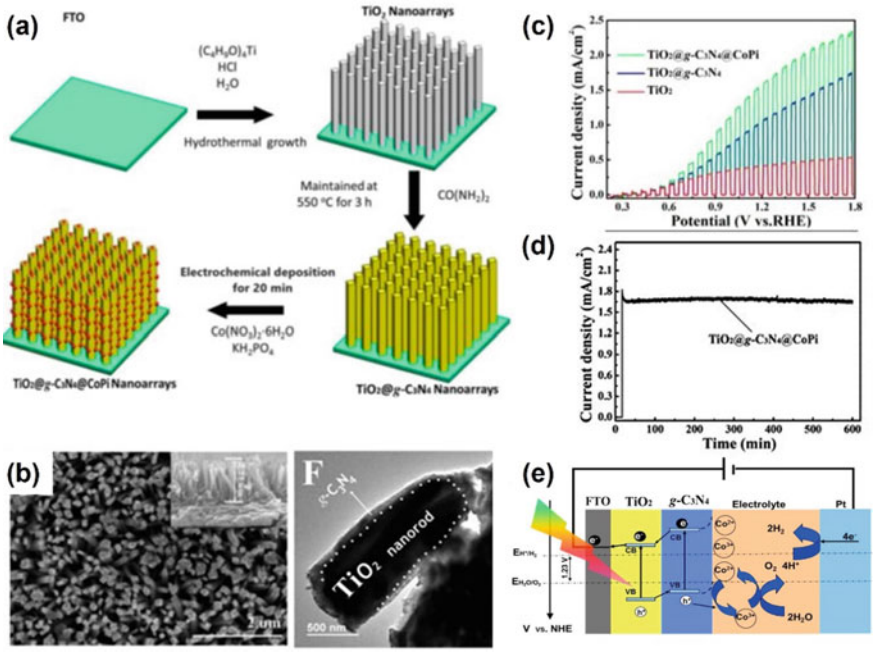

Fig. 6 **a** Illustration of the preparation of CCNRs. **b** Scanning electron microscope (SEM) and transmission electron microscope (TEM) images of TiO_2@g-C_3N_4 NRs. **c** Photocurrent density versus potential curves for pristine TiO_2 NRs, TiO_2@g-C_3N_4 NRs, and CCNRs. **d** Chronoamperometry (I–t) of CCNRs in seawater with a three-electrode system at 1.23 V_{RHE} for 10 h. **e** Diagram of transfer and separation of photogenerated charges and holes in the CCNRs heterostructure

contrast, $Cd(OH)_2$ is produced by hydrolysis of cadmium ions. These processes cause reformation of insoluble hydroxides of the metal ions [43].

Messinger et al. carried out a systematic analysis of the PEC for H_2 generation performance of TiO_2 coated with CoOx- and NiOx-functionalized microstructured p-Si photoelectrodes (p-Si/TiO_2). After removal of surface SiO_2 by reductive cleaning of commercial p-Si wafers, wet etching was performed to produce high-aspect ratio microstructured p-Si electrodes (Fig. 8a). The "as-synthesized" p-Si photoelectrodes were subsequently spincoated by treatment first with a TiO_2 sol and then with either a NiO_x or CoO_x sol. Each spin-coating step was followed by drying at room temperature and calcination at 380 °C. SEM views (Fig. 8b) show that use of the combined sol–gel and spin-coating protocols causes formation of a protective TiO_2 overcoating and film of the co-catalysts that completely covers the p-Si. PEC cells with p-Si/TiO_2/NiO_x as photoelectrodes display excellent photoelectrochemical performance in simulated seawater (pH 8.4), shown by an unprecedented high photocurrent density of 10 mA cm^{-2} at an applied potential of −0.7 V_{RHE} and 20 mA cm^{-2} at −0.9 V_{RHE} (Fig. 8c). When operating in simulated seawater at a

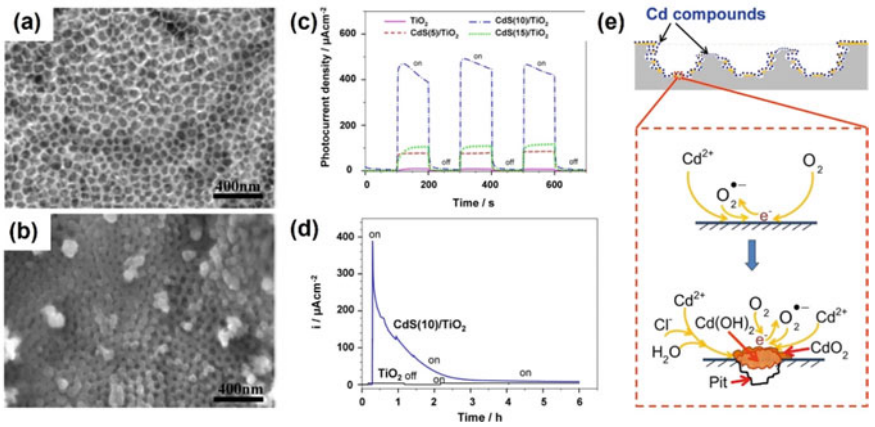

Fig. 7 **a** FE-SEM images of anodized nanoporous TiO_2. **b** FE-SEM images of CdS(10)/TiO_2 nanocomposite. **c** Comparison of PEC activities at various dipping cycles (5, 10 and 15) under intermittent visible light ($\lambda > 400$ nm) illumination. **d** photocoupling potential variation test for CdS/TiO_2 nanocomposite film in 0.5 M NaCl and visible light illumination ($\lambda > 400$ nm). **e** Diagram describing precipitation of corrosion products

potential of -0.3 V_{RHE} and 1 sun illumination, the photoelectrode produces H_2 at a nearly constant rate of ca. -1.5 mA cm^{-2} over 8 h (Fig. 8d) [43].

Wu et al. designed the photoanode In_2S_3/ANP/RND array. Inspection of the SEM and TEM images (Fig. 9a) shows that it has a core-shell-structured trunk. The high-resolution (HR) TEM image, given in the inset, shows that the trunk is composed of a single-crystalline rutile TiO_2 trunk with a growth direction of [001], and that the trunk is shielded by NPs that have a lattice spacing of 0.352 nm which is the same as that of (101) anatase TiO_2. The outer layer covering of the hierarchical TiO_2 nanostructure is NPs with a lattice spacing of 0.328 nm, which is the same as the d spacing of (110) crystal planes of rhombohedral β-In_2S_3. As the J–V curves show, the onset potentials of both the ANP/RND array and In_2S_3/ANP/RND array photoanodes in SW are 0.36 V versus RHE. (Fig. 9b). ANP/RND and In_2S_3/ANP/RND array photoanodes at 1.23 V versus RHE have respective photocurrent densities of 1.42 and 1.57 mA cm^{-2}. The authors presented band diagrams for the same photoanode in alkaline and neutral electrolytes and a schematic of In_2S_3/ANP/RND array photoanode (Fig. 9c). The PEC water oxidation performance of the ANP/RND array in the neutral electrolyte can be improved by removing the drawback associated with low charge separation efficiency, which corresponds to lowering band bending at the TiO_2–neutral electrolyte interface [44–48].

Yang et al. devised a simple controlled calcination approach to synthesize TiO_2 nanofibers enriched with Ti vacancies. The nanofibers display excellent photo/electro-performance and long-term stability as photocatalysts in PEC-promoted SW splitting. The proposed mechanism for formation of V_{Ti}-TiO_2, given in Fig. 10a suggests that hydroxy groups coordinate to titanium oligomers during solvothermal process converting Ti-G/EG I to intermediate II (Fig. 10a). During the

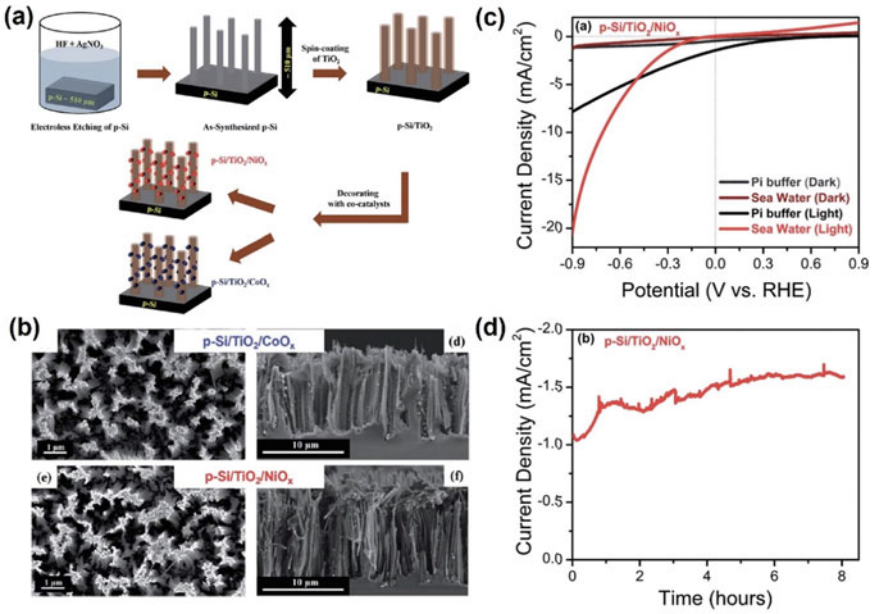

Fig. 8 **a** Representation (not to scale) of steps in the preparation of p-Si micro-wires using wet etching, coating with TiO_2 and subsequent functionalization with NiO_x or CoO_x via spin coating and sintering. **b** SEM images of planar top and cross-sectional views of as-synthesized and functionalized p-Si. **c** Linear sweep voltammograms and **d** photocurrent density of the p-Si/TiO_2/NiO_x photoelectrode recorded under 1 sun illumination in simulated seawater

initial phase of calcination, TiO_2 nanoclusters are formed and grow larger. Also, O atoms in the thermally unstable hydroxyl groups escape/migrate from the framework upon formation of anatase TiO_2 nanocrystals III (Fig. 10a). The relatively low calcination temperature enables retention of O species at the interface, which leads to distortions and concomitant generation of Ti vacancies at the O-rich interface of the amorphous crystalline phase (Fig. 10a IV). V_{Ti}-TiO_2 has a uniform structure containing fibers with 1.5–2.0 μm lengths and 30–50 nm widths (Fig. 10b). The fibers are composed of 10–20 nm nanoparticles. Analysis of J–V curves shows that under illumination, V_{Ti}-TiO_2 has the highest photocurrent density at 1.23 V versus RHE in both aqueous Na_2SO_4 (0.5 mol L^{-1}) and SSW. Specifically, the photocurrent density is 57.8 μA cm^{-2} at 1.23 V versus RHE when V_{Ti}-TiO_2 is used in SSW, which is about 26.6-, 7.8-, and 18.9-fold that of Ti-G/EG, N-TiO_2 and Comm-TiO_2, respectively (Fig. 10c). In addition to its good PEC activity, V_{Ti}-TiO_2 also shows significant stability in SSW in that 90.2% of the photocurrent is retained even after 40 h of continuous illumination (Fig. 10e). Compared with the performance of other TiO_2-based electrodes, the electrode comprised of V_{Ti}-TiO_2 supported on a Ni foam exhibits a high HER activity under irradiation with an overpotential (η, i.e., E versus RHE) of 369 mV at a catalytic current density of 10 mA cm^{-2} (Fig. 10d). The mechanism for photodriven water splitting promoted by the V_{Ti}-TiO_2 system is shown in

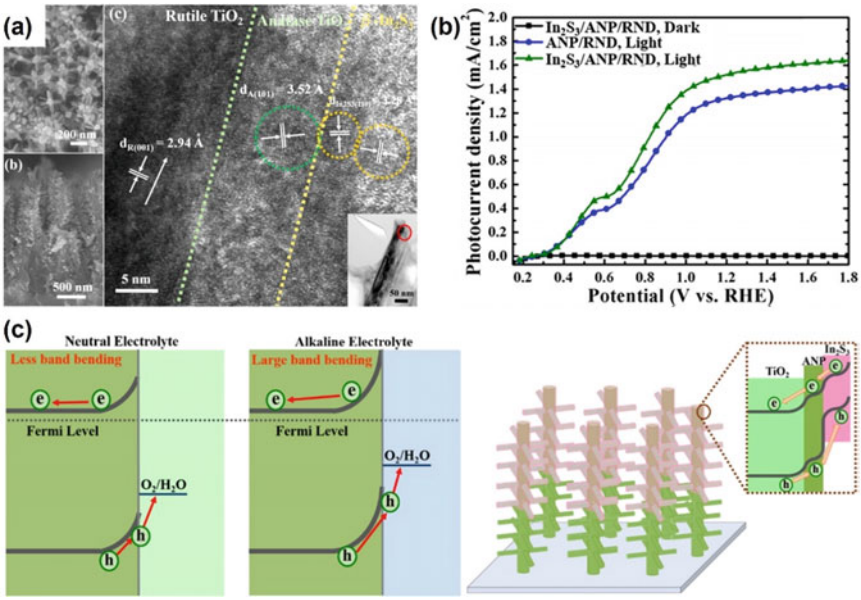

Fig. 9 **a** SEM images of an In_2S_3/ANP/RND array and HRTEM image of an In_2S_3/ANP/RND nanostructure in the inset. **b** J–V curves of ANP/RND and In_2S_3/ANP/RND photoanode arrays in seawater. **c** Band diagrams of identical photoanodes in alkaline and neutral electrolytes and a schematic of the In_2S_3/ANP/RND array photoanode

Fig. 10f. Because of the presence of Ti vacancies, valence band undergoes a negative shift, leading to narrowing of the bandgap of TiO_2. Therefore, photogenerated electrons undergo rapid migration from the VB to the CB and then transfer from the inner lattice to surface Ti vacancies as a result of a unidirectional electron trap effect. Electrons on the surface have enhanced electrical conductivity and electron transfer rates, resulting in performance enhancement of photodriven SW splitting and reduction of side reaction in high salinity systems. Also, fast H^+ adsorption on the surface caused by the presence of Ti vacancies hinders adsorption of other metal ions in seawater and significantly improves durability of the PEC system [49–51].

Metal–organic frameworks (MOFs) are substances that have high porosities and diverse photoelectrochemical properties. Afzali et. al used these materials to fabricate the PEC electrodes CoPi/MOF/TiO_2 by using a hydrothermal method. UNH and CoPi/UNH have octahedral cubic morphologies with average sizes of 90–120 nm, and that MNH and CoPi/MNH have truncated bipyramid morphologies with average sizes of about 350 nm (Fig. 11a–f). Under visible light irradiation, MOF/TiO_2, CoPi/MOF and CoPi/MOF/TiO_2 have photocurrent densities as high as 1.8 mA cm^{-2} (Fig. 11g and h). The stability of the CoPi/MOFs/TiO_2 was assessed by using chronoamperometry at 1.23 V versus RHE for 5000 s. The results show the photocurrent densities remain nearly constant during this period (Fig. 11j and l). The band energy diagrams of the heterostructured photoelectrodes are given in Fig. 11m [52].

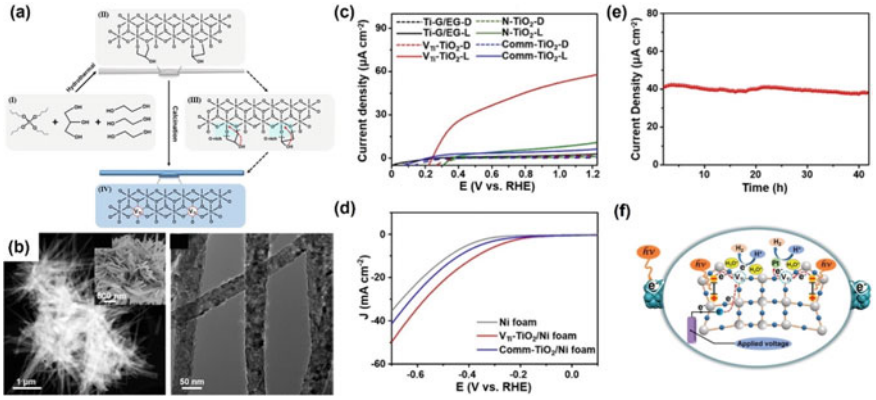

Fig. 10 **a** Representation of the mechanism of formation of V_{Ti}-TiO_2. **b** STEM, SEM and TEM images of V_{Ti}-TiO_2. **c** Linear sweep voltammograms at a scan rate of 10 mV/s of Ti-G/EG, V_{Ti}-TiO_2, N-TiO_2 and Comm-TiO_2 in simulated seawater with (L) and without (D) illumination. **d** Current density–time curve of V_{Ti}-TiO_2 under continuous illumination. **e** Polarization curves of Ni, V_{Ti}-TiO_2/Ni, and Comm-TiO_2/Ni foams for HER in simulated seawater using a potential scan rate of 5 mV/s with illumination. **f** Proposed mechanism of PC H_2 evolution and PEC H_2 evolution over V_{Ti}-TiO_2 under illumination

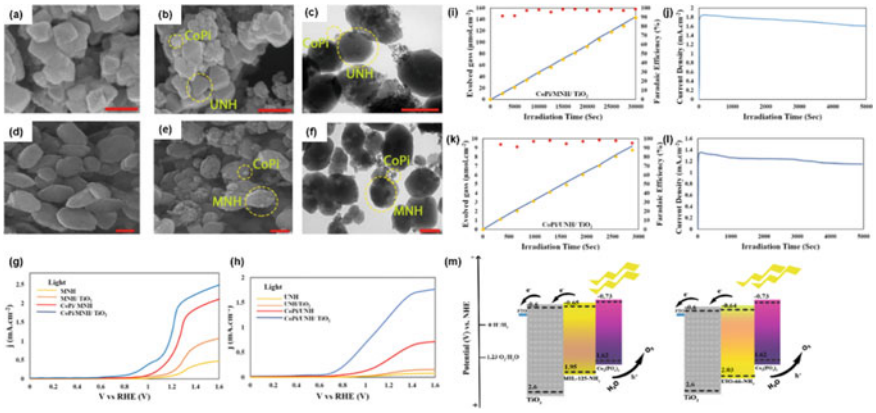

Fig. 11 FE-SEM images of **a** UNH, **b** CoPi/UNH. **d** MNH, **e** CoPi/MNH. TEM images of **c** CoPi/UNH, and **f** CoPi/MNH (scale bar 200 nm in all micrographs). **g** and **h** Linear sweep photovoltammograms of MOF composites in artificial seawater under dark and illumination conditions at 100 mW cm^{-2}. **i** and **k** Theoretical (blue line) and experimental (yellow square) O_2 evolution, along with Faradaic efficiency (red circles) and **j** and **l** Chronoamperometry of the CoPi/MOFs/TiO_2 photoelectrode at 1.23 V versus RHE under constant illumination (100 mW cm^{-2}). **m** Band energy diagram of the CoPi/MNH/TiO_2 and CoPi/UNH/TiO_2 for water oxidation

3.3.2 WO_3-based Photoelectrodes

Sun light-promoted PEC water splitting to form H_2 and O_2 is clean and uses renewable resources. Several SC materials are used as photoelectrodes for PEC, and in this group tungsten oxide (WO_3) has unique advantages in SW splitting because of its moderate bandgap (2.5–2.8 eV), excellent charge transport properties, low cost, and high stability in acidic environments. Yet, the WO_3 photoelectrode is limited by high carrier recombination and slow reaction kinetics. Current approaches to solve these problems include the formation of type-II heterojunctions and Z-type systems, crystal facet control strategies, and creation of porous structures and nanostructures.

Li et al. reported the preparation of novel inorganic–organic 2D/2D WO_3/g-C_3N_4 nanosheet arrays, which are grown on a FTO substrate using a hydrothermal growth and deposition-annealing procedure illustrated in Fig. 12a. This group also described applications of these arrays to SW splitting. TEM images show that in the WO_3/g-C_3N_4 nanosheet arrays (denoted as WO_3/g-C_3N_4 NSAs) g-C_3N_4 NSs cover WO_3 NSAs as indicated by the yellow arrow in Fig. 12b. The intimate interfacial contact existing between g-C_3N_4 and WO_3, which confirms the formation of the WO_3/g-C_3N_4 heterojunction, is clearly seen in the image given in Fig. 12c. As shown in Fig. 12d, WO_3/g-C_3N_4 NSAs achieves a current density of 0.73 mA cm^{-2} at 1.23 V versus RHE, which is two times higher than that of pristine WO_3 NSAs (0.36 mA cm^{-2}). As depicted in Fig. 12e, the current density of WO_3/g-C_3N_4 NSAs is retained after 3600 s of illumination. A possible explanation is illustrated in Fig. 12f. In WO_3/g-C_3N_4 NSAs, a well-matched type-II heterojunction exists between WO_3 and g-C_3N_4. Under illumination, the photogenerated electrons undergo thermodynamically favorable migration from the CB of g-C_3N_4 to the VB of WO_3, and then are transferred through the external circuit to the Pt electrode as part of the process for reduction of protons from SW to form H_2. Simultaneously, holes in the VB of WO_3 are transferred to the VB of g-C_3N_4 and then used to oxidize SW [53].

An efficient and stable photoanode for PEC splitting of natural seawater based on earth-abundant materials was developed by Li et al. Hydrothermal growth and deposition–annealing (DA) was employed to prepare Fe_2O_3/WO_3 nanorod arrays (Fe_2O_3/WO_3 NRs) on the surface of fluorine-doped tin oxide-coated glass (Fig. 13a). The WO_3 coating forms a film-like nanostructure on the surface of Fe_2O_3 NRs (Fig. 13b). An HRTEM image (Fig. 13c) shows that a clear interface exists between Fe_2O_3 NRs and WO_3 films. This observation demonstrates that a heterostructure rather than a physical mixture is formed between Fe_2O_3 NRs and WO_3 films. As shown in Fig. 13d, the anodes based on Fe_2O_3/WO_3 NRs display higher photocurrent densities compared with those generated using other materials and reach a maximum of 1.03 mA cm^{-2} (1.23 V versus RHE), which is 2.9 times higher than that of WO_3 films (0.36 mA cm^{-2}) and 50 times greater than that of the pristine Fe_2O_3 NRs (0.02 mA cm^{-2}). Figure 13e displays the photoresponse of Fe_2O_3/WO_3 NRs photoanode in SW at 1.23 V versus RHE for 5 h as determined using photocurrent–time (Ie–t) measurements. During the initial phase without light irradiation, the photocurrent is close to zero. Upon irradiation, the photocurrent rapidly increases to about 1 mA cm^{-2} and remains at about 65% of the initial value even after 5 h of

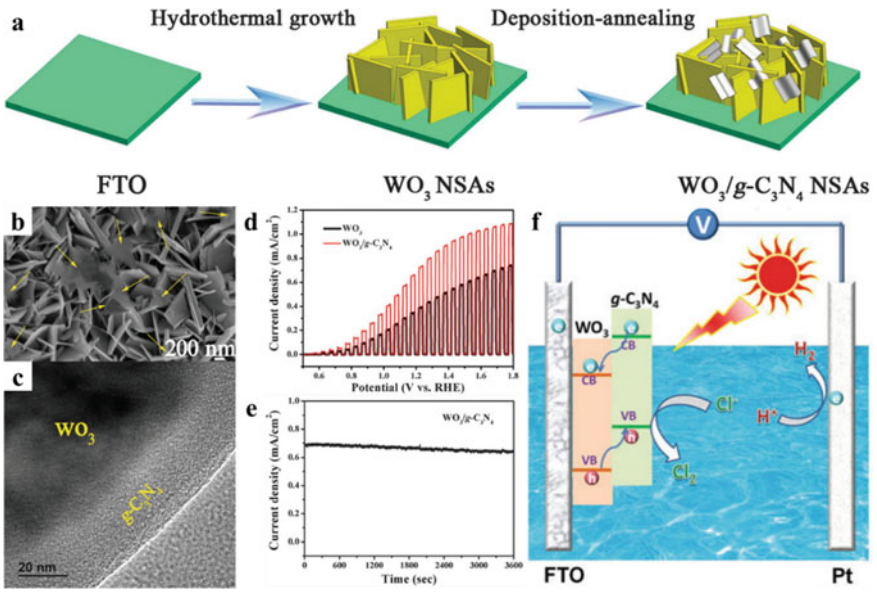

Fig. 12 **a** Schematic for the formation process of the WO_3/g-C_3N_4 NSAs; **b** SEM image of WO_3/g-C_3N_4 NSAs; **c** HRTEM images of WO_3/gC_3N_4 NSs; **d** I–V curves of WO_3 NSAs and WO_3/g-C_3N_4 NSAs measured using chopped illumination at a scan rate of 5 mV s^{-1}; **e** amperometric I–t curves of WO_3/g-C_3N_4 NSAs at 1.23 V versus RHE for 3600 s; **f** Illustration of the charge transfer process in the WO_3/g-C_3N_4 NSAs and the mechanism for PEC seawater splitting

continuous irradiation (100 mW cm^{-2}, AM 1.5G). Based on the above findings, the mechanism for operation of Fe_2O_3/WO_3 NRs photoanodes shown schematically in Fig. 13f was proposed. In this sequence, a Z-scheme system, formed between Fe_2O_3 and WO_3 in the hybrid sample, offers an effective channel for transfer of electrons from the CB of WO_3 to the VB of Fe_2O_3 followed by recombination of a majority of carriers. A minority of the electrons flow to the Pt counter electrode through the external circuit and then are used for H_2 generation. Simultaneously, photogenerated holes in the VB of WO_3 diffuse to the interface between WO_3 and electrolyte to promote the O_2 evolution reaction [53].

Liu et al. designed a facet-controlled WO_3 array, decorated with a distribution of dual co-catalysts. The process for fabrication of Ag/WO_3/ZnFe-LDH NSAs (Fig. 14a) involves initial generation WO_3 NSAs oriented perpendicular to the FTO substrate using a hydrothermal method. Then Ag NPs and ZnFe-LDH nanosheets are deposited on WO_3 by using a photoreduction method and an electrochemical synthesis process, respectively. SEM (Fig. 14b) and HRTEM image (Fig. 14c) of a selective area (red square) shows that the material has single-crystalline character, and that ZnFe-LDH nanosheets are attached to WO_3 nanosquares. All materials were found to have reproducibly rapid photocurrent responses in ON–OFF irradiation cycles, which demonstrates the improved PEC performances of Ag/WO_3/ZnFe-LDH NSAs (Fig. 14d). Furthermore, the results of long-term stability tests (Fig. 14e)

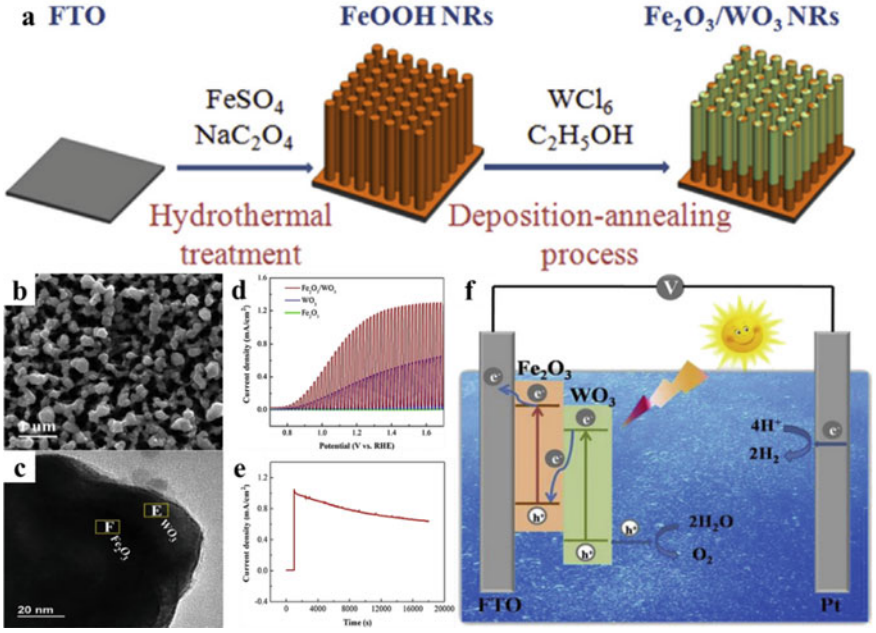

Fig.13 **a** Illustration of the process for preparation of Fe_2O_3/WO_3 NRs; **b** Top-view SEM image of Fe_2O_3/WO_3 NRs; **c** TEM image of Fe_2O_3/WO_3 NRs; **d** Photocurrent density versus potential curves for Fe_2O_3 NRs, Fe_2O_3/WO_3 NRs and WO_3 films; **e** Photostability of Fe_2O_3/WO_3 NRs in seawater (pH = 6.8) under continuous illumination; **f** Diagram for transfer and separation of photogenerated charges and holes in the Fe_2O_3/WO_3 NRs

showed that ca.90% of the initial activity exists after 24,000 s continuous illumination. Figure 14 f illustrates the mechanism of sunlight-promoted hydrogen production from SW in a PEC cell based on a $Ag/WO_3/ZnFe$-LDH NSA. Under illumination, photoexcited holes (h^+) are produced in WO_3 and then concentrate on the dominant {002} facet, while electrons (e^-) migrate to the edged {200} and {020} facets. This results in effective spatial separation of the photogenerated carriers. The plasmonic electrons of Ag generated by the LSPR effect migrate to the CB of WO_3 [54].

Shi et al. explored fabrication of a porous WO_3 film and applying this film as a photoanode for SW splitting. A WO_3 film was fabricated using the simple DA process (Fig. 15a). Inspection of Fig. 15b clearly shows that the surface morphology of the WO_3 film prepared using 5 DA cycles is smooth and that it contains many microspores. After the DA process is conducted for 25 cycles, the WO_3 film surface is rougher and WO_3 particles are larger (Fig. 15c). The WO_3 film generates a photocurrent density of 1.95 mA cm^{-2} at 1.23 V versus RHE under AM 1.5G (100 mW cm^{-2}) illumination (Fig. 15d). The stability of WO_3 film determined at 1.23 V versus RHE for 180 min (Fig. 15e) does not decay. In a suggested mechanism for operation of the WO_3 film under illumination (Fig. 15f), the WO_3 film generates electron–hole pairs, and the WO_3 CB electrons migrate to the FTO substrate, and then to the Pt

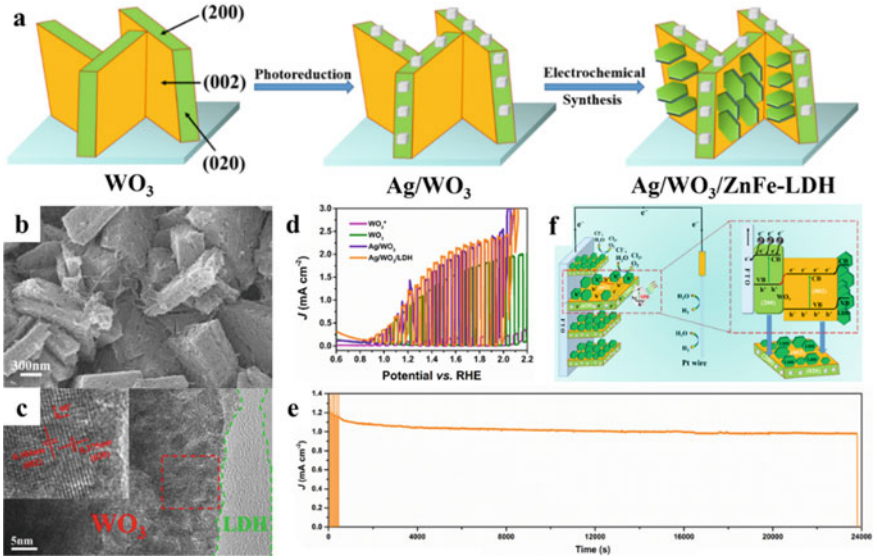

Fig.14 **a** Schematic of the fabrication of Ag/WO_3/ZnFe-LDH NSAs; **b** SEM images of Ag/WO_3/ZnFe-LDH NSAs; **c** HRTEM images of Ag/WO_3/ZnFe-LDH NSAs; **d** Photocurrent–potential curves using chopped AM 1.5 G light illumination; **e** Steady-state photocurrent 1.23 V versus RHE for Ag/WO_3/ZnFe-LDH NSAs photoanode. **f** Diagram of a PEC consisting of an Ag/WO_3/ZnFe-LDH NSAs photoanode, and a Pt counter electrode; the energy diagram for Ag/WO_3/ZnFe-LDH NSAs photoanode in the square box shows the basic mechanism for PEC seawater splitting

electrode, where they are used for reduction of protons in SW to produce hydrogen. Correspondingly, the holes in the VB of WO_3 promoted oxidation of chloride ions in SW to form Cl_2 [55].

Jadwiszczak et al. described a seawater splitting PEC cell containing a nanostructured tungsten trioxide photoanode, which has a high and stable photocurrent for production of Cl_2 with average 70% Faradaic efficiency. An SEM image of a ca.3-μm-thick mesoporous WO_3 film having pores that extend to FTO substrate is shown in Fig. 16a. The film consists of a network of individual particles with sizes of 20 to 30 nm and agglomerates including several NPs (Fig. 16b). The crystalline nature of the synthesized WO_3 was explored using TEM imaging of particles removed from the film (Fig. 16c). Figure 16d contains a linear sweep voltammetry photocurrent density–potential (j–E) plot for a ca.3-μm-thick WO_3 electrode under simulated AM 1.5G sun light (100 mW cm^{-2}) in SSW at an initial pH of 6.5. The WO_3 photoanode attained a large saturation photocurrent of 4.78 mA cm^{-2} at 0.88 V versus Ag/AgCl. Interestingly, the same photocurrent (uncorrected for the light losses within the FTO) is reached at the larger potential of 1.1 V when the WO_3 electrode was illuminated from the back side. Figure 16e shows the result of a WO_3 photoanode stability test performed in a 0.5 M NaCl at pH 2. The evolution of photocurrent as a function of time was followed at a potential of 0.76 V versus Ag/AgCl. The moderate

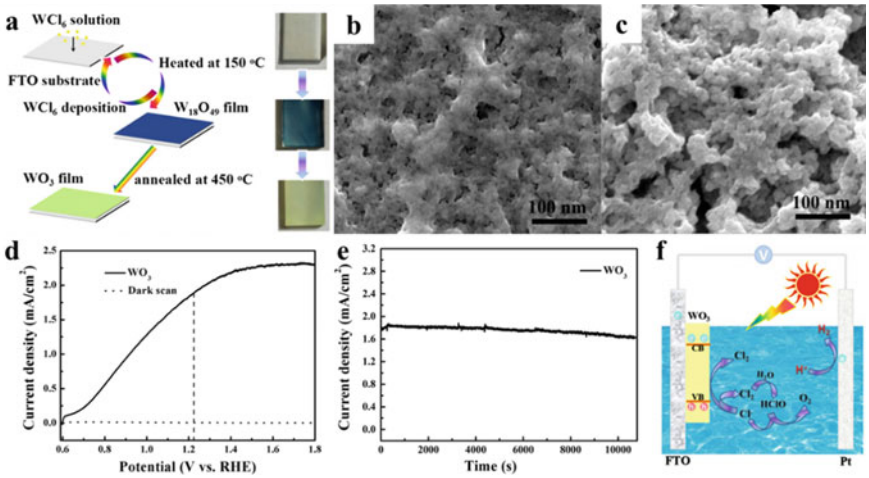

Fig.15 **a** Schematic of the preparation of the WO_3 film; **b** SEM image of the WO_3 film (5 DA cycles); **c** SEM image of the WO_3 film (25 DA cycles); **d** I–V curves of the WO_3 film; **e** Amperometric I–t curve of the WO_3 film; **f** The mechanism of PEC splitting of seawater on a WO_3 electrode

decline of the photocurrent is linked to accumulation of gas bubbles (principally O_2 cogenerated with Cl_2) within the WO_3 photoanode pores that cause a reduction of internal photoactive surface area. The latter electrode, used subsequently in a series of experiments, exhibited practically unchanged j–E behavior [56].

3.3.3 Other Metal Oxides-Based Photoelectrodes

Using Kirkendall diffusion, Patel et. al fabricated a semitransparent film of Co_3O_4, which is an earth-abundant material with a high absorption coefficient (Fig. 17a). The porous Co_3O_4 film enables an IPCE of more than 8% at an overpotential of 0.83 V in natural SW. The porous Co_3O_4 electrode exhibits remarkably high activity with an onset potential of ca.850 mV. Because stability of a PEC cell is an important issue, the performance of a PEC cell containing a Co_3O_4/FTO electrode for SW splitting and chronoamperometry (current–time characteristics) was determined using −0.34 V versus RHE (Fig. 17f). The results show that the Co_3O_4/FTO electrode has an initial current density of 2.7 mA cm^{-2} at a density of 1.6 mA cm^{-2} after 1000 s. At a current density of 25 mA cm^{-2}, a continuous jet of hydrogen bubbles along with a white precipitate is formed (Fig. 17g) [57, 58].

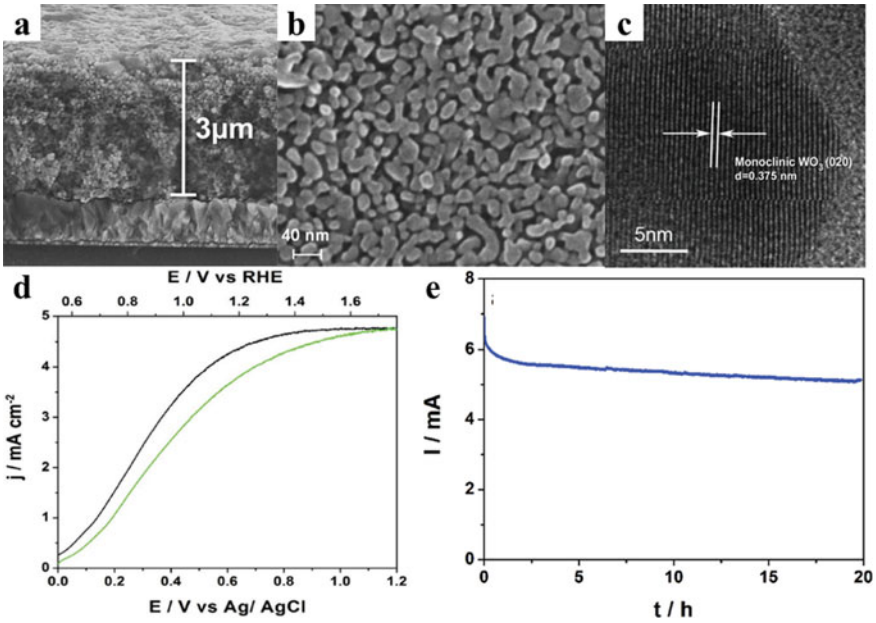

Fig.16 **a** SEM cross section and **b** top-down images of a NS WO_3 film; **c** TEM image of WO_3 removed from the substrate. **d** Photoanodic current versus potential (j–E) plots for a ca.3-μm-thick WO_3 electrode in simulated SW under AM 1.5G (100 mW cm^{-2}) illumination from the electrolyte side (black curve) and from the back side–through the FTO substrate (green trace). The latter results have not been corrected for light loss in the FTO; **e** SW splitting photocurrent–time curves recorded for a ca.1.5 cm^{-2} 3-μm-thick WO_3 photoanode illuminated with simulated sun light AM 1.5G (70–100 mW cm^{-2}) in a 0.5 M NaCl at pH 2

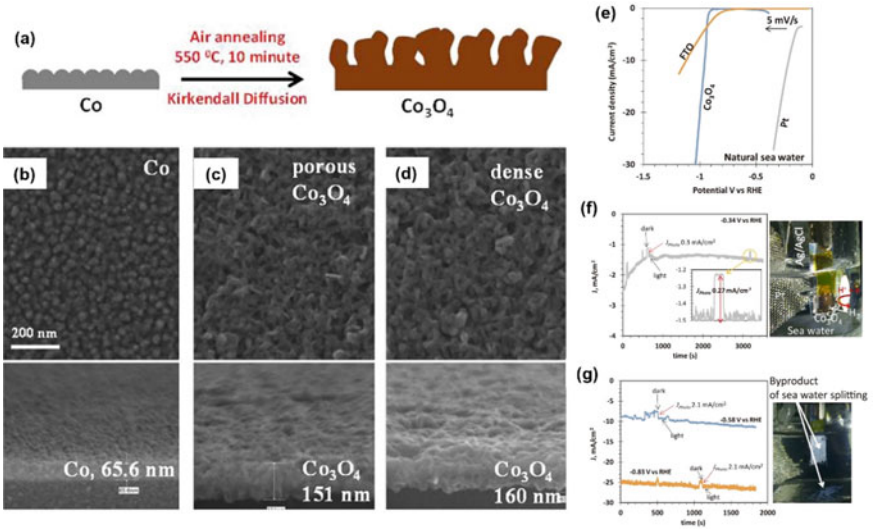

Fig. 17 **a** An illustration of the growth of porous Co_3O_4 film using Kirkendall diffusion-driven thermal oxidation. FE-SEM images of planar and cross-sectioned, **b** as deposited Co, Kirkendall diffusion grown, **c** porous, and **d** dense Co_3O_4 on the Si wafer. **e** Linear sweep voltammetry (LSV) measurements **f** J–t characteristic at an overpotential of 0.34 V versus RHE (inset shows the photoresponse after water splitting over 3000 s), and **g** J–t characteristic at over potential of 0.58 V and 0.83 V versus RHE

3.4 Non-oxide Photoelectrodes for Seawater Splitting

3.4.1 $BiVO_4$-Based Materials

The use of PEC anodes, comprised of n-type SC materials including ZnO, WO_3, $BiVO_4$, and Fe_2O_3, has been widely studied in the context of visible-light-promoted H_2 production systems. In this n-type SC family, bismuth vanadate ($BiVO_4$) is an outstanding photoanode due to its narrow bandgap energy (ca.2.4 eV), suitable CB and VB separation, earth abundance, and low cost. However, photocurrent densities produced by $BiVO_4$ anodes are well below the theoretical value of 7.5 mA cm^{-2}, because of a carrier mobility of only ca.4 $\times$ 10^{-2} $cm^2/V \cdot s$ and a hole diffusion length (Lp) of ca.70 nm. The properties enable efficient electron–hole recombination, which inhibits charge transfer and limits PEC efficiency. Doping and surface modification have been used to circumvent these hurdles and improve the PEC performance of $BiVO_4$ anodes in SW splitting.

One modification involves doping with Mo. For this purpose, RhO_2 nanoparticles, serving as a co-catalyst, were dispersed on Mo-doped $BiVO_4$ (Fig. 18a, b). An anodic photocurrent occurs with these electrodes, indicating that oxidation takes place under illumination (Fig. 18c). Dark currents (not shown here) of the $BiVO_4$, Mo-doped $BiVO_4$, and Mo-doped $BiVO_4$ with RhO_2 surface modification are approximately

several mA cm^{-2}, which is negligible compared with the photocurrents (Fig. 18c). The photocurrent of pure $BiVO_4$ at 1 V_{RHE} illuminated from the back side is about three times higher than when illuminated from the front side. In contrast, the photocurrent of Mo-doped $BiVO_4$ illuminated from the back side is about half of the value when illuminated from the front side. After Mo doping, the photocurrent is about six times higher and it increases after RhO_2 modification, especially at low potentials. Furthermore, the photocurrent arising from back-side illumination remains lower than that from the front side.

In the absence of RhO_2 modification, the photocurrent of Mo-doped $BiVO_4$ anode is about 18 mA cm^{-2} and decreases to about 12 mA cm^{-2} after 270 min illumination (Fig. 18d). After RhO_2 modification, the initial photocurrent is about 20 mA cm^{-2}, it decreases to 18.5 mA cm^{-2} within several minutes and then decreases slowly

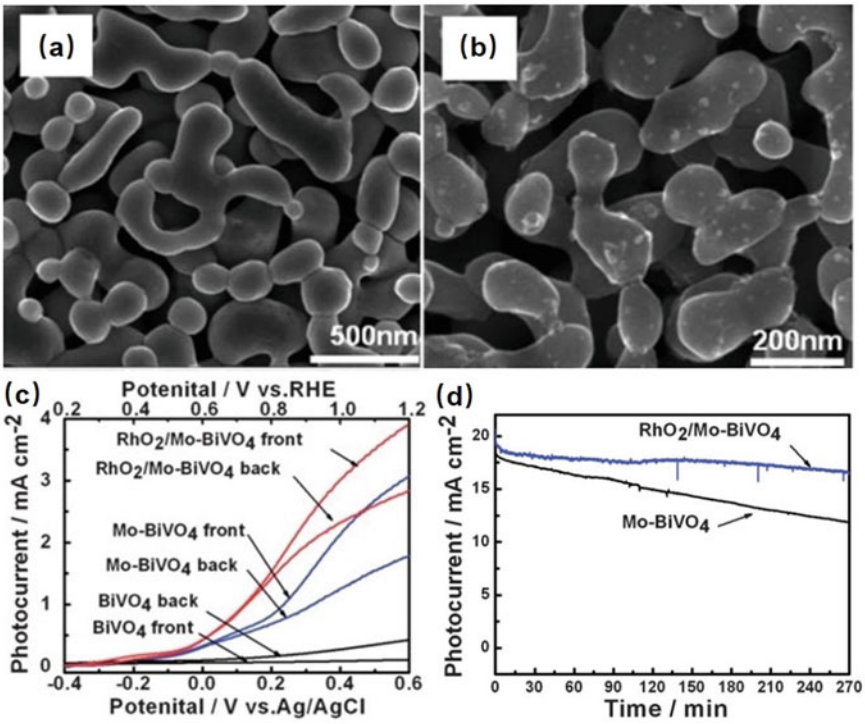

Fig. 18 **a** SEM images of Mo-doped $BiVO_4$ film surface. **b** SEM images of RhO_2 particles on the surface of Mo-doped $BiVO_4$ film. **c** Photocurrent–potential curves for $BiVO_4$, Mo-doped $BiVO_4$, and Mo-doped $BiVO_4$ with RhO_2 surface modification illuminated from the back side (FTO substrate/SC interface) and the front side (electrolyte/SC interface); electrolyte: natural seawater, a xenon lamp (full arc, $\lambda > 300$ nm). **d** Chronoamperometry (i–t) from the back side of Mo-doped $BiVO_4$ electrodes with and without RhO_2 modification in natural seawater; full-arc xenon lamp ($\lambda >$ 300 nm) with higher light intensity, a three-electrode system, the potential: 1 V versus Ag/AgCl

to 16.7 mA cm^{-2} within 270 min illumination, showing that the photostability of Mo-doped $BiVO_4$ is improved by loading with RhO_2 [21].

Figure 19a and b contains an SEM image of MoB/BVO and a TEM image of MoB/BVO. After modification of BVO by MoB, the surface becomes rough compared to that of BVO itself. Also, lattice defects exist close to the interface on the BVO side of the MoB/BVO sample, which are believed to be formed on the surface during cathodic potentiostatic polarization.

The PEC water-splitting performances of these photoanodes were determined in SSW under front one sun AM 1.5 G illumination. As can be seen by viewing Fig. 19c, pristine BVO in SW has a photocurrent of 1.45 mA cm^{-2} at 1.23 V_{RHE} with an onset potential of 0.5 V_{RHE}. The photocurrent densities of the modified Mo/BVO and B/BVO electrodes increase to 2.70 mA cm^{-2} and 3.75 mA cm^{-2} at 1.23 V_{RHE}, respectively. The photoanode obtained by further modification with MoB displays a photocurrent density of 4.3 mA cm^{-2} at the same potential, which is three times higher than that of untreated BVO. To corroborate the beneficial effect of modifying MoO_3, PEC activity and stability in SW were evaluated. Encouragingly, MoB/BVO has similar photocurrent densities in SW and SSW (inset of Fig. 19d), a 70 stability in SW (Fig. 19d). Note that an obvious fluctuation exists in the J–t curve of MoB/BVO as a consequence of alternating corrosion and passivation. In contrast, the photoresponse is larger at the initial time, suggesting that a passivated or protection layer is formed on the surface. As suggested by these above observations, an active surface remains during the entire process, which leads to stable and efficient performance. The enhanced PEC performance of MoB/BVO is a consequence of the acceleration of carrier separation which reduces electron–hole recombination at the surface.

As shown in Fig. 19e and f, the possible rate-determining steps for the process occurring on BVO are generation of *O from *OH (*OH $\rightarrow$ *O + H^+ + e) with $\Delta G = -1.19$ eV and formation of Cl_2 from *Cl and Cl^- (*Cl + Cl^- $\rightarrow$ Cl_2(g) + e) with $\Delta G = -1.29$ eV. The rate-determining step for the process occurring with MoB/BVO changes to formation of *OOH from *O (*O + H_2O $\rightarrow$ *OOH + H^+ + e) with $\Delta G = -1.32$ eV, and then to Cl_2 production with $\Delta G = -1.66$ eV. The results suggest that the chlorine evolution reaction (CER) is favored over the OER on MoB/BVO and BVO. Varying pH experiments show that Cl_2 is still produced in SSW using BVO even when the pH is higher than 9. A catalyst corresponding to a location closer to the volcano top usually have a higher electrocatalytic activity. Thus, B/BVO and MoB/BVO promote faster CERs at low overpotentials (0.10 V and 0.15 V) than BVO (0.51 V) and Mo/BVO (0.59 V) (Fig. 19g), showing that dual atom doping affects the activity of Bi.

Mo doping causes a slight change of the oxophilicity of Bi, while B doping greatly lowers its oxophilicity and leads to strong Cl adsorption, while Mo slightly tunes the adsorption energy. This is consistent with the experimental results and the enhanced PEC activity of B/BVO. Furthermore, the effects on dissolving energy of Mo and B modification of BVO are shown in Fig. 19h. The dissolving energies are in the order MoB/BVO > Mo/BVO > B/BVO > BVO, suggesting that strong bond between Mo and B helps to protect BVO from corrosion [58].

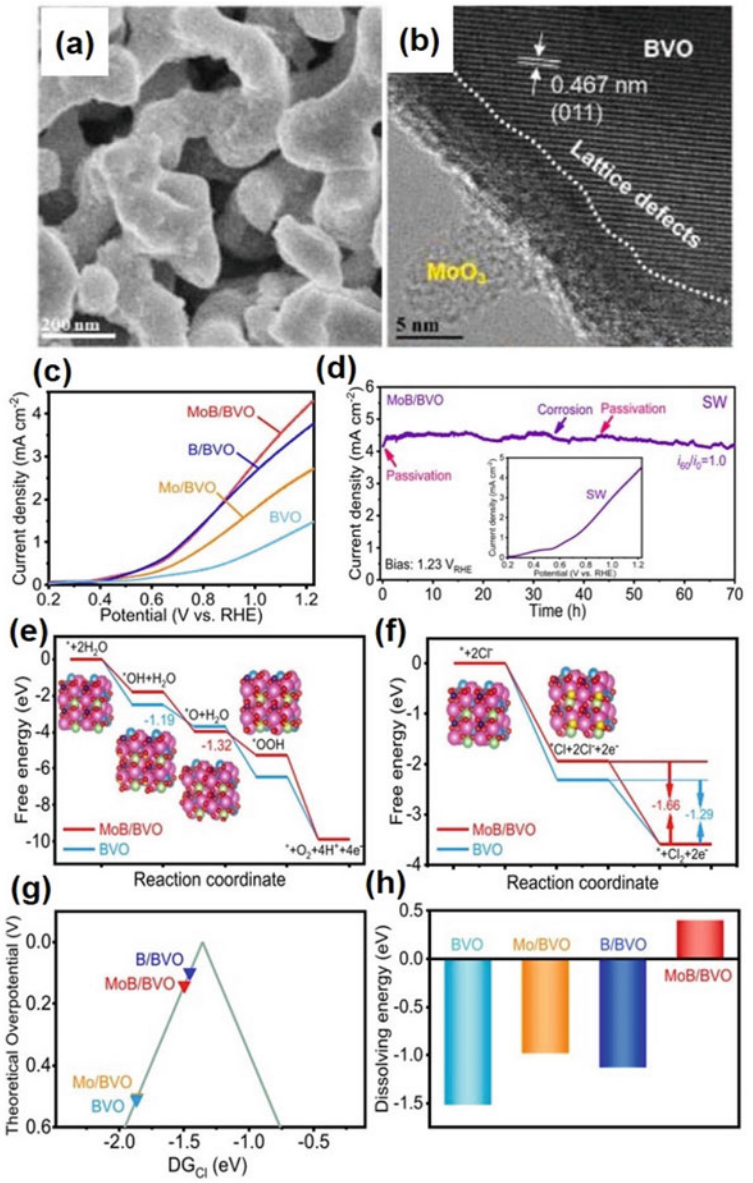

Fig. 19 **a** SEM images of MoB/BVO. **b** HRTEM images of MoB/BVO. **c** J–V curves in SSW (pH = 8) under AM 1.5 G (100 mW cm^{-2}) front-side illumination. **d** long-term durability of MoB/BVO at 1.23 V_{RHE} in SW under AM 1.5G (100 mW cm^{-2}) front-side illumination. Inset shows the J–V curve of electrode in SW under AM 1.5G (100 mW cm^{-2}) front-side illumination. **e** Results of DFT calculated Gibbs free energies for the four elementary steps of the OER. **f** Two elementary steps of the CER on BVO and MoB/ BVO. **g** Theoretical volcano plot of CER on BVO, Mo/BVO, B/BVO, and MoB/BVO. Left and right branches refer to catalysts that bind strongly and weakly to Cl^- compared with the optimal adsorption. **h** Dissolving energy of the corresponding electrodes

TEM images of NiMoOx/BVO after various times (initial, 20 h) in Fig. 20a–d show that with an increase in time, the surface of the material becomes smoother, and after 20 h a smooth amorphous layer covers on the surface (Fig. 20b and d). During the entire time, the Mo content on the surface remains relatively unchanged at 1.0–3.0 at%, suggesting a slight loss of Mo occurs to passivate the surface for protecting the BVO from corrosion.

Inspection of the linear scanning voltammetry (LSV) curves displayed in Fig. 20e shows that MoO_x/BVO has a photocurrent density of 2.06 mA cm^{-2} at 1.23 V_{RHE}, a value higher than that of pristine BVO (1.64 mA cm^{-2}). The photocurrent density of NiO_x-deposited BVO (NiO_x/BVO) is 3.02 mA cm^{-2} at 1.23 V_{RHE}, and a negative shift of the onset potential from 0.50 V_{RHE} (BVO) to 0.38 V_{RHE} takes place. Furthermore, compared to NiO_x/BVO, BVO possessing a $NiMoO_x$ layer has a photocurrent density of 3.30 mA cm^{-2} at 1.23 V_{RHE}, and the onset potential shifts to 0.50 V_{RHE}. The LSV curve and a stability test (Fig. 20f) demonstrate that $NiMoO_x$/BVO has a photocurrent of 3.0 mA cm^{-2} at 1.23 V_{RHE} in SW (inset of Fig. 20f). Also, $NiMoO_x$/BVO remains stable in SW as indicated by maintenance of 91% of the initial photoresponse after

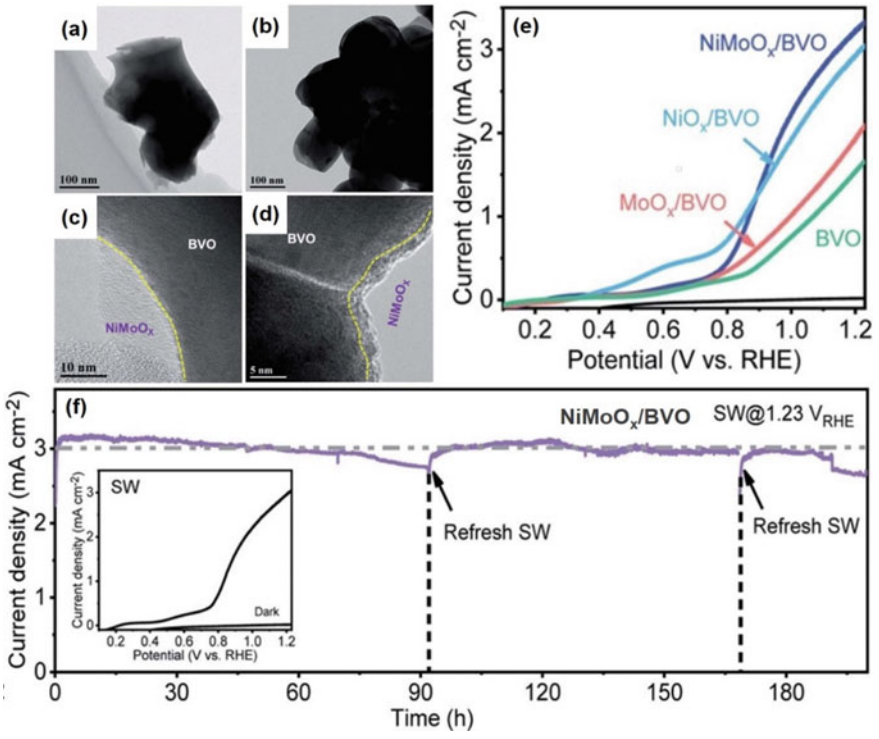

Fig. 20 **a–d** TEM images of NiMoOx/BVO after various times (initial and 20 h). **e** LSV curves of BVO, NiOx/BVO, MoOx/BVO, and NiMoOx/BVO under back-side illumination. **f** Current density of NiMoOx/BVO at 1.23 V_{RHE} in SW under back-side illumination. Inset is the LSV curve of NiMoOx/BVO in SW

190 h. This observation suggests that $NiMoO_x$/BVO in a PEC system in SW has the highest stability among other state-of-the-art materials. It should be mentioned that $Ca(OH)_2$ and $Mg(OH)_2$ deposit on the cathode during long-term operation. Thus, the electrolyte needs to be changed and cathode must be cleaned at various times during the 90-h period to avoid the deposits from influencing the PEC stability tests [59, 60].

A variety of BiFeVO NPs have very large specific surface areas that are connected by highly conductive CNTs. These features lead to high light absorption and suppression of electron–hole recombination, both of which greatly improve PEC efficiency. The architectural components of one member of this group, $BixFe_{1-x}VO_4$ @CNT (BiFeVO@CNT), are shown in Fig. 21a. The diameters of both MWCNTs and BiFeVO NPs are about 20 nm (Fig. 21b, c, and d).

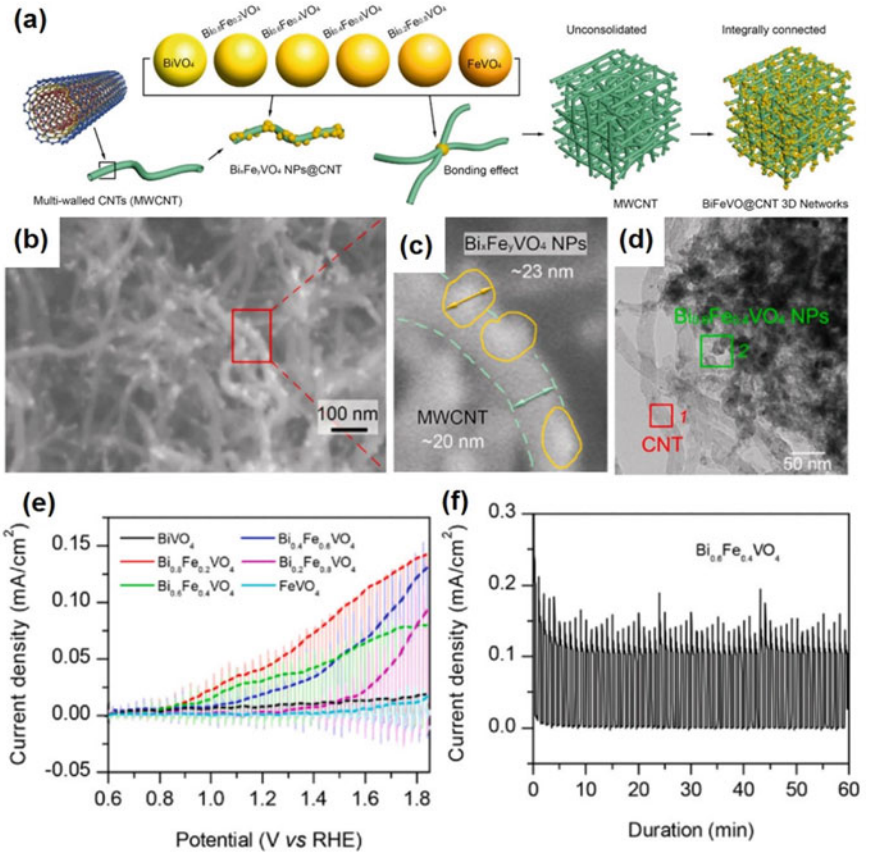

Fig. 21 **a** Sketch of the fabrication process and architectural components of $Bi_{0.6}Fe_{0.4}VO_4$ @CNT. **b** SEM images. **c** Enlarged views denoted by red squares in **b**. **d** TEM image of $Bi_{0.6}Fe_{0.4}VO_4$ @CNT. **e** LSV curves of BiFeVO@CNT photoanodes. **f** PEC stability of $Bi_{0.6}Fe_{0.4}VO_4$ @CNT in SW

The plots displayed in Fig. 21e, corresponding to PEC measurements in SW, show that $Bi_{0.8}Fe_{0.2}VO_4$ @CNTs and $Bi_{0.6}Fe_{0.4}VO_4$ @CNTs have respective 0.04 and 0.03 mA cm^{-2} PEC current densities at about 1.20 V versus RHE. However, gradually increasing the applied potential causes the current densities of $Bi_{0.4}Fe_{0.6}VO_4$ @CNTs and $Bi_{0.2}Fe_{0.8}VO_4$ @CNTs to become 1.50 and 1.78 V, respectively, which are larger than that of $Bi_{0.6}Fe_{0.4}VO_4$ @CNTs. This change may be a consequence of the fact that a gradual increase of Fe content brings about formation of higher amounts of iron oxide in the independently located electrode-surface regions of $FeVO_4$ and $BiVO_4$. The existence of these regions decreases the surface overpotential and causes the current density to increase significantly.

The PEC stability of $Bi_{0.6}Fe_{0.4}VO_4$ @CNTs in SW is indicated by its unchanging photocurrent over a 60-min period under a 1.5 V bias versus Ag/AgCl (Fig. 21f). Thus, the composite nanostructure composed of $BiVO_4$ mixed with amorphous Fe and carbon nanotubes which leads to a higher hydrogen production efficiency and stability for PEC in SW. This finding serves as a reference for designs of materials for PEC anodes for hydrogen production from SW [61].

3.4.2 N, S-Based Photoelectrodes

Along with metal oxides, different N, S-based materials, which have narrower band gaps, have also gained attention for their use in construction photoelectrodes for PEC water splitting. This has led to the development of visible light-absorbing metal sulfides such as CdS, In_2S_3, SnS_2, Bi_2S_3, and GaN. In the group of these types of metal sulfides [62–64].

In_2S_3 has attracted attention due to its meritorious features including moderate band gap, high photogenerated charge-carrier mobility, and large absorption coefficient. Sharma et al. fabricated In_2S_3/In_2O_3 nanocomposite (Fig. 22a). FE-SEM images show that In_2S_3/In_2O_3-B-5 has a uniform nanopyramid-like structure that is uniformly distributed on the FTO surface (Fig. 22b). The highly magnified F-SEM image is displayed in Fig. 22c, which shows that the bottoms of the nanopyramid In_2S_3/In_2O_3-B-5 are interlaced. The limiting photocurrent density of In_2S_3/In_2O_3-B-5 is ca. 2.99, a 2.11-fold higher value than those of In_2S_3/In_2O_3-A-5 and In_2S_3/In_2O_3-C-5 (Fig. 22f). The In_2S_3/In_2O_3 nanocomposite generates a photocurrent density of 0.83 mA cm^{-2} at 1.18 V versus RHE in SSW and an unaltered photocurrent density of up to 1000 s (Fig. 22g). In Fig. 22h, the charge separation and ready charge transport in this material are illustrated, which further inhibit the recombination process [65].

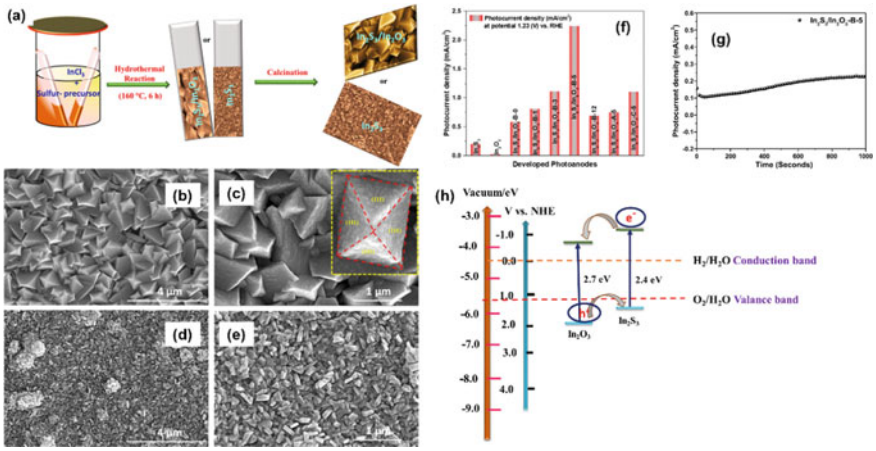

Fig. 22 **a** Representation of the creation of In_2S_3/In_2O_3 nanopyramids and nanobrick-type In_2S_3 nanostructures using the hydrothermal technique. FE-SEM images of the In_2S_3/In_2O_3-B-5 nanopyramids: **b**, **c** low and high magnification images, respectively, and **d**, **e** low and high magnification images of In_2S_3, respectively. **f** photocurrent densities of the developed photoanodes at a potential of 1.23 V versus the RHE in 0.5 M Na_2SO_4. **g** PEC stability of In_2S_3/In_2O_3-B-5 under an applied potential of 0.981 V versus the RHE for 1000 s under continuous illumination in 3.5% saline water. **h** Schematic representation of the band alignment of In_2S_3, In_2O_3 in the composite, and the charge transport mechanism

Zhou et. al. carried out studies on an interesting material comprised of few-layer cationic vacancy containing T/Td heterostructured ReS_2 nanosheets. T@Td-ReS_2 has a sheet-like rectangular structure with a plane size of 4–20 μm and thickness of 5–30 nm (Fig. 23a). Inspection of the HRTEM image reveals that a lateral 2D heterostructured interface is present between the T and Td phases having lattice fringes of 0.285 and 0.296 nm indexed to the respective (100) planes of the two phases (Fig. 23a). The nanosheets have very high HER activity with a small overpotential (η) of −173 mV (vs RHE after iR correction) and catalytic current density of -10 mA cm^{-2} (Fig. 23b, c). Moreover, the HER performance is stable for over 12 h in SSW solutions having a wide range of salinities (Fig. 23d). Figure 23e shows a representation of the transfer of "hot" electrons occurring in the lateral T-ReS_2 and Td-ReS_2 heterostructure (T@Td-ReS_2) [65].

Some studies indicate that multi-component metal sulfides have higher stabilities than those of binary metal sulfides. In one effort, Cheng et al. constructed orthorhombic Ag_8SnS_6 (Fig. 24a, b). Current density–applied voltage versus time plots for Ag_8SnS_6 in aqueous Na_2S (0.35 M) + K_2SO_3 (0.25 M) is given in Fig. 24c and d which contains current density–applied voltage curves for this material in 0.5 M NaCl in the range of 0.6–1.6 V versus RHE. The maximum PEC performance of Ag_8SnS_6 in SSW is 2.5 mA cm^{-2}. A schematic diagram describing the PEC SSW splitting process using this substance is shown in Fig. 24e [66].

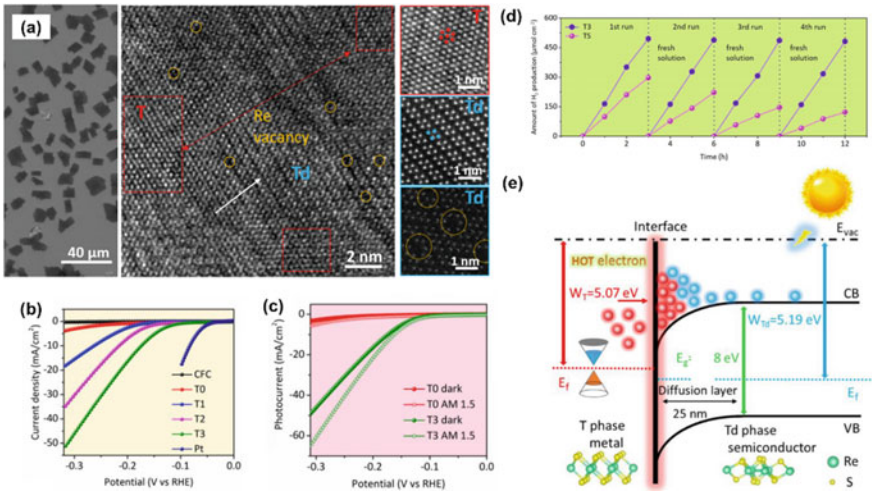

Fig. 23 **a** SEM image and HRTEM image of the lateral T@Td-ReS_2 heterostructures (the white arrow points to the lattice interspacing change from the T to Td phases) and three STEM images of T-ReS_2, Td-ReS_2 phases, and Re vacancies (marked by yellow circles). The red line indicates the distance between two adjacent T-ReS_2 clusters. **b**, **c** LSV curves. **d** LSV curves in dark and light fields. **e** Schematic of the "hot" electron transfer process between T and Td-ReS_2 phases. **f** Free energies of different active sites in the Td-ReS_2 and T@Td-ReS_2 phases. H ∗ represents the intermediate adsorbed state. **g** Calculated cationic impurity adsorption energies of T@Td-ReS_2 with V_S and V_{Re}. **h** Schematic illustration of cationic adsorption on the T@Td-ReS_2 nanosheets with V_{Re} in seawater

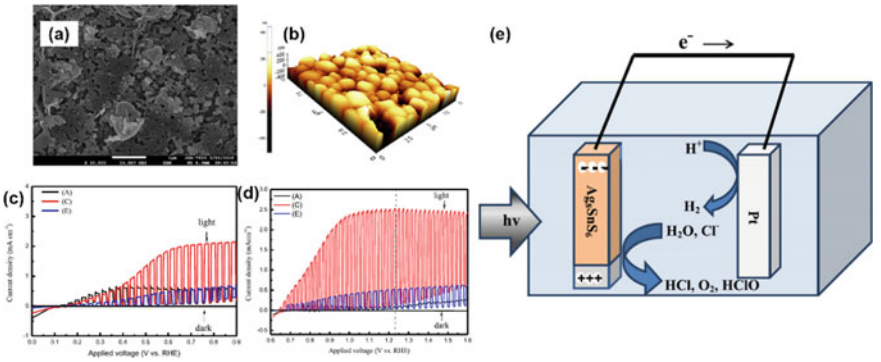

Fig. 24 FE-SEM (**a**) and AFM (**b**) images of orthorhombic Ag_8SnS_6. **c** Current density–applied voltage plots in the range of 0–0.9 V versus RHE. **d** Current density–applied voltage plots in the range of 0.6–1.6 V versus RHE. **e** Schematic diagram of a PEC cell using Ag_8SnS_6 photoelectrode in 0.5 M NaCl solution

PEC cells with photoelectrodes comprised of III-nitride SCs, e.g., $Al_xGa_{1-x}N$ and $In_xGa_{1-x}N$, have received attention because their band-edge potentials are in the range needed for water splitting. Lee et al. produced a AlGaN/GaN heterostructure on a sapphire substrate that has production rates of H_2 of 95.5 μmol cm^{-2} h in SW. Figure 25a depicted top views of constructs of working electrodes labeled WE-I ($Al_{0.2}Ga_{0.8}N$/GaN heterostructure) and WE-II (u-GaN single layer). These electrodes have a working area of 1 × 1 cm^2 sliced from respective wafers with u-GaN layer and undoped $Al_{0.2}Ga_{0.8}N$/ u-GaN layer, and epoxy glue preventing contact between the electrolyte and Ti/Al contact. Inspection of Fig. 25b, d shows that the typical photocurrent density of the PEC reaction using WE-I is higher than that using WE-II. Besides, a higher H_2 and HCOOH production rate is achieved by WE-I than WE-II (Fig. 25c, e). A preliminary result of an evaluation of the stability of this system is given in 24 d [67] (Table 2).

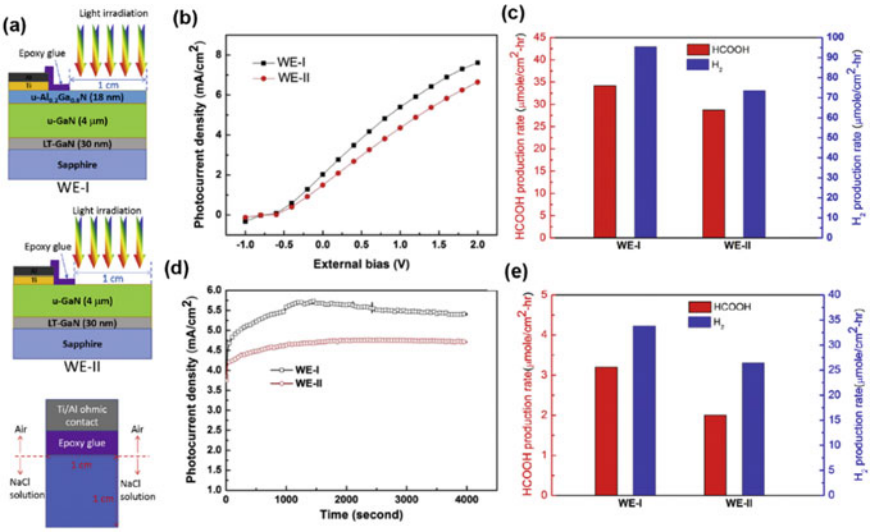

Fig. 25 **a** Schematic of working electrode layer structures: WE-I with $Al_{0.2}Ga_{0.8}N$/GaN heterostructure, WE-II with u-GaN single layer, top view of working electrodes. Arrows indicate the incident direction of light during the PEC process. **b** Photocurrent density (Jph) as a function of external bias voltage, **d** photocurrent density versus time. The applied bias to the working electrodes was maintained at 1.0 V versus the reference electrode (Ag/AgCl). **c** Typical production rates of H_2 and HCOOH for PEC processes conducted at a bias of 1 V. **e** Production rates of H_2 and HCOOH when additional biases are supplied by using a-Si solar cell

Table 2 Summary of the PCE performance of several PEC systems including the water sources, HER performances, and light sources

Photocatalyst			Water source	HER performance	Light source	Refs.
Metal oxides-based materials	TiO_2-based materials	TiO_2 nanotubular	3.5 wt.% NaCl	3 mA cm^{-2} at 1.4 V	Simulated sunlight (AM1.5G)	[27]
		TiO_2 nanotubular	Natural seawater	105 μmol cm^{-2} h^{-1}	UV–VIS (350–450 nm)	[39]
		TiO_2 nanotubular	Natural seawater	215 μmol cm^{-2} h^{-1}	UV–VIS (350–450 nm)	[68]
		TiO_2 nanotubular	Natural seawater	270 μmol cm^{-2} h^{-1}	UV–VIS (350–450 nm)	[69]
		Pt/TiO_2 nanotubular	Natural seawater	277 μmol cm^{-2} h^{-1}	UV–VIS (350–450 nm)	[70]
		Fe_2O_3–TiO_2	artificial seawater	2.0 mA cm^{-2} at 1.23 V vs. RHE	Simulated sunlight (AM1.5G)	[40]
		TiO_2@g-C_3N_4	Natural seawater	1.6 mA cm^{-2} at 1.23 V vs. RHE	Simulated sunlight (AM1.5G)	[7]
		CdS/TiO_2	0.5 M NaCl solution	0.494 mA cm^{-2}	VIS ($\lambda > 400$ nm)	[43]
		p-Si/TiO_2/NiO_x	Artificial seawater	10 mA cm^{-2} (0.7 V_{RHE}); 20 mA cm^{-2} (0.9 V_{RHE})	Simulated sunlight (AM1.5G)	[29]

(continued)

Table 2 (continued)

Photocatalyst			Water source	HER performance	Light source	Refs.
		GO/TiO_2	Artificial seawater	73.14 μmol cm^{-2} h^{-1}	UV–VIS (320–780 nm)	[71]
		In_2S_3/Anatase/Rutile TiO_2	Artificial seawater	1.57 mA cm^{-2} at 1.23 V vs. RHE	Simulated sunlight (AM1.5G)	[72]
		Bi shell-BiOI core microspheres/TiO_2	Artificial seawater	1.42 mA cm^{-2} at 1.23 V vs. RHE	Simulated sunlight (AM1.5G)	[73]
		TiO_2	Artificial seawater	57.8 μA cm^{-2} at 1.23 V vs. RHE	UV–VIS	[21]
		CoPi/MOF/TiO_2	Simulated seawater	1.8 mA cm^{-2}	Simulated sunlight (AM1.5G)	[74]
	WO_3-based materials	WO_3/g-C_3N_4 nanosheet arrays	Natural seawater	0.73 mA cm^{-2} at 1.23 V versus RHE	Simulated sunlight (AM1.5G)	[53]
		a-Fe_2O_3/WO_3 nanorod arrays	Natural seawater	1 mA cm^{-2} at 1.23 V vs RHE	Simulated sunlight (AM1.5G)	[75]
		Ag/WO_3/ZnFe-LDH NSAs	Natural seawater	38.18 μmol h^{-1}	Simulated sunlight (AM1.5G)	[54]
		WO_3	Simulated seawater	4.5 mA cm^{-2} at 0.76 V versus Ag/AgCl	Simulated sunlight (AM1.5G)	[55]
		WO_3	Natural Seawater	1.95 mA cm^{-2} at 1.23 V vs RHE	Simulated sunlight (AM1.5G)	[56]
	Other metal oxides-based materials	Co_3O_4	Natural seawater	J = 25 mA cm^{-2}, η = 0.8 V	Simulated sunlight (AM1.5G)	[57]

(continued)

Table 2 (continued)

Photocatalyst			Water source	HER performance	Light source	Refs.
Other oxides-based materials	$BiVO_4$-based materials	$BiVO_4$	Natural sea water	2.16 mA cm^{-2}	Solar (AM 1.5G,100 m W cm^{-2})	[21]
		$MoB/BiVO_4$	Natural sea water	4.30 mA cm^{-2}	Solar (AM 1.5G,100 m W cm^{-2})	[74]
		$NiMoO_x/BiVO_4$	Simulated seawater Natural sea water	3.30 mA cm^{-2} 3.0 mA cm^{-2}	Solar (AM 1.5G,100 m W cm^{-2})	[59]
		$BiVO_4$	Natural sea water	0.6 mA cm^{-2}	Solar (AM 1.5G,100 m W cm^{-2})	[9]
		$Bi_xFe_{1-x}VO_4$@CNTs	Natural seawater	0.1 mA cm^{-2} at 1.5 V versus Ag/AgCl	500 W xenon arc lamp	[61]
Non-oxidized based materials	N, S-based materials	T@Td-ReS_2	Simulated seawater	−173 mV (vs. RHE at −10 mA cm^{-2})	Simulated sunlight (AM1.5G)	[76]
		In_2S_3/In_2O_3	Simulated seawater	0.83 mA cm^{-2} at 1.18 V vs. RHE	Simulated sunlight (AM1.5G)	[65]
		Ag_8SnS_6	Simulated seawater	2.5 mA cm^{-2} at 1.23 V vs. RHE	Simulated sunlight (AM1.5G)	[66]
		AlGaN/GaN	Natural seawater	95.5 μmol cm^{-2} h^{-1}	300W Xe lamp	[67]

4 Implementation

4.1 Introduction

Solar energy is a key renewable resource that could meet the world's energy needs in an environmentally sustainable manner. However, the intermittency of sunlight requires that cost-effective energy storage methods be incorporated in large-scale solar utilities. Ideal approaches that can be utilized for this purpose involving storing solar energy in the form of chemical bonds in energy-dense substances, like H_2. However, another drawback of solar energy facilities is that they are solar flux limited, which necessitates the use of large land for them to generate levels of energy. Land area is costly and has potential environmental consequences. Thus, the availability of affordable land and need for high solar output make desert environments desirable. However, the scarcity of water resources in these regions is not compatible with the use of water splitting to generate H_2 [77].

4.2 Efficiency and Cost

4.2.1 Overall Solar-to-Hydrogen Conversion Efficiency (η_{STH})

PEC water-splitting cell performance is quantified most often by using solar-to-hydrogen conversion efficiency (η_{STH}). The η_{STH} value is directly related to the capability of a photoabsorbing material to generate hydrogen under unassisted conditions and, consequently, it is used to compare the solar-induced water-splitting efficiencies of PEC devices. The η_{STH} value is defined as the amount of chemical (H_2) energy produced by incident solar energy. Under these conditions, the voltage versus reference electrode or the open-circuit potential is insignificant. For a two-electrode PEC, η_{STH} corresponds to the rate of hydrogen production (mmol of H_2/s) multiplied by the change in Gibbs free energy required for water splitting (237 kJ/mol of H_2 at 25 °C) divided by the incident solar power density, as shown in Eqs. 4 and 5

$$\eta_{STH}(\%) = \left[\frac{\text{mmol of } H_2/\text{s} \times 237 \text{ kJ mol}^{-1} \times \eta_F}{P_{Total}(\text{mW cm}^2) \times \text{Illuminated area}(\text{cm}^2)}\right]_{AM1.5G} \times 100\% \quad (4)$$

$$\eta_{STH}(\%) = \left[\frac{J_{SC}\left(\text{mA cm}^{-2}\right) \times 1.23(V) \times \eta_F}{P_{Total}(\text{mW cm}^2) \times \text{Illuminated area}(\text{cm}^2)}\right]_{AM1.5G} \times 100\% \quad (5)$$

where J_{sc} is the normalized short-circuited photocurrent density in mA cm^{-2}, 1.23 V is the thermodynamic redox potential of water, η_F is the Faradaic efficiency for HER, and P_{Total} is the normalized intensity of incident light illuminating the SC surface, in mW cm^{-2}. Faradaic efficiency η_F, related to the ability of a photoelectrode to

produce the desired gas (H_2 or O_2), is the ratio of the actual gas generated defined time period as expressed in Eqs. 6 and 7,

$$\eta_F = \frac{Actual\ gas\ generated(\frac{mmol}{cm^2 s})}{Theoretical\ gas\ generated(\frac{mmol}{cm^2 s})} \times 100\% \tag{6}$$

$$\eta_F = \frac{Actual\ gas\ generated(\frac{mmol}{cm^2 s})}{\frac{Q}{2F}} \times 100\% \tag{7}$$

where Q represents the amount of electrical charge utilized and F is the Faradaic constant (ca. 96,500 C/mol).

For one sun illumination and a Gibbs free energy (237.13 MJ kg^{-1} at 25 °C and 1 atm), η_F corresponds to a H_2 production rate of ca. 150 μmol h^{-1} cm^{-2} or a photocurrent density of ca. 8 mA cm^{-2} for a PEC cell with a 100% theoretical maximal Faradaic efficiency. To obtain that level of efficiency, a photocatalysts would need to have an absorption edge higher than 600 nm and an apparent quantum yield (AQY) of 60%, calculated using Eq. 8, with N_{H2} and $N_{photons}$ being the numbers of generated H_2 molecules and incident photons, respectively [3, 78].

$$AQY(\%) = \frac{numbers\ of\ used\ electrons\ for H_2}{numbers\ of\ incident\ photons} = \frac{2N_{H_2}}{N_{photons}} \cdot 100\% \tag{8}$$

4.2.2 Photocurrent Density (j_p)

The generated photocurrent density (j_p), related to the ability of a photoelectrode to promote the water-redox reaction, is determined with respect to 1.23 V versus RHE for a photoanode and 0 V versus RHE for a photocathode. Before measuring j_p–V, the electronic-conductivity type of the SC needs to be determined because it governs the direction that the potential scan should be swept. Under biasing or illumination conditions, a minority of the charge carriers in a p-type SC and n-type SC drive the respective HER and OER (Fig. 26, region (III)). Forward biasing results in the formation of an accumulation layer in the region of space charge that is unfavorable for chemical reactions (Fig. 26, region II). Biasing carried out at a higher reverse bias (Vdark-onset) causes the Schottky barrier to lower and/or the breakdown of the SC, thereby generating a significant amount of dark current (Fig. 26, region (IV)). In this case, the SC behaves more like a metal to produce more dark current than the photocurrent. Therefore, biasing should be given from $V_{dark\text{-}onset}$ to V_{onset} for j_p-V measurements [79].

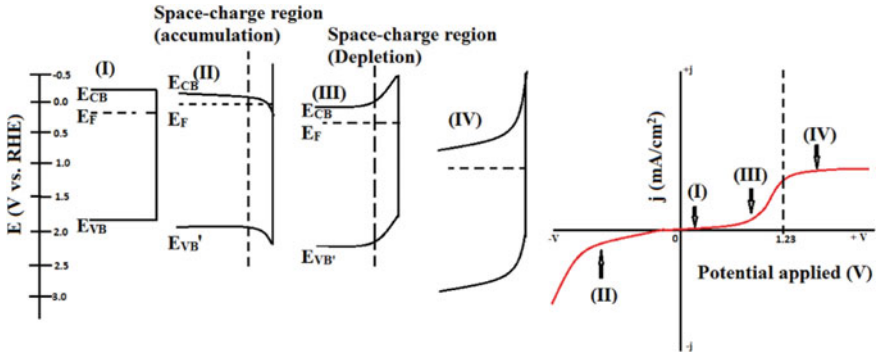

Fig. 26 Influence of biasing on band edges of a photoanode. (I) Electrode at flat band potential; (II) Electrode at the potential < flat band potential; (III) Electrode at potential > flat band potential; (IV) Electrode at a large reverse-bias potential, causing the saturation of photocurrent. The corresponding jp–V plot is given to the right of the figure

4.2.3 Incident Photon-to-Current Conversion Efficiency (IPCE)

The incident photon-to-current conversion efficiency (IPCE) is the ratio of the output flux of electrons producing hydrogen to the incident photon flux when an electrode is illuminated by using monochromatic light. IPCE data, accumulated using zero-bias or short-circuit conditions, can be integrated over the wavelength range of the solar spectrum to determine the highest STH efficiency possible. IPCE is experimentally determined using a potentiostat in a chronoamperometric mode and measuring photocurrent densities at different wavelengths. At a given wavelength, IPCE is expressed in Eq. 9,

$$IPCE(\lambda) = \frac{|j_p(\mathrm{mA/cm^2})| * c1239.8(V \times \mathrm{nm})}{P_{\mathrm{mono}}(\mathrm{mW\ cm^{-2}})\lambda(\mathrm{nm})} \tag{9}$$

where 1239.8 (V × nm) is the product of the speed of light (c) and Planck's constant (h), P_{mono} is the power density of the monochromatic light, and λ is the wavelength of incident light at which P_{mono} is observed. Alternatively, IPCE can be expressed in Eq. 10

$$IPCE(\lambda) = \frac{\text{no. of electrons generated/cm}^2\text{/s}}{\text{no. of photons incident/cm}^2\text{/s}}. \tag{10}$$

The assumption is that all generated electrons (and holes) produce H_2 (and O_2) instead other by-products, which means that the Faradaic efficiency, η_F, for gas evolution is ca. 100%. However, it has been recommended that H_2 and O_2 evolution be quantified to determine the η_F for overall water splitting. IPCE is useful in evaluating device performance in terms of electrons generated per incident photon when the spectral variation of the photon energies is considered. IPCE is best described

by using the following example. When equal numbers of photons at two different wavelengths are incident on two photoactive materials, and an equal number of electrons are generated at both wavelengths for both materials, then the IPCE of both materials is the same independent of whether differences exist in their energy levels [78].

4.2.4 Applied Bias Photon-to-Current Efficiency (ABPE)

When a bias is applied to the photoelectrode, the efficiency characterization parameter becomes the applied bias photon-to-current efficiency (ABPE). ABPE is the photocurrent density per incident photon absorbed as given in Eq. 11,

$$\eta_{\mathrm{ABPE}} = \left[\frac{|\mathrm{j_p}(\mathrm{mA\,cm^{-2}})| \times [1.23 - |V_\mathrm{b}|] \times \eta_\mathrm{F}}{\mathrm{P_{Total}}(\mathrm{mWcm^2}) \times \text{Illuminated area}(\mathrm{cm^2})} \right] \tag{11}$$

where $\mathrm{j_p}$ represents the photocurrent density and $\mathrm{V_b}$ is the potential applied between the WE and the CE. In determining the inherent performance of an electrode, ABPE can be used to determine the optimum existing between the maximum path corresponding to the photon absorption and the effective charge transfer diffusion length of a material.

The IPCE and ABPE parameters are diagnostic of the efficiencies of the PEC systems that are related by the expression in Eq. 12,

$$ABPE = \frac{IPCE}{absorptance} \tag{12}$$

where absorptance is the ratio of e^-/h^+ pairs produced per photon per area, which is measured using the Beer–Lambert law.

Using the characterization parameters described above, it is possible to create a fundamental flowchart (Fig. 27) that can be used for the design of industrial-level PEC system for photoelectrochemical hydrogen production [80].

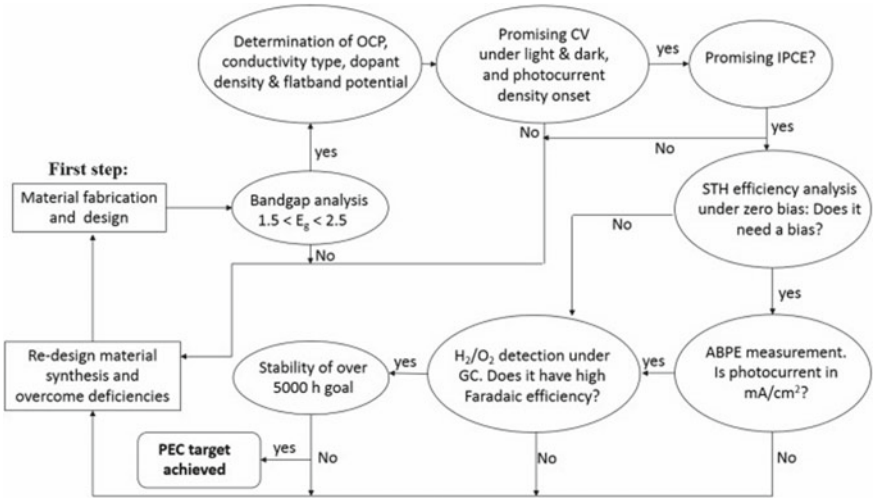

Fig. 27 Possible flowchart for a single photoelectrode-based PEC device

4.3 PEC Systems and Devices

4.3.1 Types of PEC Systems

PEC cells, having the possible configurations summarized in Fig. 28, contain either an n-type photoanode–H_2 evolution catalytic cathode (HEC) (Fig. 28a) or a p-type photocathode–O_2 evolution catalytic anode (OEC) (Fig. 28b). The single light-absorbing PEC systems require bias voltages to compensate for over voltages and other losses. For water splitting in which both the HER and OER occur, a light absorber is employed in a tandem photoanode–photocathode cell (Fig. 28c). In contrast to employing an electrocatalytic system for water splitting, using a PEC cell enables reduction or possible elimination of the externally supplied power (external bias) through use of a photoelectrode generated voltage (V_{ph}). If the sum of V_{ph} is larger than E(H_2/H_2O) + overpotentials of HER/OER (ca. 1.6 V), the PEC cell can promote water splitting without using an applied bias (Fig. 28c) [16].

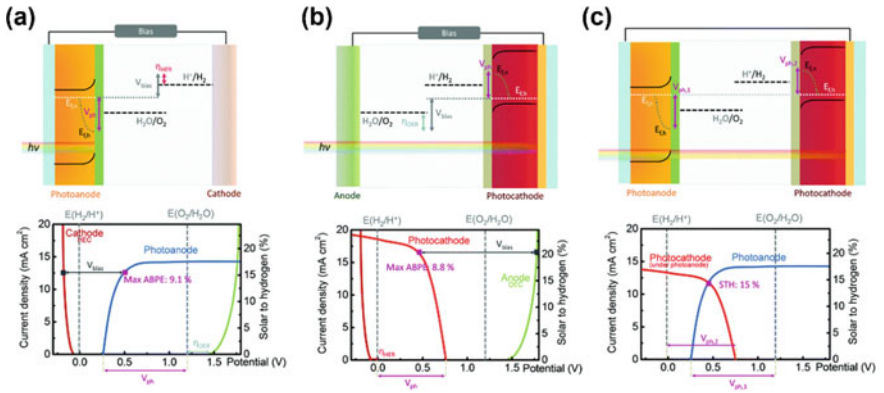

Fig. 28 Types of PEC cells for water splitting. **a** Photoanode–HEC cathode, **b** photocathode–OEC anode, and **c** photoanode–photocathode tandem cell for unbiased overall water splitting. Description and denotation are reproduced from Ref. 49 with permission from Elsevier B.V., copyright 2017

4.3.2 Scale-Up Devices

Owing to cost competitiveness concerns, criteria used to select materials for large-scale devices could be different from those employed to create laboratory devices. Complexity is the major difference between PV–EC and PEC systems, which often employ similar materials. Jacobsson et al. established a criterion for accessing whether the photoelectrode or light absorber functions inside or outside the electrolyte. Recently, Yao and Li suggested that materials such as c-Si, a-Si, GaAs, GaP, CdS, CdSe, ZnTe, and $CuInGaSe_2$ should be classified as PV grade, and TiO_2, Fe_2O_3, $BiVO_4$, TaON, Ta_3N_5, Cu_2O, and $CaFe_2O_4$ as non-PV grade. The classifications result from the fact that PV-grade material-based photoelectrodes often have similar or the same structures and geometries as those of PV materials. Ronge et al. also cited lower complexity as a potential merit of a PEC over PV–EC system, which would directly affect costs of a large-scale system [81].

The complexity of a material can be represented by numbers of "layers", where reducing the number of layers would reduce complexity and the cost in developing a PEC system. As shown in Fig. 29, highly active photoelectrodes (photocurrents above ca. 10 mA cm^{-2} at short-circuit voltage) always comprised of more than two layers (protection + electrocatalyst). Use of a light absorber that is more air- and water-stable would be one approach to reducing the complexity of a photoelectrode because it would not require use of a protection protocol. Hence, capital costs of a materials which are directly related to complexity should be balanced by their efficiencies so that an efficient, stable, and cheap material would be ideal. However, materials of this type are not yet available [82].

To obtain η_{STH} values above 10%, J_{ph} of ca. 8.13 mA cm^{-2} needs to be generated by the water-splitting reaction, so that the bandgap needs to be smaller than ca. 2.3 eV. But materials other than those of PV grade that achieve J_{ph} above 8.0 mA cm^{-2} are rare (Fig. 29). For example, the best metal oxide-based photoanode developed so far,

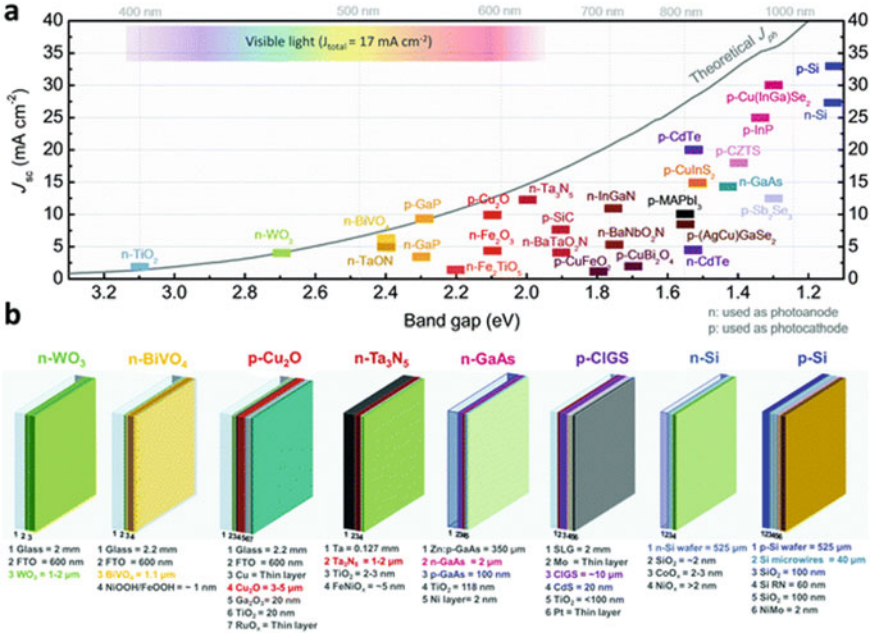

Fig. 29 **a** Reported photocurrent densities under short-circuit conditions (Jsc) of photoelectrodes for PEC water splitting under standard conditions: 1.0 sun, short-circuit condition of 1.23 V_{RHE} for photoanode and 0.0 V_{RHE} for photocathode. **b** Known composition of photoelectrodes in **a**

$BiVO_4$, has a value that is lower that this theoretical limit. The Cu_2O photocathode has the highest J_{ph} (10 mA cm^{-2} at 0.0 V_{RHE}) as well as a photovoltage of ca. 1.0 V, which are excellent for a light-absorbing metal oxide. Semi-stable Ta_3N_5 has J_{ph} ca.12 mA cm^{-2} at 1.23 V_{RHE}. Besides these materials, most others that lead to photoelectrodes that have J_{ph} above 8.0 mA cm^{-2} employ PV-grade light absorbers with buried junctions and protection layers, which makes the system have a degree of complexity.

As mentioned above, most high-performance PEC water-splitting systems utilize PV-grade light absorbers and noble metal-based electrocatalysts. Even if a high-efficiency system were to be developed, it might not be practical if it is composed of rare and precious materials. Hence, element abundance is an important criterion to use when creating scaled-up systems. In Fig. 30a, data for Earth crust abundances, annual production levels, and pure form costs of common elements are given. The data demonstrate that global production levels of materials (from U.S. Geological Survey 2018) do not necessarily parallel their abundances, but rather they reflect demand. Since renewable H_2 production will create an enormous market, current research in this area should give more attention to substituting highly functional earth-abundant materials for those that have high value. Figure 30b summarizes the three important aspects of elements in materials used in PEC water-splitting systems. Moreover, it has

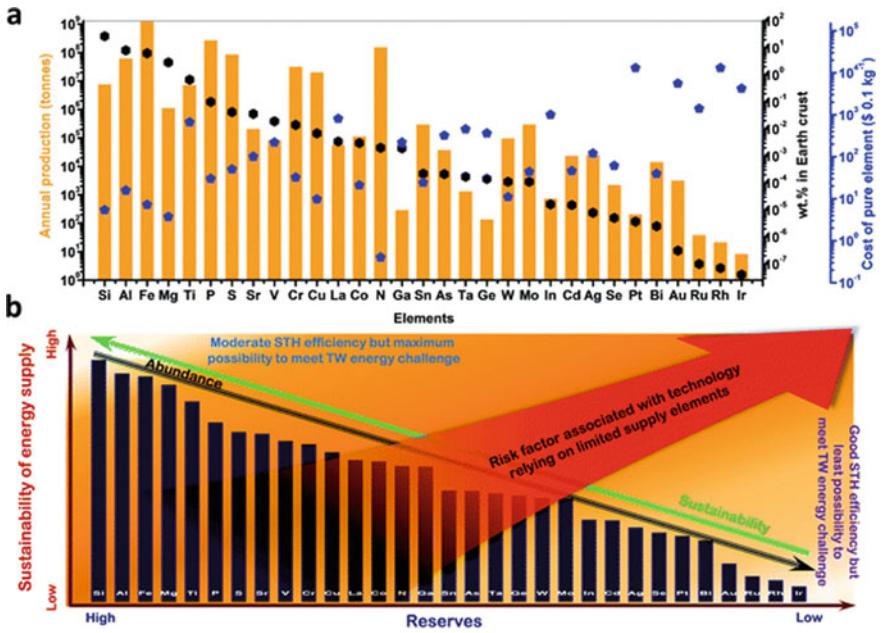

Fig. 30 **a** Annual production, abundance, and cost (pure form) of common elements in materials employed in PEC water splitting. **b** Relation between earth abundance, available reserves, and supply risk of photoactive materials used for energy production

been proposed that a relationship exists between sustainable clean energy production, and availability and earth abundance of photoactive materials [34, 83].

In addition to the choice of materials, fabrication methods need to be carefully selected for designing a suitable scaled-up PEC system. First, it is important to consider the applicability of laboratory fabrication techniques including metal–organic chemical vapor deposition, atmospheric pressure chemical vapor deposition, atomic layer deposition, sol–gel or solution-based coating via spray pyrolysis, and spin coating. In general, solution-based methods are carried out under ambient conditions, and that do not require very high or low pressure, temperature, and a desirable vacuum or inert gas environment. Large-scale fabrication of PV-grade materials (GaP, a-Si, CIS, etc.) requires development of strategies that are well established in other PV applications. However, III/V materials are typically generated using MOCVD and similar methods that require an O_2-free atmosphere, a cost-related issue that needs to be considered.

Many metal oxide-based SCs are air stable meaning that the process needed for fabrication can be conducted using ambient conditions. The hydrothermal method was employed to prepare a WO_3 nanoparticle array film with sizes above 400 cm^2 (Fig. 31a). Also, the hydrothermal method was used to synthesize FeOOH from Fe salts at 80–120 °C. This substance is then converted into Fe_2O_3 which is widely

used for Fe_2O_3 nanorod film fabrication (Fig. 31d). Figure 31e shows a schematic for sequential electrodeposition to produce Cu_2O films ca.50 cm^2 FTO [84].

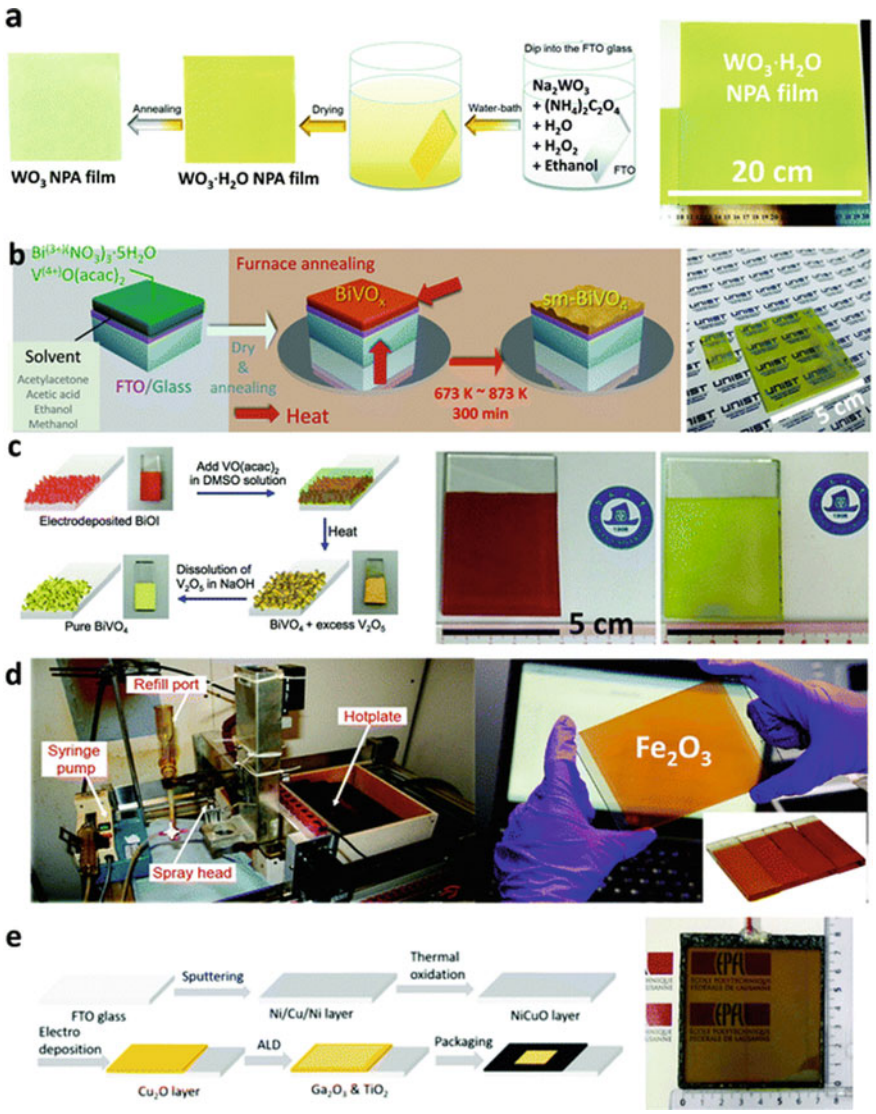

Fig. 31 Solution methods for photoelectrode preparation on a modest scale (>5 cm^2). **a** Hydrothermal synthesis of WO_3 NPA films on substrates of various sizes. **b** Metal–organic decomposition deposition of $BiVO_4$ on FTO. **c** Electrodeposition of BiOI (red) and thermal conversion to $BiVO_4$ films (yellow). **d** Hydrothermal synthesis of Fe_2O_3. **d** Spray pyrolysis deposition of Fe_2O_3 in a large area (>100 cm^2). **e** Electrodeposition of Cu_2O films with a sequential deposition process

Metal–organic decomposition (MOD), a scalable fabrication method devised by Galembeck et al., was first used to prepare $BiVO_4$ by Sayama et al. This approach utilizes metal precursors (e.g., acetate, acetyl acetate, or oleate) that are decomposable in organic solvents (e.g., acetylacetonate, acetic acid, or methanol). Materials made by using MOD can be used for deposition through a variety of methods including drop casting, spin coating, screen printing, and spray pyrolysis. Yao et al. described fabrication of $BiVO_4/WO_3$/FTO employing drop casting MOD $BiVO_4$ on substrates with areas as large as 25 cm^2. This group also found that the efficiency of the process dropped by 50% when the film size is 2.0 cm^2. Kim and Lee described a microwave-assisted method for a short time (5–8 min) requiring synthesis of $BiVO_4$ using a MOD precursor which contrast with the typical 60–300 min requiring traditional thermal synthesis method (Fig. 31b). MOD is a sol–gel method that has been widely applied on a variety of scales.

Electrodeposition is a useful method to produce light-absorbing materials. As described in a recent review by Kang and Choi, electrodeposition is one of the most useful methods for generating non-PV-grade photoelectrodes, such as TiO_2, WO_3, Fe_2O_3, $BiVO_4$, $CuWO_4$, CIGS, and CZSS. Electrocatalysts such as MOOH (M = Co, Fe, Ni, Mn, etc.), RuO_2, various metal alloys, and Pt can also be deposited on large scales using electrodeposition. Specifically, Choi and co-workers used electrodeposition and thermal conversion of BiOI to create highly porous $BiVO_4$ on FTO which has an extremely high efficiency for use in PEC water oxidation (Fig. 31c) [85, 86].

The overall efficiency for producing a scaled-up device will be lower than that involved in generating a corresponding small-scale laboratory device owing to unique factors involved that are qualitatively pictured in Fig. 32. Figure 32a and b shows a photoanode and photocathode pair with respective bandgaps of 1.84 eV and 1.23 eV and their tandem cell (D4), which was calculated by Pinaud et al. The value of η_{STH} is 22% [87].

When a device is scaled up to ca.1 m or larger sizes, problems not usually encountered in small scales arise (Fig. 32c, d). First, fabrication of larger devices requires different methods and is usually accompanied by introduction of spatial defects that lead to increase in total ohmic resistance which lowers the efficiency. Another potentially problematic issue with large solar hydrogen production systems is separation of gases, which is usually performed using a membrane. Unlike the extensive efforts that have been given to developing fuel cells and PEM electrolyzers, only a few studies have been carried exploring membranes that can be utilized for PEC cells. The results of these investigations showed that a surprisingly high fuel separator derived high energy loss which is incurred when even a high-quality membrane is used.

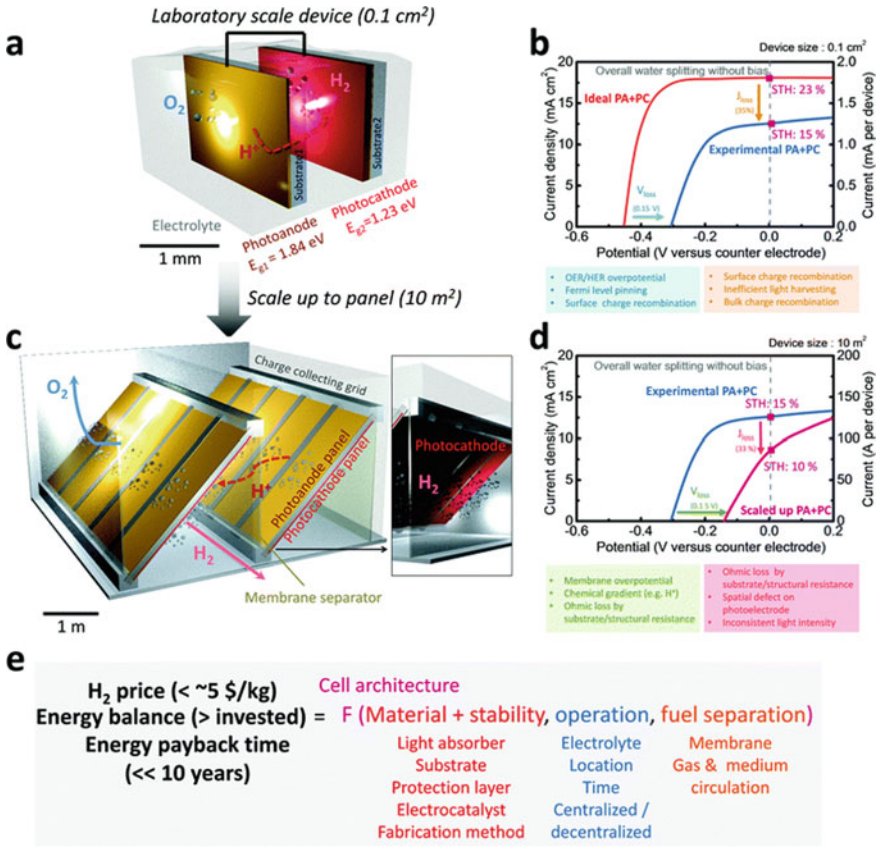

Fig. 32 **a** Device model on the experimental scale. **b** J–V curves of an ideal device with no energetic loss and a real experimental device with known loss mechanisms. **c** Scaled-up tandem photoelectrochemical device based on cell architecture. **d** J–V curves of the experimental device and the scaled-up device with expected energy losses. **e** Efficiency loss in scaled-up photoanode–photocathode tandem cells

PV–EC methods have already been demonstrated to be applicable to large-scale solar H_2 production, but it is unusual to find actual demonstrations of the large-scale effectiveness of PEC cells. Owing to rapid developments in laboratory-scale PEC water-splitting technologies taking place in the past decade, small but increasing numbers of PEC demonstration projects have been carried out. These case studies are invaluable in developing prototypes that can be employed to evaluate the techno-economic feasibility of larger PEC water-splitting plants or solar H_2 production farms.

As mentioned above, the first problem confronting in scale-up of a PEC system is the need for large photoelectrodes in which efficiencies in a two-electrode mode will be lowered owing to the sheet substrate resistance. In this regard, mimicking the production of solar cells, covering a substrate with a conductive grid, should reduce

efficiency loss. Lee et al. fabricated 130 cm^2 WO_3/FTO films by screen printing a WO_3 nanoparticle paste synthesized by sol–gel precipitation (Fig. 33a). Enlarging the size of the WO_3/FTO caused decrease in J_{ph} at 1.23 V_{RHE} from 2.63 mA cm^{-2} to 1.5 mA cm^{-2} to 1.18 mA cm^{-2} for 0.36, 4.8 and 130.6 cm^2 photoanode. In contrast, embedding an Ag grid in the film was beneficial, as exemplified by the observation that the 4.8 cm^2 photoanode experiences a 130% enhancement in its photocurrent density over a photoanode of the same size without an Ag grid. However, the efficiency is large in contrast to those of similarly sized photoanodes described so far. Under 1 sun, the tandem cell containing a photoanode with a large area (130.56 cm^2) produced 3 mL min^{-1} of H_2 [88].

A detailed study of the operation of an actual large-scale PEC cell, which addresses majority of issues of scaled-up PEC cells discussed so far, was conducted by Vilanova et al. (Fig. 34). These workers created a planar PEC cell, called a "Cool PEC cell". The cell containing a large Fe_2O_3/FTO photoanode (50 cm^2) was found to function for 1008 h, which is one of the longest operation times for a-Si solar cell-based photoanode with 0.45 mA cm^{-2} at 1.6 V. This effort demonstrated that the cool PEC cell has only negligible effects on blocking of light by gas bubbles, a serious problem in large-scale systems [89].

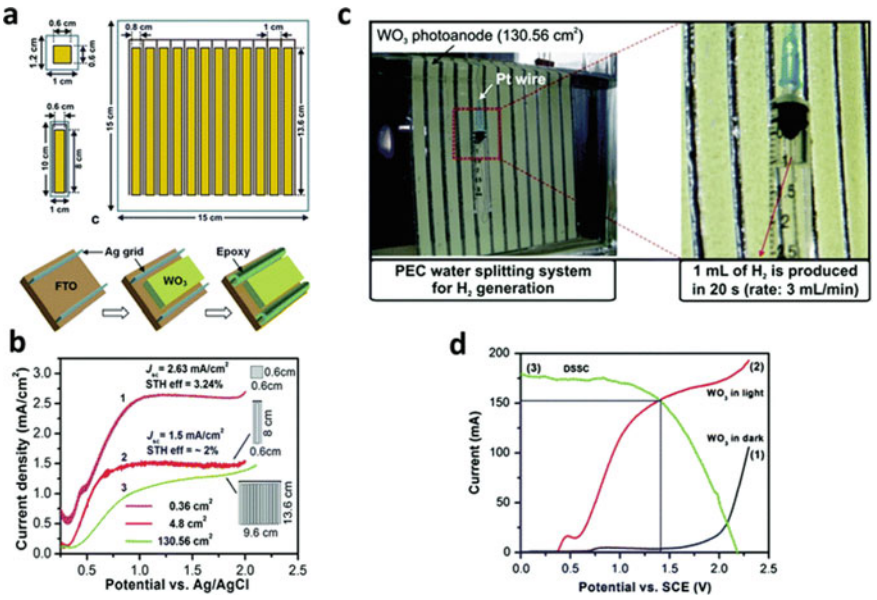

Fig. 33 Large-scale WO_3 photoanode-DSSC tandem cell. **a** Schematic diagram of small area WO_3 photoanodes with Ag grid-embedded FTO as substrate. **b** J–V curves of photoanodes in 0.5 M H_2SO_4 electrolyte under 1 sun illumination. **c** Experimental PEC set-up with WO_3 photoanode, platinum counter electrode, and calibrated cylindrical syringe for gas collection immersed in 0.5 M H_2SO_4. **d** Operating point of a scaled-up WO_3 photoanode

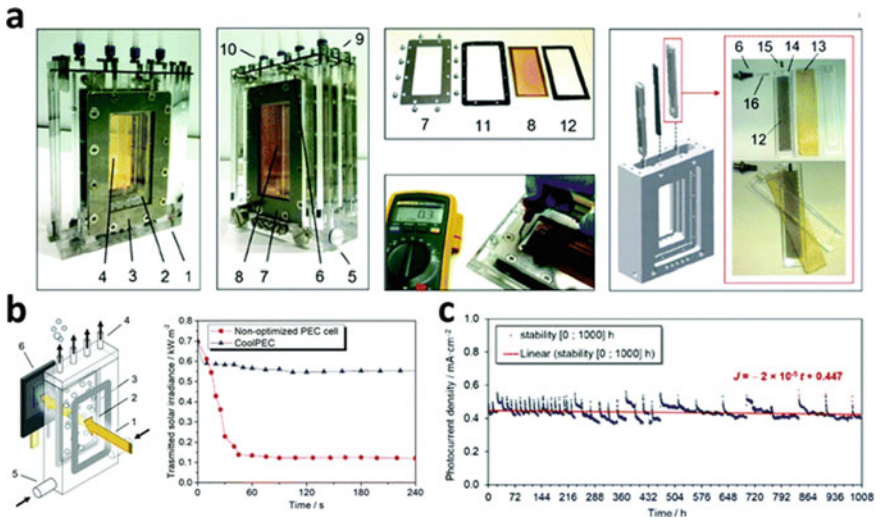

Fig. 34 **a** Cool PEC cell. 1—acrylic embodiment; 2—front window; 3—front stainless steel frame; 4—internal acrylic plate dividing the WE compartment; 5—main electrolyte inlet; 6—external screw; 7—back stainless steel frame; 8—back window; 9—acrylic cap; 10—electrolyte outlet; 11—internal gasket; 12—external gasket; 13—platinized-Ti mesh; 14—ion-exchange membrane; 15—acrylic holders; 16 and 17—metal connectors between the Pt–Ti mesh and the external screw. **b** Assessment of light trapping due to bubble accumulation inside the PEC cell. 1—simulated sunlight (1000 W m^{-2}); 2—front window; 3—back window; 4—electrolyte outlet; 5—electrolyte inlet; 6—Si calibrator used to monitor the solar irradiance reaching the outer surface of the back window. **c** Long-term stability of a hematite photoelectrode under a constant bias of 1.6 V

The reactor by Vilanova et al. was used in a PECDEMO's demonstration of a large-scale PEC cell, which investigated many issues facing scale-up including development of photoelectrode materials. For this purpose, large photoelectrodes comprised of $BiVO_4$, Cu_2O, and Fe_2O_3 were fabricated. A Mo metal grid was deposited on FTO glass to create a large area $BiVO_4$ electrode (>50 cm^2) (Fig. 35a). The $BiVO_4$-based system with dimensions of 3.6 × 3.6 cm^2 and with a grid produced using repetitive mosaic spray pyrolysis with mask generated at a modest current of ca. 70 mA at a bias of 1.23 V_{RHE} (Fig. 35b), which is much lower than that obtained using a 1.0 cm^2 scale device. Also, a four-stripe-type Cu_2O photocathode with metal grid lines was generated by the PECDEMO project group (Fig. 35c). The large-scale system with two grids comprised of Au and Ag was shown which had a significantly improved performance demonstrating the importance of the substrate design.

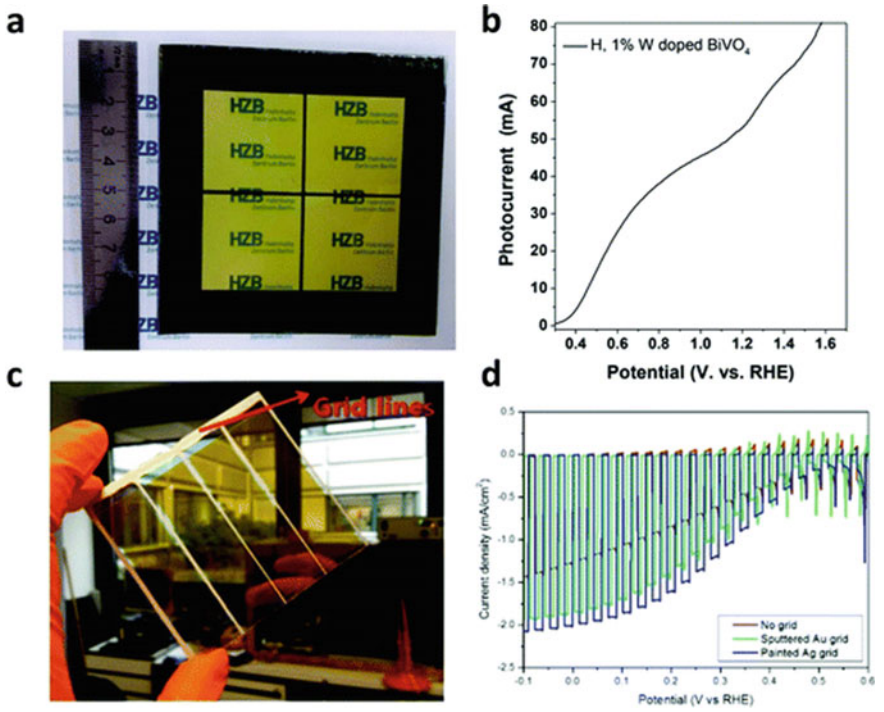

Fig. 35 Fabrication of a large-scale photoelectrode conducted by PECDEMO. **a** Large area $BiVO_4$. **b** J–V curve of large area $BiVO_4$. **c** Large area Cu_2O photocathode with grid lines (50.4 cm^2 active area). **d** Linear sweep voltammetry scans of large area Cu_2O photocathode for the vertical PEC cell under chopped illumination (0.6 sun) in the pH 5 electrolyte

As expected, photoanodes with large areas (50 cm^2) have slightly lower performances than their laboratory (ca.1.0 cm^2) counterparts, but they are plagued by the high instability of $BiVO_4$. For example, etching of $BiVO_4$ on FTO occurs, which is an indicator of corrosion. But replacement of a W:$BiVO_4$ photoanode with Co-Pi as OEC in 0.1 M KPi as electrolyte by a Co-Ci/W:$BiVO_4$ photoanode led to a near 70–100 h stability in aqueous bicarbonate. This finding emphasizes the importance of choosing the OEC and electrolyte. Moderate stability with the same OEC and electrolyte on a laboratory scale was also observed by Kim et al.

$BiVO_4$-heterojunction tandem cells containing an intrinsic thin layer (HIT) Si PV or Fe_2O_3–HIT Si PV were tested using outdoor sunlight and a planar "vertical" or solar concentrator with angled illumination (Fig. 36). The device, tested at the SoCRatus facility of the German Aerospace Center (DLR), had a maximum unbiased current density of 1.88 mA cm^{-2} ($\eta_{STH} = 2.3\%$) for $BiVO_4$–HIT Si PV and 0.52 mA cm^{-2} ($\eta_{STH} = 0.74\%$) for Fe_2O_3–HIT Si PV. For the "angled" device tested at UPorto, the actual illumination area was much larger (ca. 200 cm^2) because a reflection concentrator was used (Fig. 36a and b). Operation for 15–48 h led to no significant degradation of efficiency, but the efficiency of 50 cm^2 laboratory devices

are much higher. Thus, the $BiVO_4$–HIT Si PV tandem cell has $\eta_{STH} = 0.2\%$ and the Fe_2O_3–HIT Si PV tandem cell has only $\eta_{STH} = 0.058\%$ in the "angled" device (Fig. 36e and f). Even though the light concentrator-based system was expected to achieve a much higher level of operation, observation made on III/V light absorbers showed that this level was not reached. One of the numerous issues confronting scale-up of PEC cells is the large intermittence of illumination, which is exemplified by the variation of η_{STH} ranges from 0.42% to 0.12% for 8 d (Fig. 36f) [90].

In addition, Tolod et al. used the Artiphyction project to investigate a new approach, which they called TRL5 development. In this effort, they explored a 1.6 m^2 scale-up $BiVO_4$-based photoelectrodes in PEC–PV tandem cells (Fig. 37). A smaller 64 cm^2 module in a $BiVO_4$-Si tandem cell had a η_{STH} of 3%, which decreased to 2% during the long-term operation because of several factors including bubble formation [90].

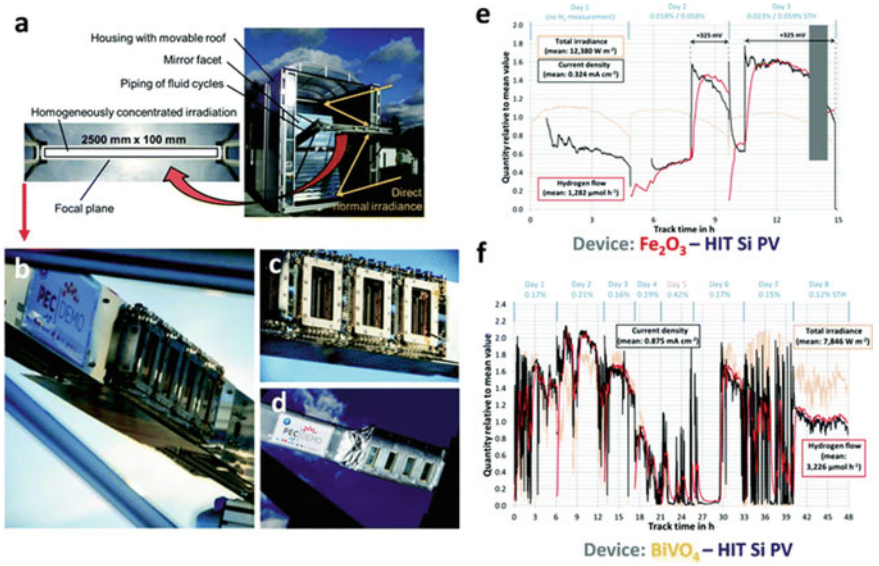

Fig. 36 Demonstration of operation of a PEC cell with a solar concentrator based on angled illumination. **a** DLR's test facility SoCRatus with its main components. **b** Prototype module in acrylic embodiment composed of four individual 50 cm^2 PEC cells mounted in the focal plane of the SoCRatus (here without reflective shields). **c** Modular prototype with Fe_2O_3 and **d** $BiVO_4$ photoelectrodes. **e** Total irradiation on the prototype, average current density, and hydrogen flow relative to the respective mean values as well as average η_{STH} without and with bias voltage associated with Fe_2O_3 photoelectrodes. Gray field refers to test of single compartments. **f** Total irradiation on the prototype, average current density, and hydrogen flow relative to the respective mean values as well as average η_{STH} associated with $BiVO_4$ photoelectrodes. The η_{STH} achieved from the device is marked on the upper side of the graph

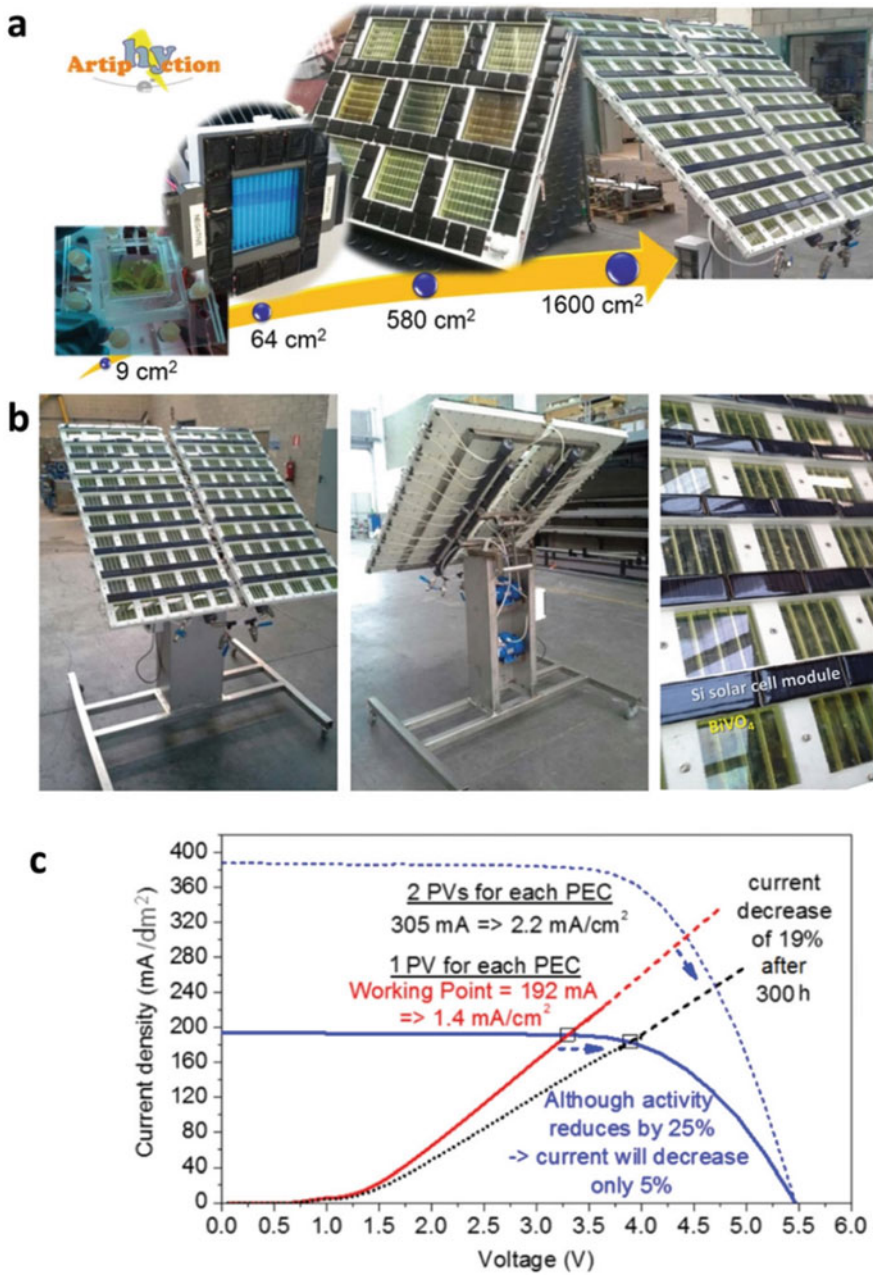

Fig. 37 **a** Large-scale PEC cell device from the Artiphyction prototype. **b** Photograph and magnified view of the 1.6 m^2 prototype comprised of 100 PEC cell modules. **c** J–V plots for a single PEC window

5 Challenges

5.1 Unassisted STH Conversion Inefficiency

Low STH conversion efficiencies of PEC cells arise because of three main reasons including (1) high recombination rates of charge carriers and low electrode/electrolyte interfaces catalytic activities, (2) improper band-edge positions of the SC, and (3) low or inappreciable generation of depletion regions owing to poor crystallinity. An effective approach to enhance conversion efficiency involves modification of the properties of the SC/liquid junction. Chen and co-workers showed that increase of photocurrent density and efficiency occurs when the morphology of α-Fe_2O_3 is changed into nanorods and the bandgap energy is tuned with Sb_2S_3 doping [91]. Boda et al. [92] showed that tuning the bandgap energy of TiO_2 through addition of $ZnFe_2O_4$ led to a three times larger current density. The conversion efficiency of InP was also enhanced by scaled addition of Pt nanoparticles. It has been shown by recent studies that N doping influences the performance of photoelectrodes significantly. Replacement of O by N atoms in some metal oxides using anionic substitution resulted in lowering bandgap energies and enhancing stability. The reason for this effect is that energies of N orbitals are higher than those of 2p O orbitals. In one example, the bandgap energy of Ta_2O_5 was transformed from 3.9 eV to 2.4 eV due to increasing nitridation (Fig. 38) [93].

5.2 Self-oxidation/reduction Promoted Photocorrosion

Besides the need for performance improvement, the important goal is the approaches that enhance the stability of a PEC cell. Except for a few studies which show that the stability of a PEC device is about 50 h, most others indicate that the PEC devices are stable for only 25 h. The use of organometal halide perovskites (OMHP) could be an approach to improve device stability. Non-PV-grade materials have higher inherent stabilities than their PV-grade counterparts. However, the passivation layer's sensitivity to the SCr/electrolyte junction might lead to electrode degradation. This problem could be avoided by preventing direct contact between the electrode and aqueous electrolyte using a HER/OER catalyst overlayer. Catalysts such as $NiCrO_x$ improve interfacial charge transfer and serve as an anti-corrosion layer. Transition metal oxides such as $ZnFe_2O_4$ also stabilize $BiVO_4$, and up to 50–100-nm-thick TiO_2 coatings have been recently used for photocathode stabilities. This type of coating introduces electronic defects and enhances hole conduction, while being sufficiently transparent [94, 95].

Another approach to address the photocorrosion issue is to optimize tuning of the electrolyte composition. This process can be blocked by V^{5+} ion saturation of the electrolyte. Similar methods can be applied to other materials only when the

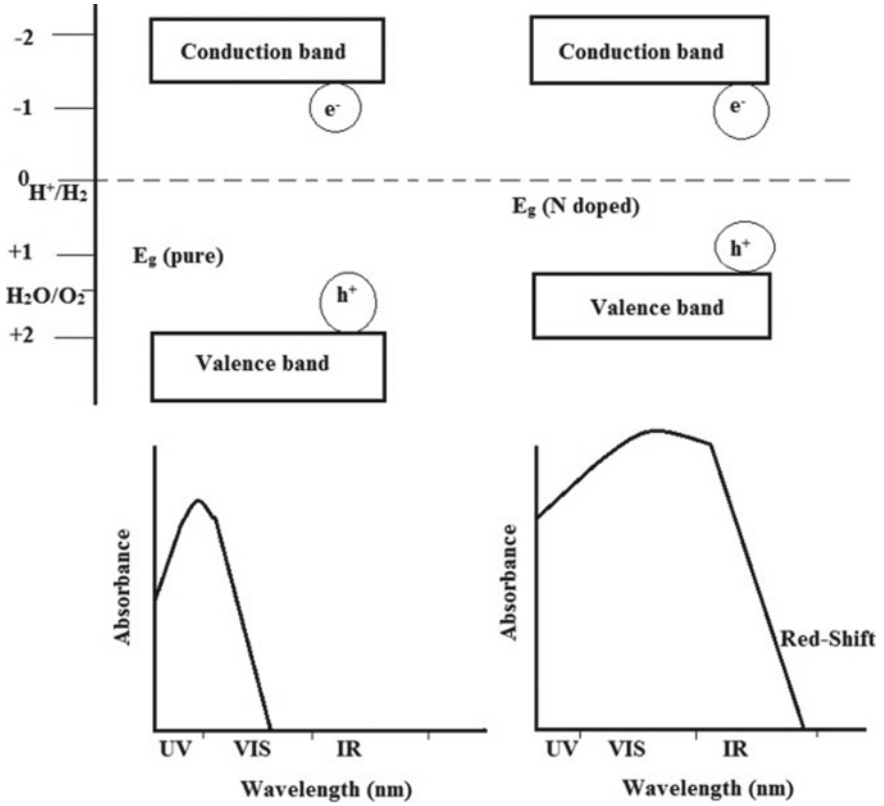

Fig. 38 Bandgap energy change by N replacement in a photoactive SC material

electrochemical phenomena responsible for material instability in the liquid medium can be identified.

5.3 Scale-Up for Creating Practical PEC Devices

From the time of the early studies by Fujishima and Honda in 1972, advances have not been made in the development of a practical scaled-up PEC system. Although research aimed at efficiency and stability enhancement needs to continue, an effort is needed for scale-up of some of the more promising PEC devices developed so far. Some of the important issues that should receive attention in this regard are the absorption/collection and intensity of incident light. Note that, at this time, current densities of commercial electrolyzers are in the range of 0.5–2 A cm^{-2}, and that these values are higher than the highest level in PEC devices (ca.10 mA cm^{-2}). These data suggest that generating the same level of current would require use of a

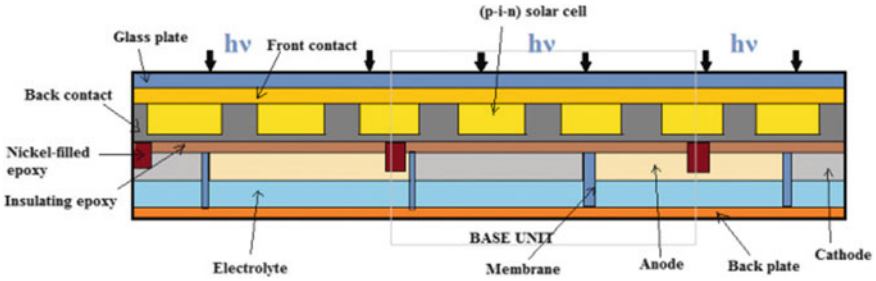

Fig. 39 Diagram of a PEC system developed by Turan and co-workers

PEC device having an electrode-active area that is 50–200-fold larger than those of currently developed systems (ca.1 cm^2). One of the most cost- and efficiency-affective solar–hydrogen generators are integrated systems comprised of an electrolyzer and group III–V PV-based solar concentrator. Also, effective scale-up can be brought about by using multiple repetitive cycles in a continuous flow and electrode-surface regeneration system rather in a one-cycle batch reactor, and to use. For example, Turan and co-workers created a PEC water-splitting device, the area of which is 64 cm^2, in which 13 continuous base modules are connected by laser patterning. The resulting large-scale devise had a stable STH efficiency of 3.9% and worked for 40 h (Fig. 39) [96].

Reactors having multiple porous electrodes or reflectors could also be applied in a PEC devise to enhance light absorption. In this way, unabsorbed light can be diverted into another electrode or a PV unit. A multi-tube, multi-pass reactor, comprised of optical fibers coated with a photocathode material, which has an effective surface area that is larger than that of the photoactive material, is developed by Ray and Beenackers [97].

6 Summary and Outlook

Solar energy-promoted water splitting using photovoltaic-, photocatalyst-, and photoelectrode-driven systems has been profoundly studied during the past 50 years. Efforts in this area during the last 10 years have led to the discovery of significantly improved systems that have STH levels close to 2% (PC), 3% (PE–PE), 8% (PEC–PV hybrid), 19% (buried junction PV), and 30% (PV–EC with PEM electrolyzer). Moreover, rapid progress is being made in studies of other PC and PEC technologies. In recent years, PEC SW splitting is attracting increased attention, and its practical use for hydrogen production has great potential.

In current research studies, the utilization of natural light has not been emphasized and most of the systems probed still utilize both co-catalysts and sacrificial agents to improve photocatalytic performances. Moreover, conversion efficiencies of most PEC systems remain low and most lack high stability. It is worth noting that

although H_2 production efficiencies are lower in SW, this source should be employed in continuing studies. At present, the great attention given to assessing the influence of ions in seawater on the photoelectrode has created a firm foundation for the mechanism of H_2 production by seawater splitting. We propose that two issues should be given greater attention when designing efficient seawater H_2 production photocatalysts. These include (1) stabilities of materials in that they should resist oxidation by Cl_2, ClO_4^-, and other agents and (2) materials that take advantage of ions in SW to generate high value-added products.

In consideration of practical applications, it is necessary to develop scale-up techniques for PEC SW splitting. Several demonstration projects to scale up PEC solar hydrogen production systems are ongoing. Thus far, investigations of PEC cells have been carried out only on ca.1 m^2 scales. In spite of this, the efforts have led to the identification of many problems and challenges associated with material scale-up, and system balancing and operation. The results of these projects along with techno-economic assessments indicate that PEC water splitting by systems developed so far is not competitive with PV-EC devices. Their STH should be above 10% and their lifetimes need to be >10 years for PEC cells to be competitive, suggesting that material development needs to occur in parallel with scale-up and demonstration efforts [98–101].

Scientific breakthroughs are still needed in this area. The revelation of developing low-cost, high-efficiency SCs will be of great significance, not only for PEC water-splitting hydrogen production, but also for PV and other solar energy conversion approaches. Great challenges exist in this area, but the benefits are even greater. We believe that continuing in-depth research in the future will make H_2 production by PEC SW splitting a practical alternative for producing fuels.

References

1. Fujishima A, Honda K (1972) Electrochemical photolysis of water at a semiconductor electrode. Nature 238:37–38
2. Tachibana Y, Vayssieres L, Durrant JR (2012) Artificial photosynthesis for solar water-splitting. Nat Photon 6:511–518
3. Hamdani IR, Bhaskarwar AN (2021) Recent progress in material selection and device designs for photoelectrochemical water-splitting. Renew Sust Energ Rev 138:110503
4. Indrawirawan S, Sun H, Duan X et al (2015) Nanocarbons in different structural dimensions (0–3D) for phenol adsorption and metal-free catalytic oxidation. Appl Catal B 179:352–362
5. Rodriguez CA, Modestino MA, Psaltis D, Moser C (2014) Design and cost considerations for practical solar-hydrogen generators. Energy Environ Sci 7:3828–3835
6. Ichikawa S (1997) Photoelectrocatalytic production of hydrogen from natural seawater under sunlight. Int J Hydrogen Energ 22:675–678
7. Li YG, Wang RR, Li HJ, Wei X, Feng J, Liu K et al (2015) Efficient and stable photoelectrochemical seawater splitting with TiO_2@g-C_3N_4 nanorod arrays decorated by Co-Pi. J Phys Chem C 119:20283–20292
8. Ayyub MM, Chhetri M, Gupta U et al (2018) Photochemical and photoelectrochemical hydrogen generation by splitting seawater. Chem 24:18455–18462

9. Ayyub MM, Chhetri M, Gupta U, Roy A, Rao CNR (2018) Photochemical and photoelectrochemical hydrogen generation by splitting seawater. Chemistry 24:18455–18462
10. Yao Y, Gao X, Meng X (2021) Recent advances on electrocatalytic and photocatalytic seawater splitting for hydrogen evolution. Int J Hydrogen Energ 46:9087–9100
11. Dominey RN, Lewis NS, Bruce JA, Bookbinder DC, Wrighton MS (1982) Improvement of photoelectrochemical hydrogen generation by surface modification of p-type silicon semiconductor photocathodes. J Am Chem Soc 104:467–482
12. Wang GM, Ling YC, Wang HY, Lu XH, Li Y (2014) Chemically modified nanostructures for photoelectrochemical water splitting. J Photoch Photobio C 19:35–51
13. Fang F, Wang Y, Shen LW, Tian G, Cahen D, Xiao YX, Chen JB, Wu SM, He L, Ozoemena KI, Symes MD, Yang X-Y (2022) Interfacial carbon makes nano-particulate RuO2 an efficient, stable, pH-universal catalyst for splitting of seawater. Small 18:202203778
14. Kumari S, Turner WR, Kumar B, Spurgeon JM (2016) Solar hydrogen production from seawater vapor electrolysis. Energy Environ Sci 9:1725–1733
15. Labrador NY, Songcuan EL, De Silva C, Chen H, Kurdziel SJ, Ramachandran RK et al (2018) Hydrogen evolution at the buried interface between Pt thin films and silicon oxide nanomembranes. ACS Catal 8:1767–1778
16. Hisatomi T, Domen K (2017) Introductory lecture: sunlight-driven water splitting and carbon dioxide reduction by heterogeneous semiconductor systems as key processes in artificial photosynthesis. Faraday Discuss 198:11–35
17. Nam W, Oh S, Joo H et al (2010) Preparation of anodized TiO_2 photoanode for photoelectrochemical hydrogen production using natural seawater. Sol Energy Mater Sol Cells 94:1809–1815
18. Bae D, Seger B, Vesborg PCK et al (2017) Strategies for stable water splitting via protected photoelectrodes. Chem Soc Rev 46:1933–1954
19. Guo L-J, Luo J-W, He T, Wei S-H, Li S-S (2018) Photocorrosion-limited maximum efficiency of solar photoelectrochemical water splitting. Phys Rev Appl 10:1–16
20. Styring S (2012) Artificial photosynthesis for solar fuels. Faraday Discuss 155:357–376
21. Luo W, Yang Z, Li Z, Zhang J, Liu J, Zhao Z et al (2011) Solar hydrogen generation from seawater with a modified $BiVO_4$ photoanode. Energy Environ Sci 4:4046–4051
22. Sun Q, Cheng T, Liu Z, Qi L (2020) A cobalt silicate modified $BiVO_4$ photoanode for efficient solar water oxidation. Appl Catal B Environ 277:1–9
23. Millero FJ, Feistel R, Wright DG, McDougall TJ (2008) The composition of standard seawater and the definition of the reference-composition salinity scale. Deep Sea Res Oceanogr Res Pap 55:50–72
24. Oener SZ, Ardo S, Boettcher SW (2017) Ionic processes in water electrolysis: the role of ion-selective membranes. ACS Energy Lett 2:2625–2634
25. Pan C, Takata T, Nakabayashi M, Matsumoto T, Shibata N, Ikuhara Y et al (2015) A complex perovskite-type oxynitride: the first photocatalyst for water splitting operable at up to 600 nm. Angew Chem Int Ed Engl 54:2955–2959
26. Zhu C, Liu Ca, Fu Y et al (2019) Construction of CDs/CdS photocatalysts for stable and efficient hydrogen production in water and seawater. Appl Catal B-Environ 242:178–185
27. Raja KS, Mahajan VK, Misra M (2006) Determination of photo conversion efficiency of nanotubular titanium oxide photo-electrochemical cell for solar hydrogen generation. J Power Sources 159:1258–1265
28. Li C, Luo Z, Wang T, Gong J (2018) Surface, bulk, and interface: rational design of hematite architecture toward efficient photo-electrochemical water splitting. Adv Mater 30:1–23
29. Kawde A, Annamalai A, Amidani L et al (2018) Photo-electrochemical hydrogen production from neutral phosphate buffer and seawater using micro-structured p-Si photo-electrodes functionalized by solution-based methods. Sustain Energ Fuels 2:2215–2223
30. Shinagawa T, Takanabe K (2017) Towards versatile and sustainable hydrogen production through electrocatalytic water splitting: electrolyte engineering. Chemsuschem 10:1318–1336
31. Young JL, Steiner MA, Döscher H, France RM, Turner JA, Deutsch Todd G (2017) Direct solar-to-hydrogen conversion via inverted metamorphic multi-junction semiconductor architectures. Nat Energy 2:17028

32. Morales-Guio CG, Tilley SD, Vrubel H, Graẗzel M, Hu X (2014) Hydrogen evolution from a copper(I) oxide photocathode coated with an amorphous molybdenum sulphide catalyst. Nat Commun 51–57
33. Yang Y, Niu S, Han D, Liu T, Wang G, Li Y (2017) Progress in developing metal oxide nanomaterials for photoelectrochemical water splitting. Adv Energy Mater 7:1–26
34. Kim MK, Sim WH, Choi M, Lim H, Kwon Y, Jeong HM (2019) Electrochemically Li-intercalated TiO_2 nanoparticles for high performance photocatalytic production of hydrogen. Catal Today 359:23–27
35. Hu J, Lu Y, Liu XL, Janiak C, Geng W, Wu SM, Zhao XF, Wang LY, Tian G, Zhang YX, Su BL, Yang X-Y (2020) Photoinduced terminal fluorine and Ti^{3+} in $TiOF_2/TiO_2$ heterostructure for enhanced charge transfer. CCS Chem 2:1573–1581
36. Xiao S, Lu Y, Li X, Xiao BY, Wu L, Song JP, Xiao YX, Wu SM, Hu J, Wang Y, Chang GG, Tian G, Lenaerts S, Janiak C, Yang X-Y, Su BL (2018) Hierarchically dual-mesoporous TiO_2 microspheres for enhanced photocatalytic properties and lithium storage. Chem Eur J 24:13246–13252
37. Simamora AJ, Hsiung TL, Chang FC, Yang TC, Liao CY, Wang HP (2012) Photocatalytic splitting of seawater and degradation of methylene blue on CuO/nano TiO_2. Int J Hydrogen Energy 37:13855–13858
38. Xiao P, Chen W, Wang X (2015) A review of phosphide-based materials for electrocatalytic hydrogen evolution. Adv Energy Mater 5:1500985
39. Joo H, Bae S, Kim C et al (2009) Hydrogen evolution in enzymatic photoelectrochemical cell using modified seawater electrolytes produced by membrane desalination process. Sol Energy Mater Sol Cells 93:1555–1561
40. Barreca D, Carraro G, Gasparotto A et al (2015) Fe_2O_3-TiO_2 Nano-heterostructure photoanodes for highly efficient solar water oxidation. Adv Mater Interfaces 2:1500313
41. Williams G, Seger B, Kamat PV (2008) TiO_2-graphene nanocomposites. UV-assisted photocatalytic reduction of graphene oxide. ACS Nano 2:1487–1491
42. Li Y, Cao C, Xie X, Zhang L, Lin S et al (2018) Enhanced photoelectrochemical performance of TiO_2 nanotube arrays with coexisted Pt nanoparticles and Co-Pi cocatalysts. Appl Surf Sci 436:337–344
43. Boonserm A, Kruehong C, Seithtanabutara V et al (2017) Photoelectrochemical response and corrosion behavior of CdS/TiO_2 nanocomposite films in an aerated 0.5 M NaCl solution. Appl Surf Sci 419:933–941
44. Yang JS, Wu JJ (2018) Toward eco-friendly and highly efficient solar water splitting using In_2S_3/Anatase/Rutile TiO_2 dual-staggered-heterojunction nanodendrite array photoanode. ACS Appl Mater Inter 10:3714–3722
45. Jiang F, Gunawan Harada T, Kuang Y, Minegishi T, Domen K, Ikeda S (2015) $Pt/In_2S_3/CdS/Cu_2ZnSnS_4$ thin film as an efficient and stable photocathode for water reduction under sunlight radiation. J Am Chem Soc 137:13691–13697
46. Wu SM, Wang YT, Xiao ST, Wang LY, Tian G, Chen JB, Liu JW, Shalom M, Yang X-Y (2022) A spatial homojunction of titanium vacancies decorated oxygen vacancies in TiO_2 and its directed charge transfer. Nanoscale 14:13373–13377
47. Wu SM, Wang YT, Xiao ST, Zhang YX, Tian G, Chen JB, Zhao XF, Janiak C, Shalom M, Bahnemann DW, Wang LY, Yang X-Y (2022) Design and synthesis of TiO_2/C nanosheets with a directional cascade carriers transfer. Chem Sci 13:7126–7131
48. Xiao ST, Wu SM, Dong Y, Liu JW, Wang LY, Wu L, Zhang YX, Tian G, Janiak C, Shalom M, Wang YT, Li YZ, Jia RK, Bahnemanni DW, Yang X-Y (2020) Rich surface hydroxyl design for nanostructured TiO_2 and its hole-trapping effect. Chem Eng J 400:125909
49. Zhang YX, Wu SM, Tian G et al (2021) Titanium vacancies in TiO2 nanofibers enable highly efficient photodriven seawater splitting. Chem 27:14202–14208
50. Lu Y, Liu Xl, He L, Zhang YX, Hu ZY, Tian G, Cheng X, Wu SM, Li YZ, Yang XH, Wang LY, Liu JW, Janiak C, Chang GG, Li WH, Van Tendeloo G, Yang X-Y, Su BL (2020) Spatial heterojunction in nanostructured TiO_2 and its cascade effect for efficient photocatalysis. Nano Lett. 20:3122–3129

51. Lu Y, Liu YX, He L, Wang LY, Liu XL, Liu JW, Li YZ, Tian G, Zhao H, Yang XH, Janiak C, Lenaerts S, Yang X-Y, Su BL (2020) Interfacial co-existence of oxygen and titanium vacancies in nanostructured TiO_2 for enhancement of the carrier transport. Nanoscale 12:8364
52. Afzali N, Keshavarzi R, Tangestaninejad S et al (2021) Multifunctional approach to improve water oxidation performance with MOF-based photoelectrodes. Appl Mater Today 24:101159
53. Li Y, Wei X, Yan X et al (2016) Construction of inorganic-organic 2D/2D WO(3)/g-C(3)N(4) nanosheet arrays toward efficient photoelectrochemical splitting of natural seawater. Phys Chem Chem Phys 18:10255–10261
54. Liu J, Xu S-M, Li Y et al (2020) Facet engineering of WO_3 arrays toward highly efficient and stable photoelectrochemical hydrogen generation from natural seawater. Appl Catal B-Environ. 264:118540
55. Shi Y, Li Y, Wei X et al (2017) Facile preparation of porous WO_3 film for photoelectrochemical splitting of natural seawater. J Electron Mater 46:6878–6883
56. Jadwiszczak M, Jakubow-Piotrowska K, Kedzierzawski P et al (2019) Highly efficient sunlight-driven seawater splitting in a photoelectrochemical cell with chlorine evolved at nanostructured WO_3 photoanode and hydrogen stored as hydride within metallic cathode. Adv Energy Mater 10:1903213
57. Patel M, Park W-H, Ray A, Kim J, Lee J-H (2017) Photoelectrocatalytic sea water splitting using Kirkendall diffusion grown functional Co_3O_4 film. Sol Energy Mater Sol Cell 171:267–274
58. Kikuchi R, Nakamura T, Tamura S, Kaneko Y, Hato K (2017) Fundamental semiconducting properties of perovskite oxynitride $SrNbO_2N$: epitaxial growth and characterization. Chem Mater 29:7697–7703
59. Guo X, Liu X, Wang L (2022) NiMoOx as a highly protective layer against photocorrosion for solar seawater splitting. J Mater Chem A 10:1270–1277
60. Lv Q, Han J, Tan X, Wang W, Cao L, Dong B (2019) Featherlike NiCoP holey nanoarrys for efficient and stable seawater splitting. ACS Appl Energy Mater 2:3910–3917
61. She X, Ma G, Zhang L et al (2022) Floc-like CNTs jointed with $Bi_xFe_{1-x}VO_4$ nanoparticles for high efficient and stable photoelectrochemical seawater splitting. J Alloy Compd 893:162146
62. Guo L, Yang Z, Marcus K, Li Z, Luo B, Zhou L, Wang X, Du Y, Yang Y (2018) MoS_2/TiO_2 heterostructures as nonmetal plasmonic photocatalysts for highly efficient hydrogen evolution. Energy Environ Sci 11:106–114
63. Dong Y, Chen SY, Lu Y, Xiao YX, Hu J, Wu SM, Deng Z, Tian G, Chang GG, Li J, Lenaerts S, Janiak C, Yang X-Y, Su BL (2018) Hierarchical MoS_2@TiO_2 heterojunctions for enhanced photocatalytic performance and electrocatalytic hydrogen evolution. Chem-Asian J 13:1609–1615
64. Zhu C, Liu C, Fu Y, Gao J, Huang H, Liu Y, Kang Z (2019) Construction of CDs/CdS photocatalysts for stable and efficient hydrogen production in water and seawater. Appl Catal B Environ 242:178–185
65. Sharma MD, Mahala C, Basu M (2020) Photoelectrochemical water splitting by In_2S_3/In_2O_3 composite nanopyramids. ACS Appl Nano Mater 3:11638–11649
66. Cheng K-W, Tsai W-T, Wu Y-H (2016) Photo-enhanced salt-water splitting using orthorhombic Ag_8SnS_6 photoelectrodes in photoelectrochemical cells. J Power Sources 317:81–92
67. Lee M-L, Liao P-H, Li G-L et al (2019) Enhanced production rates of hydrogen generation and carbon dioxide reduction using aluminum gallium nitride/gallium nitride heteroepitaxial films as photoelectrodes in seawater. Sol Energy Mater Sol Cells 202:110153
68. Nam W, Oh S, Joo H, Sarp S, Cho J, Nam B-W, Yoon J (2010) Preparation of anodized TiO_2 photoanode for photoelectrochemical hydrogen production using natural seawater. Sol Energy Mater Sol Cell 94:1809–1815
69. Oh S, Nam W, Joo H et al (2011) Photoelectrochemical hydrogen production with concentrated natural seawater produced by membrane process. Sol Energy 85:2256–2263
70. Nam W, Oh S, Joo H et al (2011) Preparation of Pt deposited nanotubular TiO_2 as cathodes for enhanced photoelectrochemical hydrogen production using seawater electrolytes. J Solid State Chem 184:2920–2924

71. Yuan X, Xu Y, Meng H et al (2018) Fabrication of ternary polyaniline-graphene oxide-TiO_2 hybrid films with enhanced activity for photoelectrocatalytic hydrogen production. Sep Purif Technol 193:358–367
72. Wu SM, Liu XL, Lian XL, Tian G, Janiak C, Zhang YX, Lu Y, Yu HZ, Hu J, Wei H, Zhao H, Chang GG, Van Tendeloo G, Wang LY, Yang X-Y, Su BL (2018) Homojunction of oxygen and titanium vacancies and its interfacial n-p effect. Adv Mater 30:1802173
73. Li F, Dong B, Feng S (2019) Bi shell-BiOI core microspheres modified TiO_2 nanotube arrays photoanode: improved effect of Bi shell on photoelectrochemical hydrogen evolution in seawater. Int J Hydrog Energy 44:29986–29999
74. Gao R-T, Guo X, Liu S et al (2022) Ultrastable and high-performance seawater-based photoelectrolysis system for solar hydrogen generation. Appl Catal B-Environ 304:120883
75. Li Y, Feng J, Li H et al (2016) Photoelectrochemical splitting of natural seawater with α-Fe2O3/WO3 nanorod arrays. Int J Hydrog Energy 41:4096–4105
76. Zhou G, Guo Z, Shan Y et al (2019) High-efficiency hydrogen evolution from seawater using hetero-structured T/Td phase ReS2 nanosheets with cationic vacancies. Nano Energy 55:42–48
77. Paracchino A, Laporte V, Sivula K, Gratzel M, Thimsen E (2011) Highly active oxide photocathode for photoelectrochemical water reduction. Nat Mater 10:456–461
78. Hamdani IR, Bhaskarwar AN (2021) Recent progress in material selection and device designs for photoelectrochemical water-splitting. Renew Sust Energ Rev 138:110503
79. Bott AW (1998) Electrochemistry of semiconductors. Curr Sep 17:87–91
80. Chen ZB, Jaramillo TF, Deutsch TG et al (2010) Accelerating materials development for photoelectrochemical hydrogen production: standards for methods, definitions, and reporting protocols. J Mater Res 25:3–16
81. Ma X, Zhang J, Wang B, Li Q, Chu S (2018) Hierarchical Cu_2O foam/g-C_3N_4 photocathode for photoelectrochemical hydrogen production. Appl Surf Sci 427:907–916
82. Chu S, Cui Y, Liu N (2017) The path towards sustainable energy. Nat Mater 16:16–22
83. Kim JH, Hansora D, Sharma P et al (2019) Toward practical solar hydrogen production - an artificial photosynthetic leaf-to-farm challenge. Chem Soc Rev 48:1908–1971
84. Dias P, Schreier M, Tilley SD et al (2015) Transparent cuprous oxide photocathode enabling a stacked tandem cell for unbiased water splitting. Adv Energy Mater 5:1501537
85. Huang K, Li C, Meng X (2020) In-situ construction of ternary Ti_3C_2 MXene@TiO_2/$ZnIn_2S_4$ composites for highly efficient photocatalytic hydrogen evolution. J Colloid Interface Sci 580:669–680
86. Parkinson B, Balcombe P, Speirs JF, Hawkes AD, Hellgardt K (2019) Levelized cost of CO_2 mitigation from hydrogen production routes. Energy Environ Sci 12:19–40
87. Pinaud BA, Benck JD, Seitz LC et al (2013) Technical and economic feasibility of centralized facilities for solar hydrogen production via photocatalysis and photoelectrochemistry. Energy Environ Sci 6:1983–2002
88. Lee WJ, Shinde PS, Go GH et al (2011) Ag grid induced photocurrent enhancement in WO_3 photoanodes and their scale-up performance toward photoelectrochemical H_2 generation. Int J Hydrogen Energ 36:5262–5270
89. Vilanova A, Lopes T, Spenke C et al (2018) Optimized photoelectrochemical tandem cell for solar water splitting. Energy Storage Mater 13:175–188
90. Tolod KR, Hernandez S, Russo N (2017) Recent advances in the $BiVO_4$ photocatalyst for sun-driven water oxidation: top-performing photoanodes and scale-up challenges. Catalysts 7:13
91. Chen D, Liu Z, Zhou M et al (2018) Enhanced photoelectrochemical water splitting performance of α-Fe_2O_3 nanostructures modified with Sb_2S_3 and cobalt phosphate. J Alloys Compd 742:918–927
92. Boda MA, Shah MA (2018) Fabrication of $ZnFe_2O_4$/TiO_2 nanotube array composite to harness the augmented photocurrent density under visible light. Appl Phys A 124:55
93. Dabirian A, van de Krol R (2015) High-Temperature ammonolysis of thin film Ta_2O_5 photoanodes: evolution of structural, optical, and photoelectrochemical properties. Chem Mater 27:708–715

94. Hu J, Lu Y, Zhao XF, Tang YQ, Li YZ, Xiao YX, Hu ZY, Su BL, Yang X-Y (2020) Hierarchical TiO_2 microsphere assembled from nanosheets with high photocatalytic activity and stability. Chem Phys Lett 739:136989
95. Hu J, Zhao T, Geng W, Lu Y, Zhao XF, Li YZ, Tang YQ, Liu JW, Wang LY, Janiak C, Yang X-Y, Su BL (2019) Synthesis of hydrophobic and hydrophilic TiO_2 nanofluids for transformable surface wettability and photoactive coating. Chem Commun 55:9275–9278
96. Turan B, Becker JP, Urbain F et al (2016) Upscaling of integrated photoelectrochemical water-splitting devices to large areas. Nat Commun 7:1–9
97. Ray AK, Beenackers AACM (1998) Development of a new photocatalytic reactor for water purification. Catal Today 40:73–83
98. Blommaerts N, Asapu R, Claes N, Bals S, Lenaerts S, Verbruggen SW (2017) Gas phase photocatalytic spiral reactor for fast and efficient pollutant degradation. Chem Eng J 316:850–856
99. Asapu R, Claes N, Bals S, Denys S, Detavernier C, Lenaerts S et al (2017) Silver-polymer core-shell nanoparticles for ultrastable plasmon-enhanced photocatalysis. Appl Catal B-Environ 200:31–38
100. Lu Q, Hutchings GS, Yu W, Zhou Y, Forest RV, Tao R et al (2015) Highly porous nonprecious bimetallic electrocatalysts for efficient hydrogen evolution. Nat Commun 6:6567
101. Xiang C, Chen Y, Lewis NS (2013) Modeling an integrated photoelectrolysis system sustained by water vapor. Energy Environ Sci 6:3713–3721

Photovoltaic Electrocatalytic Seawater Splitting

Yu-Xuan Xiao, Fei Yu, Xiong Yang, and Xiao-Yu Yang

Abstract Hydrogen generation through photovoltaic electrocatalytic seawater splitting is a highly desirable for economically and cleanly harvesting solar energy. Important developments have come from studies of this technology that focus on enhancing the efficiencies and stabilities of these systems for solar-to-hydrogen (STH) application. Herein, we introduce the fundamental principles of photovoltaic electrocatalytic seawater splitting, and discuss recent progress that has been made in developing improved photovoltaic electrocatalytic seawater splitting strategies for STH conversion, giving major attention to studies aimed at developing the novel electrocatalysts. Finally, some of the remaining challenges in this area and the outlook for future advances are presented.

Keywords Photovoltaic electrocatalysis · Seawater splitting · Solar energy · Hydrogen production · Materials characterization · Mechanism research · Sustainable energy cycle · Hydrogen energy industrialization

1 Introduction

Water splitting driven by sun light is a highly desirable technology for sustainable hydrogen (H_2) generation [1–4]. Photovoltaic electrocatalytic water splitting is an interesting method for clean generation of H_2 because it overcomes the shortcomings

Y.-X. Xiao (✉)
School of Chemical Engineering and Technology, Sun Yat-sen University, Zhuhai 519082, China
e-mail: xiaoyx63@mail.sysu.edu.cn

F. Yu · X. Yang
School of Materials Science and Engineering, Wuhan University of Technology, Wuhan 430070, China

X.-Y. Yang
State Key Laboratory of Advanced Technology for Materials Synthesis and Processing (Wuhan), Foshan Xianhu Laboratory of the Advanced Energy Science and Technology Guangdong Laboratory (Xianhu Hydrogen Valley, Foshan), Laoshan Laboratory (168 Wenhai Middle Rd, Jimo District, Qingdao), Wuhan University of Technology, Wuhan, Hubei, China

X.-Y. Yang (ed.), *Photo-Driven Seawater Splitting for Hydrogen Production*,
https://doi.org/10.1007/978-981-99-0510-2_4

of nonstorable electricity power [5]. Moreover, hydrogen is directly produced in these systems by using only economical solar energy and water. However, industrial level photoelectrolysis requires a huge amount of freshwater, which is unfriendly to the already limited water resources [6]. Although seawater is available in near limitless quantities on the earth, its employment in the water-splitting process presents many challenges owing mainly to the instability of component materials [7, 8]. One of the greatest challenges to utilizing seawater in the splitting process is the presence of chloride anions that lead to electrochemical chlorine evolution as well as corrosion of the metal electrocatalysts [9]. Thus, developing novel materials for photovoltaic (PV) electrocatalytic (EC) seawater splitting devices is an important goal. In addition, wide application of PV systems for solar-to-hydrogen (STH) conversion is severely restricted by the low power conversion efficiencies (PCE) of the PV component and the high prices and low stabilities of noble-metal ect [10]. As a result, large-scale application of photovoltaic electrocatalytic (PVEC) seawater splitting systems remains problematic.

2 Principles

With the continuing population growth and economic development of society, traditional energy production mainly based on fossil fuel combustion is encountering many problematic issues, such as high cost, low storage amount of resources, high pollution and greenhouse emission [11–14]. Hydrogen possesses advantageous features as a fuel that are associated with the cleanliness of its combustion, high storage capacity and heating value [15–20]. As a result, this gas could soon become a competitive alternative to fossil fuels. Because sun light and water are two of the inexhaustible and evenly distributed resources available, H_2 production from water has become a major goal of several efforts. Importantly, a combination of sunlight conversion and water splitting systems is highly attractive for this purpose. Because seawater is the most abundant water form on the earth [21, 22], electrolytic splitting form seawater is the most desirable method for large-scale H_2 generation. Below, we describe the underlying principles for operation of photovoltaic and electrocatalytic components of systems to carry out solar based seawater-to-hydrogen conversion.

2.1 PV Cells

A PV system designed to generate electrical power is comprised of multiple components including a solar energy collection unit and a light-to-electricity converting unit. PV systems are rated in terms of their peak kilowatt (kWp) output, which is the amount of electrical power delivered when the sun is directly overhead on a clear day [23, 24]. Owing to the importance of this technology, extensive research has

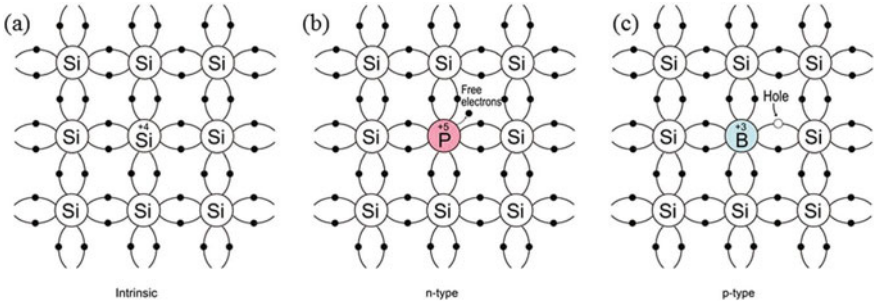

Fig. 1 Schematic illustration for different kinds of semiconductors

been carried out to develop devices that have enhanced efficiency. This has become a rapidly growing industry whose size since 2002 has doubled every two years.

The physical basis for the operation of PV cells, which convert sunlight into electricity directly, is the promotion of an electron in a semiconductor material from a lower energy state to a higher one by absorbing a photon of light. In semiconductors, bonding and antibonding molecular orbitals formed by the overlap of atomic orbitals have closely spaced energies in regions called valence bands corresponding to the highest energy occupied molecular orbitals (HOMOs) and conduction bands (corresponding to lowest energy unoccupied molecular orbitals (LUMOs) [25, 26]. The difference between the energies of the valence and conduction bands is called the bandgap energy. At 0 K, electrons will fill the valence band of a semiconductor, whereas a large electron deficiency for the conduction band. Upon excitation caused by the absorption of a photon of light, electrons will transfer from the valence band to the conduction band, leaving a hole in the valence band creating what is known as charge carriers. Pure semiconductors usually own poor conductivity, thus doping to the semiconductors is often applied to form extrinsic semiconductors. As shown in Fig. 1, donor-doped (for example, P into Si) n-type semiconductors have heteroatoms that possess more valence electrons than the host ones, while acceptor-dope (for example, B into Si) p-type semiconductors have heteroatoms with fewer valence electrons [24].

2.2 Electrocatalytic Seawater Splitting

In the hydrogen generating component of a PVEC device, electricity produced in the PV cell is used to drive EC hydrogen production from seawater, a process that takes place via two redox half-reactions including the cathodic hydrogen evolution reaction (HER) and the anodic oxygen evolution reaction (OER) [27–34]. A two electron-proton transfer process is involved in HER, while a multi-electron transfer process for OER involving loss of four protons for each evolved oxygen molecule and occurring through several intermediates. Depending on the pH of the medium,

the redox processes involved in water splitting take place by two different pathways [35, 36]. In an acidic electrolyte, the coupled redox reactions are those given in the equations below [37–39],

$$\text{Cathode: } 2H^+(aq) + 2e^- \rightarrow H_2(g) \tag{1}$$

$$\text{Anode: } H_2O(1) \rightarrow 2H^+(l) + 0.5O_2(g) \tag{2}$$

while in an alkaline electrolyte and neutral seawater, the redox reactions are those depicted in Eqs. (3) and (4) [39–41].

$$\text{Cathode: } 2H_2O(l) + 2e^- \rightarrow 2OH^-(aq) + H_2(g) \tag{3}$$

$$\text{Anode: } 2OH^- \rightarrow H_2O(l) + 2e^- + 0.5O_2(g) \tag{4}$$

Under standard conditions, the Gibbs free energy (ΔG) for water electrolysis will change 237.2 kJ mol^{-1}, which corresponds to an equilibrium potential of 1.23 V. Nevertheless, the voltage required for water electrolysis is practically higher than 1.23 V due to the existence of kinetic barriers and poor energy efficiencies for the catalytic processes [42]. Though many catalytic electrode materials have good performance towards water electrolysis, many factors, including high onset potentials, low mass diffusion rates, solution concentration, electrode resistances, etc., still limit the wide application of water electrolysis. The factors will usually result in high overpotentials to drive the catalytic reactions or poor durability during the splitting process [43]. As a result, a major challenge in investigations of seawater electrolysis lies in the design of scalable ECs with outstanding efficiencies and durabilities.

A significant problem facing the HER at the cathode is the existence of dissolved cations (Na^+, Mg^{2+}, Ca^{2+} etc.), bacteria/microbes and small particulates for direct seawater splitting. These factors will poison the electrode, degrade the catalysts, thus leading to poor durability [22, 38, 44–46]. For example, when the electrolysis current increases, the pH near the electrode surface dramatically increases, leading to precipitation of metal hydroxides (such as $Ca(OH)_2$ and $Mg(OH)_2$) which will clog the active sites of catalysts. Even at moderate current densities, an increase of 5–9 pH units will occur near the electrode surface (Fig. 2) [47]. To address the negative effects of pH fluctuation, buffers or additives are usually required to stabilize the pH of the electrolyte. In addition, other strategies like those using electrolysis cells that contain membranes to separate the precipitates from the cathode have been employed to overcome this problem.

In addition, reactions at the cathode of metal ions dissolved in seawater can also take place at certain electrocatalytic potentials (Fig. 3a). Hence, it is of great significance to limit the harmful electrochemical processes in ECs for HER in seawater. For this purpose, utilizing membranes to separate catalysts and seawater (Fig. 3b),

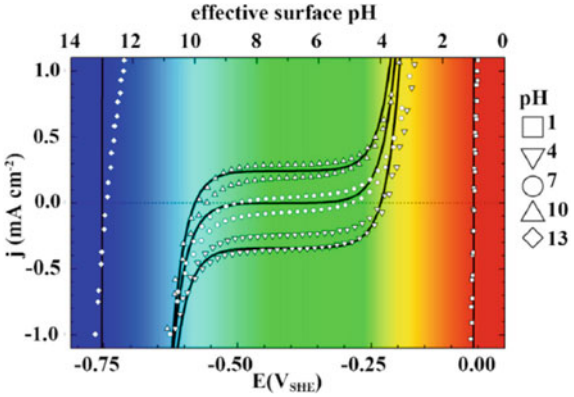

Fig. 2 The relationship between the current density with the surface pH [47]

utilizing catalysts with high corrosion resistance (Fig. 3c), or incorporating permselective blocking layers on catalysts (Fig. 3d) are possible approaches to instill high stability of ECs for seawater HER [38].

On the other hand, there are large number of anions (such as Cl^-) that are electrochemically active to interfere with the anodic OER. Considering all possible anions and their corresponding standard redox potentials, chloride oxidation should be the major process competing with the OER at the anode [22]. This issue was revealed by Bennett in 1980, who found direct seawater electrolysis will result in high current

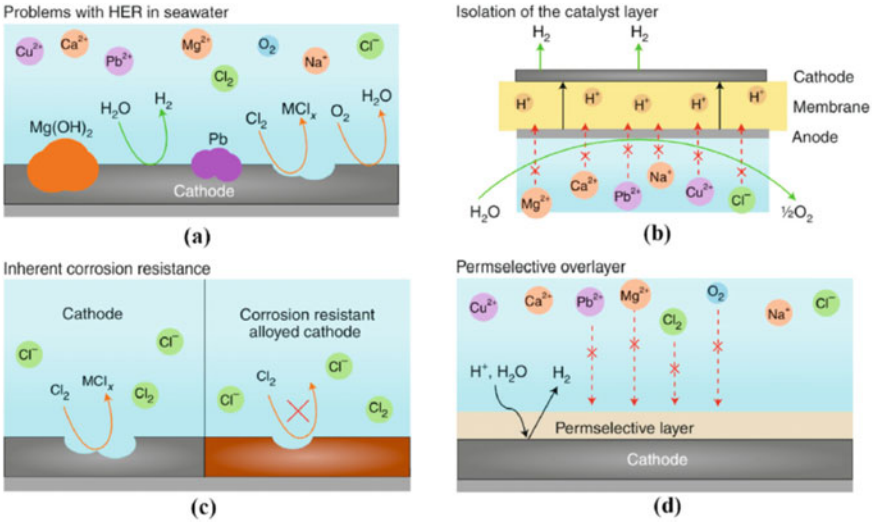

Fig. 3 Problems occur for HER in seawater and their possible solutions [38]

efficient formation of hydrogen at the cathode, along with a large quantity of chlorine at the anode in the form of hypochlorite. Redox reactions of chloride ion in aqueous solution can follow several pathways that depend on pH, applied potentials and chloride concentration.

Strasser et al. conducted detailed analysis of seawater electrolysis, giving rise to a calculated Pourbaix diagram for OER and chloride chemistry (Fig. 4) [9]. The diagram shows that the chlorine evolution reaction (ClER) taking place mainly at a pH less than 3 and hypochlorite occurring predominantly at a pH higher than 7.5 are the main competitive reactions with OER [9, 22]. Moreover, under high anodic potentials, generation of hypochlorous acid is the dominant reaction for pH 3–7.5. Under acidic conditions, ClER occurs by the pathway given in Eq. 5, while hypochlorite will form in alkaline conditions by the route displayed in Eq. 6 [48, 49].

$$2Cl^-(aq) \rightarrow Cl_2O(g) + 2e^-(E_0 = 1.36\ V\ versus\ SHE) \tag{5}$$

$$Cl^-(aq) + 2OH^-(aq) \rightarrow 2ClO^-(aq) + H_2O(l) + 2e^- \quad (E_0 = 0.89\ V\ versus\ SHE) \tag{6}$$

It can be found from Eqs. 5 and 6 that both processes are two-electron transfer reactions, which means they are more kinetically favorable compared to OER with four electrons transferred. Even though OER is more thermodynamically favorable, ClER has a much larger rate, which is responsible for a higher overpotential required for OER than ClER. As a result, a high selectivity of materials for OER is required for the seawater electrolysis.

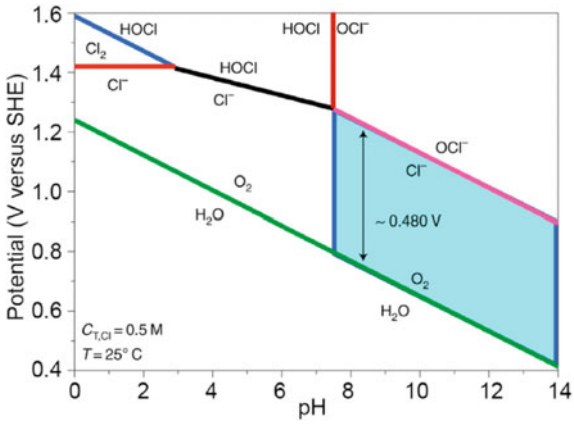

Fig. 4 OER Pourbaix diagram in artificial seawater [9]

2.3 Historical Development PVEC Seawater Splitting Systems

As mentioned above, harvesting energy directly from sunlight is highly desirable to fulfill the World's clean energy needs. Solar energy is an inexhaustible natural resource that is available on the earth's surface [50]. But some earth criteria should be noticed to fully utilize solar energy worldwide. Firstly, environmentally benign means should be used for the conversion, storage and distribution of solar energy. Next, energy provided in this manner must delivered with a stable and constant flux. Thirdly, a steadily conversion efficiency is vital in regards to the daily and seasonal variability of sunlight. Finally, perhaps the most important criteria are that the energy production goals should be cost-effective [51].

Several different approaches to convert solar energy into other forms of energy have been explored. PV and photoelectrochemical (PEC) cells, and solar-thermal systems are being developed to produce electricity from sunlight [50]. Alternatively, sunlight can be used to generate fuels either directly by using PEC cells or indirectly by using sunlight to generate electricity to drive the EC process [52–54]. The latter technology utilizes either discrete, stand-alone units or integrated systems called PVEC hybrid systems. Fuels can also be generated by using thermochemical systems [55].

PVEC systems have the highest STH conversion efficiency among the three solar hydrogen production protocols. Integrated, partially integrated and non-integrated strategies have been employed for coupling the PV and electrolytic water splitting components of PVEC systems (Fig. 5) [56]. Khaselev and Turner first fully investigated the PVEC device to produce hydrogen through water splitting in 1998 [57]. This system has greater than 10% STH efficiency. A self-operating integrated photoelectrocatalytic device comprised of a photoanode and a double junction solar cell was found to have a 8.1% increased STH efficiency [58]. Luo et al. used a hybrid system comprised of a perovskite PV cell and NiFe oxides as the EC with a 12.3% STH efficiency [59]. Bonke et al. fabricated a PVEC based on a multi-junction solar cell with Ni electrodes with a STH efficiency as high as 22.4%.

The efficiencies of PVEC systems are determined by the performance of the PV cell and the EC component. Although the overall hydrogen production efficiencies of hybrid PVEC systems are already at industrial levels, the solar cells employed in these devices are relatively complicated and expensive making the cost far greater than that of hydrogen generated from fossil fuels. Neglecting costs, PVEC systems have the highest feasibility for generation of hydrogen needed in special aerospace, navigation and military applications.

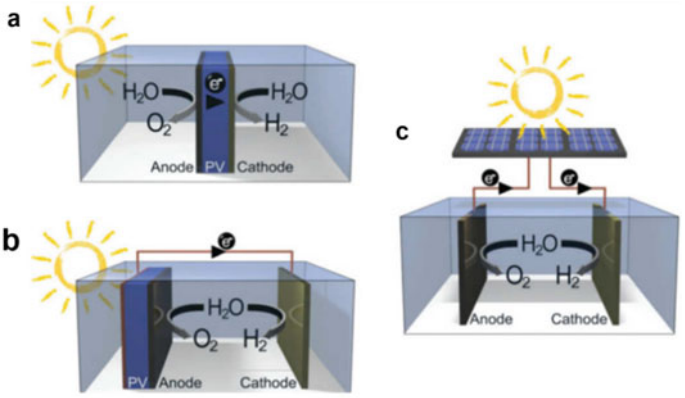

Fig. 5 Three methods to fabricate the photovoltaic and electrolytic water splitting system

3 Progress Made in Designing Efficient PVEC Seawater Splitting Systems

PV cells in PVEC devices for EC seawater splitting usually utilize monocrystalline, polycrystalline and triple-junction amorphous silicon, perovskites, and composite films. For example, an integrated PVEC system designed by Hsu et al. contained a PV cell comprised of a triple-junction solar cell connected to an electrocatalytic cell [60]. In addition, Kuang et al. [61] fabricated a perovskite based PV cell using a spin coating and thermal evaporation method. Briefly, an organic solution was spin coated on ITO-coated glass. Then spin-coating was employed to deposit the perovskite, and then a 130 nm layer of silver was applied thermal evaporation through a shadow mask. Wu et al. [62] designed an efficient solar-driven self-powered seawater splitting system composed of a Si PV cell, connected via a micro-array zinc-ion battery (m-ZIB) to an electrolytic cell containing a NiCo-layered double hydroxide (LDH) cathode and Zn anode. In the device, the Si PV cell absorbs sunlight to produce electricity to power the battery, and then drives the electrocatalytic HER and OER.

The development of PV cells is at a highly mature state. At this time, commercial silicon and perovskite-based PV cells are widely used for many light conversion purposes. Thus, PV cells of these types have been employed to simplify experimentation that is greatly needed to better understand materials and conditions required to optimize EC seawater splitting. Thus, in the discussion below, we do not describe recent investigations of the PV systems. Rather this section mainly discusses recent advances made in the development of electrode materials and conditions used for EC seawater splitting. Coverage of the electrode materials is divided into four metal-based categories, including platinum and nickel-based materials, metal containing compounds, and metal/metallic compound composites.

3.1 Metals

3.1.1 Platinum

Kumari et al. [63] developed a PVEC system that produces hydrogen by solar energy induced splitting of water vapor present under near-surface ocean conditions. In this effort, an amorphous-Si (a-Si)-based PV cell was utilized to drive electrolysis of water in humid air (80% relative humidity). The reversible fuel cell contained a membrane electrode assembly (MEA) with Pt/C catalyst particles deposited using a standard hot press method on both sides of a Nafion proton-exchange membrane (Fig. 6) [64–67]. The anode and cathode were comprised by stainless steel grids with, and the gas diffusion part was comprised by carbon Toray paper sheets with separate gas inlet and outlet ports at both anode and cathode.

Plenty of studies have been conducted to assess various features of the system developed by Kumari et al. In Fig. 7a is shown the J–V behaviors of the proton exchange membrane (PEM) electrolyzer using liquid deionized (DI) water and seawater as feedstocks. The plots show that the system displays that the initial J–V performances using both feedstocks are similar in association with a current density of ~60 mA cm^{-2} under a potential of 1.6 V. Potentiostatic measurements showed that after 60 h operation at 1.6 V, the feedstock system experiences only a small change while the electrolyzer using seawater displayed an apparent decline in current density. After 60 h, seawater fed PEM electrolyzer had a nearly negligible electrolysis current of <2 V.

The J–V behavior with water vapor in N_2 saturated seawater fed to both electrodes (Fig. 7b) showed that with an increasing $N_2(g)/H_2O(g)$ flow rate, the mass-transport-limited electrolysis current density increases. Meanwhile, with a 20 sccm flow rate applied to each electrode, the faradaic efficiency for cathodic H_2 production was 93%, and the H_2:O_2 production ratio was 2:1.15.

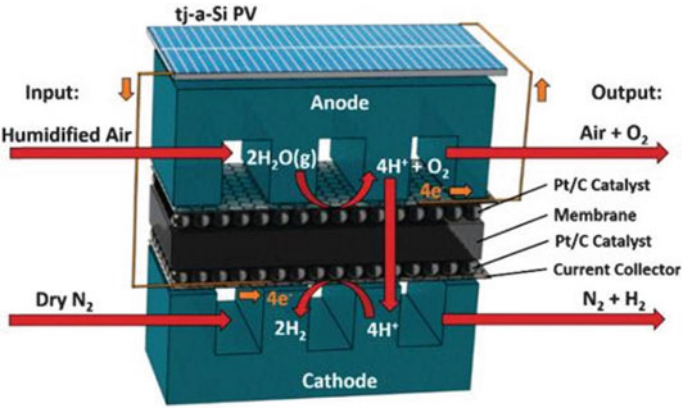

Fig. 6 Schematic illustration of the junction of MEA with a-Si-based PV cell

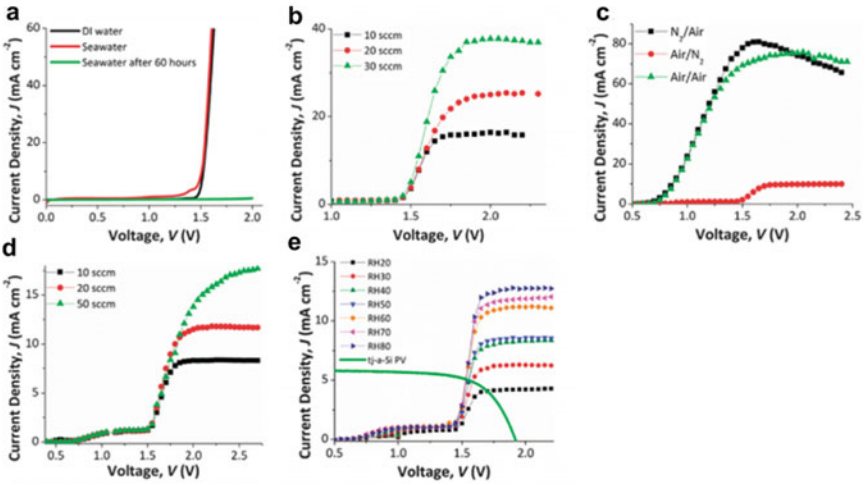

Fig. 7 J–V behaviors of the a-Si-based PV cell driven electrolysis system

The J–V behaviors to investigate the effects of using seawater humidified air versus N_2 as the carrier gas were also evaluated. Negligible current densities were found at <0.75 V in each case. When the humid air and N_2 carrier gas were present at both electrodes, the current density was still low until V > 1.5 V where J increased to and plateaued at ~11 mA cm^2 at >1.7 V. Nevertheless, when humid air was fed to both electrodes, the onset potential for generating an observable current decreased to ~0.7 V, after which it rises rapidly and reaches a density of ~70 mA cm^2 at >1.5 V. The PEM electrolyzer behaved similarly when N_2 gas was fed to the anode and air to the cathode.

The performance of the PEM electrolyzer as a function of humid air flow at the anode and N_2 at the cathode was also evaluated (Fig. 7d). At a 10 sccm flow rate to the anode, a limiting current density of ~8 mA cm^2 was found and it rose to over 18 mA cm^2 with the increase of the flow rate to >50 sccm. A decrease in relative humidity at the anode caused a decrease in the limiting current density. With a 20 sccm flow of humidified air to the anode and 10 sccm of dry N_2 to the cathode, the current density >12 mA cm^2 is produced at a relative humidity (RH) ~80% (RH80) and <4 mA cm^2 at RH ~20% (RH20). The J–V performance of one sun illuminated a-Si-based PV was evaluated to assess operation of the solar-driven electrolysis system (Fig. 7e). A power-conversion efficiency of 7.9% was found for the system.

In Fig. 8a, plots of electrolysis current densities vs time are given for a system with dry N_2 flow to the cathode and RH80 air to the anode humidified by seawater or DI water. In these experiments, a steady potential of 1.6 V was applied to the PEM electrolyzer, which is close to the expected operating potential when driven by the a-Si-based PV cell. The initial current density for electrolysis of water in seawater humidified air was high, but after 50 h it continuously dropped to <2 mA cm^2. In contrast, when electrolysis was conducted using either air humidified by

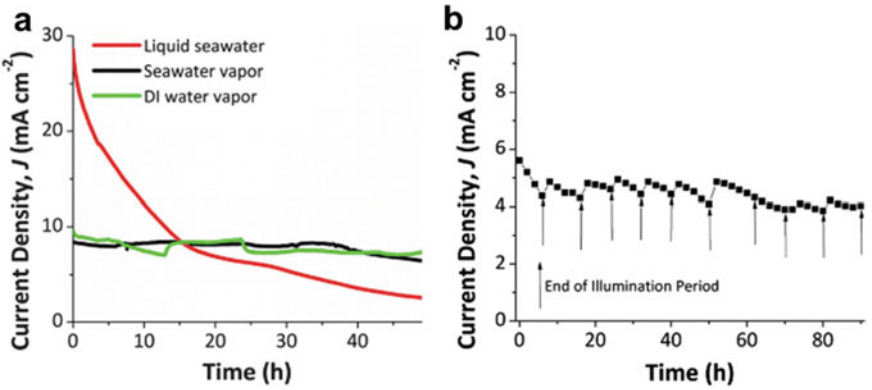

Fig. 8 Durability tests of the a-Si-based PV cell driven electrolysis system

using seawater or DI water (80% relative humidity), the current density quickly rose and stabilized for >50 h at ~7–8 mA cm^2.

Comparisons between the J–V behaviors of a PEM electrolyzer with seawater, or seawater or DI water humidified air, before and then over an extended time period are given in Fig. 8b. In liquid seawater, the initial current density at 1.6 V was 56.5 mA cm^2 and it decreased to 0.2 mA cm^2 after 50 h. In contrast, the limiting current density with seawater vapor feedstock reached ~11 mA cm^2 initially and dropped modestly to ~8 mA cm^2 after the 50 h. However, the current density of the seawater vapor-fed remained 6–7 mA cm^2 at 1.6 V during the measurement time.

3.1.2 Platinum/Titanium

Davis et al. developed a scalable PVEC device for solar-driven H_2 production from water [68]. The electrolyzer in this device produces high purity H_2 without needing active pumping of the electrolyte. An important feature governing the operation of this system is the use of novel Pt coated Ti mesh electrodes. They put forward a design of membraneless PV-electrolyzer prototype that can potentially be further assembled into a large-scale, floating solar hydrogen producing rig, as displayed in Fig. 9a. This novel device enables efficient H_2 and O_2 separation and collection without using membranes. The side-views of electrolysis cells are displayed in Fig. 9b, c. The small angle between the electrodes and the presence of the active EC only on the outer surfaces of the mesh electrodes are two notable features. These types of electrodes, called “asymmetric electrodes”, in contrast with symmetric electrodes have catalysts coated on both sides. In this way. separation of the produced gas is improved by directing bubbles to float upwards in an unimpeded manner.

The membraneless mesh electrode was tested in an electrochemical cell. The electrolyzer shown in Fig. 10a comprised by a rectangular container holding the electrolyte that has two glass windows on the front and back sides to allow for in situ

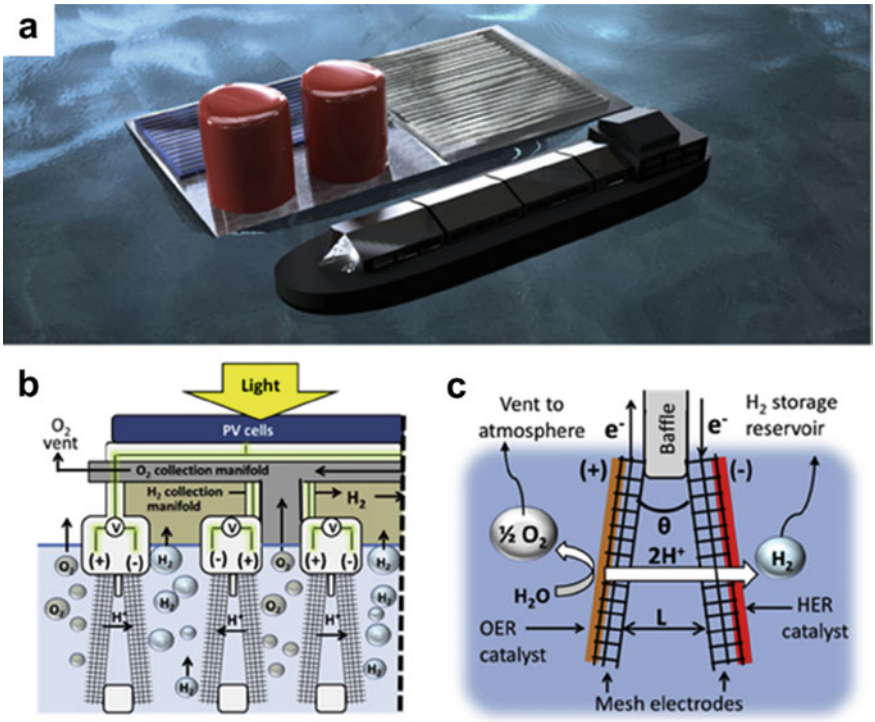

Fig. 9 Schematic illustration of the membraneless PV-electrolyzer prototype

high speed video side-view imaging of gas bubble evolution. The second component located in the cell body, is a lid through which mesh electrodes are inserted. The lid contains two 3 mL gas collection chambers above the anode and cathode that are separated by a 1 mm barrier. Although the two opposing mesh electrodes span the cell from top to bottom, electrolysis only takes place in the lower portion where the electrodes are submerged in electrolyte. Each collection chamber is capped with a rubber septum to exclude surrounding air. Prior to operation of the cell, the electrolyte is syringed into the collection chambers. During the electrolysis reaction, product gas bubbles flow into and displace the electrolyte in the collection chambers.

The separation process utilizing an asymmetric mesh electrode was visualized by a high-speed video camera. An image of the operation of an "asymmetric" electrode, in which the Pt coated sides face outwards, is shown in Fig. 10b. When the electrolyte has sufficiently conductivity and the gap between the two electrodes is small, low solution resistance occurs because dissolved ionic species which do not experience buoyancy forces readily pass through the mesh holes. Inspection of the image in Fig. 10b shows that bubble nucleation primarily occurs on the outside faces of the asymmetric electrodes. When the bubble size grows to a point at which the buoyancy force exceeds that of surface adhesion, it detaches from the electrode and rises into the overhead

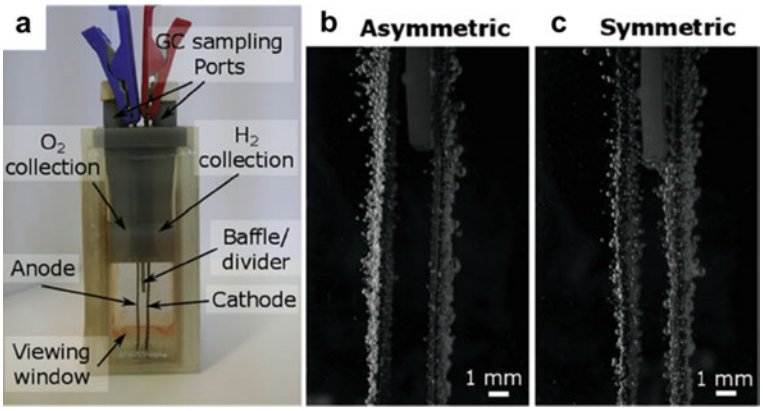

Fig. 10 Photographic image of an electrolysis cell and the bubble growth image on asymmetric and symmetric electrodes

collection chamber. Passive membraneless electrolyzer containing asymmetric mesh electrodes operate with minimal product "cross-over", which is defined by the event involving transport of the product generated at one electrode across the electrode gap and collected in the other collection chamber. A still frame image of bubble formation on symmetric electrodes, having Pt deposited on both sides, is given in Fig. 10c. In contrast, bubble growth on asymmetric electrodes takes place primarily on the outside surfaces. In the latter case, after arriving at the region between electrodes, the bubbles experience local convection causing them to rise into either collection chamber, resulting in loss of product purity.

The voltage efficiency associated with electrolysis by both the asymmetric and symmetric electrodes can be assessed using two-electrode current–voltage (IV) curves. For the trigger of electrochemical water splitting, the applied voltage should be larger than the potential difference between OER and HER ($\Delta E_0 = 1.23$ V at standard conditions). The voltage efficiency of the electrolyzer is equal to ΔE_0 divided by the operating voltage. The IV characteristics of parallel ($\theta = 0°$) asymmetric and symmetric electrodes in 0.5 M H_2SO_4 are displayed in Fig. 11a. At 100 mA cm^{-2} current density, the electrolysis efficiencies are 50.6 and 53.4% for the asymmetric and symmetric electrodes, respectively. The symmetric electrodes have relatively higher efficiency, which is owing to the existence of higher active surface area. When difference in the Pt surface areas is accounted for, the I–V curves for the asymmetric and symmetric electrodes are coincident (Fig. 11b). IV characteristics of asymmetric electrodes that have different separation angles are given in Fig. 11c. At 100 mA cm^{-2} current density, a decreased efficiency to 48.8% was found at an angle of 30°. The loss is associated with an increased solution resistance as the separation distance increases. When the curves are ohmic resistance corrected, the plots become coincident.

The product collection efficiency of an electrolyzer can be less than 100% because of several factors, including dissolution losses, back reaction and H_2 bubbles that are

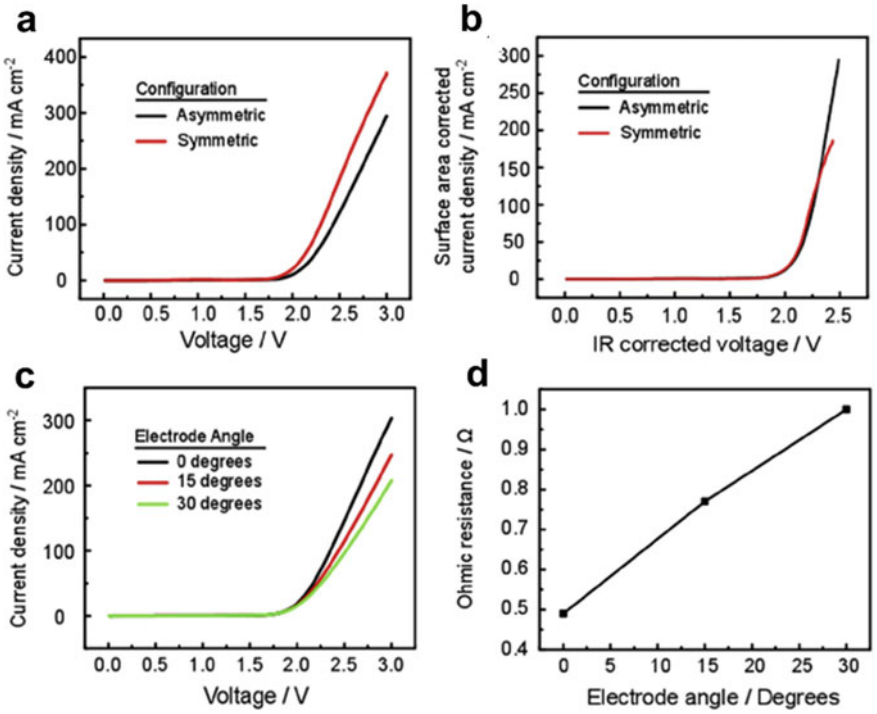

Fig. 11 OER tests of the membraneless electrolyzer

not collected. In this study, the membraneless electrolyzer H_2 collection efficiency was determined by measuring the time dependent increase in the volume of H_2 collected in the overhead chamber. The time dependence of volumes of H_2 and O_2 arriving in the lid during constant 40 mA cm^{-2} current electrolysis, using asymmetric electrodes held at a separation angle of 30°, is displayed in Fig. 12a. The error bars in the plot are 95% confidence intervals at each average collection time of collection in three independent measurements. According to the stoichiometries of the processes, the ratio of the relative rates of H_2 and O_2 collection is 2:1 ratio. In the plot, solid lines are theoretical rates of product generation. A comparison of the slopes of plots of experimental and predicted data shows that the volumetric collection efficiencies for H_2 and O_2 are 83.0% and 83.8%, respectively (Fig. 12b).

A successful demonstration of the viability and selectivity of buoyancy driven product separation, the membraneless design was used to construct a bench scale floating PVEC module. As shown in Fig. 13a, the system is comprised of two sets of asymmetric electrodes with an angle of 30°, wired in parallel and connected to four parallel-connected c-Si PV panels, each of which consisted of 6 sub-cells that are connected in series. The entire module was then placed in a 1 L reservoir of 0.5 M H_2SO_4 (Fig. 13b), where it floats on the surface as a result of the high buoyancy of the

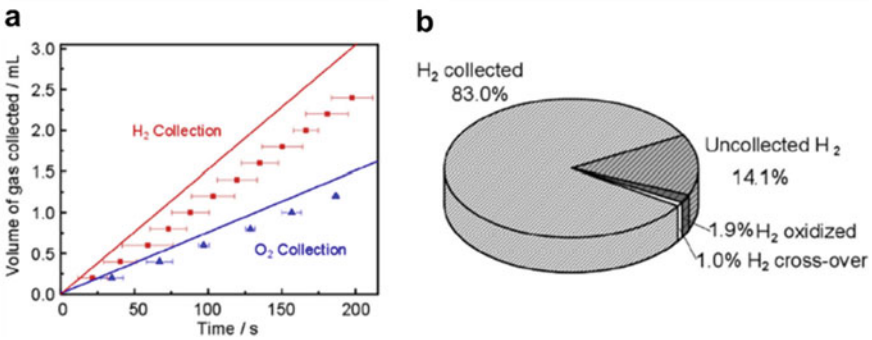

Fig. 12 Hydrogen production of the membraneless electrolyze

void-containing 3D-printed raft. H_2 collected in the interior reservoir was sampled through a sealed port and subjected to GC analysis.

Figure 13c shows the predicted performance of the PVEC device, estimated by using the intersection of individually generated IV curves of the electrolyzer and PV panels. The performance of the four PV was determined under illumination using

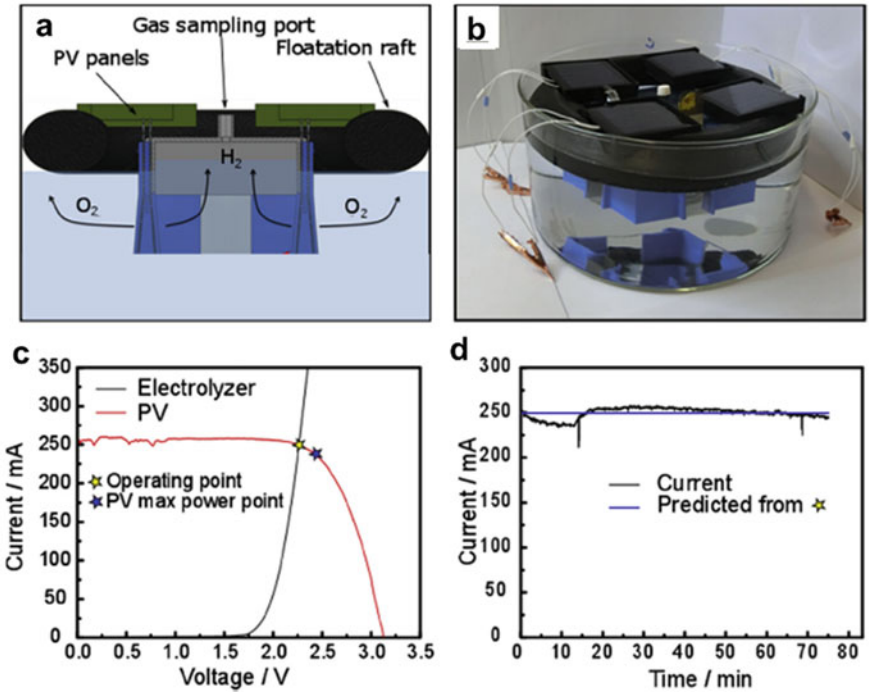

Fig. 13 The floating PVEC module and its solar driven hydrogen production performance

an unfiltered halogen lamp with a solar AM 1.5 power intensity (100 mW cm^{-2}). Analysis of the resulting IV curve shows that the system has a photovoltaic efficiency (η_{PV}) at the maximum power point of 10.0%. The 2-electrode IV curve for the two pairs of asymmetric electrodes indicates that the water electrolysis current begins to increase at an applied voltage of ~1.7 V, and then exponentially rises as the voltage is increased above this voltage. The electrolyzer (η_e), coupling (η_c), and solar-to-hydrogen (STH) efficiencies (η_{STH}) can be determined from the intersection of the two IV curves. The efficiency of the electrolyzer is calculated to be $\eta_e \approx 54\%$, and the coupling efficiency is calculated to be 98%. These observations indicate that the PV and electrode arrangements are almost perfectly matched. Combining all these efficiencies, the STH conversion efficiency (η_{STH}) is predicted to be 5.3%. The floating PVEC module was tested under continuous illumination in 0.5 M H_2SO_4 for 75 min. The plot of the operating current of the device as a function of time given in Fig. 13d reveals that the system experiences stable operation. During operation, H_2 was collected underneath the central lid while O_2 was allowed to vent to the atmosphere. After the H_2 collection chamber was filled, the gas was analyzed using GC. After subtracting the O_2 component associated with air (based on an N_2:O_2 ratio of 79:21), the purity of the collected H_2 gas was determined to be 98%.

3.2 Intermetallic Compounds

3.2.1 Nickel

Gao et al. developed a nickel foam (NF) based monolithic electrode that has extraordinary performance for both HER and OER in neutral aqueous media [69]. The electrode, which has karst landform features, has a surface that is composed of metallic Ni valleys and Ni/α-$Ni(OH)_2$ heterostructure towers. It is worth noting that the electrode can reversibly and flexibly switch between the HER and OER with long-term stability. Combined with a PV cell, this bifunctional electrode containing EC cell exhibited a high STH conversion efficiency of 16.5% towards natural seawater splitting.

As shown in Fig. 14, to prepare the karst NF electrode, a piece of the NF was directly etched in 0.5 M H_2SO_4, which created a karst landform-featured surface of NF within minutes with a Ni/α-$Ni(OH)_2$ interface.

Figure 15 shows the scanning electron microscope (SEM) characterization of karst NF. Compared to the original NF (Fig. 15a–c), the as-prepared karst NF inherits the 3D skeleton of NF and contains metal domains that are roughened to produce a typical karst morphology comprised of arrays of tall towers and deep valleys. Transmission electron microscope (TEM) images indicate that the towers have a length of ~500 nm and width of 100–200 nm. High resolution TEM (HRTEM) images show that the lattice spacing of 0.205 nm in the central region can be ascribed to metallic Ni (111) facets, and the lattice fringes with spacing of 0.159 nm are indexed to the (110) facets of α-$Ni(OH)_2$, which arises from the epitaxial conversion of Ni.

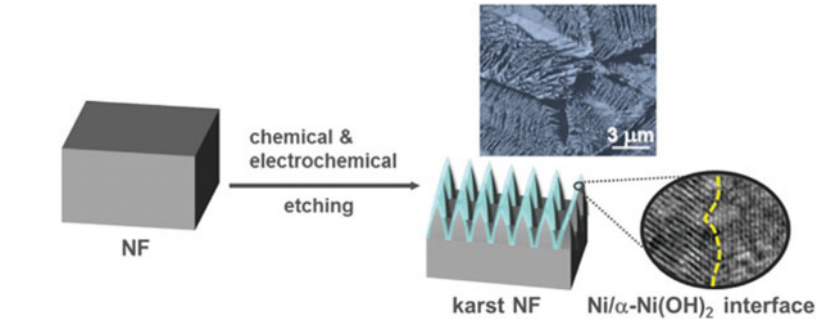

Fig. 14 Illustration of the synthesis of karst NF electrode

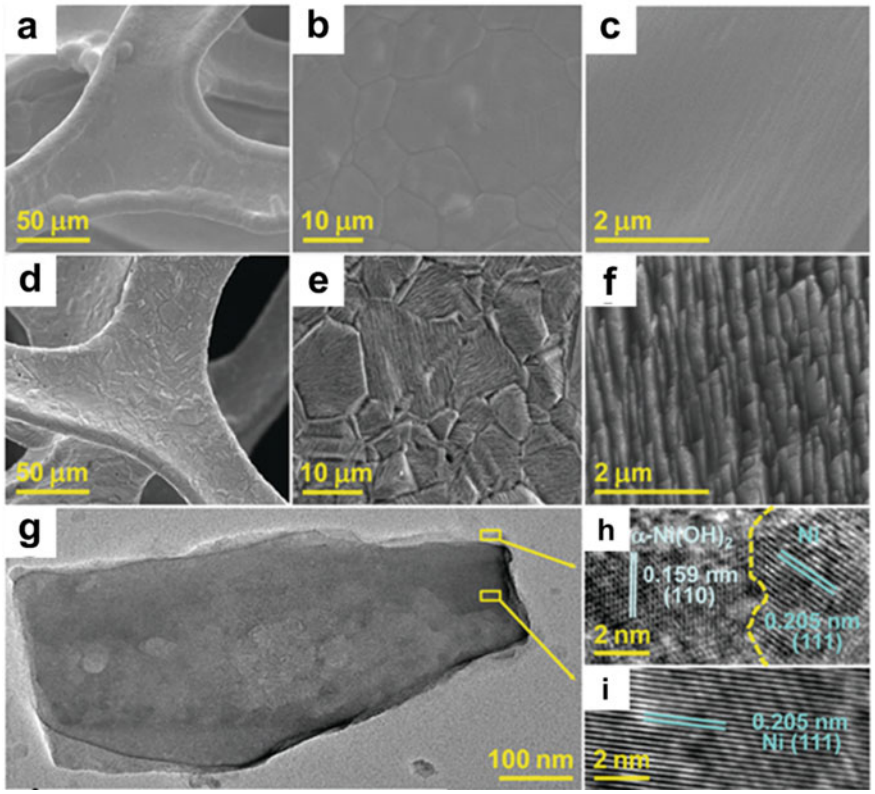

Fig. 15 SEM characterization of karst NF electrode

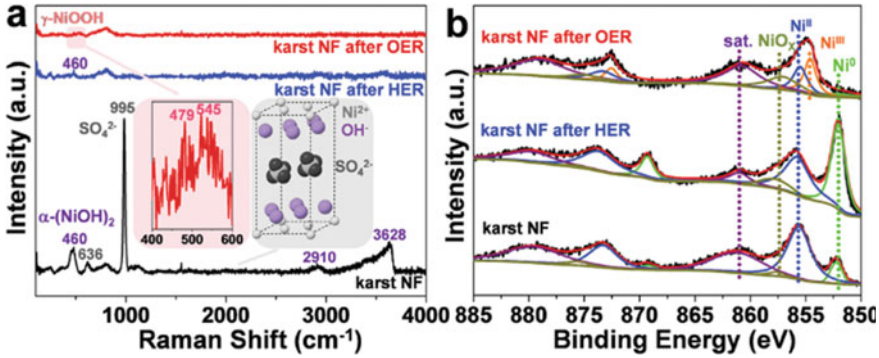

Fig. 16 Raman and XPS spectra characterization of karst NF

As shown in Fig. 16a, Raman bands at 460, 2910 and 3628 cm^{-1} correspond to the respective lattice 2nd order O–H bending and O–H stretching modes of α-$Ni(OH)_2$. The additional peaks at 636 ($\nu 4$) and 995 ($\nu 1$) cm^{-1}, associated with vibrational modes of SO_4^{2-}, are shifted to higher frequencies in contrast to those of free SO_4^{2-} as a result of adjacent cations interactions. Moreover, the weak band at 804 cm^{-1} corresponds to surface NiOx. As shown in the X-ray photoelectron spectroscopy (XPS) spectra in Fig. 16b, Ni $2p_{3/2}$ main peaks at 852.0 and 855.6 eV in the Ni 2p region confirms that Ni^0 and Ni^{II} states exist on the surface of the catalyst. Notably, the Ni^0 binding energy is slightly lower for Ni–$Ni(OH)_2$ than that it is for Ni metal (~852.6 eV), indicating charges are present in the Ni side. Furthermore, the binding energy of $Ni(OH)_2$ is slightly higher for Ni–$Ni(OH)_2$ than it is for $Ni(OH)_2$ (~854.9 eV), indicating a deficiency of charges on the $Ni(OH)_2$ side.

The electrochemical performance of the karst NF in 1.0 M phosphate buffered saline (PBS) solution was determined by using linear sweep voltammetry (LSV) (Fig. 17). Compared with blank NF that has a very low activity, karst NF exhibits a much lower overpotentials (at 10 mA cm^{-2}) of 110 mV for HER and 432 mV for OER. In contrast to most electrocatalysts that do not promote both the HER and OER in neutral solutions, karst NF has superior bifunctional activity in near neutral solutions. The karst NF achieves larger currents than does Pt/C, indicating the existence of enhanced mass diffusion. Moreover, the Tafel slopes for HER and OER are 99 and 249 mV dec^{-1}, the former of which indicates that the Volmer step is rate-limiting, while the latter indicates a slow discharge process occurs, as a result of the occurrence of strong pre-catalytic events.

The durability of the karst NF electrode was also tested and shown in Fig. 17d. The steady current densities during 10 h for HER and OER confirm its stability under neutral conditions. The decrease in signals for Ni(II) and increase for those of Ni(0) in the XPS spectrum shows that 10 h after the HER was promoted by chronoamperometry at −0.21 V without iR compensation, a portion of α-$Ni(OH)_2$ is transformed to metallic Ni. The weak Raman peaks also indicates that reduction

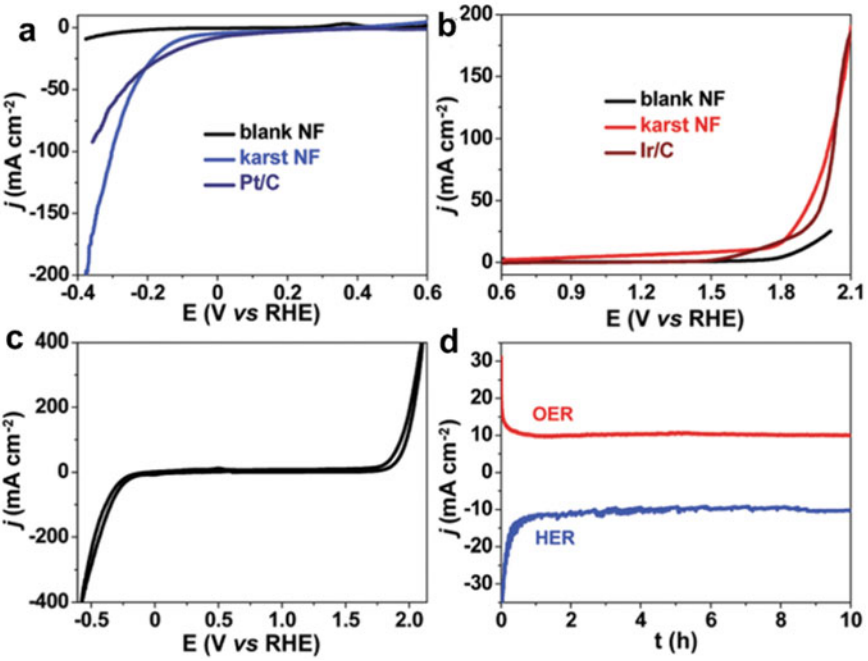

Fig. 17 HER and OER electrocatalytic performance tests of karst NF

of α-Ni(OH)$_2$ after the HER. Finally, after 10 h durability test, the surface Ni(II) was transformed to γ-NiOOH as reflected in Raman peaks at 479 and 545 cm^{-1}.

To demonstrate an application to EC STH, a karst NF||karst NF two-electrode cell was fabricated for water and seawater splitting. In regards to the Pt/C||Ir/C counterpart, the much inexpensive NF based cell requires much lower voltages of 2.2 V to drive current densities of 100 mA cm^{-2} in PBS solution (Fig. 18a). In natural seawater, 10 mA cm^{-2} current density was obtained at an applied bias of 1.79 V, a value that is superior to even that in PBS solution. An evaluation of the long-term stability of this cell at a constant current density of 10 mA cm^{-2} (Fig. 18b) showed that compared with the attenuation of activity occurring with the Pt/C||Ir/C cell, a stable cell voltage was maintained for the karst NF||karst NF cell after 24 h electrolysis. However, in natural seawater, the cell voltage has a dramatical decline owing to the complex composition of seawater. The karst NF-based cell was then connected to a commercial silicon solar PV cell to create a PVEC device for seawater splitting (Fig. 18c). The Si solar cell exhibits an open-circuit voltage of 2.3 V with a photon-current conversion efficiency of 25.5% at a sun radiation of 70 mW cm^{-2}. A current density of 9.4 mA cm^{-2} was generated in the integrated seawater splitting process with oxygen and hydrogen produced on each electrode (Fig. 18d). The electric-to-hydrogen conversion efficiency was 64.7%, and the overall STH conversion efficiency was 16.5%.

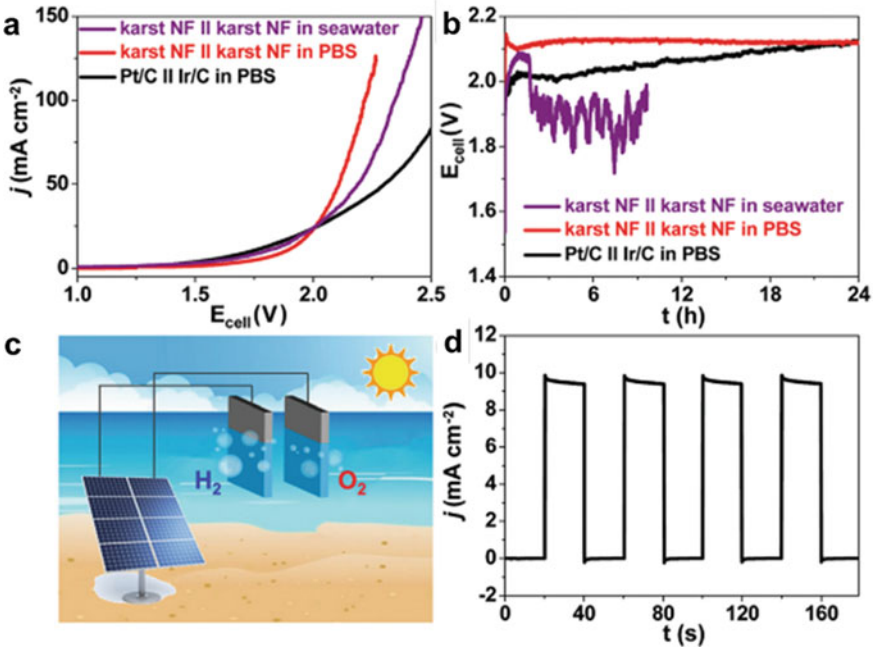

Fig. 18 Solar driven water splitting tests of karst NF electrode

The Peak Force scanning electrochemical microscope (PF-SECM) schematic and images of karst NF shown in Fig. 19a–d indicate that the 3D topographical profile of the electrode surface has valley (dark) and tower areas (bright). Peak currents for the HER occur mainly in valley areas of the karst NF, as reflected by the presence of dark areas in the topographical profile and blue-white areas in the electrochemical profile. In contrast, as indicated by bright areas in the topographical profile and the pink-red areas in the electrochemical profile, peak currents for the OER are present in tower areas. The deep valley areas correspond to exposed metallic sites at which formation of Ni–H_{ad} takes place, and the tower areas contain hydroxides for oxygen evolution. Thus, different locations in the Ni/α-$Ni(OH)_2$ heterostructures are responsible for promoting the individual HER and OER. Ni–H_{ad} generated by the metallic sites for subsequent hydrogen formation and the other site assists water dissociation by accepting the leaving hydroxide anion, giving hydroxides that are the evolution sites for the OER. Finally, polarization of the electrodes at the interface between the sites helps electron depletion to occur on the Ni^{II} to boost OER.

Figure 19e shows the density of states (DOS) associated with different models. For Ni–$Ni(OH)_2$ heterostructure, a strong metallic nature was found as expected. On the other hand, the partial DOS of the α-$Ni(OH)_2$ in the Ni/α-$Ni(OH)_2$ has continuous spin-up bands through the Fermi level, illustrating some semi-metallic nature on the surface of $Ni(OH)_2$. As a contrast, the DOS of pure $Ni(OH)_2$ indicates that it has the normal semiconductor properties, which could enhance electrolysis by improving

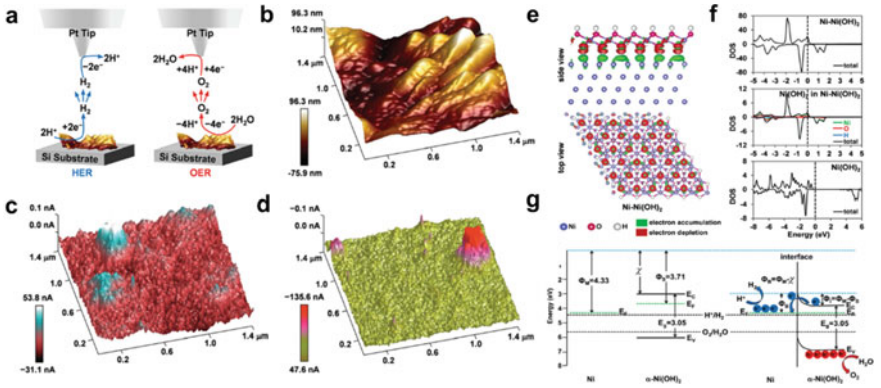

Fig. 19 SECM characterization and DOS calculation of the karst NF

charge transfer. The band structures and electrostatic potential calculations enable determination of the energy levels of the Ni metal and the $Ni(OH)_2$ semiconductor (Fig. 19f). Because the work function of the n-type semiconductor is smaller than the metal, a zone of charge and upward band bending occurs along with a depletion of electrons in the semiconductor to maintain the same of the Fermi level positions. Electron polarization happens when a heterostructure between the two components forms, which is consistent with the results shown in Fig. 19g. The redistribution of electrons at the Ni/α-$Ni(OH)_2$ interface causes upward band bending to occur in the semiconductor. Metal becomes more negatively charged, which is favorable for formation of the key M–H intermediate. Also, electron redistribution away from Ni(II) at the heterojunction interface enhances accumulation of positive holes to boost the OER.

3.2.2 Metal Sulfide

Gnanasekar et al. [70] developed the vanadium disulfide (VS_2)/amorphous carbon (AC) heterostructure as the seawater splitting electrode. To construct this electrode, two-dimensional VS_2 nanoparticles were highly uniformly deposited on AC using an optimized one-step chemical vapor deposition method (Fig. 20).

SEM (Fig. 21a, b) shows that the growth of VS_2 on AC takes place in a uniform manner to produce VS_2 particles with a size range from 50 to 200 nm, which is owing to the coalescence and Oswald ripening (Fig. 21c). HRTEM confirms the presence of a layered structure of VS_2 grown on AC, which can be seen through the selected area electron diffraction (SAED) patterns in Fig. 21d. Element mapping images shown in Fig. 21e–i shows the homogeneous distribution of V and S on the carbon skeleton.

The Raman spectrum of bare AC exhibits fingerprint D-, G-, and 2D-band carbon vibrations at 1350, 1576 and 2704 cm^{-1}, respectively. In contrast, the spectrum of the VS_2/AC heterostructure contains characteristic VS_2 peaks at 140, 281 and 405 cm^{-1},

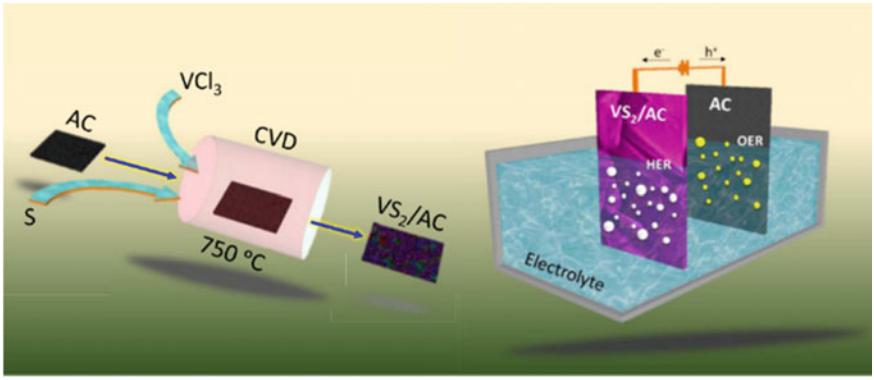

Fig. 20 Schematic illustration for the synthesis ofVS_2/AC

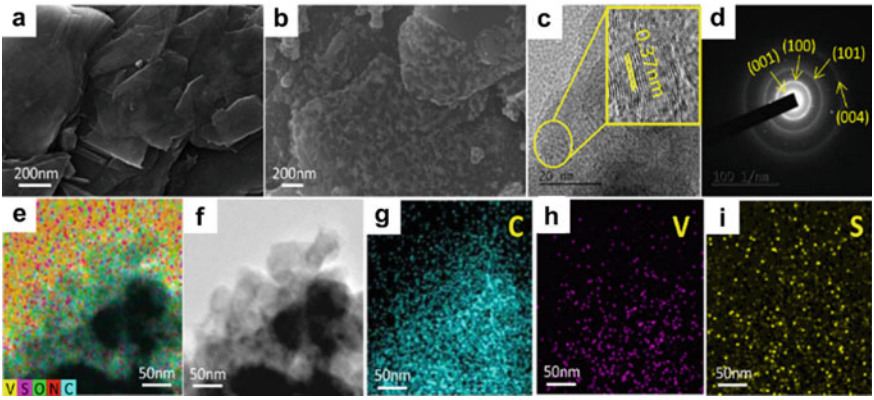

Fig. 21 SEM characterization of VS_2/AC

which are attributed to E_{1g}, E_{2g} and A_{1g} in-plane and out-of-plane VS_2 vibrations, respectively (Fig. 22a). Furthermore, the X-ray diffraction (XRD) patterns of the VS_2/AC electrodes in Fig. 22b contain peaks at 17.9, 32, 37.2 and 41.4° that can be indexed to (001), (100), (101) and (011) planes of VS_2, respectively, along with characteristic carbon diffraction peaks associated with AC. The XPS results show that the characteristic C peaks are located at 285.0 and 286.0 eV, which correspond to sp^2 and sp^3 hybridized carbons (Fig. 22c). In addition, the presence of a band associated with C–O bonds at 288.3 eV indicate the occurrence of surface oxidation, which is corroborated by the presence of absorbed of oxygen on the AC surface (Fig. 22c). Similarly, prominent divalent core level orbital peaks at 165.5 and 164.5 eV are associated with S $2p_{1/2}$ and S $2p_{3/2}$. On the other hand, the presence of two peaks at 166 and 169.3 eV are attributed to the low-coordinate-state sulfur ions and metal sulfur species (Fig. 22d). In addition, strong binding energy peaks are present for

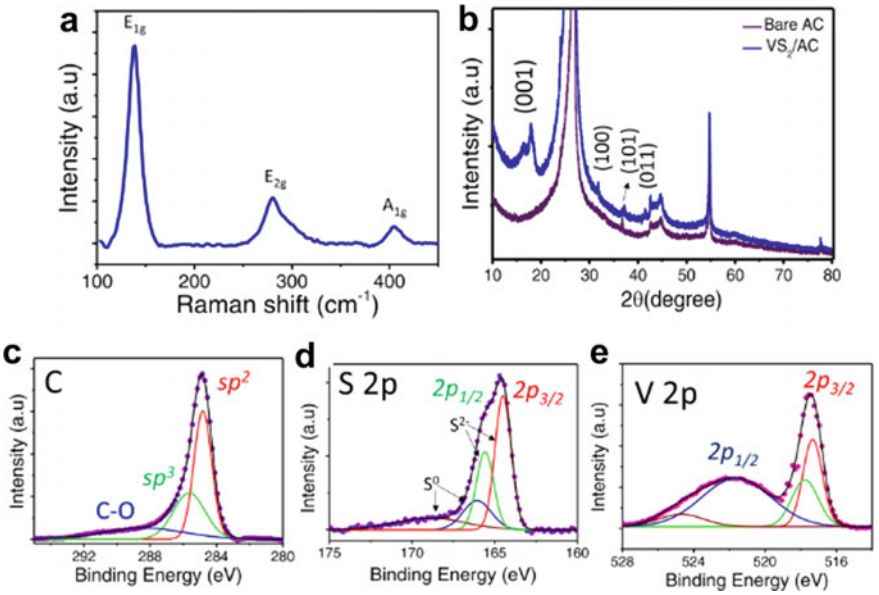

Fig. 22 Structural characterization of VS_2/AC

V $2p_{3/2}$ and V $2p_{1/2}$ at 517.4 and 522.0, corresponding to the V^{4+} and V^{2+} valence states, respectively (Fig. 22e).

Figure 22 shows the HER performance of VS_2/AC. MoS_2/AC, bare AC and a commercial Pt rod were also tested for comparison. VS_2/AC exhibits a low onset potential of −11 mV, much lower than those of MoS_2/AC (−75 mV) and pristine AC (−127 mV) but slightly higher than that of commercial Pt (−7 mV) (Fig. 23a). Moreover, the overpotential (a current density of −50 mA cm^{-2}) of VS_2/AC electrocatalyst is −61 mV, while −299 mV for MoS_2/AC and −1.01 V for pristine AC, respectively. Both VS_2/AC and Pt have small Tafel slopes of 28 and 22 mV dec^{-1}, respectively, while there are relatively large ones for bare AC (105 mV dec^{-1}) and MoS_2/AC (245 mV dec^{-1}), respectively (Fig. 23b). These results suggested that the Volmer–Heyrovsky kinetic mechanism is the main kinetic-limiting step. An electrochemical impedance spectroscopy (EIS) study was conducted to probe the charge transfer characteristics of the VS_2/AC electrode. The Nyquist plot (Fig. 23c) and fitting analysis indicate the existence of a low charge transfer resistance (R_{ct}) of 6.7 Ω, which is 12 and 70 times lower than that of MoS_2/AC and pristine AC, respectively. The small R_{ct} indicates that the source of the superior HER performance of VS_2/AC is the high availability of multiple active sulfur sites. In addition, the Nyquist plot reveals that interfacial resistance (R_S) at the AC–VS_2 junction is absent, confirming the monolithic nature of the heterostructure. The C_{dl} of VS_2/AC is estimated to be 27.44 mF/cm^2 (Fig. 23e), a value that is seven times larger than that of standalone AC (5.03 mF/cm^2). This observation confirms that the presence of abundant VS_2/AC heterostructure active surface sites is responsible for the sustained EC hydrogen

production. The durability results over 1500 cycles demonstrate that VS_2/AC has superior stability under acidic electrolyte conditions, with a negligible shift taking place in the onset potential and a minor shift of overpotential at 200 mA/cm^2 of −81 mV (Fig. 23f). Further, the J–T graph in Fig. 23g demonstrates that the heterostructure has long-term stability, and the HER performance of the VS_2/AC heterostructure is comparable to those of previously described VS_2-based electrocatalysts (Fig. 23h). The results highlight that the VS_2/AC electrode has an outstanding performance comparable to Pt electrode.

First-principles calculations were performed to gain information about hydrogen adsorption by the electrode. A model with single layer of VS_2 on a graphite stack (VS_2/graphite) was established to represent VS_2/AC. A comparison of various sites on the VS_2 side of the VS_2/graphite shows that hydrogen prefers to adsorb on the top of sulfur sites (Fig. 24a). The Gibbs activation free energy for hydrogen (ΔG_H^*) obtained are given in Fig. 24b. Compared to the ΔG_H^* of 1.62 eV for graphite and 2.13 eV for MoS_2/graphite, the small ΔG_H^* of 0.24 eV for VS_2/graphite indicates a fast charge transfer between the VS_2/graphite and the adsorbed hydrogen. Bader charge analysis suggest that sulfur atoms are electron sufficient in the VS_2/graphite (−0.68 e) than in the MoS_2/graphite (−0.54 e), as displayed in Fig. 24c.

To further analyze the solar driven HER performance in seawater, VS_2/AC was tested and it showed an onset potential of −56 mV, and a potential of −0.53 V to reach −200 mA/cm^2 (Fig. 25a). In this regard, LSV using a two-electrode configuration

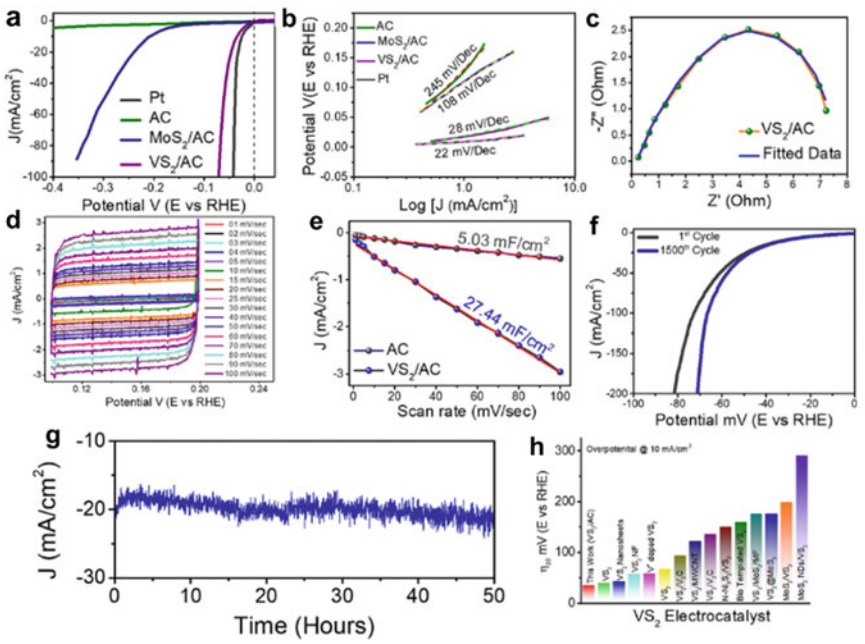

Fig. 23 HER performance of VS_2/AC

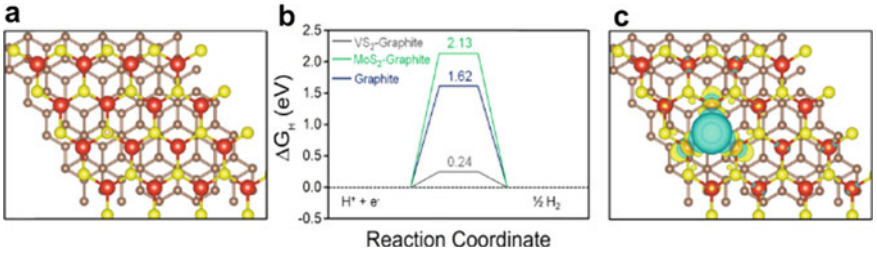

Fig. 24 First-principles calculations of VS_2/graphite

with VS_2/AC as the cathode and AC as the anode, and seawater as the electrolyte was investigated. The results show that VS_2/AC with iR (without iR) exhibits an onset potential of −0.26 (−0.11) V and achieves η_{250} at −1.06 (−2.1) V. Moreover, to determine that chlorine evolution and hypochlorite formation do not take place during the EC reaction, and to quantify hydrogen production, GC analysis was conducted during a 30 h process using a constant applied bias of −50 mA/cm^2 (Fig. 25b). Most importantly, the ratio of O_2/H_2 generated by seawater splitting is near the standard calibration ratio of 1:2. A HER rate of ~0.97 mmol/cm^2 was observed for each 6 h reaction periods. The EC system has a Faradic efficiency (FE) of 62.7% in natural seawater. Chronopotentiometry studies were performed to evaluate long-term, large-scale HER production of VS_2/AC at a constant current of −250 mA/cm^2 in a two-electrode configuration for 21 d (Fig. 25c). Moreover, solar powered chronopotentiometry at −250 mA/cm^2 was monitored daily for 9 h periods for 21 d to evaluate the real-time HER performance (Fig. 25d). A commercial solar cell was used as the power. The performance of VS_2/AC is much higher than those reported for other seawater electrocatalytic systems in Fig. 25e. Besides, VS_2/AC exhibits excellent stability with nearly unchanged potential (Fig. 25f).

3.2.3 Metal Phosphate

Kim et al. [71] developed a method of synthesizing the cobalt–iron–phosphate ((Co,Fe)PO_4) EC based on phosphidation, as shown in Fig. 26. To create this material, (Co,Fe)OOH was first grown on iron foam by means of surface corrosion in a $CoCl_2$ aqueous solution. Then (Co,Fe)OOH was transformed to $(Co,Fe)_3O_4$ by high-temperature treatment, and nanoneedle shaped (Co,Fe)PO_4 was generated by phosphidation.

Morphology characterization of (Co,Fe)PO_4 were analyzed by using SEM. The results show that (Co,Fe)PO_4 exits as thin nanosheets after phosphidation (Fig. 27a, b). TEM images were recorded to obtain information about surface morphology and phase changes taking place in the synthetic process. The results show (Co,Fe)PO_4 that has a nanoneedle shape (Fig. 27c). Furthermore, phase information was gained by analysis of SAED patterns. As shown in Fig. 27d–g, Fe_3O_4 and $FePO_4$ phases

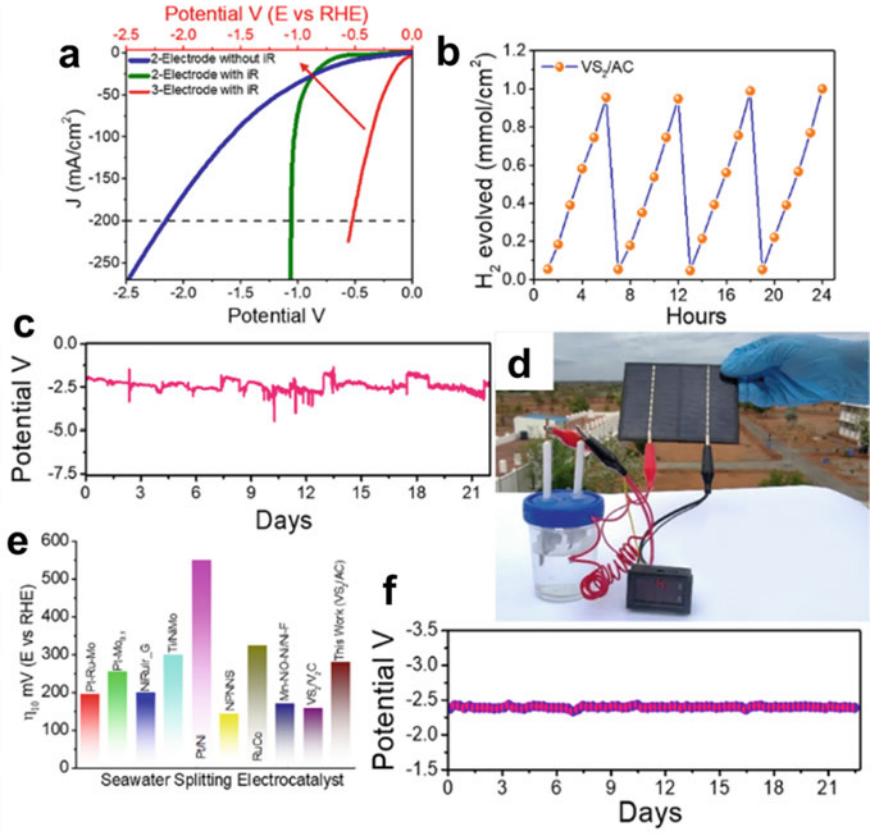

Fig. 25 Solar driven HER performance of VS_2/AC in seawater

can be clearly seen. Moreover, Co, Fe, O and P elements are uniformly dispersed from the EDS mapping result on (Co,Fe)PO_4 (Fig. 27h).

The XPS results of $(Co,Fe)_3O_4$ and (Co,Fe)PO_4 are shown in Fig. 28. The XPS survey spectra in Fig. 28a clearly displayed that Co, Fe, P and O elements are contained in $(Co,Fe)_3O_4$ and (Co,Fe)PO_4. High-resolution XPS of the these elements are displayed in Fig. 28b–e. Obviously, the binding energies of O 1s, Co 2p and Fe 2p increase upon phosphidation, indicating an electron transfer from $(Co,Fe)_3O_4$ to (Co,Fe)PO_4. The change in the local charge-density distribution will be beneficial for reducing the energy barrier, and facilitate the adsorption and desorption processes during HER.

The HER performance of (Co,Fe)PO_4 in different electrolytes (alkaline condition, alkaline artificial seawater and alkaline seawater) was carried out and shown in Fig. 29a. (Co,Fe)PO_4 exhibits a higher HER activity than Pt/C at a high current density in real alkaline seawater (Fig. 29b). Faraday's efficiencies (FE) were determined using the amount of H_2 gas generated (Fig. 29c). The FEs of (Co,Fe)PO_4 are

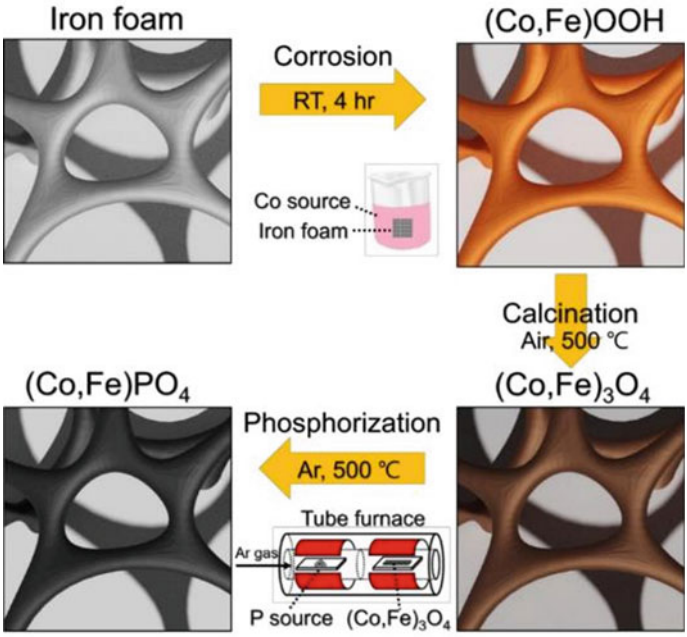

Fig. 26 Schematic for pathway used to synthesize $(Co,Fe)PO_4$ grown on iron foam

>98.6, 96.5, and 96.3% in alkaline condition, alkaline artificial seawater and alkaline seawater, suggesting that most electrons participating in the reaction are consumed during the HER. The durability of $(Co,Fe)PO_4$ for the HER was tested by applying a constant current density in different electrolytes for periods over 72 h (Fig. 29d–f). The constancy of the potentials indicate that this material has high stability in all electrolytes during the continuous operation.

To further evaluate the solar driven seawater splitting applications, an EC system comprised of a two-electrode alkaline water electrolyzer, with $(Co,Fe)PO_4$ and NiFeOOH, which is known to be an optimal OER catalyst, serving as the respective cathode and anode was used for alkaline natural seawater splitting (Fig. 30a). A cell voltage of 10 mA/cm^2 was utilized via reverse-sweeping CV to avoid oxidation current interference. The plot in Fig. 30b shows an excellent activity for overall seawater splitting in alkaline natural seawater for the NiFeOOH||$(Co,Fe)PO_4$ electrolyzer. Only a low voltage of overpotential of 395 mV was required to drive the current density of 10 mA cm^{-2} for the electrolyzer, demonstrating that it has a better overall water-splitting activity than the benchmark of IrO_2||Pt/C electrolyzer in both alkaline condition and alkaline seawater (Fig. 30b). Moreover, the FEs of the NiFeOOH||$(Co,Fe)PO_4$ electrolyzer are 97.4 and 99.0% for the respective HER and OER in alkaline seawater (Fig. 30c). Compared to recently reported transition metal-based electrolyzers, NiFeOOH||$(Co,Fe)PO_4$ electrolyzer exhibits a comparable or even better performance in alkaline seawater (Fig. 30d). The durability of

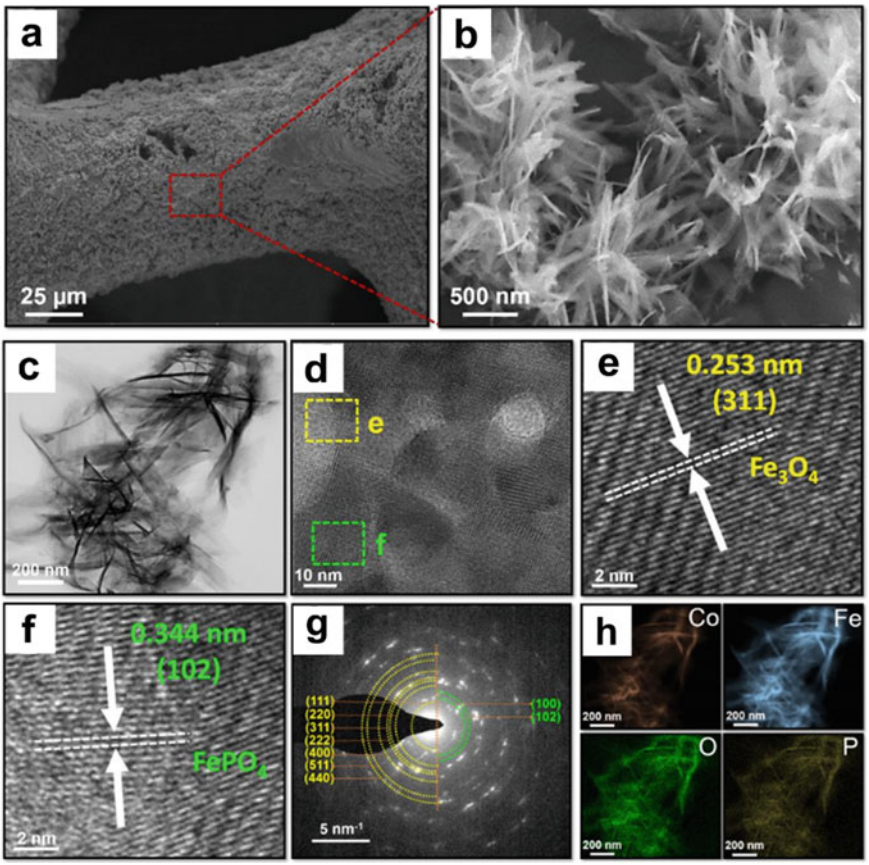

Fig. 27 Morphology characterization of $(Co,Fe)PO_4$

the $(Co,Fe)PO_4$ based electrolyzer was confirmed by the observation that the voltage at a constant current density for 50 h in alkaline seawater, and negligible decline of potential can be found for the $(Co,Fe)PO_4$ electrolyzer (Fig. 30e). To test its use in a PVEC seawater splitting system, a commercial silicon solar cell was wired to the NiFeOOH||$(Co,Fe)PO_4$ electrolyzer (Fig. 30f). In Fig. 30g the J–V curve of the commercial silicon solar cell is shown. A 12.8% of STH efficiency was calculated for the electrolyzer. When PVEC seawater splitting device is driven using natural sunlight, a continuous release of H_2 and O_2 bubbles occurs from both electrodes (inset of Fig. 30f).

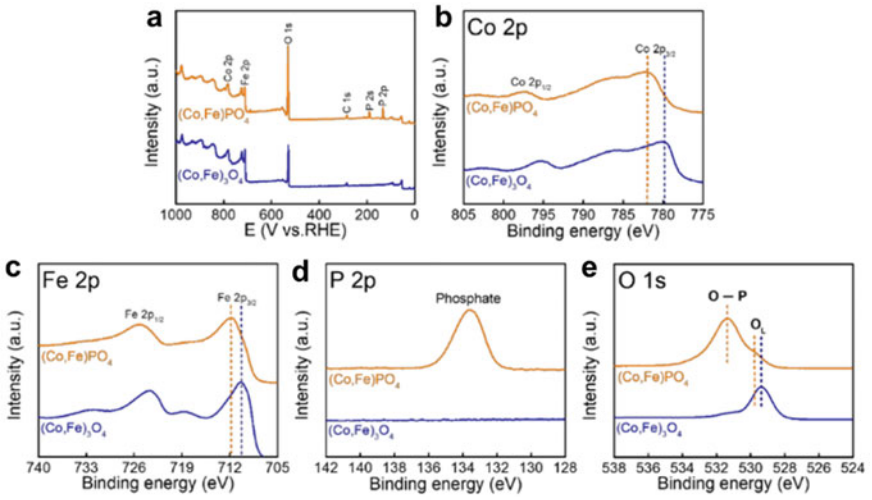

Fig. 28 XPS analyses of $(Co,Fe)_3O_4$ and $(Co,Fe)PO_4$

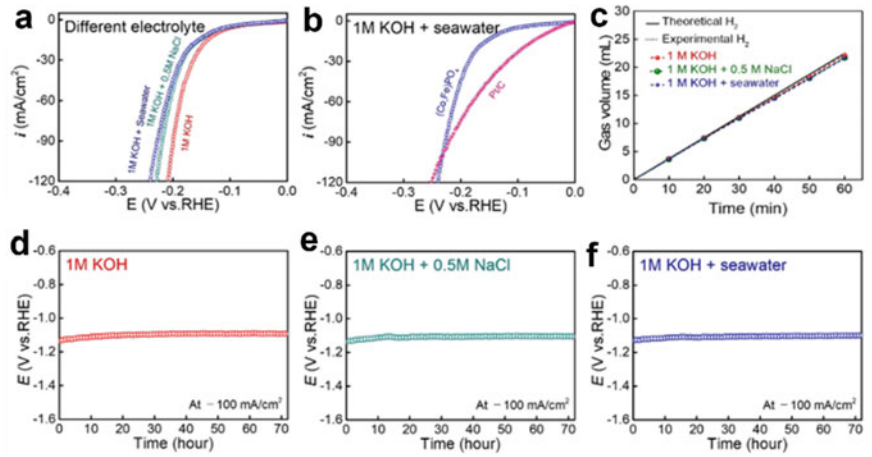

Fig. 29 HER performance of $(Co,Fe)PO_4$

3.2.4 Metal Carbide

By using density functional theory (DFT) calculations to predict the selectivity of gas-evolving catalysts, Hsu et al. [60] designed a seawater-splitting device equipped with an economical electrocatalyst comprised of transition metals Fe, Co, Ni and Mo. Guided by this information, nanoneedles of basic cobalt carbonate (BCC) were first grown on carbon cloth (CC) by a facile chemical bath deposition method (Fig. 31a, b). Then a thin layer of zeolite imidazole framework (ZIF-67) was grown on the

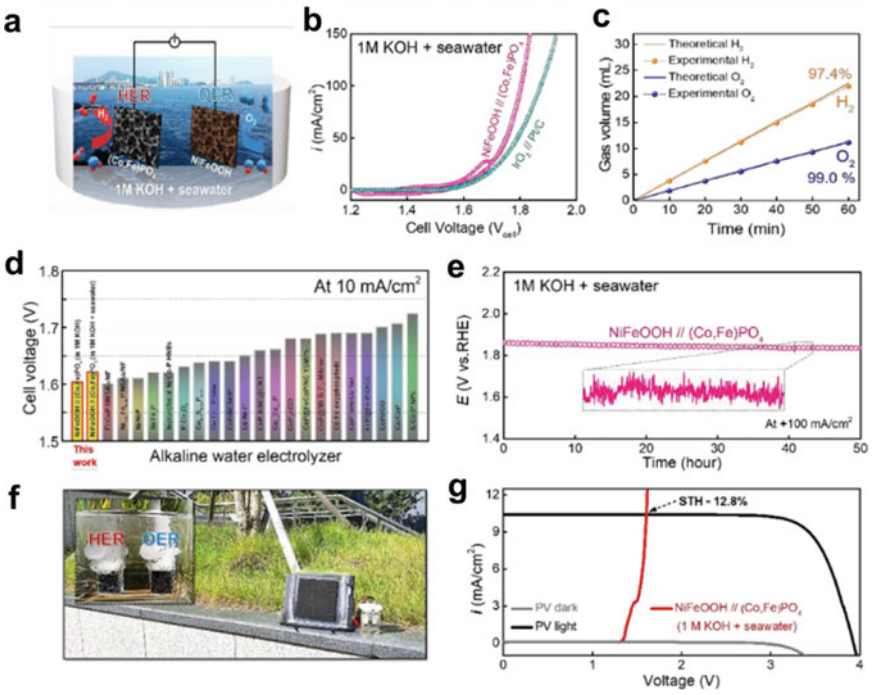

Fig. 30 Solar driven seawater splitting application of $(Co,Fe)PO_4$ based electrolyzer

surface of BCC nanoneedles (z-BCC, Fig. 31c), followed by converting ZIF-67 to $Co_2[Fe(CN)_6]\cdot nH_2O$ (MHCM-z-BCC, Fig. 31d) by dipping in sodium ferrocyanide solution. Inspection of TEM images revealed that MHCM-z-BCC has an obvious core–shell structure with a 20 nm thick shell covered on BCC nanoneedles (Fig. 31e–h). The EDS mapping results indicate that the nanoneedle center is Co- and O-rich and the surface is Fe-, N- and C-rich.

Analysis of the X-ray diffraction patterns (Fig. 32a) showed that all major diffraction peaks of BCC and MHCM-z-BCC can be indexed to those of basic cobalt carbonate, and that diffraction peaks associated with metal hexacyanometallate are absent. The presence of CN-ligands in MHCM-z-BCC was confirmed by inspecting its FT-infrared spectrum (Fig. 32b). which contains a characteristic peak at 2100–2200 cm^{-1}. X-ray photoelectron spectroscopy (XPS) measurements (Fig. 32c–f) further demonstrate that elemental Co, Fe, O, and N are present in MHCM-z-BCC.

The as-prepared MHCM-z-BCC was incorporated with NiMoS to form a MHCM-z-BCC||NiMoS device for HER application. In Fig. 33a are displayed the HER performance of MHCM-z-BCC||NiMoS water splitting device in a neutral-buffered electrolysis. The results indicate that MHCM-z-BCC||NiMoS drives a small overall water splitting applied voltage of 1.7 V compared to Pt||Pt (2.0 V), but larger than what

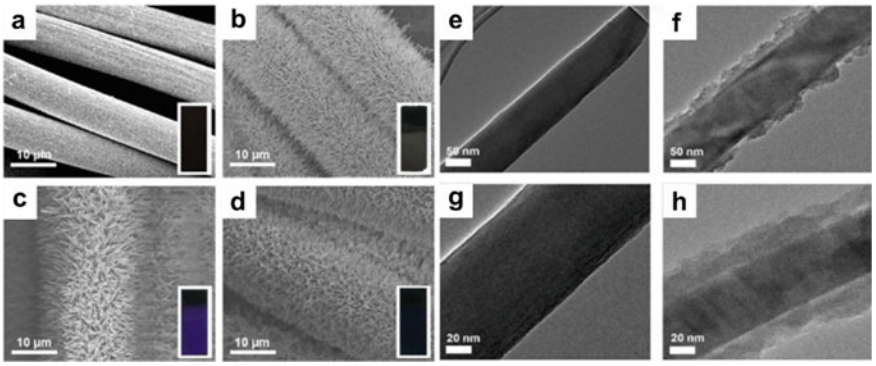

Fig. 31 Morphology characterization of MHCM-z-BCC

IrO_2||Pt drives (1.6 V). However, MHCM-z-BCC||NiMoS displays the smallest overpotential of 2.1 V at the current density of 10 mA cm^{-2}, which is 100 and 320 mV smaller than those of the IrO_2||Pt and Pt||Pt systems. As shown in Fig. 33b, c, the MHCM-z-BCC/NiMoS device has high stability with nearly 100% retention of its initial current density occurring after 10 h in a neutral-buffered electrolysis. The IrO_2||NiMoS device created by substituting the MHCM-z-BCC electrode with IrO_2, undergoes a substantial current decay at the beginning, and only a 33% current density remained after 10 h. Similarly, the analogous MHCM-z-BCC/Pt system undergoes 50% decay in current density during the first hour, and finally retained only 36% of its initial current density. On the other hand, the Pt/IrO_2 system has the lowest stability with its catalytic current density being 18% lower than its initial value. These results show that noble metal-based electrocatalysts are ineffective for seawater splitting in a neutral pH medium. During water electrolysis, H^+ and OH^- ions are rapidly consumed at the cathode and anode, respectively, which leads to localized changes in pH that can lead to performance attenuation caused by corrosion or even destruction of the electrode materials. As shown in Fig. 33c, the extraordinary electrochemical stability of the MHCM-z-BCC/NiMoS based system was verified by the finding that the pH of the buffered electrolyte is well maintained at ~6.8.

Studies were then conducted on the MHCM-z-BCC||NiMoS system in seawater, collected from a nearby coastal site with its pH adjusted to 8 using the NaH_2PO_4/Na_2HPO_4 buffer. The results show that anode only produces O_2. Moreover, o-tolidine tests were performed to determine if free chlorine is present in the electrolyte during long-term seawater electrolysis. Three different electrodes, including MHCM-z-BCC||NiMoS, IrO_2||Pt and Pt||Pt, were used and compared. After continuous operation for 12 h, IrO_2/Pt and Pt/Pt systems produced Cl_2 of 50 and 22 μmol L^{-1}, respectively. However, MHCM-z-BCC||NiMoS did not generate any Cl_2 even after 100 h. Similar trends are seen in o-Tolidine tests on the three different electrode combinations at an applied voltage of 2.5 V. The results are consistent with those arising from computational studies and confirm the superior selectivity of the MHCM-z-BCC electrode toward the OER in seawater (Fig. 34a). The FE of the

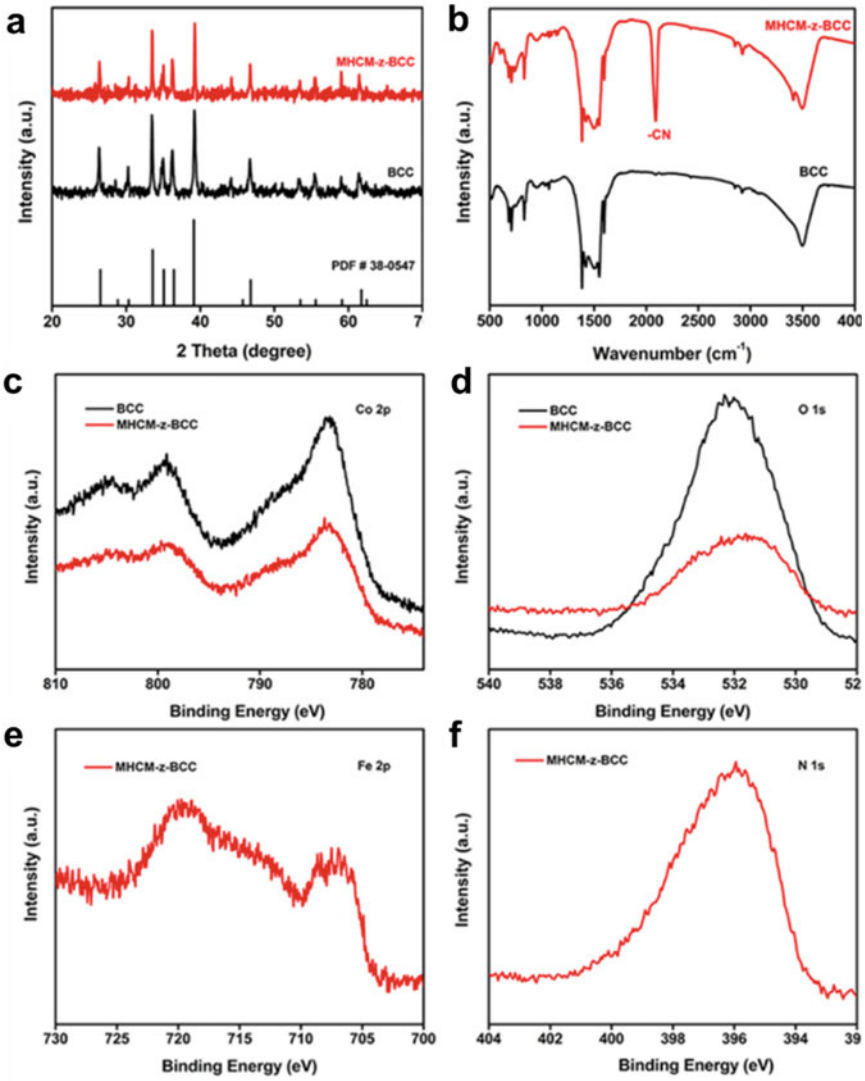

Fig. 32 Structural characterization of MHCM-z-BCC

system in seawater was evaluated by concurrently collecting the evolved H_2 and O_2 over the cathode and anode, respectively. Both MHCM-z-BCC and NiMoS electrodes demonstrate near 100% FE with a stoichiometric H_2:O_2 ratio of 2:1 (Fig. 34b).

To create an integrated PVEC system containing this electrode combination, the MHCM-z-BCC||NiMoS cell was wired to a triple-junction solar cell (Fig. 35a). Under natural solar irradiation, such integrated systems can promote spontaneous H_2 and O_2 evolution. As shown in Fig. 35b, by using the intersection of the J–V curve of the solar

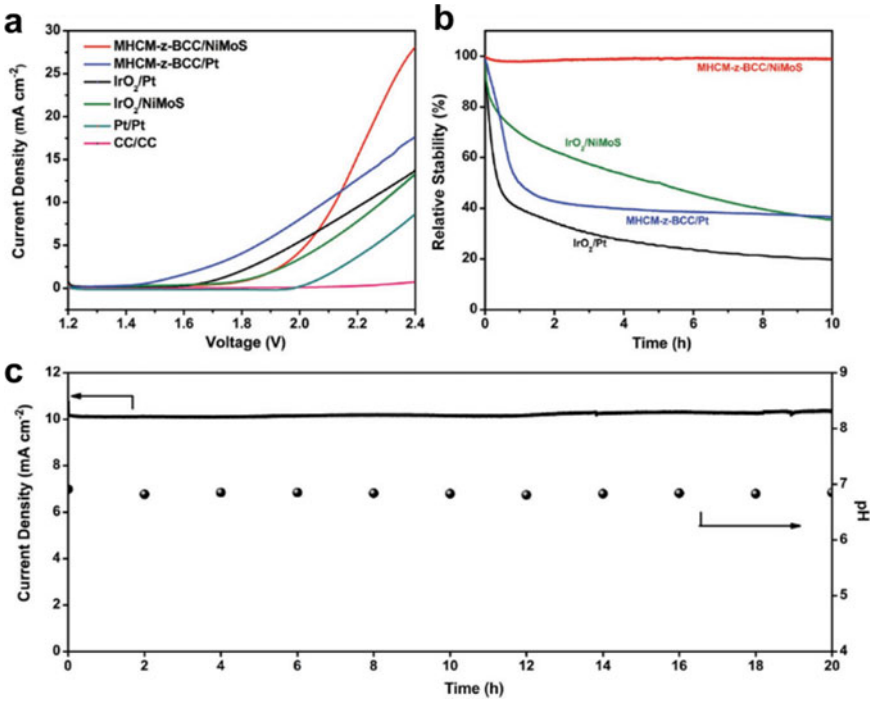

Fig. 33 Electrochemical performance of MHCM-z-BCC‖NiMoS device for water splitting

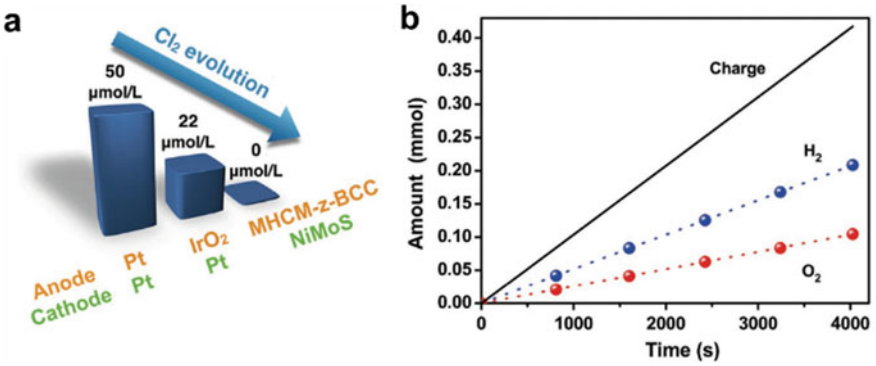

Fig. 34 Comparison of Cl_2 production of different electrodes

cell and the polarization curve of the electrolysis device, the operating current density of the system was estimated to be 14.6 mA cm^{-2}. The actual operating current density under chopped simulated solar illumination is ~14.6 mA cm^{-2}, which corresponds to a high STH efficiency of 17.9%. After over 15 consecutive on/off illumination cycles, the system still remains a constant outstanding performance (Fig. 35c), and

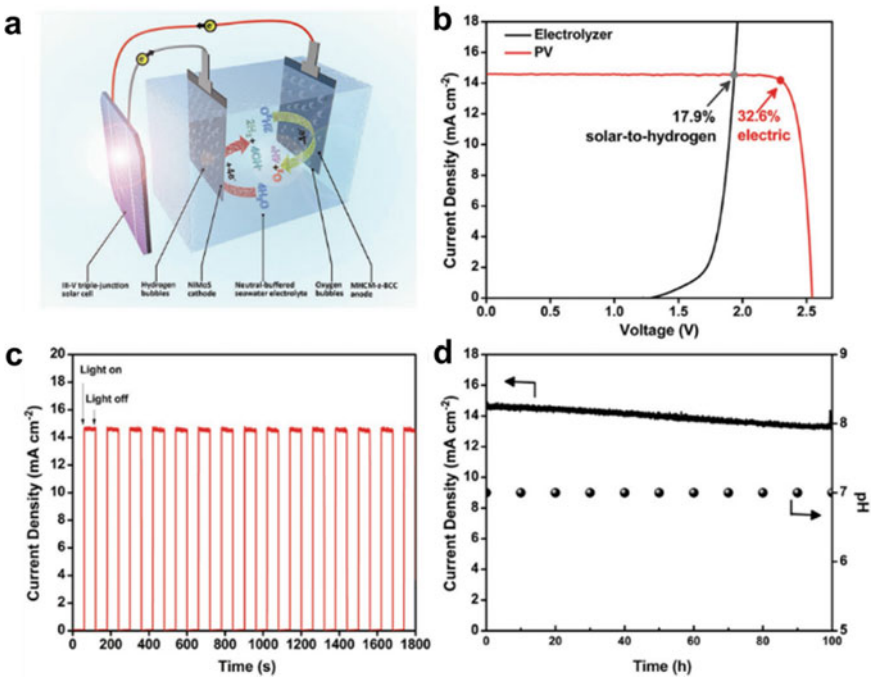

Fig. 35 Solar driven hydrogen production application of MHCM-z-BCC||NiMoS cell

the absence of spike-like features indicates that photogenerated charge carriers are utilized efficiently. Moreover, the durability test showed after 100 h of continuous illumination, ~90% of its initial activity was retained (Fig. 35d).

To further get insight into the mechanisms of the processes promoted by MHCM-z-BCC anode/NiMoS cell, the OER and ClER catalyzed by $Fe_4[Fe(CN)_6]3{\cdot}nH_2O$ (Prussian blue, PB) and its analog $Co_2[Fe(CN)_6]$ as the model MHCM catalysts were explored using DFT calculations (Fig. 36). A well-established four-step mechanism was employed as a model to investigate the OER kinetics (Fig. 36a–c). Thermodynamic analysis suggests that formation of intermediate *OOH is rate-determining in the OER on both Fe centers (Sites A and B) in pristine PB crystals. This corresponds to a theoretical overpotential (η_{OER}) of 0.61–0.85 V. In contrast, formation of the metal–oxo intermediate is rate limiting in the OER at the Co centers in $Co_2[Fe(CN)_6]$, leading to an apparently reduced η_{OER} of 0.46–0.67 V. Meanwhile, the CER promoted by the four catalysts were studied using the two-step Volmer–Heyrovsky mechanistic model, which involves Cl^- adsorption followed by release of Cl_2 (Fig. 36d–f). The results show that, unlike processed promoted by precious metal-based catalysts, evolution of O_2 is favored over Cl_2 evolution on the surface of PB and its analog.

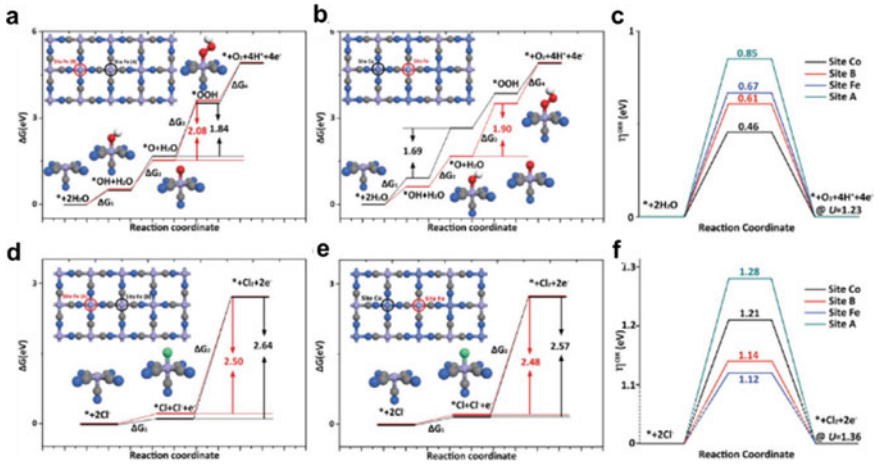

Fig. 36 DFT calculations results for OER and ClER

3.2.5 Metal Phosphide/Metal Hydroxide

In an interesting study, Wu et al. [62] developed a solar-driven self-powered PVEC water splitting system that uses a PV cell to provide stable voltage to drive a m-ZIB array in the seawater electrolyzer. The new miniature energy storage device not only harvests light efficiently, it also reduces the bulky connections of non-integrated systems. More impressively, electrodes based on earth-abundant materials have advantageous features that are reflected in the electrochemical performance of the ZIB including impressive electrocatalytic activity toward overall water splitting and robust resistance to corrosion in alkaline seawater. In the effort, a Co-based metal–organic framework zeolitic imidazole framework (ZIF-L) array was uniformly grown on the surface of pre-treated Ni foam using a co-precipitation method. The formed Co-MOF was used as an in-situ sacrificial template to construct NiCo-LDH having a three-dimensional network architecture via an ion exchange process. Upon thermal annealing at 300 °C under a PH_3 atmosphere, NiCoP/NiCo-LDH@NF having a retained network structure is produced (Fig. 37a). The highly integrated, hierarchical heterostructure facilitates carrier transport and electrolyte penetration.

The fabrication process was monitored using TEM. Inspection of TEM images show that NiCoP/NiCo-LDH has a thin nanosheet texture (Fig. 38a–d). Moreover, it can be clearly found from the HRTEM image that the lattice fringes correspond with the (111) plane of NiCoP and (110) plane of NiCo-LDH (Fig. 29e). EDS results verify that Ni, Co, P and O are homogeneously distributed (Fig. 38e). XPS spectra shows a Ni 2p peak is present in the spectra for NiCo-LDH and NiCoP/NiCo-LDH but absent in that for ZIF-L. For Co 2p spectrum displayed in Fig. 38g, peaks at 793.5 and 778.9 eV can be assigned to the Co $2p_{1/2}$ and Co $2p_{3/2}$ of Co species involved in Co–P bonding. Oxidized Co species can be found at the peaks of 798.3 and 782.1 eV

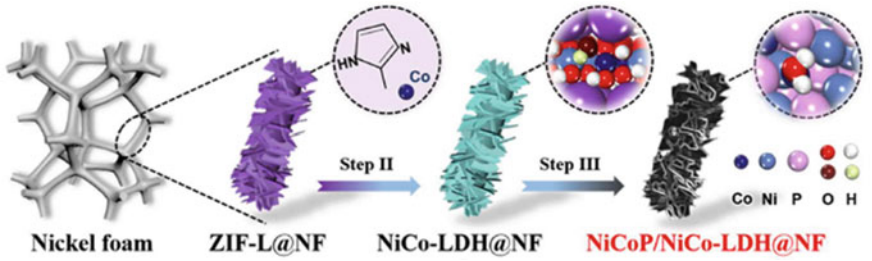

Fig. 37 Schematic illustration of the synthesis of NiCoP/NiCo-LDH@NF

and the two satellite peaks at 802.7 and 785.6 eV. Two main signals at 853.5 and 876.2 eV in the Ni 2p spectra matches Ni $2p_{1/2}$ and Ni $2p_{3/2}$ in the Ni–P compound, and peaks at 855.2 and 874.6 eV along with satellite peaks at 861.9 and 880.6 eV are associated with the corresponding oxidized species (Fig. 38h). The P 2p spectrum of the as-obtained heterostructure shown in Fig. 38i contains peaks at 129.3 and 129.8 eV ascribed to P $2p_{3/2}$ and P $2p_{1/2}$ in Ni–Co–P. That the binding energies of phosphorus atoms in this species are slightly lower than that elemental P (130.0 eV), suggests a small degree of charge density is transferred from Ni/Co centers to P. The peak at 133.5 eV is associated with the oxidized form of P, which might arise by exposure to air. As shown in Fig. 38j, a strong peak located at 532.8 eV is present in the O 1 s spectrum, implying the presence of a P–O bonding.

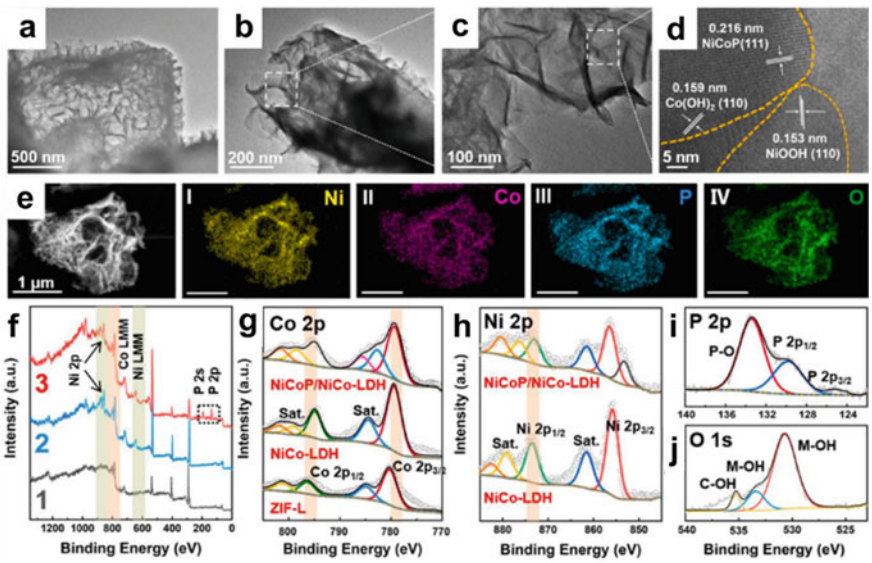

Fig. 38 Morphology and structural characterization of NiCoP/NiCo-LDH

To determine if NiCoP/NiCo-LDH heterostructures have outstanding catalytic performances, they were used to promote the HER and OER in an alkaline simulated seawater electrolyte. As can be seen by viewing the LSV curves in Fig. 39a, d, the NiCoP/NiCo-LDH@NF catalyst has excellent activity for the HER and OER, in association with overpotentials of 213 and 350 mV to maintain a current density of 50 mA cm^{-2}, respectively. The impressive HER and OER performances were verified by the observation that the Tafel slopes are small (65 and 73 mV dec^{-1} for the respective HER and OER 9, Fig. 39b, e) indicative of rapid catalytic kinetics. Despite the fact that the performance in simulated seawater is close to that in 1 M KOH, both the HER and OER activities are slightly lower. The decrease might be due to the interference caused by chlorides in the active sites of the electrodes. Also, the EIS testing results display the same trend (Fig. 39c, f) by showing that the heterostructure catalyst has larger R_{ct} values for both the HER and OER in simulated seawater compared to those in alkaline freshwater.

To gain more information about the electrocatalytic activity of the NiCoP/NiCo-LDH heterostructure toward water splitting, DFT calculations were carried out. Specifically, the free energy for oxygen redox in the OER occurring NiCo-LDH (110) surface in an alkaline environment was calculated. At steady state, all surface O sites of NiCo-LDH (110) in an alkaline environment are saturated by H and the metal sites in this material are saturated by top OH (Fig. 31a (1)). Thus, two types of surface hydroxides exist on the edge, one being two-metal coordinated bridged (M–OH–M) and the other one-metal top coordinated (M–OH), both of which play an important role in the OER. The reaction begins by deprotonation of a two-metal

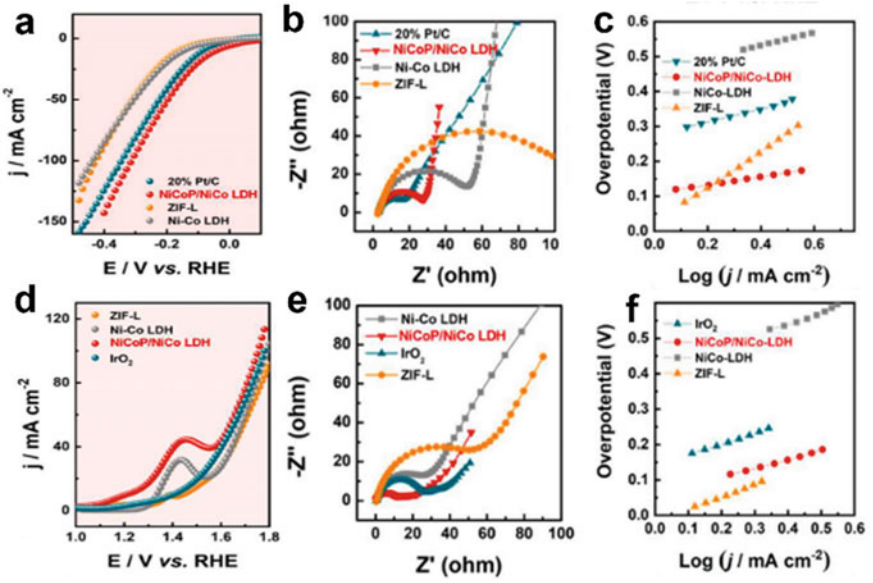

Fig. 39 HER and OER tests for NiCoP/NiCo-LDH

coordinated bridge OH via a Mars van Krevelen-type mechanism to form an O-bridged center (M–O–M) (Fig. 40a (2)). This bridge *O radial is stabilized by the neighboring Co and Ni atoms, which lowers the free energy barrier for the process to $\Delta G_{limit} = 1.53$ eV (Fig. 40b). The *O radials then react with additional OH^-, forming the surface *OOH species (Fig. 40a (3)), which reacts further with OH^-, giving an intermediate that undergoes deprotonation to produce O_2 (gas) and a vacancy (V_O) (Fig. 40a (4)). Note that the vacant O site 'hops' from the original bridge site (M–V_O–M) to the left top site (M–V_O), which stabilizes the vacancy site and lowers the free energy barrier of the reaction to only 0.76 eV. In Fig. 40c the free energy diagram of the HER promoted on a NiCoP (111) surface in an alkaline environment is given. In the process, H_2O is activated on the Co top site of the NiCoP (111) in association with a bond angle change from 104.45 to 105.38° caused by the existence of states with a Co d orbital that is emptier than the Ni d orbital. Thus, a relatively low barrier of 0.14 eV is found for water dissociation, indicating that NiCoP has a good water splitting performance. The energy for *H desorption taking place after *OH desorption is 0.58 eV, indicating an excellent catalytic ability. In Fig. 40d the projected DOS on the semiconducting NiCo-LDH (110) surface and the metallic NiCoP (111) surface is shown. The d orbitals of Co and Ni atoms close to the Fermi level benefit charge transport and which is a reason why the catalysts have excellent oxidation and reduction ability for the OER and HER.

A prototype PV-mZIB-OWS hybrid PVEC system was then constructed to assess the efficiency for production of hydrogen. The photo-charge/discharge curves of the PV-mZIB integrated device with increased current densities under simulated sunlight, given in Fig. 41a, show that when the current density returns to 1 mA cm^{-2}, the discharge behavior of the integrated device returns to the initial state, demonstrating

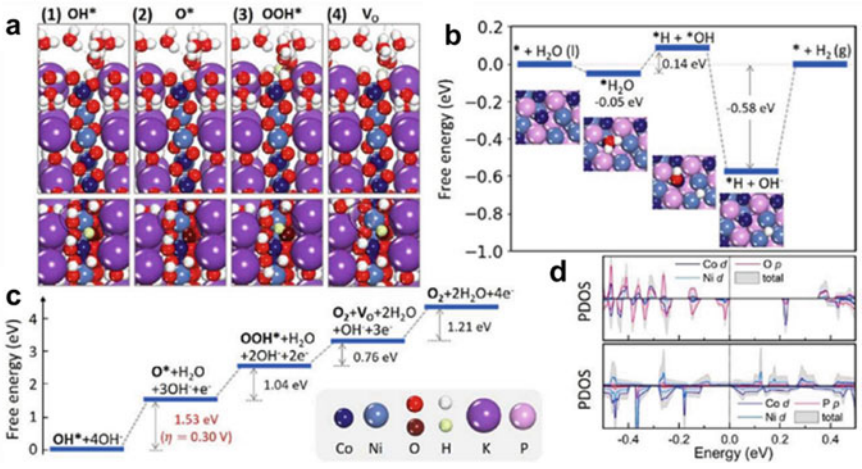

Fig. 40 DFT calculation results of NiCoP/NiCo-LDH

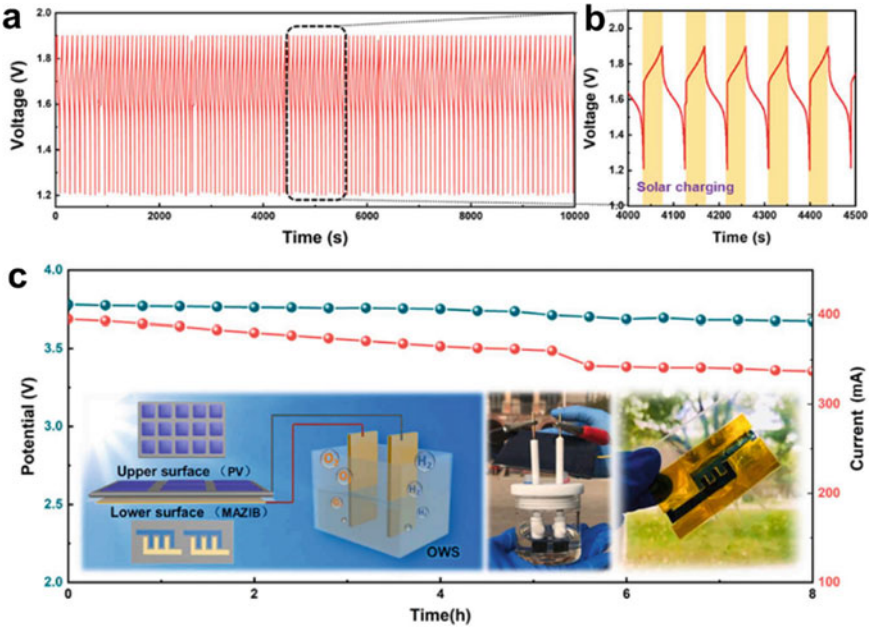

Fig. 41 Solar driven hydrogen production application of the PV-mZIB-OWS system

its excellent rate performance. Inspection of Fig. 41a, b further shows that photo-charge/discharge cycle performance of this system at a light intensity of 4 W cm^{-2} and a discharge rate of 1 mA cm^{-2} remains high. As such, the integrated energy unit has good stability over many cycles, reflected by the observation that it retains a high capacitance retention rate of 97.3% after 100 charge/discharge cycles. This finding ensures that the system has a stable output voltage for the HER and OER. In Fig. 41c the voltage-current–time curve of the overall system is presented, which demonstrates that the device functions continuously for at least 8 h. The inset in Fig. 41c contains a conceptual diagram of the device and the photographic images of the working system.

3.2.6 Metal Disulfide@Metal Carbide

Wang et al. [72] developed a novel electrocatalytic material $VS_2@V_2C$, which they prepared by a simple hydrothermal method. In the sequence, fewer layer V_2C nanosheets, produced by liquid-phase etching and ultrasonic-assisted vacuum freeze-drying, were subjected to a simplified one-step hydrothermal process, which was then used to prepare $VS_2@V_2C$ composites in which V_2C nanosheets are uniformly coated by VS_2 nanosheets. The synthesis process and surface morphology are shown in the schematic diagram (Fig. 42).

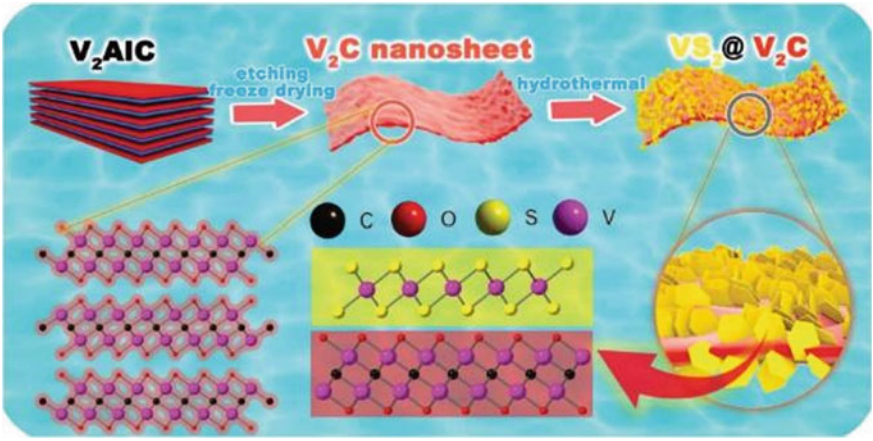

Fig. 42 Schematic illustration of the synthesis and surface morphology of the $VS_2@V_2C$

XRD spectra given in Fig. 43a indicate the pure-phase of VS_2, accordion-like V_2C, V_2C nanosheets and $VS_2@V_2C$. $VS_2@V_2C$ contains a sharp peak near 7.5°, which can be indexed to V_2C. The (002) crystal plane of the nanosheets with a small number of layers are responsible for shift of this peak as compared to one in the spectrum of the accordion multilayer V_2C obtained by liquid-phase etching. This change might be owing to the periodic changes of the original crystal structure. The results of XPS analysis of the catalyst materials are shown in Fig. 43b–d. Two peaks at 517.1 and 524.4 eV are found to be V^{4+} ions, corresponding to the $2p_{3/2}$ and $2p_{1/2}$ orbital split spin states in V_2C and VS_2, respectively. The S^{2-} ion, derived from VS_2 nanosheets, is associated with characteristic peaks in the XPS spectrum at 163.2 and 162.1 eV, respectively. The absence of other sulfur peaks shows that that the composite has a good correspondence with 1T-VS_2. In addition to participating in bonds with vanadium atoms in the V_2C nanosheets, carbon atoms also involved in planar C–C bonds with the carbon atoms in adjacent cells, C–O double bonds. As seen in Fig. 43d, the spectrum contains characteristic peaks at 284.8 eV for the C–C bond, 286.4 eV for the V–C bond and 288.8 eV for the C–O bond. Analysis of the environment in which the carbon atoms are located shows that the V_2C nanosheets are retained in the composite material without oxidation or decomposition. Moreover, the pore diameter of ca. 18 nm is found for both V_2C and $VS_2@V_2C$, and a higher porosity of $VS_2@V_2C$ compared to that of V_2C is due to the large number of vertical inlays of VS_2 nanosheets which cause widening of the specific surface area (Fig. 43e). Viewing Fig. 43f, which contains a diagram of the crystal structure of $VS_2@V_2C$ along the V_2C (101) crystal plane, shows that a one-by-one-layer interface is composed of 8 layers of atoms.

TEM image in Fig. 44a shows that few layers of V_2C nanosheets were produced by the synthetic method. Also, some thin nanosheets of V_2C created in this way are completely mutually separated, but vulnerable to easy agglomeration due to the van der Waals force which tends to reduce the overall specific surface area. By viewing

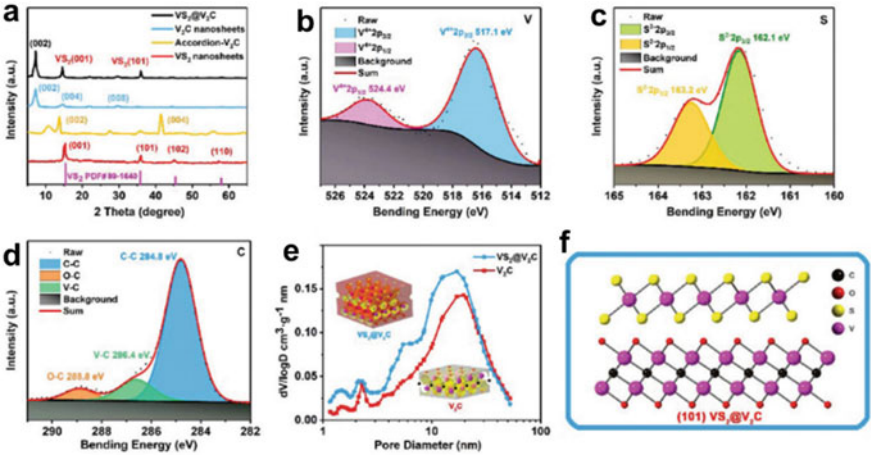

Fig. 43 Structural characterization of $VS_2@V_2C$

the image in Fig. 44b of the surface morphology of $VS_2@V_2C$, it is observed that large numbers of VS_2 nanosheets are uniformly and vertically inlaid on the V_2C nanosheets. The V_2C matrix has a thickness of ca. 50 nm, which is close to the width of the VS_2 nanosheets. This type of vertical mosaic structure is beneficial for avoiding stacking of V_2C matrices and increasing the specific surface area of the composite material enabling formation of a stable cross-mechanical structure. Also, this structural feature hinders reunion of sheets on the electrode, creates channels for electron migration, reduces interface resistance, and promotes mass and proton exchange during the catalysis. TEM image of the phase interface of the composite displayed in Fig. 44c shows areas labeled 1 and 2 that correspond to the respective vanadium carbide matrix and VS_2 nanosheets. Figure 44d shows the more detailed phase analysis, where the red lines correspond to the uniformly arranged 8 atomic layers of V_2C corresponding to the (002) crystal plane. The V_2C has a single-layer thickness of 0.62 nm and the interlayer separation of 0.45 nm. As can be seen by inspecting region 2 in the diagram, VS_2 corresponds to the (102) crystal plane. The yellow lines in Fig. 44e connects 20 corresponding atomic layers, with the distance between the layers being 0.2 nm. The element mapping of $VS_2@V_2C$ in Fig. 44f–i shows that V is distributed uniformly throughout the composite, and carbon in the matrix layer is more prevalent. Also, the sulfur distribution is larger than that of C and this element is positioned in the nanosheet perpendicular to V_2C. The electron diffraction pattern in Fig. 44j indicates the (102) crystal plane of VS_2, whereas the diffraction ring of V_2C is blurred by covering on the matrix material.

Inspection of the HER curves of the catalyst materials shows that the catalytic activity of $VS_2@V_2C$ is greatly enhanced in contrast to when V_2C is not in the composite (Fig. 45a). V_2C, OG-$VS_2@V_2C$ and $VS_2@V_2C$ display the overpotentials of 572, 304, and 164 mV at the current density of 20 mA cm^{-2}, respectively. Moreover, Pt/C, $VS_2@V_2C$, OG-$VS_2@V_2C$ and V_2C electrodes exhibit the Tafel

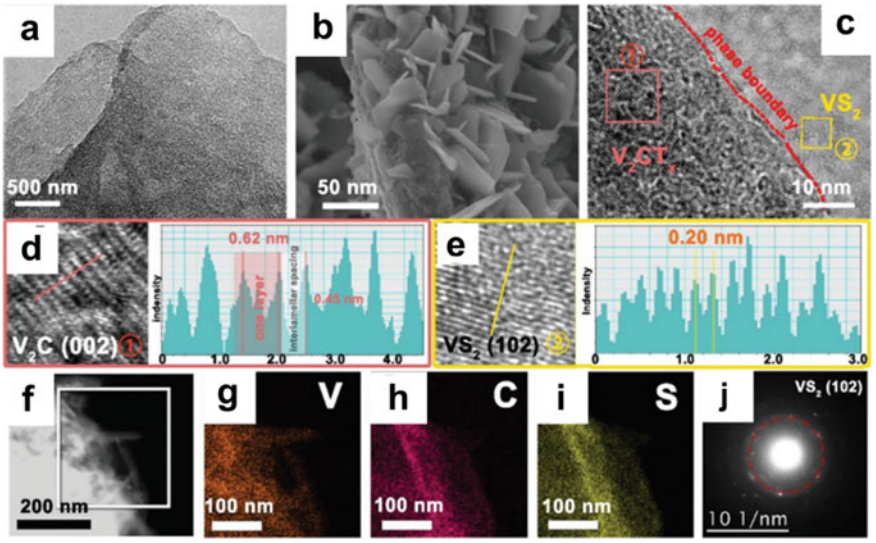

Fig. 44 Morphology characterization of $VS_2@V_2C$

slopes of 30.4, 47.6, 84.7 and 119.0 mV dec^{-1} at a pH of 13.8, respectively (Fig. 45b). According to this result, Tafel process is the main catalytic kinetic reaction during the HER, in which two adsorbed hydrogen atoms combine on the electrode surface to produce hydrogen. The Tafel slopes in seawater at various pH values and the overpotentials of $VS_2@V_2C$ for HER are summarized in Fig. 45c, d. The results show that as pH increases, the Tafel slope and hydrogen evolution overpotential first increases and then decreases. This behavior is a result of the low degree of spontaneous hydrolysis in neutral seawater and a rapid increase in reaction resistance. Figure 45e, f, which contains a list of the electrocatalytic performances of VS_2-based materials observed in studies during recent years. The data show that the new $VS_2@V_2C$ heterogeneous catalyst has excellent performances in both acidic and alkaline environments.

As the graph in Fig. 46a shows, under conditions where the overpotential is maintained at 500 mV, the $VS_2@V_2C$ having different thicknesses have significantly different in catalytic performances, and abilities to maintain stable current densities. $VS_2@V_2C$ films with different catalyst loadings were prepared by using the spin coating method. When the loading is increased to 0.4 mg cm^{-2}, current densities are obtained up to 152 mA cm^{-2}. However, with increasing loading, the overpotential of the electrode decreases and the current density increases, due to the decrease in the square resistance of the film (Fig. 46a). As shown in Fig. 46b, the results of durability tests were performed with an overpotential of 500 mV for 200 h show that stable current densities are maintained. The inset in Fig. 46a shows that surface of a 0.4 mg cm^{-2} $VS_2@V_2C$ film is flat, uniformly thick and mechanically flexible. A comparison of square resistance of the as-prepared V_2C and OG-$VS_2@V_2C$ films under the same conditions shows that $VS_2@V_2C$ has the best conductivity. Also, a

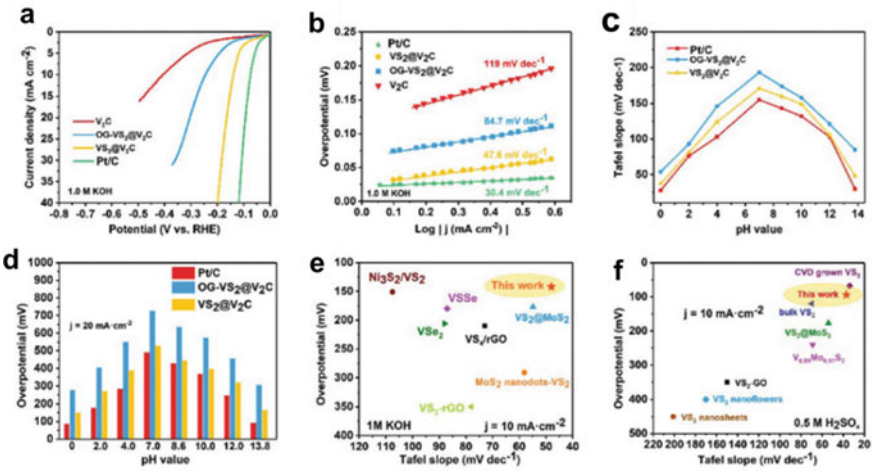

Fig. 45 HER performance of $VS_2@V_2C$

PVEC device, comprised of a solar cell, a $VS_2@V_2C$ electrode, a reference electrode, a counter electrode, and a hydrogen collecting device were assembled in Fig. 46c. Moreover, Fig. 46d shows that as the reaction continues the Faraday efficiency of the catalyst gradually increases and stabilizes at about 99.2%.

The improved catalytic performance of $VS_2@V_2C$ can be ascribed to its higher electrical conductivity and carrier mobility. To further get insight into the high catalytic performance of the material, crystal models representing VS_2 and $VS_2@V_2C$ were built for simulation studies (Fig. 47a, b). In the model, 1T-VS_2 crystals cover the vanadium carbide surface, and oxygen are the functional atoms on the V_2C surface. The band structure diagrams of the above two models for the situation were calculated and compared where hydrogen atoms are not absorbed, (Fig. 47c, d). Through calculation, it is found that 1T-VS_2 has a semi-metallic energy band character shown in Fig. 47d. Owing to the component of a conductor and a semi-metal, different band dispersions exist near the Fermi level of $VS_2@V_2C$, resulting in the altering of band structure and electron transport at the interface. To further investigate the reason for high HER performance of $VS_2@V_2C$, the Gibbs free energies associated with adsorption of hydrogen atoms were calculated. It was showed that $VS_2@V_2C$ has a significantly reduced energy required for hydrogen atom adsorption, thereby promoting the binding of active hydrogen atoms and facilitating the desorption of hydrogen molecules from the surface. Further, the charge-density distribution on the (101) plane of $VS_2@V_2C$ was also calculated (Fig. 47f). The blue areas in the plot corresponds to the charge depletion, the red area represents the charge accumulation region, and the green area represents the vacuum layer. V_2C is the main electron donor, and the inner V atom provides the charge required for electron migration. In Fig. 47g a flow chart for the heterogeneous catalytic HER on $VS_2@V_2C$ is shown. In the process, V_2C provides a rapid and continuous supply of electrons for

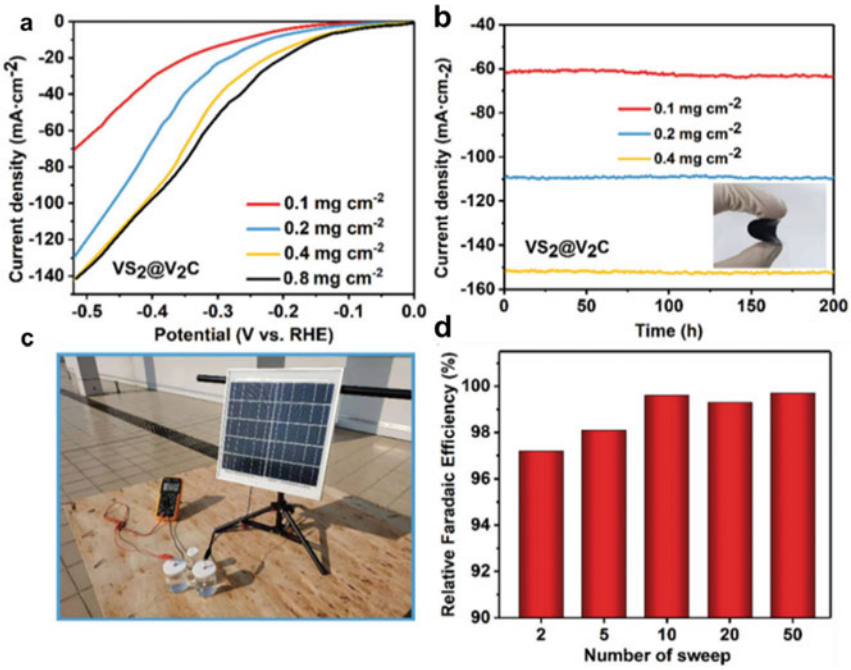

Fig. 46 Solar driven hydrogen production application of $VS_2@V_2C$

the VS_2 nanosheets. Such accumulation of electrons on VS_2 induces rapid hydrated protons adsorption, and hydrogen is produced by the Heyrovsky pathway on the VS_2 nanosheet surface.

3.3 Metal/Intermetallic Composites

3.3.1 Metal/Metal Sulfides

Kuang et al. [61] devised a multilayer anode comprised of a uniform layer of nickel–iron hydroxide electrocatalyst on a NiS_x layer on NF (denoted as NiFe/NiS_x-NF). The NiFe/NiS_x-NF (Ni^3 for brevity) anode was prepared by first transforming the surface of NF to NiS_x by solvothermal reaction with elemental sulfur in toluene. Then, NiFe hydroxide was electrodeposited via reduction of nitrate in a solution of $Ni(NO_3)_2$ and $Fe(NO_3)_3$ (Ni:Fe = 3:1) (Fig. 48).

SEM characterization clearly shows that a rough surface was formed after the surface sulfidation and the NiFe deposition (Fig. 49a–c). The cross-sectional EDS revealed that the NiS_x layer on the Ni foam is as thick as ~1–2 μm, and the NiFe layer on the top of the NiS_x layer is as thick as ~200 nm (Fig. 49c, d).

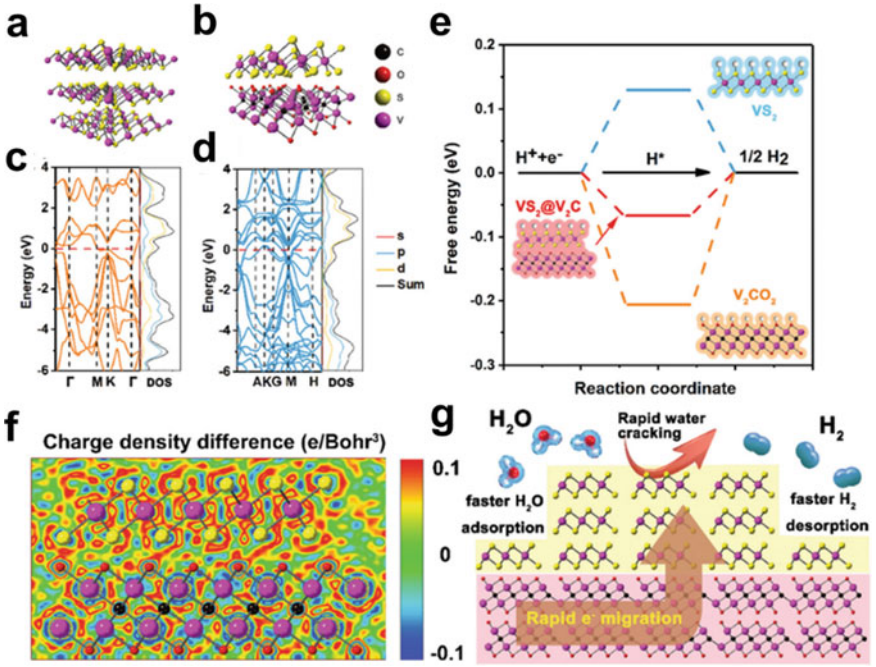

Fig. 47 DTF calculation results of $VS_2@V_2C$

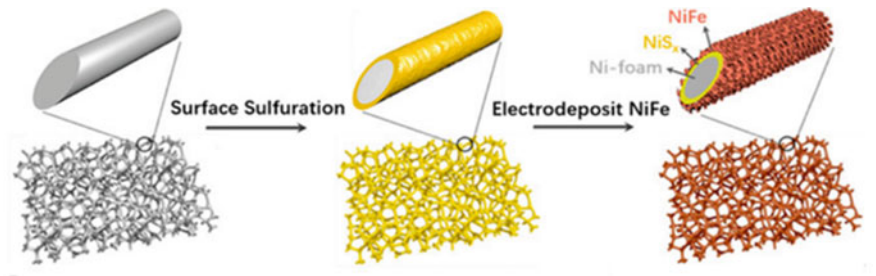

Fig. 48 Schematic illustration of the synthesis process of $NiFe/NiS_x$-NF

To test the surface chemical bonds, the Ni^3 electrode was first activated in alkaline simulated seawater (1 M KOH and 0.5 M NaCl). The Raman spectrum of the Ni^3 electrode contains two characteristic peaks of NiFe LDHs vibrational modes centered at 470 and 540 cm^{-1} and S–O vibrations peaks centered around 1,230, 1,440 and 1,590 cm^{-1} (Fig. 50a). This observation suggests that Ni^3 anode went through etching during the activation process, which caused the oxidation of the sulfides, leading to the formation of sulfate ions that migrate to the NiFe catalyst layer. Together with carbonate ions known to exist in KOH solution, sulfate ions intercalate into the NiFe LDH. Note that the NiFe-LDH is nearly amorphous in nature having only a low

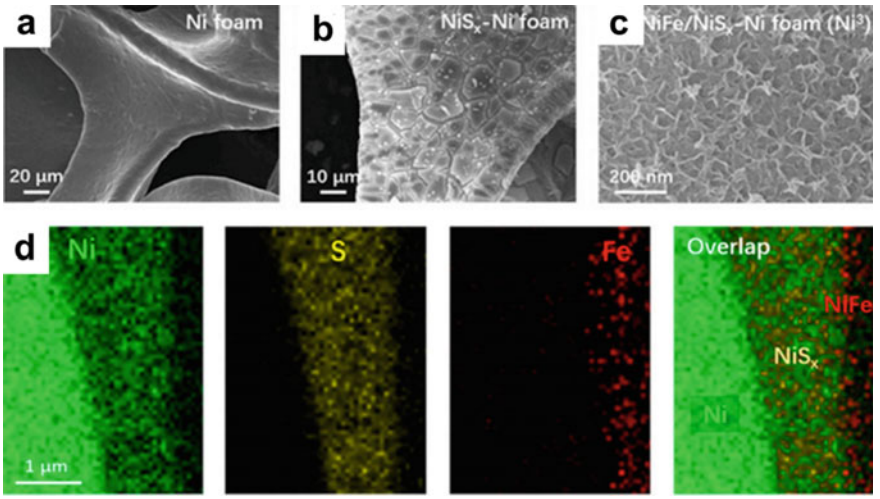

Fig. 49 SEM characterization of NiFe/NiS_x-NF

degree of crystallinity. Moreover, the secondary ion mass spectrometry mapping shows that both sulfate and carbonate species are present, proving the formation of a NiFe-LDH layer intercalated with two types of polyanions (Fig. 50b).

The OER performance in alkaline simulated seawater, was measured using anodically activated Ni^3 and in a three-electrode configuration (Fig. 51a). CV analysis showed that the electrode has an onset potential of 30 mV and a high current density of 400 mA/cm^2 at an overpotential of $\eta = 510$ mV, which are better than those of electrodeposited NiFe and NiFe-LDH (Fig. 51b). The observed oxidation peak at ~1.44 V of $Ni^{2+} \rightarrow Ni^{3+}$ suggests that increased numbers of electrochemically active sites for OER are created by anodic activation. The Ni^3 anode was then paired with a

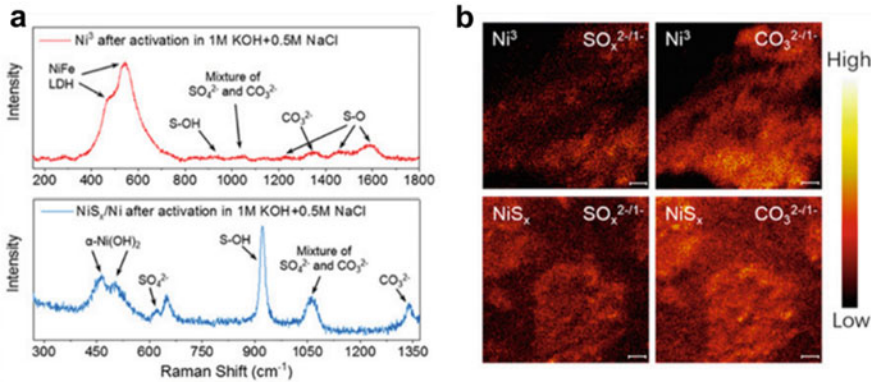

Fig. 50 Structural characterization of the Ni^3 electrode

highly active Ni-NiO-Cr_2O_3 HER cathode (a ~0.37 V overpotential to drive a HER current density of 500 mA/cm^2) in a two-electrode device to split alkaline seawater. The electrolyzer was found to operate continuously (current density of 400 mA/cm^2 under a voltage of 2.12 V, Fig. 51c) without decay for more than 1,000 h in alkaline simulated seawater (Fig. 51d). In addition, the activity of this electrode pair in electrolytes with higher NaCl concentrations (1.0 or 1.5 M NaCl) than those in seawater were assessed (Fig. 51d). Due to the higher NaCl concentrations, the electrolyzers showed lower resistance and a lower respective cell voltages of 2.02 V at a current density of 400 mA/cm^2. The electrolysis system does not corrode or undergo a voltage increase over more than 1,000 h of operation under these conditions, suggesting that the anode possesses impressive activity and stability anode for electrolysis in high-salinity water. Furthermore, the system functions in a stable manner under conditions that are typically used in the industry (1.72 V at a current density of 400 mA/cm^2 in 6 M KOH + 1.5 M NaCl at 80 °C (Fig. 51c, d)).

Tests showed that activated Ni^3 electrode in simulated alkaline seawater electrolyte has a 750 mV overpotential in order to reach the high OER current density of 1,500 mA·cm^{-2} (Fig. 52a). After iR compensation, the actual overpotential is ~0.38 V (Fig. 52b), which is 110 mV lower than chloride oxidation potential (0.49 V). Relative Faraday tests running at different current densities show that the oxygen generation efficiency is nearly 100% (Fig. 52c). Moreover, the two-electrode electrolysis in simulated alkaline seawater displays cell voltages of 2.44 V for current densities of 1000 mA cm^{-2} without apparent decline for over 500 h (Fig. 52d). To assess whether this EC system can be used for hydrogen generation when coupled with an inexpensive solar cell, the activated Ni^3 anode and a Ni-NiO-Cr_2O_3 cathode in simulated alkaline seawater operating for 5 h at 20 mA/cm^2 was connected to a perovskite solar cell in a side-by-side tandem cell. The tandem cell (without electrolyzer) has

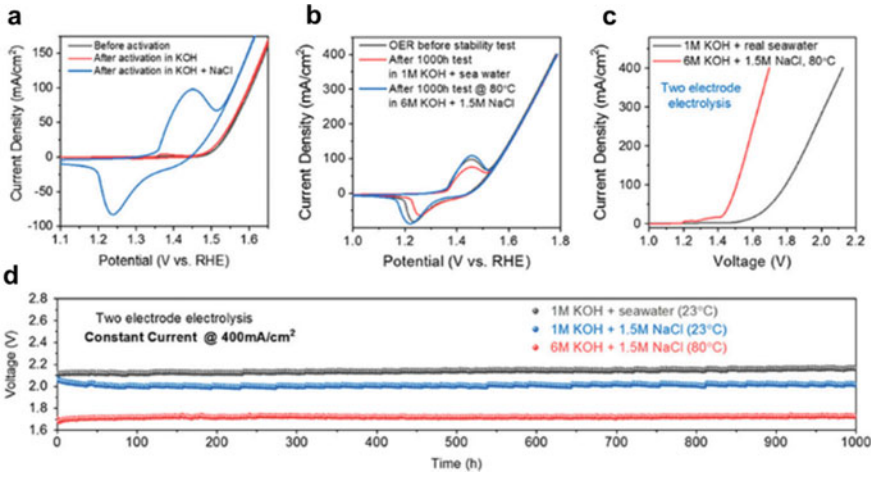

Fig. 51 OER performance of Ni^3 electrode in alkaline simulated seawater

a maximum power conversion efficiency of 16% under a simulated sunlight of 100 mW cm^{-2}. The operating current density of the solar cell–electrolyzer combination is a 9.7 ± 0.1 mA cm^{-2} (Fig. 52e). A STH efficiency of 11.9 ± 0.1% was obtained for the light-driven electrolysis, which is comparable to those of similar systems that utilize pure water. Furthermore, the integrated solar-driven seawater-splitting system operates stably for 20 h without obvious decay in its STH efficiency (Fig. 52f). A high-current test of the electrolyzer paired with a commercial Si solar cell (5 V, 1 A) using real sunlight and seawater, showed that the system operates at the impressively high current of ~880 mA under a photovoltage of 2.75 V (Fig. 52g).

It is interesting to note that activation of Ni^3 electrode in simulated alkaline seawater plays a key role in forming a chloride-repelling passivation layer. This conclusion is based on the observation that multivalent anion (sulfate and carbonate) passivated Ni^3 layers on hydrous metal oxide surfaces enhance cation selectivity and repel chloride anions. Hence, it appears that by using carefully designed anodes and electrolytes the chloride corrosion problem can be avoided without the need for desalination procedures.

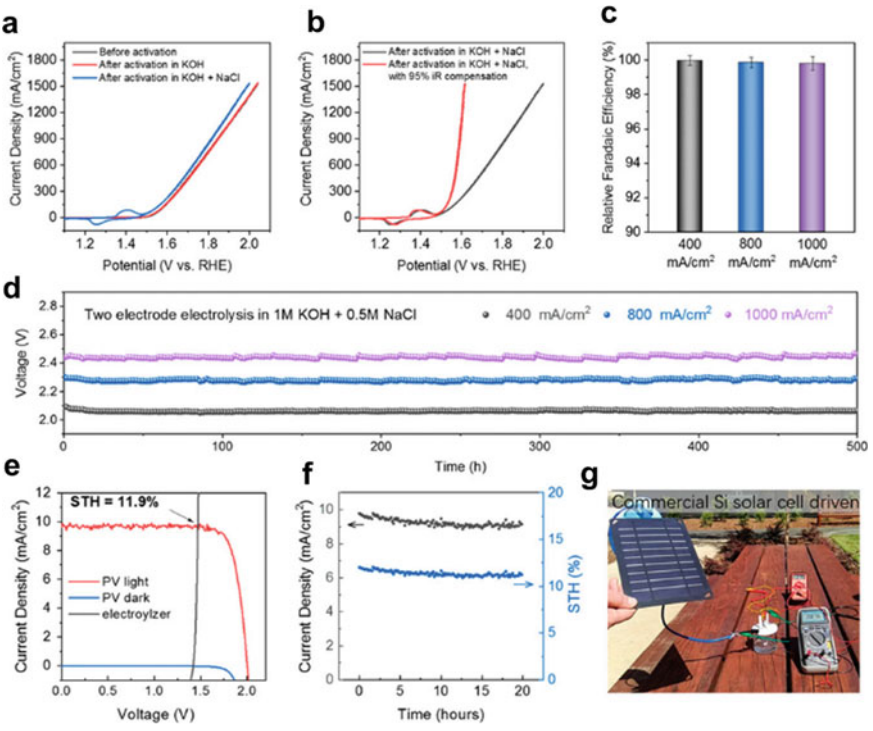

Fig. 52 Solar driven hydrogen production application of Ni^3 anode

3.3.2 Metal/Metal Oxide

Liu et al. [73] used systematic DFT calculations to predict that hydroxylation (OH^-) and the heterointerface existing on NiO coupled with metallic Cu will results in a reduced energy barrier for water dissociation and an enhanced HER. Motivated by these results, an electrochemical method was developed by this group to carry out KOH induced OH^- modification of NiO to form HOM-NiO. Rapid hydrogen spillover occurs at the heterointerface between HOM-NiO and Cu, leading to an enhancement of the rate of the HER. A study of this HOM-NiO/Cu couple using in situ XAS and electrochemical simulations verifying that it has advantageous properties for HER including enhanced water dissociation, reduced oxophilicity that enable efficient adsorption of water and accelerated hydrogen spillover. These properties are responsible for the superb HER activity of the HOM-NiO/Cu couple reflected in 33 and 310 mV overpotentials at respective current densities of 10 and 1000 mA cm^{-2} in 1.0 M KOH.

A working model for the operation of a three-electrode system based on this material is displayed in Fig. 53a, b. Specifically, when the counter electrode releases oxygen and protons into the solution, the working electrode, NiO/Cu_2O/Cu gains electrons that are used to preferentially reduce surficial Cu(I) to produce Cu(0). Meanwhile, OH^- spontaneously adsorbs on cationic Ni species.

Notably, analysis of SEM images shows that the reductive CV process does not significantly change the morphology of NiO, which is comprised of interacted nanowires with a diameter of about 200 nm. Moreover, NiO nanoclusters exist on the Cu surface in an irregular manner along with a crystal heterointerface (Fig. 54a–d).

Before structural characterization, the catalyst was first treated by applying 15 cycles of cyclic voltammetry in a 1 M KOH. HOM-NiO/Cu show an unusual onset potential, which then gradually decreases until overlapping occurs around the HER potential range, and no hydrogen bubble evolution occurs (Fig. 55a). This phenomenon is associated with irreversible reduction of Cu_2O, which occurs first due to its higher redox potential (0.3168 V). After that, HER takes place if all active components are thoroughly exposed, and finally HOM-NiO/Cu is produced

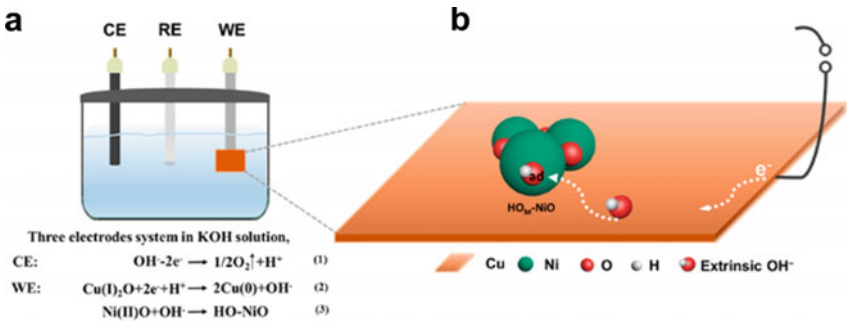

Fig. 53 Schematic illustration of the formation of NiO catalyst through three-electrode system

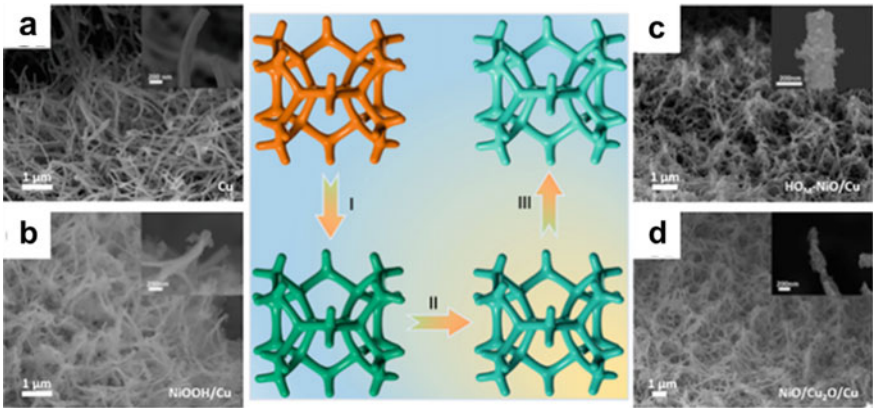

Fig. 54 SEM characterization of HOM-NiO/Cu

Therefore, overlapped cyclic voltammetry scans are generated during the subsequent 15th through 30th cycles, and then hydrogen generation begins (Fig. 55b) when the active electrocatalyst is fully formed. Impressively, the HOM-NiO/Cu has a highly enhanced HER performance, with a smaller Tafel slope than those of NiO/Cu and Cu individually (Fig. 55c).

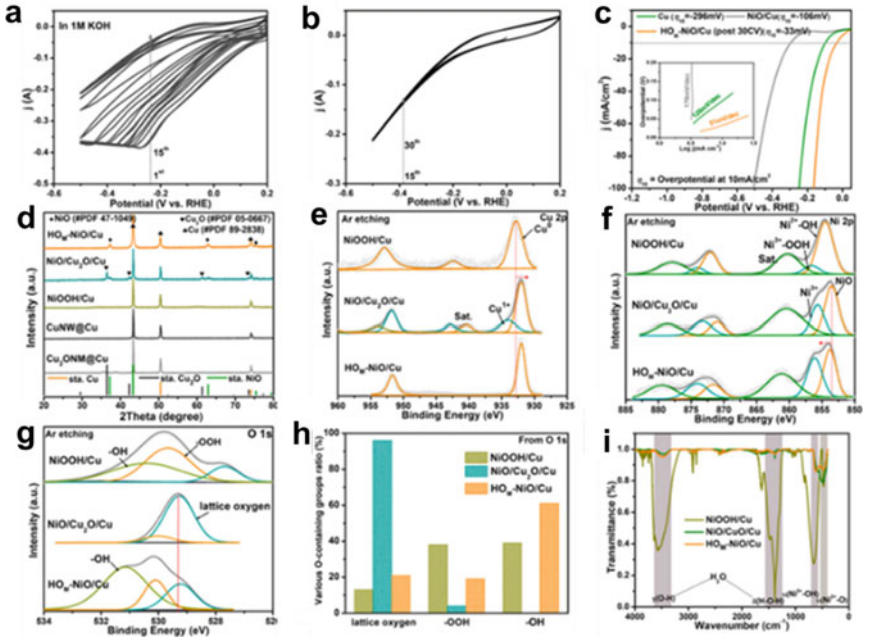

Fig. 55 Structural characterization of HOM-NiO/Cu

XRD analysis was used to follow evolution of the catalyst during the first 15 CV cycles by monitoring the retention of crystalline NiO retaining metallic Cu and the disappearance of $Cu^{I}_{2}O$ (Fig. 55d). The results are identical to those arising from Cu 2p XPS under Ar gas etching and, as a result, show that the major event at the surface is transfer of an electron between Cu and NiO at the heterointerface with consequent conversion to Cu(0) having a lower binding energy (Fig. 55e), indicating that an. The oNi 2p spectra show that a band associated with the binding energy in NiOOH/Cu is preserved throughout the process. In addition, a positive shift of the Ni^{2+} band toward a higher binding energy occurs after activation (Fig. 55f), demonstrating that electrons are lost from Ni sites as adsorption of additional OH^{-} occurs. The respective absence and rise of –OOH and –OH bands in O 1s XPS spectra before and after hydroxylation (Fig. 55g, h) and the emergence of the Ni^{2+}–OH vibrational band in the FT infrared spectrum (FT-IR) of HOM-NiO/Cu (Fig. 55i) further confirms that extrinsic OH^{-} is absorbed on Ni centers.

X-ray absorption energy near-edge structure (XANES) spectroscopy was carried out to evaluate the surface composition of the Ni. The Ni-edge XANES spectra of NiO in Fig. 56a contains a typical adsorption feature of Ni. For NiO/Cu, the absorption edge occurs at a higher energy than NiO, suggesting that the oxidation state of Ni in NiO is larger than +2 because of the heterointerface with Cu (Fig. 56a). Pre-edge adsorption of Ni in HOM-NiO/Cu is more positive after electrochemical adjustment, revealing that hydroxylation increases the valence state of Ni (larger than +2) by withdrawing electrons from the Ni center, an observation that is consistent with the Ni 2p XPS results. In addition, information about the coordination environment of these materials comes from analysis of Fourier transforms of extended X-ray absorption fine structure (EXAFS) (Fig. 56b). The coordination numbers of Ni in the Ni–O and Ni–M bonds increases upon hydroxylation from 5.6 and 12.3, and NiO/Cu to 6.0 and 13.6, respectively. This is caused by formation of an additional bond with OH^{-} and the presence of a heterointerface between NiO–Cu, which can be distinctly differentiated from NiOOH/Cu. Similar results come from the wavelet transforms of EXAFS of the Ni K-edge, especially informative is the observation of slightly more intense Ni–O (4 $Å^{-1}$) and Ni–Ni(Cu) (7 and 10 $Å^{-1}$) scattering in the HOM-NiO/Cu contour map relative to that of NiO/Cu (Fig. 56c–f).

The effects of altering several controllable parameters during the synthesis of HOM-NiO/Cu were explored. In Fig. 57a HER polarization curves of HOM-NiO/Cu produced under optimal conditions are shown. Cu and NiO/Cu exhibit inferior HER activity, with a high overpotential of 106 mV at 10 mA cm^{-2} and a high Tafel slope of 120 mV dec^{-1}. The activity of HOM-NiO/Cu is significantly higher, with an overpotential of 33 mV and a Tafel slope of 51 mV/dec, which is smaller and comparable to that of Pt/C/Cu (39 mV, 46 mV/dec) (Fig. 57b). The efficient HER kinetics of the HER promoted by HOM-NiO/Cu is proved by a higher turnover frequency. Impressively, HOM-NiO/Cu shows an enhanced activity over that of Pt/C and it even exceeds those of most reported Ni-based catalysts under 1 M KOH conditions at a high overpotential (250 mV) (Fig. 57c). The polarization curve of HOM-NiO/Cu, along with its morphology and chemistry remain nearly unchanged after 3000 cycles, showing that this material has high durability (Fig. 57d).

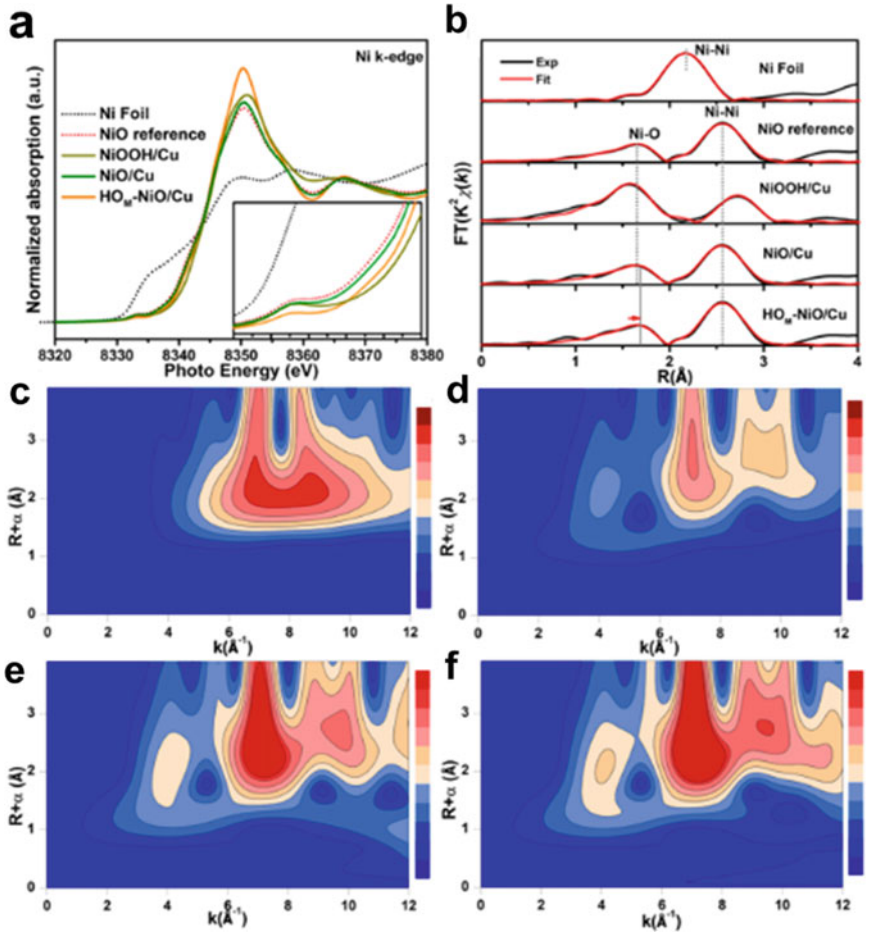

Fig. 56 XANES characterization of HOM-NiO/Cu

Because NiOOH/Cu has excellent activity for the OER, a coupled cell of HOM-NiO/Cu||NiOOH/Cu was assembled. This coupled cell has an overall water splitting performance that is superior to that of Pt/C||RuO_2 (Fig. 58a). This cell has a Faraday efficiency of nearly 100% with a stoichiometric H_2:O_2 ratio of 2:1, and excellent long-term stability in both alkaline condition and simulated seawater for 100 h and. The PVEC device, created by connecting this electrode combination to a solar cell illuminated by simulated sunlight, has a predicted operating current density of 16.8 mA cm^{-2} (Fig. 58b). The PVEC device was found to have a STH efficiency of 20.7% in 1 M KOH, 20.63% in simulated seawater, and 15.25% in PBS. Also, that unassisted photocurrents are produced during illumination by using 1600 s highlights the continuity and steadiness of this electrolyzer.

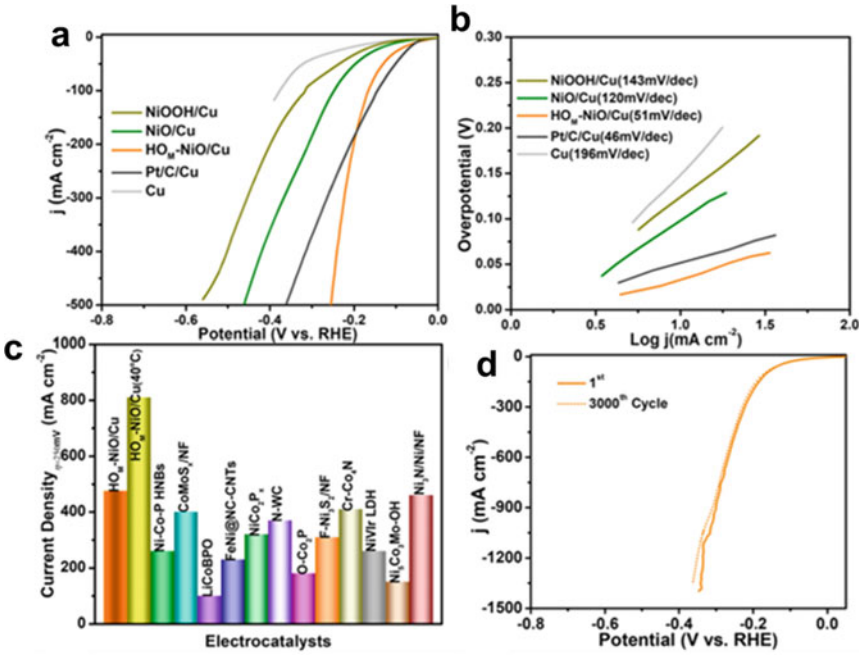

Fig. 57 HER performance of HOM-NiO/Cu electrode

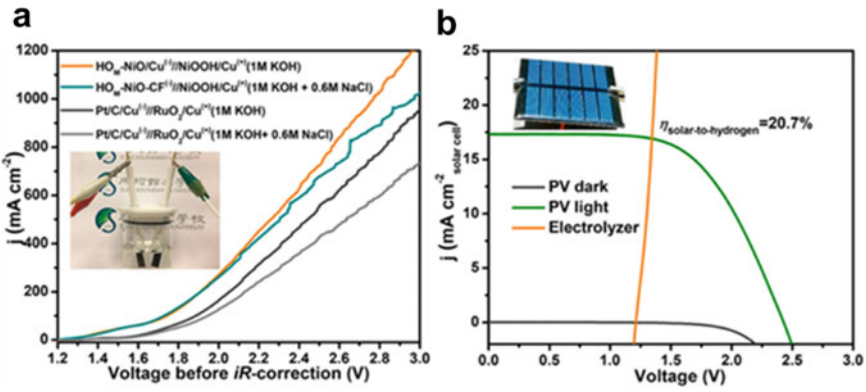

Fig. 58 Light driven hydrogen production application of HOM-NiO/Cu||NiOOH/Cu cell

In situ XAFS was performed on HOM-NiO/Cu under working conditions to determine the structural change of the material and XANES spectra at the Ni k-edge were recorded at various overpotentials (Fig. 59a). The adsorption edge of Ni shifts to a higher energy upon application of the external overpotential, suggesting that the higher oxidation state of Ni is a result of water adsorption. Upon further increasing the overpotential, the higher oxidation state remains in a defined range, which is in

accordance with the slight fluctuation of Ni adsorption edge occurring at −0.05 and −0.1 V. As shown in Fig. 59b, the EXAFS spectra show that the Ni–O shell during the EC reaction remains unchanged even over long periods at various potentials even though the Ni–Ni bonding strength slightly increases. This phenomenon is ascribed to the strong interaction between NiO and Cu, in which Cu transfers electrons. These observations suggest that the active material in this system might be NiO at the surface and bulk phase of HOM-NiO/Cu and also stable with reasonable changes. To gain information about the source of the improved HER kinetics of HOM-NiO/Cu, the consequence of hydroxylation and the heterointerface were investigated in detail. The obtained electrochemical data strongly indicate that OH^- promotes dissociation and weakens oxophilicity, further reinforcing the validity of the DFT predictions.

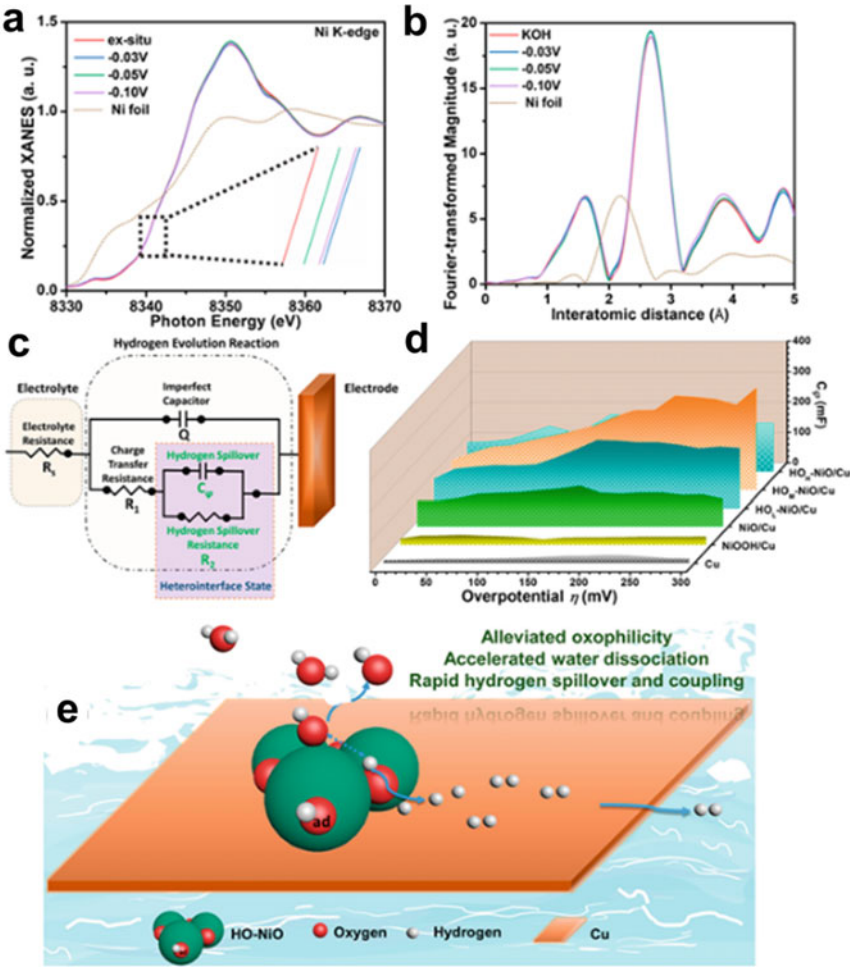

Fig. 59 Mechanistic investigations of the hydrogen spillover on HOM-NiO/Cu

The kinetic-determining step of the HER in this electrocatalytic process is the H* coupling (Heyrovsky–Tafel step) that proceeds on Cu sites. As a result, channeling H* migration from the original sites (O in NiO) to Cu through the interfacial pathway is significant. EIS analysis was employed to track the migration of H* over the active surface centers during the HER (Fig. 59c). The first parallel components in the plots, Q and R_1, where Q is an imperfect capacitor and is a C_{dl} reflect charge transfer kinetics. Larger Q and smaller R_1 values indicate greater active surface area and faster charge-transfer kinetics for the HER, respectively. Apparently, HOM-NiO/Cu has the highest intrinsic active surface area and lowest charge-transfer resistance. The second parallel components, C_φ and R_2, where C_φ and R_2 represent the respective pseudo capacitance and hydrogen adsorption resistance, reflect the charge (majority being H*) adsorption behavior on the catalyst surface. The derived curves of hydrogen adsorption capacitance (C_φ) versus overpotential are given in Fig. 59d. Notably, current development increases when the overpotential is less than 200 mV until a slightly fluctuating region is reached, indicating that hydrogen adsorbed on catalyst surfaces becomes saturated at a higher overpotential. Greater hydrogen adsorption values occur with smaller R_2 values in all HOM-NiO/Cu samples. This indicates the largest hydrogen coverage on the HOM-NiO/Cu surface, which is similarly seen in previous studies. As a result, the spillover of hydrogen from HOM-NiO toward coupling centers (Cu) is thermodynamically spontaneous (Fig. 59e).

4 Industrialization

4.1 PV Cells

Most solar cells manufactured at the current time are composed of single crystalline silicon and have efficiencies at a production-scale level as high as 23%, while most have efficiencies that fall in the 17–19% range. However, Graetzel et al. have discussed how solution-processed solar cells could become competitive if they could have a lower cost and a higher efficiency, which is one important approach that will be competitive with other rapidly advancing techniques. Polycrystalline-silicon PV systems usually have efficiencies of 14–16%, although the results of recent efforts indicate that refinement of bulk polysilicon production could lead to efficiencies that are similar to that of single-crystal silicon at a lower cost. Half the cost of a solar PV module lies in the cost of PV-grade silicon. In conventional cell production, about half the silicon is lost in transforming bulk silicon to 150–200-μm-thick wafers. When modest light-trapping techniques are used, functional wafers can be less than 50 μm thick. Other approaches to lowering the cost of silicon-based PV devices include the use of single-crystal epitaxial growth and a lift-off process pursued by Solexel of Milpitas, California, and kerf-less manufacturing that enables direct fabrication of this wafers from large and aligned grains.

The other competitive PV systems utilize direct-gap semiconductors such as CdTe or copper-indium-gallium-selenide (CIGS), in which only a thin film (less than 1 μm) is needed to absorb solar radiation. Thin-film solar cells, deposited on light and low-cost substrates, have advantages associated with transportation and installation. Nevertheless, thin-film deposition on the heterosubstrate introduces defects, greatly limiting the production-scale efficiency of CdTe and CIGS thin-film solar cells to 12–14%. If production introduced defects in CdTe thin films can be eliminated carrier lifetimes and efficiencies would be enhanced. An understanding of the origins of defects, as well as ways to reduce and control them are required for such reduction. The role of interfaces is a crucial aspect of solar cells and gaining a thorough understanding of this issue requires significant investment in research and development.

Despite the improvements in materials, online monitoring and control systems are needed to improve quality control. Currently, panels comprised of CdTe thin films have the lowest cost (~$0.70 W^{-1}). Owing to the financial discount applied to new solar systems that are expected to have 20–25 year performances, new PV technologies need to be created that remain competitive with advances made in more established technologies. When the efficiency is increased from 17 to 20%, the costs of panels and others would significantly be reduced, which could have a transformative effect on the market similar to that expected for polycrystalline silicon cells with an efficiency of over 18%. In the United States in 2011–2012, utility-scale solar photovoltaic systems are being installed at an unsubsidized cost of about $150 MWh^{-1} (Fig. 60), which is consistent with Bloomberg News Energy Finance estimates. Utility scale solar photovoltaic systems are projected to produce between $60 and 120 MWh^{-1} in ideal areas. The lowest levelized cost of energy (LCOE) for combined-cycle natural gas at a cost of $3–4 per million British thermal units is about $50–60 MWh^{-1} in the United States. Although LCOE is important, other significant issues are time of delivery, LCOE at various size scales and the potential for energy storage.

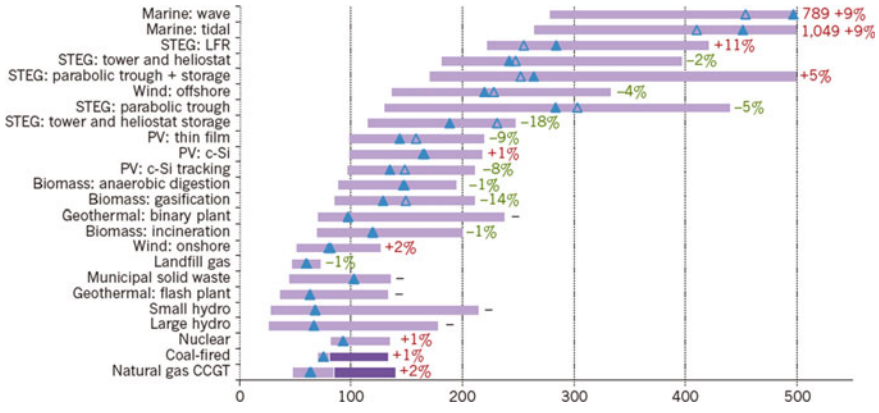

Fig. 60 Levelized costs of energy for quarter three of 2012 (dollars/megawatt-hour) [75]

Thin-film solar cells composed of direct-gap III–V semiconductors are attractive because of their high carrier mobilities and their previously demonstrated superior optoelectronic properties. This enables III–V semiconductor cells to achieve a high efficiency that is close to the practical upper limit. For example, III–V devices have solar-cell efficiencies of about 29%, which approaches the Shockley–Queisser limit of 33.5% for a single bandgap material [74]. Although high-quality films have been created on crystalline substrates, solar applications of these types of bulk materials would be cost-prohibitive. Thus, a major challenge is to develop methods to create crystalline III–V thin films on low-cost substrates such as plastics or sheet metals. Good progress is being made in devising methods for large scale manufacturing of solar cells that are generated by lift-off of thin crystalline GaAs layers grown epitaxially from bulk crystals.

4.2 Electrocatalytic Seawater Splitting

While hydrogen could have an impact on the transportation sector, its sustainable production will have a far greater short-term effect on decarbonizing the industrial sector [16, 27, 76–78]. Indeed, pure and mixed forms of hydrogen play key roles in energy-demanding industrial chemical processes [64, 79–83]. At the current time, more than 110 Mt of hydrogen is produced per year, 95% derived by CO_2 emitting reforming of fossil fuels and only 4% through electrolysis of water. The overriding reason for the low market penetration made by water electrolysis is associated with the price for hydrogen production. Hydrogen produced by reforming fossil-fuels has a cost of $1.3–1.5 per kg, while green (renewable-powered) water electrolysis now has a cost >$4 per kg of H_2 and needs to be ~$2 per kg to become cost competitive.

At the current time, the two main EC technologies employed commercially utilize alkaline electrolysis and proton exchange membrane (PEM) systems [13, 84, 85]. However, PEM water electrolysis commercialization has encountered large hurdles [86]. For example, PEM electrolyzers usually include noble metals, such as Pt as the cathodic catalyst and Ru/Ir-based oxide as the anodic catalyst, because of their corrosion resistance in acidic media [65, 87, 88]. Other less expensive transition-metal-based catalysts have poor anti-acid corrosion properties. Although many efforts have been made for the design of new inexpensive catalysts for PEM water electrolysis, the efforts face considerable challenges owing to the need to maintain high current densities, especially at high operational potentials and temperatures. Moreover, the instability of catalysts and polymer membranes in acidic media shortens lifetimes of PEM water electrolysis systems, further increasing investment costs (Table 1). Hence, the cost will be greatly increased and the widespread application of PEM water electrolysis will be limited due to the inevitable use of noble metal catalyst [81, 89–91].

The International Renewable Energy Agency put forward a report in which the total capital expenditure for an alkaline electrolysis system, including the power supply and installation, in 2017 is about $787.5 per kW, a value that is much lower

Table 1 Comparisons of the parameters, pros and cons of alkaline and PEM water electrolysis systems [39]

Parameter	Alkaline water electrolysis	PEM water electrolysis
Catalysis	Ni-based catalysts	Pt-, Ru-, Ir-based catalysts
Electrolytes	20–40 wt% KOH	Nafion membrane
Cell temperature (°C)	50–80	50–80
Cell voltage (V)	1.8–2.4	1.8–2.2
Current density (mA cm^{-2})	200–400	600–2000
Voltage efficiency (%)	60–80	60–80
System lifetime (y)	20–30	10–20
Advantages	Non-noble metal catalysts Long-term stability Low capital cost Mature commercialization	High current density High-purity hydrogen Compact device
Disadvantages	Low current density Corrosive electrolyte Noncompact device	Noble metal catalysts Poor durability High capital cost Initial commercialization

than $1260 per kW for a PEM electrolysis set-up. Although a rapidly decreased cost of PEM electrolysis systems can be expected by 2025, alkaline electrolysis still holds the economic high ground $504 per kW versus $735 per kW. An overview of commercial systems indicates that about 13 manufacturers of electrolyzers that utilize alkaline media could have single-stack capacities up to 6 MW, whereas only three manufacturers of PEM electrolysis systems can generate stacks that operate on the MW scale [92]. Moreover, the hydrogen production capacity of alkaline electrolyzers is ten times higher than that of PEM electrolyzers (hundreds of $Nm^3\ h^{-1}$ vs tens of $Nm^3\ h^{-1}$). Therefore, alkaline water electrolysis has clear advantages over acidic water electrolysis utilizing a PEM system for large-scale and low-cost hydrogen production by water splitting [8, 93].

Owing to factors associated with the water feed, maintenance and capital costs, a direct seawater electrolyzer (DSE) will have a lower efficiency and higher cost than those of a conventional electrolyser (see Fig. 61) [94]. Firstly, there are complicated compositions in natural seawater, including ions, bacteria/microbes and solid impurities, which inevitably lead to either the low catalytic efficiencies or physical/chemical interference with the components. As a result, it is necessary to filtrate or purify the

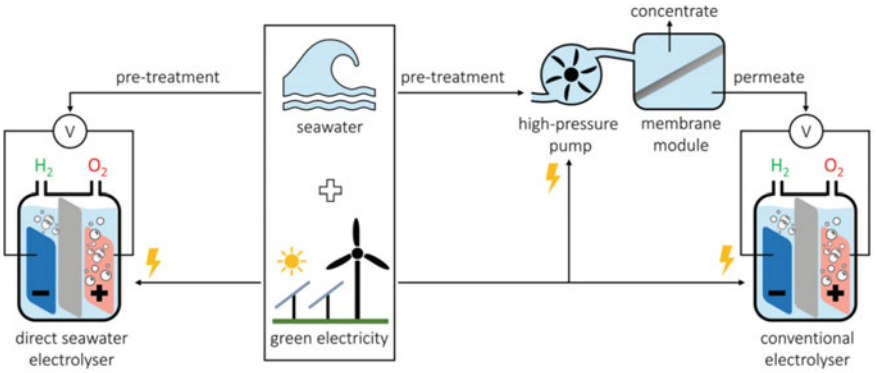

Fig. 61 Ways to generate hydrogen from seawater and green electricity

seawater before its direct use in seawater splitting. Secondly, HER and OER electrocatalysts with long-term durability are challenging because the active sites suffer from blockage and corrosion during seawater splitting. On this point, identifying suitable membranes to separate the catalyst from the seawater source or developing catalysts that have inherent anti-corrosion properties are potential approaches to improve the long-term stability of HER/OER ECs in seawater. Thirdly, the OER selectivity in seawater splitting faces great challenges due to the competing ClER [95].

4.3 Photovoltaic Electrocatalytic Seawater Splitting

Module efficiency is a useful parameter when comparing different hydrogen production technologies and purities of final products. Module efficiency is the module label power divided by the product of module area in meters and the irradiance at standard test conditions (1000 W/m) (module label power/(module area × 1000 W/m)). In Fig. 62 the efficiencies for best research level PVEC cells developed to date are shown. However, these efficiencies may be lower in the context of industrial manufacturing. In current module data sheets, module efficiency of 20% corresponds to a module area efficiency of 200 W/m. In Fig. 63 the expected average module efficiencies for modules under mass production using different cell technologies are displayed. The voltage efficiency of water electrolysis is 60–80% as discussed in Sect. 4.2 and Table 1. Considering the above data, the STH of photovoltaic electrocatalytic seawater splitting is 12–16%.

The global weighted average LCOE of utility scale solar PV derived energy fell by 7% from $0.061/kWh to $0.057/kWh in 2020, and the global weighted-average installation cost of utility-scale solar PV fell by 12% in 2020 to $883/kW. The percentage reduction in LCOE was lower than the 13% reduction occurring in 2019 because the large decline in total installation costs occurring in 2020 was partially offset by a reduction in the global weighted average capacity factor of new projects.

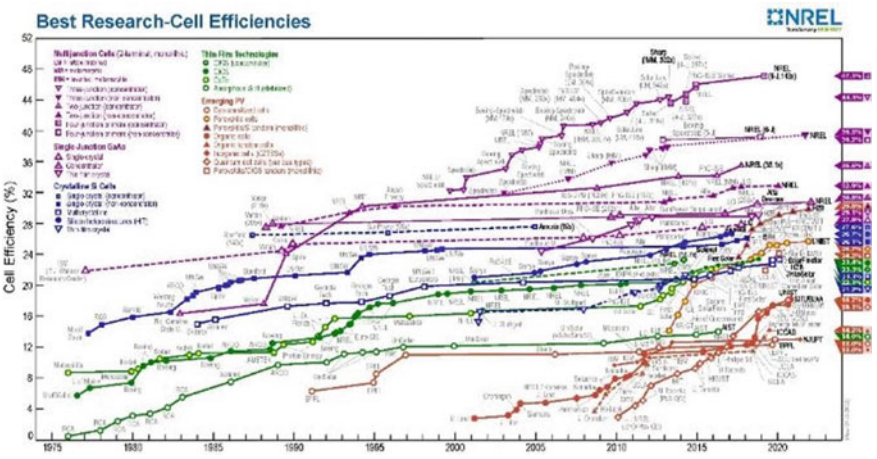

Fig. 62 Highest research-cell efficiencies

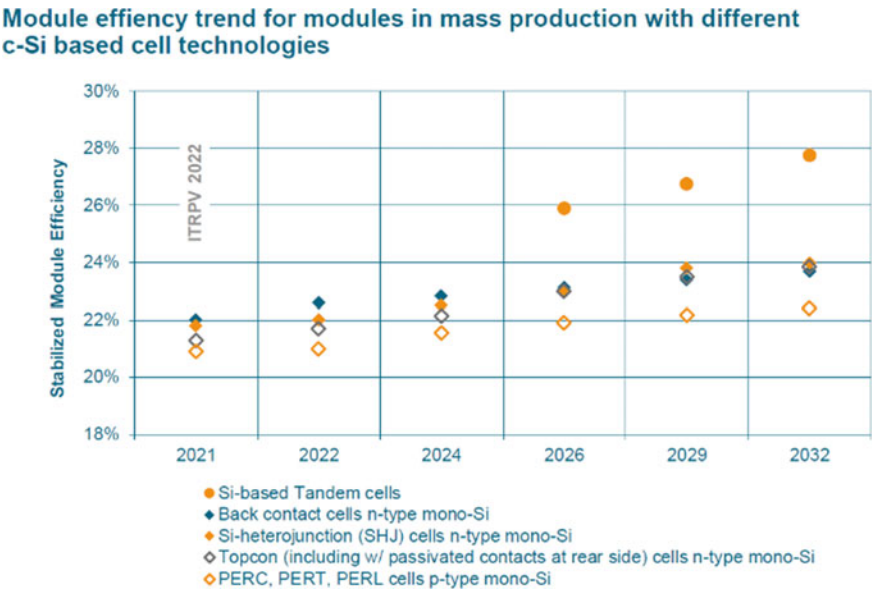

Fig. 63 Average module area efficiencies of different c-Si solar cell technologies under mass production [96]

The capacity factor reduction was driven by the fact that deployment in 2020 was greater in areas with poorer solar resources than in 2019. Similar to the situation for consumption of onshore wind derived energy, China was the largest market for new PV technologies, accounting for an estimated 45% of the new utility scale capacity added in 2020 [96].

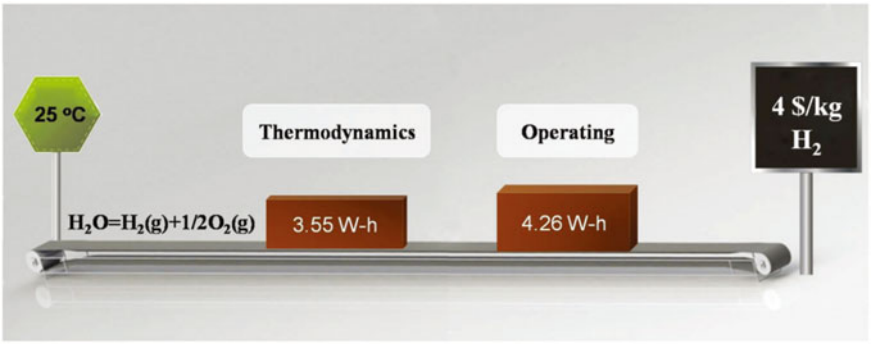

Fig. 64 Dissection of the energy input for production of hydrogen by electrolysis [98]

Hydrogen can be readily produced via electrolysis using only water and electricity as inputs on almost any scale. This process is well-established but requires a high input of electrical energy to produce hydrogen. From a thermodynamic perspective, 1 L of hydrogen at 25 C requires a minimum input of 3.55 kWh of electrical energy, and this quantity increases to around 4.26 kWh when electrochemical cell losses are taken into account [96]. If the electrolysis process is carried out at high temperatures (HT), solar derived heat can be utilized. In this case, solar energy can contribute up to 1/3 of the energy required to produce at around 1000 °C [97]. Under ideal conditions, 3.55 kWh electric power is required to produce 1 L of hydrogen, which becomes 4.26 kWh when energy losses are taken into consideration. The cost of one kilogram of hydrogen produced through water electrolysis in China is estimated to be $4, slightly higher than the contemporary market price (Fig. 64) [98]. The cost goal of overall commercial power in China is $0.028–$0.079. Considering all the above factors, the price of hydrogen derived from renewable sources is $3.01–$4.14, which has met the standard put forward in G20 ($2.5–6.0/$kg_{hydrogen}$). However, this price is much higher than that of hydrogen produced by steam reforming of methane.

Even though present in seawater, carbonate and borate ions have concentrations that are too low to sustain high current densities [11]. In most cases, industrially relevant current densities have been reached using seawater containing a borate buffer or additives. Furthermore, seawater is essentially a non-buffered electrolyte. Thus, a change in pH takes place near the electrode surface during electrolysis, resulting in precipitation of salts as well as degradation of the catalyst and electrode. Other issues involved when direct seawater electrolysis is employed include the presence of other ions or impurities which limit the long-term durability of catalysts and membranes. Direct seawater splitting still remains at the initial stage and far removed from commercialization, despite large efforts that have been devoted to developing this technology. However, the direct seawater splitting technology could be a sole alternative in areas inaccessible to fresh water, while accessible to seawater and renewable solar, wind and geothermal derived electricity [22, 99]. Over the past few decades, lots of research has been conducted on direct seawater electrolysis

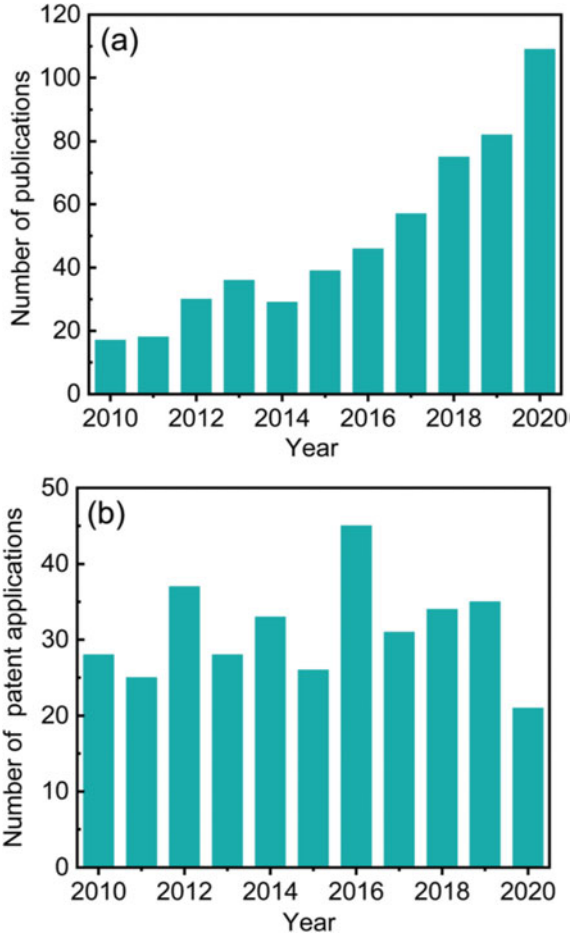

Fig. 65 **a** Annual number of publications and patent applications [11]

(Fig. 65). In the last decade, >700 scientific publications and >340 patent applications have arisen from these efforts, which translate into funding allocations amounting to millions of dollars. Therefore, hydrogen production using a combination of solar cell and direct seawater splitting has a large potential for future use in commerce.

5 Conclusion

A strategy to facilitate low cost and high STH efficiency is a fundamental goal of studies aimed identifying renewable and sustainable energy sources. In order to attain the US. Department of Energy's device efficiency target of over 10%, new stable, efficient photocatalyst materials that operate under solar irradiation are required.

The fundamentals of PVEC seawater splitting and recent progress made in developing novel electrocatalysts are described in this chapter. The ultimate target of the research field is to design and construct a cost-effective, highly efficient and stable solar-driven system comprised of a PV cell and an electrocatalytic seawater splitting system for seawater hydrogen production. In the device, the PV cell that converts solar energy to electricity and the electrocatalytic seawater splitting system utilizes electricity for electrocatalytic hydrogen production. To achieve high STH efficiencies, dual component systems of this type need to be highly efficient in promoting photovoltaic power conversion and highly durable during electrocatalytic seawater splitting. Owing to their highly mature nature, commercial silicon or perovskite-based PV cells are widely used in greatly needed experimental investigations aimed at gaining a better understanding of and designing new materials for electrocatalytic seawater splitting step.

The past several years have witnessed many innovations that have been made in devising new electrode materials, nanoarchitecture designs which address the main hurdles facing development of this technology. During this period, Noble and transition metal, metallic and metal-metallic composites have been developed for use in electrodes for efficient photovoltaic electrocatalytic seawater splitting. Pt-based electrodes, the first to be highly investigated for this purpose, have STH efficiencies of 5–6% together with a hydrogen production durability of 50 h. It should be noted that the fact that PV cells with a relatively low PCE of 7.9–10% were employed in these studies and this might be the main reason for the relatively low STH efficiencies of the Pt based devices. In any event, despite their use of expensive Pt, these efforts provided new ideas that stimulated the development of new electrocatalytic seawater splitting systems. For example, Karst landform-featured nickel foam (NF) was developed as a monolithic electrode for high performance photovoltaic HER and OER of neutral seawater. The karst NF was easily fabricated by using chemical and electrochemical etching, which formed Ni/amorphous $Ni(OH)_2$ heterostructures. This NF derived electrode, which can reversibly and flexibly switch between HER and OER, has long-term viability and a high STH efficiency of 16.5%. This inexpensive, flexible, robust and easily obtained bifunctional electrode was demonstrated to have great potentials for water splitting applications.

Although less costly transition metals can be used as substitutes for the Pt electrode, they are often vulnerable to corrosion in seawater. Novel metallic compounds, including metal carbides, phosphorites, hydroxides and sulfides, were developed as electrocatalysts for efficient and durable PVEC seawater splitting. These materials, which have special electronic structures, highly efficiently facilitate water splitting with high STH of 17.9% and have superior durabilities of 200 h. Inspired by the properties of these materials, substances in which transition metals are combined with metallic compounds have attracted increasing attention. The studies revealed that combining a high activity transition metal with a highly stable metallic compound leads to a catalyst that displays excellent PVEC seawater splitting performance that have STH efficiencies as high as 20.63% in simulated seawater.

6 Perspectives

Before presenting our thoughts about the aims of future research in the area PVEC seawater splitting, it is significant to note that the various metrics employed for evaluation serve as the basis for critical evaluations of the comparative advantageous and disadvantageous features. We believe that it is imperative that researchers utilize a common set of appropriate metrics to describe the performances of new PV and electrocatalytic devices along with those of PVEC systems derived from these components. Moreover, the methods used to measure and/or calculate STH efficiencies need to be properly described to facilitate accurate comparisons of data between laboratories.

Hydrogen production from photovoltaic electrocatalytic seawater splitting is an effective renewable energy conversion process. Despite tremendous achievements accomplished thus far, more progress is needed before the commercialization of PVEC water splitting technology with economically beneficial. As discussed above, hydrogen is produced in these systems through a two-stage process in which the photovoltaic process converts solar energy to electricity and then the electrocatalytic process uses the electricity for seawater splitting. As a result, the overall STH efficiency of a PVEC system is a multiple of the PCE with electric-to-hydrogen (ETH) efficiencies. Currently, the efficiency for seawater hydrogen production is in the 75–85% range, or even over 90%, while photovoltaic PCE is only 20–30%. When combined, these results show that the current STH efficiency level is ~20%. Since the photovoltaic cells are already commercialized, it is difficult to imagine that a great breakthrough will be made to significantly increase PCE. Therefore, persistent efforts in this area should focus on device design, and on understanding the fundamentals of the electrocatalytic seawater splitting process and developing new electrode materials. Some of the suggestions for studies that are needed for these purposes are given below.

(1) Electrolyzers. The complicated composition of natural seawater that contains a variety of dissolved ions, bacteria/microbes and solid impurities/precipitates inevitably leads to either decreased efficiency of electrocatalysts in seawater electrolyzers, and/or physical/chemical interference with the electrolysis components. As a result, new filtration/purification systems should be developed for use in pretreatment procedures in direct seawater splitting systems.
(2) Durability. Long-term stability for the HER and OER is an important feature because they suffer from blockage and corrosion during seawater splitting. On this point, developing suitable membranes that separate the catalyst from seawater is an important goal as is designing catalysts with inherent anti-corrosion abilities.
(3) ClER. It is challenging to promote the OER in seawater splitting due to competition with the ClER. Studies are required to devise ways of overcoming this problem. Some possible approaches that address this issue are employing alkaline seawater electrolytes, developing catalysts that have selective OER active sites, and/or using Cl^- blocking layers over the electrocatalysts.

(4) Mechanism. To gain more insight into the reaction mechanisms for the processes involved in seawater splitting, developing advanced characterization techniques is necessary, especially in situ microscopy, spectroscopy and chromatography. In addition, studies that combine in situ characterization data and theoretical calculations are required to understand the dynamic evolution of electrocatalysts under real working conditions.
(5) Commercialization. At present, most studies focus mainly on laboratory level systems of seawater splitting. A significant effort is needed to design and scale-up novel electrocatalyst and PVEC systems for seawater splitting to meet the requirement of industrial-scale H_2 production. Hence, already successful industrial freshwater splitting systems should serve as models.

However, nowadays only far from satisfactory performances can be obtained for seawater splitting, breakthroughs should evolve in the near future from in-depth research and optimization investigations. It is expected the material discussed in this chapter will help the efforts of researchers targeted at establishing appropriate seawater PVEC systems for sustainable hydrogen production.

Acknowledgements This work was supported by National Key Research and Development Program of China (2022YFB3805600, 2022YFB3805604), National Natural Science Foundation of China (22293020), Sino-German Center COVID-19 Related Bilateral Collaborative project (C-0046), FRFCU (2021qntd13), National 111 project (B20002), Program for Changjiang Scholars and Innovative Research Team in University (IRT_15R52), Guangdong Basic and Applied Basic Research Foundation (2021A1515111131, 2022A1515010137), and Shenzhen Science and Technology Program (JCYJ20210324142010029, GJHZ20210705143204014, KCXFZ20211020170006010).

References

1. Wang Z, Li C, Domen K (2019) Recent developments in heterogeneous photocatalysts for solar-driven overall water splitting. Chem Soc Rev 48:2109–2125
2. Liang J, Han X, Qiu Y, Fang Q, Zhang B, Wang W, Zhang J, Ajayan PM, Lou J (2020) A low-cost and high-efficiency integrated device toward solar-driven water splitting. ACS Nano 14:5426–5434
3. Yin H, Zhao S, Zhao K, Muqsit A, Tang H, Chang L, Zhao H, Gao Y, Tang Z (2015) Ultrathin platinum nanowires grown on single-layered nickel hydroxide with high hydrogen evolution activity. Nat Commun 6:6430
4. Chen C, Kang Y, Huo Z, Zhu Z, Huang W, Xin HL, Snyder JD, Li D, Herron JA, Mavrikakis M, Chi M, More KL, Li Y, Markovic NM, Somorjai GA, Yang P, Stamenkovic VR (2014) Highly crystalline multimetallic nanoframes with three-dimensional electrocatalytic surfaces. Science 343
5. Tang J, Liu T, Miao S, Cho Y (2021) Emerging energy harvesting technology for electro/photocatalytic water splitting application. Catalysts 11:142
6. Lu X, Pan J, Lovell E, Tan TH, Ng YH, Amal R (2018) A sea-change: manganese doped nickel/nickel oxide electrocatalysts for hydrogen generation from seawater. Energy Environ Sci 11:1898–1910
7. Tong W, Forster M, Dionigi F, Dresp S, Sadeghi Erami R, Strasser P, Cowan AJ, Farràs P (2020) Electrolysis of low-grade and saline surface water. Nat Energy 5:367–377

8. Ying J, Jiang GP, Cano ZP, Han L, Yang XY, Chen ZW (2017) Nitrogen-doped hollow porous carbon polyhedrons embedded with highly dispersed Pt nanoparticles as a highly efficient and stable hydrogen evolution electrocatalyst. Nano Energy 40:88–94
9. Dionigi F, Reier T, Pawolek Z, Gliech M, Strasser P (2016) Design criteria, operating conditions, and nickel-iron hydroxide catalyst materials for selective seawater electrolysis. Chemsuschem 9:962–972
10. Qi J, Zhang W, Cao R (2018) Solar-to-hydrogen energy conversion based on water splitting. Adv Energy Mater 8:1701620
11. Khan MA, Al-Attas T, Roy S, Rahman MM, Ghaffour N, Thangadurai V, Larter S, Hu JG, Ajayan PM, Kibria MG (2021) Seawater electrolysis for hydrogen production: a solution looking for a problem? Energy Environ Sci 14:4831–4839
12. Pu Z, Zhao J, Amiinu IS, Li W, Wang M, He D, Mu S (2019) A universal synthesis strategy for P-rich noble metal diphosphide-based electrocatalysts for the hydrogen evolution reaction. Energy Environ Sci 12:952–957
13. Wang PT, Jiang KZ, Wang GM, Yao JL, Huang XQ (2016) Phase and interface engineering of platinum-nickel nanowires for efficient electrochemical hydrogen evolution. Angew Chem-Int Ed Engl 55:12859–12863
14. Xing Z, Han C, Wang D, Li Q, Yang X (2017) Ultrafine Pt nanoparticle-decorated $Co(OH)_2$ nanosheet arrays with enhanced catalytic activity toward hydrogen evolution. ACS Catal 7:7131–7135
15. Cao Z, Chen Q, Zhang J, Li H, Jiang Y, Shen S, Fu G, Lu BA, Xie Z, Zheng L (2017) Platinum-nickel alloy excavated nano-multipods with hexagonal close-packed structure and superior activity towards hydrogen evolution reaction. Nat Commun 8:15131
16. Wang P, Zhang X, Zhang J, Wan S, Guo S, Lu G, Yao J, Huang X (2017) Precise tuning in platinum-nickel/nickel sulfide interface nanowires for synergistic hydrogen evolution catalysis. Nat Commun 8:14580
17. Zhao Z, Liu H, Gao W, Xue W, Liu Z, Huang J, Pan X, Huang Y (2018) Surface-engineered PtNi-O nanostructure with record-high performance for electrocatalytic hydrogen evolution reaction. J Am Chem Soc 140:9046–9050
18. Cheng X, Li Y, Zheng L, Yan Y, Zhang Y, Chen G, Sun S, Zhang J (2017) Highly active, stable oxidized platinum clusters as electrocatalysts for the hydrogen evolution reaction. Energy Environ Sci 10:2450–2458
19. Ramani S, Sarkar S, Vemuri V, Peter SC (2017) Chemically designed CeO_2 nanoboxes boost the catalytic activity of Pt nanoparticles toward electro-oxidation of formic acid. J Mater Chem A 5:11572–11576
20. Xie Y, Cai J, Wu Y, Zang Y, Zheng X, Ye J, Cui P, Niu S, Liu Y, Zhu J, Liu X, Wang G, Qian Y (2019) Boosting water dissociation kinetics on Pt-Ni nanowires by N-induced orbital tuning. Adv Mater 31:e1807780
21. Dresp S, Dionigi F, Loos S, de Araujo JF, Spori C, Gliech M, Dau H, Strasser P (2018) Direct electrolytic splitting of seawater: activity, selectivity, degradation, and recovery studied from the molecular catalyst structure to the electrolyzer cell level. Adv Energy Mater 8
22. Dresp S, Dionigi F, Klingenhof M, Strasser P (2019) Direct electrolytic splitting of seawater: opportunities and challenges. ACS Energy Lett 4:933–942
23. Coridan RH, Nielander AC, Francis SA, McDowell MT, Dix V, Chatman SM, Lewis NS (2015) Methods for comparing the performance of energy-conversion systems for use in solar fuels and solar electricity generation. Energy Environ Sci 8:2886–2901
24. Jiang C, Moniz SJA, Wang A, Zhang T, Tang J (2017) Photoelectrochemical devices for solar water splitting—materials and challenges. Chem Soc Rev 46:4645–4660
25. Li R (2017) Latest progress in hydrogen production from solar water splitting via photocatalysis, photoelectrochemical, and photovoltaic-photoelectrochemical solutions. Chin J Catal 38:5–12
26. Alaaeddin MH, Sapuan SM, Zuhri MYM, Zainudin ES, Al-Oqla FM (2019) Photovoltaic applications: status and manufacturing prospects. Renew Sustain Energy Rev 102:318–332

27. Liu Y, Yu HZ, Wang Y, Tian G, Zhou L, de Torresi SIC, Ozoemena KI, Yang XY (2022) Hierarchically fractal Co with highly exposed active facets and directed electron-transfer effect. Chem Commun 58:6882–6885
28. Chen JB, Ying J, Xiao YX, Dong Y, Ozoemena KI, Lenaerts S, Yang XY Stoichiometry design in hierarchical CoNiFe phosphide for highly efficient water oxidation. Sci China-Mater
29. Wang XS, Zheng Y, Sheng WC, Xu ZCJ, Jaroniec M, Qiao SZ (2020) Strategies for design of electrocatalysts for hydrogen evolution under alkaline conditions. Mater Today 36:125–138
30. Sheng W, Zhuang Z, Gao M, Zheng J, Chen JG, Yan Y (2015) Correlating hydrogen oxidation and evolution activity on platinum at different pH with measured hydrogen binding energy. Nat Commun 6:5848
31. Yu HZ, Wang Y, Ying J, Wu SM, Lu Y, Hu J, Hu JS, Shen L, Xiao YX, Geng W, Chang GG, Janiak C, Li WH, Yang XY (2019) Hydrogen evolution enhancement over a cobalt-based Schottky interface. ACS Appl Mater Interfaces 11:27641–27647
32. Wang Z, Ren X, Shi X, Asiri AM, Wang L, Li X, Sun X, Zhang Q, Wang H (2018) A platinum oxide decorated amorphous cobalt oxide hydroxide nanosheet array towards alkaline hydrogen evolution. J Mater Chem A 6:3864–3868
33. Yu FY, Lang ZL, Yin LY, Feng K, Xia YJ, Tan HQ, Zhu HT, Zhong J, Kang ZH, Li YG (2020) Pt-O bond as an active site superior to Pt(0) in hydrogen evolution reaction. Nat Commun 11:490
34. Feng Y, Guan Y, Zhang H, Huang Z, Li J, Jiang Z, Gu X, Wang Y (2018) Selectively anchoring Pt single atoms at hetero-interfaces of γ-Al_2O_3/NiS to promote the hydrogen evolution reaction. J Mater Chem A 6:11783–11789
35. Liu G, Xu Y, Yang T, Jiang L (2020) Recent advances in electrocatalysts for seawater splitting. Nano Mater Sci
36. Zheng J, Sheng WC, Zhuang ZB, Xu XB, Yan YS (2016) Universal dependence of hydrogen oxidation and evolution reaction activity of platinum-group metals on pH and hydrogen binding energy. Sci Adv 2:e1501602
37. Anantharaj S, Aravindan V (2020) Developments and perspectives in 3d transition-metal-based electrocatalysts for neutral and near-neutral water electrolysis. Adv Energy Mater 10
38. Tong WM, Forster M, Dionigi F, Dresp S, Erami RS, Strasser P, Cowan AJ, Farras P (2021) Electrolysis of low-grade and saline surface water (vol 5, pg 367, 2020). Nat Energy 6:935–935
39. Yu ZY, Duan Y, Feng XY, Yu X, Gao MR, Yu SH (2021) Clean and affordable hydrogen fuel from alkaline water splitting: past, recent progress, and future prospects. Adv Mater 33:e2007100
40. Jin HY, Guo CX, Liu X, Liu JL, Vasileff A, Jiao Y, Zheng Y, Qiao SZ (2018) Emerging two-dimensional nanomaterials for electrocatalysis. Chem Rev 118:6337–6408
41. Liu YW, Xiao C, Huang PC, Cheng M, Xie Y (2018) Regulating the charge and spin ordering of two-dimensional ultrathin solids for electrocatalytic water splitting. Chem 4:1263–1283
42. Sultan S, Tiwari JN, Singh AN, Zhumagali S, Ha M, Myung CW, Thangavel P, Kim KS (2019) Single atoms and clusters based nanomaterials for hydrogen evolution, oxygen evolution reactions, and full water splitting. Adv Energy Mater 9
43. Li XM, Hao XG, Abudula A, Guan GQ (2016) Nanostructured catalysts for electrochemical water splitting: current state and prospects. J Mater Chem A 4:11973–12000
44. Oh BS, Oh SG, Hwang YY, Yu HW, Kang JW, Kim IS (2010) Formation of hazardous inorganic by-products during electrolysis of seawater as a disinfection process for desalination. Sci Total Environ 408:5958–5965
45. Zheng JJ (2017) Seawater splitting for high-efficiency hydrogen evolution by alloyed PtNix electrocatalysts. Appl Surf Sci 413:360–365
46. Liu E, Li J, Jiao L, Doan HTT, Liu Z, Zhao Z, Huang Y, Abraham KM, Mukerjee S, Jia Q (2019) Unifying the hydrogen evolution and oxidation reactions kinetics in base by identifying the catalytic roles of hydroxyl-water-cation adducts. J Am Chem Soc 141:3232–3239
47. Katsounaros I, Meier JC, Klemm SO, Topalov AA, Biedermann PU, Auinger M, Mayrhofer KJJ (2011) The effective surface pH during reactions at the solid-liquid interface. Electrochem Commun 13:634–637

48. Zhang L-N, Li R, Zang H-Y, Tan H-Q, Kang Z-H, Wang Y-H, Li Y-G (2021) Advanced hydrogen evolution electrocatalysts promising sustainable hydrogen and chlor-alkali co-production. Energy Environ Sci 14:6191–6210
49. Zhuang L, Li J, Wang K, Li Z, Zhu M, Xu Z (2022) Structural buffer engineering on metal oxide for long-term stable seawater splitting. Adv Funct Mater 32
50. Walter MG, Warren EL, McKone JR, Boettcher SW, Mi QX, Santori EA, Lewis NS (2010) Solar water splitting cells. Chem Rev 110:6446–6473
51. Lewis NS (2007) Toward cost-effective solar energy use. Science 315:798–801
52. Steinfeld A (2005) Solar thermochemical production of hydrogen—a review. Sol Energy 78:603–615
53. Rosen MA (2010) Advances in hydrogen production by thermochemical water decomposition: a review. Energy 35:1068–1076
54. Li X, Fan L, Li Z, Wang K, Zhong M, Wei J, Wu D, Zhu H (2012) Boron doping of graphene for graphene-silicon p-n junction solar cells. Adv Energy Mater 2:425–429
55. Blankenship RE, Tiede DM, Barber J, Brudvig GW, Fleming G, Ghirardi M, Gunner MR, Junge W, Kramer DM, Melis A, Moore TA, Moser CC, Nocera DG, Nozik AJ, Ort DR, Parson WW, Prince RC, Sayre RT (2011) Comparing photosynthetic and photovoltaic efficiencies and recognizing the potential for improvement. Science 332:805–809
56. Bonke SA, Wiechen M, MacFarlane DR, Spiccia L (2015) Renewable fuels from concentrated solar power: towards practical artificial photosynthesis. Energy Environ Sci 8:2791–2796
57. Khaselev, Turner (1998) A monolithic photovoltaic-photoelectrochemical device for hydrogen production via water splitting. Science (New York, N.Y.) 280:425–427
58. Pihosh Y, Turkevych I, Mawatari K, Uemura J, Kazoe Y, Kosar S, Makita K, Sugaya T, Matsui T, Fujita D, Tosa M, Kondo M, Kitamori T (2015) Photocatalytic generation of hydrogen by core-shell WO_3/$BiVO_4$ nanorods with ultimate water splitting efficiency. Sci Rep 5
59. Luo JS, Im JH, Mayer MT, Schreier M, Nazeeruddin MK, Park NG, Tilley SD, Fan HJ, Gratzel M (2014) Water photolysis at 12.3% efficiency via perovskite photovoltaics and Earth-abundant catalysts. Science 345:1593–1596
60. Hsu S-H, Miao J, Zhang L, Gao J, Wang H, Tao H, Hung S-F, Vasileff A, Qiao SZ, Liu B (2018) An Earth-abundant catalyst-based seawater photoelectrolysis system with 17.9% solar-to-hydrogen efficiency. Adv Mater 30:1707261
61. Kuang Y, Kenney MJ, Meng Y, Hung W-H, Liu Y, Huang JE, Prasanna R, Li P, Li Y, Wang L, Lin M-C, McGehee MD, Sun X, Dai H (2019) Solar-driven, highly sustained splitting of seawater into hydrogen and oxygen fuels. Proc Natl Acad Sci USA 116:6624–6629
62. Wu Y, Tian Z, Yuan S, Qi Z, Feng Y, Wang Y, Huang R, Zhao Y, Sun J, Zhao W, Guo W, Feng J, Sun J (2021) Solar-driven self-powered alkaline seawater electrolysis via multifunctional earth-abundant heterostructures. Chem Eng J 411:128538
63. Kumari S, Turner White R, Kumar B, Spurgeon JM (2016) Solar hydrogen production from seawater vapor electrolysis. Energy Environ Sci 9:1725–1733
64. Shen L, Ying J, Ozoemena KI, Janiak C, Yang XY (2022) Confinement effects in individual carbon encapsulated nonprecious metal-based electrocatalysts. Adv Funct Mater 32
65. Ying J, Li J, Jiang GP, Cano ZP, Ma Z, Zhong C, Su D, Chen ZW (2018) Metal-organic frameworks derived platinum-cobalt bimetallic nanoparticles in nitrogen-doped hollow porous carbon capsules as a highly active and durable catalyst for oxygen reduction reaction. Appl Catal B-Environ 225:496–503
66. Ying J, Lenaerts S, Symes MD, Yang XY Hierarchical design in nanoporous metals. Adv Sci
67. Ying J, Hu ZY, Yang XY, Wei H, Xiao YX, Janiak C, Mu SC, Tian G, Pan M, Van Tendeloo G, Su BL (2016) High viscosity to highly dispersed PtPd bimetallic nanocrystals for enhanced catalytic activity and stability. Chem Commun 52:8219–8222
68. Davis JT, Qi J, Fan X, Bui JC, Esposito DV (2018) Floating membraneless PV-electrolyzer based on buoyancy-driven product separation. Int J Hydrogen Energy 43:1224–1238
69. Gao X, Chen Y, Sun T, Huang J, Zhang W, Wang Q, Cao R (2020) Karst landform-featured monolithic electrode for water electrolysis in neutral media. Energy Environ Sci 13:174–182

70. Gnanasekar P, Eswaran MK, Palanichamy G, Ng TK, Schwingenschlögl U, Ooi BS, Kulandaivel J (2021) Sustained solar-powered electrocatalytic H_2 production by seawater splitting using two-dimensional vanadium disulfide. ACS Sustain Chem Eng 9:8572–8580
71. Kim C, Lee S, Kim SH, Park J, Kim S, Kwon S-H, Bae J-S, Park YS, Kim Y (2021) Cobalt–iron–phosphate hydrogen evolution reaction electrocatalyst for solar-driven alkaline seawater electrolyzer. Nanomaterials 11:2989
72. Wang Z, Xu W, Yu K, Feng Y, Zhu Z (2020) 2D heterogeneous vanadium compound interfacial modulation enhanced synergistic catalytic hydrogen evolution for full pH range seawater splitting. Nanoscale 12:6176–6187
73. Liu Y, Liu X, Wang X, Ning H, Yang T, Yu J, Kumar A, Luo Y, Wang H, Wang L, Lee J, Jadhav AR, Hu H, Wu M, Kim MG, Lee H (2021) Unraveling the synergy of chemical hydroxylation and the physical heterointerface upon improving the hydrogen evolution kinetics. ACS Nano 15:15017–15026
74. Miller OD, Yablonovitch E, Kurtz SR (2012) Strong internal and external luminescence as solar cells approach the Shockley-Queisser limit. IEEE J Photovolt 2:303–311
75. Chu S, Majumdar A (2012) Opportunities and challenges for a sustainable energy future. Nature 488:294–303
76. Dong Y, Ying J, Xiao YX, Chen JB, Yang XY (2021) Highly dispersed Pt nanoparticles embedded in N-doped porous carbon for efficient hydrogen evolution. Chem-Asian J 16:1878–1881
77. Jia MP, Shen L, Tian G, de Torresi SIC, Symes MD, Yang XY Superior electrocatalysis delivered by a directional electron transfer cascade in hierarchical CoNi/Ru@C. Chem-Asian J
78. Xu J, Liu T, Li J, Li B, Liu Y, Zhang B, Xiong D, Amorim I, Li W, Liu L (2018) Boosting the hydrogen evolution performance of ruthenium clusters through synergistic coupling with cobalt phosphide. Energy Environ Sci 11:1819–1827
79. Xiao YX, Ying J, Tian G, Yang X, Zhang YX, Chen JB, Wang Y, Symes MD, Ozoemena KI, Wu JS, Yang XY (2021) Hierarchically fractal PtPdCu sponges and their directed mass- and electron-transfer effects. Nano Lett 21:7870–7878
80. Wang D, Xin HL, Hovden R, Wang H, Yu Y, Muller DA, DiSalvo FJ, Abruna HD (2013) Structurally ordered intermetallic platinum-cobalt core-shell nanoparticles with enhanced activity and stability as oxygen reduction electrocatalysts. Nat Mater 12:81–87
81. Wang Y, Yu HZ, Ying J, Tian G, Liu Y, Geng W, Hu J, Lu Y, Chang GG, Ozoemena KI, Janiak C, Yang XY (2021) Ultimate corrosion to Pt-Cu electrocatalysts for enhancing methanol oxidation activity and stability in acidic media. Chem-Eur J 27:9124–9128
82. Xiao YX, Ying J, Tian G, Zhang XQ, Janiak C, Ozoemena KI, Yang XY (2021) PtPd hollow nanocubes with enhanced alloy effect and active facets for efficient methanol oxidation reaction. Chem Commun 57:986–989
83. Xiao Y-X, Ying J, Tian G, Tao Y, Wei H, Fan S-Y, Sun Z-H, Zou W-J, Hu J, Chang G-G (2019) Highly dispersed PtPd on graphitic nanofibers and its heavy d-π effect. Appl Catal B 259:118080
84. Zhao G, Rui K, Dou SX, Sun W (2018) Heterostructures for electrochemical hydrogen evolution reaction: a review. Adv Funct Mater 28
85. Yan Y, Zhang R, Yu Y, Sun Z, Che R, Wei B, LaGrow AP, Wang Z, Zhou W (2021) Interfacial optimization of PtNi octahedrons@Ti_3C_2MXene with enhanced alkaline hydrogen evolution activity and stability. Appl Catal B: Environ 291
86. Carmo M, Fritz DL, Merge J, Stolten D (2013) A comprehensive review on PEM water electrolysis. Int J Hydrogen Energy 38:4901–4934
87. Ying J, Jiang GP, Cano ZP, Ma Z, Chen ZW (2018) Spontaneous weaving: 3D porous PtCu networks with ultrathin jagged nanowires for highly efficient oxygen reduction reaction. Appl Catal B-Environ 236:359–367
88. Ying J, Yang XY, Hu ZY, Mu SC, Janiak C, Geng W, Pan M, Ke X, Van Tendeloo G, Su BL (2014) One particle@one cell: highly monodispersed PtPd bimetallic nanoparticles for enhanced oxygen reduction reaction. Nano Energy 8:214–222

89. Ying J (2021) Atomic-scale design of high-performance Pt-based electrocatalysts for oxygen reduction reaction. Front Chem 9
90. Xiao YX, Ying J, Chen JB, Dong Y, Yang X, Tian G, Wu JS, Janiak C, Ozoemena KI, Yang XY (2022) Confined ultrafine Pt in porous carbon fibers and their N-enhanced heavy d-π effect. Chem Mater 34:3705–3714
91. Shen L, Ying J, Tian G, Jia MP, Yang XY (2021) Ultralong PtPd alloyed nanowires anchored on graphene for efficient methanol oxidation reaction. Chem-Asian J 16:1130–1137
92. Buttler A, Spliethoff H (2018) Current status of water electrolysis for energy storage, grid balancing and sector coupling via power-to-gas and power-to-liquids: a review. Renew Sustain Energy Rev 82:2440–2454
93. Jang SW, Dutta S, Kumar A, Hong YR, Kang H, Lee S, Ryu S, Choi W, Lee IS (2020) Holey Pt nanosheets on NiFe-hydroxide laminates: synergistically enhanced electrocatalytic 2D interface toward hydrogen evolution reaction. ACS Nano
94. Hausmann JN, Schlogl R, Menezes PW, Driess M (2021) Is direct seawater splitting economically meaningful? Energy Environ Sci 14:3679–3685
95. Schmidt O, Gambhir A, Staffell I, Hawkes A, Nelson J, Few S (2017) Future cost and performance of water electrolysis: an expert elicitation study. Int J Hydrogen Energy 42:30470–30492
96. Results ITRfPI
97. Badwal SPS, Giddey SS, Munnings C, Bhatt AI, Hollenkamp AF (2014) Emerging electrochemical energy conversion and storage technologies. Front Chem 2
98. Wang J, Xu F, Jin H, Chen Y, Wang Y (2017) Non-noble metal-based carbon composites in hydrogen evolution reaction: fundamentals to applications. Adv Mater 29
99. Coro G, Trumpy E (2020) Predicting geographical suitability of geothermal power plants. J Clean Prod 267

Solar Thermochemical Water-Splitting

Tian Zhao and Xiao-Yu Yang

Abstract Solar thermochemical hydrogen (STCH) water cracking technology is recognized as an essential method for sunlight-driven "green" H_2 production and is presently being pursued by the research and development community. The latest techno-economic analysis (TEA) of the STCH water splitting method illustrates the promise of low-cost hydrogen utilization with renewable energy inputs. Remarkably, the entire solar spectrum can be used in the STCH system. For the STCH system, the discovery of a new redox-active material that can reduce the solar input requirement per mole of H2 produced while retaining favourable thermodynamic and kinetic attributes of water splitting is the biggest challenge of the technology. In addition, this ideal redox-active material should exhibit fast redox kinetics, high cycling, high thermal stress, high thermal conductivity and oxygen ion conductivity, and low cost. At present, the theoretical efficiency of many cycles exceeds 40% and, even though still in the research phase, has the potential to be realized for large-scale industrialization. Thus, it offers more energy resilient solutions for long-term energy storage and has the potential to enable low-cost H_2 production.

Keywords Solar thermochemical hydrogen · High temperature · Water-Splitting

1 Preface

The solar thermochemical hydrogen (STCH) water-splitting process is an important method for sunlight-driven "green" hydrogen generation. This approach, currently being explored intensively by the research and development community, could

T. Zhao (✉)
School of Chemical Engineering and Technology, Sun Yat-Sen University, Zhuhai 519082, China
e-mail: zhaot33@mail.sysu.edu.cn

X.-Y. Yang
State Key Laboratory of Advanced Technology for Materials Synthesis and Processing (Wuhan), Foshan Xianhu Laboratory of the Advanced Energy Science and Technology Guangdong Laboratory (Xianhu Hydrogen Valley, Foshan), Laoshan Laboratory (168 Wenhai Middle Rd, Jimo District, Qingdao), Wuhan University of Technology, Wuhan, Hubei, China

X.-Y. Yang (ed.), *Photo-Driven Seawater Splitting for Hydrogen Production*,
https://doi.org/10.1007/978-981-99-0510-2_5

become a cost-effective and sustainable alternative to fossil fuel derived energy on the Earth.

In a STCH water-splitting reactor, a set of successive chemical reactions are carried out to produce oxygen and hydrogen in a spatially separated manner. Water is the single consumed reactant in this process, and one or more materials actively take part without being "net" consumed. One example of STCH water splitting employs the two-step off-stoichiometric metal oxide (MO_x) cycle, in which hydrogen is generated in a highly endothermic reduction reaction of MO_x at high temperatures that simultaneously generates the reduced form $MO_{x-\delta}$. In the second step of the cycle, oxygen is produced in a mildly exothermic reoxidation of $MO_{x-\delta}$ at low temperatures to reform MO_x.

It is obvious that the materials undergoing reduction/oxidation are of key importance in determining the efficiencies of the overall water-splitting processes. Several two-step metal oxide cycles have been utilized to drive efficient STCH water splitting, such as the ZnO/Zn, SnO_2/SnO, CeO_2/CeO_2-δ, Fe_3O_4/FeO, MFe_2O_4/MFe_2O_4-δ, CeO_2-xSnO_2/$Ce_2Sn_2O_7$, and manganese oxide-based cycle. Also, multi-cycles have been utilized for STCH.

A recent techno-economic analysis (TEA) demonstrates that the STCH water-splitting approach holds promise for producing low-cost hydrogen using renewable resources including SW and the entire spectrum of sunlight. The implementation of practical STCH water splitting systems requires the discovery of novel redox-active materials that minimize the solar input requirement per mole of H_2 produced while retaining maximum water-splitting thermodynamic and kinetic parameters. Moreover, an ideal redox-active material needs to display high cyclability, thermal stress resistance and thermal and oxygen ion conductivity, along with having a low cost. Many of the redox materials uncovered thus far have been shown to promote hydrogen production cycles that have theoretical efficiencies of over 40%, but additional investigations are needed to develop systems that attain these yields on large-scale industrial levels.

2 Principle of Solar Thermochemical Hydrogen (STCH) Water-Splitting

2.1 The Basic Principles for STCH Water Splitting

Hydrogen is an attractive sustainable energy source because it can be employed as a high-quality environmentally clean energy carrier and it can be produced using a variety of diverse primary energy sources. More importantly, H_2 exhibits a very high electrochemical activity in fuel cells, theoretically generating electricity at a rate of up to 83%. Thus, H_2 production technologies have received great attention in the global scientific community, whose efforts have focused on devising clean and renewable ways of generating this gas in large scale and at low cost. At the present

time, ~95% of hydrogen worldwide comes primarily from fossil fuels. Although easily performed, this method requires rapidly depleting fossil fuels and produces unwanted hydrocarbon byproducts [1]. Electrochemical production of hydrogen is also used in industrial settings, where electricity used to form this gas comes mainly from sustainable energy generating systems such as solar and wind power. However, the cost of employing this method is comparatively high owing to the high cost of electricity.

Cost-competitive "green" hydrogen generation could have applications to many industrial processes including those for transportation, chemical synthesis, iron and steel production, fertilizer synthesis and biorefining. Moreover, hydrogen has the potential of being utilized to meet long-term, terawatt scale energy storage demands [2]. STCH water-splitting is undoubtedly an important approach for sunlight-driven "green" hydrogen generation and the STCH water-splitting approach has promise for generating low-cost hydrogen from renewable energy sources. It is known that water can be directly split into hydrogen and oxygen at significant efficiencies (>4%) using temperatures exceeding 2500 K, but it is difficult/costly to produce these high temperatures as well as to separate hydrogen and oxygen under these conditions before explosive combination occurs. Solar hydrogen production using thermochemical cycles, which circumvent these problems, is a promising approach that has a high theoretical efficiency (>40%) because of the fact that it can utilize the entire solar spectrum [3–5]. Although still at a research stage, this method has the potential of achieving large-scale hydrogen generation.

2.2 Mechanism of STCH Water Splitting

STCH water splitting uses sunlight to create the temperatures needed to produce hydrogen and oxygen from water. In contrast to other systems, in STCH water-splitting reactors, the combustion problem is avoided by using consecutive chemical reactions to form O_2 and H_2 at different times and separated locations [6]. In the process, water is the solely consumed reactant, and one or more materials actively participate in the process without being "net" consumed.

Methods for thermochemical hydrogen production can be divided into two main categories involving either a two-step cycle with a metal oxide or a multistep cycle using copper-chlorine or sulfur [7, 8]. Up to the current time, two-step redox active off-stoichiometric metal oxide (MO_x) thermochemical cycles have garnered the most attention. In the two-step cycle, the thermal reduction (TR) and water splitting (WS) reactions take place in separate steps to interconvert the oxidized and reduced form of a metal, MO_x, for which the parent M has multiple oxidation states [9]. Equations (1)-(3) below summarize reactions involved in the two-step off-stoichiometric metal oxide cycle,

Thermal reduction step (TR step)

$$\text{Reduction: } \frac{1}{\delta} MO_x \rightarrow \frac{1}{\delta} MO_{x-\delta} + \frac{1}{2} O_2 \tag{1}$$

Water splitting step (WS step)

$$\text{Oxidation: } \frac{1}{\delta} MO_{x-\delta} + H_2O \rightarrow \frac{1}{\delta} MO_x + H_2 \tag{2}$$

$$\text{Netreaction: } H_2O \rightarrow H_2 + \frac{1}{2} O_2 \tag{3}$$

where M is Fe, Sn, Zn or Ce, MO_x is the corresponding higher-valence metal oxide and $MO_{x-\delta}$ is the corresponding lower-valence metal oxide.

The overall two-step metal oxide cycle for STCH water-splitting is illustrated in Fig. 1. The first step involves a highly endothermic reduction reaction, which requires a high temperature. The enthalpy change in metal-oxide reduction (normally in the 250–500 kJ/mol range for H_2 production) must be higher than that of the water-splitting reaction at the reoxidation temperature [10]. Concentrated solar thermal devices can provide this level of thermal energy in a cost-effective renewable form. One approach involves focusing sunlight reflected from a mirror array on a receiver/reactor, in which an active material is heated and the reduction process occurs. The second step is mildly exothermic reoxidation, which takes place at lower temperatures. The degree of reduction or off-stoichiometry (δ) reduction is a strong function of both temperature and O_2 pressure. To avoid the reverse reaction, released oxygen needs to be removed from the system prior to initiation of the reoxidation process. The efficiency of the reoxidation reaction is highly dependent on both temperature (T_{OX}) and the amount of excess reactant steam relative to available oxygen ion vacancies. At higher reoxidation temperatures, a larger amount of excess steam is available, whereas at lower temperatures, a larger amount of sensible heat needs to be released. Moreover, after reduction, a corresponding amount of heat needs to be injected to raise the temperature required for another reduction step.

As mentioned above, the type of STCH water splitting involves two reactions, in which two electrons during reduction are lost from one oxygen atom in the anionic lattice within the solid-state MOx material and for the oxidation process the two electrons nominally move to the cationic lattice.

Compared to other methods, those based on two-step thermochemical cycles for hydrogen production have several advantageous characteristics, including that (1) hydrogen and oxygen are produced in different processes and do not need to be separated, (2) each step occurs at a lower, redox material dependent temperature than that needed for direct water thermolysis (>1500 °C), and (3) direct use of solar energy is possible but the required operating temperatures present engineering challenges.

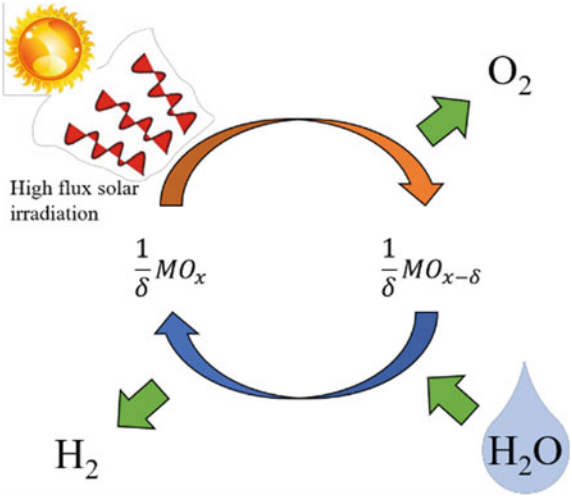

Fig. 1 Schematic of a two-step redox active off-stoichiometric metal oxide (MO_x) thermochemical cycle for STCH water-splitting

3 Materials Used for STCH Water Splitting

At the present time, many redox reaction couples have been explored for use in two-step STCH processes including volatile metal oxide couples (e.g., Zn/ZnO and SnO_2/SnO), phase change stoichiometric oxides (e.g., Fe_3O_4/FeO and metal-substituted ferrites) or multistep couples (e.g., hybrid sulfur and manganese oxide-based cycles). Among those probed for use in thermochemical water-splitting, redox active off-stoichiometric metal oxide (MOx) thermochemical cycles utilizing cerium-based oxides or perovskites have received the greatest attention. To attain negative Gibbs free energies for the combined steps, the enthalpy and entropy changes in the thermochemical cycle must correspond to the standard enthalpy and entropy changes for direct water splitting ($\Delta H \geq 286$ kJ/mol and $\Delta S \geq 49.55$–57.80 J/mol/K (500–1800 K)) [11]. The thermodynamic expressions for these steps (TR and WS)N are given in Eqs. (4)–(7).

$$\Delta G_{TR} = \Delta H_{red} - T_{TR}\left(\Delta S_{red} + \frac{1}{2} S^{O_2}_{T_{TR}}\right) \leq 0 \tag{4}$$

$$\Delta G_{WS} = -\Delta H_{red} - \Delta H^{H_2O}_{f,T_{WS}} - T_{WS}(-\Delta S_{red} + S^{H_2}_{T_{WS}} - S^{H_2O}_{T_{WS}}) \leq 0 \tag{5}$$

$$\Delta H_{cycle} = \Delta H_{TR} + \Delta H_{WS} \geq 286 \text{ kJ/molh} \tag{6}$$

$$\Delta S_{cycle} = \Delta S_{TR} + \Delta S_{WS} \geq 49.55 - 57.80 \text{J/mol/K} \tag{7}$$

Inspection of these relationships shows that the thermochemically active oxides having lower reduction enthalpies and higher reduction entropies are more readily

reduced ($\triangle G \propto 1/T_{TR}$). Furthermore, the entropy decrease associated with the step (WP) involving conversion of H_2O to H_2 is greater than that of the increase for reoxidizing oxides because the latter involves the generation of a gas from a solid, This makes the WS step exoergic and explains why some oxides like Co_3O_4 and Mn_3O_4, which are reduced at lower temperatures, cannot be used in two-step thermochemical water-splitting cycles. Therefore, in this process, the TR step is furnished at least 286 kJ/mol to support the energy requirements for WS step (Eqs. (6)).

ZnO and SnO_2 are reduced at lower temperatures than Fe_3O_4, which makes the former more useful in thermochemical cycles. Commonly, temperatures required for the TR step in both the ZnO/Zn cycle and CeO_2/Ce_2O_3 systems are above 1500 °C. Doping systems including CeO_2/m-ZrO_2 and Fe_3O_4/m-ZrO_2 systems have been utilized to circumvent this problem. Although doping systems have the ability to reduce the required temperature and improve cycling stability of the material, they might cause a reduction in hydrogen yields. For the dual purposes of reducing reduction temperature and increasing hydrogen yield, composite metal oxide systems have been utilized. An example is the composite spinel ferrite (MFe_2O_4), which releases oxygen at high temperatures and forms $MFe_2O_{4-\delta}$ enriched with oxygen vacancies. During hydrolysis, oxygen vacancies in $MFe_2O_{4-\delta}$ fill with water as the oxygen source and H_2 are released.

Developments made in research on metal oxide (MOx) thermochemical cycles are reviewed in the following section.

3.1 ZnO/Zn

The ZnO/Zn cycle is considered to be a volatile cycle because pyrolysis of ZnO generates Zn (g) and O_2 in the TR step (Eqs. (8) and (9)) [12].

TS step

$$ZnO_{(s)} \overset{2350K}{\rightarrow} Zn_{(g)} + 0.5O_2 \tag{8}$$

WS step.

$$Zn_{(s)} + H_2O_{(g)} \overset{850K}{\rightarrow} ZnO_{(s)} + H_{2(g)} \tag{9}$$

The reduction step in this cycle is highly endothermic (ZnO → Zn, $\Delta G = 0$,) so it requires a high temperature (2340 K). Weidenkaff et al. [13, 14] found that two factors affect this cycle including (1) recombination of zinc vapor with oxygen generated in the TR step that reduces the rate of decomposition zinc oxide, and (2) ZnO thin film formation takes place on the Zn during hydrolysis that prevents further reaction. Thus, the key to the success of this process is effectual separation of Zn vapor from O_2. Weidenkaff et al. used a tube furnace with a temperature gradient

to transform Zn (g) to Zn (s) under an inert atmosphere (N_2, Ar), which enables effectual separation of Zn (g) and O_2. The decomposition rate of ZnO was found to be proportional to temperature and inert gas mass flow rate and inversely proportional to oxygen partial pressure (Fig. 2). The results of simulation studies by Abanades et al. [15] are consistent with the findings of Weidenkaff et al.

Fletcher et al. [16] devised a method for direct electrolysis of ZnO (l), which generates Zn (g) and oxygen at various electrodes. This process requires tiny electrical energy and avoids recombination of Zn and oxygen. Nevertheless, the temperature for this process must exceed 2248 K to melt the ZnO, and at 2400 K, the pressure needs to be larger than 2.6 bar to obstruct boiling of liquid ZnO. This temperature is much higher than those to which most electrode materials are exposed. In a related study, Wegner and the coworkers [17] developed an aerosol reactor comprised of three controlled temperature zones in which mixing, nanoparticle formation and hydrolysis occur. The Zn nanoparticles entrained in the gas stream enables simple and continuous control of the feed stream employed to remove product gases.

Steinfeld and the coworkers [18, 19] proposed a method to analyze energy efficiencies and determine the best energy effectiveness and irreversibility of the ZnO/Zn cycle. The results revealed that the largest exergy efficiency could reach 29%, and that irreversibility is most related to return of unused light from the solar reactor and Zn (g) quenching. A cost evaluation for industrialization of a water-splitting process using this cycle showed that the cost of hydrogen would be 0.13–0.15 $/kW h (5 $/kg H_2). Notably, an economic assessment of the ZnO/Zn cycle [20] revealed that a cost of 7.98 $/kg is associated with H_2 generation, which is higher than that predicted by Steinfeld [18, 19] due to the assumed costs that differ from that used at the factory scale. Finally, Lange and the coworkers [21] using temperature-entropy figures connected with a pinch-point test to analyze the ZnO/Zn two-step thermochemical water-splitting process, showed that the required temperature is in the technically feasible range but the energy conversion efficiency is lower than that needed for practical applications. Moreover, it was noted that the energy conversion efficiency is lowered as a consequence of irreversibility associated with incomplete heat recovery and inert gas quenching. In addition, reduction of the partial pressure of oxygen during reduction lowers the reduction temperature while the cycle efficiency only slightly decreases (Fig. 3).

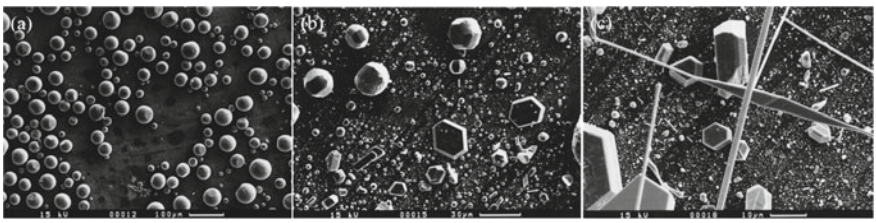

Fig. 2 SEM images of **a** ZnO/Zn deposited droplets at $T > 693$ K, **b** boundary at $T = 693$ K and **c** hexagonal prismatic crystals at $T < 693$ K. Reproduced from Ref. [13] with permission from Elsevier

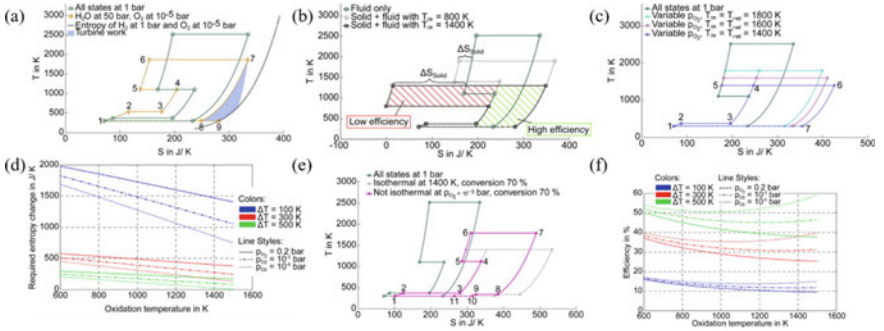

Fig. 3 T-S diagram of production of 1 mol of hydrogen. Reproduced from Ref. [21] with permission from Elsevier

3.2 SnO_2/SnO

Commonly, pyrolysis of Sn(IV) oxide to form Sn(0) is not practical for the TR step of a thermochemical cycle because it requires ultra-high temperatures ($SnO_2 \rightarrow$ Sn, $\Delta G = 0$, at 2647 °C). Obtaining metal tin from its oxide at lower temperatures requires a reducing agent such as C or CH_4 but the processes form byproducts such as CO/CO_2, and produce Sn(l) instead of Sn(s), which is an unsatisfactory substrate for the ensuing hydrolysis reaction. Therefore, a viable alternative was devised that utilizes the SnO_2/SnO system in a volatile cycle that is similar to that of the ZnO/Zn system (Eqs. 10 and 11).

TR step

$$SnO_{2(s)} \rightarrow SnO_{(g)} + 0.5O_2 \tag{10}$$

WS step

$$SnO_{(s)} + H_2O_{(g)} \overset{850K}{\rightarrow} SnO_{2(s)} + H_{2(g)} \tag{11}$$

Charvin et al. [22] proposed an operational scheme for a tin-based process using thermodynamic equilibrium calculations. Computations suggest that the SnO2/SnO/Sn regime has two hydrogen producing routes, the first of which proceeds through a three-step cycle (called the Suryaou cycle). In this route, SnO_2 is first heated and reduced to form SnO, then placed at 600 °C for 15 min to promote full disproportionation ($2SnO \rightarrow SnO_2 + Sn$) before hydrolysis of Sn/SnO. The second H_2 producing pathway occurs in two steps. When pure SnO was reacted with steam at 525 °C for 18 min, H_2 was fabricated at a rate of 13.6 mL/min/g. While SnO was found to be more oxidized than Sn, the hydrolysis rate of SnO was greater than the conversion rate of Sn.

The results of simulation studies by Abanades [23] showed that the amount of inert gas used in the SnO_2/SnO cycle affects the reduction of SnO_2, and that the reduction yield decreases with a decrease in the N_2:SnO_2 ratio. At a ratio of 50:1, the pyrolysis rate is about 70%. A parallel investigation demonstrated that reductive conversion of SnO_2 to SnO occurs at 1600 °C under normal pressures and that gaseous products are quenched to generate nanoparticles having a SnO mass fraction of 54% and an average diameter of 10–50 nm. Reduction of the partial pressure of oxygen causes an increase in reduction yield. Furthermore, the temperature of an effective hydrolysis reaction is > 470 °C and the maximum temperature above which SnO undergoes disproportionation is 600 °C. In another effort, Leveque et al. [24] calculated that the activation energy of H_2O oxidation by the Sn/SnO_2 couple is 53 ± 1 kJ/mol (Fig. 4).

In a recent effort, Abanades et al. [25, 26] explored the ZnO/Zn and SnO_2/SnO cycles at about 1900 K. The gaseous products of ZnO and SnO_2 pyrolysis were quenched by using an inert gas. In each case, about 50% of the recovered product is with a relatively high specific surface area (20–60 m^2/g). The mass fractions of recovered Zn and SnO were 48 and 72 wt%, respectively. Hydrolysis reactions were conducted in a bed reactor with controllable temperature and heating rate. After 30 min at 800 K, the conversion rate of the SnO-SnO_2 hydrolysis process is 80%, and that of the Zn-ZnO hydrolysis is 55%. The hydrogen yields for water-splitting promoted by both the ZnO and SnO_2 systems were 6 mmol/g. Abanades et al. [27] also determined the activation energies of the SnO and Zn in water-splitting processes. By testing the molar fractions (f_{mol}) of the reduced species in powders produced

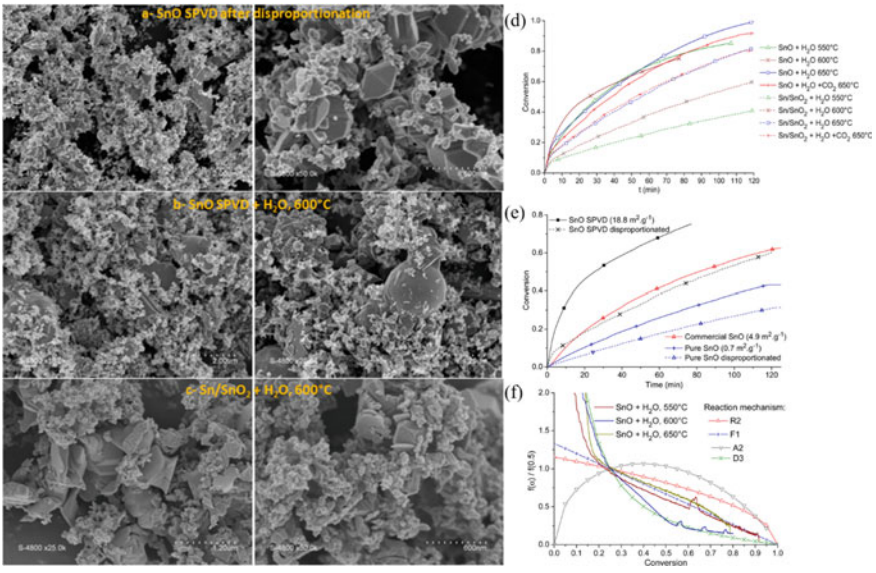

Fig. 4 SEM images of various Sn/SnO_2 species and their oxidation reactivities. Reproduced from Ref. [24] with permission from American Chemical Society

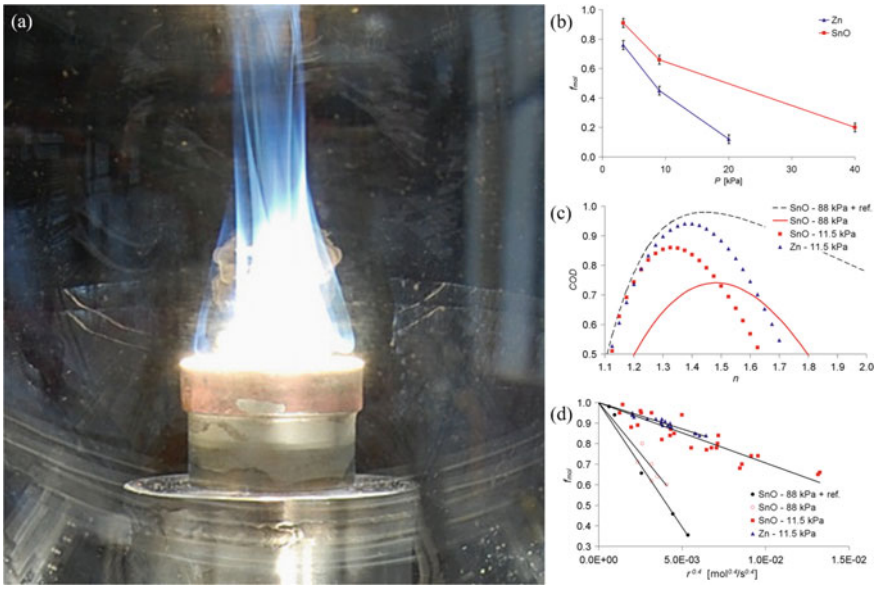

Fig. 5 **a** Image during reduction of a SnO_2 pellet under collected solar irradiation. **b** Influence of total pressure on mole fractions of reduced species formed by solar flux induced ZnO and SnO_2 reductions. **c** Coefficient of determination (COD) for fitting molar fraction (f_{mol}). **d** Experimentally determined mole fraction of reduced species versus reduction rate (μmol/min). Reproduced from Ref. [27] with permission from Elsevier

in ZnO and SnO_2 reductions, it was disclosed that the reoxidation rate of Zn was qualitatively higher than that of SnO (Fig. 5).

In another investigation, Bhosale et al. [28] used the thermodynamics database to elucidate factors determining the thermal reduction and hydrolysis temperatures in the SnO_2/SnO cycle. The analysis showed that, at equilibrium obtained at 1 bar pressure, SnO_2 can be totally reduced when temperature is over 2380 K. Reducing the O_2 partial pressure to 10^{-3} bar enables the reduction process to be conducted at 1780 K.

3.3 $CeO_2/CeO_{2-\delta}$

Abanades et al. [26] were the first to propose using the $CeO_2/CeO_{2-\delta}$ cycle shown in Eqs. (12) and (13) for thermochemical water-splitting.

TR step

$$GeO_2 \rightarrow GeO_{2-\delta} + \frac{\delta}{2} O_2 \tag{12}$$

WS step

$$GeO_{2-\delta} + \frac{\delta}{2} H_2O \rightarrow GeO_2 + \delta H_2 \quad (13)$$

These workers [26] found that at pressures of 100–200 mbar, the TR step in the process produces non-stoichiometric $CeO_{2-\delta}$ ($\delta \approx 0.5$) at a reaction temperature of ~2000 °C. Also, at 400–600 °C, $CeO_{2-\delta}$ reacts rapidly with water vapor present in the air. By employing thermogravimetric analysis, Panlener et al. [29] studied how different non-stoichiometric amounts of CeO_2 are generated using different temperatures and oxygen partial pressures. The results suggest that thermal reduction is favored at lower oxygen partial pressures and higher temperatures.

Chueh et al. [30] conducted studies in which porous cylindrical CeO_2 was heated directly in a solar hollow reactor. The solar reactor exhibited an apparent absorptance in excess of 0.94, close to the blackbody limit. At temperatures between 1420 and 1640 °C, the CeO_2 reduction rate reached 90%, while the hydrogen production rate peaked at $7.6 \times 10^2 \pm 0.8 \times 10^2$ mL/min (STP) and averaged $3.1 \times 10^2 \pm 0.3 \times 10^2$ mL/min. Over more than 500 cycles of operation, the CeO_2 system produces H_2 rapidly and steadily, with a solar-to-fuel energy conversion efficiency of 0.7–0.8% that is mainly limited by the system. Chueh and the coworkers [31] also used 15% samarium-doped ceria (SDC) for STCH water-splitting. This study showed that $Sm_{0.15}Ce_{0.85}O_{1.925-\delta}$ proved to be very stable, with no significant change in hydrogen yield after more than 50 cycles.

Abanades and the coworkers [32] have analyzed the characteristics of ceria-based oxide nanoparticles, prepared using a Pechini-derived polymeric route. The experiment resulted in pure CeO_2 nanopowders with better activity than commercial CeO_2. Furthermore, an investigation probing the effects of metal additives on a mixture CeO_2-MO_x showed that doping with zirconium (IV) lowers the temperature required for a reduction and increases the yield. The hydrolysis reaction of material formed by reduction at 1500 °C is 1045 °C, and the hydrogen yield is ~0.24 mmol/g, which is lower than that promoted by undoped CeO_2.

Meng and the coworkers [33], in studies of the Pr-doped ceria-based oxide, $Ce_{1-x}Pr_xO_{2-\delta}$ (x = 0, 0.05, 0.1, 0.2, 0.3), discovered that Pr^{2+} does not interact with H_2O (g), but rather with 5 or 10 mol% Pr^{2+} to CeO_2 material to facilitates forming of O_2 and H_2. The H_2 yield is closely related to the hydrolysis temperature, with an optimum temperature of 1023 K. The authors also investigated the reaction of lithium-doped cerium-based oxides, $Ce_{1-x}Li_xO_{2-\delta}$ ($x = 0, 0.05, 0.1, 0.2, 0.3$) [34]. The results show that when the Li^+ content is increased, the O_2 yield first increases and then decreases, while the H_2 yield gradually decreases.

In their study of the thermochemistry of the CeO_2–ZrO_2 system, Gal and the coworkers [35] have found that there is a linear increase with increasing Zr content at 1400 °C. Moreover, the addition of other dopants (Y, La, Pr, or Gd) does not cause an increase in the reduction rate. Additionally, reducing the reaction pressure significantly increases the reduction yield. Gokon and the coworkers [36] were able to use a CeO_2-based thermochemical system to promote the stable production of O_2

and H_2. However, at 1550 °C, due to the release of O_2 associated with the formation characteristics of the reduced phase $CeO_{2-\delta}$, the oxygen yield starts to decrease. The conversion of Ce(IV) to Ce(III) in the cubic lattice during thermal reduction involves the diffusion of oxygen, which is enhanced at higher pyrolysis temperatures. The hydrolysis temperature was found to be 1000 °C and the hydrogen yield remained almost constant over six cycles. When $T_H \geq 1400$ °C, $CeO_{2-\delta}$ reacts rapidly with steam to form H_2 at a rate that reaches 2.5–6.8 Ncm^3/min/g (Fig. 6).

Hathaway et al. [37] performed an evaluation of the cerium dioxide thermochemical cycle occurring in a high flux solar simulator at an equivalent temperature. The results showed that the isothermal methods for separating CO_2 or water in this way are not attractive.

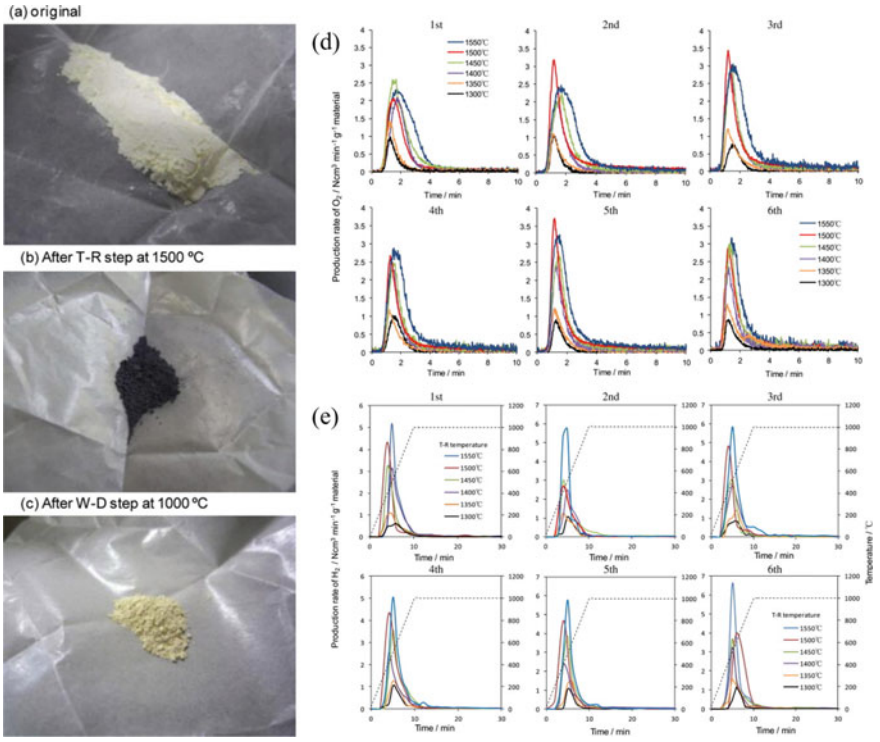

Fig. 6 Image of CeO_2 species and the oxygen/hydrogen production rate. Reprinted with permission from Ref. [36]

3.4 Fe_3O_4/FeO Cycle and $MFe_2O_4/MFe_2O_{4-\delta}$

The Fe_3O_4/FeO thermochemical cycle is one of the earliest used for driving water-splitting. The reaction pathway followed in this process is displayed in Eqs. (14), (15). The temperature of the thermal reduction step in this cycle is > 2000 °C, at which the rapid decay of Fe_3O_4 by severe sintering and melting results in deactivation of key materials.

TR step

$$Fe_3O_4 \rightarrow 3FeO + \frac{1}{2}O_2 \tag{14}$$

WS step

$$3FeO + H_2O \rightarrow Fe_3O_4 + H_2 \tag{15}$$

Steinfeld et al. [38] found that Fe_3O_4 decomposes into FeO at a temperature of 1875 K or above. FeO (l) is further converted to FeO (g), and at these higher temperatures would the ratio of FeO (g) in the mixture is large which is detrimental to the hydrolysis reaction. Similar to processes of this type occurring in other cycles, FeO recombines with oxygen at a high temperature, so fast quenching or an oxygen-free environment is required. Charvian and the coworkers [39] found that when Fe_2O_3 was used as a feedstock, the reduction product FeO was oxidized to form Fe_3O_4 rather than Fe_2O_3 in a hydrolysis reaction. Simulation studies by this group showed that Fe_2O_3 is not totally reduced to FeO, and it forms non-stoichiometric wustite, $Fe_{1-y}O$. In air, the reduction products formed from Fe_2O_3 were Fe_3O_4 and FeO, whereas in an inert atmosphere only FeO was formed. When Nakamura et. Al. [40] first made the Fe_3O_4/FeO cycle publicly available, they noted that the rate of hydrolysis reaction of the non-chemically stoichiometric $Fe_{1-y}O$ was greater than that of FeO.

Kodama et al. [41] made two important discoveries from the investigation of the Fe_3O_4/FeO cycle. Firstly, pure Fe_3O_4 can be reduced at low oxygen partial pressure, and Fe_3O_4 becomes dense, sintered and smooth during the process. Secondly, when Fe_3O_4 is supported by yttria-stabilized zirconia (YSZ), the reduction product FeO does not melt in the YSZ lattice, so it can be converted to Fe_3O_4 during hydrolysis. Also, Gokon and the coworkers [42] demonstrated that Fe_3O_4 loaded on ZrO_2 could be converted to FeO. It was found that Fe_3O_4/m-ZrO_2 had significantly higher reduction rates and hydrogen yields.

At 1600 °C, the reduction rate of Fe_3O_4/m-ZrO_2 reaches 60%, and at 1400–1500 °C monoclinic ZrO_2(m-ZrO_2) transformed into tetragonal ZrO_2(t-ZrO_2) without a phase change. Finally, during the reduction process, iron ions do not enter the ZrO_2 lattice (Fig. 7).

Although the theoretical yield for hydrogen production using the Fe_3O_4/FeO system is good, the reduction temperature and pressure are very high. These high

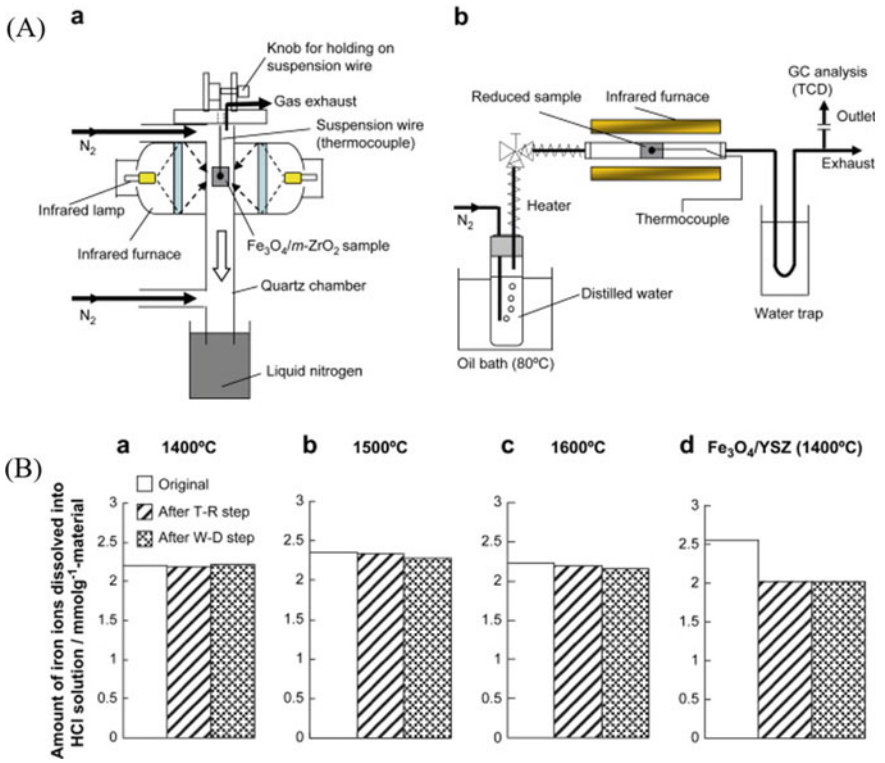

Fig. 7 **A** Apparatus for analysis of the (a) T-R and (b) W-S steps of the water-splitting thermochemical cycle. **B** Changes in the amounts of Fe ions from Fe_3O_4 dissolved in HCl. Reprinted with permission from Ref. [42]

temperatures exceed the boiling point of Fe_3O_4, where gasification and sintering occur to seriously affect efficiency. Partial doping with other metal cations forms spinel ferrites, MFe_2O_4 (where M is Ni, Zn, Co, Mn or others), whose reduction can be carried at reduced temperatures.

For example, Ehrensberge et al. [43] demonstrated that Mn and Fe_2O_3 can be utilized to form a composite oxide that promotes optimal H_2 production. Compared to the Fe_3O_4/FeO cycle, the hydrogen yield of Mn ferrites was not reduced and no irreversible segregation occurred during the process, but the reduction reaction temperature was reduced. Han and the coworkers [44] tested several spinel ferrites employing a reduction temperature of 1200 °C with a hydrolysis temperature of only 800 °C. The experiment revealed that the $NiFe_2O_4$ system not only generated more hydrogen than the other ferrites, but that it was highly durable and the hydrogen yield remained almost constant after repeated cycles.

Allendorf and the coworkers [45] developed a thermodynamic model for the prediction of several M-Ferrites (M = Fe, Co, Ni or Zn). The predicted components after thermal reduction showed that the stability of M ferrites was on the order of

$Fe_3O_4 > CoFe_2O_4 > NiFe_2O_4 > ZnFe_2O_4$. Fresno and the coworkers [46] expressed NFSA, CFSA, ZFSA, CZFSA and CZFSA for many ferrites were evaluated for their activity. The results show that the hydrogen yield after one cycle decreases in the order of NFSA > NZFSA > ZFSA > CZFSA, and the H_2/O_2 molar ratio becomes lower in the same order, which is considered to indicate the potential for recoverability. Of these ferrites, NFSA is the best in terms of hydrogen yield and recoverability.

Doping with other metal cations can effectively reduce temperatures for the reduction reaction, but the sintering problem remains. Attempts have been made to solve this problem by loading with other oxides. In one example case, Kodama and the coworkers. Reference [47] revealed for the first time that manganese ferrite ($MnFe_2O_4$) particles loaded on ZrO_2 have both high hydrogen production activity and durability because sintering of the iron oxide does not occur. After repeated cycles, in contrast to unsupported ferrite $MnFe_2O_4/ZrO_2$ retains a high activity between 1000–1400 °C. Kodama and the coworkers [48] investigated a two-step hydrolysis cycle using ZrO_2 loaded Co-ferrite, and compared the results to those previously reported for ZrO_2-supported Mn-ferrite ($Mn_{0.36}Fe_{2.64}O_4/ZrO_2$) [37]. At T_H = 1400/1300 °C and T_L = 1000 °C, $Co_{0.42}Fe_{2.58}O_4/ZrO_2$ has a higher reactivity than $Mn_{0.36}Fe_{2.64}O_4/ZrO_2$. At 1400 °C, ~40−60% of the sample is reduced, and $Co_xFe_{3-x}O_4/ZrO_2$ (with x = 0.4–0.7) has the best activity (Fig. 8). Kodama et al. [49] also investigated the $Ni_xFe_{3-x}O_4$/m-ZrO_2 system and found that the reactivity increases with increasing amount of doping x, and reaches a maximum at x = 1.0. Compared with that of unsupported $NiFe_2O_4$, $Ni_xFe_{3-x}O_4$/m-ZrO_2 has a higher hydrogen yield and that this yield remains unchanged over multiple cycles. Even compared with the $CoFe_2O_4$/m-ZrO_2 cycle mentioned above, the one occurring in $Ni_xFe_{3-x}O_4$/m-ZrO_2 has a higher activity. A comparison of activities of $NiFe_2O_4$ and $NiFe_2O_4$/m-ZrO_2 at 1300 °C/700–900 °C showed that the latter gives a higher hydrogen yield, but the effect of hydrolysis temperature (optimally 700 °C) on the properties of the material is not as significant as that of the carrier.

Scheffe et al. [50] showed that $CoFe_2O_4$ on Al_2O_3, prepared by using atomic layer deposition, has a 200–300 °C lower reduction temperature. At 1200 °C/1000 °C, the H_2 yield of $CoFe_2O_4/Al_2O_3$ is four times higher than that of $CoFe_2O_4$, and no significant sintering or deactivation occurred during multiple cycles. Muhich et al. [51] produced a filtering method to establish the practicality of thermochemical water-splitting using various oxide reduction raw materials. When the method was applied to doped-hercynite, $FeAl_2O_4$ and $CoAl_2O_4$ cycles, it was shown that the redox process facilitated by the aluminate family members of the spinel material proceeds through an O-vacancy rather than a stoichiometric mechanism. Undoped hercynite ($FeAl_2O_4$) also proved to be a viable material for thermochemical water cracking as its H_2 production capacity was higher than that of conventionally doped iron pyroxene materials.

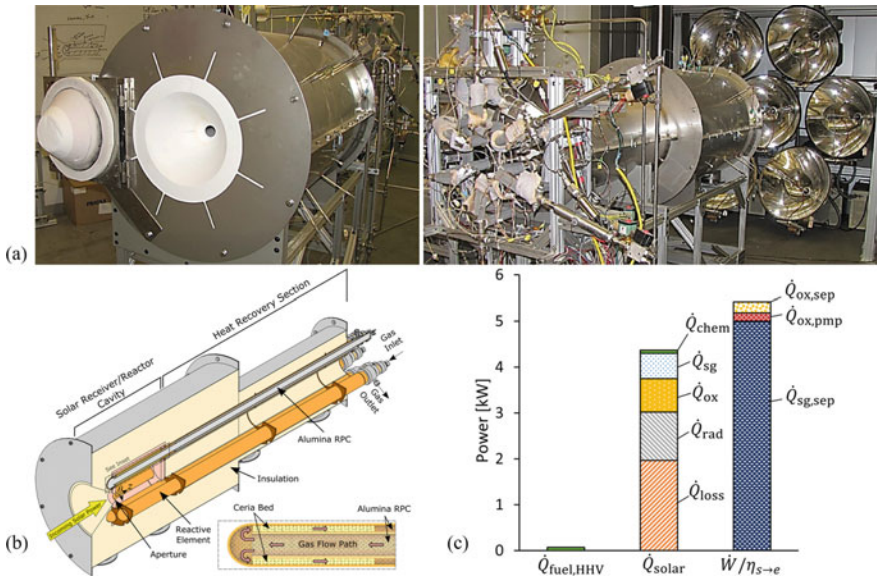

Fig. 8 Images of the isothermal reactor. Reprinted with permission from Ref. [37]

3.5 Perovskites (ABO_3)

To address the low reduction levels and high operating temperatures associated with two-step STC fuel production using CeO_2, alternatives have been developed, including calcium titanite in the general form ABO_3, similar to that used in oxygen permeable membranes, solid oxide fuel cells and metal air cells. The redox reactions occurring in cycles involving perovskites are given in Eqs. (16) and (17).

TR step

$$ABO_{3-\delta_{ox}} \rightarrow ABO_{3-\delta_{red}} + \frac{\delta_{\text{red}} - \delta_{\text{ox}}}{2} O_2 \tag{16}$$

WS step

$$ABO_{3-\delta_{red}} + (\delta_{\text{red}} - \delta_{\text{ox}}) H_2O \rightarrow ABO_{3-\delta_{ox}} + (\delta_{\text{red}} - \delta_{\text{ox}}) H_2 \tag{17}$$

In comparison to CeO_2, perovskites promote O_2 precipitation in the high-temperature reduction step and enables the use of significantly lower operating temperatures. Although the use of larger than stoichiometric amounts results in a higher upper limit for fuel production, the oxidation reaction must be sufficiently favourable to allow the reduced chalcocite to adequately replenish the oxygen lost during the reduction process. This is an issue for many perovskites explored to date,

showing why excess oxidants are used to increase the thermodynamic driving force [52, 53]. However, considering the large number of possible compositions including at least 27 elements suitable for the A-site cation and 35 for the B-site, perovskites have greater flexibility for thermodynamic tuning than doped CeO_2.

Scheffe et al. [54] developed lanthanum-strontium-manganese (LSM) perovskites as a novel material for two-step STCH water-splitting. The extent of reduction of $La_{0.65}Sr_{0.35}MnO_3$ (LSM35) is approximately twice as large as CeO_2. However, unlike CeO_2, LSM35 does not completely deoxidize under any of the conditions studied. The degree of reduction of LSM-based perovskites at the same temperature and p_{O2} have been shown to increase with increasing Sr^{2+} content. However, this increase was accompanied by a decrease in water-splitting activity (Fig. 9). In addition, the introduction of a divalent dopant at the A-site leads to a mixed Mn^{3+}/Mn^{4+} valence and the higher Mn^{4+} content (caused by the higher Sr^{2+} dopant concentration) increases the degree of reduction [55]. From a thermodynamic perspective, the partial molar enthalpy of LSM perovskites reduction decreases monotonically with increasing Sr^{2+} content. Because the entropy remains relatively constant, this increase removes the energetic penalty for reduction [56] that results in a decrease in operating temperature and a greater ΔT between redox steps. In general, $La_{1-x}Ca_xMnO_3$ (LCM) perovskites achieve higher extents of reduction than do $La_{1-x}Sr_xMnO_3$ (LSM) perovskites. This observation suggests that the improved redox properties of LCM-based perovskites are due to having an orthogonal crystal structure rather than the rhombic structure of LSM perovskites.

Analogous to LSM perovskites, during reduction of LCM perovskites during reductions, O_2 evolution increase with increasing Ca^{2+} dopant concentration. In addition, LCM perovskites have a reduced tendency to oxidize compared to CeO_2. $La_{1-x}Ba_xMnO_3$ (LBM) perovskites facilitate lower levels of O_2 release and fuel production compared to LSM chalcocite, while also following similar reduction and oxidation yield trends [57, 58]. The trends suggest that the size, tolerance factor (τ) and size variance factor ($\sigma 2$) of the rare earth ions are important factors in determining the feasibility of STCH water-splitting. Specifically, O_2 evolution during reduction increases with decreasing rare-earth ion size and, thus, decreasing τ. Perovskites with almost identical τ and different $\sigma 2$ exhibit different redox properties, for example, perovskites with higher $\sigma 2$ start to reduce at lower temperatures. Among the perovskites, $Y_{0.5}Sr_{0.5}MnO_3$ (YSM50) and $Y_{0.5}Ca_{0.5}MnO_3$ (YCM50) have the largest reduction yields. YSM50 and YCM50 show excellent O_2 evolution and fuel yields compared to CeO_2.

LSM- and LCM-based perovskites with Al^{3+} B-site doping (LSMA and LCMA) release more O_2 during reduction than do CeO_2, and Al^{3+} dopant free LSM- and LCM-based perovskites under comparable conditions. For example, the evolution of O_2 during the reduction of $La_{0.6}Sr_{0.4}Mn_{0.4}Al_{0.6}O_3$ (LSMA6446) is approximately eight times greater than that of CeO_2 and reduction begins at the lower temperature of 300 K. Furthermore, the extent of reduction of $La_{0.6}Sr_{0.4}Mn_{0.6}Al_{0.4}O_3$ (LSMA6464) is 13 times larger than that of CeO_2 and 150% greater than that of LSM40 under the same reduction conditions [59]. Reduction extents are also

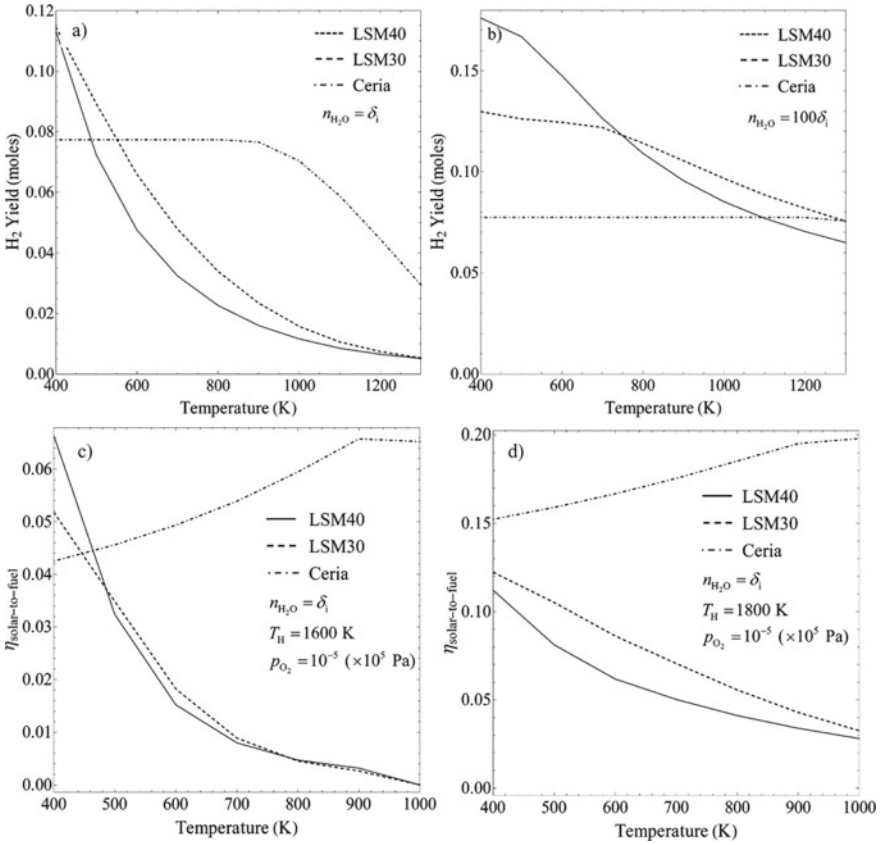

Fig. 9 Predicted equilibrium H_2 yields of LSM30, LSM40, and ceria as a function of the oxidation temperature. Reprinted with permission from Ref. [54]

enhanced when Ca^{2+}, rather than Sr^{2+}, is doped into the A-site. For example, $La_{0.6}Ca_{0.4}Mn_{0.6}Al_{0.4}O_3$ (LCMA6464) experiences a greater extent of reduction than LSMA6464. LSMA-based materials have notably improved fuel yields compared to that of CeO_2, as demonstrated by the observation of McDaniel et al. [60] of 9− and sixfold improvements in H_2 yields (Fig. 10).

3.6 Polymetallic Oxides

Ruan et al. [61] devised a novel CeO_2-$x SnO_2/Ce_2Sn_2O_7$ system, in which an uneven distribution of CeO_2 and SnO_2 react at 1400 °C to form stable $Ce_2Sn_2O_7$ and Sn (IV) is not reduced. The steps in the water-splitting process promoted by this material are shown in Eqs. (18) and (19).

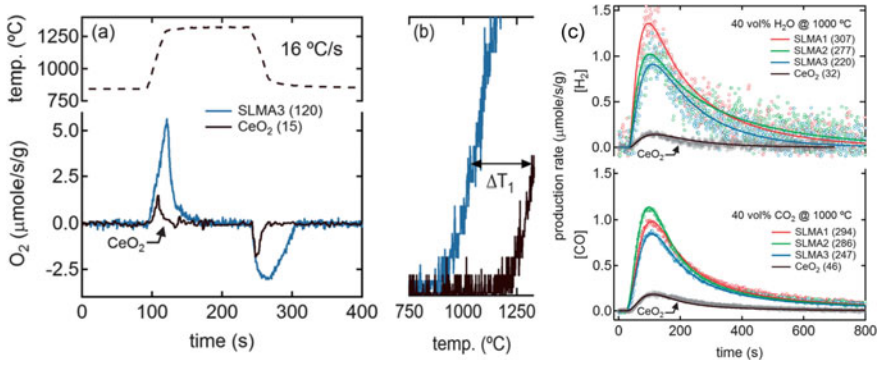

Fig. 10 O_2, H_2 and CO production rates. Reprinted with permission from Ref. [60]

TR step

$$GeO_2 + SnO_2 \overset{1400^{\circ}C}{\rightarrow} \frac{1}{2}Ge_2Sn_2O_7 + \frac{1}{4}O_2 \tag{18}$$

WS step

$$\frac{1}{2}Ge_2Sn_2O_7 + \frac{1}{2}H_2O \overset{800^{\circ}C}{\rightarrow} GeO_2 + SnO_2 + \frac{1}{2}H_2 \tag{19}$$

The oxygen evolution rate of $CeO_2{-}xSnO_2$ is significantly higher than that of CeO_2. For all $CeO_2{\_}xSnO_2$ ($x = 0.05$–0.20), the oxygen evolution is significantly higher than that of pure CeO_2 and it increases in a linear fashion with increasing SnO_2 content.

Shang et al. [62] described the new four metal cationing oxides, $(FeMgCoNi)O_x$ ($x \approx 1.2$) (PCOs). This study demonstrated that during the water-splitting cycle, the PCOs do not fully undergo a transition into a single phase, but instead, they experience a reversible phase change between a reduced rock salt and an oxidized spinel phase. The experimental results also showed that the PCOs do not display a degradation in performance over 10 cycles under the two conditions. Even at 1100 °C, the PCOs have a considerably high hydrogen yield (Fig. 11).

Liang et al. [63] developed a biphasic $Ce_{0.9}Pr_{0.1}O_{2-\delta}{-}Pr_{0.6}Sr_{0.4}FeO_{3-\delta}$ O_2 transport membrane, which converts a 2:1 ratio of H_2O and CO_2 into synthesis gas via a one-step low temperature (<1000 °C) thermochemical reaction (Fig. 12).

Seo et al. [64] used microwaves for continuous thermochemical hydrogen production. The catalyst used in experiments conducted by these workers was nickel oxide containing a polyvinylpyrrolidone (PVP) coating on the surface of a macroporous structure. The organic components on the surface of nickel oxide have dipole moments that enable microwave irradiation to promote generation of vibration and

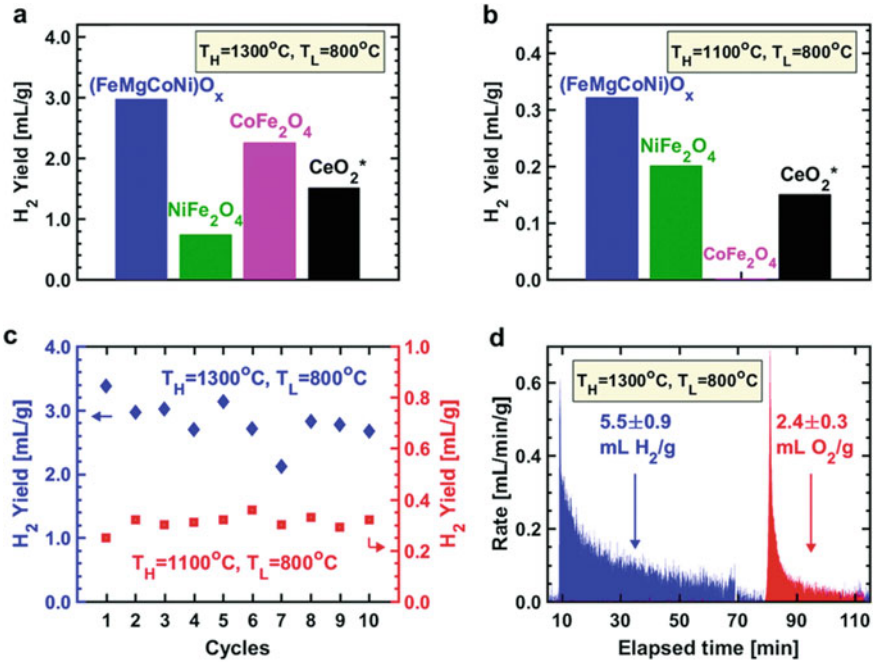

Fig. 11 Thermochemical water-splitting performance for short cycles. Reprinted with permission from Ref. [62]

rotational motion to cause rapid heating. In the water-splitting process catalyzed by this material, ~750 μmol/g of hydrogen are continuously generated.

3.7 Sulfur Family

Among the numerous thermochemical cycle schemes developed thus far, those that fall in the sulfur family operate by recycling sulfur through oxidation state changes. In general, the processes occurring in these systems involve more than two steps (referred to as multistep cycles), and in this respect, their chemistry is more complex than that of the two-step cycle based on metal oxides [65]. The common feature is that all of these rely on the decomposition reaction of sulfuric acid as a high-temperature heat absorption reaction. The actual temperatures required are in the range of 1000–1200 K, well below the temperatures required for the high-temperature step of the metal oxide cycle based on redox pairs. On the other hand, major limitations of sulfur-based cycles are associated with the corrosive environments present in the stepwise reactions involved in sulfuric acid production. However, technical solutions are available to make sulfur-based thermochemical cycle attractive for commercial

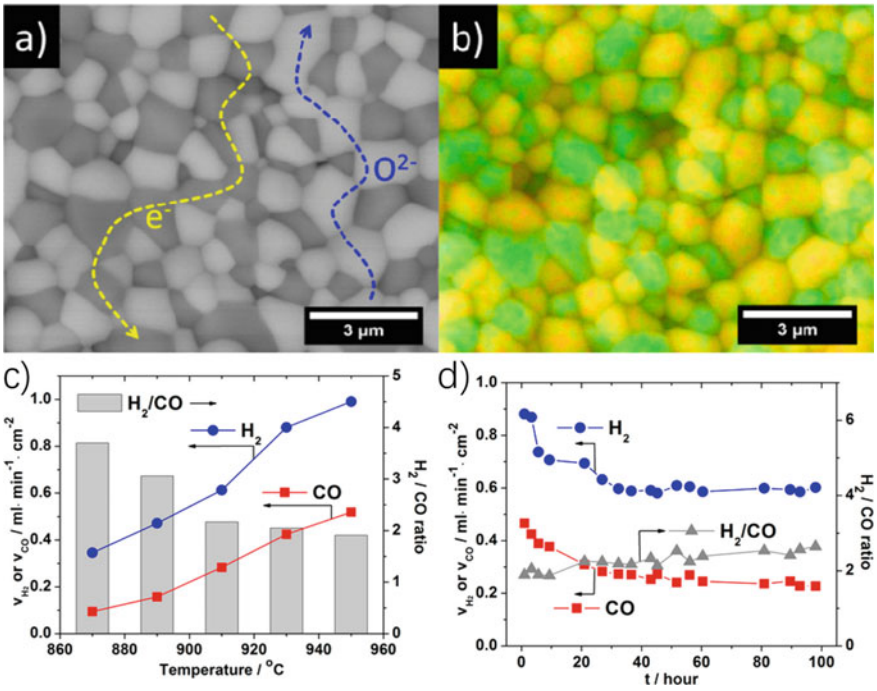

Fig. 12 Backscattered electron micrographs (BSEM) and EDXS images of the CPO-PSFO membrane. Reprinted with permission from Ref. [63]

grade deployment. In fact, these types of cycles are considered potentially suitable for screening analyses under the U.S. Department of Energy (DOE) Hydrogen Program.

The best known of these is the sulfur-iodine cycle, also known as the Ispra Mark 16 cycle or the General Atomics Cycle, originally proposed and developed in the USA by General Atomics in the mid- seventies (Fig. 13). The three basic reactions in the cycle are given in the following scheme [66].

	Reaction		Temperature (K)
Sulfuric acid decomposition	1a	$H_2SO_4(aq) \rightarrow H_2O(g) + SO_3(g)$	723–773
	1b	$SO_3(g) \rightarrow SO_2(g) + ½\ O_2(g)$	973–1073
Bunsen reaction	3	$2H_2O + SO_2 + I_2 \rightarrow H_2SO_4 + 2HI$	300–400
HI decomposition	4	$2HI \rightarrow I_2(g) + H_2(g)$	400–1000

The Bunsen reaction in the sequence proceeds exothermically and produces two immiscible concentrated aqueous acid phases. The distillation required to separate the HI and H_2SO_4 is very energy intensive, which has a direct negative impact on the efficiency of the overall cycle. One of the main challenges in the sulfur-iodine cycle is to reduce the need for large amounts of residual water and iodine and to find

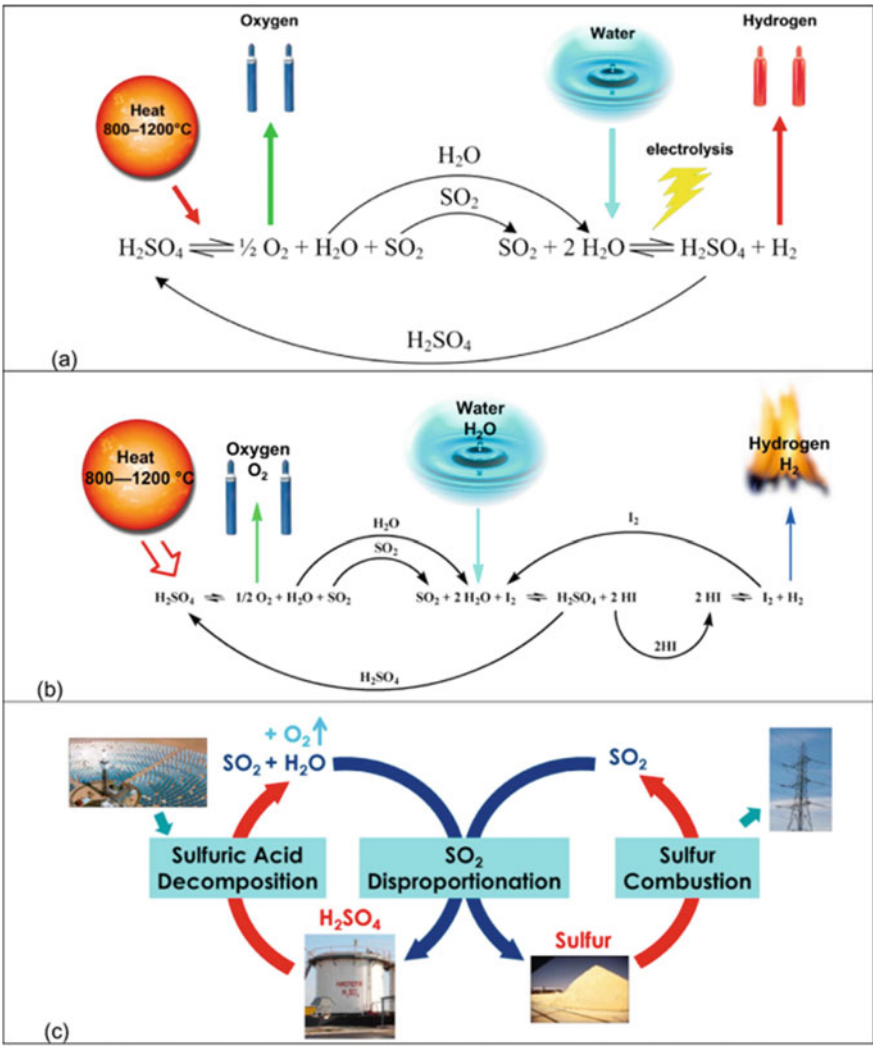

Fig. 13 Schematics of the reaction sequences of three sulfur-based cycles. Reprinted with permission from Ref. [66]

alternative separation processes that consume less energy than distillation. Following the Bunsen reaction, HI and H_2SO_4 are decomposed by the processes displayed in steps 4, and 1a and 1b of the scheme. HI decomposition to form I_2 and H_2 slightly absorbs heat, it involves the circulation of a large amount of product and requires the evaporation of a large amount of water.

Sulfur based cycles are composed of processes that serve as key steps in the industrial, solar energy promoted decomposition of sulfuric acid that occurs at temperatures clearly lower than 1200 K. All steps in these processes have been validated

and have reached a level of maturity sufficient for the development of small-scale demonstration industrial plants. However, further improvements in catalysts and construction materials are required before this technology can be employed at a full-size industrial level. The economics and flexibility of sulfuric acid-based thermochemical cycles would be enhanced if they operate as open cycles in combination with sulfuric acid production or with desulfurization of flue-gas or natural gas. In these systems, part of the energy required comes from raw sulfur, sulfur-containing ores or sulfur dioxide (Fig. 13).

4 Reactor

The structure and reactor design of the STCH water-splitting are essential to optimize the overall performance. Two conceptually different reactor system designs exist for the device, one in which both the TR and WS processes take place in the same reactor and the other where they occur in different reactors. In one configuration (Fig. 14a), the metal oxide stays in the same chamber and the TR and WS processes take place sequentially to yield temporally separated O_2 and H_2. To enable quasi-continuous H_2 production and minimize wastage of sun energy, two (or more) reactors are put in concurrent systems alternating between O_2 and H_2 production. In the second configuration (Fig. 14b), the metal oxide repetitively moves from one reactor to another, with reduction occurring in the sun irradiated reaction chamber and reoxidation reaction taking place in the dark reaction chamber. Thus, the manufacture of H_2 is consecutive and the partition of O_2 and H_2 takes place spatially. In addition, the latter configuration contributes to heat recovery, which is essential for organizing high efficiency. Technologically, the two approaches to the design of a system of this type incorporate a moving bed of particles (or other forms) and counter-rotating rings [67, 68]. The moving particle concept offers greater operational flexibility, as particles can be stored and used on demand. Although this approach can improve the plant's capacity factor, it eliminates the opportunity for solid–solid heat recovery. On the other hand, the reverse rotary ring reactor is a simpler system where the reactor and heat exchanger are contained in a single unit, but the strong coupling of the two reaction rates limits the opportunity to vary the residence time of each reaction independently.

STCH reactors demand a high factor of concentration (at least 2500) to limit re-radiation losses ($\sim T^4$), which in conjunction with optical losses contribute to collection losses. These factors require the desired collection area to be > 5000 times larger than the receiver aperture area. After the defocusing and before being absorbed by the active materials, the collected sunlight has an affective absorbing flux of C > 200–500. In addition, the STCH reactor is typically located in a centralized H_2 production plant with a minimal size of 1 MW to balance system costs.

Thermochemical processes promoted by a high flux solar simulator (HFSS) were performed to determine kinetics and performances [69]. At the present time, te results of pilot plant scale studies have verified the use of thermochemical cycles

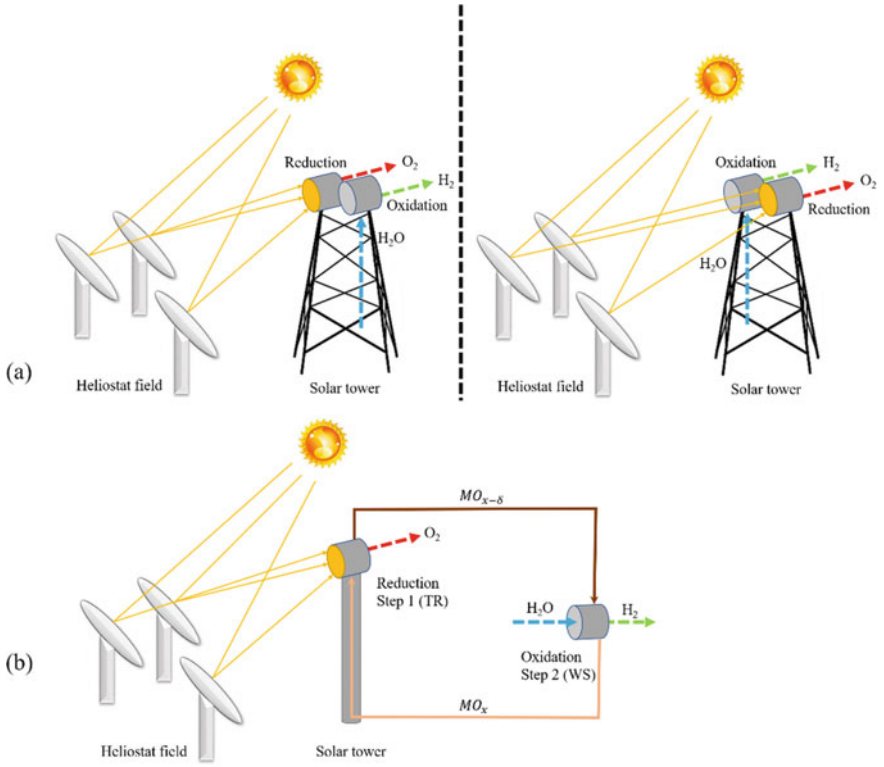

Fig. 14 Schematic of device architectures for **a** two fixed-bed alternating reactors STCH system, and **b** moving particle STCH continuous production system

of cerium oxide and iron oxide [70], and provided an important reference point to guide further development. When the energy consumed to separate the inert gas from air or gaseous products (E_{inert}) is added, the solar-to-fuel energy conversion efficiency can be expressed by the relationship in Eq. 20.

$$\eta_{solar-to-fuel} = \frac{HHV}{Q_{solar} + E_{inert}} \tag{20}$$

While inert gas quenching increases the solar energy input needed, recovery of the inert gas increases the energy input. Currently, a method to effectively recycle the inert gas that leads to optimal efficiency remains a hurdle.

4.1 Reactor for Volatile Metal Oxides

Several strategies including packed bed, aerosolized and entrained flows, and dynamic feed in a rotating chamber, have been utilized to design reactors in which volatile cycles are employed. Typically, the reaction particles are directly heated by solar radiation and the gas phase is trapped by a continuously inert gas stream and delivered to the reactor outlet. A filtration unit at the outlet then separates the solid gas mixture to collect particles that can be used in the next reaction. Abanades and the coworkers [15] developed a continuous-feed solar reactor comprising a linear mirror with a horizontal axis and a parallel concentrator with a solar flux concentration of up to 1600 W/cm^2 (Fig. 15). The water-cooled rotary cylinder chamber is situated at the focus of the thickener and the reaction chamber is separated from the ambient air by a glass window. The particles used in the process continuously enter the cavity through a screw feeder and are heated using direct solar radiation.

Koepf et al. [71] carried out a pilot scale study of ZnO dissociation in a 1 MW solar furnace. The solar furnace consists of a heliostat, a rotating chamber and a quenching unit that operates during the day and cools to ambient temperature at night. These workers found that over a 13 d operation period, the dissociation rate of zinc oxide is as high as 28 g/min, and 28 kg of reactants were consumed. Although no hydrolysis reaction takes place, the experimental results reveal that (1) the quench unit requires a large gas flow to completely cool the reduced product, (2) collection of particles with up to 44% zinc molar content, (3) the reduction yield is high, and (4) development of an effective quenching technology is needed to increase $\eta_{\text{solar-to-fuel}}$ (3.5%).

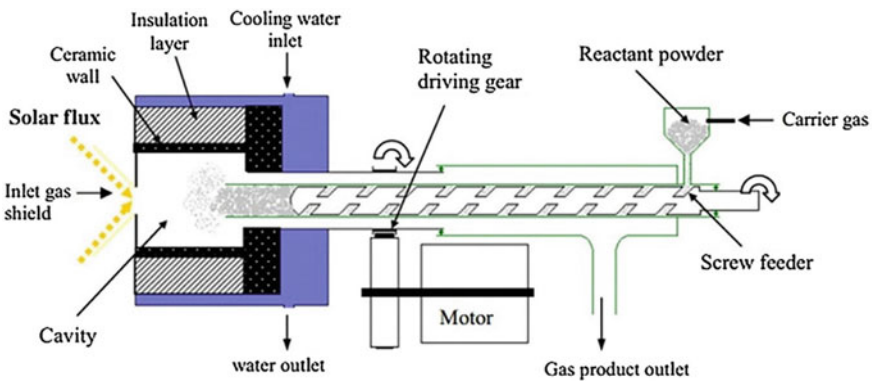

Fig. 15 Schematic of the solar reactor which was made by Abanades et al. Reprinted from Ref. [15]

4.2 Reactor for Non-Volatile Metal Oxides

Gokon et al. [72] explored a thermochemical system exploiting $NiFe_2O_4$/m-ZrO_2/MPSZ ceramic foam in a double quartz tube reactor. The $NiFe_2O_4$/m-ZrO_2/MPSZ ceramic foam was located on a porous quartz plate fixed inside a quartz tube (Fig. 16a) at the focal point of a 7-kW xenon lamp. The hydrolysis reactions were performed in another quartz tube (Fig. 16b).

The material supporting the catalyst has a significant impact on the performance of the system. Studies by Vidales et al. [73] demonstrated that a reactor consisting of silicon carbide porous ceramic foam has three advantageous features, including (1) Reactants are immobilized on the silicon carbide receiver, thus preventing the availability of reactants and the recovery of raw materials, (2) the entire cycle takes place in the same reactor, and (3) due to the high surface area of porous silicon carbide, proper gas–solid contact and high mass transfer at the interface are ensured. Lorentzou et al. [74] studied the properties of nickel ferrites having either a porous disk or honeycomb monolithic structure, which were prepared using different molding processes. Although not as efficient as powder constructions in hydrogen production, the honeycomb monolithic structure is fully formed from the active material and is an ideal material for recycling, which eliminates the interaction between the active and inert structures.

Processes utilizing reactant powders can be performed in solar radiation-driven thermochemical reactors in which fluidized beds are directly heated. Gokon et al. [75] demonstrated that hydrogen can be generated using a reactor containing an internal circulating fluidized bed (Fig. 17) topped with a glass window.

Traditionally, temperature changes introduce thermal stress on the reactor during two-step thermochemical cycles [76]. Hoskins et al. [77] was the first to develop a pilot scale potentially commercially feasible sequential isothermal thermochemical hydrogen generation system using a high-throughput solar furnace. In the device, two fluidized beds with iron aluminate (iron spinel) particles are situated in a solar chamber operating isothermally. During an 8 h operation period, the batch heater

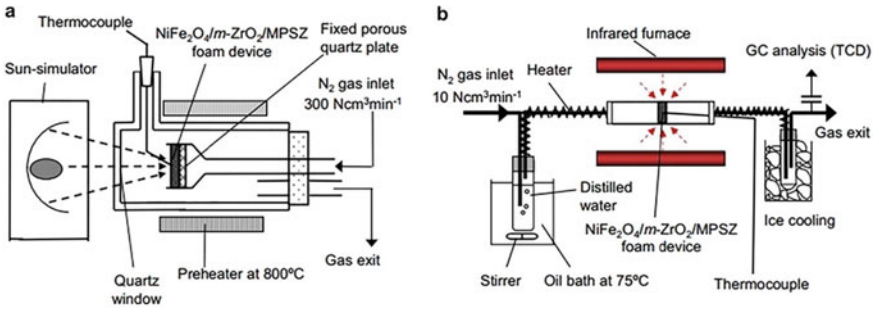

Fig. 16 Device using $NiFe_2O_4$/m-ZrO_2/MPSZ ceramic foam. Reprinted from Ref. [72]

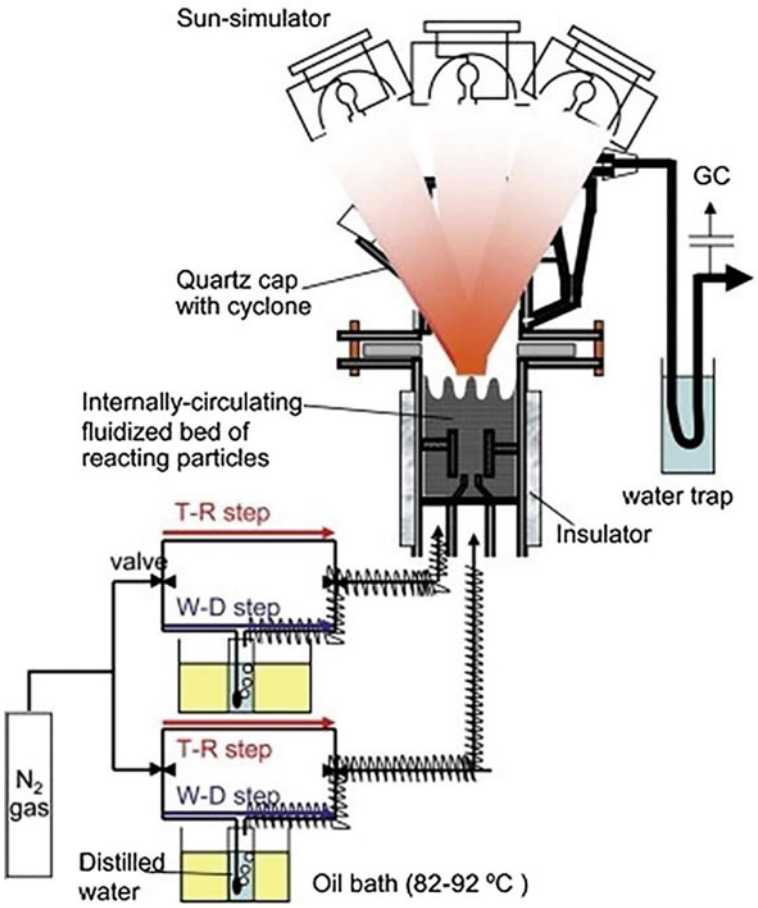

Fig. 17 Schematic of an internal circulating fluidized bed reactor (reprinted from Ref. [75])

process optimized for the redox cycle yields 5.3 L of H_2 with an average production of 597 μmol H_2/g. However, as reactor temperatures can change dramatically throughout cloudy periods, appropriate reactor materials and advanced control systems are required to maintain constant temperatures and hydrogen production rates.

5 Perspectives for Solar Thermochemical Seawater-Splitting

Over the past few decades, most of the research in this area has focused on developing high-performance metal oxides that actively participate in thermochemical hydrogen

production using high-purity freshwater. However, large-scale hydrogen production utilizing electrolysis of high-purity freshwater would either consume large quantities of this increasingly scarce source or the availability of expensive water purification systems [78]. At the present economic development, population growth and urbanization levels, the demand for drinking water has increased significantly. About 22% of the world's population live in China and the nation has only 8% of the world's fresh water resources. The imbalance between water supply and demand is more serious in China's coastal areas than inland areas, due to higher levels of population and industry. China's 11 coastal provinces have only 1,915 m^3 of water per capita (by the end of 2010). These provinces are situated on 1800 km of coastline, equivalent to 13.7% of China's geographical area and 43.0% of its population (by the end of 2010). Therefore, utilization of STCH to produce hydrogen using seawater, the most abundant water resource on earth (~97%), is highly intriguing in the context of sustainable energy production.

At the present time, studies of seawater splitting are at an early stage, and none yet have been aimed at solar thermochemical seawater-splitting. But this does not prevent us from looking forward to the development of solar thermochemical seawater-splitting.

5.1 Desalinating Seawater for STCH

Under high-temperature conditions, salt in seawater causes corrosion of STCH equipment, which greatly affects service lifetimes. One possible strategy is to develop seawater desalination technologies, especially in economically developed coastal areas. The level of urbanization in the 11 coastal provinces of China compared to the national level, which in 2009 was 57.7% in the coastal areas, compared to the national average of 48.3% [79].

The water supply situation in the coastal areas of China reveals that water stress in coastal areas is higher than in the country as a whole. The total water supply accounts for 51.1% of the water supply capacity in the coastal areas and 50.4% of the national water supply capacity. In addition, the public water supply system in the coastal zone serves a higher proportion of the population. Per capita water consumption in the coastal zone is 185.2 L/person/d, compared to the national average of 171.4 L/person/d.

At present, the coastal areas have made greater progress in economic and industrial development compared to the inland, which has led to greater pressure on water resources in the coastal areas. In 2010, the gross domestic product (GDP) of coastal areas was RMB 24.6 trillion, accounting for 61.3% of the national GDP. However, water resources in the coastal areas only accounted for 28.6% of the national total. The total water consumption in coastal areas is 248 trillion cubic meters, accounting for approximately 41.2% of the country's total water consumption. Coastal areas utilize about 28.1% of water resources, compared to a national average of 19.5%.

In summary, the imbalance between water supply and demand in coastal areas has worsened over the past decades due to increased economic development, growing populations and urbanization. In the coming two decades, these factors will become even more important in coastal areas. This is particularly true for the Pearl River Delta, the Yangtze River Delta and the Bohai Sea Rim. One of the greatest challenges to China's development is how to address the growing imbalance between water supply and demand. Thus, for the economically developed coastal areas, it is feasible to develop industrial level seawater desalination technologies, and the desalinated seawater could be used for many purposes including STCH water-splitting to produce H_2.

5.2 Seawater Electrolysis for Hydrogen Production via Solid Oxide Electrolyzer Cell (SOEC)

Recent years have seen advances in the development of low-temperature water electrolysis technologies, such as those associated with alkaline and proton exchange membrane water electroliers [80, 81]. Solid oxide fuel cells (SOFCs) have been popular for decades and extensive research has been carried out on these systems to explore SOFC fabrication techniques, electrode development and operating parameters [82]. The reversal of SOFCs consisting of solid oxide electrolyzer cells (SOEC) has recently received a lot of attention because of their advantages over cryogenic electrolysis in terms of efficient H_2 production.

In the early 1980s, steam electrolysis for hydrogen production in SOEC attracted interest as an alternative to low-temperature water electrolysis [84]. From a thermodynamic point of view, high-temperature electrolysis of steam using SOEC is a promising technology compared to low-temperature water electrolysis because it is more thermodynamically and kinetically favourable at high temperatures and therefore requires less electrical energy per mount of produced hydrogen [85, 86]. The increase in operation temperature results in a lower electrical energy requirement for steam electrolysis and, therefore, a lower cost of hydrogen production.

Currently, most water electrolysis technologies are based on the utilization of freshwater. However, less than 1% of freshwater on the Earth is accessible at an affordable cost, whereas 97.5% of water on the Earth is in the form of seawater which has an almost unlimited abundance. Electricity generated by renewable energy technologies (such as offshore wind and wave farms) can be used for the direct electrolysis of steam, and these technologies are more common in areas where seawater is abundant. Developments relating to electrode materials for low-temperature seawater electrolysis have been used to solve problems such as the production of chlorine at the anode and the gradual accumulation of insoluble precipitates at the cathode [87, 88]. In contrast, the electrolysis of seawater with high-temperature steam using SOEC is still a new area of research to be explored.

Chan and the coworkers investigated two issues related to seawater electrolysis using button cell SOECs [89]. The first involves the purity of steam produced from seawater and the second involves contamination by sea salt of the Ni-YSZ fuel electrode and its effect on electrochemical performance and device degradation. A test, conducted using a button cell consisting of Ni-YSZ as a fuel electrode, YSZ as electrolyte and LSCF-GDC as an air electrode, demonstrated that these problems can be overcome and that SOECs are feasible for direct seawater electrolysis. In this study, the in-situ and non-in-situ properties of SOEC were investigated using pure water and simulated seawater-generated vapour and SOEC fuel electrodes contaminated with sea salt. The results showed that no contaminants were found in the seawater-generated vapor, so the electrolysis of pure water and seawater-generated water vapor had almost the same initial performance in terms of current–voltage curves and impedance spectra. The degradation rate in seawater electrolysis was also similar to that in normal water electrolysis. Post-run analysis showed that sodium chloride is not present on the surface, cross-section and electrode–electrolyte interface of the Ni-YSZ fuel electrode. Therefore, direct contamination of the SOEC fuel electrode by sea salt, which affects the electrochemical performance of the cell, does not occur. Furthermore, the uncontaminated and contaminated cells have similar initial properties. The degradation rate of the contaminated cells is also close to that of the uncontaminated cells. Post-run analysis confirmed that sea salt does not react with the electrode material and is lost during operation at a typical temperature of 800 °C [89]. Thus, this method might be suitable for large-scale hydrogen production from seawater.

6 Challenges and Outlook

Although the technological readiness level (TRL) of direct solar hydrogen production technology is significantly lower in terms of proven scale and lifetime, it has unique characteristics compared to low-temperature electrolysis (LTE). For example, direct solar-to-hydrogen pathways can be utilized in locations that do not have reliable electrical grid infrastructures, as they can avoid the need for electricity transmission lines. For STCH water-splitting, the largest demonstration facility comprised of three fixed-bed reactors with two containing $NiFe_2O_4$ and one CeO_2 as redox-active materials have a capacity in the range of 750 kW [90]. No reports about the efficiency of this system have appeared. The experimental maximum efficiency of the thermochemical cycle was 5.25% in a 4.1 kW fixed-bed reactor with CeO_2 operating in a solar simulator [91].

New STCH based systems, which are comprised of new redox-active materials that have lower solar input requirements per mole of H_2 produced and good water-splitting thermodynamics is a major challenge. In addition, the ideal redox-active material should exhibit fast redox kinetics, high cyclability, high thermal stress, high thermal conductivity and oxygen ion conductivity as well as low cost. Currently, researchers in this field consider ceria to be the most advanced material, as it is the

most studied material. However, ceria is very difficult to reduce, requiring reduction temperatures of up to 1500 °C or higher, or very low O_2 partial pressures (e.g., very high sweep currents).

Materials similar to ceria but with a lower enthalpy change of reduction (e.g., 15% lower) and a similar or slightly lower entropy change of reduction will be more readily reduced with adequate reoxidation thermodynamics and kinetics. However, it may not be possible to maintain a solid state entropy change at the ceria level during the reduction process while reducing the enthalpy change [92].

Considering the design of the STCH system, the reduction in heat loss and heat demand of the auxiliary system will result in an increase in overall system efficiency close to the theoretical value. Effective heat recovery systems are required to optimally select the temperature difference between the reduction reaction (O_2 production) and the reoxidation reaction (H_2 production) without adversely affecting the STCH conversion efficiency while utilizing a higher degree of reduction and water conversion yield (i.e., limiting the amount of excess steam). The challenge of developing a cost and performance effective solid–solid heat exchange system is reflected in the fact that 80% effectiveness has not yet been achieved [93]. The removal of oxygen from reduction reactors is another issue that has received more attention, although not enough in practical applications. The technical approach to achieving the necessary low oxygen partial pressures must be energetically efficient and economical. Presently, a second-law efficiency of 10% for N_2-O_2 separation is deemed to be acceptable in electrically driven devices. The thermally driven oxygen adsorption/desorption cycle can be developed to improve STCH conversion efficiency by using internal and low mass process heat [94]. Although less studied, the H_2/H_2O separation process is also critical to achieve high STCH conversion efficiency. Recovering latent heat is often more challenging than achieving efficient gas–gas heat exchange, as efficiencies in excess of 90% have been reported for gas phase recovery at high temperatures [37, 95]. An ideal H_2/H_2O partitioning process would involve reusing the residual in-process heat from the reoxidation reactor and separating the two substances in the gas phase. More generally, the choice between finding the optimum operating conditions or the ideal material has not yet been agreed among workers in the field.

Due to the high solar flux and high temperature of the STCH unit, the receiver/reduction reactor is one of the most risk-prone critical components of the water separation unit. The reactor needs to be fabricated with materials that are resistant to severe thermal shock and that can operate in high-temperature and oxidizing environments. Moreover, materials in the reactor, heat exchange and heat integration and separation are also important in designing devices that can be used for large scale hydrogen production. So far, most of the focus has been on finding a material that is as good as cerium dioxide in terms of reduction and reoxidation performance. From a materials perspective, the design of a reoxidation reactor is less challenging than a reduction reactor. The heat captured during reoxidation plays a crucial role in improving the efficiency of STH conversion as it can be used repeatedly to drive all auxiliary processes. Currently, no reactors have been developed with designs that address this issue.

The capabilities of STCH water-splitting systems can be extended to other important processes such as CO_2 and N_2 reduction [9]. Redox-active metal oxide-based cycles can be applied directly to CO_2 cracking and/or combined CO_2/H_2O cracking to produce CO/syngas respectively. Since the Gibbs free energy change for CO_2 splitting is lower than that of the water-splitting at high temperatures, cycles that carry out these processes are less energy-demanding than that for water-splitting. Other applications of the STCH system, in which the oxygen affinity of reduced (oxygen-deficient) metal oxides is utilized, include oxygen pumping, inert gas purification and the production of N2 from air [96]. In addition, the principle behind STCH extends to redox-active metal nitrites, which release nitrogen to react with H_2 to produce ammonia [97].

In conclusion, direct solar hydrogen production through STCH water cracking, while not yet cost competitive with more recent methods such as LTE using electrons, can be a unique alternative and complementary method in certain parts of the world where the grid is not yet fully deployed. They can also provide a more resilient solution for long-term energy storage.

References

1. Holladay JD, Wang Y, Jones E (2004) Chem Rev 104:4767
2. Ardo S, Fernandez Rivas D, Modestino MA, Schulze Greiving V, Abdi FF, Alarcon Llado E, Artero V, Ayers K, Battaglia C, Becker JP, Bederak D, Berger A, Buda F, Chinello E, Dam B, Di Palma V, Edvinsson T, Fujii K, Gardeniers H, Geerlings H, Hashemi SMH, Haussener S, Houle F, Huskens J, James BD, Konrad K, Kudo A, Kunturu PP, Lohse D, Mei B, Miller EL, Moore GF, Muller J, Orchard KL, Rosser TE, Saadi FH, Schüttauf JW, Seger B, Sheehan SW, Smith WA, Spurgeon J, Tang MH, van de Krol R, Vesborg PCK, Westerik P (2018). Energy Environ Sci 11:2768.
3. Zhu X, Wang H, Wei Y, Li K, Yan D (2010) Progress in Chemistry 22:1010
4. Scheffe JR, Steinfeld A (2014) Mater Today 17:341
5. Hosseini SE, Wahid MA (2016) Renew Sustain Energy Rev 57:850
6. Funk JE (2001) Int J Hydrogen Energy 26:185
7. Tadokoro Y, Kajiyama T, Yamaguchi T, Sakai N, Kameyama H, Yoshida K (1997) Int J Hydrogen Energy 22:49
8. Teo ED, Brandon NP, Vos E, Kramer GJ (2005) Int J Hydrogen Energy 30:559
9. Lu Y, Zhu L, Agrafiotis C, Vieten J, Roeb M, Sattler C (2019) Prog Energy Combust Sci 75
10. Bayon A, de la Calle A, Stechel EB, Muhich C (2022). Energy Technology 10
11. Meredig B, Wolverton C (2009). Physical Review B 80
12. Bilgen E, Ducarroir M, Foex M, Sibieude F, Trombe F (1977) Int J Hydrogen Energy 2:251
13. Weidenkaff A, Steinfeld A, Wokaun A, Auer PO, Eichler B, Reller A (1999) Sol Energy 65:59
14. Weidenkaff A, Reller AW, Wokaun A, Steinfeld A (2000) Thermochim Acta 359:69
15. Abanades S, Charvin P, Flamant G (2007) Chem Eng Sci 62:6323
16. Fletcher EA (1999) Ind Eng Chem Res 38:2275
17. Wegner K, Ly HC, Weiss RJ, Pratsinis SE, Steinfeld A (2006) Int J Hydrogen Energy 31:55
18. Steinfeld A (2002) Int J Hydrogen Energy 27:611
19. Loutzenhiser PG, Meier A, Steinfeld A (2010) MATERIALS 3:4922
20. Charvin P, Stephane A, Florent L, Gilles F (2008) Energy Convers Manage 49:1547
21. Lange M, Roeb M, Sattler C, Pitz-Paal R (2014) Energy 67:298
22. Charvin P, Abanades S, Lemont F, Flamant G (2008) AlChE J. 54:2759

23. Abanades S (2012) Int J Hydrogen Energy 37:8223
24. Leveque G, Abanades S, Jumas J-C, Olivier-Fourcade J (2014) Ind Eng Chem Res 53:5668
25. Chambon M, Abanades S, Flamant G (2011) AlChE J. 57:2264
26. Chambon M, Abanades S, Flamant G (2009) Int J Hydrogen Energy 34:5326
27. Chambon M, Abanades S, Flamant G (2010) Chem Eng Sci 65:3671
28. Bhosale RR, Kumar A, Sutar P (2017) Energy Convers Manage 135:226
29. Panlener RJ, Blumenthal RN, Garnier JE (1975) J Phys Chem Solids 3611:1213
30. Chueh WC, Falter C, Abbott M, Scipio D, Furler P, Haile SM, Steinfeld A (2010) Science 330:1797
31. Chueh WC, Haile SM (2009) Chemsuschem 2:735
32. Abanades S, Legal A, Cordier A, Peraudeau G, Flamant G, Julbe A (2010) J Mater Sci 45:4163
33. Meng Q-L, Lee C-I, Kaneko H, Tamaura Y (2012) Thermochim Acta 532:134
34. Meng Q-L, Lee C-I, Shigeta S, Kaneko H, Tamaura Y (2012) J Solid State Chem 194:343
35. Le Gal A, Abanades S, Bion N, Le Mercier T, Harle V (2013) Energy Fuels 27:6068
36. Gokon N, Sagawa S, Kodama T (2013) Int J Hydrogen Energy 38:14402
37. Hathaway BJ, Chandran RB, Gladen AC, Chase TR, Davidson JH (2016) Energy Fuels 30:6654
38. Steinfeld A, Sanders S, Palumbo R (1999) Sol Energy 65:43
39. Charvin P, Abanades S, Flamant G, Lemort F (2007) Energy 32:1124
40. Nakamura T (1977) Sol Energy 19:467
41. Kodama T, Nakamuro Y, Mizuno T (2004) J SolEnergy Eng 128:3
42. Gokon N, Murayama H, Umeda J, Hatamachi T, Kodama T (2009) Int J Hydrogen Energy 34:1208
43. Ehrensberger K, Frei A, Kuhn P, Oswald HR, Hug P (1995) Solid State Ionics 78:151
44. Han SB, Kang TB, Joo OS, Jung KD (2007) Sol Energy 81:623
45. Allendorf MD, Diver RB, Siegel NP, Miller JE (2008) Energy Fuels 22:4115
46. Fresno F, Fernandez-Saavedra R, Belen Gomez-Mancebo M, Vidal A, Sanchez M, Rucandio MI, Quejido AJ, Romero M (2009) Int J Hydrogen Energy 34:2918
47. Kodama T, Wada Y, Yamamoto T, Tsuji M, Tamaura Y (1995) J Mater Chem 5:1413
48. Kodama T, Kondoh Y, Yamamoto R, Andou H, Satou N (2005) Sol Energy 78:623
49. Kodama T, Gokon N, Yamamoto R (2008) Sol Energy 82:73
50. Scheffe JR, Li J, Weimer AW (2010) Int J Hydrogen Energy 35:3333
51. Muhich CL, Ehrhart BD, Witte VA, Miller SL, Coker EN, Musgrave CB, Weimer AW (2015) Energy Environ Sci 8:3687
52. Cooper T, Scheffe JR, Galvez ME, Jacot R, Patzke G, Steinfeld A (2015) Energ Technol 3:1130
53. Ezbiri M, Takacs M, Theiler D, Michalsky R, Steinfeld A (2017) J Mater Chem A 5:4172
54. Scheffe JR, Weibel D, Steinfed A (2013) Energy Fuels 27:4250
55. Demont A, Abanades S, Beche E (2014) J Phys Chem C 118:12682
56. Yang C-K, Yamazaki Y, Aydin A, Haile SM (2014) J Mater Chem A 2:13612
57. Demont A, Abanades S (2014) RSC Adv 4:54885
58. Demont A, Abanades S (2015) J Mater Chem A 3:3536
59. Takacs M, Hoes M, Caduff M, Cooper T, Scheffe JR, Steinfeld A (2016) Acta Mater 103:700
60. McDaniel AH, Miller EC, Arifin D, Ambrosini A, Coker EN, O'Hayre R, Chueh WC, Tong J (2013) Energy Environ Sci 6:2424
61. Ruan C, Tan Y, Li L, Wang J, Liu X, Wang X (2017) AlChE J. 63:3450
62. Zhai S, Rojas J, Ahlborg N, Lim K, Toney MF, Jin H, Chueh WC, Majumdar A (2018) Energy Environ Sci 11:2172
63. Liang W, Cao Z, He G, Caro J, Jiang H (2017) ACS Sustain Chem & Eng 5:8657
64. Seo K, Jeong S-M, Lim T, Ju S (2018) RSC Adv 8:37958
65. Agrafiotis C, Roeb M, Sattler C (2015) Renew Sustain Energy Rev 42:254
66. Sattler C, Roeb M, Agrafiotis C, Thomey D (2017) Sol Energy 156:30
67. Diver RB, Miller JE, Allendorf MD, Siegel NP, Hogan RE (2008) J Sol Energy Eng-Trans ASME 130
68. Lapp J, Davidson JH, Lipinski W (2013) J Sol Energy Eng-Trans ASME 135
69. Smestad GP, Steinfeld A (2012) Ind Eng Chem Res 51:11828

70. Yadav D, Banerjee R (2016) Renew Sustain Energy Rev 54:497
71. Koepf E, Villasmil W, Meier A (2016) Appl Energy 165:1004
72. Gokon N, Murayama H, Nagasaki A, Kodama T (2009) Sol Energy 83:527
73. Villafan-Vidales HI, Abanades S, Caliot C, Romero-Paredes H (2011) Appl Therm Eng 31:3377
74. Lorentzou S, Pagkoura C, Zygogianni A, Karagiannakis G, Konstandopoulos AG (2017) Int J Hydrogen Energy 42:19664
75. Gokon N, Mataga T, Kondo N, Kodama T (2011) Int J Hydrogen Energy 36:4757
76. Muhich CL, Evanko BW, Weston KC, Lichty P, Liang X, Martinek J, Musgrave CB, Weimer AW (2013) Science 341:540
77. Hoskins AL, Millican SL, Czernik CE, Alshankiti I, Netter JC, Wendelin TJ, Musgrave CB, Weimer AW (2019) Appl Energy 249:368
78. Liu G, Xu Y, Yang T, Jiang L (2020) Nano materials science
79. Zheng X, Chen D, Wang Q, Zhang Z (2014) Chem Eng J 242:404
80. Manabe A, Kashiwase M, Hashimoto T, Hayashida T, Kato A, Hirao K, Shimomura I, Nagashima I (2013) Electrochim Acta 100:249
81. Ehteshami SMM, Chan SH (2013) Chem Eng Sci 98:282
82. Liu Y, Hao X, Wang Z, Wang J, Qiao J, Yan Y, Sun K (2012) J Power Sources 215:296
83. Kong J, Sun K, Zhou D, Zhang N, Mu J, Qiao J (2007) J Power Sources 166:337
84. Isenberg AO (1981) Solid State Ionics 3–4:431
85. Holladay JD, Hu J, King DL, Wang Y (2009) Catal Today 139:244
86. Stempien JP, Sun Q, Chan SH (2013) Energy 55:647
87. Ghany NAA, Kumagai N, Meguro S, Asami K, Hashimoto K (2002) Electrochim Acta 48:21
88. Baniasadi E, Dincer I, Naterer GF (2013) Int J Hydrogen Energy 38:2589
89. Lim CK, Liu Q, Zhou J, Sun Q, Chan SH (2017) J Power Sources 342:79
90. Gonzalez-Pardo A, Denk T, Vidal A (2020) Lessons learnt during the construction and start-up of 3 cylindrical cavity-receivers facility integrated in a 750 kW solar tower plant for hydrogen production. In: International conference on concentrating solar power and chemical energey systems (Solarpaces 2019)
91. Marxer D, Furler P, Takacs M, Steinfeld A (2017) Energy Environ Sci 10:1142
92. Lange M, Roeb M, Sattler C, Pitz-Paal R (2016) Entropy 18
93. Kong H, Kong X, Wang H, Wang J (2019) Int J Hydrogen Energy 44:19585
94. Ermanoski I, Stechel EB (2020) Sol Energy 198:578
95. Banerjee A, Chandran RB, Davidson JH (2015) Appl Therm Eng 75:889
96. Farr TP, Nguyen NP, Bush HE, Ambrosini A, Loutzenhiser PG (2020) Materials 13:5123
97. Michalsky R, Parman BJ, Amanor-Boadu V, Pfromm PH (2012) Energy 42:251

Photo-Driven Biocatalytic Seawater Splitting

Wei Geng, Zi-Qian Yi, and Xiao-Yu Yang

Abstract Hydrogen is considered as one of the most promising energy sources because of its wide sources, zero carbon emissions, and high conversion efficiency. Biological hydrogen production, to convert organic matter or water into hydrogen by using the metabolism of organisms themselves, has shown great potential in green hydrogen industry due to its unique advantages of low cost, zero carbon emission, and mild reaction conditions. Hydrogen production from seawater has aroused widespread interest among researchers. The high salinity of the seawater will lead to the inactivation of cells. Therefore, it is necessary to design a cell protection strategy to keep long term stable of microorganisms even in harsh environments such as seawater. Cell nanoencapsulation is a method inspired by nature to enhance their durability or functionalize them, in which the nanomaterials self-assemble on cell surface forming an artificial shell with "cell in shell" structure. Among them, artificial photosynthetic biohybrid system with semiconductor materials have attracted wide attention for solar-driven hydrogen production. Huge improvements have been achieved in the past decade because that such biohybrid systems may overcome the limitations of natural and artificial photosynthesis. In this chapter, we have thoroughly reviewed this new artificial biohybrid system both enzyme-based and cell-based that can be exploited to target hydrogen production. The mechanism and its application to the preparation of artificial hybrid system with highly advanced functional materials are discussed. In the end, the design direction of next-generation artificial hybrid system creating is prospected.

Keywords Biological hydrogen production · Artificial biohybrid system · Cell nanoencapsulation · Semi-artificial photosynthesis · Enzymatic

W. Geng (✉)
School of Chemical Engineering and Technology, Sun Yat-Sen University, Zhuhai 519082, China
e-mail: gengw6@mail.sysu.edu.cn

Z.-Q. Yi · X.-Y. Yang
State Key Laboratory of Advanced Technology for Materials Synthesis and Processing (Wuhan), Foshan Xianhu Laboratory of the Advanced Energy Science and Technology Guangdong Laboratory (Xianhu Hydrogen Valley, Foshan), Laoshan Laboratory (168 Wenhai Middle Rd, Jimo District, Qingdao), Wuhan University of Technology, Wuhan 430070, China

X.-Y. Yang (ed.), *Photo-Driven Seawater Splitting for Hydrogen Production*,
https://doi.org/10.1007/978-981-99-0510-2_6

1 Introduction

While advances made in the energy industry in recent years have resulted in increased productivity, global energy consumption has also grown dramatically. This increase has led to a global energy crisis caused by increases in energy prices and by fossil fuel combustion promoted climate change and air pollution. In this context, hydrogen has received increasing attention as an energy generator, due to its being renewable and clean. Notably, combustion of hydrogen has a high specific heat and it produces water solely. Consequently, the application of hydrogen as a large-scale energy source in areas such as the automotive industry has progressed significantly [1]. Hydrogen is generally produced by water electrolysis [2], the water–gas shift reaction [3], and as a byproduct of petroleum refining [4, 5]. Among the currently available methods, those relying on biological processes for production of this gas are the most cost-effective. Importantly, approaches that utilize living organisms that produce hydrogen and biofuels by hydrogenase-catalyzed processes are highly attractive. Thus, a sufficient supply of this energy source could be created using organisms, and inexhaustible supplies of water, carbon dioxide and sunlight [6].

Recently, artificial photosynthetic biohybrids have attracted much attention to highly efficient biohydrogen production [7]. These systems integrate biocatalytic machinery with synthetic materials in a manner that combines the strengths of each while overcoming their limitations. In these hybrid systems, microbes function as catalysts to drive the overall endergonic series of chemical reactions that generate hydrogen. In addition, synthetic materials including dyes, electrocatalysts, semiconductors, electrodes, and mediators have been utilized as scaffolds to immobilize biocatalysts and functional components [8]. Those materials also protect fragile bioorganisms enabling sustainable stability in unfavorable environments [9–11].

Artificial biohybrids are powerful tools for transforming light energy into hydrogen [12]. Unlike in microbial electrosynthesis, biohybrids serve as stand-alone systems that do not require external electron input. Furthermore, catalytic conversion efficiencies of the biohybrids can be enhanced by upregulating key enzyme components using nanoparticles [13]. The formed bio-nanomaterials have enhanced levels of hydrogen production using light illumination [14]. Importantly, the interface between materials and bioorganisms plays a key role in low efficient electron transfer [15].

Up-scale production of biohybrid system is a challenging issue [16]. Moreover, many other issues need to be addressed to increase the scale of biohybrid-promoted hydrogen production to reach industrial levels, including the biocompatibility of nanomaterials and cost. We believe that current efforts aimed at designing efficient large-scale artificial biohybrid processes will revolutionize hydrogen production from water and sunlight. In this chapter, we provide background information that will the understanding of processes and mechanisms involved in bio-hydrogen production, Next, we describe and discuss investigations which have led to important contributions to artificial photosynthesis.

2 Hydrogen-Producing Enzymatic Processes in Organisms

Organisms produce hydrogen through many biological pathways. The two types of enzymes that promote processes that lead to hydrogen production are hydrogenases and nitrogenases. Hydrogenases catalyze the direct generation of hydrogen by reducing protons by electrons, while nitrogenases produce this gas as a by-product of nitrogen fixation [17].

2.1 Nitrogenases

Cyanobacteria can reduce molecular nitrogen to form ammonia and hydrogen. Nitrogenases are multiprotein complexes each consisting of a dinitrogenase (molybdenum-iron protein or protein I) and its specific reductase (iron protein or protein II). The dinitrogenases are $\alpha 2\beta 2$ heterotetramers composed of α and the β subunits having molecular weights of about 220–240 kDa [18]. The heterotetramers contain a [4Fe-4S] cluster and two ATP active sites. Dinitrogenase reductases are 60–70 kDa homodimers comprised of subunits encoded by *NifH* [19]. The conversion efficiencies of nitrogenases are lower than those of [FeFe]-hydrogenases and [NiFe]-hydrogenases (see below) [20]. In eukaryotic green algae, HydA localizes to the chloroplast as maturation occurs [21]. The several forms of nitrogenases that exist are classified based on the metal cofactors they contain. The most common of these are Mo nitrogenases, and two other groups are V-nitrogenases and Fe-nitrogenases [22]. V-nitrogenases and Fe-nitrogenases are enzyme homologs, which lack additional subunits (VnfG or AnfG). The three nitrogenases catalyze hydrogen evolution (Eqs. 1–3) with different efficiencies [23].

The most studied members of the Mo-nitrogenase family are oxygen-sensitive metalloenzyme complexes. Perhaps the most common Mo-nitrogenases are those present in *Azotobacter vinelhandii*, *Klebsiella pneumoniae,* and *Clostridium pasteurianum* [24–28]. The ferritin cycle in these bacteria can promote reduction of nitrogen and production of hydrogen [29, 30].

$$\begin{aligned} &\text{Mo} - \text{nitrogenase}: \ N_2 + 8H^+ + 8e^- + 16ATP \\ &\quad \rightarrow 2NH_3 + H_2 + 16ADP + P_i \end{aligned} \tag{1}$$

$$\begin{aligned} &\text{Fe} - \text{nitrogenase}: \ N_2 + \ 21H^+ + 21e^- + 42ATP \\ &\rightarrow 2NH_3 + 7.5H_2 + 42ADP + 42P_i \end{aligned} \tag{2}$$

$$\begin{aligned} &\text{V} - \text{nitrogenase}: \ N_2 + \ 12H^+ + 12e^- + 24ATP \\ &\quad \rightarrow 2NH_3 + 3H_2 + 24ADP + 24P_i \end{aligned} \tag{3}$$

2.2 *Hydrogenases*

Three different types of hydrogenases exist relying on the nature of the metal cluster at the reaction center. Included in this group are the two most important hydrogenases, [NiFe]-hydrogenase and [FeFe]-hydrogenase [31–34], which contain CO and CN ligands bound to metal centers, and are irreversibly inactivated by oxygen. Structural analysis shows that the [4Fe-4S] cluster is a source of electrons for the [2Fe-2S] core where protons bind to iron portion in the [2Fe-2S] core and are reduced to produce hydrogen.

In cells, these hydrogenases exist in either soluble forms in the cytoplasm or in membrane-bound forms [35]. [NiFe]-hydrogenases trend to take part in hydrogen consumption, whereas [FeFe]-hydrogenases generally produce hydrogen [36]. In addition, [NiFe]-hydrogenases are constitutively expressed, whereas expression of [FeFe]-hydrogenases requires anaerobic induction [37, 38].

2.2.1 [FeFe]-Hydrogenases

[FeFe]-hydrogenases are present in various organisms, but mainly anaerobic bacteria, especially those in fermenting organisms (for example, bacillus). [FeFe]-hydrogenases, found in algae (eg., *Chlorella*), have 100 times higher catalytic activities than those of other hydrogenases [39]. In 2001, the first algal [FeFe]-hydrogenase gene from *Scenedesmus obliquus* was cloned in 2001 [40, 41], and [FeFe]-hydrogenase genes were subsequently produced for *Chlamydomonas* [42, 43] and *Chlorella vulgaris* [44, 45]. Fe-S clusters exist in bacterial [FeFe]-hydrogenases and are necessary for electron transport. *Chlorella* contains two the [FeFe]-hydrogenases, HydA1 and HydA2 [46].

2.2.2 [NiFe]-Hydrogenases

[NiFe]- and [FeFe]-hydrogenases differ in many ways. For the most part, [NiFe]-hydrogenases catalyze hydrogenation and, as such, are likely to have been key enzymes functioning in the advent of modern respiratory metabolism [32]. [NiFe]-hydrogenases, which are more abundant in nature than [FeFe]-hydrogenases [47], are present in archaea and anaerobic and aerobic bacteria, but not in eukaryotes. Although genetically unrelated, [NiFe]- and [FeFe]-hydrogenases have many similarities including active sites containing 1) ligands CO- and CN-coordinated to iron, and 2) a binuclear metal center. In general, [NiFe]-hydrogenases catalyze both hydrogen evolution and uptake, while [FeFe]-hydrogenases only promote hydrogen evolution [36]. Moreover, the conversion efficiencies of [FeFe]-hydrogenases are typically 10–100 times higher than those of [NiFe]-hydrogenases [36]. However, several exceptions to this categorization exist. [NiFe]-hydrogenases consist of at least two subunits [35].

3 Semi-artificial Photosynthetic Biohybrids for Hydrogen Production

3.1 Hydrogen Production Through Photosynthesis

In currently operating biogas production facilities, biomass is fermented by microorganisms to generate H_2, methane, and CO_2. Because of photosynthesis in microorganisms, the biogas production process indirectly utilizes solar energy. Almost all photosynthetic microorganisms contain hydrogenases. So, it shows the great potential to produce H_2 by solar energy directly. This was first discussed by Gaffron in 1937, in a report describing H_2 production in green algae [48].

Oxygenic photosynthesis is driven on charge separation between two reaction centers (Fig. 1). In the sequence, photosystem II (PSII) oxidizes water while releasing molecular oxygen and protons (reaction 5). Electrons produced in this system are transferred to photosystem I (PSI). A reaction then occurs in PSI to generate a highly reducing electronic state that promotes reduction of ferredoxin (Fd, reaction 6). The second light-induced reaction creates electron carriers that have a sufficiently high reduction potential to conduct CO_2 reduction through the Calvin–Benson–Bassham (CBB) cycle or H_2 production by hydrogenases (reaction 7)

$$\begin{aligned} &2H_2O + 8h\nu \rightarrow \ O_2 + 2H_2 \\ &E^0 = +1.23\ \text{V} \end{aligned} \tag{4}$$

$$\begin{aligned} &2H_2O + 4h\nu \rightarrow \ O_2 + 4H^+ + 4e \\ &\text{PSII},\ E^{0'} = +820\ \text{mV} \end{aligned} \tag{5}$$

$$\begin{aligned} &4e^-(0\ \text{mV}) + 4h\nu \rightarrow \ 4e^-(-430\ \text{mV}) \\ &\text{Plastoquinol (PSII)} \rightarrow \ \text{Fd (PSI)} \end{aligned} \tag{6}$$

$$\begin{aligned} &4H^+ + 4e^- \rightarrow \ 2H_2 \\ &\text{Hydrogenase},\ E^{0'} = -410\ \text{mV} \end{aligned} \tag{7}$$

Because ferredoxin functions as an electron donor, a natural pathway exists for electrons to promote H_2 production by hydrogenases. However, two main obstacles stand in the way of utilizing the high efficiency of this "dream" reaction. One hurdle is associated with the fact that most active hydrogenases are sensitive to oxygen O_2. Moreover, competitive pathways exist for carbon fixation by the CBB cycle (Fig. 1). In microorganisms, carbon fixation is necessary for growth. The CBB cycle is the main function of the electrons extracted from water. Only when this metabolic pathway is inhibited, H_2 production will operate to relieve the buildup of excess electrons and avoid stress.

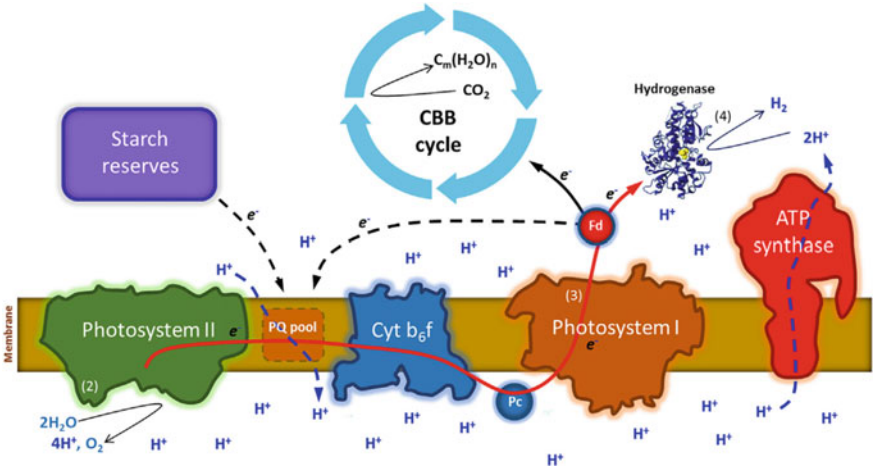

Fig. 1 The scheme of H_2 production in microorganism

Approaches have been developed to overcome this problem. One involves temporal separation of photosynthetic growth and H_2 production in which PSII activity and the presence of O_2 are inhibited after the photosynthetic growth phase using sulfur deprivation [49]. Starch degradation serves as one electron source for H_2 production under the anaerobic conditions (Fig. 1). This strategy is suboptimal because solar energy is stored temporarily in biomass and thus H_2 production is not continuous. In a search for a more direct approach, efforts have been made to promote solar-driven H_2 production by introducing semi-artificial materials in non-natural photosynthesis systems [50].

3.2 Semi-artificial Photosynthetic Biohybrids

In nature, solar energy is used in photosynthesis to produce O_2 and organic compounds from CO_2 [51]. This process is comprised of light and dark reactions (Fig. 2) [52]. In light reactions, PSII absorbs photons and uses the energy in its excited state to oxidize water and release protons and O_2. The energized electrons (e^-) are transported to PSI [53]. Then, ATP synthesis is conducted by the electrochemical potential gradient maintained by cross-membrane transport of protons [54]. Then NADPH and ATP are utilized to form CO_2 that is converted to carbohydrates via the Calvin cycle [55]. Although the quantum efficiency (QE) of charge separation in natural photosynthesis can be as high as 100% [56], organisms evolved using this pathway for survival rather than maximization efficiency. For example, photorespiration and photodamage caused by long light exposure or high light illuminate are harmful to photosystem [57]. An alternative energy-consuming process, self-repair reversal of photodamage, causes decreases in solar conversion efficiency. Because

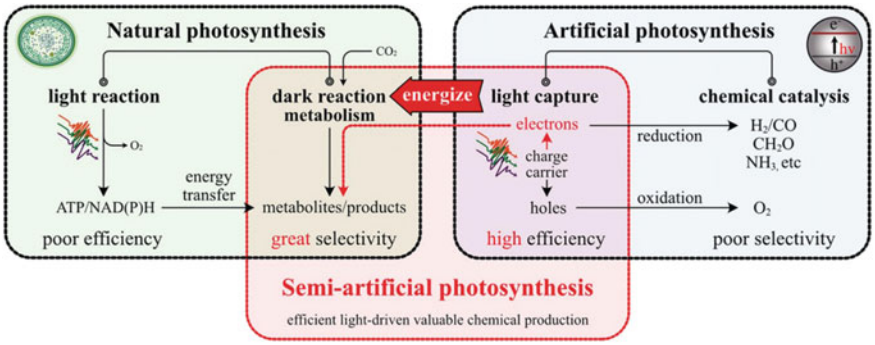

Fig. 2 Schematic of semi-artificial photosynthesis which combines the advantages of the natural photosynthesis and artificial photosynthesis

of these factors, photosynthetic efficiencies are actually 20% of the solar intensity absorbed, and the solar-to-biomass (STB) efficiency is only 1–2% for photosynthetic microorganisms [58] and less than 0.1% in most plants [7].

In artificial photosynthetic systems, semiconductor-based materials harvest solar energy to generate high-energy electron donors, which can participate in photoreductive reactions such as H_2 production, CO_2 reduction, and N_2 fixation (Fig. 2). Light-capturing efficiencies of semiconductors can be promoted by using structural modification, band structure regulation, and defect construction [59]. In comparison to semiconductors, biological pigments such as chlorophylls and carotenoids absorb solar light only within specific wavelength ranges [60]. By using artificial photosynthetic systems comprised of semiconductors, several excellent photocatalytic CO_2 reduction processes have been developed that have as high as 20% of STC conversion efficiencies, which are significantly higher than those of phototrophic organisms [61–63]. This feature has stimulated the development of artificial photosynthesis systems to generate methanol or higher alcohols (liquid sunshine) [64]. However, the attainment of this goal is confronted by scale-up issues. The solar conversion efficiencies of artificial photosynthetic systems are highly dependent on the presence of impurities in catalysts, which are attenuated in the liquid phase and prone to reactions [7]. Also, the self-replicating properties of microorganisms are difficult to mimic in artificial catalysts. Furthermore, artificial systems are restricted by their lack of chemical selectivity, which prevents simulation of the specific nature of C_{2+} product formation from CO_2 that occurs in natural photosynthesis [65]. In spite of the promoted selectivity, production of complex multi-carbon-based products using artificial photosynthetic systems is still rare [66, 67].

In light of the restrictions outlined above, semi-artificial photosynthetic biohybrid (SAPS) systems, also known as photosynthetic biohybrid systems, have been explored in recent years [7]. One system of this type consists of a photosensitizer as a light-harvesting component (Fig. 3). The photosensitizers are materials such as photoelectrodes, nanoparticles, photosensitive dyes, and photochromic molecules. In addition, enzymes or bacteria are used as react centers for production of long carbon

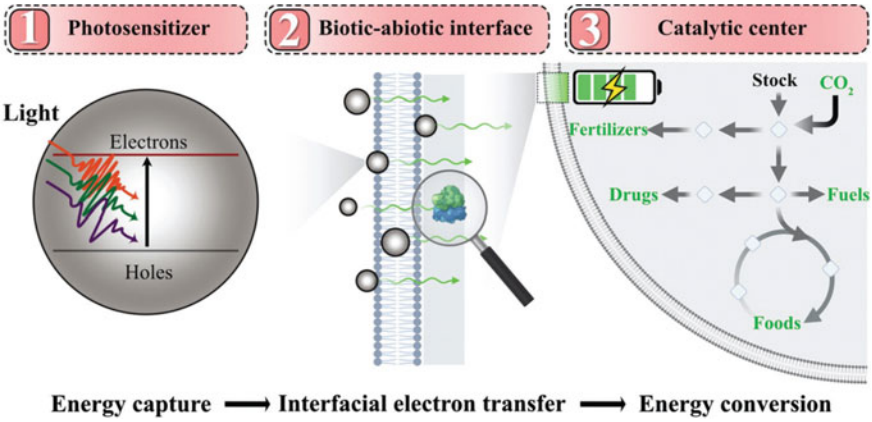

Fig. 3 Schematic of a semi-artificial photosynthesis system

chain substances from simple building blocks (CO_2, H_2O, and N_2) through precisely synchronized catalytic processes. Therefore, the photosynthetic biohybrids combine the advantages of natural and artificial photosynthetic systems to promote light-driven generation of valuable chemicals (Fig. 2). The semi-artificial photosynthetic biohybrids are classified into enzyme-based and cell-based systems. In enzyme-based semi-artificial photosynthetic biohybrids, pure enzymes such as [FeFe]-hydrogenase (H_2ase), CO dehydrogenase, and [MoFe]-nitrogenase are used in combination with photoelectrodes or semiconductor nanoparticles [68–70]. These systems, which display nearly 100% product selectivities, can utilize rationally designed photosensitive materials that have maximized charge flow to active center [71]. A recent report systemically summarized the key variables that govern the optimization of product production that facilitate interactions between biomolecules and synthetic materials [72]. Furthermore, although cell-free semi-artificial photosynthetic biohybrids can be designed to utilize the full solar spectrum [9], the inherent instabilities and laborious purification processes needed to produce requisite enzymes hinder its applications.

A timeline of pioneering studies leading to the history of enzyme-based and cell-based SAPSs is given in Fig. 4. The earliest report of a cell-based SAPS, in which *Clostridium butyricum* is composited with TiO_2 and methyl viologen (MV) for H_2 production [73], dates back to the 1980s. Although research on bioelectrochemistry (BEC), especially efforts related to microbial electrosynthesis (MES) [74], has progressed in the twenty-first century, studies focusing on cell-based SAPSs have been sparse. In the first decade of the twenty-first century, investigations of light-driven chemical or biomass-producing systems, in which nanomaterials or electrodes are utilized in combination attracted interest with regard to cell-based SAPSs [75, 76]. Cell-based systems employ natural or synthetic photosensitive materials as electron donors as locations in which critical reactions occur [65]. Importantly, the unique and sophisticated metabolic processes taking place in organism systems can be utilized

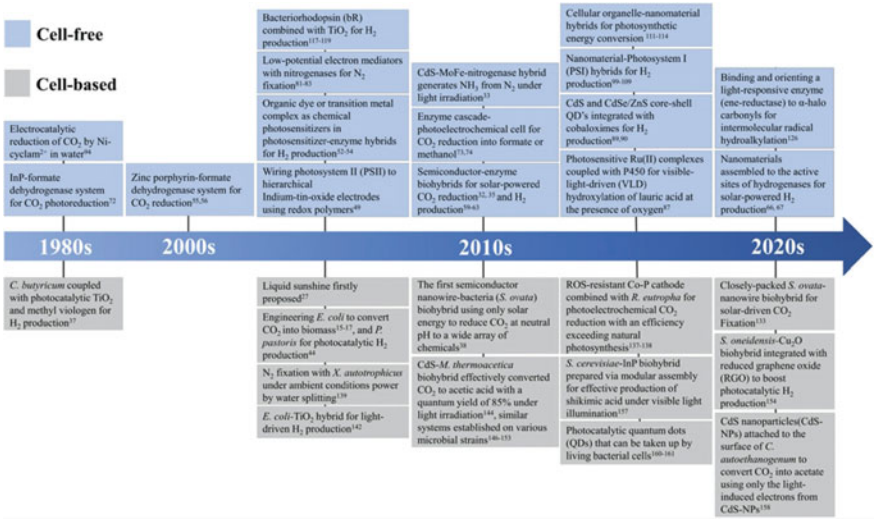

Fig. 4 Timeline of studies of enzyme-based and cell-based semi-artificial photosynthesis systems

to produce chemicals. Moreover, product diversity can be expanded in cell-based hybrids by using synthetic biology [7]. Also, the self-repair and self-replication properties of live cells endow cell-based systems with potentially high stability and scalability. Although the development of cell-based systems is at an early stage, these benefits suggest that it will have wide commercial use in carbon–neutral solar energy conversion [77].

To design efficient SAPSs for commercialization, it is critical to first understand and maximize the interfacial electron transfer process. However, mechanisms for electron transfer are still unclear, especially those taking place in cell-based systems. In the case of enzyme-based SAPSs, photosensitizers can be precisely designed to bind to enzyme active centers based on a consideration of the surface properties (electrostatics, covalent binding) of the enzymes. Furthermore, interfacial electron transfer in enzyme-based systems can be explored by using spectroscopic techniques. For instance, in vitro electron transfer from CdS to the hydrogenase has been probed utilizing transient absorption (TA) decay kinetics [78]. Also, X-ray absorption spectroscopy (XAS) has been utilized to determine oxidation states of metal centers in the enzymes which govern the specificity of electron transfer from photosensitizers to biocatalysts [79]. Unfortunately, application of these techniques in studies of whole-cell systems is made difficult by interactions that occur between metabolic processes and potential interference in making spectroscopic measurements in vivo. Also, electron transfer in the cell-based systems can take place through either direct or indirect pathways [80–82]. To enhance the efficiencies of SAPSs, investigations of interfacial biotic-abiotic redox communication are required.

3.2.1 Material-Microorganism Electron Transfer

A fundamental question about semi-artificial photosynthetic biohybrids is how cells utilize the electron generated by nanoparticles in pathways for product production. Studies of charge transfer in bioelectrochemical systems provide fundamental knowledge about these processes. Although autotrophic bacteria commonly apply H_2 as energy, many of them have evolved the ability to construct direct electrical contacts by which they can transport electrons to and from electrodes [83]. As a result, the mechanism by which electron transfer occurs between an anode and electron-donating bacteria has been studied [84, 85]. Membrane-bound proteins transfer electrons across cell membranes [86] via processes involving surface-displayed cytochromes and flavins [87]. In addition, it has been demonstrated that oxidation reactions of inorganic mineral oxides mediate electrostatic interactions on surface-displayed hemeoproteins. For example, Fukushima et al. reported that MtrF, a terminal extracellular electron transfer protein from *Shewanella oneidensis* MR-1, combine with mineral oxides using a three-dimensional, positively charged pocket (Fig. 5a) [88]. As well, bacteria have extracellular polymers, termed microbial nanowires [81, 89], that are involved in redox processes. Cryoelectron microscopy was used to investigate the structure of *Geobacter sulfurreducens* that are responsible for long-range electron transport (Fig. 5b) [90]. The results show that the nanowires consist of hexaheme cytochrome OmcS with heme groups assembled within 3–6 Å (Fig. 5c).

The platform in cell-nanoparticle hybrids enables spectroscopic exploration of the mechanisms of charge transfer between biotic/inorganic interfaces. Knowledge about the material–microorganism interface in these systems can be utilized to design efficient solar-to-biomass conversion systems [65]. An efficient H_2-producing device

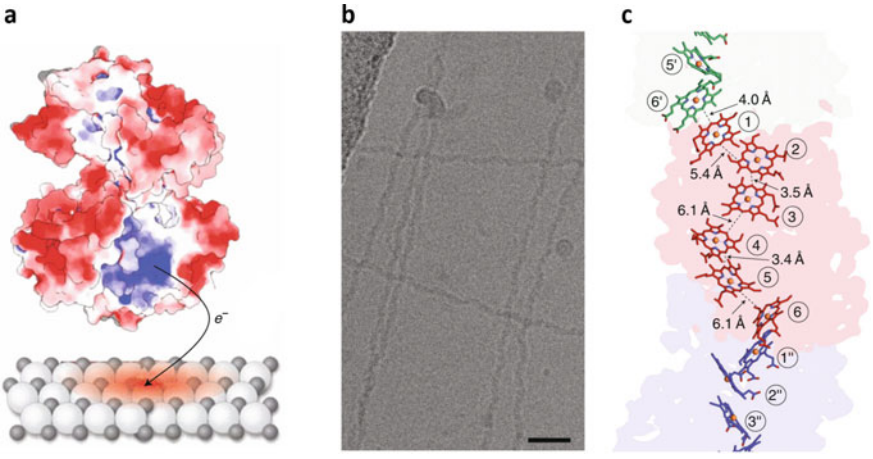

Fig. 5 Mechanisms of electron transfer in microbial cells. **a** Modeling of electron transport from MtrF to material. **b** Cryoelectron microscope graph of nanowires (scale bar, 200 Å). **c** Schematic of metal cluster hemes dense-packed in nanowires

needs to have a high efficiency for solar energy harvest and a high selectivity for specific catalytic reactions [59]. Solid-state materials like inorganic semiconductors [91] have the photoelectronic properties needed for electron transport and solar-to-electricity conversion. In addition, non-photosynthetic microbes that possess efficient H_2-producing biochemical pathways can be bioengineered to use in cell–nanoparticle hybrids. The beneficial features of materials and microorganisms can be used advantageously to create systems that undergo semiconductor-driven biochemical processes that form H_2 with efficiencies [92].

Two mechanisms for electron transfer between materials and microorganisms, including mediated and un-mediated, have been explored. In mediated route, a soluble redox shuttle electrochemically regenerated at the electrode–solution interface provides reducing equivalents in the microbes [92–94]. Oxidation of the reducing equivalents causes reduction of $NAD(P)^+$ to form NAD(P)H. These efficient systems contain an H_2-generating electrocatalyst coupled with H_2-oxidizing or CO_2- or N_2-reducing bacterium [92, 93, 95]. These synthesized systems show 10% solar-to-biomass energy conversion efficiencies [92], which are an order of magnitude greater than those of plant-based photosynthesis systems [96]. The design of these systems takes advantage of earlier research that provided an understanding and optimization of the H_2 evolution reaction [97]. In a biological context, the basic process is a consequence of the robust, native autotrophic metabolism occurring in various microorganisms that leads to CO_2 fixation to generate materials [98], molecules [99], biomass, and proteins [92, 93]. Alternative systems that utilize redox mediators such as formate [100], phenazines, and viologens [101] have also been developed [75, 102].

3.2.2 Cytoprotection in SAPSs

SAPSs are promising platforms to promote conversion of CO_2, N_2, and H_2O to biomass [65]. However, autotrophic organisms such as *M. thermoacetica* that have specialized metabolic pathways cannot stable in the high level of photon required for photosynthesis. In addition, enzymes like Rubisco, hydrogenases, and nitrogenases are usually oxygen sensitive [103]. Sacrificial agent used to prolong separation of photo-generated electron become depleted during the photosynthetic process. To circumvent these problems, a novel strategy was developed in which cystine is reduced to cysteine by TiO_2 nanomaterials [104]. Although this approach enhances the yield of the process converting CO_2 to acetate, photoanodic TiO_2 nanocatalysts lead to the creation of deleterious reactive oxygen species (ROS) [105]. To elevate the applicability of photosensitized organisms to solar-to-biomass conversion, it is imperative to design cytoprotection strategies that possess long-term stability in reaction environments.

In nature, there are number of examples of cytoprotection systems. For example, diatoms generate silica by forming shells to thwart environmental stresses [106]. In addition, cyanobacteria produce extracellular polymers that absorb light in the damaging high-energy UV range [107]. Therefore, approaches involving directly

coating cells with charged polymers [108], and inorganic [109, 110], and metal–organic framework materials (MOFs) [111] have been employed to protect against mechanical stresses, thermal and radiation [112]. As mentioned above, *E. coli* was encapsulated by CdS nanoparticles in a system for hydrogen production [113]. Because of oxygen sensitivity, the *E. coli*-CdS composites were entrapped in silica to enhance stability. Also, charged polymers were deposited on the membranes of the cells to provide a scaffold for deposition of silica. This protocol led to the generation of a stability-enhancing local anaerobic microenvironment within the cell core (Fig. 6a, b).

Another strategy involves encapsulation of the photosensitized cells in the hydrogel. Owing to the presence of a soft structure with well-developed microvoids, alginate hydrogel enables unencumbered proliferation of cells [114]. Also, the alginate gel scavenges ROS including superoxides, hypochlorites, and peroxides [115]. Thus, hydrogel encapsulation of *M. thermoacetica*-AuNCs leads to an increase in the efficiency of photosynthetic acetate production [116].

MOFs are microporous materials that can enhance biocompatibility [117, 118]. Because of their advantages in thermal and chemical stability, and facilitation of gas absorption, MOFs have interesting applications in mixed gas sequestrations and CO_2 electrocatalysis [119, 120]. For example, the results of studies by Liang and coworkers demonstrate that a zeolitic imidazolate framework (ZIF) can be selectively

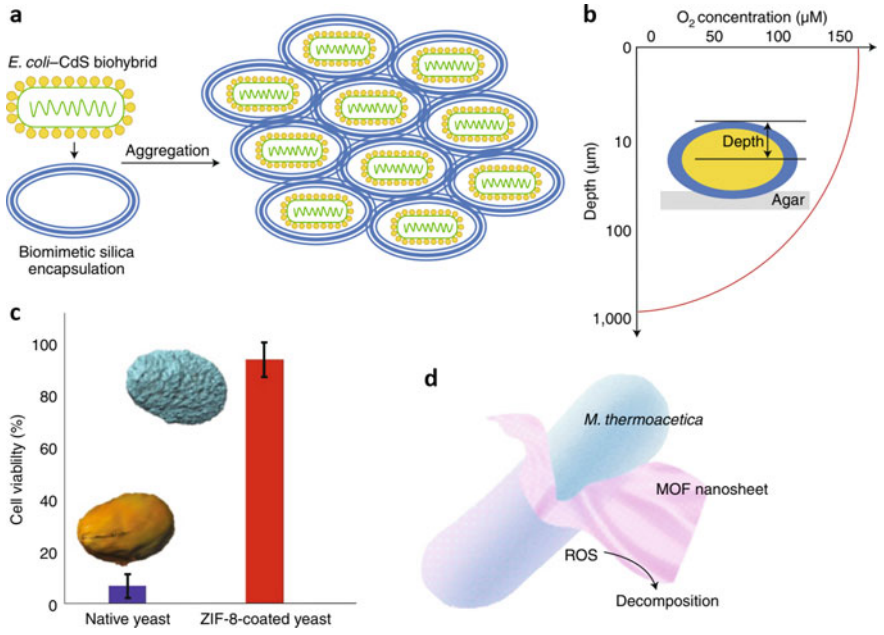

Fig. 6 Cytoprotection for microbes. **a** *E. coli* hybrid with CdS is entrapped in silica. **b** Oxygen concentration decreases with depth. **c** Schematic of ZIF coatings on living cells. **d** Schematic of MOF nanosheet coating *M. thermoacetica* against ROS damage

in vitro precipitated on yeast [111]. Remarkably, the crystallized ZIF coating prolongs the viability of yeast under adverse environmental conditions (Fig. 6c). However, the rigidity of nanoshell prevents cell proliferation and induces formation of a dormant state. Additionally, the ZIF coating might not fully cover the yeast cell membrane. In this light, Ji et al. reported a technology to entrap *M. thermoacetica* in flexible MOF nanosheets (Fig. 6d) [121]. The MOF layer does not block cell division. Comparing with native *M. thermoacetica*, nanosheet-coated *M. thermoacetica* undergoes decay at a remarkably lower rate when exposed to the ROS H_2O_2. The enhanced lifetime is a consequence of decomposition of ROS promoted by the surface zirconium clusters. As a result, MOF-encapsulated *M. thermoacetica*-CdS promotes carbon fixation even under oxidative stress, and it has a 200% increased acetate production efficiency over that of the bare biohybrid.

4 Hydrogen Production in Enzyme-Based SAPSs

4.1 [FeFe]-Hydrogenase

4.1.1 Single-Walled Carbon Nanotube

[FeFe]-hydrogenases, containing clusters comprised of one iron and one nickel center [122], can catalyze the redox interconversion of molecular hydrogen and protons. Owing to the low cost and high efficiency, [FeFe]-hydrogenases have been the good alternatives to noble metal catalysts for solar-driven H_2 production [123–125]. Moreover, [FeFe]-hydrogenases have high efficiency at zero overpotential and are highly stable [125, 126], both of which are needed for industrial solar hydrogen conversion applications.

In a recent study, Drazenka Svedruzic et al. determined the highly active SWNT/CaH_2ase-based electrodes (Fig. 7) [127]. The electrocatalytic performance of electrodes having a high m-SWNT content compared with those of Pt-group catalysts, and their proton reduction and H_2 oxidation performances exceeded those of other H_2ase-based electrodes. The m-SWNT showed the advantages in the construction of electroactive enzyme-based electrodes for potential applications.

In this study, SEM was used to observe the surface morphologies of bare C-cloth and C-cloth/SWNT electrodes. Images of bare C-cloth reveal the presence of nanoparticles ranging from 10 to 100 nm showing nanoscale roughness (Fig. 8a). Spraying with small amounts of SWNTs does not obviously change the surface morphology as can be seen by viewing images (Fig. 8b, c). The image in Fig. 8d shows that the morphology of an 84% m-SWNTs on C-cloth substrate is clearly dominated by that of the C-cloth, but SWNTs ranging about 20–110 nm are in contact with and bridge the C-cloth particles, suggesting that good electrical transfer between the C-cloth and SWNT.

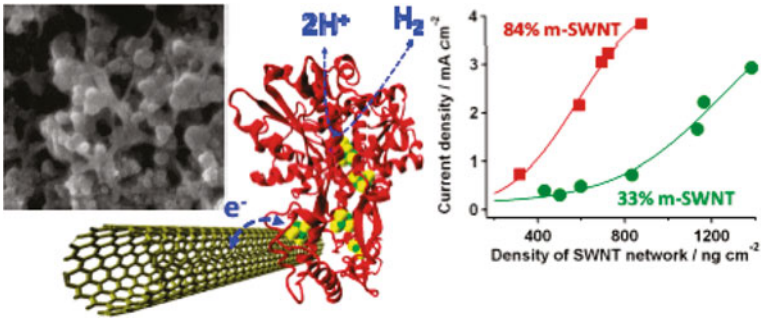

Fig. 7 Hydrogen production of biosystem with [FeFe]-hydrogenase immobilized on single-walled carbon nanotube (SWNT)

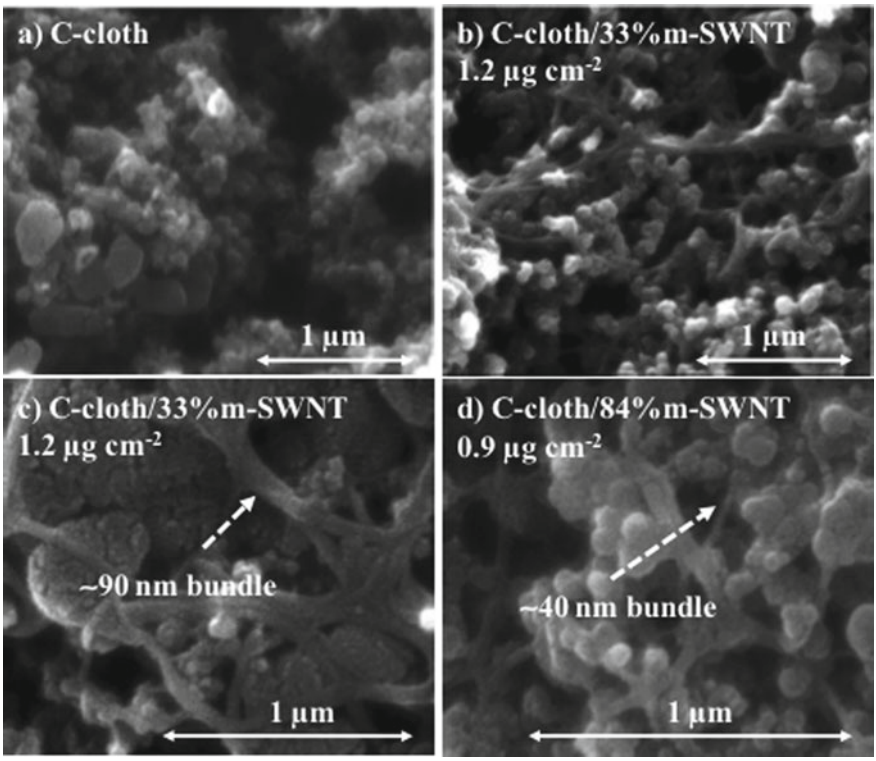

Fig. 8 SEM graphs of synthesized biological electrodes. **a** bare electrode of C-cloth; **b**, **c** electrode of C-cloth by adding 33% m-SWNT with 1.2 μg cm^{-2} areal density; **d** electrode of C-cloth by adding 84% m-SWNT with 0.9 μg cm^{-2} areal density

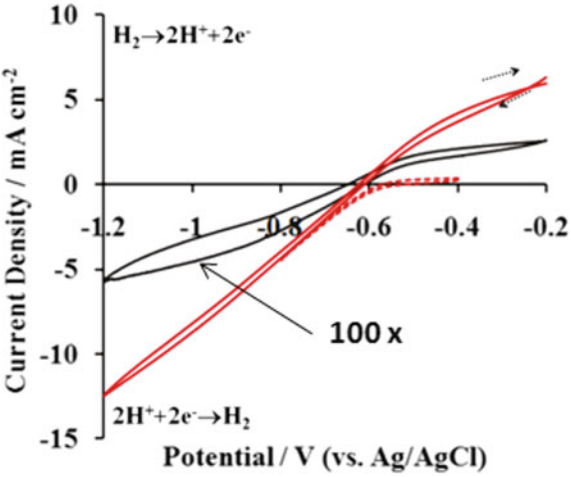

Fig. 9 CVs for CaH_2ase immobilized on electrode of bare C-cloth (black) and C-cloth composite 84% m-SWNT (red)

CVs of these materials demonstrate that the current by using a C-cloth/SWNT electrode (84% m-SWNT) are enlarged more than 200-fold that of the bare C-cloth electrode. Under the experimental conditions, points of zero current for C-cloth/CaH_2ase and C-cloth/SWNT/CaH_2ase electrodes (from Fig. 9) occur at potentials of −0.633 and −0.622 versus Ag/AgCl, respectively. This result demonstrates that the addition of the SWNT network does not change the CaH_2ase operating potential or the Hþ/H_2 equilibrium on the electrode surface.

Figure 10 contains plots that show the dependence of CaH_2ase-based electrode performance. The data show that films with higher m-SWNT content display higher catalytic currents at fixed SWNT coverage. Additionally, the current density increases with the amount of SWNTs. The change in current density of the highest m-SWNT is the largest. The results suggest that the CaH_2ase on s-SWNTs does not affect the externally measured catalytic current as much as it does on m-SWNTs.

4.1.2 Carbon Dots

Comparing with traditional semiconductors [128–130], quantum dots [68, 131–133] metal-free light harvesters have lower toxicities and costs. Their high water dispersibilities [134–136], photostabilities, and tunabilities of absorption above 600 nm [137] make carbon dots (CDs) exceptional in this group for use as photosensitizers in solar fuel production systems [138–144]. These features have motivated studies of their biotechnological applications [145–147]. Compositing CDs and hydrogenases is a promising strategy to create biohybrid systems for hydrogen production [148]. Hydrogenases are specific proteins that contain abundant active sites. Thus, they require pathways for electron and proton shuttling [149–152].

In one recent study, Katerina Hola et al. prepared CDs for use as the photosensitizer to drive reactions of the artificially maturated [FeFe] hydrogenase (Fig. 11) [153].

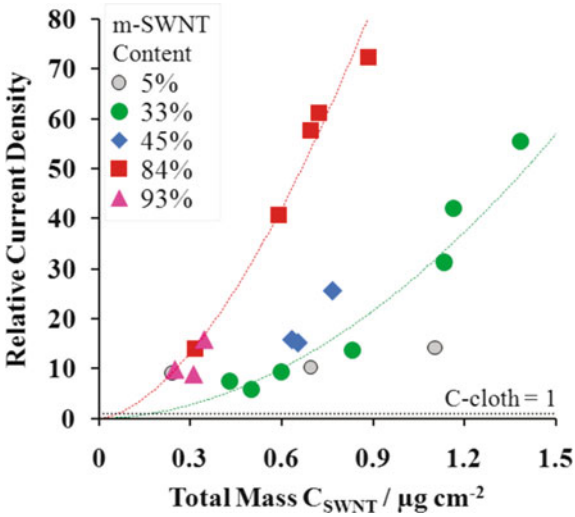

Fig. 10 Proton reduction current density curves of CaH_2ase immobilized C-cloth electrode with increasing the amount of m-SWNT

The possibility of producing the [FeFe] hydrogenase using standard heterologous expression technologies also significantly simplifies the catalyst production.

The negative charges on the surfaces of the L-aspartic acid (AspCD) particles provide an ideal interface for inducing the [FeFe] hydrogenase. Specifically, CrHydA1, [FeFe] hydrogenase from Chlamydomonas reinhardtii, is positively charged which is near its active site (Fig. 12), which serves as an ideal site for attachment to the CDs. Because CDs are smaller than the hydrogenases, the possibility exists that several CDs interact with the hydrogenase to form numbers of light-harvesting centers. However, considering the size of the CDs and that of the

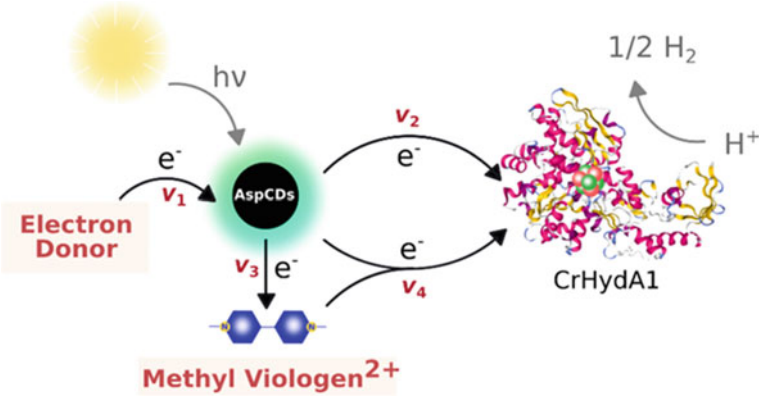

Fig. 11 Schematic of biohybrid system with CDs and hydrogenases for hydrogen production

positively charged area (see Fig. 12c), it is likely that at most two CDs are close enough to the active site to participate in the transmission of electron.

In both the presence and absence of the MV^{2+}, H_2 production is promoted by the biohybrid AspCDs/CrHydA1 when various sacrificial electron donors are employed. In the system using EDTA as the sacrificial donor, the produced hydrogen during the first hour of light illuminating is 0.14 ± 0.05 μmol and it increases by a factor of 6 (0.77 ± 0.08 μmol H_2) when MV^{2+} is present as the mediator. This result indicates that the electrostatic interaction is not sufficient to promote direct electron transfer to the enzyme. In contrast, the process occurring in the presence of TEOA has a higher H_2 evolution efficiency during the first hour in the absence of MV^{2+} (0.62 ± 0.11 μmol) than when this mediator is present (0.33 ± 0.09 μmol) (Fig. 13a). These results show that the negative charged AspCD interact strongly with the positive charged CrHydA1 as compared to those not containing EDTA. Because the pH of the solution is identical in the two cases, the difference in photocatalysis is likely associated with the nature of the sacrificial electron donor.

The results of assays show that the AspCDs and CrHydA1 hybrids along with electron donors (EDTA) and the redox mediators (MV^{2+}) produce H_2, at which time the hydrogen accumulation plateaus when MV^{2+} is absent (Fig. 13). The observation

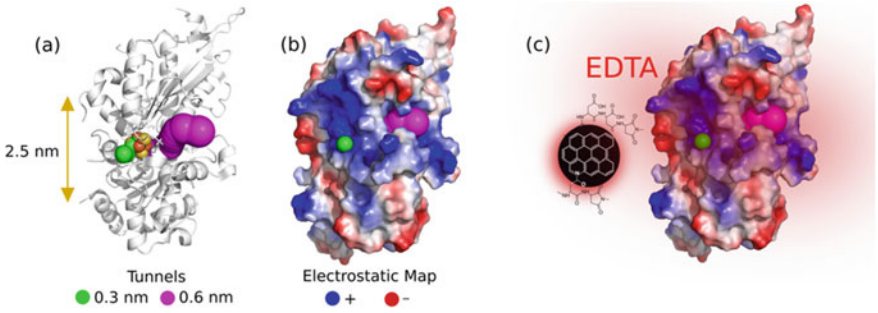

Fig. 12 **a** Crystal structure model of CrHydA1); **b** Electrostatic map of CrHydA1; and **c** Influence of EDTA on the interaction between AspCDs and CrHydA1

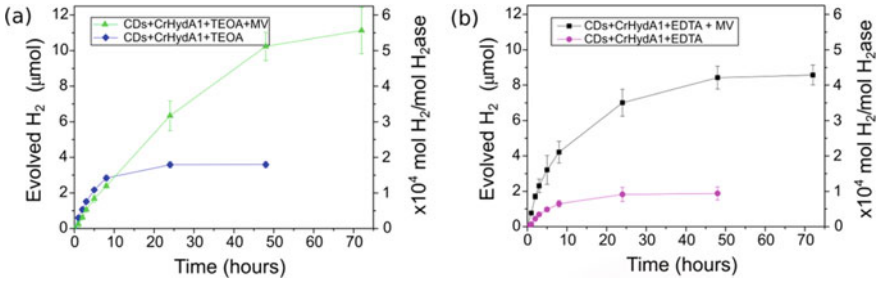

Fig. 13 Hydrogen evolution under light illumination of the hybrid system of AspCDs and CrHydA1 in the present of TEOA (**a**) or EDTA (**b**) with and without MV^{2+}

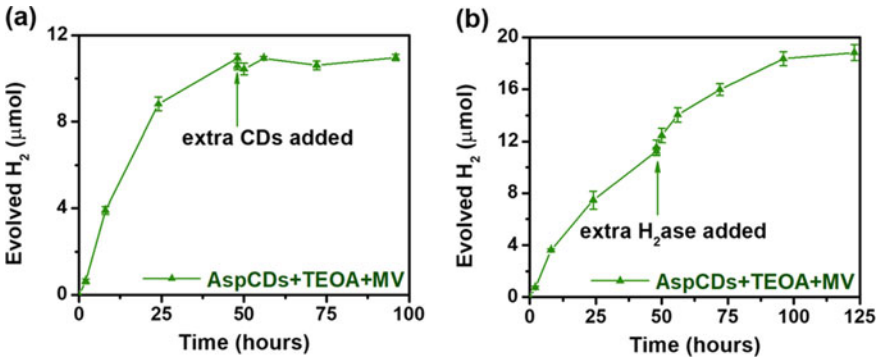

Fig. 14 Hydrogen evolution of hybrid electrode in the presence of TEOA and MV^{2+} by adding extra AspCDs (**a**) or CrHydA1 (**b**)

that the presence of excesses of either AspCDs or CrHydA1 does not elongate the time over which hydrogen evolution takes place shows that both AspCDs and CrHydA1 are deactivated over extended operation times. In contrast, MV^{2+} increases the stability of the artificial system by enabling almost linearly increasing hydrogen production (Fig. 13a). In accord with this proposal is the finding that adding new AspCDs with MV^{2+} after hydrogen production ceases has only a negligible effect on extending hydrogen evolution (Fig. 14a), but hydrogen production is restarted by addition of CrHydA1 (Fig. 14b).

4.1.3 TiO_2

In microalgae and cyanobacteria, H_2 is produced via a [FeFe]hydrogenase ([FeFe]-H_2ase), which catalyzes reduction of protons to form H_2 [154]. A semi-artificial hybrid comprised of PSII and H_2ase has been developed for light-driven water splitting that does not require the participation of PSI. This design of PEC, inspired by the features of dye-sensitized solar cells [155], enables replacement of PSI by a rationally designed diketopyrrolopyrrole (dpp) dye having an absorption profile complementary to that of PSII. The PEC system, which does not require dual light absorption, contains a tandem photoanode consisting of PSII connected to the dye-sensitizer TiO_2. Efficient electron transfer between PSII and dpp was realized by adding the polymer poly(1-vinylimidazole-co-allylamine)-Os(bipy)$_2$Cl (P_{Os}).

Measurements showed that the new PEC tandem cell has a photoanodic current onset potential of approximately −0.5 V versus the standard hydrogen electrode (SHE) (Fig. 15). The IO-TiO_2@dpp@P_{Os}-PSII electrode shows a more than 0.5 V shift towards negative potential. This property makes the new electrode a promising candidate for use in overall water splitting. Studies showed that potential-independent steady-state photocurrent occurs at Eapp > −0.2 V versus SHE (Fig. 15b).

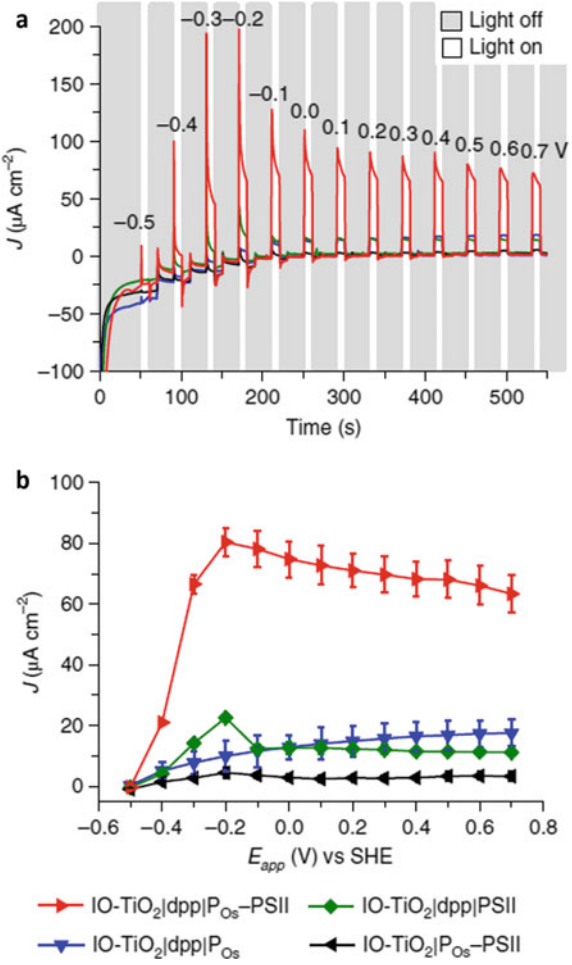

Fig. 15 **a** Chronoamperometry curves of different electrodes in cycles with light on or off. **b** Photocurrent density of different electrodes

Control systems containing only one component of the photoanode exhibit only marginal photoactivity. The small background photoresponses arising from IO-TiO_2@dpp@PSII and IO-TiO_2@dpp@P_{Os} (Fig. 15), and their similarity to the response of IO-TiO_2@dpp are associated with the occurrence of stoichiometric electron transfer from photoexcited dpp (dpp*) to TiO_2 without regeneration and photocatalytic turnover of the dye. The observation of a low photocurrent arising from the system lacking P_{Os} (IO-TiO_2@dpp@PSII) supports the conclusion that an insufficient direct electronic interaction exists between PSII and dpp when the redox polymer is not present. Also, no significant photocurrents arise from systems lacking dpp (IO-TiO_2@P_{Os}-PSII (Fig. 2), IO-TiO_2, IO-TiO_2@P_{Os}, and IO-TiO_2@PSII).

These findings are in accord with the more positive reduction potentials of PSII's QB and P_{Os} relative to the CB of TiO_2, which causes unfavorable electron transfer. Observation made in studies of the newly developed semi-artificial system demonstrates that a functional biotic–abiotic interface can be assembled for controlled electron transfer in an artificial Z scheme.

IO-TiO_2, IO-TiO_2@P_{Os}, IO-TiO_2@PSII, and IO-TiO_2@P_{Os}—PSII produced negligible photocurrents under all wavelengths of monochromatic light illumination (Fig. 16a). PSII-free electrodes loaded with dpp gave photocurrent responses that match the absorption spectrum of dpp, showing that the origin of background current is photooxidation of dpp. For the IO-TiO_2@dpp@P_{Os}-PSII system, the photocurrent onset occurred at $\lambda = 620$ nm with a maximum being reached at approximately 560 nm, which are consistent with the overlapping absorption spectra of PSII and dpp, and the requirement for simultaneous excitation of both components.

For the purpose of probing dpp, continuous excitation of PSII (t) in IO-TiO_2@dpp@P_{Os}-PSII (Fig. 16b) was carried out. This led to a wavelength dependent action profile that mimics the UV–vis spectrum of dpp and the results of single-wavelength excitation experiments. In comparison to the latter, the scan profile contains a maximum at $\lambda = 550$ nm, but the magnitude of the photocurrent is 40% higher. The overall dual excitation promoted photocurrent cross-section (Fig. 16b) is approximately two times higher than those of the individual components (Fig. 16a).

An artificial PEC cell was constructed using an IO-TiO_2@dpp@P_{Os}-PSII photoanode and an IO-ITO@H_2ase cathode separated by a glass frit membrane. The data in Fig. 17 demonstrate that this system promotes solar-driven water splitting. Chronoamperometry measurements over longer irradiation times (Fig. 17a) were performed to minimize charging effects. Upon simulated solar light irradiation, the system has a current density of 28 ± 5 μA cm^{-2} at an applied voltage (Uapp) 0 V (Fig. 17b). The magnitude of the photocurrent is similar to that of a two-electrode system comprised of a Pt rather than an IO-ITO@H_2ase cathode. This finding is consistent with the photocurrent limitation by IO-TiO_2@dpp@P_{Os}-PSII. Comprised of an IO-TiO_2@H_2ase cathode, the two-electrode system was observed to exhibit similar behavior, even though less charging occurred because of the matched Fermi levels of IO-TiO_2.

After one hour of continuous light irradiation of the semi-artificial PEC device at Uapp = 0.0 V, H_2 is generated (0.06 μmol H_2 cm^{-2}) with a Faradaic efficiency (ηF) of 76%. However, a reliable analysis of formed O_2 can not be performed because of the detection limit of the apparatus. At Uapp = 0.3 V, O_2 and H_2 evolutions (Fig. 20c) were $\eta F = 88 \pm 12\%$ and $82 \pm 10\%$, respectively, and the solar-to-hydrogen conversion efficiency is about $0.14 \pm 0.02\%$. The PSII-based turnover frequency was 2.5 ± 0.3 mol O_2 (mol PSII)$^{-1}$ s^{-1}, calculated on the basis of the quantities of O_2 and PSII.

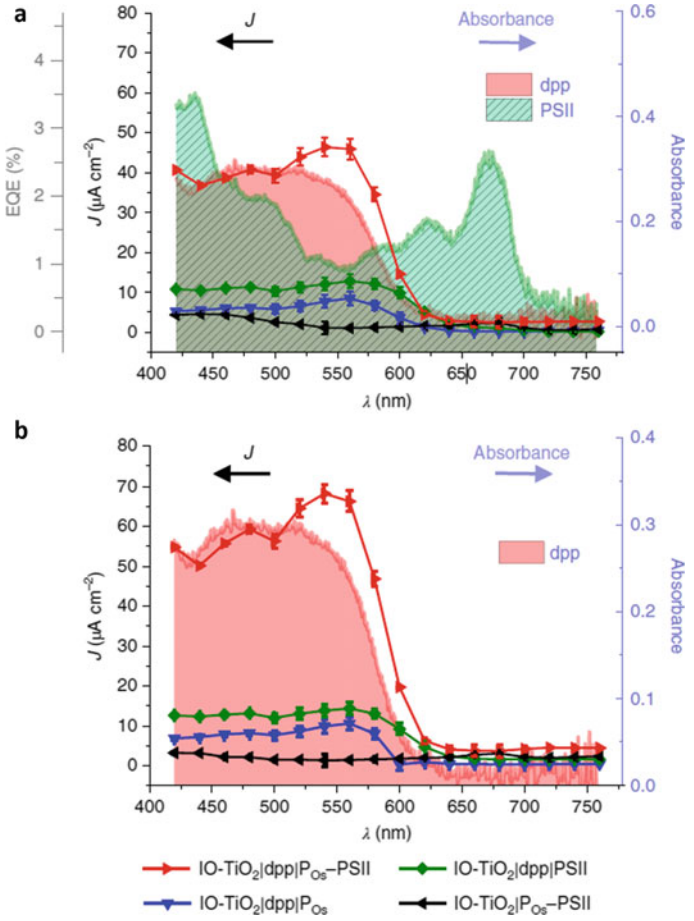

Fig. 16 **a** Single-wavelength photocurrent action spectra and **b** dual-wavelength photocurrent action spectra of PSII-dye photoanodes

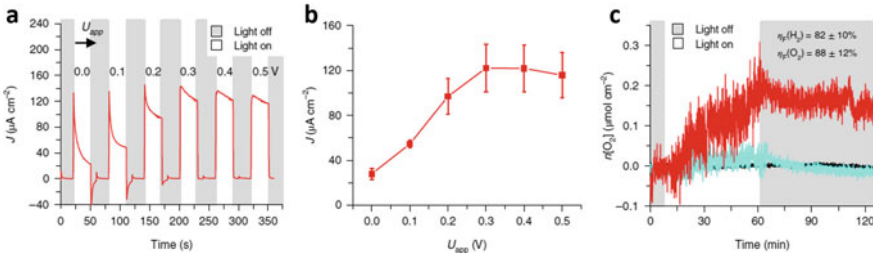

Fig. 17 **a** Chronoamperometry curve of the constructed PEC cell for overall water splitting. **b** Photocurrent density for the constructed PEC cell determined in a. **c** Quantification of O_2 and H_2 evolution at each photoanode

4.2 [NiFeSe]-Hydrogenase

4.2.1 Perovskite

A perovskite-H_2ase photocathode has been developed for use in a water splitting system (Fig. 18) [156]. The photoanode, comprised of an encapsulation that protects the photo-absorber while providing a porous and biocompatible TiO_2 scaffold for the enzyme, is combined with the water oxidation photoanode $BiVO_4$ for bias-free, tandem PEC production of H_2 and O_2. The system takes advantage of the fact that enzymes have been incorporated with high loading into hierarchically structured porous, inverse opal (IO) metal oxide scaffolds.

Linear sweep voltammetry (LSV) of the synthesized PVK@IO-TiO_2@H_2ase electrode showed that it has a cathodic onset potential of +0.8 V versus RHE and a photocurrent density of approximately −5 mA cm^{-2} at 0 V versus RHE. Controlled potential photoelectrolysis (CPPE) of water was conducted at +0.4 V versus RHE, and gas chromatography was used to determine H_2 evolution yields. The CPPE results demonstrated that the photocathode is stabile in that it promotes the water splitting reaction for a 12 h period (Fig. 19b). The electrode fails to work after 12 h, in which water is likely to entry the electrode to break the perovskite. The stability of the equivalent PVK-Pt device was found to be comparable, which indicates that decay of the perovskite limits longevity. The H_2ase electrode generates 258 ± 55 μmol H_2 cm^{-2} of H_2, whereas the enzyme-free counterpart produces <1 μmol H_2 cm^{-2} (Fig. 19c).

The $BiVO_4$ photoanode is used as the current-limiting light absorber (Fig. 20a). Due to the high O_2 resistance of [NiFeSe] H_2ase, the two photoelectrodes directly construct the PEC cell without the separated membrane. Under bias-free condition, the device obtained a current density of about 1.1 mA cm^{-2} and an onset potential

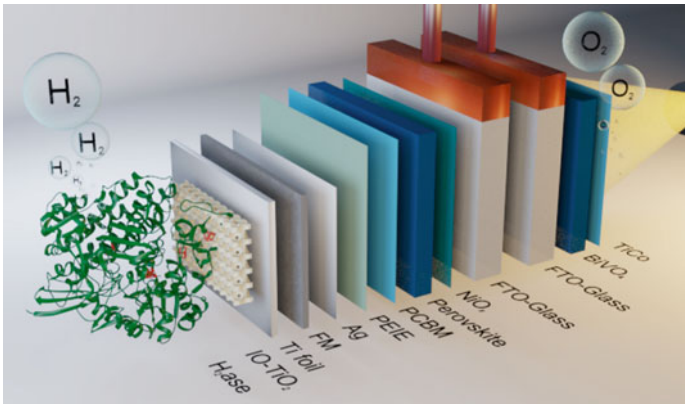

Fig. 18 Schematic of semi-artificial hybrid system consisting of H_2ase, perovskite and $BiVO_4$

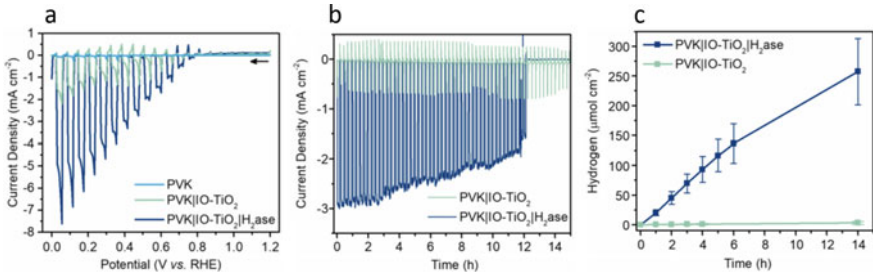

Fig. 19 **a** LSV curve of different photocathodes. **b** CPPE of photocathodes with or without H_2ase. **c** Hydrogen evolution of photocathodes with or without H_2ase

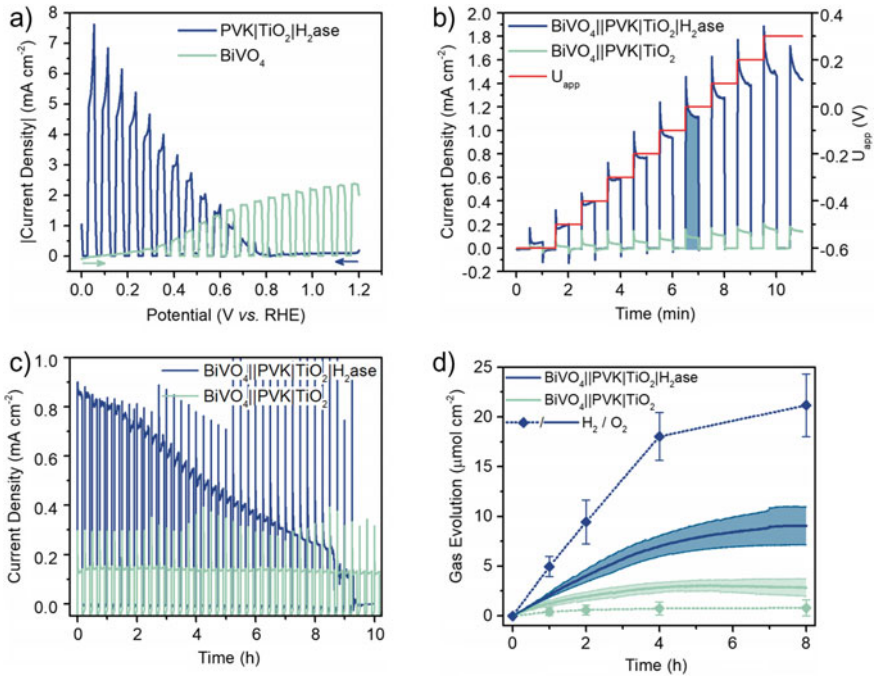

Fig. 20 **a** LSV curves of photocathode and photoanode. **b** Potential chronoamperometry of the constructed device with or without H_2ase. **c** CPPE of the constructed device with or without H_2ase. **d** Hydrogen evolution of the constructed device with or without H_2ase

of about −0.6 V (Fig. 20b). In view of the bias-free CPPE curve, the photocurrent continually decreases over 8 h, because the enzyme desorption, inactivation, or reorientation cause the destruction of film (Fig. 20c). The Faradaic efficiency (FE) of this PEC cell is about 82 ± 3% for H_2 and 50 ± 8% for O_2 (Fig. 20d). The solar-to-hydrogen efficiency of the system is 1.1%.

5 Hydrogen Production by Bacterial-Based Semi-artificial Biohybrids

5.1 Shewanella Oneidensis MR-1

5.1.1 Cu_2O + rGO

Flexible and thin Reduced graphene oxide (RGO) sheets with high specific surface areas and excellent electron transport mobilities serve as an area for efficient electron collection as well as for fast electron migration [157–159]. Thus, in contrast to soluble electron mediators, RGO is a superior solid-state support material for electron relay between different nanoparticles. Moreover, RGO also exhibits high biocompatibility and, as a result, it can be used to effectively bridge cellular MRPs [160, 161] which then distribute electrons into cells. As a result, RGO serves as an ideal support and electron mediator for whole-cell SAPSs for efficient solar H_2 production.

Considering its band position and visible light-promoted photocatalytic activity, Cu_2O is an ideal semiconductor for SAPSs construction [162–164]. Based on this knowledge, Hongqiang Shen et al. designed an RGO-supported SAPS, in which the RGO is used as the electron collector between semiconductor nanoparticles and cells by efficiently wiring the MRPs (Fig. 21) [165]. This guarantees that collected electrons are efficiently distributed into the cells. Specifically, in the Cu_2O/RGO/SW SAPSs, RGO enables efficient electron flow between Cu_2O and SW cells, which should lead to efficient solar H_2 production.

In the fabrication process, Cu_2O/RGO nanocomposites entrapped SW cells through the hydrophobic interactions by simple mixing. Transmission electron microscope (TEM) and scanning transmission electron microscope (STEM) indicated that both the Cu_2O nanosheets and SW cells are supported on RGO. CLSM analysis of the Cu_2O/RGO/SW SAPSs showed that cell viability is maintained demonstrating that the Cu_2O/RGO/SW SAPSs fabrication process is viable and biocompatible (Fig. 21g). The SAPSs show the 46–80-fold higher hydrogen production performance (about 322.0 μmol/g Cu_2O) than those of Cu_2O and Cu_2O/RGO (Fig. 22). To explore the role played by RGO in the SAPSs, the formed Cu_2O/SW SAPSs only exhibited a low level of H_2 production of 8.3 μmol/g Cu_2O.

5.1.2 CdS

It is well known that the dissimilar metal reduction bacterium, SW, possesses an extracellular electron transfer (EET) chain, through which in the metal-reducing (Mtr) pathway [80, 166, 167] electrons are delivered to extracellular inorganic materials [168, 169]. However, when the SW is employed as a biocatalyst for reduction reactions like that used in hydrogen production from water, electron transfer between an extracellular semiconductor and bacteria must take place reversibly. SW

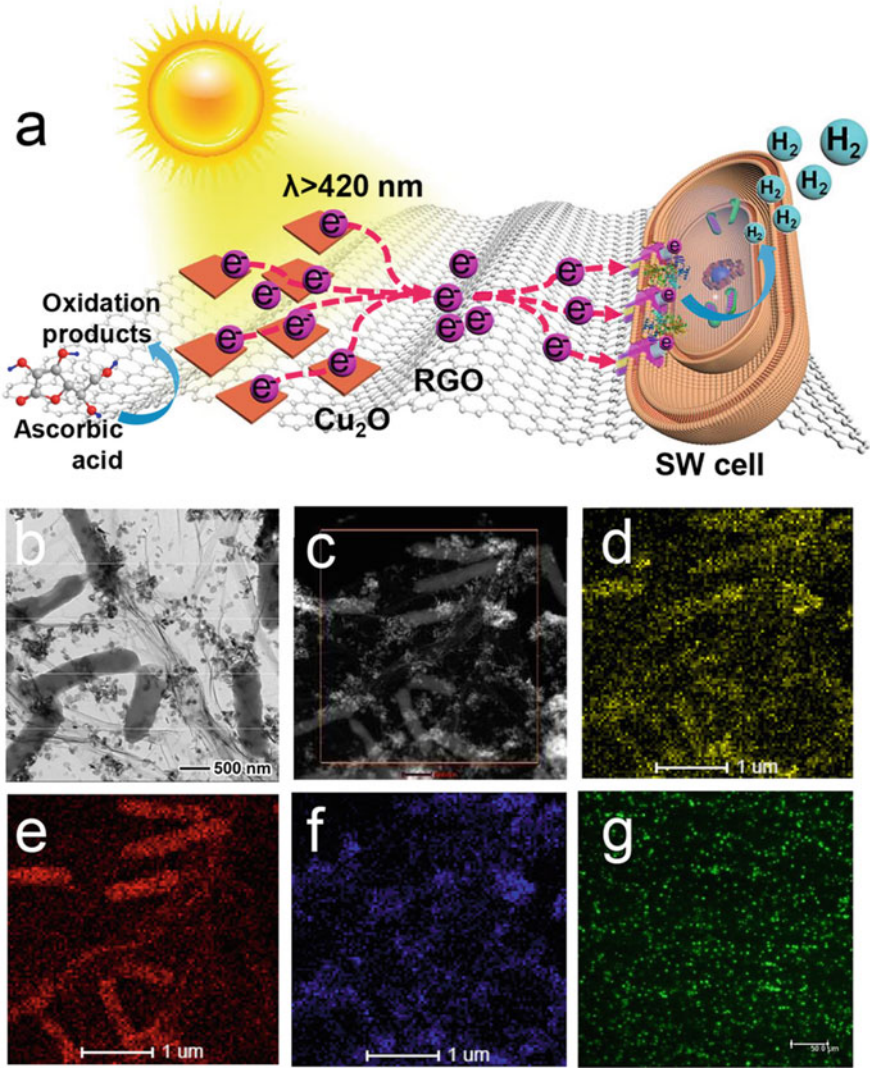

Fig. 21 **a** Schematic of the hybrid system. **b** TEM image of the hybrid system. **c** STEM image and EDS mapping images of **d** O, **e** C, and **f** Cu. **g** CLSM image of this hybrid system

contains two periplasmic hydrogenases [170], which accept electrons from an extracellular semiconductor [171]. Although remaining largely unnoticed, these observations suggest that it should reverse the EET chain of SW by using a biotic-abiotic system with semiconductor nanoparticles. Also, owing to its powerful reducing and detoxification capacities, SW serves as a bio-nano-factory for fabricating multifunctional nanoparticles [172, 173]. This enables its use in hybrid photosynthetic systems employed in fundamental mechanistic studies.

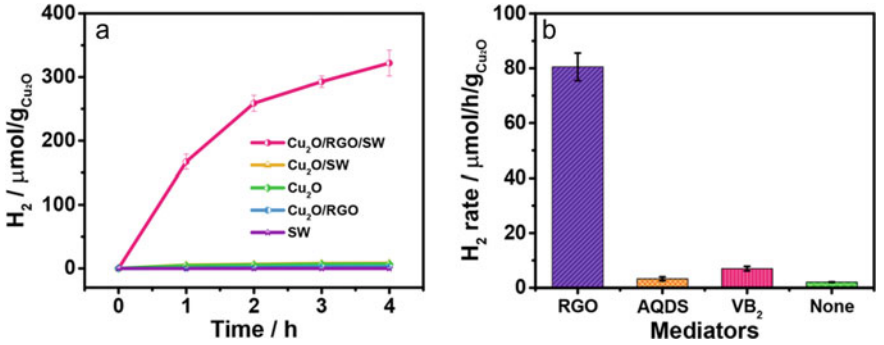

Fig. 22 **a** Light-driven H_2 production of each material under the light. **b** Average rate of H_2 production using different various electron mediators

In a recent proof of concept study, a hybrid photosynthetic system in which SW is coupled with biogenic CdS nanoparticles was constructed (Fig. 23) [174]. In the SW-CdS photosynthesis mimicking system, biogenic CdS nanoparticles cause SW to be active in light-driven hydrogen generation. The results of this study, detailed below, show that the contribution and direction of EET in the biotic–abiotic photosynthetic system are well defined, highlighting its key role in light-driven hydrogen generation. The results provide important insight into the design of biotic-abiotic photosynthetic systems.

Inspection of a TEM image of SW CdS nanoparticles shows that the formed nano-sized particles are located mainly in the extracellular space and are attached to the outer membranes of the cells for the most part (Fig. 24a). The magnified TEM image (Fig. 24b) shows that few biosynthesized nanoparticles (1 ± 1.4 nm) are in the periplasm of SW cells. Energy dispersive spectroscopy (EDS) revealed that the

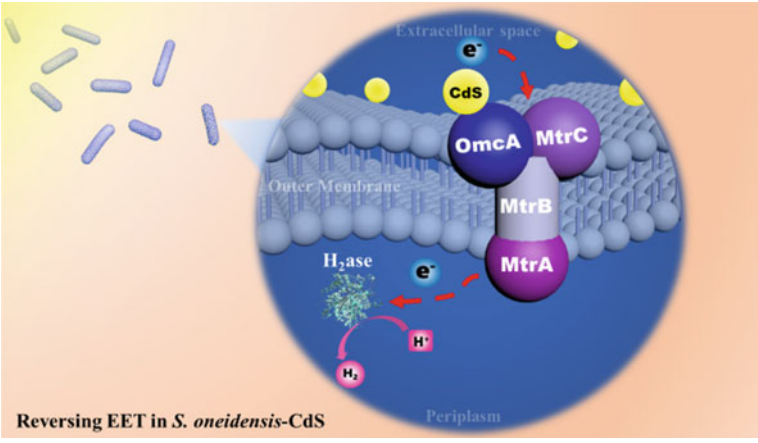

Fig. 23 Electron transfer route for hydrogen production in biohybrid systems

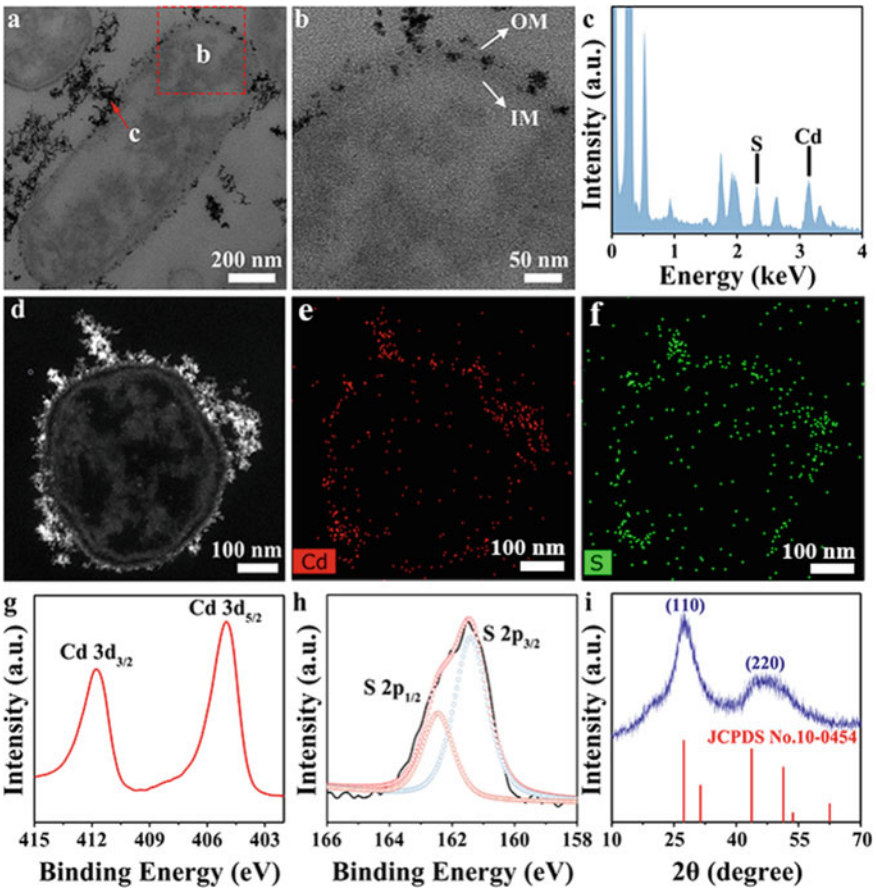

Fig. 24 **a**, **b** TEM iamge of SW-CdS. **c** EDS spectrum of particles on cells. **d**–**f** STEM image and EDS mapping of SW-CdS: **e** S and **f** Cd. XPS of CdS: **g** Cd 3d and **h** 2p. **i** XRD of CdS

major components are Cd and S in an approximate 1:1 ratio (Fig. 24c). To determine the location of CdS nanoparticles more precisely, high-angle angular dark field-scanning transmission electron microscopy–energy-dispersive spectroscopy (HAADF-STEM-EDS) mapping was performed on the hybrid photosynthetic system (Fig. 24d–f). As expected for microbial cells, signals associated with P arise from the entire cell. In comparison, S and Cd are annularly arranged around the cell (Fig. 24e,f), confirming that assembled CdS nanoparticles are located both in the extracellular space and within the periplasm of SW.

A high hydrogen generation efficiency under light illumination is achieved by using SW-CdS (Fig. 25a). After 72 h illumination, the total hydrogen yield promoted by SW-CdS is about 362.44 ± 119.69 μmol/mg, which is about 711-fold higher than that produced by using only SW (0.51 ± 0.13 μmol/mg) and 4.36-fold higher than that generated by SW (dead)-CdS (83.05 ± 17.08 μmol/mg). The results reveal that

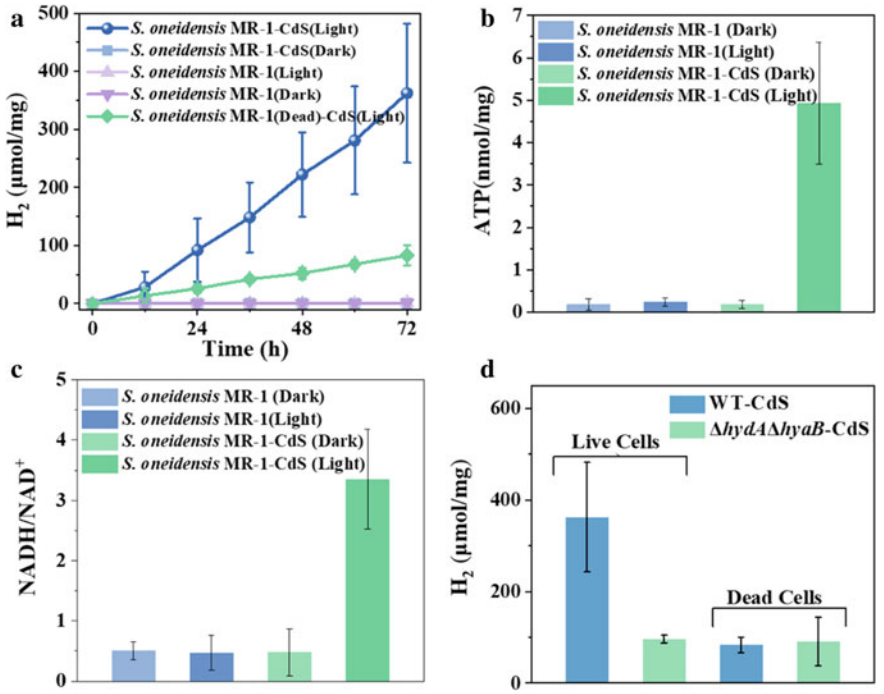

Fig. 25 **a** Hydrogen production of SW with or without CdS in dark or light. **b** ATP level of different experiments under 72 h irradiations. **c** NADH/NAD^+ ratio assay of different experiments. **d** Hydrogen production of WT-CdS and *ΔhydAΔhyaB* with live or dead cells

a synergistic effect between SW and CdS nanoparticles in the hybrid photosynthetic system facilitates hydrogen production. Specifically, bacteria-promoted activity for hydrogen generation is activated by the illumination of self-anchored semiconductors. During the 72 h process, hydrogen generation by SW-CdS exhibits a nearly linear relationship with time, and an average rate of 5.03 ± 1.67 μmol/(mg h). Thus, the SW-CdS photosynthetic system performs highly efficiently and has high stability. To investigate whether the photoexcited electrons can be delivered from the biogenic CdS nanoparticles to create cellular energy, intracellular ATP and NADH/NAD + ratios in different groups were determined after 72 h illumination (Fig. 25b, c). The highest ATP and NADH/NAD + ratios were obtained using the WT-CdS photosynthetic system under light illumination, indicating that CdS-generated photoexcited electrons can be taken up and converted into cellular reducing power and a proton motive force (PMF). In this and a previous study, Hexing Han et al. showed that SW cells transmit electrons from the electrode to activate oxygen reduction in a way that enables the production of cellular energy.

5.1.3 $CuInS_2$/ZnS Quantum Dots

A novel approach to the design of artificial photosynthetic biohybrids for hydrogen production utilizes whole cells expressing hydrogenases. These systems should have advantages over those employing purified hydrogenases due to their ease of fabrication and high stability. Thus far, two general types of whole-cell based biohybrid systems have been developed, one based on an extracellular photosensitized biohybrid and the other a cytoplasmic photosensitized biohybrid [175, 176]. In the extracellular photosensitized biohybrid, electrons are delivered from excited states of extracellular photosensitizers to the hydrogenase in the cell through redox mediators or membrane-bound redox-active proteins. However, because it is a transmembrane process, electron transfer is slow. In the cytoplasmic photosensitized biohybrid system, interfacial electron transfer between the excited photosensitizer and enzyme occurs in the cytoplasm, thereby avoiding energy loss because it is not a transmembrane process. Also, it is known that gram-negative bacterial cells have periplasmic space between the outer membrane and cytoplasm [177]. Compared with the cytoplasm, the periplasm is located close to the outer membrane, making light absorption by its constituent photosensitizer favorable. Furthermore, locally high hydrogenase concentrations exist in the periplasm space, which causes electron transfer between the hydrogenases and excited photosensitizer to take place more rapidly. Recognition of these features gives new insight into strategies for the development of more efficient whole-cell biohybrid systems.

In a recent effort, Bifu Luo et al. fabricated SAPSs by mixing biocompatible quantum dots with a cell that expresses hydrogenases in its periplasm [171]. The system QDs/SW SAPSs, comprised of $CuInS_2$/ZnS quantum dots (QDs) and SW cells (Fig. 26), displays continuous H_2 production under visible light irradiation at higher levels than those of bare QDs or SW cells.

Confocal laser scanning microscope (CLSM) images of fabricated QDs/SW SAPSs showed that red fluorescence of the QDs is well dispersed in the SW cells (Fig. 27b). In addition, a TEM image of a cross-section slice was employed to show that periplasm of the SW cells contains dispersed QDs (Fig. 27c, d) as a likely

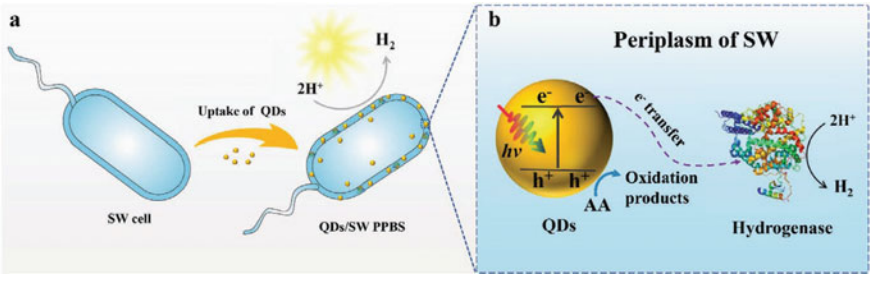

Fig. 26 **a** The synthesis of QDs/SW SAPSs. **b** The electron transfer between QDs and hydrogenase

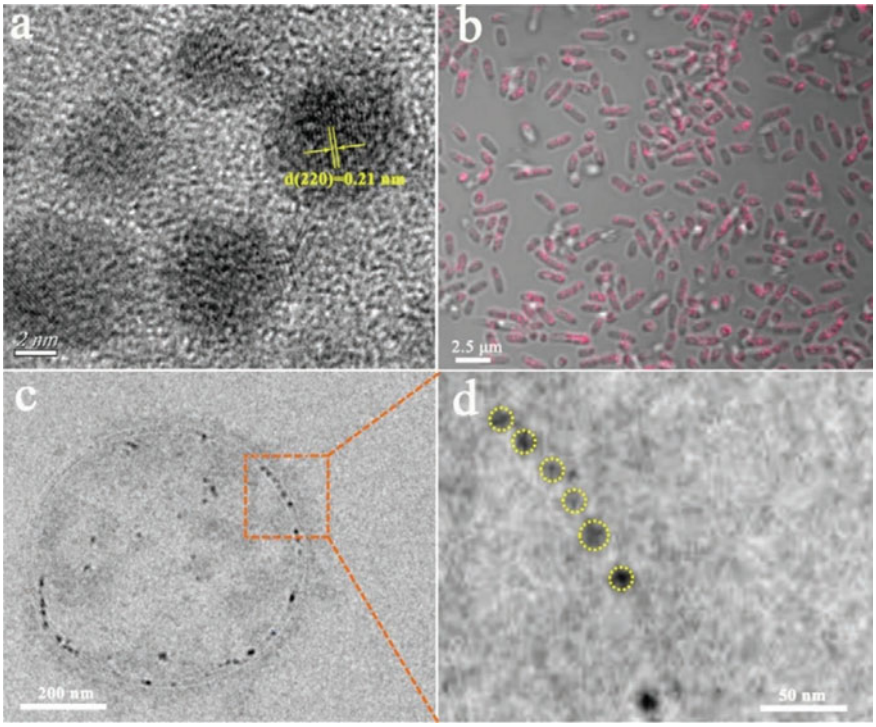

Fig. 27 **a** TEM graph of QDs. **b** CLSM graph of cells composited with QDs. **c** TEM graph of QDs/SW SAPS. **d** TEM graph of QDs on the SW cell

consequence of binding between zinc in the ZnS shell of QDs and Fe-S clusters in the hydrogenase.

As illustrated in Fig. 28a, H2 is not generated by using either irradiating bare SW cells or QDs/SW SAPSs in the dark. H_2 production by bare QDs is 57 0.2 ± 8.6 μmol under visible light irradiation for 9 h. Under the same conditions, QDs/SW SAPSs display a superior H_2 production (491.8 ± 26.6 μmol), which is 8.6-fold higher than that of bare QDs. The optimized apparent quantum efficiency (AQE) of QDs/SW SAPSs reaches 15.02% when irradiated at 475 nm. Long-term monitoring (Fig. 28b) showed that H_2 production increases in a nearly linear fashion with respect to irradiation time up to 45 h. This indicates that the durability of QDs/SW SAPSs is about 1.2 times longer than that of the most CdS/*E. coli* whole-cell biohybrid system reported to date. The viability of bacteria in the SAPSs was demonstrated by using fluorescence microscope analysis under light irradiation (Fig. 28c). However, in contrast to the observation that no bacteria are destroyed after 13 h irradiation, prolonged irradiation for 48 h brings about nearly complete bacterial death, mainly because of the occurrence of hole oxidation and a lack of an energy source for maintaining cell metabolism. This observation contrasts with previously reports indicating whole-cell hybrid system does not maintain H_2 production for more than 20 h, The

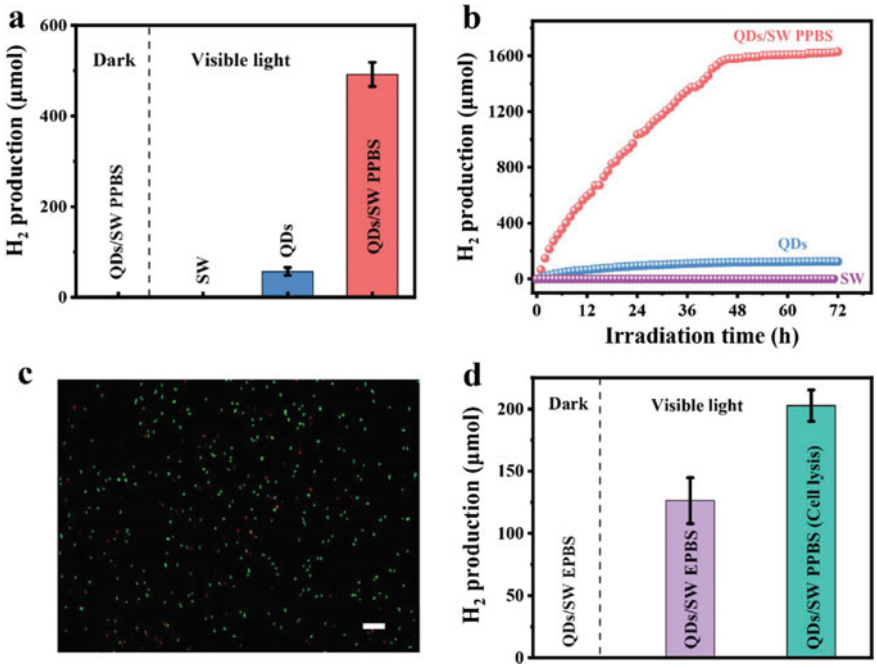

Fig. 28 **a** H_2 production of different groups. **b** H_2 production of different groups under long-time irradiation. **c** Fluorescence microscope graph of QDs/SW SAPSs after strained with LIVE/DEAD assay kit. Scale bar, 20 μm. **d** H_2 production of SAPSs with extracellular and intracellular QDs

long-term viability can be attributed to the high biocompatibility of QDs as well as the minimization of damage caused by visible light. resulting in the sustained hydrogen production capacity of QDs/SW SAPSs, where the p. To show that a large local concentration of hydrogenases in the periplasm of SW cells is responsible for the high efficiency, cells in QDs/SW SAPSs were lysed and H_2 production was then determined. Indeed, H_2 production decreased to 202.7 ± 12.6 μmol, suggesting that the unique periplasmic location results in a high hydrogenase concentration. More importantly, intracellular QDs in the periplasm are close to the hydrogenase which facilitates electron transfer and consequent improvement of the charge transport efficiency.

5.2 Escherichia Coli

5.2.1 CdS

In a recent study, Wang et al. designed a whole-cell *E. coli-CdS* hybrid system for efficient biological hydrogen production that utilizes the endogenous bacterial

[Ni–Fe]-hydrogenase and electrons photogenerated by CdS, which is present in the form of precipitated sulfide complexes as a precipitate on the bacterial cell surface (Fig. 29) [178]. TEM images of both freeze-dried and thin-sectioned samples of the *E. coli*-CdS hybrid showed that high densities of nanosized particles are present on the surface, and high-resolution TEM (HRTEM) images revealed that these nanoparticles are distributed across the periplasmic space of the *E. coli* membrane and that half of the nanoparticle surface is exposed to the extracellular environment. The precipitated nanoparticles have an average size of about 15–20 nm. In addition, scanning electron microscope (SEM) images and X-ray spectroscopy (EDX) analysis showed that protruding nodules of CdS particles exist on the cell surface of *E. coli*.

The study by Wang et al. demonstrated that about 1400 μmol of hydrogen is generated from untreated *E. coli* culture under dark conditions. In contrast, the amount generated using the *E. coli*-CdS hybrid system is slightly lower when the system is irradiated with visible light (VL) with an intensity lower than 500 W m^{-2}. However, the hydrogen generation significantly increased with increasing VL intensity and reaches a maximum at an intensity of 2000 W m^{-2}. This amount corresponds to an increase of ~30% over that of untreated E. coli. Hydrogen produced from both the untreated *E. coli* culture and the hybrid system over 3 h decreases with increasing light intensities higher than 2000 W m^{-2}. However, hydrogen production from the hybrid system is still significantly ($p < 0.05$) higher than that of the control. In addition, hydrogen production using CdS nano particles, isolated from the hybrid, increases

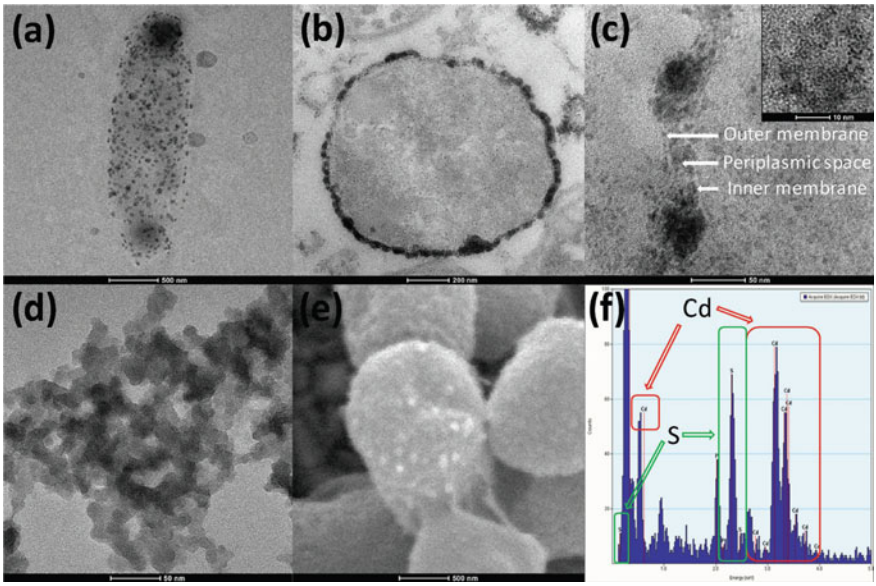

Fig. 29 **a** TEM image of *E. coli-CdS* hybrid system. **b** TEM image of the thin-section of the hybrid system. **c** TEM image of nanoparticles on cell surface. **d** TEM image of synthesized CdS. **e** SEM image of nanoparticles on cell surface. **f** EDX analysis of CdS nanoparticles

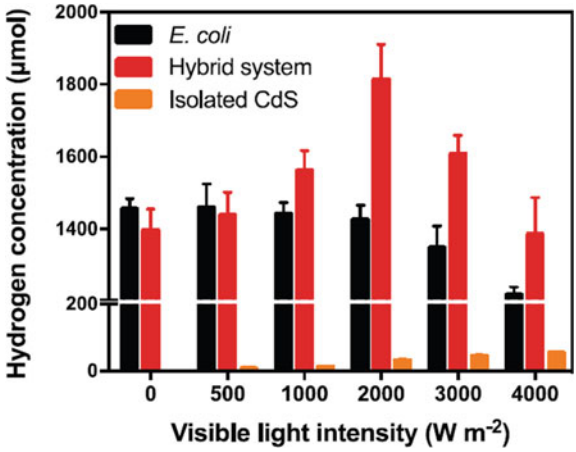

Fig. 30 Hydrogen production of synthesized hybrid system and controls

with increasing light intensity to a lesser extent than that of the hybrid system under the same conditions. From a material chemistry point of view, the results suggest that the hydrogen production efficiencies of semiconductors are significantly enhanced by incorporating them into biological hybrids (Fig. 30).

Information about the mechanism for electron transfer in this biohybrid comes from the observation that no hydrogen is generated by the heat-treated hybrid system (Fig. 31). This finding indicated that the surface CdS of the hybrid system does not generate hydrogen in the absence of the biological components and that additional hydrogen evolution is not directly generated by surface CdS promoted water electrolysis. This outcome might be partially due to hydrogen bonding between water molecules and e organic components of bacterial cells, such as phospholipids and peptidoglycans. It was also found that an increase in the concentration of Cr(VI), a widely used electron scavenger in photocatalysis studies, causes a decrease in extra hydrogen evolution. This observation suggests that the interaction between photogenerated electrons and *E. coli* is inhibited by Cr(VI) and totally quenched by 0.5×10^{-3} M Cr(VI). In addition, compared with hydrogen production promoted by irradiation of untreated *E. coli* with visible light at 2000 W m^{-2}, the amount of hydrogen evolved from the system comprised of untreated *E. coli* mixed with isolated CdS nanoparticles id not significantly enhanced. The results show that close contact between the CdS nanoparticles and *E. coli* is essential for electron migration.

The photoexcited electrons produced by light absorption by surface CdS particles can interact with bioactive components for injection into the hydrogen production pathway (Fig. 32). A portion of these electrons can take part in glycolysis, which results in higher levels of pyruvate formation. The lactate fermentative pathway can also be inhibited by the photogenerated electrons, leading to a lower consumption of pyruvate and a consequent a higher concentration of formate. This process would enhance FHL activity, leading to more rapid consumption of formate and a

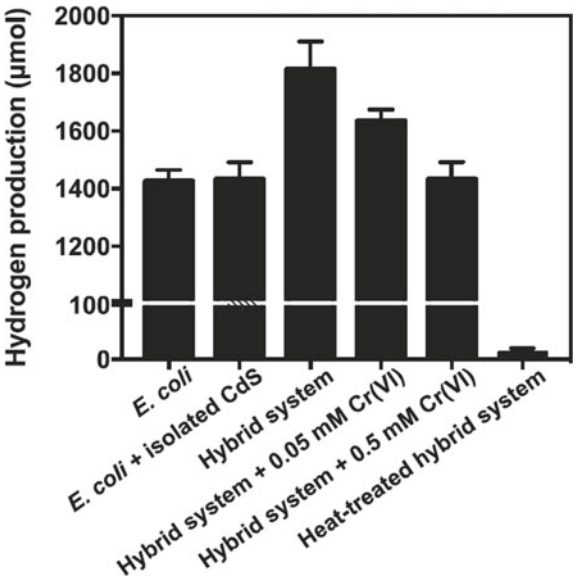

Fig. 31 Hydrogen production of different systems under various treatments

higher hydrogen production efficiency. In addition, an elevation of the intracellular NADH/NAD ratio caused by the photogenerated electrons could also benefit the hydrogen production process.

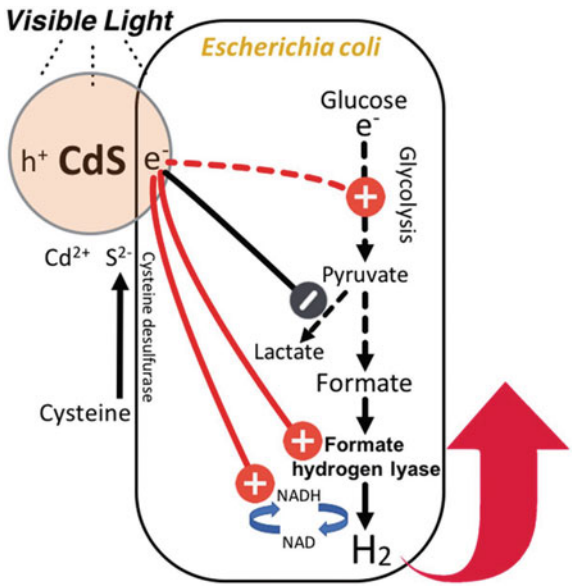

Fig. 32 Schematic of the electron transfer from solar light to cell for hydrogen production

5.2.2 CdS + Silica

Zhao et al. devised a whole-cell photocatalytic hydrogen production system that is comprised of a biocompatible light-capturing inorganic semiconductor, engineered E. coli cells as a biocatalyst, and a protective shell against oxygen. Guided by this study, Wei Wei and co-workers recently developed engineered E. coli cells for photocatalytic hydrogen production under aerobic conditions (Fig. 33) [113]. The system combines the biosynthetic capability of CdS nanoparticles with surface-displayed heavy metal-binding proteins and biocatalysis by oxygen-tolerant [Ni–Fe]-hydrogenase. The fusion protein expression plasmid, including the *E. coli* outer-membrane protein A (OmpA) and the PbrR protein, was transformed into *E. coli* strain BL21. Expression of PbrR protein on the surface of *E. coli* cells was induced using arabinose, and precipitation of CdS nanoparticles on the cell surface was trigged by adding Cd^{2+} to the culture medium. As the TEM images show, Cd^{2+} accumulates on the cell surface as <50 nm uniform nanoparticle clusters. Furthermore, EDX analysis of a randomly chosen area containing the CdS nanoparticles confirmed the elemental composition.

Trace amounts of H_2 are produced by the engineered *E. coli* cells in the presence or absence of CdS in the absence of light as a result of anaerobic fermentation mediated by the endogenously expressed hydrogenase (Fig. 34). However, under illumination by a 350-W Xe lamp, the engineered *E. coli* cells (1×10^8) carrying CdS nanoparticles form 13.40 ± 1.20 μmol H_2 after 6 h and up to 81.80 ± 7.39 μmol after 24 h. These values are significantly higher than those of other systems. In addition, the

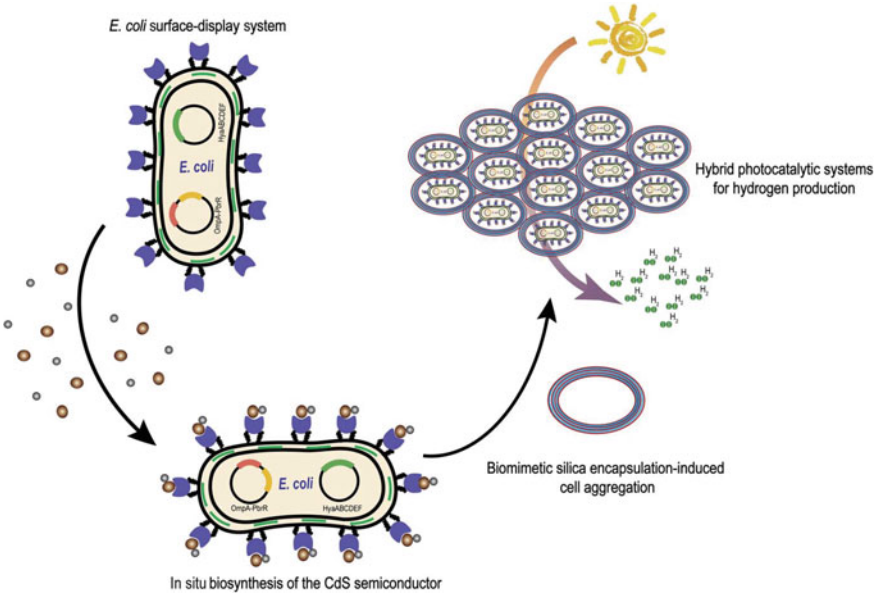

Fig. 33 The synthesis of hybrid photocatalytic system

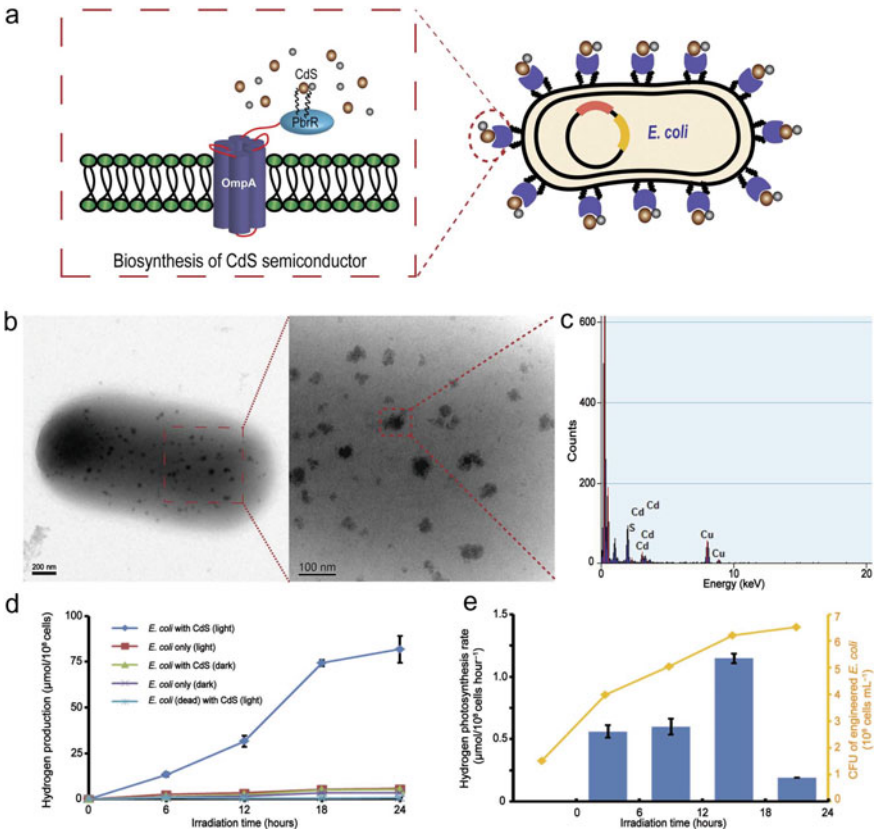

Fig. 34 **a** Schematic of CdS engineered cell. **b** TEM images of hybrid photocatalytic system. **c** EDX analysis of nanoparticle on the cell. **d** H_2 production of different groups under anaerobic condition. **e** H_2 photosynthesis rate under long-time light illumination and relative cell viability

rate of H_2 generation using the hybrid system increases from 0.56 to 1.15 μmol/10^8 cells per hour in the first 18 h and then decreases due to bacterial death (Fig. 34e). The results demonstrate that H_2 production by the newly engineered *E.coli* cell-CdS hybrid system under anaerobic conditions is directly related to the presence of the biosynthesized CdS semiconductor and the activity of the whole-cell biocatalyst.

5.2.3 TiO_2

Balasubramani Ramprakash et al. used this material to create a sodium alginate encapsulated hybrid system (TiO_2/MV^{2+}/*E.coli*) and evaluated its hydrogen production efficiency under aerobic and anaerobic conditions (Fig. 35) [179]. They anticipated that TiO_2 nanoparticles would utilize light energy to generate electrons, which would be transferred into E. coli by the electron mediator (MV^{2+}). Finally, in this

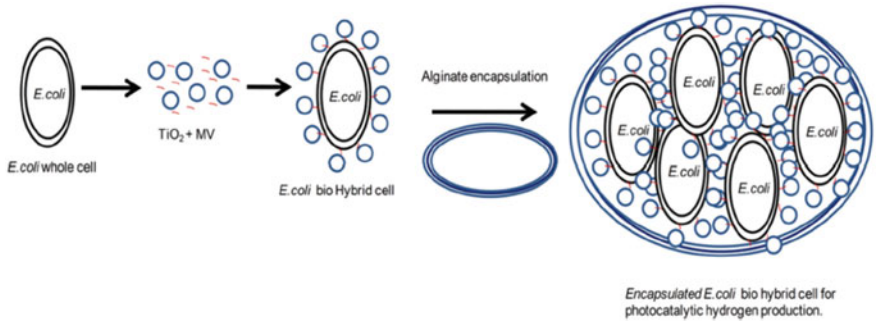

Fig. 35 Schematic of the encapsulated hybrid system

system, the inorganic semiconductor (TiO_2) and *E. coli* (NiFe) hydrogenases are encapsulated to protect against oxygen.

In the effort, *E. coli* cells were grown in LB medium for about 6 h at 37 °C. Then, 200 μL of the preculture was centrifuged for 10 min at 12,000 g to obtain cell pellets, which were resuspended in 50 mL of 50 mM MOPS medium supplemented with 0.375 mM TiO_2 anatase along with 5 mM MV^{2+} (electron mediator) to form the hybrid system. After a desired incubation period, the cell pellets were subjected to centrifugation at 12,000 g for 10 min and then suspended in 1 mL of 0.9% NaCl, containing 4 mL of 2.5% sodium alginate and mixed well. The sodium alginate hybrid cell suspension was placed in a sterile syringe and droplets were ejected into 100 mL of a stirred 100 mM $CaCl_2$. The generated encapsulated hybrid cell beads were used for hydrogen production (Fig. 36).

Under anaerobic conditions (Fig. 37a), hydrogen production by the non-encapsulated hybrid steadily increases up to 18 h and reaches a maximum at around 24 h corresponding to a yield of 3.6 mmol H_2/mmol glucose. After 24 h hydrogen production ceases. On the other hand, with the encapsulated hybrid system hydrogen production is slow but steadily increases up to 36 h to reach a maximum yield of 3.1 mmol H_2/mmol glucose after 48 h. Following the 48 h period, no hydrogen production occurs. These results clearly demonstrate that under anaerobic conditions the hybrid system without encapsulation more efficiently generates hydrogen than the encapsulated hybrid system. This is due to the fact that the interaction between light and the nanoparticles is affected by encapsulation. In contrast, under aerobic conditions hydrogen production by the encapsulated hybrid system steadily increases up to 42 h and reaches a maximum at 48 h that corresponds to a yield of 2.4 mmol H_2/mmol glucose, which is threefold higher than the hydrogen yield of unencapsulated hybrid system (0.8 mmol H_2/mmol glucose) at 48 h (Fig. 37b). This observation suggests that, as expected, alginate encapsulation is essential for protection of the oxygen-sensitive hydrogenase of E. coli.

The hydrogen-producing ability of this system under natural sunlight was also investigated. The results demonstrate that the encapsulated hybrid system under anaerobic conditions has the highest hydrogen yield. This observation demonstrates

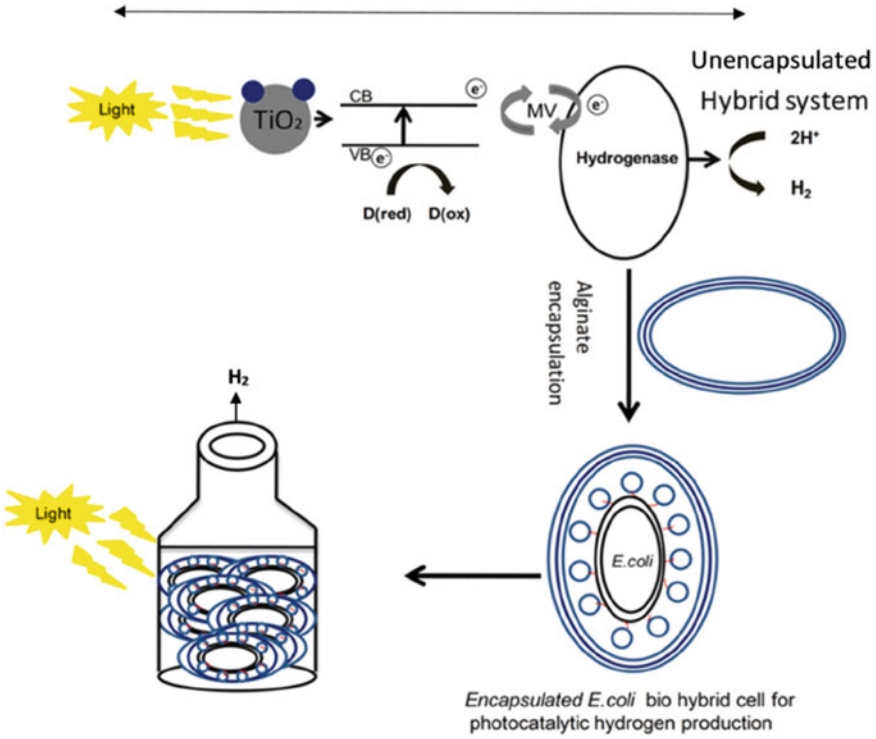

Fig. 36 Schematic of light-driven hydrogen production of biohybrids

that the encapsulated hybrid system effectively utilizes natural sun light to form hydrogen under natural condition.

5.2.4 $CdSe_xS_{1-x}$

In a proof-of-concept study, Shuo Cui et al. constructed a coupled inorganic–biohybrid system for fermentative hydrogen production that is comprised of an industrial E. coli strain and bacterial self-assembled $CdSe_xS_{1-x}$ as the intracellular semiconductor (Fig. 38) [180]. The inorganic–biohybrid system, $CdSe_xS_{1-x}$ NPs, was synthesized in-vivo by *E. coli* cells. The proposal that biosynthesized Cd- and Se-rich nanoparticles are formed inside the cells is evidenced by the HAADF-TEM image and energy-dispersive X-ray spectra.

The optimal biohybrid, prepared using 1 mM Cd and 0.25 mM Se group, exhibits a hydrogen-producing activity of 70.2 μ mol/10^8 cells (Fig. 39). The coupled hybrid exhibits a light-to-hydrogen AQE of about 27.6%, which is higher than all other inorganic–biohybrids explored to date. Under intermittent irradiation, the inorganic-bio hybrid has a 2.9-fold higher hydrogen production rate than that of pure E. coli, while

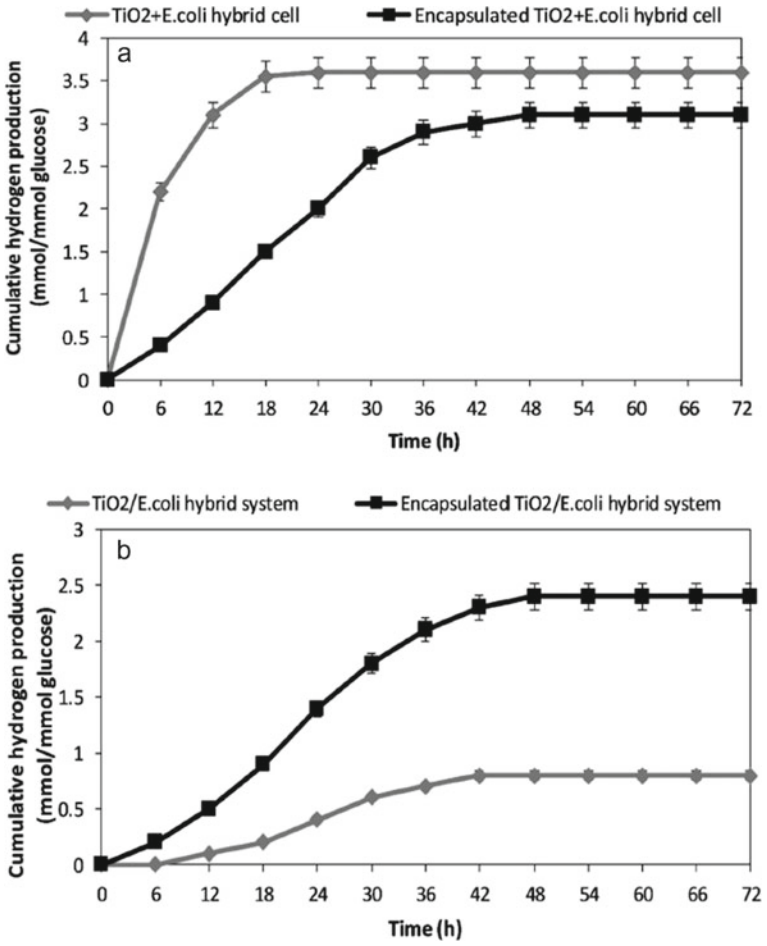

Fig. 37 **a** Hydrogen production of hybrid system with or without encapsulation under anaerobic condition. **b** Hydrogen production of hybrid system with or without encapsulation under aerobic condition

the extracted bio-NPs have only a negligible hydrogen production ability. Notably, a system created by physically mixing external bio-NPs with *E. coli* displays a slightly enhanced activity relative to that of pure *E. coli*. These results show that synergy exists between the cells and intracellular bio-NPs and that the location of the bio-NPs critically determines the degree of synergy. Specifically, sluggish electron transfer from the external bio-NPs to intracellular enzymes severely restricts utilization of the photoelectrons, a limitation that is removed by co-localization of bio-NPs and enzymes.

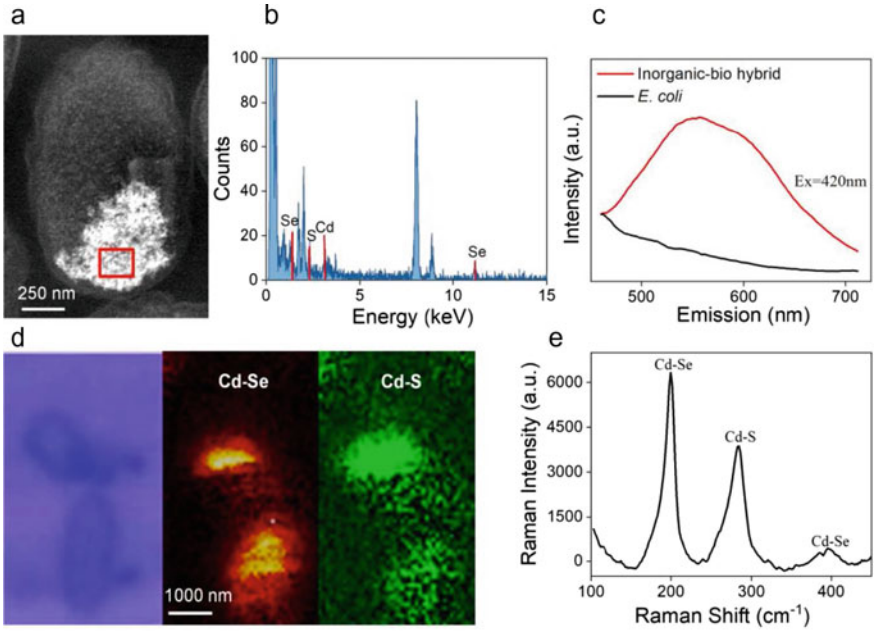

Fig. 38 **a** STEM image of hybrid cells. **b** EDX analysis of nanoparticles on cell surface. **c** Photoluminescence spectra cells before and after hybridization. **d** Raman mapping of hybrid cell. **e** Raman spectrum of hybrid cells

The photocatalytic activity of the $CdSe_xS_{1-x}$ NPs does not decrease during the irradiation period. Cd leaching from the bio-NPs was found to be only 0.0056% and 0.0035% after 6 h under light and dark conditions, respectively (Fig. 40).

5.3 Chlorella

5.3.1 Hydrogels

Jinhui Wu and coworkers created a hydrogel, comprised of living Chlorella and chaperone inside the impermeable casing can produce H_2 continuously for 60 h upon exposure to light (Fig. 41) [181]. These workers showed that the algae-bacteria hydrogel generates hydrogen, which promotes chronic diabetic wound healing by reducing oxidative stress and inflammation. Accordingly, these workers devised a patch-like wound dressing that is filled with gel beads containing live microorganisms, When the patch is exposed to light, the patch continuously delivers hydrogen into the environment of the wound.

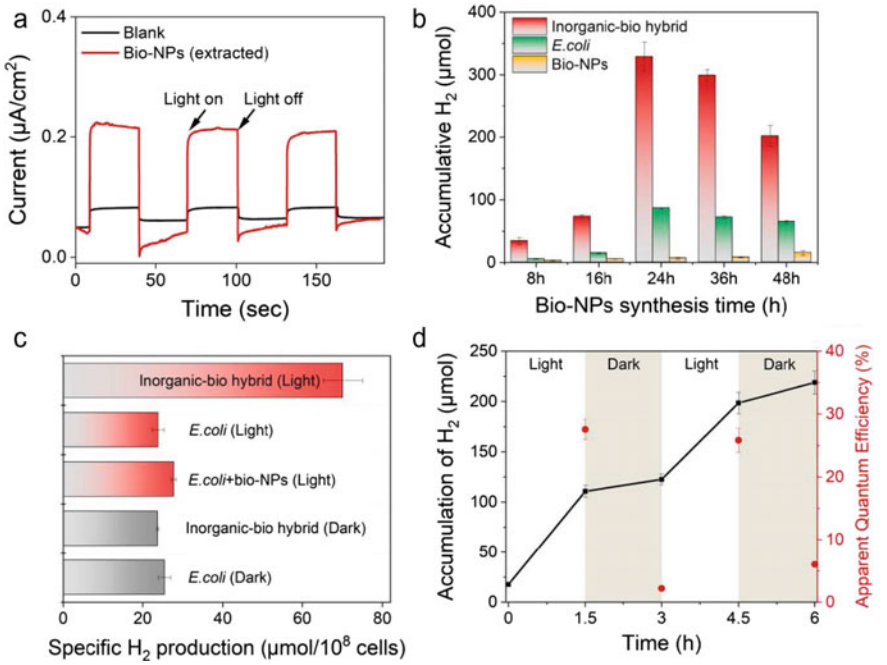

Fig. 39 **a** Photocurrent of bio-NPs. **b** Hydrogen production of three groups for different times. **c** Hydrogen production rate of each group in dark or light. **d** Continue hydrogen production under intermittent irradiation and relative quantum efficiency

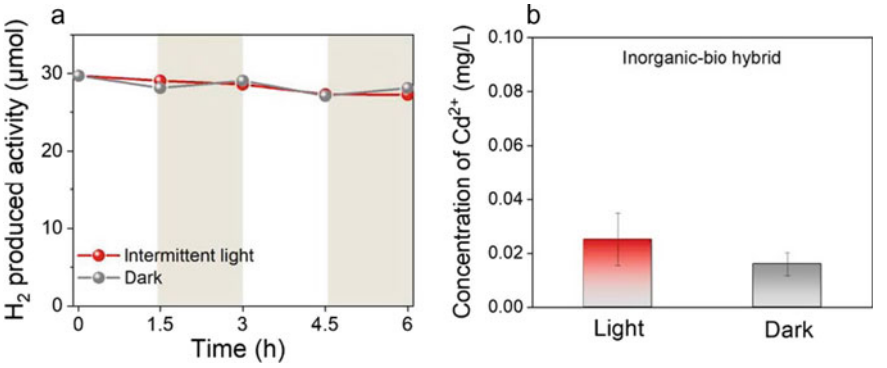

Fig. 40 **a** Hydrogen production of bio-NPs under dark or intermittent light. **b** Concentration of released Cd^{2+} after 6 h

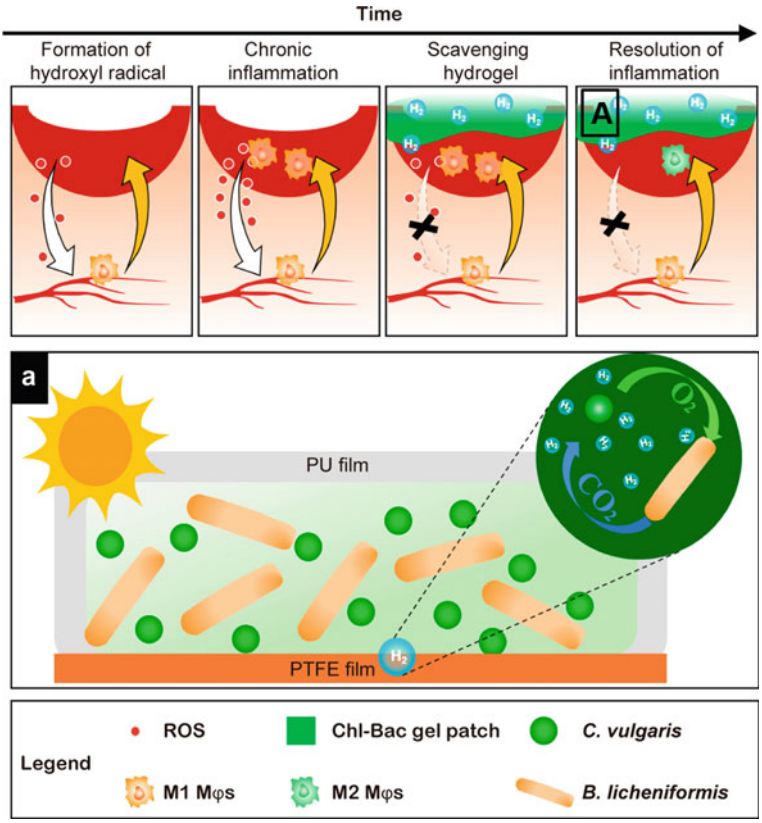

Fig. 41 The synthesis of Bactria-Chalorella cell-based gel

5.3.2 Silica

Tang et al. found that green algae aggregates through silicification promote sustainable photobiocatalytic hydrogen production even in air [182]. The core–shell structure of the green algae aggregates could balance the activity of hydrogenase and the production of electron (Fig. 42). The rationally designed green algae aggregates are a viable and green system for solar-induced water splitting to produce H_2 and O_2.

Chlorella pyrenoidosa is a unicellular alga with a prominent pyrenoid in its chloroplast, and can be cultured on a large commercial scale. Poly(diallyldimethylammonium chloride) (PDADMAC) mimics silicification proteins to induce in situ deposition of silica on cell surfaces. This technique was applied to *Chlorella pyrenoidosa*, which after biomimetic modification forms self-aggregating silicified *C. pyrenoidosa* cells. Upon visible light irradiation, the 100 mm aggregates release H_2 continuously at a constant speed of 0.35 $\mu molH_2\ h^{-1}$ (mg chlorophyll)$^{-1}$, which is 2.75 times the instantaneous conversion of biomass to fuel in nature (Fig. 43). More importantly, H_2 production occurs over at least a 48 h

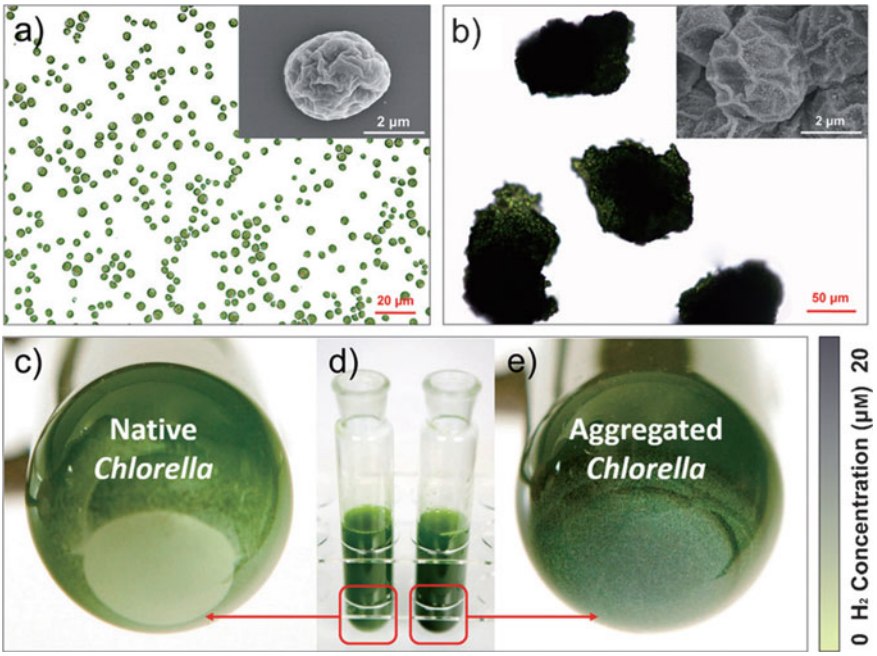

Fig. 42 Optical microscope and SEM images: **a** Native cells. Scale bars: 20 mm (inset 2 mm). **b** Silica aggregated cells. Scale bars: 50 mm (inset 2 mm). **d** Optical images of cells cultured with WO_3 powders in tube: **c** Native cells. **e** Aggregated cells

period. Native Chlorella does not have hydrogenase activity in vivo or in vitro, because the hydrogenase is inactivated by environmental oxygen. The in vivo hydrogenase activity of Chlorella aggregates gradually rises in the first 24 h, and then stays at a steady rate of 4 $\mu molH_2\ h^{-1}$ (mg chlorophyll)$^{-1}$ which is significantly higher than the rate of H_2 production under Ar. An in vitro study confirmed that the aggregates have hydrogenase activity with a sustained increase in the rate of hydrogen production during the first 24 h.

From a mechanism perspective, H_2 production does not occur on the surfaces of the 100 mm aggregates (Fig. 44). In addition, the concentration of produced hydrogen increases as the depth in the aggregates increases and reaches a maximum at the core. This profile suggests that H_2 is generated in core. In contrast, the O_2 concentration decreases as the depth increases, and the O_2 concentration at center of the core center is nearly zero. The distribution of these gases in Chlorella aggregates suggests that spatial–functional differentiation (SFD) takes place between cells.

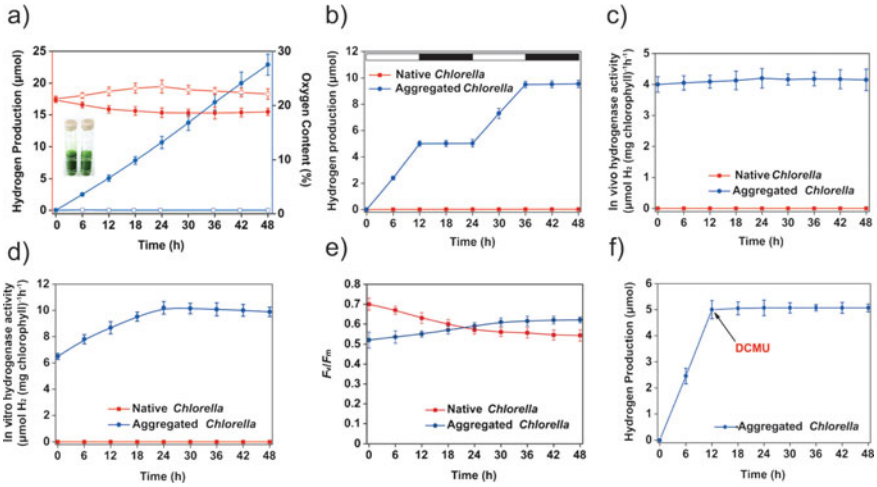

Fig. 43 **a** H_2 and O_2 concentration curve of two groups in 48 h. **b** Sustainable hydrogen production of two groups for 48 h. **c** Activity of in vivo hydrogenase for 48 h. **d** Activity of in vitro hydrogenase for 48 h. **e** Quantum yield of two groups in 48 h. **f** Influence of DCMU in silica aggregated cell for hydrogen production

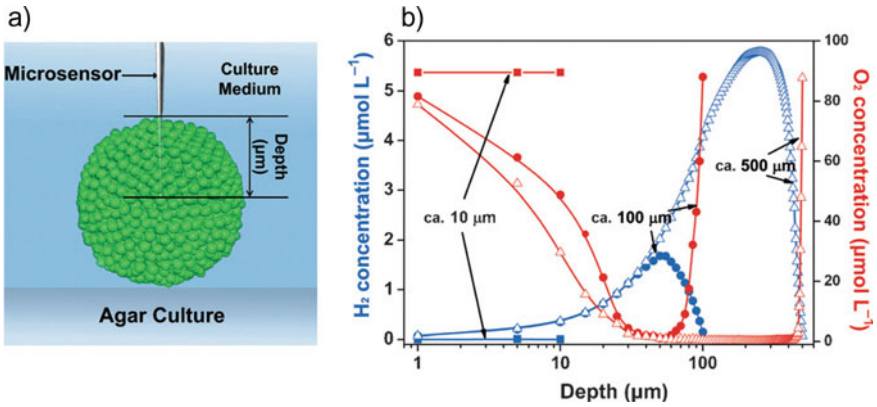

Fig. 44 **a** Schematic of hydrogen electrode and oxygen electrode test. **b** H_2 and O_2 concentration with depth in different silica aggregated cells

5.3.3 Polydopamine and Laccases

All kinds of artificial cell walls like nanoshells composed of inorganic materials [183–185], polymers [186–188], or metal–organic frameworks [189] and having dynamic, adaptive, and self-healing characteristics have been thoroughly investigated. The results demonstrated that the constructed "cell in shell" structure confers a number of properties on living cells such as UV filtering and increased tolerance to hazards.

Owing to these effects, single-cell nanoencapsulation has potential application in various fields [190–192].

Huang designed a new biological hydrogen production system comprised of an enzyme-modulated anaerobic layer which is formed around single *C. pyrenoidosa* by the self-assembly of dopamine, laccase, and tannic acid (Fig. 45) [193]. In this way, an anaerobic balance is established in the layers by a laccase-based oxygen-consuming reaction between photosynthetic production and mitochondrial respiration's consumption of oxygen. These processes can be used to reversibly activate hydrogenases by switching from photosynthetic O_2 production to H_2 production.

The polydopamine (PDA) shell is formed on the bacterial surface by the oxidative polymerization of dopamine in a pH 8.5 buffer solution (Fig. 46). This shell promotes adhesion of various substrates to the encapsulated cells. Thus, PDA's interaction with laccase's amine or thiol molecules results in the spontaneous binding of laccase. Owing to the presence of an Atto425NHS ester label on laccase, the modified cells display bright blue fluorescence that can be observed by using a confocal fluorescence microscope (Fig. 46i). Although the coated cells have increased roughness, their decreased Young Qs modulus (0.12 GPa) relative to those of the native bacterial cells (0.78 GPa) indicates that formed layer is loose and flexible (Fig. 46g). Addition of tannic acid (TA) to a solution of the PDA coated cells causes generation of a TA–laccase–PDA layer, which was visualized as green fluorescence FITC labeled TA was used.

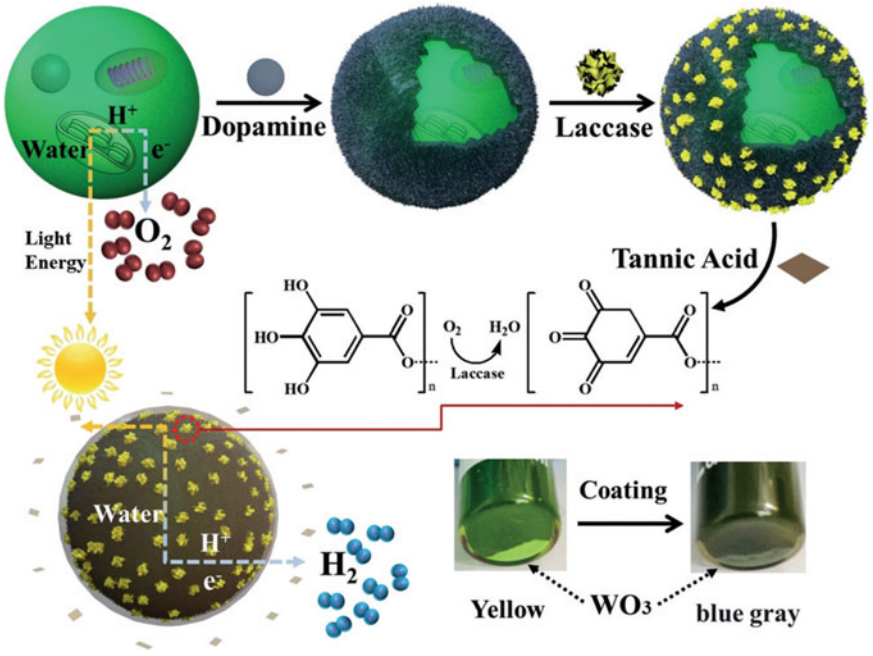

Fig. 45 Schematic of the synthesis of dopamine-laccase encapsulated Chlorella cells

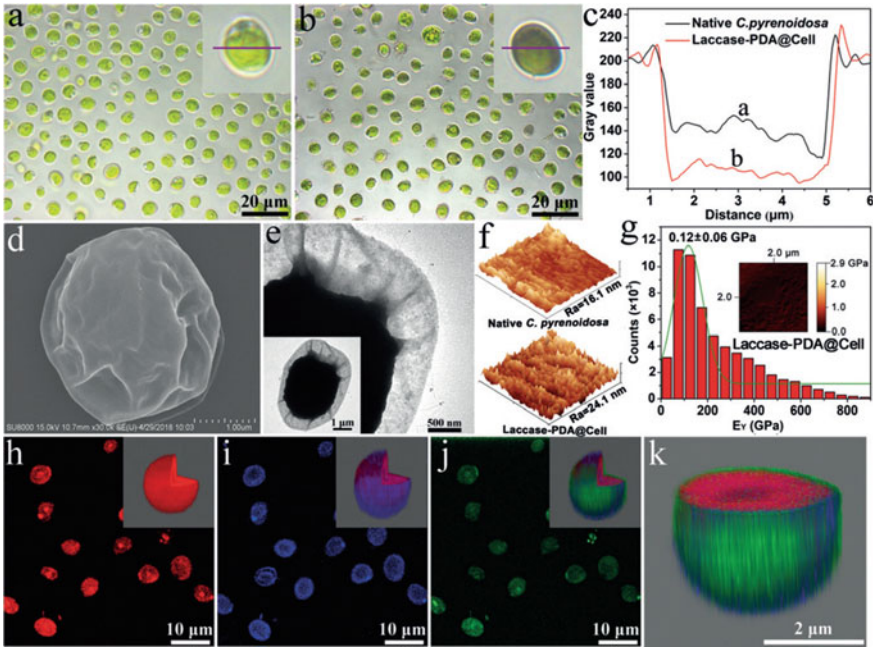

Fig. 46 Optical microscope images of **a** native cells and **b** cells coated by laccase and polydopamine. **c** Surface contrast of native *C. pyrenoidosa* and Laccase-dopamine-coated cell. **d** SEM and **e** TEM images of the coated cell. **f** AFM image of native C. pyrenoidosa and coated cell. **g** Young's modulus and statistical histograms with single peak fitting to a Gaussian curve for coated cells CLSM images of **h** native cells and coated cells, **i** Laccase-PDA@cell, **j** TA-Laccase-PDA@cell

A quantitative study showed that, when 10 mg mL^{-1} of TA is used for fabrication, the coated cells hydrogen continuously at a rate of 0.32 $\mu molH_2\ h^{-1}$ (mg chlorophyll)$^{-1}$ over 7 days. The H_2 production efficiency of the constructed system is 1.6-fold enhanced, much higher than that of native cells in Ar. Without the oxygen-consuming layer, the O_2 produced by photosynthesis in the PSII center would inactivate the hydrogenase. Interestingly, under the same conditions (TA, 10 mg mL^{-1}), an anaerobic environment is created around the coated cell as a result of an acceleration of the oxygen-consuming reaction caused by an increase in laccase content. Moreover, using smaller amounts of TA, H_2 production terminates earlier owing to the depletion of TA and consequent switching of the coated *C. pyrenoidosa* cells back to the normal photosynthesis.

Similar to other fabricated shells that protect the cells against various external stresses, the novel TA-laccase-PDA layer plays a role in increasing the viability of the coated cells in solution, resulting in a long-term stable H_2 production. In conclusion, this study showed that laccase and polydopamine can be used to encapsulate individual *C. pyrenoidosa* cells (Fig. 47d). In the presence of TA, the laccase-induced

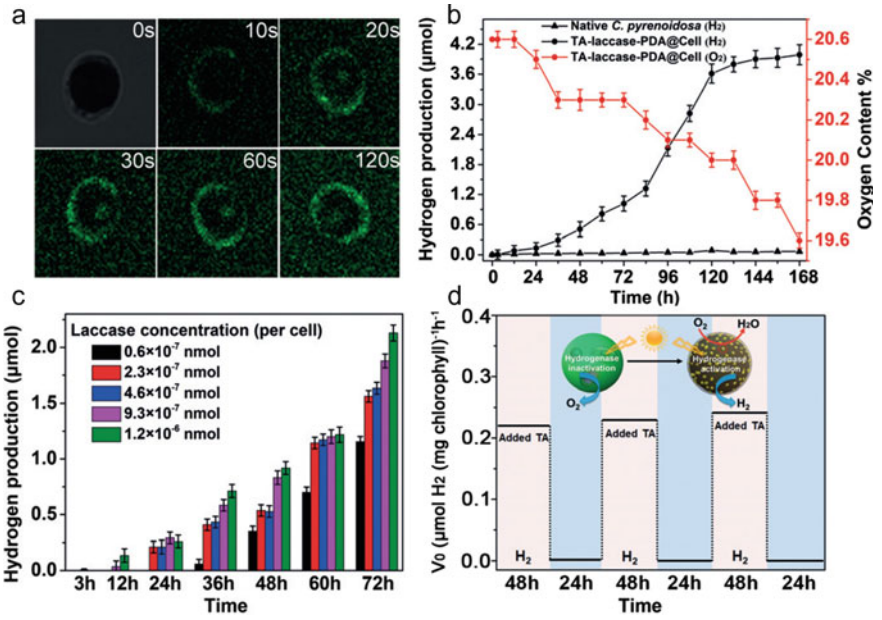

Fig. 47 **a** Confocal fluorescence microscope images of Laccase-PDA@cell's surface containing FITC-labeled tannin acid. **b** H_2 and the content of O_2 in the headspace of sealed tubes. **c** H_2 production from the Laccase-PDA@cell having different laccase contents. **d** The addition of TA enables the coated cells to switch functions between oxygen and hydrogen production

oxygen-consuming reaction takes place within the formed layer, creating an anaerobic microenvironment around cells, which makes it possible for H_2 to be produced despite in an aerobic environment. Importantly, switching the coated cells between H_2 and O_2 production can be modulated by controlling the TA content.

5.3.4 PEG Gel and Co-culture with *E. Coli*

In a recent study, Zhijun Xu et al. utilized the aqueous two-phase separation property of dextran-in PEG emulsion droplets to immobilize living algal cells in the form of dispersible microscale microbial reactors that were capable of both aerobic and hypoxic photosynthesis in sunlight under air (Fig. 48) [194]. Each emulsified droplet can trap a large number of cells to produce a suspension of algal colonies, which are subsequently compressed hyperosmotically into compact multicellular spheroids. The results show that the formation of a hypoxic microniche inside the spheroid is the source of the dual photosynthetic behavior. Thus, the production of oxygen and hydrogen production processes occur at the surface and core of the reactor respectively. In summary, aqueous two-phase separated droplets can be used as vectors to control the organization of algal cells and photosynthesis in synthetic microspaces and to assemble photobiomicroreactors with multiple functions from the bottom up.

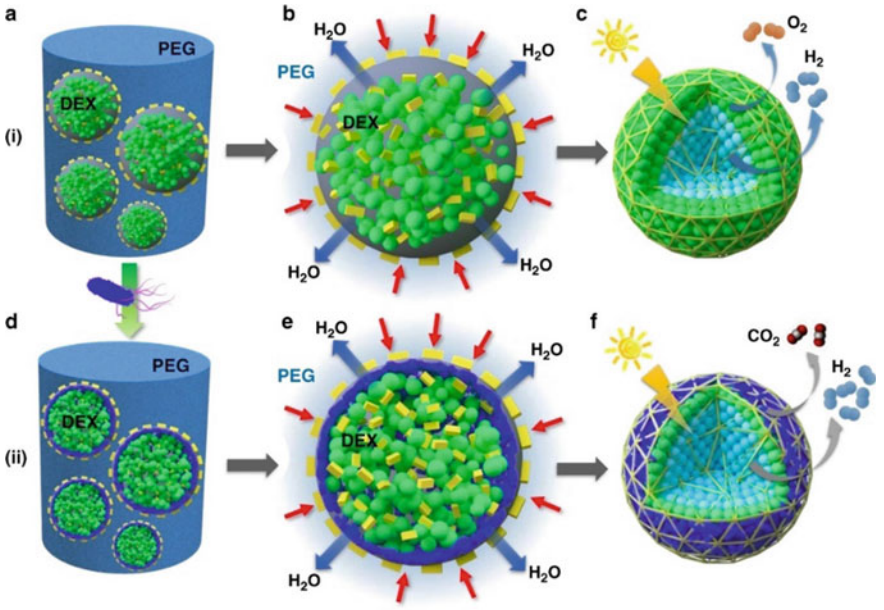

Fig. 48 Schematic of living micro-reactors based on droplets with multiple cells

The results showed that, when Chlorella cells containing spheroids are exposed to light, they can continue to produce hydrogen for 96 h (Fig. 49). In contrast, when both native Chlorella cells or non-osmotically compressed dextran-in-PEG emulsion droplets containing loosely aggregated algal cells are exposed to light in air, only a minimal level of hydrogen is produced. Similarly, when the mean size of the Chlorella cell-based spheroids is reduced to 22 μm, the amount of hydrogen produced in air is negligible because the proportion of aerobic surface area increases and the oxygen production intensifies. Interestingly, when the average size of the microbial spheroids was increased to 165 μm, hydrogen production was reduced by approximately 50%, due to the significantly reduced level of light available to the algal cells located deep in the core of the spheroids.

In an alternative method, the external wall of bacteria was PEGylated to increase their solubility in the continuous phase prior to emulsification at 200 rpm. As a result, *E. coli* cells are adsorbed at the dextran/PEG interface rather than being sequestered inside the emulsion droplet, and Chlorella cells are present in high concentrations (Fig. 50). Subsequently, hypertonicity produced multicellular spheroids (mean size = 90.8 μm) with a spatially algal/bacterial core–shell structure i.e., tightly arranged chlorella encased in a thin layer of *E. coli*. Exposure of the hybrid spheroids in a sealed vial to sunlight in an air environment resulted in rapid hydrogen production and a gradual increase in hydrogen concentration in the bottle, which stabilized after 84 h… At the same time, oxygen content in the vial decreases from 20.6% to 18.9% within 60 h, consistent with the onset of hypoxic photosynthesis in the closely packed

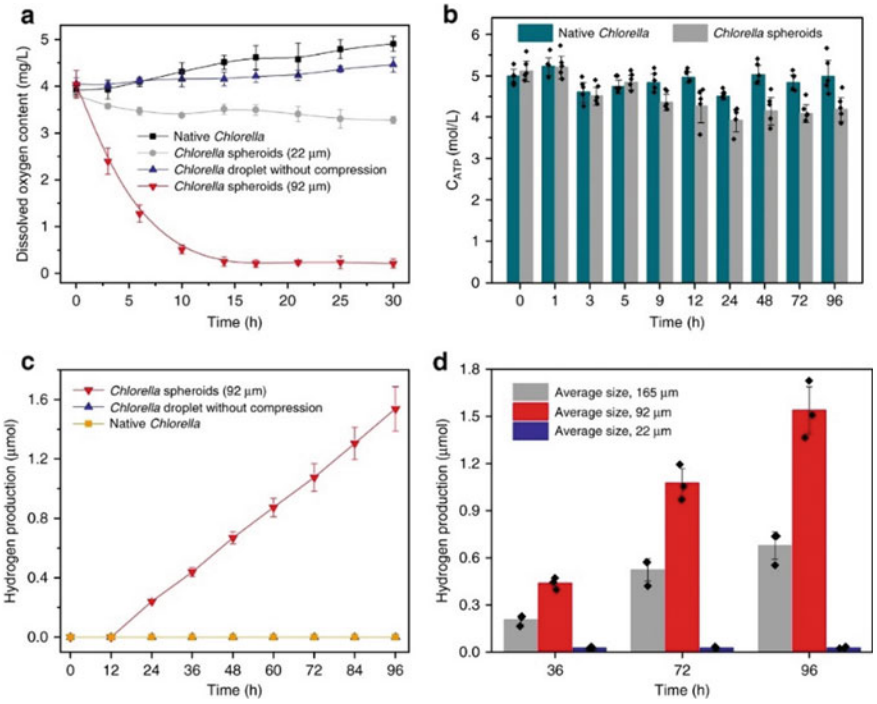

Fig. 49 **a** Dissolved oxygen concentration in suspensions of native Chlorella cells, Chlorella-loaded w/w dextran-in-PEG emulsion droplets, and Chlorella multicellular spheroids over time. **b** Changes in the concentration ATP in native free Chlorella cells and Chlorella cells over time. **c** Hydrogen concentrations in suspensions of native Chlorella cells, Chlorella-loaded w/w dextran-in-PEG emulsion droplets, and Chlorella multicellular spheroids were measured over time. **d** Time-dependent production of hydrogen for Chlorella multicellular spheroids. Hydrogen production for Chlorella multicellular spheroids over time

Chlorella cells. In contrast, mixtures of the Chlorella spheroids along with free E. coli cells do not have enhanced photosynthetic hydrogen production. Compared to microreactors containing only Chlorella cells, the hybrid spheroids exhibit superior hydrogen production performance, as evidenced by a shorter induction period and an increased initial level of hydrogen production. In addition, the rate of hydrogen production in the hybrid spheroids is 3.2 times the instantaneous biomass-to-fuel conversion that occurs in nature (0.20 μmol H_2 (mg chlorophyll)$^{-1}$ h^{-1}).

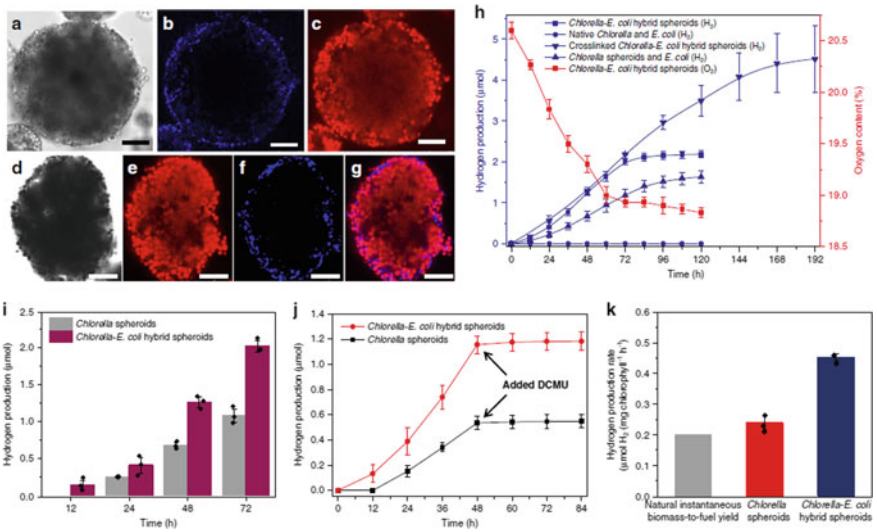

Fig. 50 Hydrogen production from heterogeneous micro-reactors in air. a-c Bright-field image (**a**), and blue and red CLSM images (**b**, **c**) of w/w dextran-in-PEG emulsion droplet with captured red algal and surface-adsorbed bacterial cells. scale bars, 25 μm. **d**–**f** Confocal bright field microscope image of Chlorella/*E. coli* multicellular spheroid (**d**) and corresponding red **e** and blue **f** CLSM images. **g** Overlay image of (**e**) and (**f**) showing the core–shell spatial organization. Scale bars in (**d**–**g**), 20 μm. **h** Hydrogen concentrations in different biohybrid systems; corresponding decrease in oxygen content for the algal/bacterial cell spheroids is also shown. **i** Time versus hydrogen production for Chlorella cell-based spheroids and Chlorella*/E. coli* hybrid core–shell spheroids at different time periods. **j** Time versushydrogen production for Chlorella spheroids and Chlorella/E. coli hybrid core–shell spheroids. **k** hydrogen production rates for Chlorella multicellular spheroids and Chlorella/E. coli hybrid spheroids and for the natural instantaneous biomass-to-fuel yield

5.4 Chlamydomonas Reinhardtii

5.4.1 Chemoenzymatic Cascade Engineering

Green algae are widespread photoautotrophs that contain [FeFe]-hydrogenases (H_2ase), utilize sunlight to produce H_2 [195, 196]. Jie Chen et al. developed a system for the efficient production of hydrogen gas using green algae, which was designed to operate through a chemoenzymatic cascade (CEC) (Fig. 51). CECs, consisting of a series of consecutive catalytic or non-catalytic enzymatic and chemical reactions in a one-pot system. The CEC possessed a combination of a variety of functions, including oxygen depletion, pH retention, and induction of cell aggregation induction, that activate hydrogenase for long-term H_2 production in a local anaerobic environment while maintaining green algae vitality [197].

The *C. reinhardtii* ($OD_{750} = 0.25$) were cultured in gastight glass tubes with a CEC system which contains approximately 0.1 KU mL^{-1} of GOx, 10 KU mL^{-1} of CAT, 50 mM of glucose, and 150 mmol of $Mg(OH)_2$. A large excess of CAT

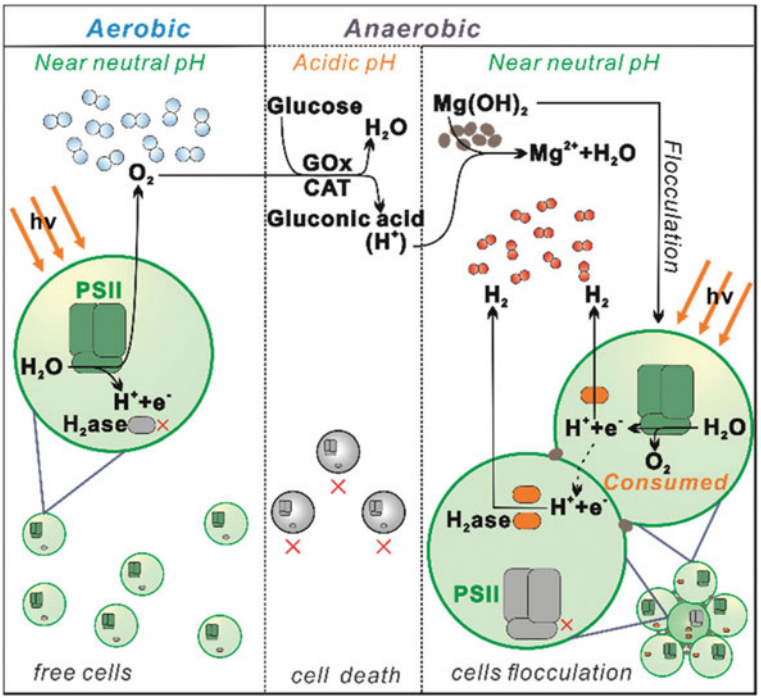

Fig. 51 Schematic for sustainable H_2 production with green algae

is used to rapidly remove H_2O_2 produced by glucose oxidation. Upon illumination with a 6300 lx, only a small amount of H_2 is produced in the first several days, however, the amount increases markedly after 6 d and by day 10 its concentration reaches 19.41 μmol, about 300 times that of day 2 and about 100 times that of day 4, respectively. It is worth noting that H_2 production increased steadily over a period of up to 26 days. The total yield of H_2 reaches 34.67 mmol H_2 L^{-1}, which exceeds the yield of the sulfur-deprived algae (6.62 μmol H_2 L^{-1}). The average rate of H_2 production was 0.44 μmol H_2 h^{-1} (mg chlorophyll)$^{-1}$, which is 3.22 times 3.2 times of the instantaneous biomass-to-fuel in nature [0.20 μmol H_2 h^{-1} (mg chlorophyll)$^{-1}$] (Fig. 52).

5.4.2 Sulfur-Deprivation

Sulfur-deprived cells of *C. reinhardtii* has the highest hydrogen production capacity among those of other photobiological systems. In a study, Alena Volgusheva et al. analyzed changes in PSII content and activity during hydrogen production in the wild type (WT) and the state transition mutant 6 mutant (Stm6) of *C. reinhardtii* (Fig. 53) [198]. The latter mutant was reported to have an enhanced H_2 yield. These workers

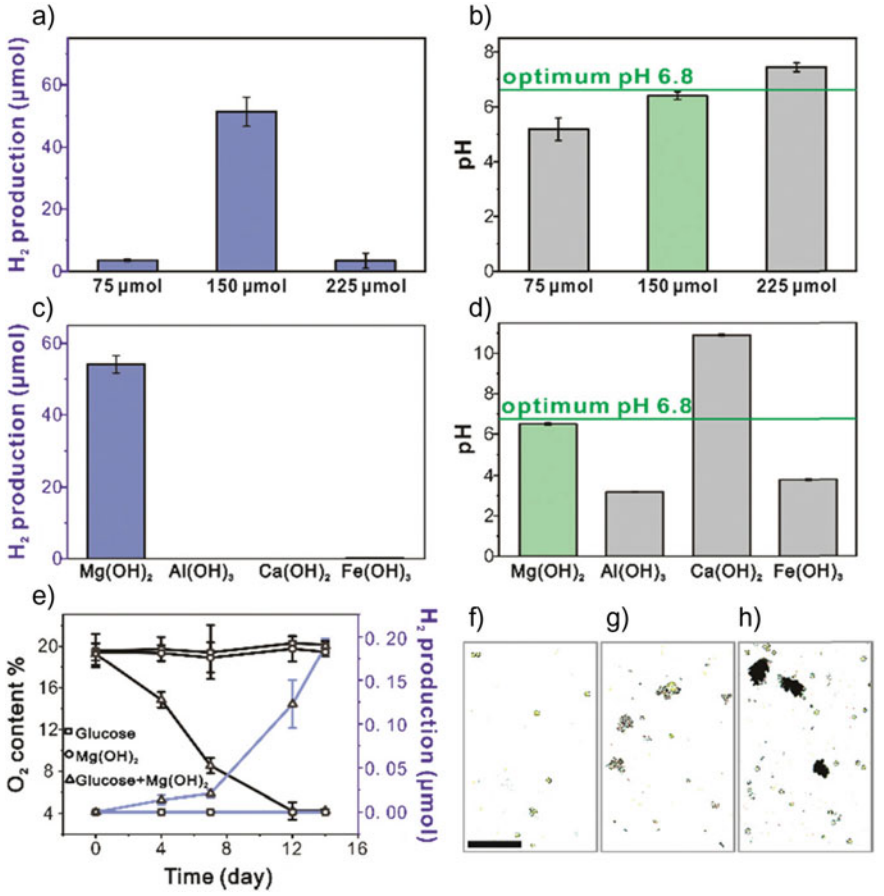

Fig. 52 **a**–**b** H_2 production and pH from culture systems with different $Mg(OH)_2$ content. **c**–**d** H_2 production and pH from the culture systems with different content insoluble metal hydroxides. **e** Plots of H_2 production versus O_2 content. **f**–**h** Optical microscope images of different systems

quantified the decrease in the amount of PSII and showed that by altering the redox state of the quinone acceptors in PSII, the PQ pool generated when deprived of S and subsequent H_2 production, acceptor side reactions in PSII can be controlled.

In the initial phase of this effort, researchers observed that the changes in hydrogen and oxygen concentrations over time during the cultivation of *C.reinhardtii* under S-deprived conditions can be divided into four phases, including oxygen production, oxygen depletion, anaerobic and hydrogen production. The whole process takes place in WT and Stm6 mutant cells, but their time dependence differs. Specifically, the Stm6 mutant can reach the anaerobic phase 15 h earlier than WT cells, which is attributed to combined effects of reduced oxygen-production capacity and increased respiration rate in the mutant. Stm6 mutant cells have a shorter anaerobic phase, with H_2 production detectable only a few hours after the onset of anaerobiosis. In addition, the Stm6

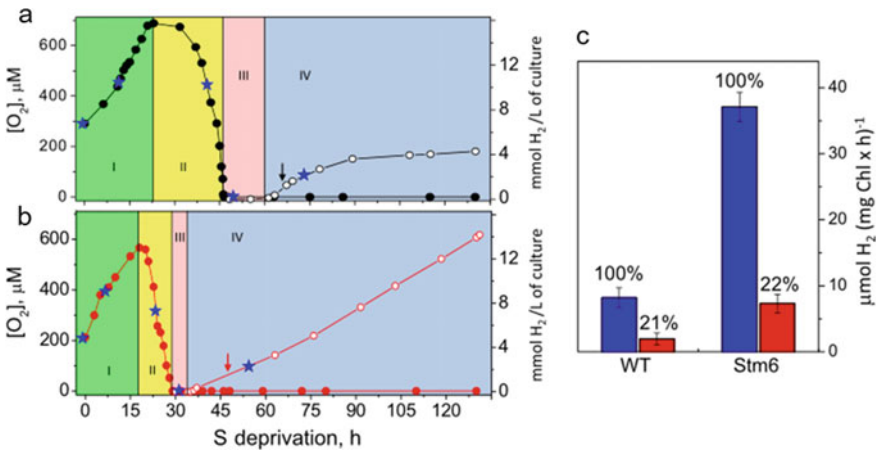

Fig. 53 The concentration of dissolved O_2 and produced H_2 during incubation of WT (**a**) and the Stm6 mutant (**b**). (**c**) Hydrogen production by WT and the Stm6 mutant under S-deprived conditions and the effect of DMCU

mutant can produce hydrogen consistently and steadily throughout 130 h, exhibiting a stability that far exceeds that of WT cells. (3,4-Dichlorophenyl)-1,1-dimethylurea (DCMU) specifically inhibits PSII by disrupting the electron transfer pathway. It has been reported that the addition of DMCU partially inhibits hydrogen production during S-deprived cultivation of *C. reinhardtii*, which indicates that hydrogenase utilizes the electrons from PSII. The addition of DCMU to both WT and Stm6 mutants reduced hydrogen production by 80%, suggesting that PSII plays an important role in the evolution of photosynthetic hydrogen.

Volgusheva and co-workers analyzed the activity of PSII during S-deprived cultivation of *C. reinhardtii*. During the hydrogen production, they quantified the function of PSII centers that lead to charge separation and S-state advancement and supply electrons to the PQ pool. The results indicate that most of the electrons used for H_2 synthesis originate from the water splitting of PSII, a conclusion confirmed by the inhibition of H_2 production by DCMU. The results also indicate that hydrogenase takes electrons from the PQ pool, which partially unblocks the PSII electron transfer from QA- to plastoquinone, thus allowing electrons from water oxidation to be used in PSII for hydrogen generation.

Moreover, Volgusheva et al. found that the amount of PSII in operation is positively correlated with the rate of hydrogen production. In the Stm6 mutant, both the amount of hydrogen produced and the amount of PSII were four times higher than in the WT. The larger amount of remaining PSII centers reflects that the redox environment of the thylakoid membrane is altered in the Stm6 mutant, which leads to an earlier anaerobic phase, an important prerequisite for preservation of PSII during illumination under S-deprived conditions.

5.4.3 Alga-Bacteria Co-culture

Neda Fakhimi et al. recently conducted a study of algal–bacterial co-culture for synergistic biological hydrogen production [199]. They found that algal hydrogen photoproduction in this system occurs only when green alga *C. reinhardtii* is independently co-cultured with bacterial in medium with sugar. Among them, co-cultures with P. putida showed significantly higher levels of H_2 production (40.8 mL $H_2 \cdot L^{-1}$, 6.3 times, $P < 0.0001$). Co-culture with *E. coli* increased hydrogen production (35.1 mL $H_2 \cdot L^{-1}$,1.6 times, $P > 0.05$), while co-culture with R. etli did not significantly increase. Because none of the bacteria produce H_2 in a monoculture, hydrogen production in the co-culture system attributes to the algae. The co-culture scan enhance capacity to prolong the hypoxia phase ($P < 0.0001$) which is beneficial for H_2 production.

Hydrogen photoproduction in co-cultures is associated not only with anaerobic induction but also with the ability of bacteria to produce acetic acid. By integrating photosynthesis and fermentative production in the co-culture of Chlamydomonas and E. coli and using glucose as an energy source, results in a 60% increase H_2 production compared to the sum emanating from the respective monocultures (Fig. 54). This synergy is attributed to the ability of the algae to consume the acetic acid excreted by the bacteria. This work could open up new possibilities for designing systems for biohydrogen production from industrial wastes.

In a recent study, Ban et al. observed that bacterium *Pseudomonas sp.* strain D assists photo-mediated H_2 production by Chlamydomonas reinhardtii and could significantly promote hydrogen production by the green algae Chlorella and Scenedesmus [200]. In strain D partnered algal–bacterial co-culture, the oxygen in the system is rapidly consumed by bacterial growth, creating a completely anaerobic environment that allows the algal hydrogenase to be activated. Moreover, algal–bacterial synergy improved algal H_2 production by slowing the reduction of chlorophyll, enhancing starch accumulation, and maintaining protein content. This study suggests a proposal for the design of efficient and durable algal–bacterial synergistic systems to enhance light-mediated biological hydrogen production.

The results of a study suggested that co-culturing algae with *Escherichia coli* or *Bacillus subtilis* only slightly improves H_2 production, but that co-culture by adding *Pseudomonas sp.* strain D can significantly increase the production of H_2 (Fig. 55).

The hydrogen production from Co-cultures of this bacterium with *C. protothecoides*, *C. pyrenoidosa*, *Chlorella sp.* WFY, *Scenedesmus sp.* WFY, and *S. obliquus* can reach 2.3–9.0 times greater than that generated by algal cells grown in pure culture (Fig. 56).

5.4.4 $NaHSO_3$ Treatment

Weimin et al. suggested a way in which $NaHSO_3$ treatment could enhance H_2 production by algae. The mechanism for this action related to the changes in O_2 content and hydrogenase activity caused by $NaHSO_3$ [201]. This suggestion was assessed

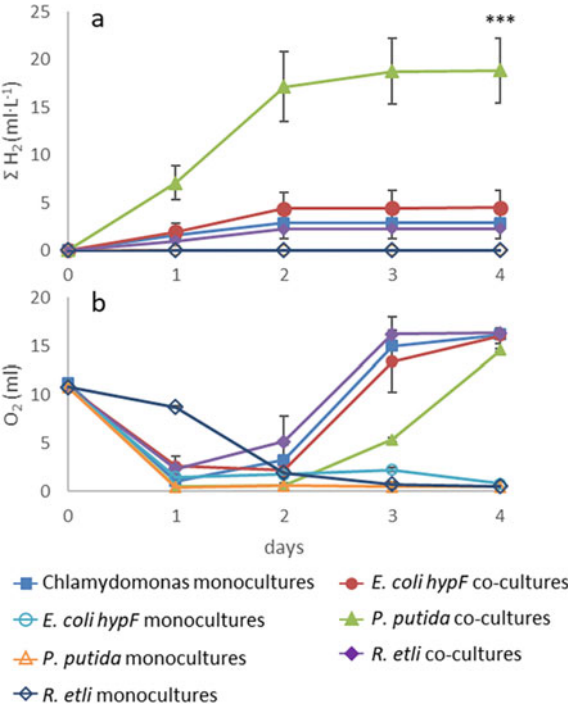

Fig. 54 Changes in H_2 (**a**) and O_2 (**b**) concentrations in the headspace over 4 days

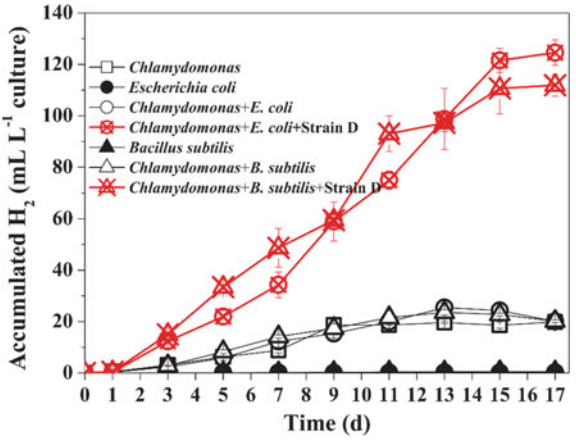

Fig. 55 Hydrogen production by co-culture of *Chlamydomonas reinhardtii* and bacteria

possibility by determining the effects of $NaHSO_3$ and S-deprived on H_2 production in *C. reinhardtii*.

The results showed that the H_2 formation rate of C. reinhardtii is maximized by using approximately 13 mM $NaHSO_3$ and that the increased production level is approximately 200 times higher than that of untreated cells (Fig. 57). Therefore,

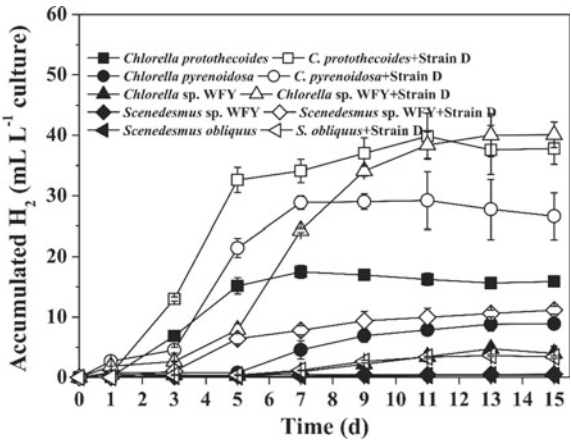

Fig. 56 Hydrogen production by co-culture of algae with *Pseudomonas sp.* strain D

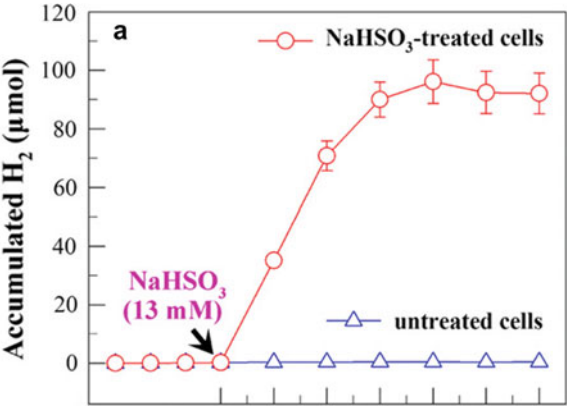

Fig. 57 Effect of $NaHSO_3$ treatment on H_2 production

treatment with an O_2 reductant appears to be an effective strategy for increasing the photobiological hydrogen production capacity of microalgae.

5.4.5 Pulse Illumination Protocol

At the current time, H_2 photosynthesis in algal cultures requires a temporary separation of hydrogen- and oxygen-producing reactions. *C. reinhardtii* cultures that reached anoxic conditions in the dark then produced H_2 under illumination, before the onset of O_2 evolution, while S-deprived cells showed the opposite behavior (Fig. 58). Although the maximum H_2 photoproduction activity is higher in dark-adapted cells than it is in S-deprived algae, the latter system produces H_2 over a much longer period of time and in a higher yield. To sustain H_2 production in dark-adapted algae, it is possible use low light and high cell density conditions to prevent the accumulation

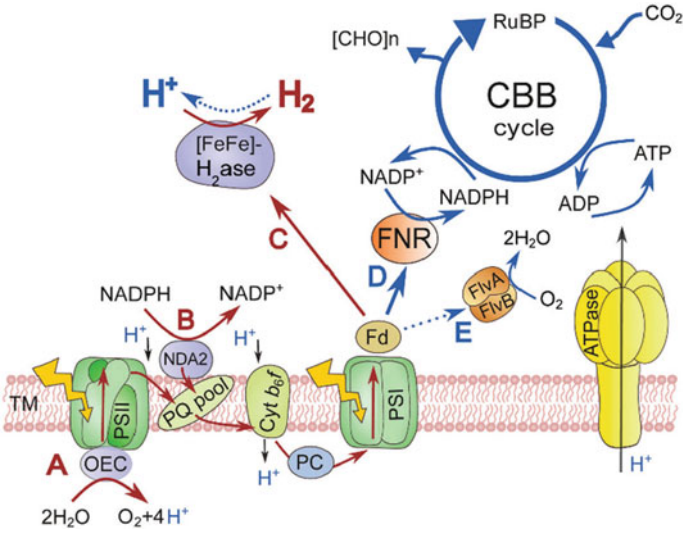

Fig. 58 Schematic of the hydrogen photoproduction and metabolic pathways in the chloroplasts of green alga *C. reinhardtii*. **A**–**C** direct biophotolysis of water; **B**, **C** indirect biophotolysis of water; **D** NADPH production and CBB cycle; **E** light-dependent oxygen reduction

of oxygen due to active respiration [202]. Alternatively, H_2 production can be driven at high light intensities by transporting photosynthetic electrons to hydrogenases to avoid transport to Calvin-Benson-Bassham (CBB) cycle, while controlling of the intracellular O_2 level. Although Rubisco deficiency has been reported to promote hydrogen production in green algae, the yield of H_2 is not high, most likely because only a small amount of photosynthetic electrons flow to the hydrogenase [203]. Nevertheless, partial inactivation of the CBB cycle does significantly increasethe H_2 photoproduction [204].

Hydrogenases are produced in algae under dark anaerobic conditions and can acts as an alternative electron sink to promote oxygenic photosynthesis by eliminating excess accumulated electrons in PETC. Photoactivation of the CBB cycle requires time dependent photosynthetic productivity by using fluctuating light. Kosourov et al. proposed that a series of short light pulses could enable algal photosynthesis in the production of only H_2 as long as each light pulse was short enough to prevent the flow of electrons to the CBB cycle and the accumulation of O_2 as much as possible (Fig. 59) [205]. In order to verify this assumption, a series of experiments were carried out with *C. reinhardtii* was subjected to short light pulses (1–5 s) interrupted by a longer dark phase(3–9 s) and with low background illumination (3 μmol photons m^{-2} s^{-1}) instead of dark phases. The results of experiments performed in anaerobic vials showed that pulsed irradiation of the algae produce H_2 continuously for at least 3 d. The process occurs in the absence of acetate and at a low cell density, suggesting that self-shading in the suspension is not responsible for inducing H_2 production. *C. reinhardtii* produces rapidly H_2 within the first 6 h, with its maximum hydrogen production

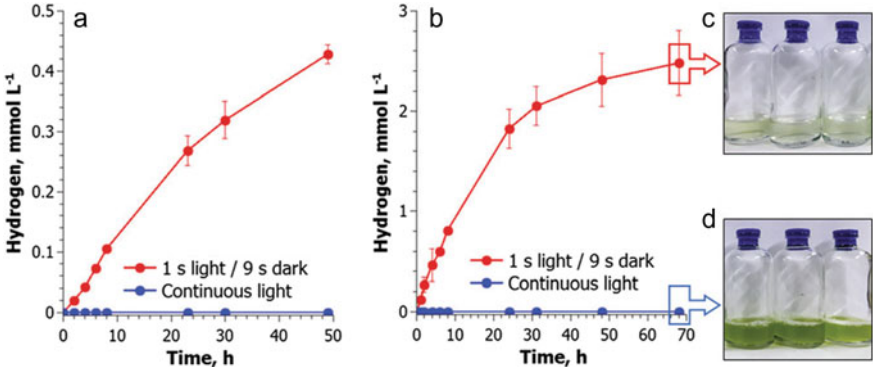

Fig. 59 Long-term stability of H_2 production by different types of *C. reinhardtii* cultures, photoautotrophic (**a**) and photoheterotrophic (**b**). No growth under pulsed light (8.8 mg mL^{-1}; **c**), increased biomass under continuous light (26 mg mL^{-1}; **d**)

rate exceeding that of sulfur-deprived algae and then the rate declined. Moreover, the maximum conversion efficiency of H_2 production from pulse-illuminated algae during the first 8 h was 1.6–1.7% (2–2.2% if upper H_2 gas combustion energy is assumed).

These findings demonstrate that H_2 photoproduction in green algae becomes sustainable when the illumination protocol for growing algal cultures is changed from continuous light to a series of short light pulses. In addition, the results provide strong evidence that CO_2 fixation competes with the [FeFe]-H_2ase enzyme for the photosynthetic electrons and demonstrate that an approach exists for eliminating this competition.

5.5 Other Microorganisms

5.5.1 Rhodopseudomonas Palustris

Conjugated polymers (CPs) have highly delocalized π-conjugated backbones in the main chain and semiconductor properties. As a result, they can be used as photosensitizers for light-induced hydrogen formation [206–208]. Compared with photosensitizer dyes and inorganic semiconductors, CPs have excellent photoelectric properties in electrochemical devices, light harvesting capabilities, light stability for CO_2 reduction, tunable energy levels in photovoltaic cells, and biocompatibility with natural organisms [209–211]. Owing to these outstanding properties, we designed a CP-based bio-optical composite to augment photosynthesis by R. palustris. In this study, Zijuan Wang et al. constructed the efficient bio-hybrid photocatalytic

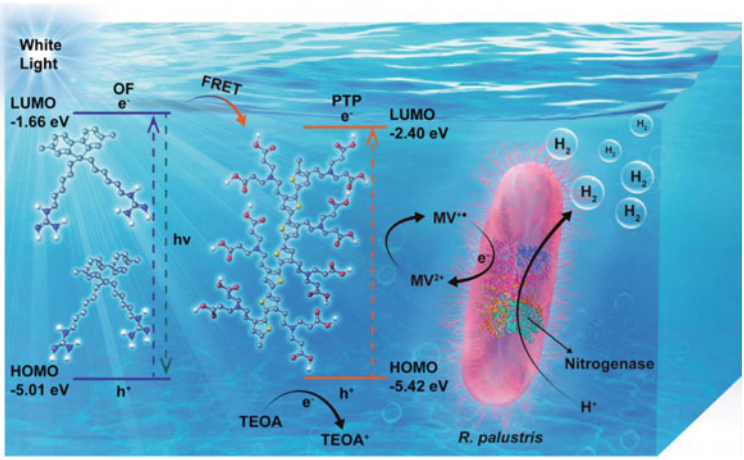

Fig. 60 Schematic of the electron transfer route of the hybrid photocatalysis during hydrogen production

hydrogen production complex, OF/PTP/MV^{2+}/TEOA/R. palustris, in which water-soluble oligofluorene (OF) and polythiophene (PTP) serve as photosensitizers, and R. palustris acts as a biocatalyst (Fig. 60) [212].

As shown in Fig. 61, under visible light, fluorescence resonance energy transfer (FRET) occurs between the OF and PTP centers in OF/PTP/MV^{2+}/TEOA/R. palustris, which amplifies the photoelectron signals that enhance electron transfer to microorganisms for hydrogen production. Moreover, MV^{2+} is present in the complex as a mediator to permeate cells and facilitate electron transfer between the OF/PTP pair and nitrogenase in R. palustris, and triethanolamine (TEOA) serves as a sacrificial electron donor. In OF/PTP/MV^{2+}/TEOA/R. palustris, separated electrons of the OF/PTP pair continuously provided by TEOA are delivered to MV^{2+} for reduction to form blue $MV^{+\cdot}$. An dthen $MV^{+\cdot}$ transfers electrons to the nitrogenase in intact R. palustris for hydrogen synthesis.

The results of this effort showed that hydrogen production using the OF/PTP/MV^{2+}/TEOA complex reaches 48.49 nmol (Fig. 62). In the absence of the OF/PTP/MV^{2+}/TEOA complex or nitrogenase, hydrogen production is about 40% of that obtained using the OF/PTP/MV^{2+}/TEOA complex. The OF/PTP/MV^{2+}/TEOA/R. palustris complex produces the largest amount of hydrogen using irradiation for 2 h, while no hydrogen is generated in the absence of R. palustris. Compared with those of other systems for hydrogen production either containing or not containing photosynthetic organisms, the OF/PTP/MV^{2+}/TEOA/R. palustris complex has excellent characteristics such as efficient hydrogen production, low-cost and simple operation.

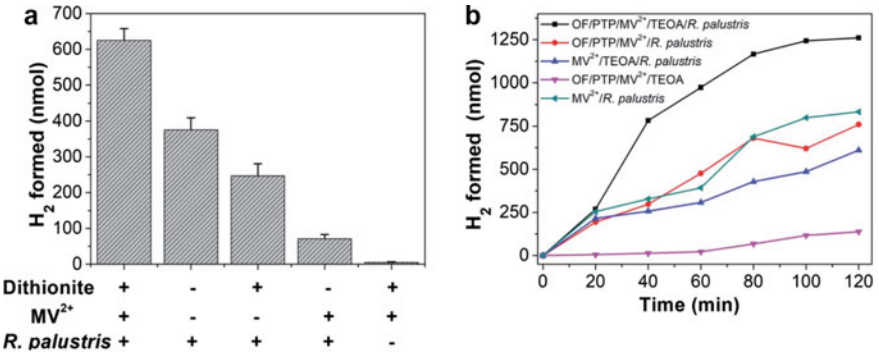

Fig. 61 **a** The effect of each component in complexes on hydrogen production. **b** H_2 production from different complexes under irradiation

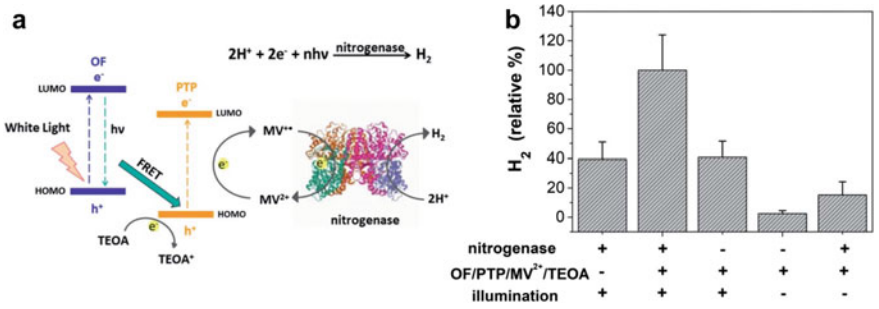

Fig. 62 **a** Mechanism of hybrid system for H_2 production. **b** The effect of each condition in hydrogen production process

5.5.2 Desulfovibrio Desulfuricans and Citrobacter Freundii

As discussed above, biohybrid systems have been devised recently to use microorganisms as catalysts, because they house complex biosynthetic pathways, are far more stable than isolated proteins, and have the power for self-renewal and reproduction [8, 77, 213]. It is also appealing that the microbes can be coupled with light-harvesting nanoparticles or nanostructured materials that have superior optical and electronic properties, high surface areas and proper sizes for ready interaction with microbes [176, 214, 215].

In a recent investigation, Monica Martins et al. determined if a self-photosensitization approach could be utilized for efficient H_2 production promoted by microorganisms that are known to express high levels of hydrogenases and/or are efficient in producing sulfide or engaging in electron exchange with external materials [216]. In this study, three new biohybrid systems were generated for light promoted H_2 production using Gram-negative bacteria, self-precipitated CdS nanoparticles and cysteine as the sacrificial electron donor (Fig. 63). *Desulfovibrio desulfuricans* was

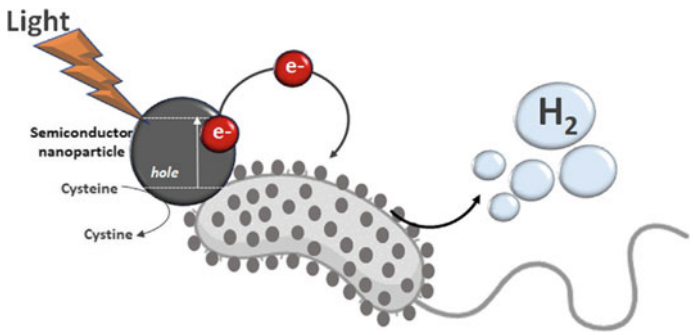

Fig. 63 Schematic of the biohybrid systems

chosen for this purpose because it is a sulfate reducing bacterium that also has high H_2 production activity. Moreover, this bacterium has the unique ability to generate sulfide from sulfate, making it able to self-produce metal nanoparticles. *Citrobacter freundii* was identified as another sulfide and/or H_2 producing bacterium, and *S. oneidensis* was selected as a H_2-producing electroactive microorganism that participates in efficient electron exchange with inorganic materials.

To generate the biohybrid systems, cells grown in the presence of a sulfur compound (sulfate for *D. desulfuricans*, cysteine and thiosulfate for *S. oneidensis* and only cysteine for *C. freundii* and *E. coli*) were incubated with $CdCl_2$. Formation of the biohybrids could be observed by creation of a yellow color, indicative of CdS formation, and consequent removal of cadmium from solution. The biohybrid systems were characterized by using SEM and SEM–EDS (Fig. 64). SEM images revealed the presence of nanoparticles on all bacteria cell surfaces (Fig. 64B/C, E/F, H/I, and K/L), whereas no particles were observed in control *E. coli* cells (Fig. 64A, D, G and J). SEM images showed the presence of a remarkable high density of CdS nanoparticles on the surface of *D. desulfuricans*, along with some extracellular CdS nanoparticle clusters (Fig. 64B/C). In the case of *C. freundii*, extracellular clusters of CdS nanoparticles were mostly observed around the cells (Fig. 64E/F). The CdS nanoparticles formed by *S. oneidensis* exist as smaller spherical spots uniformly distributed on the cell surface (Fig. 64I/H), which agrees with previous studies. In the case of E. coli, small clusters of CdS particles were observed on the cell surface (Fig. 64 K/L).

All biohybrids were found to produce H_2 upon light irradiation, albeit with different efficiencies (Fig. 65). In the presence of MV^{+2}, production of H_2 by the *D. desulfuricans*-CdS biohybrid is 10800 $\mu mol\ g_{dcw}{}^{-1}$ after 120 h, which is considerably higher than those of the other organisms including the *Soneidensis*-CdS biohybrid producing 2000 $\mu mol_{gdcw}{}^{-1}$, the *C. freundii*-CdS system 858 $\mu mol_{gdcw}{}^{-1}$ and the *E. coli*-CdS system 1200 $\mu mol_{gdcw}{}^{-1}$, even after 140 h (Fig. 65a). In the absence of MV^{+2}, H_2 production of the biohybrid systems is reduced by between 30 and 40% for all organisms (Fig. 65b), with the notable exception of the *S. oneidensis*-CdS containing biohybrid, which has identical performances in the presence and in the

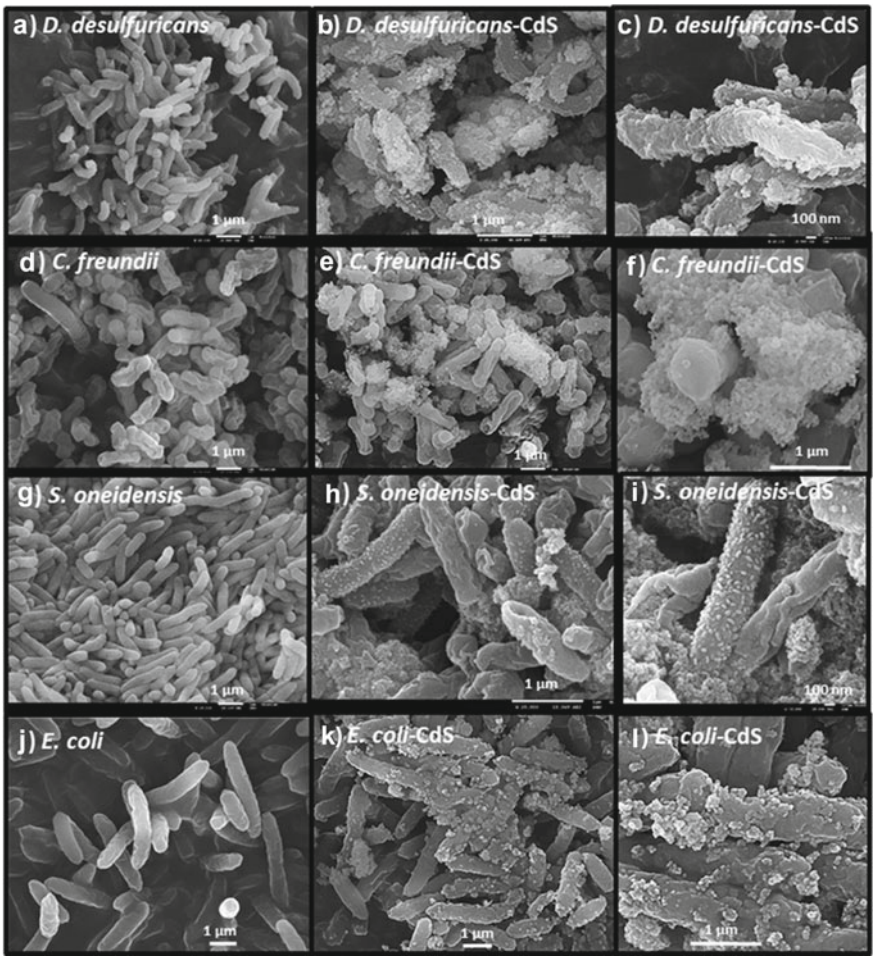

Fig. 64 SEM images of: **a**–**c** *D. desulfuricans* cells before and after CdS self-photosensitization, **d**–**f** *C. freundii* cells before and after CdS self-photosensitization, **g**–**i** *S. oneidensis* cells before and after CdS self-photosensitization, **j**–**l** *E. coli* cells before and after CdS self-photosensitization

absence of MV^{+2}. Remarkably, the *D. desulfuricans*-CdS biohybrid without MV^{+2} outperforms the other biohybrids (3790 $\mu mol_{gdcw}{}^{-1}$ of H_2) in the presence of MV^{+2}. In contrast, the *E. coli* complex displays modest activity in the absence of glucose.

The behavior of the S. oneidensis-CdS biohybrid is unusual in that it has a higher photocatalytic activity in the presence of an electron shuttlers like MV^{+2}. S. oneidensis is a well-known electroactive microorganism capable of performing extracellular electron transfer with insoluble electron acceptors/donors directly and indirectly. In direct electron transfer pathway, this bacterium establishes contact via proteins like MtrC and OmcA cytochromes on the cell surface or through cellular appendages such as conductive nanowires. On the other hand, indirect electron

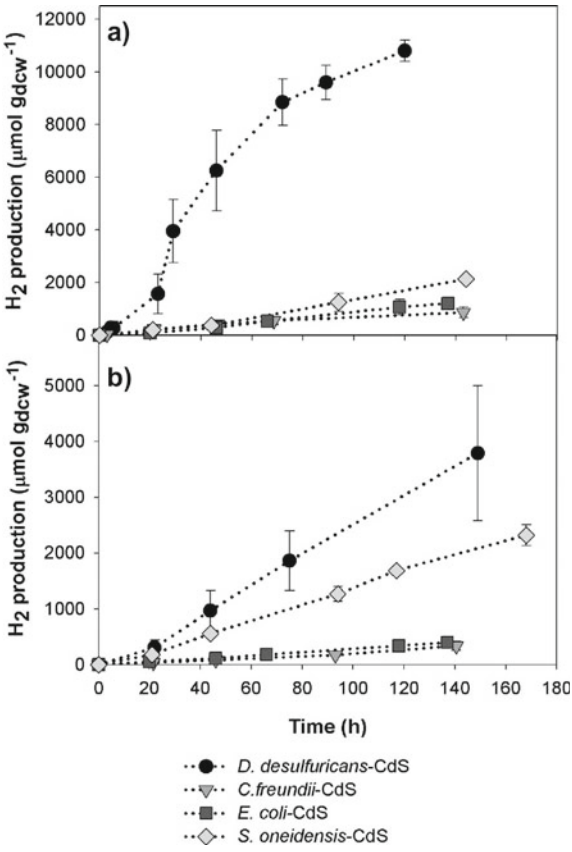

Fig. 65 Hydrogen production of different CdS self-photosensitized cells **a** with adding MV or **b** without MV

transfer occurs through S. oneidensis generated redox active compounds such as flavins. In fact, it has been reported that flavin electron shuttling is responsible for up to 75% of extracellular electron transfer by S. oneidensis. These mechanisms, and in particular flavin electron shuttling pathway, may be responsible for the ability of the S.oneidensis-CdS biohybrid to operate similarly in the presence or absence of MV^{+2}. In contrast, Rowe and colleagues reported that MV^{+2} is required for light driven H_2 production by a photocatalytic system composed by Soneidensis and the chemical photosensitizer eosin Y.

Overall, the most efficient biohybrid system was found to be the one containing *D. desulfuricans.* The fact that the total amounts of CdS present and the crystalline structures in the four systems are comparable, and that the *D. desulfuricans*-CdS biohybrid has a lower band gap than do *C. freundii*-CdS or *S. oneidensis*-CdS suggests that the higher H_2 production rate of the *D. desulfuricans* hybrid is related to a higher biological activity and/or more efficient electron transfer with CdS rather than to intrinsic properties of the nanoparticles produced by this organism.

6 Perspective

Microorganism-based semi-artificial hybrids have attracted much attention for producing renewable hydrogen energy. Although many attempts have been made to increase hydrogen generation in microorganisms, the current levels reached are not sufficient to make hydrogen a commercially competitive energy carrier. Thus, a need exists to uncover ways to improve the hydrogen production capacity of microorganism-based systems. Some thoughts about this matter are given here.

(1) **Charge transfer**. Advances are developed in past decade in the construction of efficient molecular and supramolecular SAPSs. The life times of charge separated states during electron transfer in artificial photosynthesis systems are reflected in their efficiencies. Longer lived charge-separated states have a higher probability to participate in subsequent processes that generated "usable" forms of energy. By viewing the examples described above, an important way is to promote electron-transfer within the system. In addition, efficiencies of energy and electron transfer can be controlled by adjusting the orientation and distance between the donor and acceptor entities, and the interaction between photoactive species and medium. Compared with "one-point" type binding, the "two-point" counterpart can be used to generate more stable supramolecular complexes having donor and acceptor centers located with defined distances and orientations. This may enable the precise control of interaction between donor–acceptor for highly efficient electron transfer.

(2) **Physical Interfaces**. One initial challenge of designing artificial photosynthetic systems is the level of biocompatibility needed for the occurrence of interactions between materials and microorganisms. Semi-artificial hybrid systems require biocompatible surfaces that enable stable combination of electrodes and microbes. Many efforts have shown that integration of microorganism and artificial electrodes can be obtained utilizing two main approaches including material surface modification and nanostructure construction. Inspired by the formation of biofilms on electrodes, it enables the control of physical interfaces. Through the research on the nanostructure of biofilm and the extracellular biopolymer of cells, the deepened understanding of bacteria enables modeling of their behavior in the form of classical colloidal particles. The results lead to the intriguing suggestion that electrophoretic deposition can be employed to positively form the bacterial biofilm to improve the combination.Finally, conducting bio-signaling through controlling functional materials represents highly interesting research directions in this area.

(3) **Cytoprotective Materials**. For improving the activity of cells, encapsulation technique has been used as an alternate approach to improve the chemical-compatibility of microorganisms. Semiconductor-microorganism hybrids usually use the ROS producing materials. Studies have proved the feasibility of encapsulation technique against various harsh conditions, such as heat, UV-light, pH, ROS, osmotic pressure and mechanical pressure. However, protective shells on cells could induce formation of dormant states that have inhibited the cell proliferation as well as metabolic activity. The dynamic shell including self-repairing and reversible functions may solve the question. Among them, the smart materials show the great

potential for encapsulation. For example, applications of materials that undergo autocatalytic proliferation, such as the reported catalytic and autocatalytic proliferating micells, to construct nano hybrids for living cells could be important in the future.

(4) **Stability Improvement**. A need exists to develop stable photosensitizers that have good light-harvesting abilities. Earlier studies have shown that carbon-based materials have promising properties for biological integration due to the stability to light and biocompatibility to organisms. In addition, the sustainabilities of cell-based hybrid system also need to be improved for practical applications. The self-reproduction ability of microorganisms is a phenomenon that might be used advantageously as a method to replace deactivated components in photosynthetic systems. Therefore, innovative approaches are needed like those used in developing inheritable biological materials. For example, it might be possible to produce a photosensitizer protein by stimulating bacteria with light. This would be an effective strategy for retaining photosensitizer loadings by increasing numbers of cells. These approaches could be applied in the semi-artificial photosynthetic biohybrid field to improve the stability of entire systems. With continued development and overlap of the chemical, biological and physical fields, it should soon become possible to devise processes based on sustainable semi-artificial photosynthetic biohybrids that lead to a carbon–neutral society.

(5) **Reaction Source**. Seawater is a potential source for hydrogen production that is needed to meet future demands. However recent techniques developed for seawater desalination or wastewater clarification are high cost and unstable. Therefore, developing general and simple strategies for seawater desalination or wastewater clarification is most desired. Algal organisms have been proposed to be a suitable alternative for these purposes. The integration of algal and materials for seawater desalination or wastewater clarification have the advantage of higher rates of growth, and the ability for cultivation using non-arable land and fresh, brackish or ocean water.

7 Conclusion

We have comprehensively reviewed advanced developments in biological hydrogen production based on artificial hybrid system. Big challenge facing the area of artificial photosynthesis is the improvement of existing fermentation systems so that they can be employed to produce hydrogen. Further research on this topic will focus on improving photosynthesis efficiencies and electron flow, immobilizing microbial cultures, and lowering the cost of bioreactors. Semi-artificial photosynthetic systems contain many interdisciplinary subjects including material science, physics, chemistry, biology, and medical science. Multidisciplinary conclusions from research will contribute to the development of semi-artificial photosynthetic system. With the improvement, the hydrogen produced through semi-artificial photosynthetic system

will exhibit the incomparable advantages in scientific research and economics, especially in seawater hydrogen production. Furthermore, technologies applied in semi-artificial photosynthetic system have the potential to be expended to applications in other fields.

References

1. Allakhverdiev SI (2012) Int J Hydrog Energy 37:8744–8752
2. Armaroli N, Balzani V (2011) Chemsuschem 4:21–36
3. Yi KB, Harrison DP (2005) Ind Eng Chem Res 44:1665–1669
4. Das D, Veziroğlu TN (2001) Int J Hydrog Energy 26:13–28
5. Westermann P, Jørgensen B, Lange L, Ahring BK, Christensen CH (2007) Int J Hydrog Energy 32:4135–4141
6. Dubini A, Ghirardi ML (2015) Photosynth Res 123:241–253
7. Kornienko N, Zhang JZ, Sakimoto KK, Yang P, Reisner E (2018) Nat Nanotechnol 13:890–899
8. Fang X, Kalathil S, Reisner E (2020) Chem Soc Rev 49:4926–4952
9. Chen Y, Li P, Zhou J, Buru CT, Đorđević L, Li P, Zhang X, Cetin MM, Stoddart JF, Stupp SI, Wasielewski MR, Farha OK (2020) J Am Chem Soc 142:1768–1773
10. Plumeré N, Rüdiger O, Oughli AA, Williams R, Vivekananthan J, Pöller S, Schuhmann W, Lubitz W (2014) Nat Chem 6:822–827
11. Li H, Buesen D, Dementin S, Léger C, Fourmond V, Plumeré N (2019) J Am Chem Soc 141:16734–16742
12. Fabian DM, Hu S, Singh N, Houle FA, Hisatomi T, Domen K, Osterloh FE, Ardo S (2015) Energy Environ Sci 8:2825–2850
13. Chen S, Takata T, Domen K (2017) Nat Rev Mater 2:17050
14. Wang Q, Domen K (2020) Chem Rev 120:919–985
15. Hurst JK (2010) Science 328:315–316
16. Su Y, Cestellos-Blanco S, Kim JM, Shen Y-X, Kong Q, Lu D, Liu C, Zhang H, Cao Y, Yang P (2020) Joule 4:800–811
17. Wang Y, Yang H, Zhang X, Han F, Tu W, Yang W (2020) Small Methods 4:1900514
18. Khetkorn W, Khanna N, Incharoensakdi A, Lindblad P (2013) Biofuels 4:535–561
19. Seefeldt LC, Peters JW, Beratan DN, Bothner B, Minteer SD, Raugei S, Hoffman BM (2018) Curr Opin Chem Biol 47:54–59
20. Srirangan K, Pyne ME, Perry Chou C (2011) Bioresour Technol 102:8589–8604
21. Meyer J (2007) Cell Mol Life Sci 64:1063
22. Berggren G, Adamska A, Lambertz C, Simmons TR, Esselborn J, Atta M, Gambarelli S, Mouesca JM, Reijerse E, Lubitz W, Happe T, Artero V, Fontecave M (2013) Nature 499:66–69
23. Chan MK, Kim J, Rees DC (1993) Science 260:792–794
24. Seto B, Mortenson LE (1974) J Bacteriol 120:822–830
25. Vandecasteele J-P, Burris RH (1970) J Bacteriol 101:794–801
26. Parejko RA, Wilson PW (1971) Proc Natl Acad Sci 68:2016–2018
27. Shah VK (1986) Methods in enzymology. Academic Press, vol 118, pp 511–519
28. Wilson TGG, Roberts ER (1954) Biochem Biophys Acta 15:390–394
29. Thorneley RNF, Lowe DJ (1984) Biochem J 224:887–894
30. Burgess BK, Lowe DJ (1996) Chem Rev 96:2983–3012
31. Vignais PM, Billoud B (2007) Chem Rev 107:4206–4272
32. Tamagnini P, Leitão E, Oliveira P, Ferreira D, Pinto F, Harris DJ, Heidorn T, Lindblad P (2007) FEMS Microbiol Rev 31:692–720
33. Tamagnini P, Axelsson R, Lindberg P, Oxelfelt F, Wünschiers R, Lindblad P (2002) Microbiol Mol Biol Rev 66:1–20

34. Thauer RK, Kaster A-K, Goenrich M, Schick M, Hiromoto T, Shima S (2010) Annu Rev Biochem 79:507–536
35. Vignais PM, Billoud B, Meyer J (2001) FEMS Microbiol Rev 25:455–501
36. Frey M (2002) ChemBioChem 3:153–160
37. Ghirardi ML (2015) Photosynth Res 125:383–393
38. Lyon EJ, Shima S, Boecher R, Thauer RK, Grevels F-W, Bill E, Roseboom W, Albracht SPJ (2004) J Am Chem Soc 126:14239–14248
39. Vogt S, Lyon EJ, Shima S, Thauer RK (2008) J Biol Inorg Chem 13:97–106
40. Florin L, Tsokoglou A, Happe T (2001) J Biol Chem 276:6125–6132
41. Wünschiers R, Stangier K, Senger H, Schulz R (2001) Curr Microbiol 42:353–360
42. Happe T, Kaminski A (2002) Eur J Biochem 269:1022–1032
43. Forestier M, King P, Zhang L, Posewitz M, Schwarzer S, Happe T, Ghirardi ML, Seibert M (2003) Eur J Biochem 270:2750–2758
44. Winkler M, Heil B, Heil B, Happe T (2002) Biochimica et Biophysica Acta (BBA)—Gene structure and expression 1576:330–334
45. Happe T, Hemschemeier A, Winkler M, Kaminski A (2002) Trends Plant Sci 7:246–250
46. Meuser JE, D'Adamo S, Jinkerson RE, Mus F, Yang W, Ghirardi ML, Seibert M, Grossman AR, Posewitz MC (2012) Biochem Biophys Res Commun 417:704–709
47. Peters JW, Schut GJ, Boyd ES, Mulder DW, Shepard EM, Broderick JB, King PW, Adams MWW (2015) Biochimica et Biophysica Acta (BBA)—Molecular Cell Research 1853:1350–1369
48. Gaffron H (1937) Biochem Z 292:241–270
49. Melis A, Zhang L, Forestier M, Ghirardi ML, Seibert M (2000) Plant Physiol 122:127–136
50. Wegelius A, Khanna N, Esmieu C, Barone GD, Pinto F, Tamagnini P, Berggren G, Lindblad P (2018) Energy Environ Sci 11:3163–3167
51. Hohmann-Marriott MF, Blankenship RE (2011) Annu Rev Plant Biol 62:515–548
52. Herek JL, Wohlleben W, Cogdell RJ, Zeidler D, Motzkus M (2002) Nature 417:533–535
53. Barber J (2009) Chem Soc Rev 38:185–196
54. Itoh H, Takahashi A, Adachi K, Noji H, Yasuda R, Yoshida M, Kinosita K (2004) Nature 427:465–468
55. Sharkey TD, Bernacchi CJ, Farquhar GD, Singsaas EL (2007) Plant Cell Environ 30:1035–1040
56. Fleming GR, Schlau-Cohen GS, Amarnath K, Zaks J (2012) Faraday Discuss 155:27–41
57. Zhu X-G, Long SP, Ort DR (2010) Annu Rev Plant Biol 61:235–261
58. Mussgnug JH, Thomas-Hall S, Rupprecht J, Foo A, Klassen V, McDowall A, Schenk PM, Kruse O, Hankamer B (2007) Plant Biotechnol J 5:802–814
59. Blankenship RE, Tiede DM, Barber J, Brudvig GW, Fleming G, Ghirardi M, Gunner MR, Junge W, Kramer DM, Melis A, Moore TA, Moser CC, Nocera DG, Nozik AJ, Ort DR, Parson WW, Prince RC, Sayre RT (2011) Science 332:805–809
60. Ma HH, Imran M, Dang Z, Hu Z (2018) Curr Comput-Aided Drug Des 8:182
61. Khaselev O, Turner JA (1998) Science 280:425–427
62. Verlage E, Hu S, Liu R, Jones RJR, Sun K, Xiang C, Lewis NS, Atwater HA (2015) Energy Environ Sci 8:3166–3172
63. Jia J, Seitz LC, Benck JD, Huo Y, Chen Y, Ng JWD, Bilir T, Harris JS, Jaramillo TF (2016) Nat Commun 7:13237
64. Shih CF, Zhang T, Li J, Bai C (2018) Joule 2:1925–1949
65. Sakimoto KK, Kornienko N, Yang P (2017) Acc Chem Res 50:476–481
66. Rosen BA, Salehi-Khojin A, Thorson MR, Zhu W, Whipple DT, Kenis PJA, Masel RI (2011) Science 334:643–644
67. Hall AS, Yoon Y, Wuttig A, Surendranath Y (2015) J Am Chem Soc 137:14834–14837
68. Brown KA, Dayal S, Ai X, Rumbles G, King PW (2010) J Am Chem Soc 132:9672–9680
69. Woolerton TW, Sheard S, Pierce E, Ragsdale SW, Armstrong FA (2011) Energy Environ Sci 4:2393–2399

70. Brown KA, Harris DF, Wilker MB, Rasmussen A, Khadka N, Hamby H, Keable S, Dukovic G, Peters JW, Seefeldt LC, King PW (2016) Science 352:448–450
71. Armstrong FA, Hirst J (2011) Proc Natl Acad Sci 108:14049–14054
72. Harris AW, Cha JN (2020) Molecular Syst Des Eng 5:1088–1097
73. Krasnovsky AA, Nikandrov VV (1987) FEBS Lett 219:93–96
74. Liu C, Gallagher JJ, Sakimoto KK, Nichols EM, Chang CJ, Chang MCY, Yang P (2015) Nano Lett 15:3634–3639
75. Nevin KP, Woodard TL, Franks AE, Summers ZM, Lovley DR (2010) mBio 1:e00103–00110
76. Lu A, Li Y, Jin S, Wang X, Wu X-L, Zeng C, Li Y, Ding H, Hao R, Lv M, Wang C, Tang Y, Dong H (2012) Nat Commun 3:768
77. Sahoo PC, Pant D, Kumar M, Puri SK, Ramakumar SSV (2020) Trends Biotechnol 38:1245–1261
78. Kornienko N, Sakimoto KK, Herlihy DM, Nguyen SC, Alivisatos AP, Harris CB, Schwartzberg A, Yang P (2016) Proc Natl Acad Sci 113:11750–11755
79. Haumann M, Liebisch P, Müller C, Barra M, Grabolle M, Dau H (2005) Science 310:1019–1021
80. Breuer M, Rosso KM, Blumberger J, Butt JN (2015) J R Soc Interf 12:20141117
81. Reguera G, McCarthy KD, Mehta T, Nicoll JS, Tuominen MT, Lovley DR (2005) Nature 435:1098–1101
82. Honda Y, Hagiwara H, Ida S, Ishihara T (2016) Angew Chem Int Ed 55:8045–8048
83. Lovley DR, Nevin KP (2013) Curr Opin Biotechnol 24:385–390
84. Lovley DR (2012) Annu Rev Microbiol 66:391–409
85. Virdis B, Millo D, Donose BC, Lu Y, Batstone DJ, Krömer JO (2016) RSC Adv 6:3650–3660
86. Kracke F, Vassilev I, Krömer JO (2015) Front Microbiol 6
87. Light SH, Su L, Rivera-Lugo R, Cornejo JA, Louie A, Iavarone AT, Ajo-Franklin CM, Portnoy DA (2018) Nature 562:140–144
88. Fukushima T, Gupta S, Rad B, Cornejo JA, Petzold CJ, Chan LJG, Mizrahi RA, Ralston CY, Ajo-Franklin CM (2017) J Am Chem Soc 139:12647–12654
89. Deutzmann JS, Sahin M, Spormann AM (2015) mBio 6:e00496–00415
90. Wang F, Gu Y, O'Brien JP, Yi SM, Yalcin SE, Srikanth V, Shen C, Vu D, Ing NL, Hochbaum AI, Egelman EH, Malvankar NS (2019) Cell 177:361-369.e310
91. Dasgupta NP, Sun J, Liu C, Brittman S, Andrews SC, Lim J, Gao H, Yan R, Yang P (2014) Adv Mater 26:2137–2184
92. Liu C, Colón BC, Ziesack M, Silver PA, Nocera DG (2016) Science 352:1210–1213
93. Liu C, Sakimoto KK, Colón BC, Silver PA, Nocera DG (2017) Proc Natl Acad Sci 114:6450–6455
94. Li H, Opgenorth PH, Wernick DG, Rogers S, Wu T-Y, Higashide W, Malati P, Huo Y-X, Cho KM, Liao JC (2012) Science 335:1596–1596
95. Marshall CW, Ross DE, Fichot EB, Norman RS, May HD (2013) Environ Sci Technol 47:6023–6029
96. Ort DR, Merchant SS, Alric J, Barkan A, Blankenship RE, Bock R, Croce R, Hanson MR, Hibberd JM, Long SP, Moore TA, Moroney J, Niyogi KK, Parry MAJ, Peralta-Yahya PP, Prince RC, Redding KE, Spalding MH, van Wijk KJ, Vermaas WFJ, von Caemmerer S, Weber APM, Yeates TO, Yuan JS, Zhu XG (2015) Proc Natl Acad Sci 112:8529–8536
97. Kibsgaard J, Tsai C, Chan K, Benck JD, Nørskov JK, Abild-Pedersen F, Jaramillo TF (2015) Energy Environ Sci 8:3022–3029
98. Verlinden RAJ, Hill DJ, Kenward MA, Williams CD, Radecka I (2007) J Appl Microbiol 102:1437–1449
99. Grousseau E, Lu J, Gorret N, Guillouet SE, Sinskey AJ (2014) Appl Microbiol Biotechnol 98:4277–4290
100. Yishai O, Lindner SN, Gonzalez de la Cruz J, Tenenboim H, Bar-Even A (2016) Curr Opin Chem Biol 35:1–9
101. Moscoviz R, Toledo-Alarcón J, Trably E, Bernet N (2016) Trends Biotechnol 34:856–865

102. Nevin KP, Hensley SA, Franks AE, Summers ZM, Ou J, Woodard TL, Snoeyenbos-West OL, Lovley DR (2011) Appl Environ Microbiol 77:2882–2886
103. Lambertz C, Leidel N, Havelius KGV, Noth J, Chernev P, Winkler M, Happe T, Haumann M (2011) J Biol Chem 286:40614–40623
104. Sakimoto KK, Zhang SJ, Yang P (2016) Nano Lett 16:5883–5887
105. Hirakawa K, Mori M, Yoshida M, Oikawa S, Kawanishi S (2004) Free Radical Res 38:439–447
106. Mishra M, Arukha AP, Bashir T, Yadav D, Prasad GBKS (2017) Front Microbiol 8
107. Ehling-Schulz M, Scherer S (1999) Eur J Phycol 34:329–338
108. Shchukin DG, Shutava T, Shchukina E, Sukhorukov GB, Lvov YM (2004) Chem Mater 16:3446–3451
109. Yang SH, Ko EH, Choi IS (2012) Langmuir 28:2151–2155
110. Yang SH, Lee K-B, Kong B, Kim J-H, Kim H-S, Choi IS (2009) Angew Chem Int Ed 48:9160–9163
111. Liang K, Richardson JJ, Cui J, Caruso F, Doonan CJ, Falcaro P (2016) Adv Mater 28:7910–7914
112. Park JH, Yang SH, Lee J, Ko EH, Hong D, Choi IS (2014) Adv Mater 26:2001–2010
113. Wei W, Sun P, Li Z, Song K, Su W, Wang B, Liu Y, Zhao J (2018) Sci Adv 4:eaap9253
114. Allan-Wojtas P, Truelstrup Hansen L, Paulson AT (2008) LWT—Food Sci Technol 41:101–108
115. Kim BJ, Park T, Park S-Y, Han SW, Lee H-S, Kim Y-G, Choi IS (2015) Chem—An Asian J 10:2130–2133
116. Cestellos-Blanco S, Zhang H, Yang P (2019) Faraday Discuss 215:54–65
117. Chem Rev 112:673–674 (2012)
118. Liang K, Richardson JJ, Doonan CJ, Mulet X, Ju Y, Cui J, Caruso F, Falcaro P (2017) Angew Chem Int Ed 56:8510–8515
119. Zhan W-W, Kuang Q, Zhou J-Z, Kong X-J, Xie Z-X, Zheng L-S (2013) J Am Chem Soc 135:1926–1933
120. Kornienko N, Zhao Y, Kley CS, Zhu C, Kim D, Lin S, Chang CJ, Yaghi OM, Yang P (2015) J Am Chem Soc 137:14129–14135
121. Ji Z, Zhang H, Liu H, Yaghi OM, Yang P (2018) Proc Natl Acad Sci 115:10582–10587
122. Fontecilla-Camps JC, Volbeda A, Cavazza C, Nicolet Y (2007) Chem Rev 107:4273–4303
123. Vincent KA, Cracknell JA, Clark JR, Ludwig M, Lenz O, Friedrich B, Armstrong FA (2006). Chem Commun. https://doi.org/10.1039/B614272A,5033-5035
124. Hambourger M, Gervaldo M, Svedruzic D, King PW, Gust D, Ghirardi M, Moore AL, Moore TA (2008) J Am Chem Soc 130:2015–2022
125. Armstrong FA, Belsey NA, Cracknell JA, Goldet G, Parkin A, Reisner E, Vincent KA, Wait AF (2009) Chem Soc Rev 38:36–51
126. Alonso-Lomillo MA, Rüdiger O, Maroto-Valiente A, Velez M, Rodríguez-Ramos I, Muñoz FJ, Fernández VM, De Lacey AL (2007) Nano Lett 7:1603–1608
127. Svedruzic D, Blackburn JL, Tenent RC, Rocha J-DR, Vinzant TB, Heben MJ, King PW (2011) J Am Chem Soc 133:4299–4306
128. Batzill M (2011) Energy Environ Sci 4:3275–3286
129. Reisner E, Fontecilla-Camps JC, Armstrong FA (2009). Chem Commun. https://doi.org/10.1039/B817371K,550-552
130. Polliotto V, Morra S, Livraghi S, Valetti F, Gilardi G, Giamello E (2016) Int J Hydrog Energy 41:10547–10556
131. Greene BL, Joseph CA, Maroney MJ, Dyer RB (2012) J Am Chem Soc 134:11108–11111
132. Li XB, Tung CH, Wu LZ (2019) Angew Chem 131:10918–10925
133. Hou W, Cronin SB (2013) Adv Func Mater 23:1612–1619
134. Baker SN, Baker GA (2010) Angew Chem Int Ed 49:6726–6744
135. Hola K, Zhang Y, Wang Y, Giannelis EP, Zboril R, Rogach AL (2014) Nano Today 9:590–603
136. Wei W, Xu C, Wu L, Wang J, Ren J, Qu X (2014) Sci Rep 4:1–7
137. Ding H, Wei JS, Zhang P, Zhou ZY, Gao QY, Xiong HM (2018) Small 14:1800612
138. Yeh TF, Teng CY, Chen SJ, Teng H (2014) Adv Mater 26:3297–3303

139. Yang P, Zhao J, Wang J, Cui H, Li L, Zhu Z (2015) ChemPhysChem 16:3058–3063
140. Martindale BC, Hutton GA, Caputo CA, Reisner E (2015) J Am Chem Soc 137:6018–6025
141. Bhattacharyya S, Ehrat F, Urban P, Teves R, Wyrwich R, Döblinger M, Feldmann J, Urban AS, Stolarczyk JK (2017) Nat Commun 8:1–9
142. Martindale BC, Hutton GA, Caputo CA, Prantl S, Godin R, Durrant JR, Reisner E (2017) Angew Chem 129:6559–6563
143. Xu X, Tang W, Zhou Y, Bao Z, Su Y, Hu J, Zeng H (2017) Adv Sci 4:1700273
144. Yan Y, Chen J, Li N, Tian J, Li K, Jiang J, Liu J, Tian Q, Chen P (2018) ACS Nano 12:3523–3532
145. Land H, Senger M, Berggren G, Stripp ST (2020) ACS Catal 10:7069–7086
146. Lubitz W, Ogata H, Rudiger O, Reijerse E (2014) Chem Rev 114:4081–4148
147. Esmieu C, Raleiras P, Berggren G (2018) Sustain Energy Fuels 2:724–750
148. Hutton GA, Martindale BC, Reisner E (2017) Chem Soc Rev 46:6111–6123
149. Schilter D, Camara JM, Huynh MT, Hammes-Schiffer S, Rauchfuss TB (2016) Chem Rev 116:8693–8749
150. Winkler M, Senger M, Duan J, Esselborn J, Wittkamp F, Hofmann E, Apfel U-P, Stripp ST, Happe T (2017) Nat Commun 8:1–7
151. Silakov A, Wenk B, Reijerse E, Lubitz W (2009) Phys Chem Chem Phys 11:6592–6599
152. Morra S, Giraudo A, Di Nardo G, King PW, Gilardi G, Valetti F (2012) PLoS ONE 7:e48400
153. Holá KI, Pavliuk MV, Németh B, Huang P, Zdražil Ls, Land H, Berggren G, Tian H (2020) ACS Catalysis 10:9943–9952
154. Khetkorn W, Rastogi RP, Incharoensakdi A, Lindblad P, Madamwar D, Pandey A, Larroche C (2017) Biores Technol 243:1194–1206
155. Xu P, McCool NS, Mallouk TE (2017) Nano Today 14:42–58
156. Edwardes Moore E, Andrei V, Zacarias S, Pereira IA, Reisner E (2019) ACS Energy Lett 5:232–237
157. Han YY, Lu XL, Tang SF, Yin XP, Wei ZW, Lu TB (2018) Adv Energy Mater 8:1702992
158. Geim AK, Novoselov KS (2010) Nanoscience and technology: a collection of reviews from nature journals. World Scientific, pp 11–19
159. Wang Y, Ding X, Wang F, Li J, Song S, Zhang H (2016) Chem Sci 7:4284–4290
160. Yong YC, Yu YY, Zhang X, Song H (2014) Angew Chem Int Ed 53:4480–4483
161. Ruiz ON, Fernando KS, Wang B, Brown NA, Luo PG, McNamara ND, Vangsness M, Sun Y-P, Bunker CE (2011) ACS Nano 5:8100–8107
162. Hou J, Cheng H, Takeda O, Zhu H (2015) Angew Chem Int Ed 54:8480–8484
163. Kim C, Cho KM, Al-Saggaf A, Gereige I, Jung H-T (2018) ACS Catal 8:4170–4177
164. Wei T, Zhu Y-N, An X, Liu L-M, Cao X, Liu H, Qu J (2019) ACS Catal 9:8346–8354
165. Shen H, Wang Y-Z, Liu G, Li L, Xia R, Luo B, Wang J, Suo D, Shi W, Yong Y-C (2020) ACS Catal 10:13290–13295
166. Hartshorne RS, Reardon CL, Ross D, Nuester J, Clarke TA, Gates AJ, Mills PC, Fredrickson JK, Zachara JM, Shi L (2009) Proc Natl Acad Sci 106:22169–22174
167. Clarke TA, Edwards MJ, Gates AJ, Hall A, White GF, Bradley J, Reardon CL, Shi L, Beliaev AS, Marshall MJ (2011) Proc Natl Acad Sci 108:9384–9389
168. Shi L, Dong H, Reguera G, Beyenal H, Lu A, Liu J, Yu H-Q, Fredrickson JK (2016) Nat Rev Microbiol 14:651–662
169. Cao B, Zhao Z, Peng L, Shiu H-Y, Ding M, Song F, Guan X, Lee CK, Huang J, Zhu D (2021) Science 373:1336–1340
170. Meshulam-Simon G, Behrens S, Choo AD, Spormann AM (2007) Appl Environ Microbiol 73:1153–1165
171. Luo B, Wang YZ, Li D, Shen H, Xu LX, Fang Z, Xia Z, Ren J, Shi W, Yong YC (2021) Adv Energy Mater 11:2100256
172. Lee J-H, Kim M-G, Yoo B, Myung NV, Maeng J, Lee T, Dohnalkova AC, Fredrickson JK, Sadowsky MJ, Hur H-G (2007) Proc Natl Acad Sci 104:20410–20415
173. Tian L-J, Li W-W, Zhu T-T, Chen J-J, Wang W-K, An P-F, Zhang L, Dong J-C, Guan Y, Liu D-F (2017) J Am Chem Soc 139:12149–12152

174. Han H-X, Tian L-J, Liu D-F, Yu H-Q, Sheng G-P, Xiong Y (2022) J Am Chem Soc 144:6434–6441
175. Zhang H, Liu H, Tian Z, Lu D, Yu Y, Cestellos-Blanco S, Sakimoto KK, Yang P (2018) Nat Nanotechnol 13:900–905
176. Honda Y, Hagiwara H, Ida S, Ishihara T (2016) Angew Chem 128:8177–8180
177. Miller SI, Salama NR (2018) PLoS Biol 16:e2004935
178. Wang B, Zeng C, Chu KH, Wu D, Yip HY, Ye L, Wong PK (2017) Adv Energy Mater 7:1700611
179. Ramprakash B, Incharoensakdi A (2020) Biores Technol 318:124057
180. Cui S, Tian L-J, Li J, Wang X-M, Liu H-Q, Fu X-Z, He R-L, Lam PK, Huang T-Y, Li W-W (2022) Chem Eng J 428:131254
181. Chen H, Guo Y, Zhang Z, Mao W, Shen C, Xiong W, Yao Y, Zhao X, Hu Y, Zou Z (2021) Nano Lett 22:229–237
182. Xiong W, Zhao X, Zhu G, Shao C, Li Y, Ma W, Xu X, Tang R (2015) Angew Chem 127:12129–12133
183. Yao S, Jin B, Liu Z, Shao C, Zhao R, Wang X, Tang R (2017) Adv Mater 29:1605903
184. Youn W, Ko EH, Kim MH, Park M, Hong D, Seisenbaeva GA, Kessler VG, Choi IS (2017) Angew Chem Int Ed 56:10702–10706
185. Li W, Liu Z, Liu C, Guan Y, Ren J, Qu X (2017) Angew Chem Int Ed 56:13661–13665
186. Niu J, Lunn DJ, Pusuluri A, Yoo JI, O'Malley MA, Mitragotri S, Soh HT, Hawker CJ (2017) Nat Chem 9:537–545
187. Song RB, Wu Y, Lin ZQ, Xie J, Tan CH, Loo JSC, Cao B, Zhang JR, Zhu JJ, Zhang Q (2017) Angew Chem 129:10652–10656
188. Su D, Liu X, Liu L, Wang L, Xie H, Zhang H, Meng X, Huang X (2018) Adv Func Mater 28:1705699
189. Liang K, Richardson JJ, Doonan CJ, Mulet X, Ju Y, Cui J, Caruso F, Falcaro P (2017) Angew Chem 129:8630–8635
190. Geng W, Wang L, Jiang N, Cao J, Xiao Y-X, Wei H, Yetisen AK, Yang X-Y, Su B-L (2018) Nanoscale 10:3112–3129
191. Jiang N, Yang X-Y, Ying G-L, Shen L, Liu J, Geng W, Dai L-J, Liu S-Y, Cao J, Tian G, Sun T-L, Li S-P, Su B-L (2015) Chem Sci 6:486–491
192. Kim BJ, Cho H, Park JH, Mano JF, Choi IS (2018) Adv Mater 30:1706063
193. Su D, Qi J, Liu X, Wang L, Zhang H, Xie H, Huang X (2019) Angew Chem 131:4032–4035
194. Xu Z, Wang S, Zhao C, Li S, Liu X, Wang L, Li M, Huang X, Mann S (2020) Nat Commun 11:1–10
195. Posewitz MC, Smolinski SL, Kanakagiri S, Melis A, Seibert M, Ghirardi ML (2004) Plant Cell 16:2151–2163
196. Happe T, Naber JD (1993) Eur J Biochem 214:475–481
197. Chen J, Li J, Li Q, Wang S, Wang L, Liu H, Fan C (2020) Energy Environ Sci 13:2064–2068
198. Volgusheva A, Styring S, Mamedov F (2013) Proc Natl Acad Sci 110:7223–7228
199. Fakhimi N, Dubini A, Tavakoli O, González-Ballester D (2019) Biores Technol 289:121648
200. Ban S, Lin W, Wu F, Luo J (2018) Biores Technol 251:350–357
201. Ma W, Chen M, Wang L, Wei L, Wang Q (2011) Biores Technol 102:8635–8638
202. Scoma A, Durante L, Bertin L, Fava F (2014) New Phytol 204:890–900
203. Hemschemeier A, Fouchard S, Cournac L, Peltier G, Happe T (2008) Planta 227:397–407
204. Pinto T, Malcata F, Arrabaça J, Silva J, Spreitzer R, Esquível M (2013) Appl Microbiol Biotechnol 97:5635–5643
205. Kosourov S, Jokel M, Aro E-M, Allahverdiyeva Y (2018) Energy Environ Sci 11:1431–1436
206. Yanagida S, Kabumoto A, Mizumoto K, Pac C, Yoshino K (1985) J Chem Soc, Chem Commun 474–475
207. Swager TM (1998) Acc Chem Res 31:201–207
208. Yong W-W, Lu H, Li H, Wang S, Zhang M-T (2018) ACS Appl Mater Interf 10:10828–10834
209. Yuan H, Zhan Y, Rowan AE, Xing C, Kouwer PH (2020) Angew Chem Int Ed 59:2720–2724
210. Gai P, Yu W, Zhao H, Qi R, Li F, Liu L, Lv F, Wang S (2020) Angew Chem Int Ed 59:7224–7229

211. Lin J-Y, Liu B, Yu M-N, Ou C-J, Lei Z-F, Liu F, Wang X-H, Xie L-H, Zhu W-S, Ling H-F (2017) J Mater Chem C 5:6762–6770
212. Wang Z, Gao D, Geng H, Xing C (2021) J Mater Chem A 9:19788–19795
213. Cestellos-Blanco S, Zhang H, Kim JM, Shen Y-X, Yang P (2020) Nat Catal 3:245–255
214. Honda Y, Watanabe M, Hagiwara H, Ida S, Ishihara T (2017) Appl Catal B 210:400–406
215. Ramprakash B, Incharoensakdi A (2020) Int J Hydrog Energy 45:6254–6261
216. Martins M, Toste C, Pereira IA (2021) Angew Chem Int Ed 60:9055–9062